



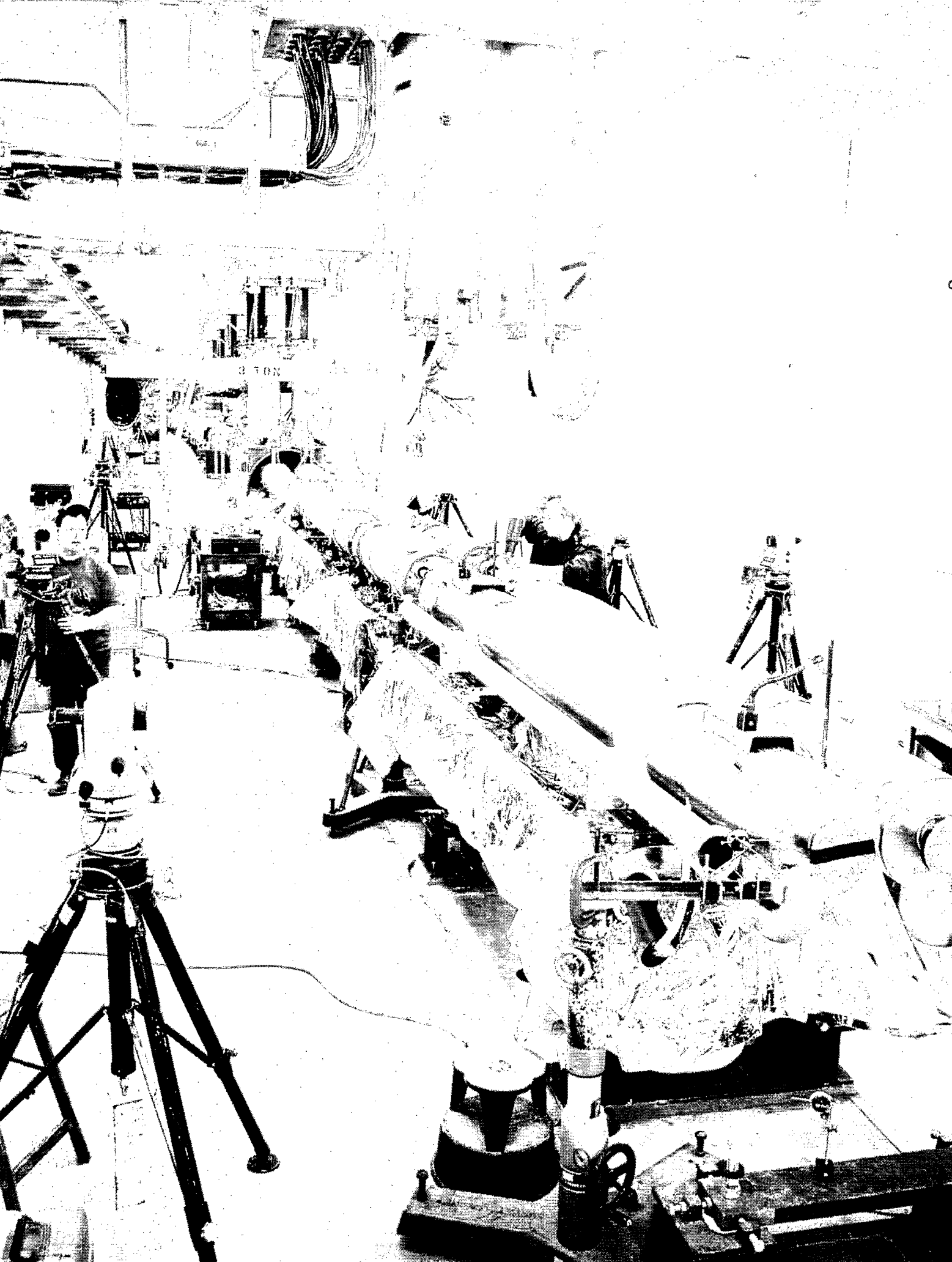
# *RHIC Summer Study '96:*

*Theory Commission on*

## *Relativistic Heavy Ion Collisions*

*July 8-19, 1996 at Brookhaven National Laboratory*

*Edited by D.L. Kanana and Y. Pang*



# RHIC '96

Proceedings of the First Summer Study on the Physics of  
Ultrarelativistic Nucleus-Nucleus Collisions at RHIC.

Brookhaven National Laboratory, Upton, NY 11973, USA

July 8-19, 1996

Edited by

David E. Kahana and Yang Pang

OFFICIAL FILE COPY

**BROOKHAVEN NATIONAL LABORATORY**  
**ASSOCIATED UNIVERSITIES, INC.**  
**UPTON, LONG ISLAND, NEW YORK 11973**

UNDER CONTRACT NO. DE-AC02-76CH00016 WITH THE

**UNITED STATES DEPARTMENT OF ENERGY**

#### DISCLAIMER

This report was prepared as an account of work sponsored by an agency of the United States Government. Neither the United States Government nor any agency thereof, nor any of their employees, nor any of their contractors, subcontractors, or their employees, makes any warranty, express or implied, or assumes any legal liability or responsibility for the accuracy, completeness, or usefulness of any information, apparatus, product, or process disclosed, or represents that its use would not infringe privately owned rights. Reference herein to any specific commercial product, process, or service by trade name, trademark, manufacturer, or otherwise, does not necessarily constitute or imply its endorsement, recommendation, or favoring by the United States Government or any agency, contractor or subcontractor thereof. The views and opinions of authors expressed herein do not necessarily state or reflect those of the United States Government or any agency, contractor or subcontractor thereof.

Printed in the United States of America  
Available from  
National Technical Information Service  
U.S. Department of Commerce  
5285 Port Royal Road  
Springfield, VA 22161

NTIS price codes:  
Printed Copy: A19; Microfiche Copy: A01

## Preface

This RHIC Theory Summer Study was held at Brookhaven National Laboratory, July 8-19, 1996. Considering its apparent success and broad attendance, one can only hope this meeting is just the first in a long series. The ostensible reason for the Study was to define and sharpen the scientific focus of the physics at RHIC. An unstated purpose was to bring together leading figures in disparate disciplines and have them forge their thoughts and ideas into a coherent whole. It is not the first time workers in hard QCD, lattice thermodynamics and the phenomenology of heavy-ion collisions have co-attended meetings, but perhaps the open format and the background presence of an accelerator actually devoted to this physics might have been expected to catalyse closer interplay of these fields.

As one summary speaker stated, the heart of the subject is phenomenology. RHIC concerns itself with producing and detecting signs of high particle and high energy density in an ultra relativistic nucleus-nucleus collision. This involves both perturbative and non-perturbative aspects of the strong interactions and necessarily can not be addressed solely by pristine theoretical algorithms. One must also borrow from and extend the techniques of the past couple of decades directed at diffraction and production in hadron-hadron collisions. The many contributions presented in this Proceedings speak eloquently to this need.

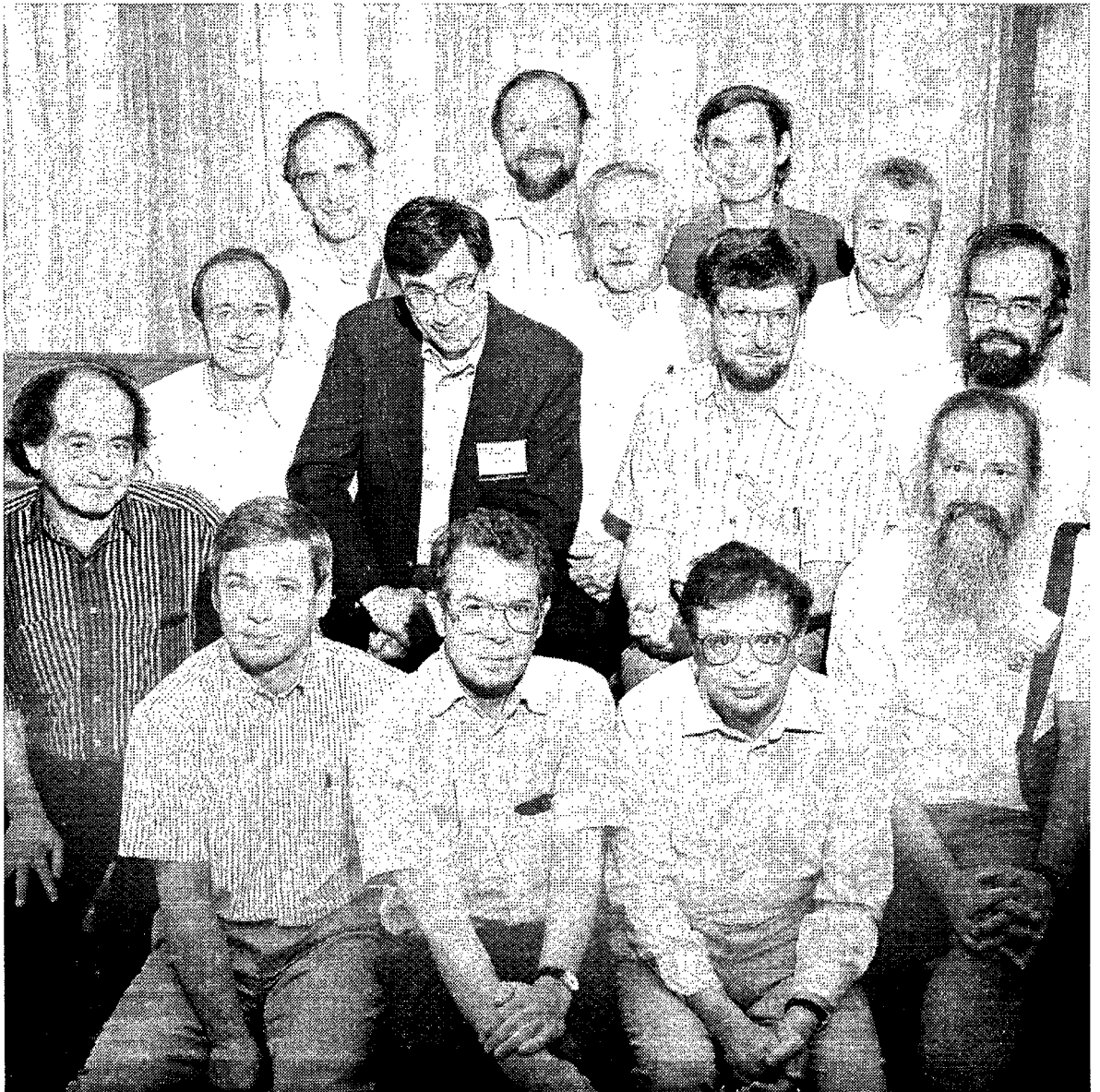
RHIC '96 was divided into four sections, each devoted to a single theoretical topic. The Proceedings reflects this. An additional section, housing presentations by experimentalists describing the RHIC detectors as well as new results at CERN, FNAL and the AGS, was added. The list of participants and the Table of Contents remind us of those speakers whose contributions, unfortunately, are absent. The entire day by day Agenda was viewed as too long and complicated to include. Nor is there any memory of the numerous parallel working sessions, except perhaps in forthcoming research.

Many peoples efforts went into making RHIC '96 possible. T. D. Lee and Tom Kirk provided the original impetus. The convenors and organisers were instrumental in defining the scope of the workshop and in selecting its attendees. The speakers themselves, in practice almost all invitees, were a most important ingredient. Special thanks are due Doris Rueger, Bonnie Sherwood, Pat Tuttle, Liz Mogavero and Mary Campbell for seeing that the workshop operated smoothly and pleasantly. Pat Yalden, in the Laboratory's Graphic Arts division, collaborated beautifully with the artist, Elinor Kahana, to produce the cover to this volume and the Workshop Poster.

I, personally, would like to thank all of the above, and my co-chairman Tom Ludlam, for their excellent cooperation.

October, 1996

Sidney Kahana



**RHIC Summer Study'96**  
**July 8-19**  
**Brookhaven National Laboratory**

**Organizers**

S. H. Kahana, Co-Chair  
T. Ludlam, Co-Chair  
V. Emery  
K. Kinder-Geiger  
M. J. Tannenbaum  
T. L. Trueman  
F. Videbaek

**Convenors**

W. Busza, <i>MIT</i>	A. H. Mueller, <i>Columbia</i>
N. Christ, <i>Columbia</i>	Y. Pang, <i>Columbia / BNL</i>
M. Creutz, <i>BNL</i>	R. Pisarski, <i>BNL</i>
M. Gyulassy, <i>Columbia</i>	J. Randrup, <i>LBL</i>
J. Harris, <i>LBL</i>	E. Shuryak, <i>Stony Brook</i>
J. Kapusta, <i>Minnesota</i>	W. Zajc, <i>Columbia</i>

# CONTENTS

Preface . . . . .	iii
Organizers and Conveners . . . . .	v

## INVITED TALKS

### Opening Talk

*To Know the Smallest We Need the Largest*

T. D. Lee xiii

### I. Thermodynamics

*Overall Position of Lattice QCD*

A. Ukawa

*The Equation of State for QCD from the Lattice*

T. Blum 3

*Continuum Limit in Lattice QCD*

S. Ohta 11

*Lattice QCD with 0, 2 and 4 Quark Flavors*

Mawhinney 17

*Improved QCD Thermodynamics*

F. Karsch 29

*Improved Lagrangians for Lattice QCD*

K. Wiese

*Hydrodynamics and Collective Behaviour in Relativistic Nuclear Collisions*

D. H. Rischke 41

*Wilson Fermions at Finite Temperature*

M. Creutz 49

*Tensor Charge of the Nucleon on the Lattice*

T. Hatsuda 55

*The Critical Points of Lattice QCD with a Non-Zero Quark Density*

M.-P. Lombardo 61

*Hadronic Ratios and the Number of Projectile Participants*

A. Muronga 67

### II. Hard Probes

*Medium-induced QCD*

Yu. L. Dokshitzer 75



<i>PQCD Analysis of Hard Scattering in Nuclei</i>	85
G. Sterman	
<i>Self-Screened Parton Cascades</i>	91
B. Müller	
<i>Minijets in Ultrarelativistic Heavy Ion Collisions at RHIC and LHC</i>	99
K. J. Eskola	
<i>Theoretical Overview of Potential of Nuclear Beams in HERA and Interface with Heavy Ion Physics</i>	111
M. Strikman	
<i>Study Parton Energy Loss in High-energy Heavy-ion Collisions</i>	123
X.-N. Wang	
<i>Gluon Density in Nuclei</i>	137
E. M. Levin	
<i>Review of <math>J/\psi</math> Production Data at Fixed-Target Energies</i>	147
R. Vogt	
<b>III. Phenomenology</b>	
<i>Non-Equilibrium QCD of High-Energy Multi-Gluon Dynamics</i>	157
K. Kinder-Geiger	
<i>Simulation of Heavy Ion Collisions at <math>\sqrt{S} = 20 - 200</math> GeV</i>	175
D. Kahana	
<i>General Cascade Program</i>	193
Y. Pang	
<i>A Realistic Model for Nuclear Collisions at RHIC</i>	203
K. Werner	
<i>Signatures of Dense Hadronic Matter in Ultrarelativistic Heavy Ion Reactions</i>	211
H. Stoecker	
<i>Equation of State in Relativistic Heavy Ion Simulation with RQMD</i>	
H. Sorge	
<i>Charm Production at RHIC</i>	221
R. Vogt	
<i>Percolation Approach and <math>J/\psi</math> Suppression in the String Fusion Model</i>	229
E. G. Ferreira	
<i>Charmonium Suppression in Nuclear Collisions</i>	235
S. Gavin	
<b>IV. Chiral Symmetry</b>	
<i>Overall View of Chiral Symmetry in Relativistic Heavy Ion Collisions</i>	
V. Rajagopal	
<i>Formation of DCCs with Linear Sigma Model</i>	247
J. Randrup	
<i>“Baked Alaska” in Relativistic Heavy Ion Collisions: Formation of Disoriented Chiral Condensate</i>	257
M. Asakawa	

<i>Disoriented Chiral Condensate</i>	
S. Gavin	
<i>Light Vector Mesons at Finite Baryon Density</i>	263
T. Hatsuda	
<i>On the Physics of a Cool Pion Gas</i>	273
M. Tytgat	
<i>New Mesons in the Chirally Symmetric Plasma</i>	279
H. A. Weldon	
<i>Dileptons from Heavy Ion Collisions and Chiral Symmetry</i>	
I. Zahed	
<i>Consequences of Partial <math>U_A(1)</math> Restoration</i>	287
X. N. Wang	
<b>V. Experiments and Detectors</b>	
<i>Recent Results from CERN-SPS</i>	
B. Jacak	
<i>Interesting Aspects of the STAR Detector and Physics Program</i>	299
T. J. Hallman	
<i>DCC Experiments at CERN</i>	
B. Wyslouch	
<i>Some Recent Results in Au+Au Collisions at AGS</i>	309
Z. Chen	
<i>The BRAHMS Experiment at RHIC</i>	321
F. Videbæk	
<i>The PHOBOS Detector at RHIC</i>	
W. Busza	
<i>Early Results from Minimax: A Disoriented Chiral Condensate Search at the Tevatron</i>	329
C. C. Taylor	
<i>Proton Stopping at AGS and CERN</i>	
J. Harris	
<i>Spin Physics at RHIC</i>	335
M. J. Tannenbaum	
<i>The PHENIX Detector at RHIC</i>	351
W. Zajc	
<b>VI. Summary</b>	
<i>The Phases of QCD</i>	369
E. Shuryak	
<i>Status of Lattice QCD</i>	
N. H. Christ	
<i>Hard Processes at RHIC</i>	385
A. H. Mueller	

*Overall View of Phenomenology*

M. Gyulassy

*Summary Talk on Chiral Symmetry and Disoriented Chiral Condensates*

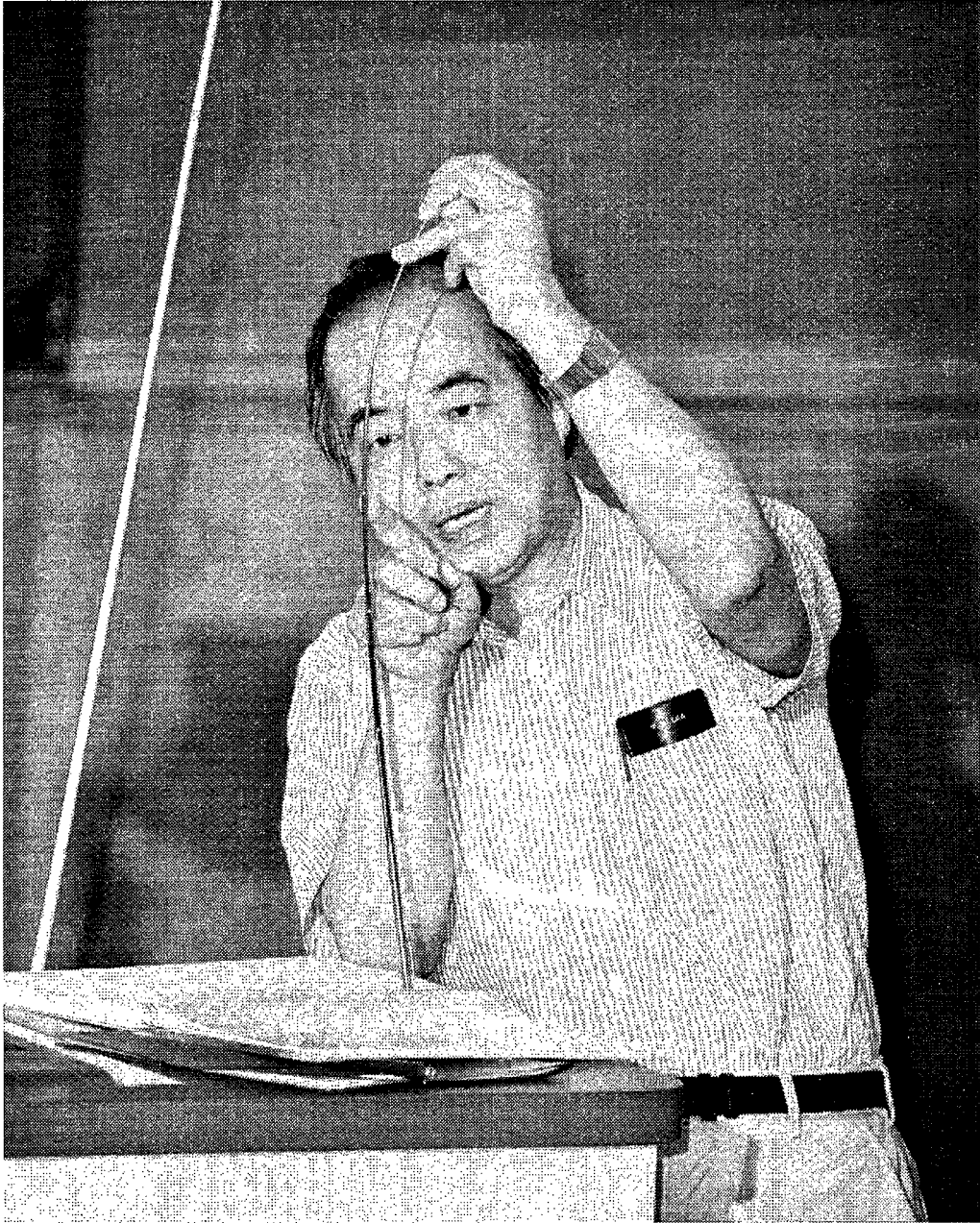
R. D. Pisarski

391

List of Participants

399

**OPENING  
TALK**



# To Know the Smallest We Need the Largest

T. D. Lee  
Columbia University, New York, NY 10027

## I. INTRODUCTION

Below is a list of some of the milestones in physics since 1870:

	<u>Nineteenth Century</u>	<u>Twentieth Century</u>
'70	Maxwell Equation	
'72	Boltzmann Equation	
'73		Asymptotic Freedom (QCD)
'74		c Quark
'75		$\tau$
'77		b Quark
'79		Gluon
'83		W, Z
'87	Hertz: Electromagnetic Wave Photoelectric Effect Michelson-Morley Experiment	
'94		t Quark
'95	Roentgen X-ray	
'96	Becquerel Radioactivity	
'97	Thomson Electron	
'99	Rutherford $\alpha$ and $\beta$ rays	
'00	Planck Formula	

Of these the discovery of the electron by Thomson in 1897 set the direction of the field "particle physics".

This leads to the theme of my talk:

**From 1897 - Present:**

*To comprehend the largest,  
we need only understand the smallest.*

**From Present - 21<sup>st</sup> Century:**

*To know the smallest,  
we need also the largest.*

One of the reasons for the change is the evolution from simple systems consisting of a few elementary particles to their merging with a complex condensate—the physical vacuum.

Let us start with one of the puzzles in modern physics: the discrepancy between symmetry and asymmetry.

## II. WHY DO WE BELIEVE IN SYMMETRY?

### ***THEORY (1996)***

QCD (strong interaction)

SU(2) X U(1) Theory (electro-weak)

General Relativity (gravitation)

---

All these theories are based on symmetry,  
but most symmetry quantum numbers are  
not conserved!

*So, why do we believe in symmetry?*

Perhaps the reason is

*Maximum Asymmetrical Possibilities = Perfect Symmetry.*

I wish to illustrate this seeming paradox by the example of the buckling of an elastic beam.

When one applies a force  $F$  to a beam, the deformation is uniform over the length of the beam if  $F$  is small. However, the beam buckles when  $F$  is larger than a critical value. This problem was solved by Euler, as shown in Figure 1(a). What I would like to call attention to is the relation between the possible buckling directions and the shape of the cross section of the beam, as illustrated in Figure 1(b).

If the cross section of the beam is a circle, then the buckling can be along any direction perpendicular to the beam. There are three important conclusions that can be drawn for such a perfect symmetrical initial state:

1) A circular cross section gives maximum (infinite) possibilities of asymmetrical buckling directions.

2) Because these different asymmetrical buckling possibilities stem from perfect circular symmetry, they are connected through rotation.

3) If we rotate very slowly from any one of these asymmetrical bucklings to another there is no energy cost. Consequently, this gives rise to a zero-energy excitation (analog of the *Goldstone-Nambu boson*).

Point 1) gives a clear illustration of the theme that perfect symmetry can generate the maximal asymmetrical possibilities. In that case, point 2) emphasizes that the complexity



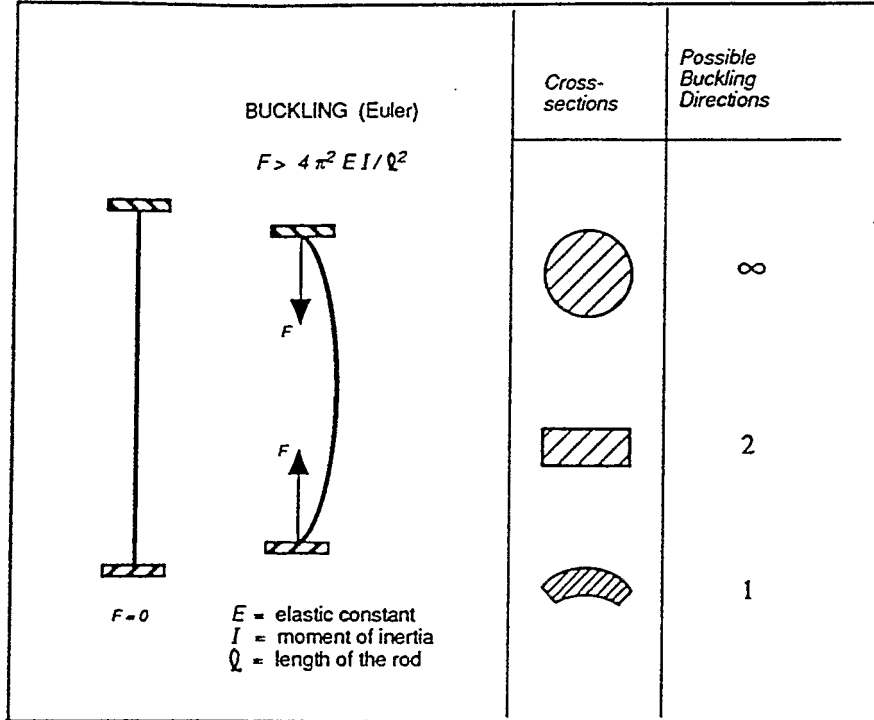


Figure 1(a)

Figure 1(b)

FIG. 1.

of all these asymmetries can be unified into a single mechanism based on perfect symmetry. Furthermore, if one is confronted with any one of these asymmetrical configurations, the underlying perfect symmetry can be verified by observing the zero-energy Goldstone-Nambu excitation.

The buckling problem illustrates how to reconcile symmetry in principle with asymmetry in manifestation. It is also an example of the *spontaneous symmetry breaking* mechanism, which relates the asymmetrical phenomena to an origin that is perfectly symmetrical, and forms the basis of the Standard  $SU(2) \times U(1)$  Model. As in the buckling example, the symmetry in physical law can generate a large variety (maximal) of asymmetries; furthermore, these asymmetrical configurations are in turn connected through the symmetry, and thereby result in the zero-mass Goldstone-Nambu boson excitation, which can be verified experimentally. However, in order to apply the spontaneous symmetry breaking mechanism to the microscopic system of elementary particles, one has to assume that the physical vacuum is not symmetric.

What is the physical vacuum? Our present view is that it has the following properties:

- 1) a state without matter,
- 2) but with energy fluctuations (virtual matter) because of interactions,
- 3) Lorentz invariant,
- 4) therefore not aether,
- 5) a complex condensate that can violate symmetry,

6) like superconductors, can undergo phase transitions.

Also, as we will discuss, it may violate  $T$  (time reversal) and  $CP$  (charge conjugation  $\times$  parity).

Even though there is no “matter” in the physical vacuum, because of the uncertainty principle the presence of interactions necessitates energy fluctuations in the vacuum, which makes it a complex system. The Lorentz invariance implies that the vacuum transforms like a scalar or pseudoscalar field; like such fields it can have complicated structures. The Relativistic Heavy Ion Collider (RHIC) at Brookhaven National Laboratory will be an effective tool to study the complex structure of the QCD vacuum, as illustrated in Figure 2 (together with some of the questions).

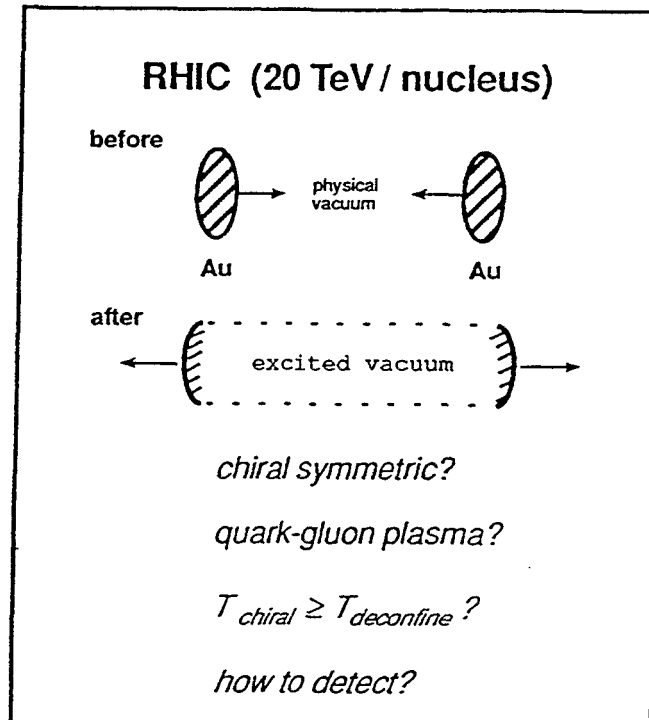


FIG. 2.

Our subsequent analysis will be divided into three parts:

- Phenomenological Models?
- How good is QCD?
- New Approaches?

### III. PHENOMENOLOGICAL MODELS

#### A. Problems

Table I gives a few of the worries concerning most of the phenomenological models.

PHENOMENOLOGICAL RESONANCE CALCULATION
<ul style="list-style-type: none"> <li>• Take the ARC model for <math>Si + Au</math> at AGS (14.6 GeV/c/nucleon). For detailed <math>\pi</math> production, there is an 8-10% difference between C.M. and Lab. system.</li> <li>• At RHIC energy, the corresponding difference may become 50-100%.</li> <li>• At AGS, thermalization could be a reasonable zeroth-order approximation.</li> <li>• At RHIC energy, the equilibrium concept is hardly applicable.</li> </ul>

TABLE I.

As a concrete example, we examine the cascade (ARC) model developed by Kahana, Pang and Schlagel [1] give by Table II.


Cascade (ARC)	
1. Initial condition	
$W_n(\vec{x}, t, \vec{p}) = \sum_i \delta^3(\vec{x} - \vec{x}_i(t)) \delta^3(\vec{p} - \vec{p}_i)$	
2. Straight line trajectories	$\vec{v}_i = \frac{\vec{p}_i}{E_i}$ $\vec{x}_i(t) = \vec{x}_i(0) + \vec{v}_i t$
3. Collision at closest approach	$d \leq \sqrt{\frac{\sigma_{total}}{\pi}}$
4. Outgoing channel selection	partial cross-sections: elastic, inelastic (productions of pion, strange, ...)
5. Momentum distribution	$\int d(\text{phase - space})  A ^2$
Repeat steps 2-5	
Y. Pang, T. J. Schlagel, S. H. Kahana	

TABLE II.

Step 3 involves a nonzero  $d$ , which makes the model violate Lorentz invariance. For applications to RHIC physics, this would be a serious problem and must be corrected.

## B. Lorentz Invariant Models

A particularly attractive approach has been developed by Y. Pang [2], based on Feynman's parton model and the relativistic Boltzmann equation. Table III summarizes Pang's method: As the parameter  $\lambda \rightarrow \infty$ , the number of partons also becomes infinite, and the cascade model becomes the relativistic Boltzmann Equation (Table IV)

<p><u>Lorentz invariance</u></p> <p><math>W(x, t, p) =</math> Boltzmann probability function  <math>= \sum_1^N \delta^3(x - x_i(t)) \delta^3(p - p_i)</math></p> <p>Decompose each particle into a large number  <math>\lambda</math> of partons  <math>N \rightarrow \lambda N \quad W \rightarrow \lambda W \quad \text{with } \lambda \rightarrow \infty</math></p> <p>Cross-section <math>\sigma \rightarrow \sigma/\lambda</math>, so that  mean free path <math>\sim W\sigma</math> fixed  collision distance <math>d = \sqrt{\sigma/\pi} \rightarrow 1/\sqrt{\lambda} \rightarrow 0</math>  <math>\therefore</math> Cascade Model <math>\rightarrow</math> Relativistic Boltzmann  Equation</p> <p><i>Y. Pang</i></p>
--

TABLE III.

<p><u>Relativistic Boltzmann Equation</u></p> $p^\mu \partial_\mu \mathcal{W}_a(\bar{x}, t, \bar{p}) = \sum_n \sum_{b_1, b_2, \dots, b_n} \int \prod_{i=1}^n \frac{d^3 \bar{p}_{b_i}}{(2\pi)^3 2E_{b_i}} \mathcal{W}_{b_i}(\bar{x}, t, \bar{p}_{b_i})$ $\sum_m \sum_{c_1, c_2, \dots, c_m} \int \prod_{j=1}^m \frac{d^3 \bar{p}_{c_j}}{(2\pi)^3 2E_{c_j}}  A_{n \rightarrow m} ^2$ $(2\pi)^4 \delta^4 \left( \sum_{i=1}^n p_{b_i} - \sum_{j=1}^m p_{c_j} \right)$ $\left[ - \sum_{i=1}^n \delta_{ab_i} \delta^3(\bar{p} - \bar{p}_{b_i}) + \sum_{j=1}^m \delta_{ac_j} \delta^3(\bar{p} - \bar{p}_{c_j}) \right]$ <p>Probability Distribution: <math>\mathcal{W}_a(\bar{x}, t, \bar{p})</math></p> <p>S-Matrix:</p> $\langle c_1, c_2, \dots, c_m   S   b_1, b_2, \dots, b_n \rangle$ $= A_{n \rightarrow m} (2\pi)^4 \delta^4 \left( \sum_{i=1}^n p_{b_i} - \sum_{j=1}^m p_{c_j} \right)$ <p><math>a, b_i, c_j = (p, n, \pi, K, \rho, \Delta, \Lambda, \Sigma, \dots)_{\text{parton}}</math></p>
--

TABLE IV.

### C. Non-uniqueness in Interpretation

Assuming that in  $Au + Au$  collisions at RHIC energy, a large increase in entropy density is observed in the central region (through, say,  $\pi\pi$  or/and  $KK$  interferometry), how can we be sure whether this signifies a transition to quark-gluon plasma (QGP), or simply the observation of Hagedorn temperature corresponding to the emergence of a very large number of broad resonances?

Another example of the non-uniqueness in interpretation is given in Figures 3–5 on  $J/\psi$  suppression. (I thank M. Gyulassy and S. Gavin for giving me these diagrams.)

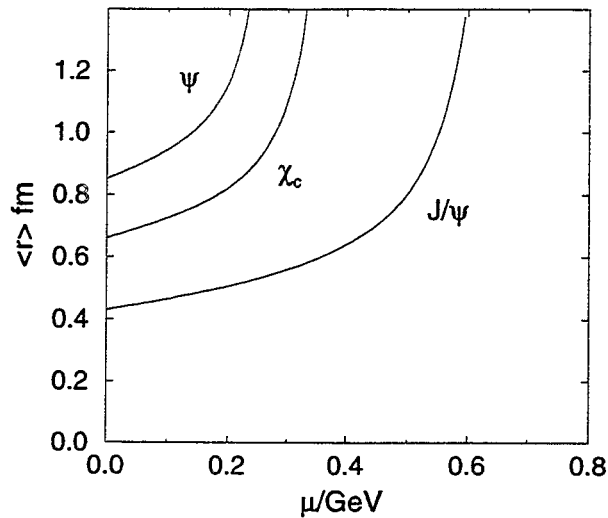


FIG. 3. Matsui and Satz predicted suppressions of  $J/\psi$  as a result of QGP formation. This figure shows the dependence of  $\psi'$ ,  $\chi_c$ , and  $J/\psi$  radii on Debye mass.

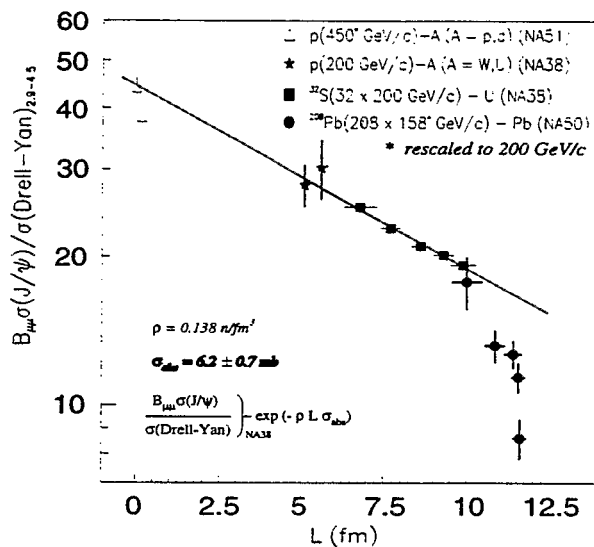


FIG. 4. NA 50 result on  $J/\psi$  to Drell-Yan ratio showing a  $J/\psi$  suppression in  $Pb + Pb$  collisions.

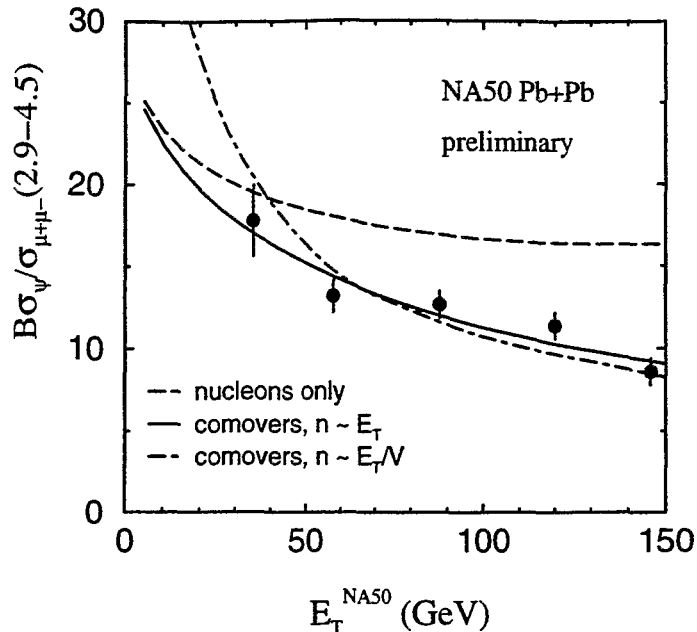


FIG. 5. Gavin and Vogt predicted  $J/\psi$  suppression in  $Pb+Pb$  collisions due to  $J/\psi$  absorption by nucleons and comovers.

#### IV. HOW GOOD IS QCD

The non-uniqueness in interpretation of RHIC physics can only be resolved when QCD can be elevated into a theory with precise predictive power.

##### A. Continuum vs. Lattice QCD

At present, there are two main approaches, the continuum QCD and the lattice QCD, for solving problems with strong interactions. Each has its own limitations, as summarized in Table V. We emphasize that the present compact form of lattice QCD is intrinsically different from the noncompact form of continuum QCD, except in the weak-coupling limit or when the lattice size equals zero. Both limits are difficult to achieve. In addition, for lattice QCD there is the problem of spurious fermion solutions.

It is well known that the Dirac equation on a discrete lattice in  $D$  dimension has  $2^D$  degenerate solutions. The usual method of removing these spurious solutions encounters difficulties with chiral symmetry when the lattice spacing  $\ell \neq 0$ , as demonstrated by the persistent problem of pion and kaon masses. On the other hand, we recall that in any crystal in nature, all the electrons do move in a lattice and satisfy the Dirac equation; yet there is not a single physical result that has ever been entangled with a spurious fermion solution. Therefore it should not be difficult to eliminate these unphysical elements (as will be discussed in the next section).

CONTINUUM QCD	LATTICE QCD
ACTION $A = -\frac{1}{4} \int F_{\mu\nu} F_{\mu\nu} d^4x$ ( $F_{\mu\nu}$ UNBOUNDED)	$A = \sum_{\square} \frac{1}{2} \text{trace} (1 - U_{\square}) + \text{c.c.}$ ( $U_{\square}$ BOUNDED)
<i>Based on Perturbative Series of Noncompact Action</i>	<i>Based on Compact Action, and often with Euclidean time</i>
Difficulties with confinement hadron spectra hadron distributions in dynamical processes	Difficulties with spurious fermion solutions (Wilson & staggered formalism) pion mass dynamical processes

TABLE V.

### V. NEED FOR A TERAFLOP MACHINE

At present, in order to remove the spurious fermion solutions, two approaches are being used in lattice QCD: the Wilson and the staggered formulation. So far, their results have large differences, as illustrated in Figure 6. (I thank N. Christ for giving me this diagram.)

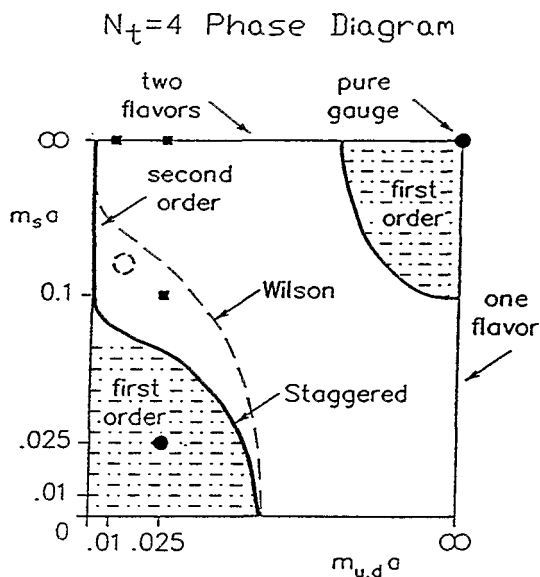


FIG. 6.

Table VI lists the need for a teraflop machine, in order to resolve this and other pressing problems of lattice QCD.

<b>NEED FOR A TERAFLOP MACHINE</b>
<p>In order to make a more definitive statement on</p> <ul style="list-style-type: none"> <li>• <i>The continuum limit of lattice QCD (by comparing staggered fermion thermodynamics at <math>N_t = 4, 8</math> and 12)</i></li> <li>• <i>The calculation of pion mass</i></li> <li>• <i>The comparison of finite temperature Wilson and staggered fermions on <math>N_t = 4</math> and 8 lattices.</i></li> <li>• <i>An improved action to study <math>N_t = 8</math> thermodynamics</i></li> </ul>

TABLE VI.

## VI. NEW APPROACHES

From the determination [3] that the  $\Lambda$ -parameter is about 230 MeV, it follows that for physics in the small domain  $\ell \ll \Lambda^{-1}$ , the continuum QCD should be applicable. Lattice QCD becomes important only for physics at large distances  $\ell > \Lambda^{-1}$ , when confinement plays a dominant role. Thus it seems reasonable that we probably only need a lattice of spacing  $\ell \lesssim 1/5$  fm, the interior of which could be studied by using continuum QCD through perturbative calculations (because of asymptotic freedom [4]).

In  $Au + Au$  collisions, the whole process occurs in a spatial dimension about 10 fm. Thus, a finite lattice of  $\sim 50^3$  points in spatial distribution might be sufficient, as illustrated in Figure 7. Thus a teraflop machine could be sufficient to resolve our present need.

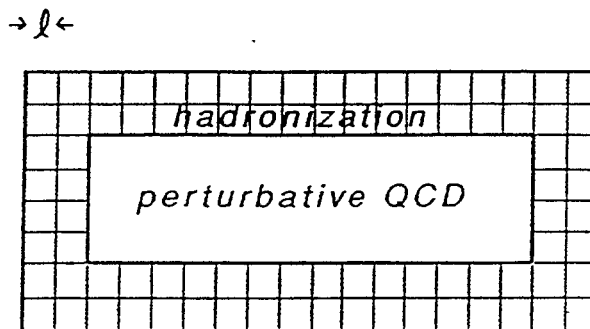


FIG. 7.



The crucial problem is how to devise an interpolation formula, connecting the continuum QCD with the lattice QCD, without taking the lattice spacing  $\ell \rightarrow 0$  limit (i.e., keeping  $\ell$  fixed at, say,  $\lesssim 1/5$  fm). There are two difficulties:

(i) spurious fermion solutions.

Both the staggered and the Wilson fermion approaches can be connected to the continuum formulation only in the limit  $\ell \rightarrow 0$ .

(ii) the noncompact action of continuum QCD vs. the compact action of lattice QCD.

Our subsequent discussions will be divided into three parts:

### A. Spurious Lattice Fermion Solutions

To see the origin of the spurious lattice fermion solutions, we may consider the replacement of the continuum equation  $-i \partial \psi / \partial x = p \psi$  by its discrete form in one space dimension:

$$-\frac{i}{2\ell} (\psi_{j+1} - \psi_{j-1}) = p_L \psi_j \quad (1)$$

where  $\psi_j$  is the value of  $\psi$  at the  $j^{\text{th}}$  site. The above equation can also be derived by setting the derivative  $\partial / \partial \psi_j$  of the discrete bilinear form

$$B_L \equiv \frac{1}{2} \left[ -i \sum_j \psi_j^\dagger (\psi_{j+1} - \psi_j) / \ell + \text{h.c.} \right] \quad (2)$$

to be zero at a constant  $\sum_j \psi_j^\dagger \psi_j$ . The lattice-eigenvalue  $p_L$  is given by

$$p_L = \frac{1}{\ell} \sin K \ell \quad (3)$$

where

$$K \ell \equiv \theta \quad (4)$$

is between  $-\pi$  and  $\pi$ . The spurious solution refers to the zero ( $p_L(\theta) = 0$ ) at  $\theta = \pi$  (which is the same as  $\theta = -\pi$ ). This is a special case of the Nielsen-Ninomiya theorem [5]: For any continuous and periodic function  $p_L(\theta)$ , if as  $\theta \rightarrow 0$   $p_L(\theta) \rightarrow K = \theta / \ell$ , then because of the periodicity  $p_L(\theta) = p_L(\theta + 2\pi)$ , there must be another zero of  $p_L(\theta)$  for  $\theta$  between 0 and  $2\pi$ . For a  $D$ -dimension cubic lattice, the corresponding wave function is a product function, the number of spurious solutions becomes  $2^D$ .

### B. Elimination of Spurious Lattice Fermion Solutions [6]

We note that on a discrete lattice, particles hop from point to point, whereas in a real crystal the lattice structure is embedded in a continuum and electrons move continuously from lattice cell to lattice cell. In a discrete system, the lattice functions are defined only on individual points (or links, as in the case of gauge fields). However, in a crystal the electron state vector is represented by the Bloch wave functions which are continuous functions in  $\vec{r}$ , and herein lies one of the essential differences.

In this new approach we shall expand the field operator in terms of a suitably chosen complete set of orthonormal Bloch functions

$$\{ f_n(\vec{K} | \vec{r}) \} \quad (5)$$

where  $\vec{K}$  denotes the Bloch wave number restricted to the Brillouin zone, and  $n$  labels the different bands. Thus,  $e^{-i\vec{K}\cdot\vec{r}} f_n(\vec{K} | \vec{r})$  has the periodicity of the lattice. The lattice approximation is then derived by either restricting it to only one band (say,  $n = 0$ ), or to a few appropriately defined low-lying bands. Since the inclusion of all bands is the original continuum problem, there is a natural connection between the lattice and the continuum in this method. By including the contributions due to more and more bands, one can systematically arrive at the exact continuum solution from the lattice approximation, as we shall see. There is a large degree of freedom in choosing the Bloch functions (1.1), as the original continuum theory has no crystal structure. These extra degrees of freedom are analogous to gauge fixing; the final answer to the continuum problem is independent of the particular choice of Bloch functions.

For the expansion of the continuum wave function  $\psi(x)$  in terms of (5), we choose the zeroth band ( $n = 0$ ) to be simply the linear interpolation of the discrete values  $\{ \psi_j \}$ ; i.e., in the zeroth-band approximation

$$\psi(x) = \sum_j \psi_j \Delta(x - j\ell) \quad (6)$$

where

$$\Delta(x) = \begin{cases} 1 - \frac{|x|}{\ell} & \text{for } |x| < \ell \\ 0 & \text{otherwise.} \end{cases}$$

Thus, at  $x = j\ell$ ,  $\psi(x) = \psi_j$ . Substitute (6) into the continuum bilinear form

$$B(\psi(x)) \equiv -i \int \psi(x)^\dagger \frac{d\psi(x)}{dx} dx. \quad (7)$$

Setting  $\partial B / \partial \psi_j = 0$  at a constant  $\int \psi^\dagger \psi dx$ , we find

$$\psi_j \propto e^{i\theta j}$$

with  $\theta$  given by (4). Correspondingly, the zeroth-band Bloch function is

$$f_0(K | x) = \sqrt{\frac{3}{N\ell(2 + \cos\theta)}} \sum_j e^{i\theta j} \Delta(x - j\ell) \quad (8)$$

where  $N$  is the total number of lattice sites. It is not difficult to construct from  $f_0(K | x)$  and the Fourier series a complete set of Bloch functions (5), which satisfy

$$\int_0^{N\ell} f_n(K | x)^* f_{n'}(K' | x) dx = \delta_{nn'} \delta_{KK'}. \quad (9)$$

Let

$$\beta_n \equiv -i \int f_n(K | x)^* \frac{\partial}{\partial x} f_n(K | x) dx. \quad (10)$$

We find for  $n = 0$

$$\beta_0 = \frac{3 \sin \theta}{2 + \cos \theta} \quad (11)$$

which, like (3), has a spurious zero solution at  $\theta = \pi$ .

If we substitute the full expansion

$$\psi(x) = \sum_n \sum_k q_n(K) f_n(K|x) \quad (12)$$

into (7), then  $\delta B / \delta \psi(x) = 0$  at a constant  $\int \psi^\dagger \psi dx$  gives  $-i \partial \psi / \partial x = p x$  where

$$p = K + \frac{2\pi m}{\ell} \quad (13)$$

with  $K$  given by (4) and  $m = \dots, -1, 0, 1, \dots$ .

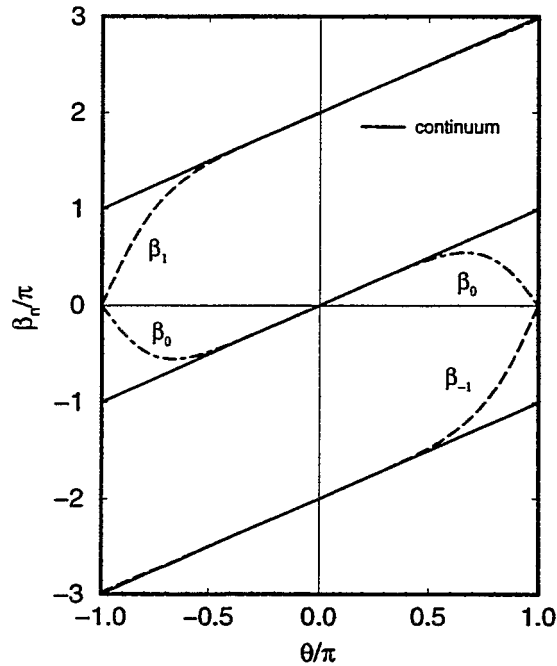


FIG. 8. The dash-dot line gives  $\beta_0 = 3 \sin \theta / (2 + \cos \theta)$  vs.  $\theta = K\ell$  and the dashed lines denote  $\beta_{-1}$  and  $\beta_1$  defined by (10). The solid lines are the continuum free-particle spectrum  $p\ell = K\ell + 2\pi m$  vs.  $\theta$ , with  $m = 0$  and  $\pm 1$ .

In Figure 8, the abscissa is  $\theta / \pi = K\ell / \pi$ , the solid line gives the exact continuum value  $p\ell / \pi$  and the different segments correspond to  $m = -1, 0, 1$ . The dashed line segments are the corresponding  $\beta_n / \pi$  defined by (10). For  $|n| > 1$ , each  $\beta_n$  deviates from the exact continuum result (13) within  $< 1\%$ . For  $|n| \leq 1$ , we see that  $\beta_0$  and  $\beta_{-1}$  are both 0 at  $\theta = \pi$ ; likewise  $\beta_0$  and  $\beta_1$  are both 0 at  $\theta = -\pi$ . Thus, the spurious solutions also extend to  $n = \pm 1$  bands. This additional unwanted degeneracy makes it easy to remove all spurious solutions, as we shall see.

Because  $f_0(K|x)$  and  $f_1(K|x)$  are not eigenfunctions of  $-i\partial/\partial x$ , the degeneracy between  $\beta_0$  and  $\beta_{-1}$  at  $\theta = \pi$  can be removed by considering the off-diagonal elements of  $-i\partial/\partial x$ . At  $\theta = \pi - \epsilon$  where  $\epsilon$  is a positive infinitesimal, we may consider only two bands,  $n = 0$  and  $-1$ ; in this subspace the operator  $-i\partial/\partial x$  becomes the following  $2 \times 2$  matrix:

$$\begin{pmatrix} 3\epsilon & \sqrt{10}/\ell \\ \sqrt{10}/\ell & -5\epsilon \end{pmatrix}. \quad (14)$$

As  $\epsilon \rightarrow 0$ , its eigenvalues are

$$\pm\sqrt{10}/\ell = \pm 1.006 \times \pi/\ell. \quad (15)$$

Similar considerations apply to  $\theta = -\pi$  by taking into account the coupling between  $n = 0$  and  $n = 1$  band. Thus, by taking into account only  $n = 0$  and  $\pm 1$ , we have removed all spurious zero-mode solutions and, in addition, the result differs from the exact continuum value by less than a few tenths of a percent for the entire range.

### C. Noncompact Lattice QCD

In order to extend the above considerations to QCD we have to construct an appropriate complete set of Bloch wave functions that is compatible with the gauge-fixing condition. Once that is done, the restriction to the  $0^{\text{th}}$  band ( $n = 0$ ) gives a noncompact formulation [7] of lattice QCD. The exact continuum theory can be reached through the inclusion of all  $n = 0$  and  $n \neq 0$  bands, without requiring the lattice size  $\ell \rightarrow 0$ . This makes it possible, at a nonzero  $\ell$ , for the lattice coupling  $g_\ell$  to act as the renormalized continuum coupling. All physical results in the continuum are, of course, independent of  $\ell$ . Table VII summarizes this new approach:

<p>at nonzero lattice size <math>\ell</math>:</p> <ul style="list-style-type: none"> <li>• <i>removal of spurious lattice fermion solutions (thereby restoring chiral symmetry)</i> <i>with R. Friedberg and Y. Pang (J. Math. Phys. 1994)</i></li> <li>• <i>Noncompact lattice QCD</i> <i>with R. Friedberg, Y. Pang and H. C. Ren (Phys. Rev. D 1995)</i></li> <li>• <i>lattice as first approximation of the continuum (keeping <math>\ell</math> fixed)</i></li> <li>• <i>a unifying Hamiltonian formalism</i> <i>distance <math>&gt; \ell</math> using lattice calculation (for confinement)</i> <i>distance <math>&lt; \ell</math> using perturbative approach (<math>\because</math> asymptotic freedom)</i></li> </ul>
--

TABLE VII.

## VII. CONCLUDING REMARK

*Large things are made of small  
And even smaller.  
To know the smallest  
We need also the largest.*

*All lie in Vacuum  
Everywhen and everywhere.  
How can the micro  
Be separate from the macro?*

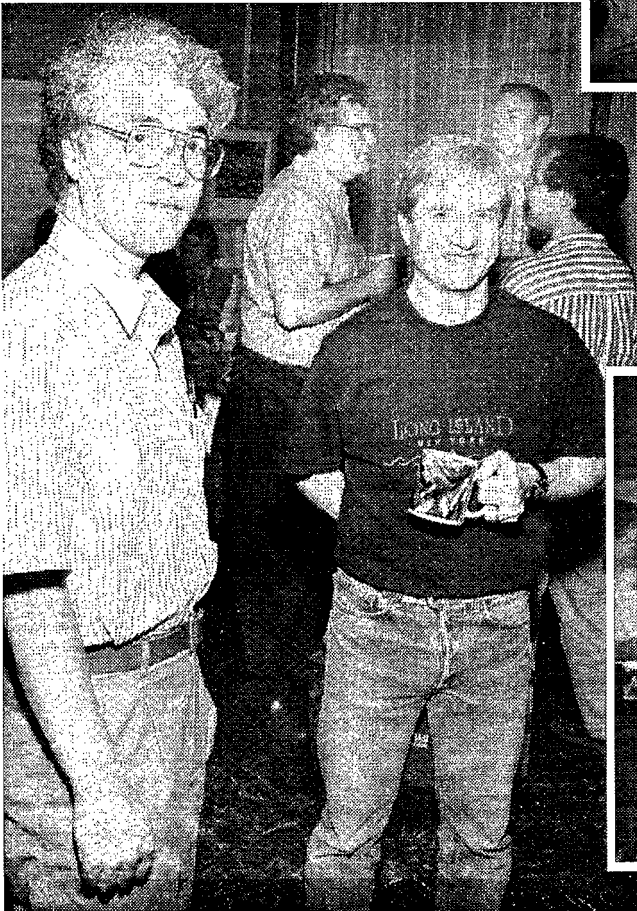
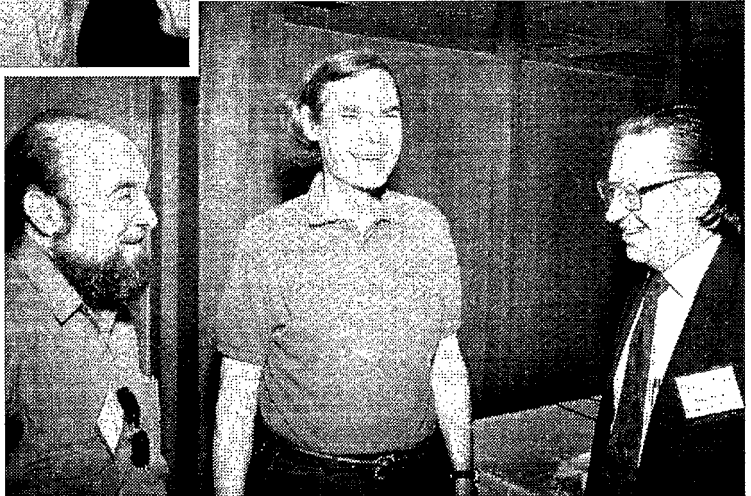
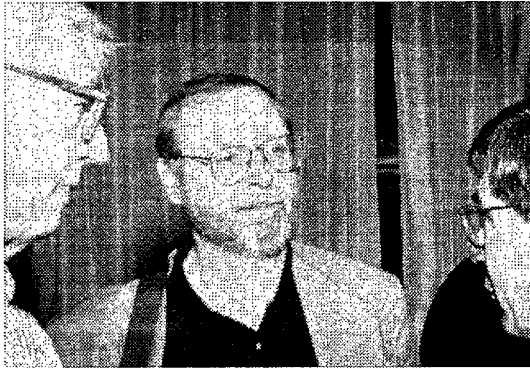
*Let Vacuum be a condensate  
Violating harmony.  
We can then penetrate  
Through asymmetry into symmetry.*

## REFERENCES

- [1] Y. Pang, T. J. Schlagel and S. H. Kahana, Physical Review Letter **68**, 2743 (1992); S. H. Kahana, Y. Pang, and T. J. Schlagel, In Proceedings of *Heavy Ion Physics at the AGS – HIPAGS '93*, edited G. S. F. Stephans, S. G. Steadman and W. L. Kehoe, 13-15 January, 1993, p. 263.
- [2] Y. Pang, in *Proceedings of CCAST Symposium/Workshop on Particle Physics at Fermi Scale*, Beijing, May 1993, Edited by Y. Pang, J. Qiu, and Z. Qiu, (Gordon Breach, New York, 1993), p451.
- [3] R. M. Barnett et al. Phys. Rev. D **54**, 1, (1996).
- [4] H. D. Politzer, Phys. Rev. Lett. **30**, 1346 (1973); D. Gross and F. Wilczek, *ibid.*, 1343. G. 't Hooft, talk at the Marseilles meeting 1972 (unpublished).
- [5] H. B. Nielsen, and M. Ninomiya, Nucl. Phys. B**185**, 20 (1981); **193**, 173 (1981).
- [6] R. Friedberg, T. D. Lee and Y. Pang, J. Math. Phys. **35**, 5600 (1994).
- [7] R. Friedberg, T. D. Lee, Y. Pang and H. C. Ren, Phys. Rev. B. **52**, 4053, (1995).

**I.**

# **Thermodynamics**



# The Equation of State for QCD from the Lattice

C. Bernard

*Department of Physics, Washington University, St. Louis, MO 63130, USA*

T. Blum\*

*Physics Department, Brookhaven National Laboratory, Upton, NY 11973, USA*

C.E. DeTar and C. McNeile

*Physics Department, University of Utah, Salt Lake City, UT 84112, USA*

Steven Gottlieb and K. Rummukainen

*Department of Physics, Indiana University, Bloomington, IN 47405, USA*

U.M. Heller

*SCRI, Florida State University, Tallahassee, FL 32306-4052, USA*

J.E. Hetrick and D. Toussaint

*Department of Physics, University of Arizona, Tucson, AZ 85721, USA*

L. Kärkkäinen

*Nokia Research Center, P.O. Box 100, FIN-33721 Tampere, Finland*

R.L. Sugar

*Department of Physics, University of California, Santa Barbara, CA 93106, USA*

M. Wingate

*Department of Physics, University of Colorado, Boulder, CO 80309, USA*

## Abstract

We give an elementary introduction to lattice calculations of the QCD equation of state and briefly review results for the case of two light flavors [1,2].

---

\*Presented by T. Blum.



## I. INTRODUCTION AND BACKGROUND

Lattice simulations have shown for some time that ordinary hadronic matter at zero temperature undergoes a dramatic crossover characterized by large increases in the entropy and energy densities of the system [3] when the temperature is raised to about 150 MeV. In the thermodynamic limit, this crossover may become a phase transition to a new state of matter, the quark-gluon plasma (QGP). The equation of state (EOS), or energy density and pressure as a function of the temperature, is important input for phenomenological models of upcoming heavy-ion collision experiments at RHIC that seek to detect the QGP. Because the phase transition occurs at relatively low temperature, a nonperturbative method is required for first principles calculations using QCD.

Generally, thermodynamic quantities are given by derivatives of the partition function. In particular, the energy density  $\varepsilon$  and pressure  $p$  are given by

$$\varepsilon = -\frac{1}{V} \left. \frac{\partial \log Z}{\partial (1/T)} \right|_V \quad \text{and} \quad p = T \left. \frac{\partial \log Z}{\partial V} \right|_T, \quad (1)$$

where  $V$  and  $T$  are the spatial volume and the temperature of the system. The partition function is given by a path integral over all possible field configurations of the Boltzmann weight,

$$Z = \int [d\mathcal{A}, d\bar{\psi}, d\psi] e^{-S_E}, \quad (2)$$

where the Euclidean space-time action is given by

$$S_E = \int_0^\tau d\tau' \int_V d^3\vec{x} \mathcal{L}_E(\mathcal{A}(\vec{x}, \tau'), \bar{\psi}(\vec{x}, \tau'), \psi(\vec{x}, \tau')), \quad (3)$$

and the integral over Euclidean time is cut off at time  $\tau$ . The above path integral corresponds to the thermodynamic partition function if  $\tau$  is identified as the inverse temperature, and the boundary conditions on the (fermion) boson fields are chosen to be (anti-) periodic.

To regularize the theory nonperturbatively,  $S_E$  is discretized on a four dimensional space-time lattice (see Fig. 1) with spacing  $a$ , so the continuum derivatives become finite differences, and the integral over space-time becomes a sum over all lattice sites. In the limit that  $a \rightarrow 0$ , the classical continuum action is recovered. The lattice spacing disappears from the lattice action; the extra factors of  $a$  are absorbed into the fields and the quark mass to make them dimensionless. Therefore the lattice spacing, or cut off, is varied implicitly by changing the bare gauge coupling,  $6/g^2$ , and the bare quark mass  $am_q$ . Explicitly,

$$S_E = \int d\tau \int_V d^3\vec{x} \left( \frac{1}{4} F_{\mu\nu} F^{\mu\nu} + \bar{\psi} (\not{D} + m) \psi \right) \rightarrow \sum_{\text{sites}} \sum_{\mu > \nu} \left( \frac{6}{g^2} \text{Re Tr } \square_{\mu\nu} \right) + \bar{\psi} M \psi. \quad (4)$$

The gauge fields,  $U_\mu(x)$ , live on the links of the lattice to maintain exact gauge invariance. They are elements of the group SU(3) and are related to their continuum counterparts by a simple exponential relation,

$$U_\mu(x) = \exp\{iga_\mu A_\mu(x)\} \approx \exp\{ig \int_x^{x+a_\mu} dy A_\mu(y)\}. \quad (5)$$

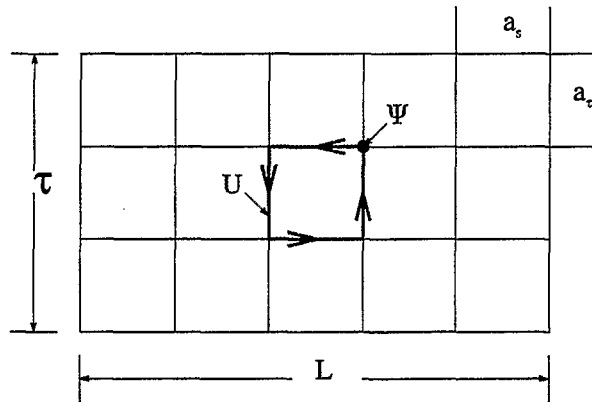


FIG. 1. The four dimensional Euclidean space-time lattice.

The quadratic part of the continuum gauge lagrangian then becomes the trace of the path ordered product of gauge links around an elementary plaquette,

$$\square_{\mu\nu}(x) = \frac{1}{3} \text{Tr} U_\mu(x) U_\nu(x + a\hat{\mu}) U_\mu^\dagger(x + a\hat{\nu}) U_\nu^\dagger(x), \quad (6)$$

which yields the standard Wilson gauge action given by the RHS of Eq. 4. The Dirac action is constructed by replacing the the  $\mathcal{D}$  operator with a finite difference operator. For Kogut-Susskind (KS), or staggered fermions, the quark fields are transformed to a spin diagonal basis which mixes the spin and flavor degrees of freedom in a complicated way, and all spin components but one are thrown away. In the limit  $a \rightarrow 0$ , the continuum action for *four* degenerate Dirac fermions is recovered. The fermion matrix for KS quarks is

$$M = 2(am_q)\delta_{x,y} + \sum_{\mu} (\eta_{\mu}(x)U_{\mu}(x)\delta_{x+a\hat{\mu},y} - \eta_{\mu}(y)U_{\mu}^{\dagger}(y)\delta_{x-\hat{\mu},y}), \quad (7)$$

where the  $\eta'_{\mu}$ s are the KS phases which correspond to the Dirac  $\gamma'_{\mu}$ s in the spin diagonal basis.

Once the lattice action has been constructed, it is straightforward to calculate observables. Integrating over the quark fields (which are Grassman variables), we obtain

$$\langle \mathcal{O} \rangle = Z^{-1} \int [dU] \mathcal{O} \det((M(U)))^{n_f/4} e^{-S_g} \quad \text{where} \quad Z = \int [dU] \det((M(U)))^{n_f/4} e^{-S_g}, \quad (8)$$

for any observable. Thus  $\det((M(U)))^{n_f/4} e^{-S_g}$  serves as a probability weight for  $n_f$  flavors of quarks, and the remaining path integral over gauge fields is done by Monte Carlo simulation. Using importance sampling to generate the gauge field configurations with the desired weight, observables become simple averages over the configurations.

Now, let's return to discussing thermodynamics on the lattice where the volume and inverse temperature are  $V = N_s^3 a_s^3$  and  $T^{-1} = N_t a_t$ .  $V$  and  $T$  are varied by changing the number of lattice sites  $N_s$ ,  $N_t$ , or the lattice spacings  $a_s$ ,  $a_t$ , or both. To simulate at finite temperature in the continuum, the prescription was to cut off the Euclidean time integral in the action at  $\tau = T^{-1}$ . This is accomplished on the lattice by taking  $N_t \ll N_s$  for the usual case when  $a_t = a_s$ . This sets the overall temperature scale. To vary the temperature around this scale, we vary the lattice spacing by adjusting  $6/g^2$  and  $am_q$ . For small  $am_q$  increasing  $6/g^2$  is roughly equivalent to raising the temperature. However one should keep in mind

that varying  $am_q$  also changes the lattice spacing and thus the temperature. Derivatives with respect to  $T^{-1}$  and  $V$  are most easily obtained by adjusting the couplings. Then, the interaction measure, or energy density minus three times the pressure is

$$\frac{\varepsilon - 3p}{T^4} = \left( -\frac{1}{V} \frac{\partial}{\partial(1/T)} - 3T \frac{\partial}{\partial V} \right) \log Z = -N_t^4 \left( \frac{\partial(6/g^2)}{\partial \ln(a)} \langle \square \rangle + \frac{\partial(am_q)}{\partial \ln(a)} \langle \bar{\psi}\psi \rangle \right), \quad (9)$$

where the rightmost expression is for KS quarks and the Wilson action, and

$$\langle \square \rangle = \frac{1}{N_s^3 N_t} \frac{\partial \log Z}{\partial(6/g^2)} \quad \text{and} \quad \langle \bar{\psi}\psi \rangle = \frac{1}{N_s^3 N_t} \frac{\partial \log Z}{\partial(m_q a)} = \frac{n_f}{4} \frac{2}{N_s^3 N_t} \langle \text{Tr } M^{-1} \rangle \quad (10)$$

are the derivatives of  $\log Z$  with respect to  $6/g^2$  and  $am_q$ . The definition of  $\square$  is given in Eq. 6, and the form of  $\bar{\psi}\psi$  results from exponentiating the quark determinant. The derivatives of  $6/g^2$  and  $am_q$  with respect to  $\log(a)$  are just the  $\beta$  function and anomalous dimension of the quark mass which have been calculated nonperturbatively from spectrum data in the literature [1]. It is important to use the nonperturbative  $\beta$  function since it differs by roughly a factor of two from the perturbative result in the region of  $6/g^2$  used for present simulations.

The pressure is obtained from

$$\frac{p}{T} = \frac{\partial \log Z}{\partial V} = \frac{\log Z}{V}, \quad (11)$$

which is just a restatement of the fact that the free energy density is independent of volume for large volumes. The derivatives of  $\log Z$ , given by Eqs. 6 and 10, are calculated rather than  $Z$  itself. These are integrated numerically with respect to  $6/g^2$  and  $am_q$  to obtain the pressure.

Together, the interaction measure and the pressure form the equation of state. The energy density (and pressure) can be calculated directly from an expression similar to Eq. 9, but with derivatives of the couplings with respect to the temporal (spatial) lattice spacing at fixed spatial (temporal) lattice spacing. These derivatives are much harder to measure, and in fact have not been calculated nonperturbatively for QCD with  $n_f \neq 0$ .

It is important to note that the physical energy and pressure are given after subtracting off their divergent vacuum, or  $T = 0$ , contributions. In practice this is done by subtracting the same quantities measured on a symmetric lattice ( $N_t = N_s$ ) from quantities measured on the finite temperature, or asymmetric, lattice ( $N_t < N_s$ ). These are often referred to (unfortunately) as cold and hot lattices, respectively. This fact more than doubles the cost of calculating the EOS since each point in the phase diagram requires two lattices.

Finally, to determine the temperature from  $T^{-1} = N_t a$ , the lattice spacing is given by by setting one observable to its physical value. For example, in the results discussed below the (zero temperature) rho mass measured in units of  $a$  is used, or  $am_\rho = a \times 770$ . Since simulations are done in the strong coupling regime, there are scaling violations. In other words, using the nucleon mass results in a different  $a$ , and therefore a different temperature. While no one has done a detailed analysis, the conventional wisdom is that these scaling violations are on the order of ten percent. Also, typically thermodynamic quantities are normalized by  $T^n$  by simply multiplying by  $N_t^n$ ; for example,  $pa^4 \times N_t^4 = p/T^4$ . While this also yields physical numbers, the values will show scaling violations depending on  $N_t$  (see below). All of these systematic errors disappear in the continuum limit.

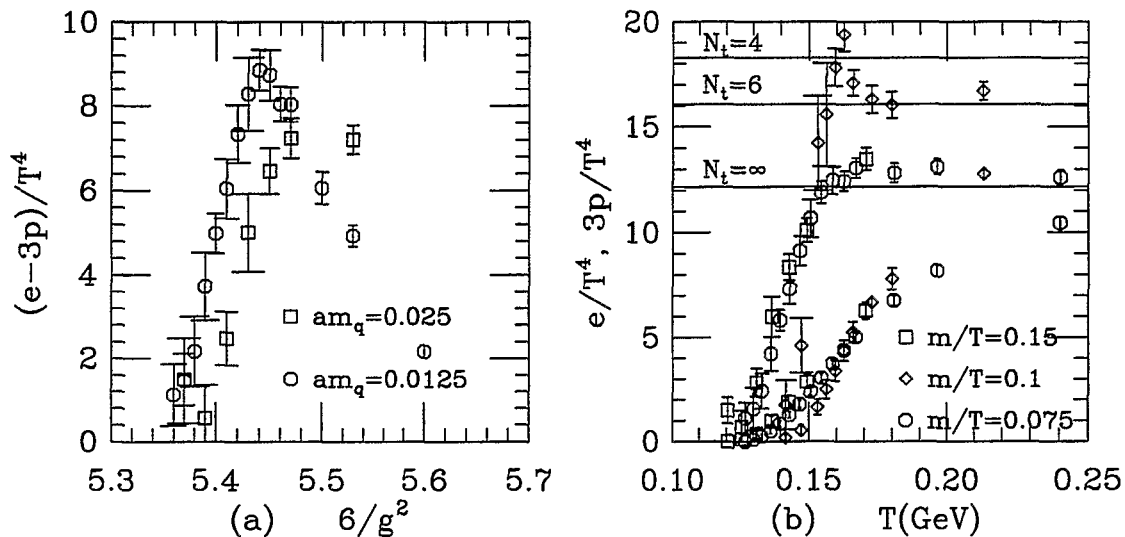


FIG. 2. (a) The interaction measure on  $N_t = 6$  lattices. (b) The EOS. The horizontal lines are Stefan-Boltzmann values for  $\varepsilon/T^4$ . The diamonds indicate an earlier result on  $N_t = 4$  lattices.

## II. RESULTS FOR $N_F = 2$

Below we briefly review recent calculations of the two flavor QCD EOS at zero chemical potential by the MILC collaboration [1,2]. Most simulations with dynamical fermions have used two light flavors because doing so cuts the computational burden in half over simulations with two light and one strange flavor. Since previous simulations have shown the critical temperature  $T_c$  to be roughly 150 MeV, it is reasonable to assume that the dynamics near  $T_c$  is governed mainly by pions, and thus two flavor simulations should capture the bulk of the physics. Fine details, like the order and universality class of the transition may of course depend on the presence of the strange quark. Also, presently there is no viable method of simulating QCD at finite chemical potential; however at RHIC, the baryon number density in the central rapidity region is expected to be small (see the contribution from J. Harris). Simulations for the EOS are also limited by computational resources to relatively small lattices ( $N_t = 4, 6$ ). Results for the pure SU(3) gauge theory and preliminary calculations with four flavors of quarks have been obtained by the Bielefeld group following a similar approach, and are also discussed in this volume by Karsch.

In Fig. 2(a) the interaction measure for  $N_t = 6$  is shown as a function of  $6/g^2$ . The two curves in the figure correspond to quark masses  $am_q = 0.0125$  and  $am_q = 0.025$ , and up to an overall shift in the coupling, appear quite similar. The interaction measure rises sharply through the crossover region (it is normalized to zero at  $T = 0$ ) and then decreases towards zero at large  $6/g^2$  (high temperature).

In Fig. 2(b) we show the  $N_t = 6$  EOS as a function of the temperature. Again, there is a rapid rise in  $\varepsilon/T^4$  which levels off around 160 MeV. The energy density is about 1 GeV/fm<sup>3</sup> at this point. The pressure rises smoothly through the crossover region but has not leveled off at the highest temperature simulated. Also shown in Fig. 2(b) is an earlier calculation

on  $N_t = 4$  lattices. There is a large finite size correction when  $N_t$  is increased from 4 to 6. This is expected from the lattice Stefan-Boltzmann results (see Fig. 2(b)). It appears that the approach to these expected asymptotic values is quite slow.

From the location of the maximum in the slope of  $\langle \square \rangle$  or  $\langle \bar{\psi}\psi \rangle$  with respect to  $6/g^2$ , the pseudocritical temperature of the transition is roughly 140 MeV (for both  $am_q = 0.025$  and 0.0125) [2]. Figure 2(b) shows that the energy density is already substantial at this point.

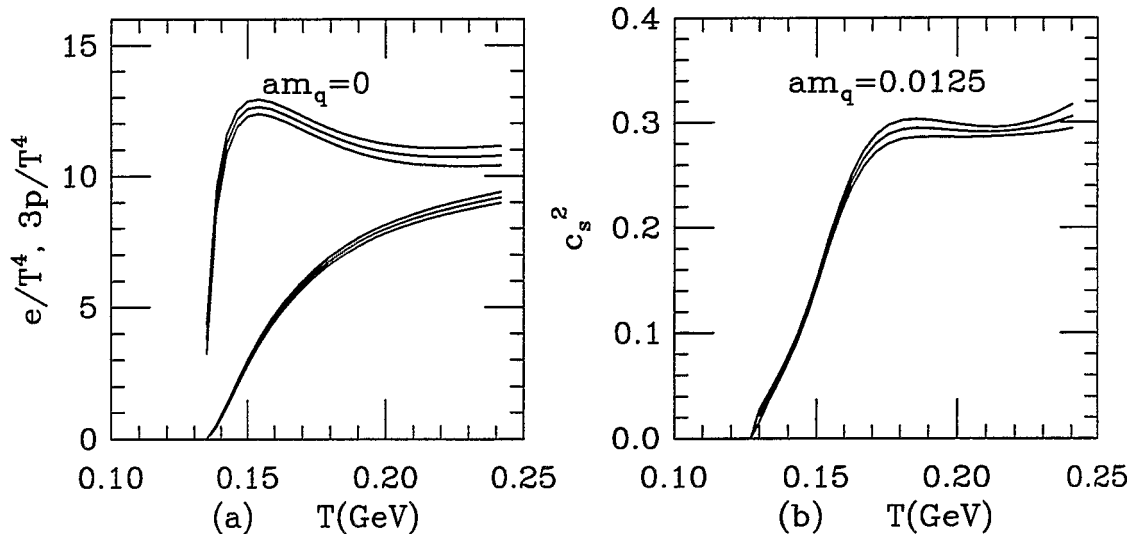


FIG. 3. (a) The EOS extrapolated to  $am_q = 0.0$  from a fit to the  $O(4)$  universal scaling function plus polynomial terms. Each set of curves indicates the central value and a one standard deviation spread resulting from the statistical uncertainty in the fit. (b) The speed of sound for  $am_q = 0.0125$  from the same fit. Both figures are taken from Ref. [2].

The light quark mass is too large in the above simulations, in the sense that the pion mass is two to four times its physical value (simulations corresponding to the physical pions would require extremely large amounts of computer time on present computers). Thus results must be extrapolated to  $m_q \approx 0$ . Such an extrapolation for the EOS is shown in Fig. 3(a), where a second order phase transition in the limit  $m_q \rightarrow 0$  has been assumed. Until recently, lattice simulations and universality arguments [5] have indicated that in the limit  $m_q \rightarrow 0$  two flavor QCD probably exhibits a second order phase transition in the same universality class as the 3d  $O(4)$  spin model [5]. However, new lattice simulations on large volumes have cast some doubt on both conclusions (see A. Ukawa's contribution to this volume). The results displayed in Fig. 3 are from a fit to an  $O(4)$  universal scaling function [6] (plus polynomial terms), although the data are fit equally well to the mean field scaling function. The appearance of the bump in the energy density just after the transition is likely an artifact of the extrapolation, although it need not be [4]. Ignoring the bump, the extrapolated EOS is quantitatively similar to the  $am_q = 0.025$  and 0.0125 results: the results depend weakly on the quark mass. The gap in  $\varepsilon/T^4$  at low temperature is due to a breakdown in the fit which, for  $am_q = 0$ , corresponds to an extrapolation in  $6/g^2$ .

The smooth interpolation of the data as a function of  $T$  also allows for a determination of the speed of sound,  $c_s^2 = (dp/dT)/(d\varepsilon/dT)$ , shown in Fig. 3(b). The speed of sound has

important experimental implications for the detection of the quark-gluon plasma (see M. Gyulassy, these proceedings). At the transition we expect  $c_s$  to be small since  $d\varepsilon/dT \gg dp/dT$ . However, just below  $T_c$ ,  $c_s$  should approach  $1/3$ , the value for a relativistic free gas of massless pions (for massive interacting pions the value will be less than  $1/3$ ), and above  $T_c$ ,  $c_s$  should again approach  $1/3$  if the system is a weakly interacting relativistic plasma. From Fig. 3(b), the second expectation is more or less borne out from the simulations. Unfortunately, while  $c_s$  is small near  $T_c$ , in the hadronic phase there is no indication of an increase, and thus no dip. Again, this is because of the difficulty in measuring  $\varepsilon$  and  $p$ , and thus their derivatives, in the low temperature hadronic phase.

## REFERENCES

- [1] T. Blum, S. Gottlieb, L. Kärkkäinen, and D. Toussaint, Nucl. Phys. B (PS) **42** (1995) 460; T. Blum, S. Gottlieb, L. Kärkkäinen, and D. Toussaint, Phys. Rev. D. **51** (1995) 5153.
- [2] C. Bernard *et al*, Nucl. Phys. B (PS) **47** (1995) 503; C. Bernard *et al*, "Thermodynamics for two flavor QCD", to appear in Nucl. Phys. B (PS), hep-lat 9608026.
- [3] See annual reviews in the Proceedings of the International Symposium on Lattice Field Theory, Nucl. Phys. B (PS), and references therein.
- [4] M. Asakawa and T. Hatsuda, hep-ph/9508360.
- [5] For universality arguments, see R.D. Pisarski and F. Wilczek, Phys. Rev. D **29** (1984) 338; K. Rajagopal and F. Wilczek, Nucl. Phys. B**399** (1993) 395; and K. Rajagopal, this workshop. For lattice results see E. Laermann and F. Karsch, Phys. Rev. D **50** (1994) 6954; C. DeTar, in Quark Gluon Plasma 2, R. Hwa, Ed., World Scientific, 1995; Y. Iwasaki, K. Kanaya, S. Kaya, T. Yoshie, "Scaling of Chiral Order Parameter in Two-Flavor QCD", hep-lat/9609022.
- [6] D. Toussaint, University of Arizona preprint AZPH-TH/96-13 (1996).

# Continuum Limit in Lattice QCD\*

Shigemi Ohta

*Institute of Physical and Chemical Research (RIKEN)  
Wako-shi, Saitama 351-01, Japan*

## Abstract

We discuss the continuum limit in lattice QCD based on our quenched staggered light hadron mass calculation at the coupling of  $\beta = 6.5$  on a  $48^3 \times 64$  lattice with quark mass  $m_q a = 0.01, 0.005, 0.0025$  and  $0.00125$  in lattice units. We observe the flavor symmetry restored for pion and  $\rho$  meson, signaling that we are close enough to the continuum. The lattice scale is estimated to be  $a^{-1} = 3.7(2)$  GeV.

## I. ASYMPTOTIC SCALING AND CONTINUUM LIMIT:

In the continuum limit the lattice cutoff is removed by sending the lattice spacing  $a$  to zero. The asymptotic freedom of QCD means the gauge coupling  $g$  is sent to zero simultaneously, since Callan-Symanzik (CS) renormalization-group coefficient

$$\beta_{\text{CS}}(g) = -a \frac{dg}{da} \quad (1)$$

is negative near the ultraviolet fixed point  $g = 0$  for number of quark flavors  $N_f < 17$ : in perturbation expansion,

$$\beta_{\text{CS}}(g) = b_0 g^3 + b_1 g^5 + O(g^7), \quad b_0 = -\frac{1}{(4\pi)^2} \frac{33 - 2N_f}{3}. \quad (2)$$

Since there is no dimensionful parameter in quenched lattice QCD other than the lattice spacing, hadron mass  $m$  in general is described as

$$m = a^{-1} f(g) \quad (3)$$

with a dimensionless function  $f$  of the dimensionless gauge coupling  $g$ . Since QCD is renormalizable, the explicit dependence of  $m$  on the cutoff  $a$  must disappear in approaching the continuum limit:

---

\*Work in collaboration with Seyong Kim, Center for Theoretical Physics, Seoul National University, Seoul, Korea. The author thanks the computation center of RIKEN for the use of VPP500/30 vector parallel super computer.

$$\frac{dm}{da} = -a^{-2}(f'\beta_{CS} + f) \rightarrow 0, \quad \text{as } a \rightarrow 0. \quad (4)$$

The differential equation  $f'\beta_{CS} + f = 0$  is easily solved to give

$$\int^g \frac{dg}{\beta_{CS}} = - \int^g \frac{df}{f} = - \ln f(g) + C, \quad (5)$$

or

$$ma = f(g) = C' \exp\left(- \int^g \frac{dg}{\beta_{CS}}\right) \simeq C' \exp\left(\frac{1}{2b_0g^2}\right). \quad (6)$$

This relation is called the asymptotic scaling. By confirming this scaling on the lattice, we can extract the continuum hadron mass value by extrapolation<sup>1</sup>. In practice, however, to confirm the asymptotic scaling in any lattice-QCD numerical calculation is a daunting task. Hadron mass calculation at a single value of the gauge coupling  $g$  on a lattice usually requires months or years of super computing at tens of GFLOPS. Calculations at multiple values of  $g$  take longer.

## II. FLAVOR SYMMETRY VIOLATION BY LATTICE:

Instead we use the violation and restoration of the flavor symmetry as an indicator of closeness to the continuum. In the current work we employ the staggered formulation of quark propagation. Unlike the original Wilson formulation, this formulation preserves a continuous U(1) remnant of the  $SU(N_f)$  flavor chiral symmetry. This allows one of the  $(N_f^2 - 1)$  Nambu-Goldstone (NG) pion modes to survive as a NG mode. Its mass  $m_\pi$  obeys the GellMann-Oakes-Renner relation  $m_\pi^2 \propto m_q$ . The other pion modes can no longer be NG mode, and will acquire heavier mass which does not obey the GMOR relation. As the lattice cutoff is removed by sending the lattice spacing and gauge coupling to zero simultaneously, this lattice violation of flavor symmetry should also be removed. The non-NG mode pion mass should gradually approach the NG-mode pion mass and eventually be degenerate. It is this signal we will be looking at in this talk<sup>2</sup>.

## III. RIKEN-SEOUL LATTICE QCD COLLABORATION:

To get a meaningful result for hadron mass, the lattice box must be large enough to contain the hadron. More accurately, a perimeter of the box must be about 2.5 fm or longer to contain a proton. On the other hand the lattice spacing must be fine enough, eg smaller

---

<sup>1</sup>The scaling relation also shows why hadron mass cannot be perturbatively expanded in terms of gauge coupling  $g$ . The hadron mass behavior as  $ma \propto \exp(1/(2b_0g^2))$  has an essential singularity at  $g = 0$ .

<sup>2</sup>This is a necessary condition for the continuum limit.



than 0.1 fm, to accurately describe the propagation of quarks and gluons [1]. In the present work [2] the lattice size is  $48^3 \times 64$  and the inverse-squared gauge coupling is  $\beta = 6/g^2 = 6.5$ <sup>3</sup>. These parameters roughly correspond to a physical box of  $(2.5 \text{ fm})^3$  and lattice spacing  $a$  of  $\sim 0.05 \text{ fm}$ . We use four different values of quark mass, 0.01, 0.005, 0.0025 and 0.00125 in lattice units or equivalently about 40, 20, 10 and 5 MeV in physical units. Since the normal up- and down-flavor quark mass is considered to be about 5 and 10 MeV respectively, we are quite close to the real world in this regard too.

We use the VPP500/30 vector-parallel super computer at RIKEN for this work. The space-like lattice size of 48 allows efficient use of a 24-node partition of the super computer. In generating the gauge configurations we use a combination of a Metropolis update sweep followed by an over-relaxation one. The separation between two successive hadron-mass calculations is 1000 such pairs of sweeps and take about 3 hours in total including the necessary disk accesses. This separation should be about equivalent with a series of earlier studies at lower cutoff or smaller volume [4]. With the current statistics of 200 configurations the autocorrelation in successive Nambu-Goldstone pion propagators at time  $t = 20$  is about 15 %. All the configurations used for the hadron-mass calculations, almost 2 Gbytes each, are stored in a tape archive. This will enable us to study hadrons with strangeness and charm in the near future. Further details on our simulation method and characteristics were already reported [2,3].

#### IV. EFFECTIVE MASS:

As is mentioned in the above, we first calculate quark propagators  $q(t, x, y, z)$  for each gauge configuration<sup>4</sup>. Next we combine them to form hadron propagators,  $P_h(t, x, y, z)$ <sup>5</sup>. For example, NG pion propagator  $P_\pi$  and non-NG one  $P_{\pi_2, \sigma}$ <sup>6</sup> are respectively given by

$$\begin{aligned} P_\pi(t) &= \sum_{x,y,z} \text{Tr}[q^\dagger(t, x, y, z)q(t, x, y, z)], \\ P_{\pi_2, \sigma}(t) &= \sum_{x,y,z} (-1)^{x+y+z} \text{Tr}[q^\dagger(t, x, y, z)q(t, x, y, z)]. \end{aligned} \quad (7)$$

Here the summation over the space coordinates is taken to project the propagator onto zero-momentum mode. Such a zero-momentum-projected hadron propagator is dominated by the ground-state mass of the hadron,  $m_h$ :

$$P_h(t) \sim \exp(-m_h t), \quad (8)$$

---

<sup>3</sup>This quantity, the inverse-squared gauge coupling  $\beta = 6/g^2$  is to be distinguished from the renormalization-group coefficient  $\beta_{\text{CS}}$ .

<sup>4</sup>Quark propagators are gauge-dependent. The color indices are suppressed here.

<sup>5</sup>Hadron propagators are gauge independent. There is no color index.

<sup>6</sup>This channel is mixed with a parity partner  $\sigma$ .

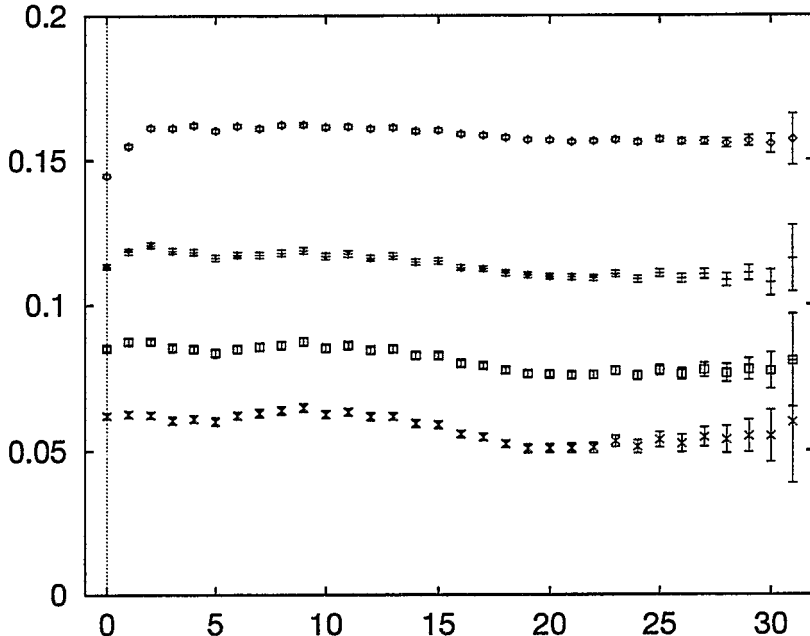


FIG. 1. Nambu-Goldstone pion effective mass at  $\beta = 6.5$  on  $48^3 \times 64$  lattice for quark mass  $m_q = 0.01, 0.005, 0.0025$  and  $0.00125$ .

at large  $t$ . In practice, however, hadron propagators suffer from various noise. So we need to try various methods in extracting the mass from them. A frequently used measure is the so-called effective mass, defined at each time slice as

$$m_{\text{eff}}(t) = \ln[P_h(t)/P_h(t+1)]. \quad (9)$$

This quantity may deviate from the true hadron mass  $m_h$  for various reasons: because of the unwanted excited states in the small- $t$  region or suffer from noise in the large- $t$  region. But we usually find a plateau in the medium- $t$  region in this quantity from which we can extract the hadron mass fairly accurately.

## V. NAMBU-GOLDSTONE PION:

Let us look at the effective mass of NG pion plotted in Figure 1. At a first glance, we observe nice long plateaus with small error bars: if we neglect first four or five points in time, the remaining points seem to align on a well defined plateau for each quark mass. Indeed if we take weighted average of the effective mass from  $t = 5$  through 31, we get pion mass estimates of 0.1592(4), 0.1135(7), 0.0812(8) and 0.0583(9) for the four quark mass values of 0.01, 0.005, 0.0025 and 0.00125 respectively. However, closer inspection of Figure 1 reveals strange wiggles and there seem to be two plateaus for each quark mass: one for a higher mass in earlier time and the other for a lower mass in later time. This tendency is more pronounced for lighter quark mass cases. Perhaps our Jack-knife analysis

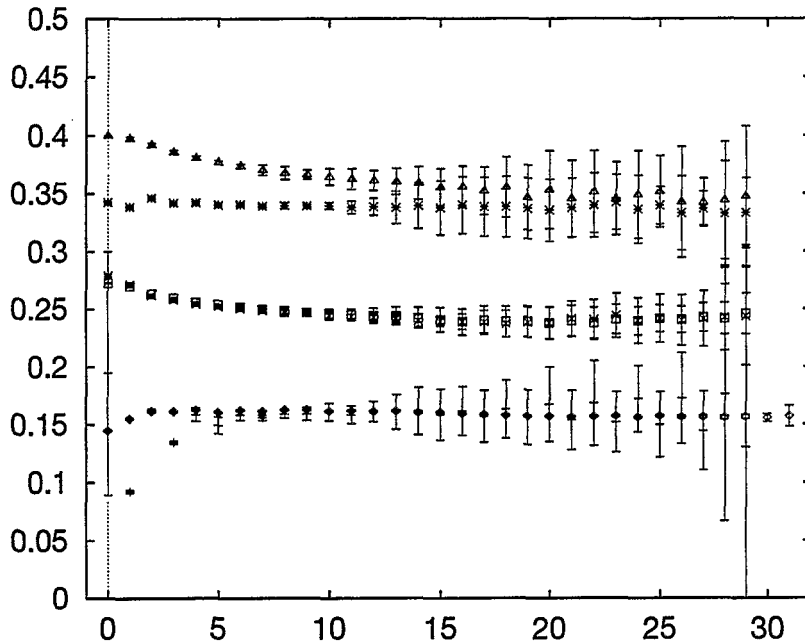


FIG. 2. Effective mass of flavor symmetry partners at  $\beta = 6.5$  on  $48^3 \times 64$  lattice for quark mass  $m_q = 0.01$ :  $N_1$  and  $N_2$  (top),  $\rho$  and  $\rho_2$  (middle) and  $\pi$  and  $\pi_2$  (bottom). All show flavor symmetry restoration.

is underestimating the error because of unexpectedly strong auto-correlation in the pion propagator. We are investigating this issue by accumulating more statistics and by trying various methods of fitting the propagator in extracting the mass [2]. Anyway we are confident that the systematic error is not very serious: it can grow only by a factor of two or so larger than the cited values of statistical error.

## VI. FLAVOR SYMMETRY RESTORATION:

In Figure 2 we plot effective mass of flavor symmetry partners: NG pion  $\pi$  and non-NG one  $\pi_2$ ,  $\rho$  and  $\rho_2$ , and  $N_1$  and  $N_2$ , for the heaviest quark mass value of 0.01. We clearly observe that  $\pi$  and  $\pi_2$  are on top of each other, and so are  $\rho$  and  $\rho_2$ . The same is observed for pions and  $\rho$  mesons for the lighter quark mass values, 0.005, 0.0025 and 0.00125, albeit with more noise. From this we conclude that the flavor symmetry is restored in the present calculation. A similar calculation at slightly smaller value of  $\beta = 6.4$  by the JLQCD collaboration still shows the violation [5]. We also observe that  $N_2$  signal, from the “even-point-wall” source, is nearly flat and  $N_1$ , from the “corner-wall” source, seems to converge with it for large  $t$ . Thus we will use  $N_2$  for nucleon mass estimation.

## VII. IMPLICATION FOR THERMODYNAMICS:

Current lattice-QCD calculations investigating the phase transition or cross over separating the low-temperature hadronic world and the high-temperature quark-gluon-plasma world are typically done on lattices with time-like extent of up to  $N_t = 12$ . On such a lattice the phase transition or cross over occurs at the inverse-squared coupling of  $\beta \leq 6.0$  or the lattice spacing  $a$  larger than 0.05 fm [1]. As many people realize, at such large lattice spacing the flavor symmetry is badly violated: there is at most one light pion and the other pions are all too heavy. This is of course unsatisfactory since pion, as the lightest hadron, should be essential in this phenomenon just like in any other low-energy hadronic physics. According to our hadron mass calculation to achieve the continuum requires  $\beta = 6.5$  or  $a \sim 0.05$  fm. A full-QCD lattice thermodynamics calculations with such spacing to be at the phase transition or cross over in turn requires  $N_t$  of about 24. In other words the linear lattice size would have to be increased by a factor of at least 2, and perhaps 4. The computational complexity would then increase by  $2^{10}$  or  $4^{11}$ . Thus we would need at least 1000 times faster computer and more efficient algorithm [6].

## VIII. PROTON SPIN STRUCTURE:

Another interesting experiment planned to use the RHIC accelerator will be investigating the spin structure of proton. As is shown in Figure 2, our signal from the  $N_2$  nucleon operator is very stable. This will allow us to calculate the moments of proton structure functions, both spin-independent and spin-dependent, very accurately if we get access to a powerful enough super computer<sup>7</sup>.

## REFERENCES

- [1] Steven Gottlieb, review talk in Proc. Int'l Symp. Lattice 96 (St. Louis, June 1996) Nucl. Phys. B (Proc. Suppl.) to be published; preprint hep-lat/9608107.
- [2] S. Kim and S. Ohta, in Proc. Int'l Symp. Lattice 96 (St. Louis, June 1996) Nucl. Phys. B (Proc. Suppl.) to be published; preprint hep-lat/9609023 (= RIKEN-AF-NP-234 = SNUTP-96-086).
- [3] S. Ohta and S. Kim, Nucl. Phys. B (Proc. Suppl.) 42 (1995) 920.
- [4] S. Kim and D.K. Sinclair, Phys. Rev. D48 (1993) 4408; Nucl. Phys. B (Proc. Suppl.) 34 (1994), 347; Phys. Rev. D52 (1995) R2614.
- [5] Talk presented by T. Yoshie for the JLQCD collaboration, in Proc. Int'l Symp. Lattice 96 (St. Louis, June 1996) Nucl. Phys. B (Proc. Suppl.) to be published; preprint hep-lat/9608144.
- [6] N.H. Christ, in these proceedings; F. Karsch, in these proceedings; M. Lombardo, in these proceedings; U. Wiese, in these proceedings.

---

<sup>7</sup>We will also need to clear the renormalon problem.

# Lattice QCD with 0, 2 and 4 Quark Flavors

Robert D. Mawhinney\*

*Columbia University, Department of Physics, New York, NY 10027, USA*

## Abstract

We have done simulations of lattice QCD with different numbers of light dynamical quarks. Since we cannot reach the continuum limit with our current computers, we have done comparisons with 0 (quenched), 2 and 4 light quark flavors with the physical volume and lattice spacing constant, when these are determined from the mass of the rho. We find a 7% ( $2\sigma$ ) difference in the nucleon to rho mass ratio for 2 and 4 quarks. More importantly, the effects of chiral symmetry breaking are dramatically decreased for the case of 4 light quarks.

## I. INTRODUCTION

The role of light dynamical quarks in QCD is not fully understood. Perturbatively, light quarks introduce screening and cause the QCD coupling constant to evolve more slowly. The role of light quarks in the low-energy non-perturbative physics of QCD is much less certain. Of major interest in the numerical study of lattice QCD is a qualitative and quantitative determination of light quark effects in low-energy hadronic physics.

In lattice QCD, many calculations have been done in the quenched approximation [1], where the effects of dynamical quarks are removed. Valence quarks can still be introduced, allowing hadron masses to be measured from the decay of two-point hadronic correlation functions, but there are no closed loops involving quarks. Some quenched calculations report hadron masses in reasonable agreement with experiment but what is not known is whether this trend will continue to weaker couplings. In addition, theoretical arguments in the context of chiral perturbation theory have given predictions for specific ways in which the fermion truncation of the quenched approximation will appear; quenched chiral logarithms. If these quenched chiral logarithms appear in numerical results they will certainly cloud the extraction of hadron masses, etc.

---

\*The two flavor calculation reported here was done at Columbia in collaboration with Shailesh Chandrasekharan, Dong Chen, Norman H. Christ, Weonjong Lee and Decai Zhu. The zero and four flavor calculations were done in collaboration with Dong Chen and Norman Christ at Columbia and Gregory W. Kilcup at the Ohio State University. This work was supported in part by the U.S. Department of Energy.

TABLE I. Parameters for the three simulations reported here. The run length, thermalization, hadron measurement frequency and jackknife block size are in time units.

	$N_f = 4$	$N_f = 2$	$N_f = 0$
volume	$16^3 \times 32$	$16^3 \times 40$	$16^3 \times 32$
$\beta$	5.4	5.7	6.05
$m_{\text{dynamical}}^a$	0.01	0.01	
evolution	HMC	HMD	HMC
run length	4450	4870	187,125
thermalization	250	250	375
acceptance rate	0.95		0.91
trajectory length	0.5	0.5	0.75
step size	0.0078125	0.0078125	0.025
CG stopping condition	$1.13 \times 10^{-6}$	$1.01 \times 10^{-5}$	
total run time	5 months	7.5 months	1.7 months

Lattice QCD calculations with dynamical fermions are less advanced. Inclusion of the fermionic determinant increases the required computer power by at least 2 orders of magnitude. Over the last few years, calculations on  $16^3 \times 32$ ,  $16^3 \times 40$  and  $20^4$  lattices have been done by a number of groups [1]. However, a full data set with various lattice spacings and volumes is not yet available. To date, very little difference has been seen between the quenched and 2 flavor calculations at zero temperature for similar volumes and lattice spacings. (At finite temperature, differences between the quenched and 2 flavor theories with staggered fermions have been seen for a number of years.)

A study of full QCD comparable to the level of current quenched calculations awaits the coming new computers which will push towards the Teraflop scale. Here we report a less ambitious calculation, which still requires about 7 Gigaflop-years of computing; a comparison of 0, 2 and 4 flavor QCD with a fixed lattice spacing and volume (in units of the rho mass extrapolated to zero valence quark mass). The calculations we report only have results for a single dynamical fermion mass, but we have calculated hadron masses and the chiral condensate for a wide variety of valence quark masses. As we detail below, even from this restricted set of simulations, we have seen pronounced effects of dynamical fermions for the four quark case.

Section II gives some details of our calculations. and section III details the valence hadron masses we measured for the three simulations and discusses the major differences between them. In section IV we use a simple model of finite volume effects to support our conclusions about the hadron mass spectrum.

## II. SIMULATION PARAMETERS

We are reporting on three different simulations whose parameters are given in Table I. The simulations were done using the 16 Gigaflop, 256-node computer at Columbia, which is just finishing its seventh year of full time computation. (Additional quenched simulations

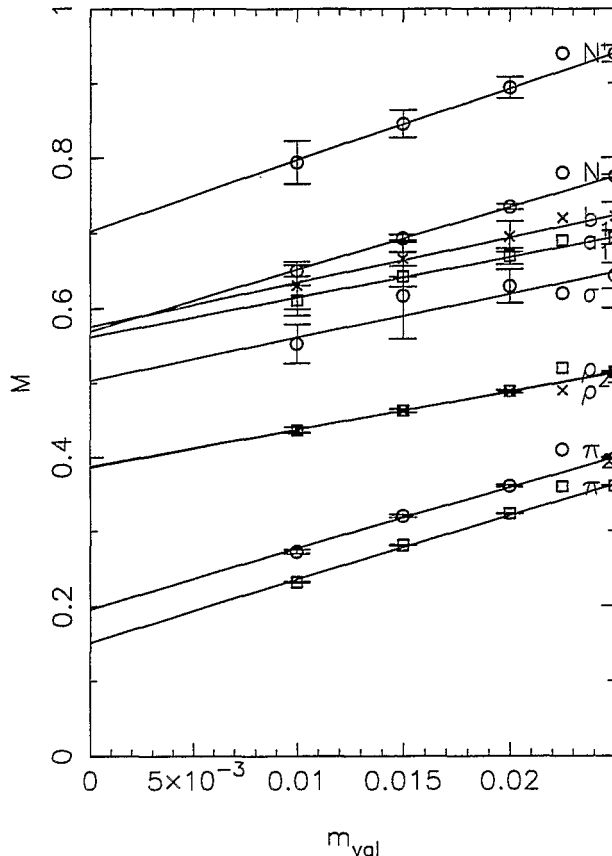


FIG. 1. Hadron masses versus  $m_{\text{val}}$  for the  $16^3 \times 32$  quenched calculation at  $\beta = 6.05$ .

were done by Greg Kilcup using the T3D at the Ohio Supercomputer Center. Some results from these are reported in [2].)

All of our simulations were done with staggered fermions. For 0 and 4 flavors, we used an exact hybrid Monte Carlo algorithm, while for 2 flavors, there is no practical exact algorithm available. The R algorithm we employed has “ $(\Delta t)^2$ ” errors, which means observables will have systematic errors of this order, where for our case  $\Delta t = 0.0078125$ . The high acceptance rate for the exact evolution, which has the same parameters as the inexact evolution (except for the conjugate gradient stopping condition), demonstrates that the  $(\Delta t)^2$  errors are negligible for the inexact case.

We have measured hadron correlators using a variety of different source sizes [3], but only report results here from  $16^3$  wall sources. With staggered fermions, the sinks which are used to select the quantum numbers of the hadronic states can be, and in some cases must be, non-local, due to the fact that the 4 components of the 4 fermionic flavors are delocalized. We have used local sinks for all the hadrons reported here.

### III. RESULTS

Figures 1, 2 and 3 are plots of hadron masses as a function of the valence quark mass. In order to compare the plots, a few major points about staggered fermions should be recalled. At any finite lattice spacing, staggered fermions exhibit flavor symmetry breaking.

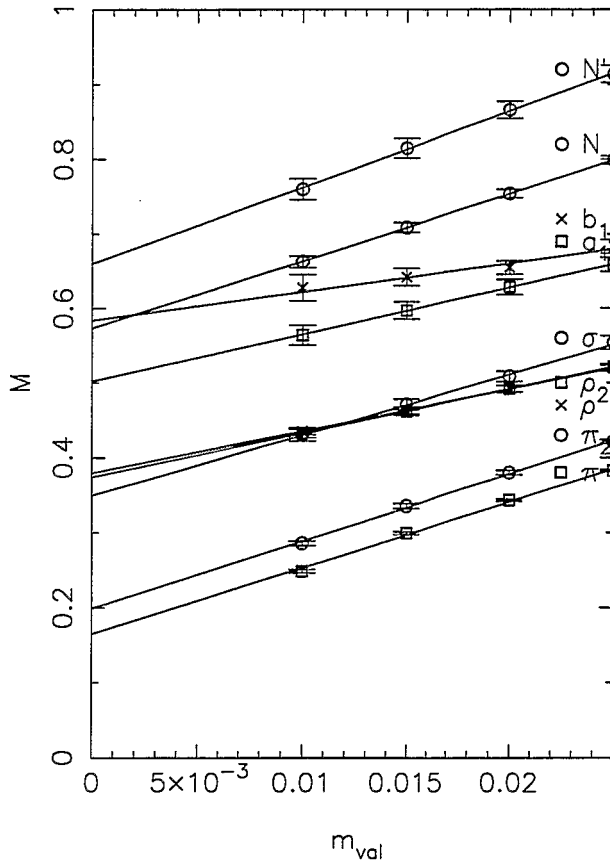


FIG. 2. Hadron masses versus  $m_{\text{val}}$  for the  $16^3 \times 40$  two flavor calculation at  $\beta = 5.7$  with  $m_{\text{dyn}}a = 0.01$ .

The particles labeled  $\rho$  and  $\rho_2$  should become degenerate in the continuum limit and are actually quite degenerate on the lattices we have studied. The  $a_1$  and  $b_1$  correspond to the continuum mesons of the same names, as does the nucleon  $N$ . The  $N'$  is the parity partner of the nucleon.

The  $\pi$  and  $\pi_2$  should also be degenerate in the limit of small lattice spacing, but they are far from degenerate for the lattices we studied. An important feature of staggered fermions is the presence of a  $U(1)$  chiral symmetry, for finite lattice spacing, when the quark mass is set to zero. (This  $U(1)$  symmetry is a subgroup of the  $SU(4)_A$  flavor symmetry of four flavor continuum QCD and must not be confused with the anomalous  $U(1)_A$  symmetry of the continuum.) This  $U(1)$  chiral symmetry of staggered fermions then leads to a Goldstone theorem for the valence pion and the prediction that  $m_\pi^2$  goes linearly to zero as the valence quark mass goes to zero. Note that it is  $m_\pi$  versus  $m_{\text{val}}$  plotted here and not  $m_\pi^2$ , which we will plot later.

The  $\sigma$  particle in these figures is related to the staggered fermion pseudo-Goldstone pion by a  $U(1)$  rotation on the valence quark lines. In the continuum, this  $\sigma$  becomes a scalar, isoscalar particle. However, the  $\sigma$  measured here does not include vacuum bubble contributions. Only quark propagators which start on the source and end on the sink are included in the correlator. This means that for the case where  $m_{\text{val}} = m_{\text{dyn}}$ , the  $\sigma$  mass reported here is not the mass for the scalar, isoscalar particle for full QCD. However, in the



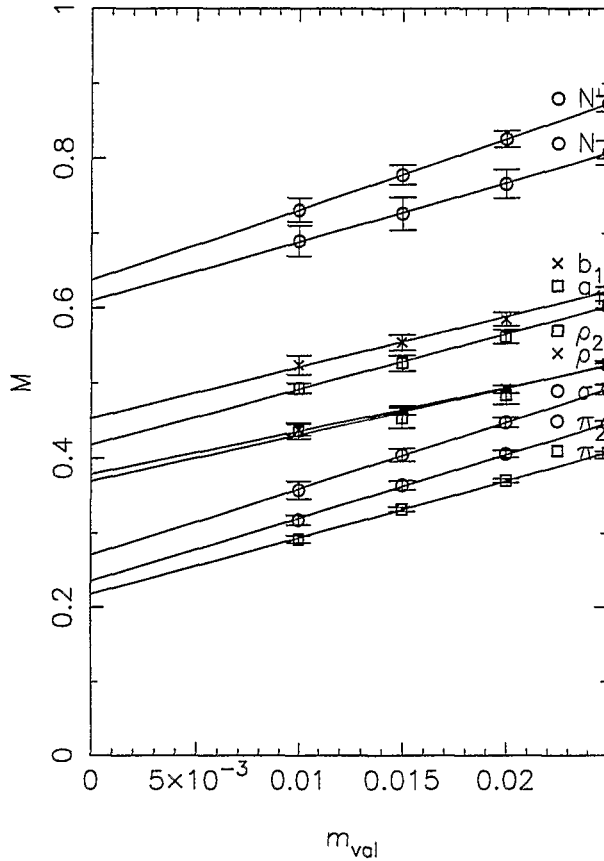


FIG. 3. Hadron masses versus  $m_{\text{val}}$  for the  $16^3 \times 32$  four flavor calculation at  $\beta = 5.4$  with  $m_{\text{dyn}}a = 0.01$ .

absence of chiral symmetry breaking, this  $\sigma$  and the  $\pi$  are degenerate.

Comparing Figures 1, 2 and 3 reveals the following features:

1. For all three calculations, the values of  $\rho$  and  $\rho_2$  agree quite closely for all valence masses and therefore in the extrapolation to  $m_{\text{val}} = 0$ . The agreement at  $m_{\text{val}} = 0$  is a result of our choice of parameters; we wanted to keep the physical volume and lattice size constant in units of the  $\rho$  mass. The fact that there is agreement for all valence masses was unexpected.
2. While  $m_\rho$  is the same for all three simulations,  $m_N$  increases as more quarks are added.
3. The mass of the  $\sigma$  decreases as the number of quark flavors is increased.  $m_\sigma$  is greater than  $m_\rho$  for the quenched calculation and clearly less than  $m_\rho$  for four flavors.
4. The splitting between parity partners ( $\pi, \sigma$ ), ( $\rho, a_1$ ) and ( $N, N'$ ) decreases as the number of dynamical quarks increases. This is evidence for much smaller chiral symmetry breaking effects as the number of dynamical quarks is increased. We will concentrate on this issue in Section IV

The variation in  $m_N/m_\rho$  as the number of dynamical quarks is increased is given in Figure 4. There is very little difference between the quenched and 2 flavor calculations for this

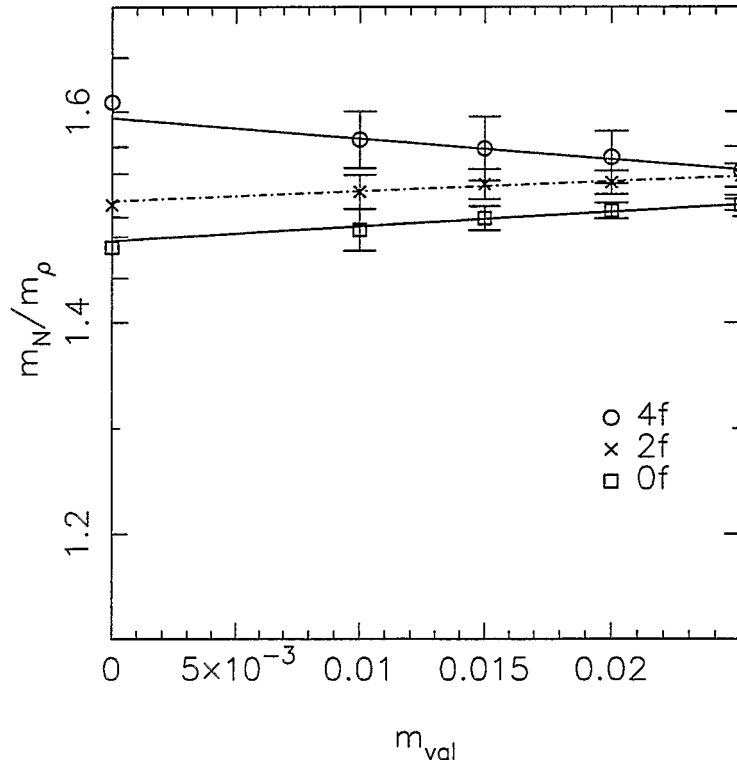


FIG. 4.  $m_N/m_\rho$  vs.  $m_{\text{val}}$  for the 0, 2 and 4 flavor calculations. The points at  $m_{\text{val}} = 0$  are the ratios of the extrapolated quantities, while the line is the extrapolation of the ratios.

quantity. This has been seen by others for  $m_N/m_\rho$  and is also true of other zero-temperature hadronic quantities like  $B_K$ . However, the four flavor calculation is quite distinct from the others. The difference between the 2 and 4 flavor results is about 7% or  $2\sigma$ . The statistical difference of  $2\sigma$  does not make an ironclad case for a difference, however as we have varied our statistical analysis this is the smallest statistical difference we have seen.

Another comparison between the three simulations is given in Figure 5, where  $m_\pi^2$ ,  $m_\sigma^2$  and  $m_{\pi_2}^2$  are plotted versus valence quark mass. As mentioned earlier, the presence of a Goldstone theorem for external quark lines means that  $m_\pi^2$  should go to zero as  $m_{\text{val}} \rightarrow 0$ . This appears to be the case for the quenched approximation, although the extrapolated value for  $m_\pi^2$  is actually 6 standard deviations away from zero. For the 2 and 4 flavor calculations, the intercept is growing relatively larger, until for the 4 flavor calculation the intercepts for  $m_\pi^2$  and  $m_\sigma^2$  are closer to each other than the intercept for  $m_\pi^2$  is to zero.

To summarize, we have observed a systematic difference in the value of  $m_N/m_\rho$  between four flavors and the other calculations. The remaining features we observe in the valence hadron spectrum are easily understood as a decreased strength of chiral symmetry breaking, except the large intercept for  $m_\pi^2$  in the limit  $m_{\text{val}} \rightarrow 0$ . In the next section we use an earlier proposal of ours for finite volume effects to understand this intercept.

#### IV. CHIRAL SYMMETRY BREAKING AND FINITE VOLUME

Before drawing conclusions about the role of light dynamical fermions in four flavor QCD, it is important to be confident that the four flavor simulation we have done has the

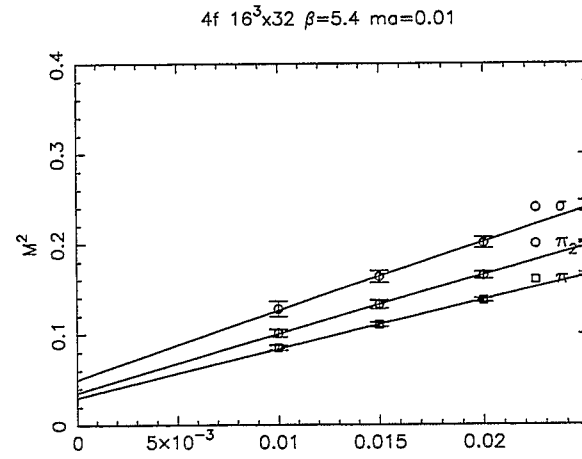
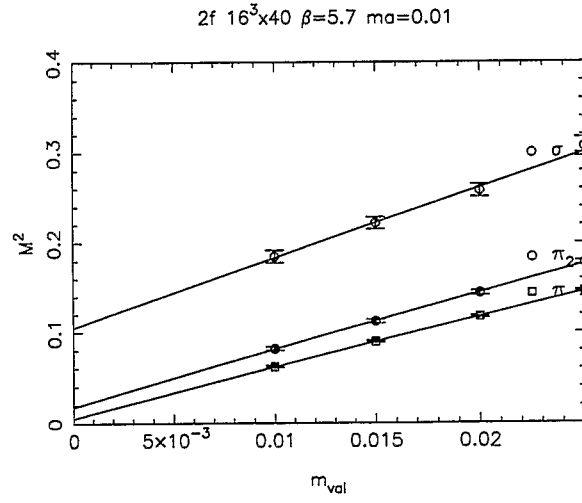
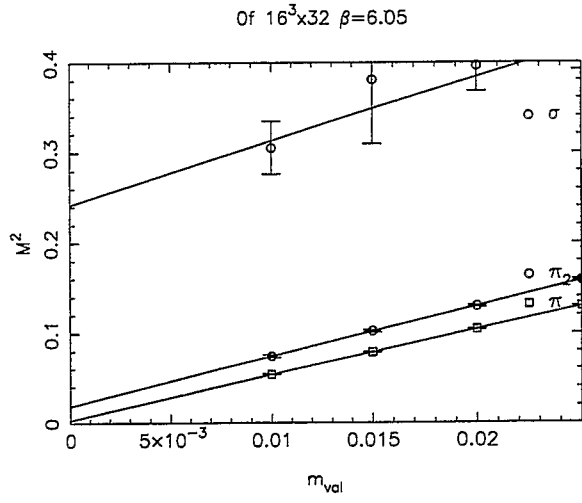


FIG. 5.  $m_\pi^2$ ,  $m_{\pi_2}^2$  and  $m_\sigma^2$  vs.  $m_{\text{val}}$  for the three simulations.

general qualitative properties associated with the continuum limit of QCD, i.e. confinement and chiral symmetry breaking. There can be unexpected phase structure in theories with many fermions [4], so we seek assurance that we are in a phase consistent with continuum QCD. Evidence for confinement comes indirectly through our hadron mass correlators; we see propagating states that fit the same functional forms as for two flavors where we do have bound hadrons. We have also measured Wilson lines and find no evidence for deconfinement.

As mentioned above the four flavor hadron spectrum shows little effect of chiral symmetry breaking. In addition, extrapolations of  $m_\pi^2$  to  $m_{val} = 0$  give a large intercept, in apparent contradiction to the Goldstone theorem. This large intercept effect has been known for some time in quenched simulations and was widely expected to be caused by finite volume effects since the intercept became closer to zero as the volume increased. Recently [5], we have proposed a simple model which can help to quantify the role of finite volume effects in quenched or partially quenched calculations. (Our 2 and 4 flavor calculations are sometimes referred to as partially quenched calculations, since we are discussing valence quark extrapolations on a set of gauge fields that were generated including the effects of quark loops.) To test whether the four flavor results we are seeing are consistent with conventional QCD, we now discuss the role of finite volume effects.

One simple effect of finite volume that has been predicted analytically and is seen numerically is a cutoff in the average eigenvalue density for the Dirac operator. We can observe this effect numerically by measuring the chiral condensate as a function of valence quark mass. In a chirally asymmetric phase, when the valence quark mass is less than the smallest eigenvalue of the Dirac operator, the valence chiral condensate goes to zero linearly with the valence quark mass.

In particular, we write the valence chiral condensate  $\langle \bar{\zeta} \zeta \rangle$  as

$$\langle \bar{\zeta} \zeta(m_\zeta) \rangle = 2m_\zeta \int_0^\infty d\lambda \frac{\bar{\rho}(\lambda, \beta, m_{\text{dyn}})}{\lambda^2 + m_\zeta^2} \quad (1)$$

where  $\bar{\rho}(\lambda, \beta, m_{\text{dyn}})$  is the ensemble average of the density of eigenvalues of the Dirac operator and  $m_\zeta$  is the valence mass for the quark fields  $\zeta$  and  $\bar{\zeta}$ . (These fields do not enter in the dynamics; they are an extra set of fermions used to probe the system.) The ensemble average can depend on the dynamical fermion mass used ( $m_{\text{dyn}}$ ) as well as  $\beta = 6/g^2$ . Our normalization is  $\int d\lambda \bar{\rho}(\lambda, \beta, m_{\text{dyn}}) = 1$ . If  $\bar{\rho}(\lambda, \beta, m_{\text{dyn}})$  is zero (or small) below some  $\lambda_{\text{min}}$ , then equation (1) gives  $\langle \bar{\zeta} \zeta(m_\zeta) \rangle$  going linearly to zero.

To relate this finite volume effect in the quenched chiral condensate to the intercept in the quenched pion mass squared, we use the fact that there is a Gell-Mann–Oakes–Renner relation on the lattice, which is independent of whether the ensemble of gauge fields is quenched or unquenched,

$$C(m_\zeta) = \frac{m_\pi^2(m_\zeta) \langle \bar{\zeta} \zeta(m_\zeta) \rangle}{m_\zeta} \quad (2)$$

where

$$C(m_\zeta) = m_\pi^2(m_\zeta) \int d^4x \langle \pi(x) \pi(0) \rangle \quad (3)$$

(The lattice version of this for staggered fermions is  $\langle \bar{\zeta} \zeta(m_\zeta) \rangle = m \sum_t C_\pi(t)$  where  $C_\pi(t)$  is the staggered fermion pseudo-Goldstone pion correlator [6].)

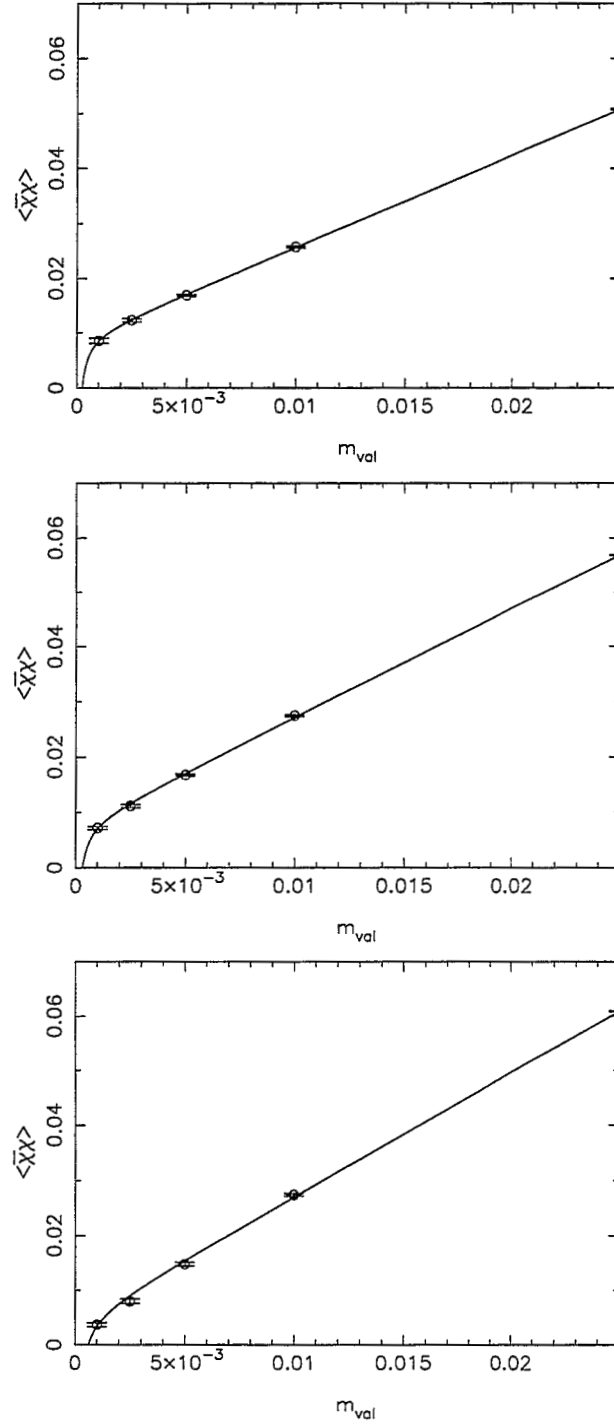


FIG. 6. Fits of  $\langle \bar{\chi}\chi \rangle$  to the form  $a_0 + a_{-1}/m_\zeta + a_1 m_\zeta$  for five values of  $m_\zeta$ . The top figure is for 0 flavors, the middle for 2 and the bottom for 4.

TABLE II. Fit parameters for fits to the form given in equation (4).

	$a_0$	$a_{-1}$	$a_1$	$\chi^2$
0f	0.00917(23)	$-2.38(53) \times 10^{-6}$	1.669(10)	1.0(17)
2f	0.00765(29)	$-2.61(17) \times 10^{-6}$	1.973(7)	7.6(52)
4f	0.00488(41)	$-3.77(19) \times 10^{-6}$	2.245(15)	15(13)

As shown in [5], the assumption that  $\bar{\rho}(\lambda, \beta, m_{\text{dyn}})$  drops dramatically below some  $\lambda_{\text{min}}$  and is constant for  $\lambda_{\text{min}} < \lambda < \lambda_0$  leads to the result that

$$\langle \bar{\zeta}\zeta(m_\zeta) \rangle = a_0 + a_1 m_\zeta + a_{-1}/m_\zeta + O(m_\zeta^2) + O(m_\zeta^{-2}), \quad (4)$$

for  $\lambda_{\text{min}} < m_\zeta < \lambda_0$ . Figure 6 shows plots of  $\langle \bar{\zeta}\zeta(m_\zeta) \rangle$  for our simulations. The curvature at  $m_\zeta \sim 10^{-4}$  is the onset of finite volume effects.

Now, assuming  $C(m_\zeta)$  is a smooth function of  $m_\zeta$  in the range  $\lambda_{\text{min}} < m_\zeta < \lambda_0$ , we have

$$m_\pi^2 = -\frac{C(0)a_{-1}}{a_0^2} + \left[ \frac{C(0)}{a_0} - \frac{C'(0)a_{-1}}{a_0^2} \right] m_\zeta + \dots \quad (5)$$

Thus a non-zero intercept for  $m_\pi^2$  can be related to the finite volume cutoff in the Dirac eigenvalue spectrum since  $a_{-1} \sim -\lambda_{\text{min}}$ .

Uncorrelated fits to our measurements of  $\langle \bar{\zeta}\zeta \rangle$  are given in Table II. The error on  $\chi^2$  is the jackknifed error on this quantity. For four flavors, we find that  $a_{-1}/a_0^2$  is about 3.6 times as large as the two flavor value, while the ratio of the  $m_\pi^2$  intercepts is about 5.6. There is clearly some  $N_f$  dependence in  $C(m_\zeta)$ , or higher order terms we have neglected in (5) are important for good quantitative agreement.

This analysis supports the conclusion that we are in a phase with chiral symmetry breaking, although the breaking is small. The small amount of breaking (small  $a_0$ ) in a finite volume (non-zero  $a_{-1}$ ) leads to a large intercept for  $m_\pi^2$ . We are investigating the possible  $N_f$  dependence of  $C(m_\zeta)$  and are working on a determination of  $f_\pi$  for the four flavor calculation.

## V. CONCLUSIONS

We have seen that increasing the number of light dynamical quarks to four does alter the valence hadron spectrum at zero temperature. The change in the nucleon to rho mass ratio is about 7% and seems resolved by our statistics. A much larger effect is seen in the amount of chiral symmetry breaking on the lattices. The hadron spectrum exhibits much less chiral symmetry breaking, which is consistent with the suppression of small eigenvalues of the Dirac operator due to the fermionic determinant.

By checking the role of finite volume effects in distorting chiral symmetry breaking, we have argued that our four flavor results are consistent with a chirally asymmetric, confining theory. To gain further evidence for the explanation proposed here, calculations of the explicit eigenvalue density are being done in collaboration with Robert Edwards from SCRI.

Of great interest is whether the effects we have seen for valence calculations done on a dynamical fermion background persist when the dynamical and valence masses are varied together. We are currently undertaking another four flavor calculation at a different dynamical quark mass to gain some insight into this question.

## ACKNOWLEDGEMENTS

We would like to thank Catalin Malareanu for measuring the Wilson lines on our lattices.

## REFERENCES

- [1] D. K. Sinclair, Nucl. Phys. **B** (Proc. Suppl.) **47** (1996) 112; S. Gottlieb, hep-lat/9608107, to appear in the proceedings of Lattice '96.
- [2] D. Chen and R. D. Mawhinney, to appear in the proceedings of Lattice '96, St. Louis, June 1996.
- [3] Dong Chen, Columbia University PhD Thesis, September, 1996.
- [4] F. R. Brown, *et. al.*, Phys. Rev. **D46** (1992) 5655.
- [5] R. D. Mawhinney, Nucl. Phys. **B** (Proc. Suppl.) **47** (1996) 557.
- [6] G. W. Kilcup and S. R. Sharpe, Nucl. Phys. **B283** (1987) 493.

# Improved QCD Thermodynamics

Frithjof Karsch

*Fakultät für Physik, Universität Bielefeld, D-33615 Bielefeld, Germany*

## Abstract

We will discuss recent advances in the calculation of thermodynamic observables using improved actions. In particular, we will discuss the calculation of the equation of state of the  $SU(3)$  gauge theory, the critical temperature in units of the string tension, the surface tension and the latent heat at the deconfinement transition. We also will present first results from a calculation of the equation of state for four-flavour QCD using an  $\mathcal{O}(a^2)$  improved staggered fermion action.

## I. INTRODUCTION

The idea that strongly interacting hadronic matter undergoes a phase transition to a new phase, the quark-gluon plasma, has been around for a long time. More than 10 years ago lattice calculations have given first direct evidence for the existence of such a phase transition and opened the way for its detailed quantitative analysis. Many of the non-perturbative features of finite temperature QCD, which have been developed in a perturbative context in order to get control over the infra-red behaviour of QCD, have since then been studied in lattice calculations. However, many of these numerical studies also had to remain on a qualitative level for a long time because the simulations on coarse lattices were hampered by large discretization errors and calculations at smaller lattice spacing suffered from poor statistical accuracy.

Indeed, it is well known that the non-zero lattice spacing introduces severe problems in thermodynamic calculations, which in the past made a direct comparison with the physics in the continuum limit difficult. For instance, already the thermodynamics of a free Bose (gluon) or Fermi (quark) gas deviates strongly from the well-known Stephan-Boltzmann result when calculated on coarse Euclidean lattices. This problem carries over to QCD. Although the plasma phase of QCD does in many respects show strong non-perturbative properties (screening masses, poor convergence of perturbation theory,...), bulk thermodynamic observables like energy density and pressure do rapidly come close to the non-interacting ideal gas limit above the QCD phase transition. The calculation of these quantities is thus expected to suffer from similarly strong cut-off effects as the ideal gas.

At high temperature the relevant contributions to thermodynamic observables result from momentum modes which are of the order of the temperature, *i.e.* the average momentum is proportional to  $T$ . However, in lattice calculations  $T$  is fixed through the temporal extent,  $N_\tau$ , of the lattice and the cut-off  $a^{-1}$ , *i.e.*  $T \equiv 1/N_\tau a$ . The relevant momenta,  $\langle p \rangle \sim 3T$ , are therefore of the order of the cut-off, where lattice and continuum dispersion relations differ



strongly from each other. Indeed this is the origin of the well-known discrepancy between the energy density of an ideal gas calculated on a finite lattice ( $\epsilon(N_\tau)$ ) and in the continuum ( $\epsilon_{\text{SB}}$ ). The cut-off dependence in finite temperature calculations thus shows up as a *finite size effect*, which should not be confused with the finite size dependence resulting from the spatial extent of the lattice. The latter is an infra-red effect and controls the approach to the thermodynamic limit.

In the next section we briefly discuss the Symanzik improved actions, which recently have been used in thermodynamic calculations. Results for the  $SU(3)$  gauge theory and four-flavour QCD are discussed in Sections 3 and 4.

## II. IMPROVED ACTIONS

During the last few years much progress has been made in dealing with the systematic discretization errors in lattice regularized quantum field theories. Various improved discretization schemes for the Lagrangian of QCD have been constructed and explored, which do show much less cut-off dependence than the prescription originally given by Wilson.

When formulating a discretized version of QCD one has a great deal of freedom in choosing a lattice action. Different formulations may differ by subleading powers of the lattice cut-off, which vanish in the continuum limit. This has, for instance, been used by Symanzik to systematically improve lattice regularized  $SU(N)$  gauge theories [1]. In addition to the elementary plaquette term appearing in the standard Wilson formulation of lattice QCD larger loops can be added to the action in such a way that the leading  $\mathcal{O}(a^2)$  deviations from the continuum formulation are eliminated and corrections only start in  $\mathcal{O}(a^4)$ . Examples for the *Symanzik improved* actions are, for instance, the actions  $S^{(1,2)}$  and  $S^{(2,2)}$ , where appropriately weighted contributions from planar (1,2) or (2,2) loops, have been added to the Wilson plaquette action,  $S^{(1,1)}$ ,

$$\begin{aligned}
S^{(1,2)} &= \sum_{x,\nu>\mu} \frac{5}{3} \left( 1 - \frac{1}{N} \text{Re Tr } \square_{\mu\nu}(x) \right) - \frac{1}{6u_0^2} \left( 1 - \frac{1}{2N} \text{Re Tr } \left( \square_{\mu\nu}(x) + \square_{\nu\mu}(x) \right) \right) \\
S^{(2,2)} &= \sum_{x,\nu>\mu} \frac{4}{3} \left( 1 - \frac{1}{N} \text{Re Tr } \square_{\mu\nu}(x) \right) - \frac{1}{48u_0^4} \left( 1 - \frac{1}{N} \text{Re Tr } \square_{\mu\nu}(x) \right) . \quad (1)
\end{aligned}$$

For  $u_0 \equiv 1$  these are examples for tree level improved actions which can systematically be further improved by adding additional loops to the action. One-loop corrections can be taken into account through  $\mathcal{O}(g^2)$  corrections to the weight factors for each loop. A non-perturbative procedure to select these weight factors has been introduced recently [2]. Here the factor  $u_0$  appearing in the definition of the Symanzik actions is determined self-consistently from plaquette expectation values [2],  $u_0^4 = \frac{1}{6N_\tau^3 N_\tau} \langle \sum_{x,\nu>\mu} (1 - \frac{1}{N} \text{Re Tr } \square_{\mu\nu}(x)) \rangle$ . This non-perturbative approach is expected to reduce the cut-off dependence also at non-vanishing values of the gauge coupling and does approach the tree level form of the action for small values of  $g^2$ . Indeed, rather encouraging results have been obtained at zero temperature for observables which are sensitive to short distance scales. Other improvement schemes based on renormalization group techniques have been developed with great success in the last years. We will not discuss them here but rather refer to recent reviews [3,4].

The importance of improved actions for thermodynamic calculations does become immediately evident from an analysis of the high temperature gluon gas on lattices of size  $N_\sigma^3 N_\tau$ . One indeed finds a strong reduction of the cut-off dependence relative to the standard Wilson formulation. For instance, the deviation of the energy density from the continuum result,  $\epsilon_{\text{SB}}$ , which has been calculated in the thermodynamic limit ( $N_\sigma \rightarrow \infty$ ) on a lattice with temporal extent  $N_\tau$  is drastically reduced,

$$\frac{\epsilon(N_\tau)}{\epsilon_{\text{SB}}} \begin{cases} 1 + \frac{30}{63} \cdot \left(\frac{\pi}{N_\tau}\right)^2 + \frac{1}{3} \cdot \left(\frac{\pi}{N_\tau}\right)^4 + \mathcal{O}(N_\tau^{-6}) & , \text{ Wilson} \\ 1 + 0 + c_I \cdot \left(\frac{\pi}{N_\tau}\right)^4 + \mathcal{O}(N_\tau^{-6}) & , \text{ Symanzik} \end{cases} \quad (2)$$

Although one has no control over the subleading corrections when setting up the systematic  $\mathcal{O}(a^2)$  improvement it turns out that in many cases not only the  $\mathcal{O}(a^2)$  corrections get eliminated but also the  $\mathcal{O}(a^4)$  corrections get reduced. In the case of the (1,2)-Symanzik action the leading  $N_\tau^{-4}$  correction is, in fact, nearly an order of magnitude smaller, *i.e.*  $c_I = 0.044$ , which is to be compared with  $1/3$  in the Wilson case. As a consequence one finds already on lattices with temporal extent  $N_\tau = 4$  that the cut-off dependence is drastically reduced in the case of Symanzik improved actions. While the Wilson action leads to nearly 50% deviations from the continuum Stephan-Boltzmann gas value on this size lattices the deviations from the continuum result are less than 2% in the case of the (1,2)-Symanzik improved action. This clearly demonstrates the importance of improved actions for the description of the high temperature phase of QCD, which asymptotically approaches the ideal gas limit ( $T \rightarrow \infty$ ).

A similar systematic improvement as discussed above for the gluonic sector can be achieved in the fermion sector. We will present first results for four-flavour QCD in Section 4. In the next section we start with a discussion of results obtained for the thermodynamics of the pure SU(3) gauge theory using tree level and tadpole improved actions [5–8].

### III. SU(3) THERMODYNAMICS

Only recently calculations with the standard Wilson action could be extended to lattices with sufficiently large temporal extent ( $N_\tau = 6$  and 8) that would allow an extrapolation of lattice results for bulk thermodynamic quantities to the continuum limit [9,10]. Computationally the step from  $N_\tau = 4$  to  $N_\tau = 8$  is quite non trivial as the computer time needed to achieve numerical results with the same statistical significance on a two times larger lattice increases roughly like  $2^{10}$ . It therefore is highly desirable to use improved actions, which suffer less from discretization errors, also for thermodynamic calculations.

We have analyzed the thermodynamics of the SU(3) gauge theory using the  $\mathcal{O}(a^2)$  improved tree level ( $u_0 \equiv 1$ ) and tadpole ( $u_0 < 1$ ) improved actions defined in Eq. 1. As discussed above it seems to be plausible that improved actions will help to reduce the cut-off dependence of thermodynamic quantities in the high temperature plasma phase. It is, however, less evident that this also is of advantage for calculations close to the deconfinement phase transition where the physics is strongly dependent on contributions from infrared modes. In addition to a calculation of the equation of state an analysis of the cut-off dependence of the critical temperature itself as well as properties of the first order deconfinement transition like the surface tension and latent heat are therefore of interest.

## A. The critical temperature

When comparing the cut-off dependence of thermodynamic observables one, of course, has to make sure that these are compared at the same value of the cut-off. On lattices with fixed temporal extent this amounts to a comparison at the same value of the temperature, which, for instance, can be defined in terms of the critical temperature for the deconfinement transition, *i.e.*  $T/T_c$ . Also the determination of this temperature scale is influenced by the finite lattice spacing and will contribute to the overall cut-off dependence of thermodynamic observables. An indication for the size of cut-off dependence in the definition of a temperature scale can be deduced from a calculation of the critical temperature in units of  $\sqrt{\sigma}$ . The ratio  $T_c/\sqrt{\sigma}$  has been studied in quite some detail at different values of the cut-off for the  $SU(3)$  gauge theory using the Wilson action. An extrapolation of these results to the continuum limit yields [10]

$$\frac{T_c}{\sqrt{\sigma}} = 0.629 \pm 0.003 . \quad (3)$$

When comparing calculations of  $T_c/\sqrt{\sigma}$  at the critical coupling for  $T_c$  on an  $N_\tau = 4$  lattice with Eq. 3 one observes a change of the ratio by roughly 10%. A calculation of this ratio with a tree level improved Symanzik action at a comparable value of the cut-off (critical coupling on a  $N_\tau = 4$  lattice) does, on the other hand, yield results which differ little from the continuum extrapolation for the Wilson action. In fact, results are within statistical errors consistent with Eq. 3. The inclusion of an additional tadpole improvement factor does yield only small modifications. Some results for the ratio  $T_c/\sqrt{\sigma}$  at the cut-off value  $aT_c = 0.25$  are given in Table I.

TABLE I. Critical temperature in units of  $\sqrt{\sigma}$  on lattices with temporal extent  $N_\tau = 4$ , *i.e.* at a value of the cut-off given by  $aT_c = 0.25$ . Infinite volume extrapolations of  $\beta_c$  for the Symanzik actions are based on lattices with  $N_\sigma = 16, 24$  and  $32$ .

action	$N_\sigma$	$\beta_c$	$T_c/\sqrt{\sigma}$
standard Wilson	$\infty$	5.69254 (24)	0.5983 (30)
(2,2) Symanzik (tree)	24	4.3995 (2)	0.624 (4)
(1,2) Symanzik (tree)	$\infty$	4.07297 (28)	0.631 (3)
(1,2) Symanzik (tadp.)	$\infty$	4.35228 (39)	0.635 (3)

It should be noted here that a recent analysis of the ratio  $T_c/\sqrt{\sigma}$  using a renormalization group improved action led to a somewhat large value [11] ( $T_c/\sqrt{\sigma} = 0.657$  (5)). Although the difference is only about 3% this does seem to be larger than the errors quoted. Here one has to keep in mind that the determination of the string tension is, in fact, quite involved. It does seem that the good consistency between the results from different actions quoted in Table I also has been achieved because the string tension has been analyzed in the same way for all cases. It seems that the slightly larger value obtained in [11] does reflect the different approach taken there to calculate the string tension rather than a different cut-off dependence for the Symanzik and renormalization group actions.

## B. Bulk thermodynamics

Bulk thermodynamic quantities like the energy density ( $\epsilon$ ) or pressure ( $p$ ) calculated with the Wilson action on lattices of size  $N_\sigma^3 N_\tau$  with  $N_\tau = 4, 6$  and  $8$  [10] show a strong cut-off dependence in the plasma phase. A first analysis with the tree level improved (2,2)-Symanzik action [5] has shown that this cut-off dependence gets drastically reduced already on a  $N_\tau = 4$  lattice. This is true also for the (1,2)-Symanzik action, the tadpole improved (1,2)-Symanzik action [7] and a fixed point action [12] which all yield results consistent with the continuum extrapolation performed for the standard Wilson action. As an example we discuss here the pressure.

The pressure can be obtained from an integration of the difference of action densities at zero ( $S_0$ ) and finite ( $S_T$ ) temperature [13],

$$\frac{p}{T^4} \Big|_{\beta_0}^{\beta} = N_\tau^4 \int_{\beta_0}^{\beta} d\beta' (S_0 - S_T), \quad (4)$$

where the zero temperature calculations are performed on a large lattice of size  $N_\sigma^4$  and the finite temperature calculations are performed on lattices of size  $N_\sigma^3 N_\tau$ . In order to compare calculations performed with different actions one has to determine a physical temperature scale. This can, for instance, be achieved through a calculation of the string tension at some value of the gauge coupling ( $\beta$ ) and at the critical coupling for the phase transition on a lattice of temporal size  $N_\tau$ . This yields  $T/T_c \equiv \sqrt{\sigma}(\beta_c)/\sqrt{\sigma}(\beta)$ . We show in Figure 1 the results of a calculation of the pressure. The strong cut-off dependence for the Wilson action is clearly seen in Figure 1a. The continuum extrapolation obtained from this calculation [10] is in good agreement with the results obtained with improved actions on lattices of temporal extent  $N_\tau = 4$  (Figure 1b).

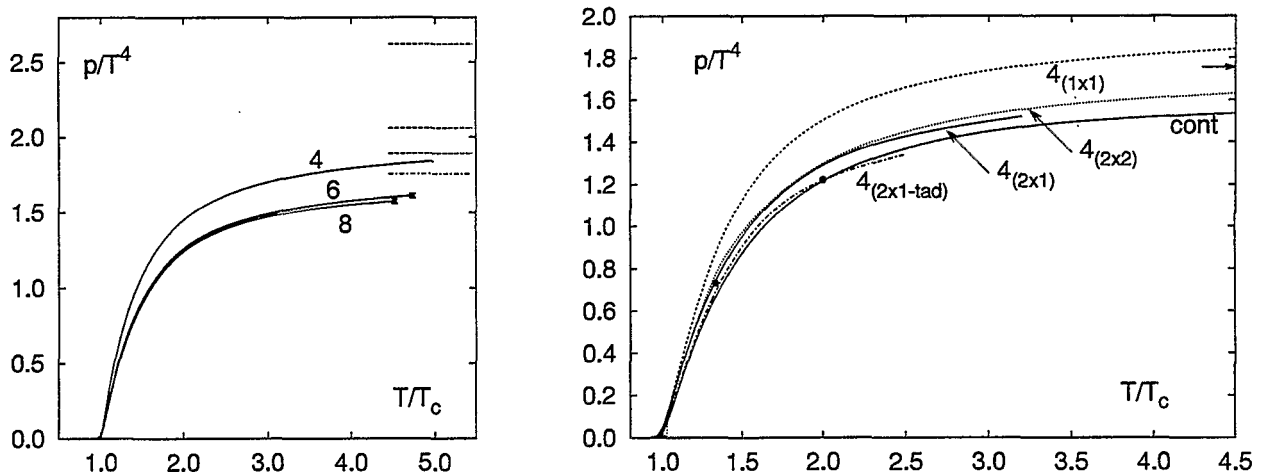


FIG. 1. Pressure of the SU(3) gauge theory calculated with the Wilson action (a) and different improved actions (b). In the latter case the temporal extent of the lattice is  $N_\tau = 4$  while it is  $N_\tau = 4, 6$  and  $8$  for the Wilson action. The solid line in (b) shows the continuum extrapolation obtained from the standard Wilson action. The dots give results from a calculation with a perfect action on a  $12^3 \times 3$  lattice [12]. The arrow indicates the continuum ideal gas value.

It thus seems that systematic errors in the calculation of the equation of state which result from the lattice discretization are well under control for the SU(3) gauge theory. In Figure 2

we show the energy density, pressure and entropy density obtained from an extrapolation of results obtained with the standard Wilson action. We note the rapid rise in all observables at

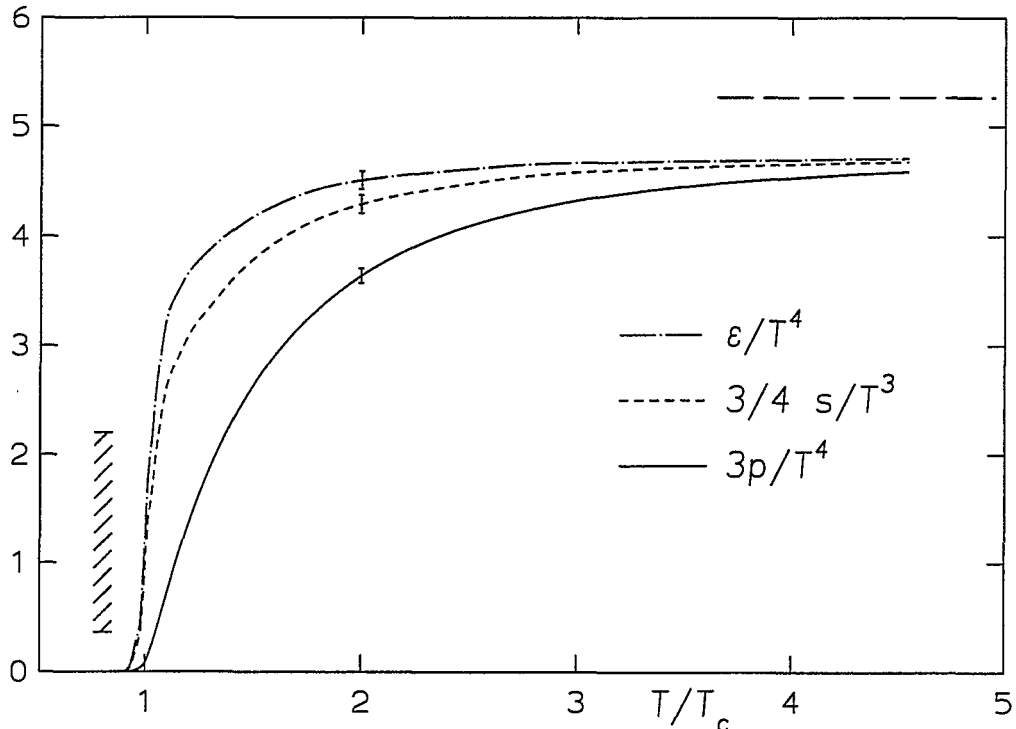


FIG. 2. Extrapolation to the continuum limit for the energy density, entropy density and pressure versus  $T/T_c$ . The dashed horizontal line shows the ideal gas limit. The hatched vertical band indicates the size of the discontinuity in  $\epsilon/T^4$  (latent heat) at  $T_c$ . Typical error bars are shown for all curves.

$T_c$  followed by a rather slow approach to the asymptotic ideal gas behaviour. The latter is in accordance with the expectation that the high temperature behaviour of QCD is controlled by a universal function, which only depends on a *running coupling* that varies logarithmically with temperature. However, the (15-20)% deviations from the ideal gas limit observed at temperatures as large as  $5T_c$  are, in fact, too large to be described by perturbation theory. The perturbative expansion of the thermodynamic potential is converging quite badly and would require a running coupling which is significantly smaller than unity [14,15]. As a consequence, the perturbative expansion does seem to converge only for temperatures much larger than  $T_c$ . In particular, the calculation of screening lengths on the lattice do, however, suggest that the running coupling is larger than unity even at  $5T_c$  [17].

A quantity which is very sensitive to deviations from the perturbative high temperature limit is the trace anomaly of the energy-momentum tensor,  $T_\mu^\mu \equiv \epsilon - 3p$ . It defines the temperature dependent gluon condensate [16]

$$\epsilon - 3p = \langle G^2 \rangle_{T=0} - \langle G^2 \rangle_T . \quad (5)$$

As the left hand side will, for high temperatures, be proportional to  $T^4$  the first term on the

right hand side,  $\langle G^2 \rangle_{T=0}$ , will soon become negligible. The temperature dependent gluon condensate may then be compared to the perturbative calculation of  $\epsilon - 3p$  [18]

$$\frac{\epsilon - 3p}{T^4} = \frac{11N^2}{12\pi^2} \left[ \frac{(N^2 - 1)}{288} g^4(T) - \frac{N^2 - 1}{16N\pi} \left( \frac{N}{3} \right)^{3/2} g^5(T) + O(g^6) \right]. \quad (6)$$

In the case of  $SU(3)$  we thus expect in the perturbative limit to find  $(\epsilon - 3p)/T^4 = 0.02322g^4 - 0.04435g^5 + O(g^6)$ . This does reflect the poor convergence of the perturbative expansion which also persists at higher orders [14,15].

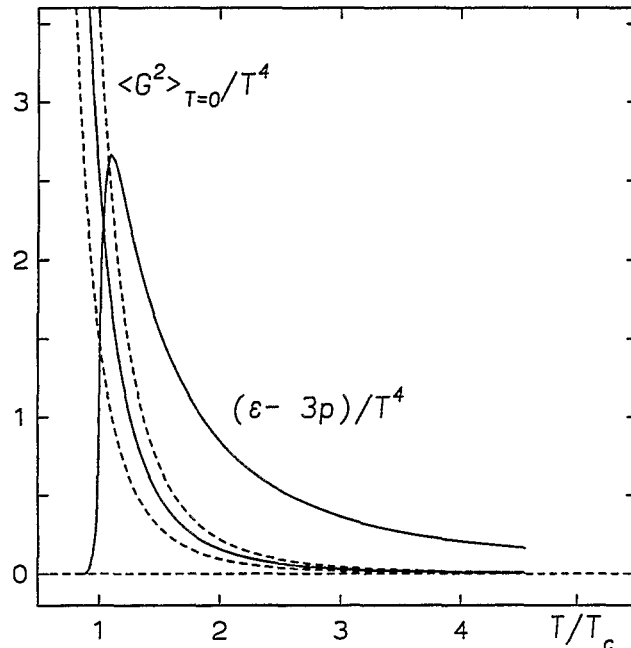


FIG. 3. The zero temperature gluon condensate divided by  $T^4$  and  $(\epsilon - 3p)/T^4$  versus  $T/T_c$ . The dashed band shows the uncertainty in the zero temperature gluon condensate value [16].

In Figure 3 we compare the contribution from the non-vanishing gluon condensate in the vacuum with the calculated  $(\epsilon - 3p)/T^4$ . It is evident, that  $\langle G^2 \rangle_{T=0}$  does contribute to the peak in this quantity. However, this contribution rapidly becomes negligible above  $T_c$ . On the other hand it is also clear from the leading order perturbative result given in Eq. 6 that this cannot give a satisfactory description of the equation of state for temperatures  $T \sim 5T_c$ . Here a running coupling  $g^2(T) \sim 2$  would be needed in order to describe the numerical results in terms of the leading order correction. However, for such a large value of  $g^2(T)$  higher order corrections clearly cannot be neglected.

### C. Surface tension and latent heat

The success of improved actions for the calculation of bulk thermodynamics even at temperatures close to  $T_c$  naturally leads to the question whether these actions also do lead to an improvement at  $T_c$  where a strong cut-off dependence has been observed previously in

the calculation of the latent heat ( $\Delta\epsilon$ ) and the surface tension ( $\sigma_I$ ). The region around  $T_c$  is, of course, a highly non-perturbative regime. However, observables like  $\Delta\epsilon$  and  $\sigma_I$ , which characterize the discontinuities at the first order deconfinement phase transition in a  $SU(3)$  gauge theory, do depend on properties of the low as well as the high temperature phase. As the latter is largely controlled by high momentum modes it may be expected that some improvement does result even from tree level improved actions.

At the  $SU(3)$  deconfinement transition  $\Delta\epsilon$  and  $\sigma_I$  have been studied on lattices up to temporal extent  $N_\tau = 6$  [19,20] using the standard Wilson action. A strong cut-off dependence has been found when comparing calculations for  $N_\tau = 4$  and 6. For this reason an extrapolation to the continuum limit has so far not been possible for these observables.

We have extracted  $\sigma_I$  [7] from the probability distribution of the absolute value of the Polyakov loop,  $P(|L|)$ , following the analysis presented in Ref. [20]. The probability distribution at the minimum is proportional to

$$P(|L|) \sim \exp(-[f_1 V_1 + f_2 V_2 + 2\sigma_I A]/T) \quad (7)$$

where  $f_i$  denotes the free energy in the phase  $i$ , and  $V_i$  is the volume occupied by that phase and  $A$  denotes the interface area of the finite system. The distribution functions for the tadpole improved actions for three different lattice sizes are shown in Figure 4. From the depth of the minimum one can extract the surface tension.

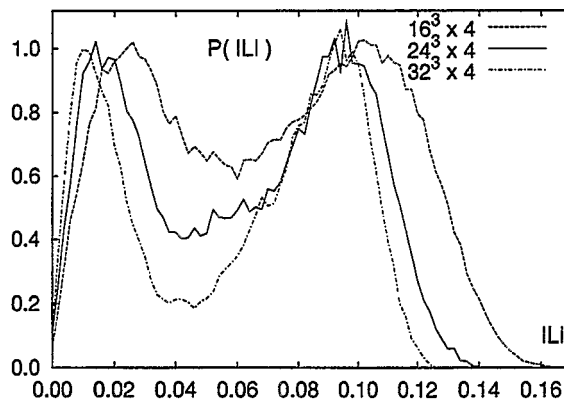


FIG. 4. Polyakov loop distributions for the tadpole improved (1,2) Symanzik action.

In Table II we give results for  $\sigma_I$  on the largest lattices considered. Clearly the surface tension extracted from simulations with improved actions on lattices with temporal extent  $N_\tau = 4$  are substantially smaller than corresponding results for the Wilson action. In fact, they are compatible with the  $N_\tau = 6$  results for the Wilson action.

The latent heat is calculated from the discontinuity in  $(\epsilon - 3p)$ . This in turn is obtained from the discontinuity in the various Wilson loops entering the definition of the improved actions,

$$\frac{\Delta\epsilon}{T_c^4} = \frac{1}{6} \left( \frac{N_\tau}{N_\sigma} \right)^3 \left( a \frac{d\beta}{da} \right) \left( \langle \tilde{S} \rangle_+ - \langle \tilde{S} \rangle_- \right), \quad (8)$$

with  $\tilde{S} \equiv S - dS/d\beta$ .

TABLE II. Surface tension and latent heat for the three improved actions and the Wilson action. Results for the Wilson action are based on data from [20] using the non-perturbative  $\beta$ -function calculated in [10].

action	$V_\sigma$	$N_\tau$	$\sigma_I/T_c^3$	$\Delta\epsilon/T_c^4$
standard Wilson	$24^2 \times 36$	4	0.0300 (16)	2.27 (5)
	$36^2 \times 48$	6	0.0164 (26)	1.53 (4)
(1,2) Symanzik (tree)	$32^3$	4	0.0116 (23)	1.57 (12)
(1,2) Symanzik (tadp.)	$32^3$	4	0.0125 (17)	1.40 (9)

The difference of action expectation values at  $\beta_c$  is obtained by calculating these in the two coexisting phases at  $\beta_c$ . In order to extract the latent heat one does still need the  $\beta$ -function entering the definition of  $\Delta\epsilon/T_c^4$  in Eq. 8. The necessary relation  $a(\beta)$  has been obtained from a calculation of  $\sqrt{\sigma}a$  (improved actions) or a determination of  $T_c a$  (Wilson action). Results for  $\Delta\epsilon/T_c^4$  are summarized in Table II.

In particular the comparison with results obtained with tadpole improved actions on even coarser lattices ( $N_\tau = 3$ ) [7] suggests that the values obtained for the latent heat with improved actions on lattices with temporal extent  $N_\tau = 4$  only have a small additional cut-off dependence. We thus may use these results to estimate the latent heat in the continuum limit. Using Eq. 3 and  $\sqrt{\sigma} = 420$  Mev we find

$$\Delta\epsilon \simeq 1.5T_c^4 = 0.23\sigma^2 = 0.9 \text{ GeV/fm}^3 \quad (9)$$

From Figure 2 we find that the energy density on the confinement side of the transition is about 1/3 of this value, the critical energy density on the plasma side thus is about  $1.2 \text{ GeV/fm}^3$ .

#### IV. FOUR-FLAVOUR QCD WITH AN IMPROVED STAGGERED ACTION

In the fermionic sector of QCD the influence of a finite cut-off on bulk thermodynamic observables is known to be even larger than in the pure gauge sector. For instance, in the staggered formulation the energy density of an ideal fermi gas differs by more than 70% from the continuum value on a lattice with temporal extent  $N_\tau = 4$  and approaches the continuum value only very slowly with increasing  $N_\tau$ . This cut-off dependence can drastically be reduced with an  $O(a^2)$  improved staggered action. We have used an improved action,  $S^I[U] = S^{(1,2)} + \bar{\psi}M\psi$ , where a higher order difference scheme (one-link and three-link terms), is used to improve the fermionic part [21]. The improved fermion matrix reads

$$M[U]_{ij} = m\delta_{i,j} + \eta_i \left( \frac{9}{16}A[U]_{i,j} - \frac{1}{48}B[U]_{i,j} \right)$$

with

$$A[U]_{ij} = \sum_{\mu} \left( U_{i,\mu} \delta_{i,j-\hat{\mu}} - U_{i-\hat{\mu},\mu}^\dagger \delta_{i,j+\hat{\mu}} \right)$$

$$B[U]_{ij} = \sum_{\mu} \left( U_{i,\mu} U_{i+\hat{\mu},\mu} U_{i+2\hat{\mu},\mu} \delta_{i,j-3\hat{\mu}} - U_{i-\hat{\mu},\mu}^\dagger U_{i-2\hat{\mu},\mu}^\dagger U_{i-3\hat{\mu},\mu}^\dagger \delta_{i,j+3\hat{\mu}} \right)$$



In the gluonic sector we use the tree level improved (1,2)-Symanzik action. With this action the overall cut-off distortion for the ideal gas limit on a  $16^3 \times 4$  lattices reduces to about 20%. We have performed simulations for two quark masses,  $ma = 0.05$  and  $0.1$  [8]. Like in the pure gauge sector the improvement is visible already close to  $T_c$ .

The general structure of the four-flavour equation of state does not differ much from that of the pure gauge theory. In fact, the temperature dependence of the pressure is very similar to that of the pure gauge theory, if we rescale the latter by an appropriate ratio of the number of degrees of freedom so that the high temperature limit coincides for both cases. This is shown in Figure 5.

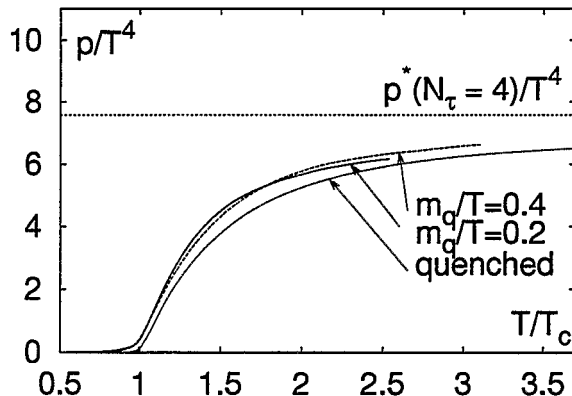


FIG. 5. Comparison between the pressure of four-flavour QCD on a  $16^3 \times 4$  lattice for two values of the quark mass and the pressure of the pure  $SU(3)$  gauge theory. The latter has been rescaled by the appropriate number of degrees of freedom of four-flavour QCD.

While the pressure is obtained in complete analogy to the pure gauge theory through an integration of action differences (Eq. 4), the calculation of energy density now also requires the determination of differences of the chiral condensates at zero and non-zero temperature as well as the cut-off dependence of the two bare couplings,  $\beta$  and  $m_q$ ,

$$\frac{\epsilon - 3p}{T^4} = -N_\tau^4 \left[ \frac{d\beta}{d \ln a} (S_0 - S_T) + \frac{dma}{d \ln a} (\langle \bar{\chi}\chi \rangle_0 - \langle \bar{\chi}\chi \rangle_T) \right] \quad (10)$$

Only in the chiral limit the derivative  $d \ln ma/da$  vanishes and  $(\epsilon - 3p)$  is again proportional only to the  $\beta$ -function,  $d\beta/d \ln a$ , as it is the case in the pure gauge sector.

Results for the energy density are shown in Figure 6. The energy density does stay close to the ideal gas limit immediately above  $T_c$ . We do observe an overshooting of the ideal gas limit close to  $T_c$  for the non-zero quark masses considered by us. This is a feature not seen before in the pure gauge sector. Whether this does persist for finite values of the quark mass or is an artefact of our present statistical accuracy has to be clarified in further more detailed investigations. The overshooting does, however, seem to disappear in an "extrapolation" to in the chiral limit, which we constructed by ignoring the term proportional to  $\langle \bar{\psi}\psi \rangle$  in the definition of the energy density [8]. This contribution of this term vanishes in the chiral limit as the derivative  $d \ln ma/da$  is proportional to the quark mass.

We note that the energy density in the critical region is larger than in the pure gauge case when expressed in units of  $T_c$ , *i.e.*  $\epsilon \sim 10T_c^4$ . However, as the critical temperature is

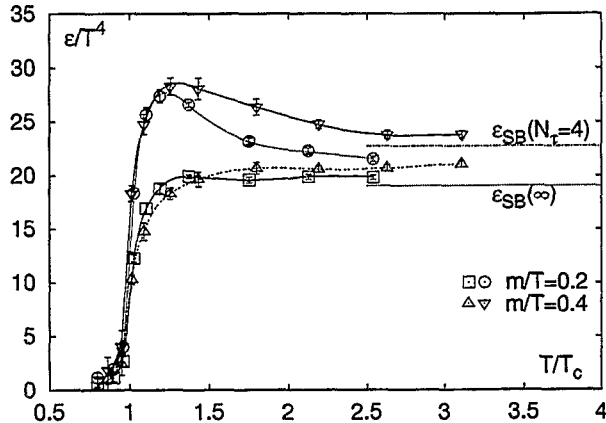


FIG. 6. Energy density of four-flavour QCD on a  $16^3 \times 4$  lattice. The lower set of curves shows an "extrapolation" to the chiral limit which has been obtained by ignoring the second term in Eq. 10 (see text).

substantially smaller than in the pure gauge theory, the critical energy density again turns out to be about  $1 \text{ GeV}/\text{fm}^3$ .

The calculations with an improved fermion action show that a strong reduction of the cut-off dependence is possible in the high temperature phase. Still a further improvement is necessary in order to reduce the cut-off dependence to only a few percent as it is the case in the pure gauge sector. In addition one would also like to achieve a reduction of the flavour symmetry breaking in the staggered action. This does not seem to be the case for the improved action we have used here.

## V. CONCLUSIONS

Thermodynamic observables of the  $SU(3)$  gauge theory and QCD studied with improved gauge and fermion actions show a drastic reduction of the cut-off dependence in the high temperature limit as well as at  $T_c$ . The major improvement effect is already obtained with tree level improved actions. The calculation of the equation of state of the  $SU(3)$  gauge theory does seem to be well under control and major sources for lattice artefacts have been eliminated. This opens the possibility to repeat quantitative studies of various other thermodynamic quantities on rather coarse lattices which so far could only be investigated on a qualitative level without reliable extrapolations to the continuum limit.

The calculation of thermodynamic quantities with improved fermion actions has just started. In this case further work is still needed in order to be able to select an appropriate action which even in the ideal gas limit has as little cut-off dependence as the Symanzik improved actions.

## REFERENCES

- [1] K. Symanzik, Nucl. Phys. B226 (1983) 187 and Nucl. Phys. B226 (1983) 205.

- [2] G.P. Lepage and P.B Mackenzie, Phys. Rev. D48 (1993) 2250.
- [3] F. Niedermayer, *Improved Lattice Actions*, hep-lat-9608097, June 1996.
- [4] T. DeGrand, *Lattice Gauge Theory for QCD*, COLO-HEP-378 (hep-ph/9610391), October 1996.
- [5] B. Beinlich, F. Karsch and E. Laermann, Nucl. Phys. B462 (1996) 415.
- [6] B. Beinlich, F. Karsch, E. Laermann and A. Peikert, *String tension and Thermodynamics from Tree Level and Tadpole Improved Actions*, in preparation.
- [7] B. Beinlich, F. Karsch and A. Peikert, *SU(3) Latent Heat and Surface Tension from Tree Level and Tadpole Improved Actions*, BI-TP 96/24, to appear in Phys. Lett. B.
- [8] J. Engels, R. Joswig, F. Karsch, E. Laermann, and B. Petersson, *Thermodynamics of four-flavour QCD with an improved staggered action*, in preparation.
- [9] J. Engels, F. Karsch and K. Redlich, Nucl. Phys. B 435 (1995) 295.
- [10] G. Boyd *et al.*, Phys. Rev. Lett. 75 (1995) 4169 and Nucl. Phys. B469 (1996) 419.
- [11] Y. Iwasaki, K. Kanaya, T. Kaneko and T. Yoshié, *Scaling in SU(3) pure gauge theory with a renormalization group improved action*, UTHEP-348, October 1996.
- [12] A. Papa, *SU(3) Thermodynamics on Small Lattices*, BUTP-96/13.
- [13] J. Engels, J. Fingberg, F. Karsch, D. Miller and M. Weber, Phys. Lett. B 252 (1990) 625.
- [14] P. Arnold and C.-X. Zhai, Phys. Rev. D50 (1994) 7603.
- [15] C.-X. Zhai and B. Kastening, Phys. Rev. D52 (1995) 7232.
- [16] H. Leutwyler, in Proceedings of the Conference *QCD - 20 years later*, (Edts. P.M. Zerwas and H.A. Kastrup), World Scientific 1993, p. 693.
- [17] U.M. Heller, F. Karsch and J. Rank, Phys. Lett. B355 (1995) 511.
- [18] J. I. Kapusta, Nucl. Phys. B148 (1979) 461.
- [19] Y. Iwasaki *et al.*, Phys. Rev. D46 (1992) 4657.
- [20] Y. Iwasaki *et al.*, Phys. Rev. D49 (1994) 3540.
- [21] S. Naik, Nucl. Phys. B316 (1989) 238.

# Hydrodynamics and Collective Behaviour in Relativistic Nuclear Collisions

Dirk H. Rischke

*Physics Department, Pupin Physics Laboratories, Columbia University,  
538 W 120th Street, New York, NY 10027, U.S.A.*

## Abstract

Hydrodynamics is applied to describe the dynamics of relativistic heavy-ion collisions. The focus of the present study is the influence of a possible (phase) transition to the quark-gluon plasma in the nuclear matter equation of state on collective observables, such as the lifetime of the system and the transverse directed flow of matter. It is shown that such a transition leads to a softening of the equation of state, and consequently to a time-delayed expansion which is in principle observable via two-particle correlation functions. Moreover, the delayed expansion leads to a local minimum in the excitation function of transverse directed flow around AGS energies.

## I. INTRODUCTION AND CONCLUSIONS

Hydrodynamics has found widespread application in studying the dynamical evolution of heavy-ion collisions [1]. It was found that compressional shock waves, first predicted by Scheid and Greiner to occur in such collisions [2], lead to collective flow phenomena like sideward deflection of matter in the reaction plane (“side-splash” and “bounce-off”) as well as azimuthal deflection out of the reaction plane (“squeeze-out”). The confirmation of these collective flow effects by BEVALAC experiments [3] was one of the main successes of the fluid-dynamical picture.

One of the primary goals of present relativistic heavy-ion physics is the creation and experimental observation of the so-called quark-gluon-plasma (QGP) phase of matter, predicted by lattice calculations of quantum chromodynamics (QCD) [4]. A class of interesting signals for the QGP, which are directly related to the QCD equation of state (EoS) as measured on the lattice, emerge from the influence of that EoS on the *collective* dynamical evolution of the system. Relativistic hydrodynamics is the most suitable approach to study these signals, since it is the only dynamical model which provides a *direct* link between collective observables and the EoS.

It was shown [5–8] that the transition to the QGP *softens* the EoS in the transition region, and thus reduces the tendency of matter to expand on account of its internal pressure. This, in turn, delays the expansion and considerably prolongs the lifetime of the system. It was moreover shown [8] that this prolongation of the lifetime (as compared to the expansion of an ideal gas without transition) is in principle observable via an enhancement of the ratio of inverse widths,  $R_{\text{out}}/R_{\text{side}}$ , of the two-particle correlation function in out- and

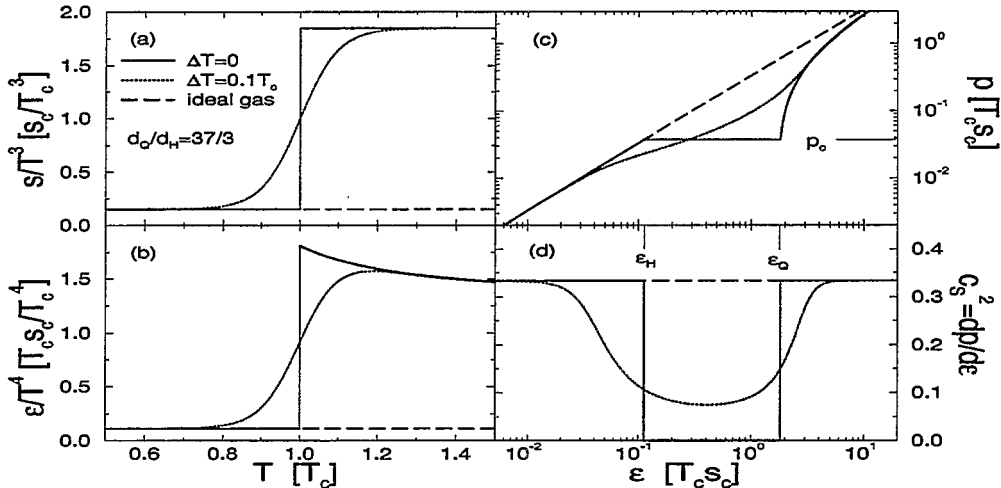


FIG. 1. Equation of state.

side-direction. (This signal was originally proposed by Pratt and Bertsch [9].) Another aspect [10,11] of the delayed expansion is the reduction of the transverse directed flow in semi-peripheral collisions that can be readily tested experimentally at fixed target energies [12].

In this paper I summarize the essential physics and observable consequences of the softening of the EoS in the transition region, namely, the time-delayed expansion and the subsequent enhancement of  $R_{\text{out}}/R_{\text{side}}$ , and the disappearance of the transverse directed flow. Natural units  $\hbar = c = k_B = 1$  are used throughout this paper.

## II. THE QCD PHASE TRANSITION AND SOFTENING OF THE EQUATION OF STATE

Available lattice data for the entropy density in full QCD can be approximated by the simple parametrization [7,8,13]

$$\frac{s}{s_c}(T) = \left[ \frac{T}{T_c} \right]^3 \left( 1 + \frac{d_Q - d_H}{d_Q + d_H} \tanh \left[ \frac{T - T_c}{\Delta T} \right] \right), \quad (1)$$

where  $s_c = \text{const.} \times (d_Q + d_H) T_c^3$  is the entropy density at  $T_c$ . Pressure  $p$  and energy density  $\epsilon$  follow then from thermodynamical relationships. For  $\Delta T = 0$ , the EoS (1) reduces to the MIT bag EoS [14] with a strong first order phase transition between QGP and hadronic phase. In that case, the ratio  $d_Q/d_H$  determines the latent heat (density) of the transition,  $\epsilon_Q - \epsilon_H \equiv 4B$ .

Fig. 1 shows (a) the entropy density and (b) the energy density as functions of temperature, and (c) the pressure and (d) the velocity of sound squared  $c_s^2 \equiv dp/d\epsilon$  as functions of energy density for  $\Delta T = 0, 0.1 T_c$ , and an ideal gas with  $d_H$  degrees of freedom for  $d_Q/d_H = 37/3$ . Figs. 1 (a,b) present the thermodynamic functions in a form to facilitate comparison with lattice data. Present lattice data for full QCD can be approximated with a choice of  $\Delta T$  in the range  $0 \leq \Delta T < 0.1 T_c$ . In the hydrodynamical context, however, Figs. 1 (c,d) are more relevant. As can be seen in (c), for  $\Delta T = 0$  the pressure stays constant in

the mixed phase  $\epsilon_H \leq \epsilon \leq \epsilon_Q$ . Hydrodynamical expansion is, however, driven by pressure *gradients*. It is therefore (the square of) the velocity of sound  $c_s^2 = dp/d\epsilon$ , Fig. 1 (d), that is the most relevant measure of the system's tendency to expand. For  $\Delta T = 0$ , the velocity of sound vanishes in the mixed phase, i.e., mixed phase matter does not expand at all on its own account, even if there are strong gradients in the energy density. For finite  $\Delta T$ , pressure gradients are finite, but still smaller than for an ideal gas EoS, and therefore the system's tendency to expand is also reduced, cf. Fig. 1 (d).

The reduction of  $c_s^2$  in the transition region is commonly referred to as “softening” of the EoS, the respective region of energy densities is called “soft region” [5–8]. For matter passing through that region during the expansion phase, the flow will temporarily slow down or even possibly stall under suitable conditions and consequently lead to a *time delay* in the expansion of the system.

### III. HYDRODYNAMICS

Hydrodynamics is defined by local energy–momentum conservation,

$$\partial_\mu T^{\mu\nu} = 0 . \quad (2)$$

Under the assumption of local thermodynamical equilibrium (the so-called “ideal fluid” approximation) the energy–momentum tensor  $T^{\mu\nu}$  assumes the particularly simple form [15]

$$T^{\mu\nu} = (\epsilon + p) u^\mu u^\nu - p g^{\mu\nu} , \quad (3)$$

where  $u^\mu = \gamma(1, \mathbf{v})$  is the 4–velocity of the fluid ( $\mathbf{v}$  is the 3–velocity,  $\gamma \equiv (1 - \mathbf{v}^2)^{-1/2}$ ,  $u_\mu u^\mu = 1$ ), and  $g^{\mu\nu} = \text{diag}(+, -, -, -)$  is the metric tensor. The system of equations (2) is closed by choosing an EoS in the form  $p = p(\epsilon)$ , i.e., as depicted in Fig. 1 (c). In the ideal fluid approximation, the (equilibrium) EoS is the *only* input to the hydrodynamical equations of motion (2) that relates to properties of the matter under consideration and is thus able to influence the dynamical evolution of the system. The final results are uniquely determined once a particular initial condition and a decoupling (“freeze-out”) hypersurface are specified.

For finite baryon density, one has to also take into account local conservation of baryon number,

$$\partial_\mu N^\mu = 0 , \quad (4)$$

where  $N^\mu = n u^\mu$  is the baryon 4–current (in the ideal fluid approximation),  $n$  is the baryon density in the local rest frame of a fluid element. In this case, the EoS has in general to be provided in the form  $p = p(\epsilon, n)$  (see Fig. 1 of Ref. [11] for an explicit example).

### IV. DELAYED EXPANSION AND TWO-PARTICLE CORRELATIONS

In this section I discuss the delayed expansion and observable consequences in the so-called Bjorken model [16] and for the EoS (1). The main assumption of Bjorken’s model is longitudinal boost invariance which implies that the longitudinal flow velocity of matter is

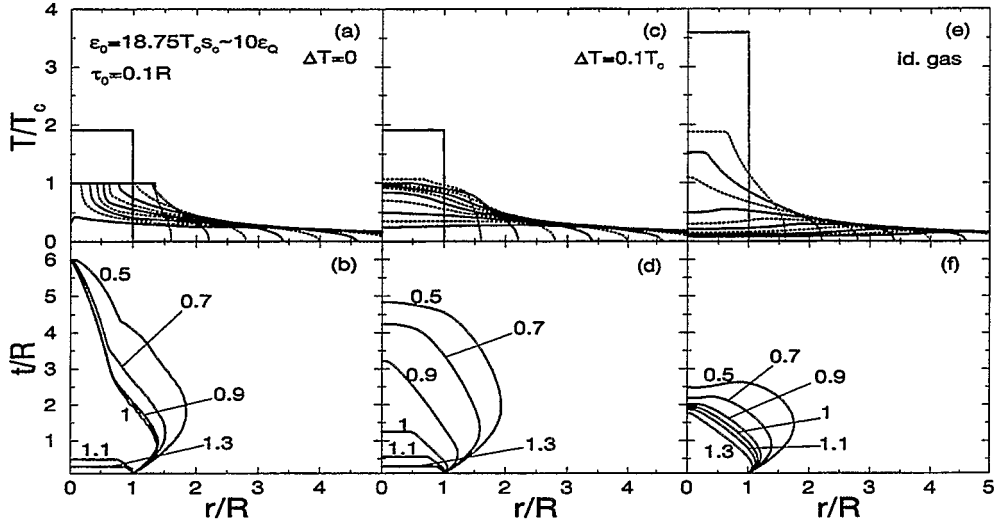


FIG. 2. Transverse expansion in the Bjorken model.

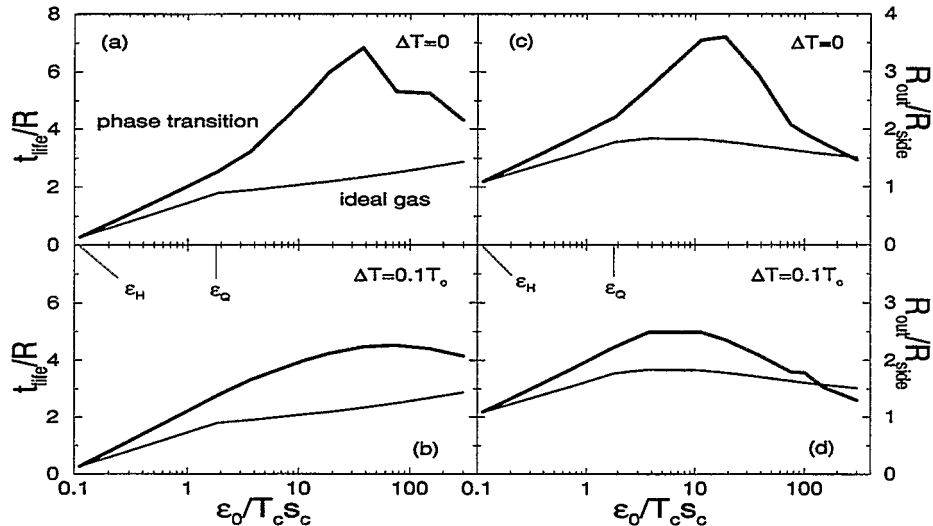


FIG. 3. Lifetimes and inverse widths in the Bjorken model.

always given by  $v^z \equiv z/t$  [16]. The initial conditions are specified at constant proper time  $\tau \equiv \sqrt{t^2 - z^2}$ . I fix  $\tau_0 = 0.1 R$ , motivated by the fact that for Au+Au collisions at RHIC energies equilibration is expected [17] to occur after 0.5 fm, while the initial radius  $R$  of the hot zone is on the order of 5 fm. Fig. 2 shows hydrodynamic solutions for the (cylindrically symmetric) transverse expansion of a “Bjorken cylinder” (at  $z = 0$ ), for an initial (homogeneously distributed) energy density  $\epsilon_0 = 18.75 T_c s_c \sim 10 \epsilon_Q \simeq 14 \text{ GeV fm}^{-3}$ . This value is expected to be reached through mini-jet production at RHIC energies [18]. As one observes, the system spends considerable time in the “soft region” of the EoS (corresponding to temperatures around  $T_c$ ), and therefore the expansion is delayed, Figs. 2 (a–d), in comparison to the ideal gas case, Figs. 2 (e,f).

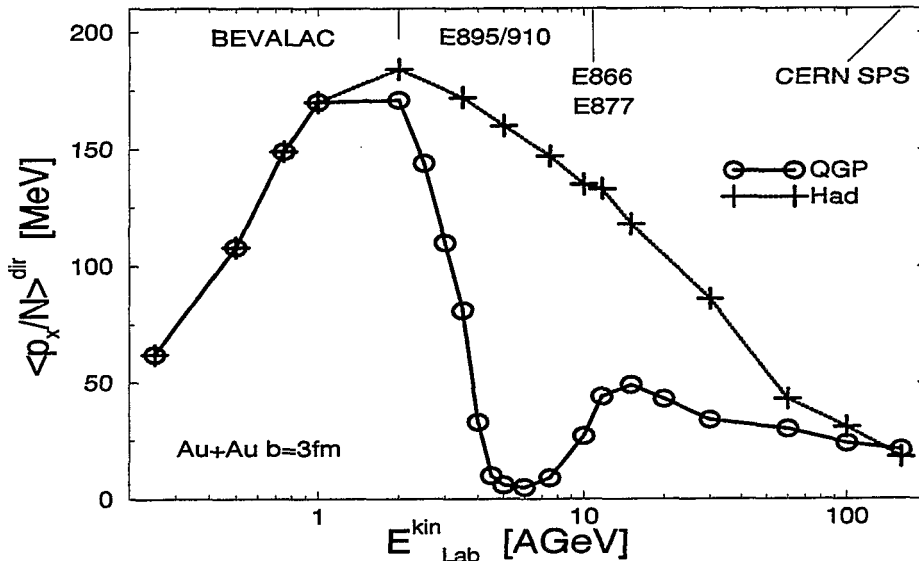


FIG. 4. The transverse directed flow as calculated from 3+1 dimensional hydrodynamics.

Figs. 3 (a,b) show the lifetime<sup>1</sup> of the system (assuming it “freezes out” at a temperature  $T = 0.7 T_c$ ) as a function of initial energy density  $\epsilon_0$  for the Bjorken expansion. One observes a distinguished maximum in the lifetime associated with the transition to the QGP. Note that this maximum of the lifetime occurs not exactly at energy densities corresponding to the “soft region” of the EoS. This is due to the fact that the strong dilution on account of the (ever present) longitudinal velocity field has to be compensated so that the systems stays long enough in the “soft” transition region. If the system were initially at rest, the maximum would (as naively expected) occur around  $\epsilon_0 \sim \epsilon_Q$  [7,8].

Figs. 3 (c,d) show the ratio of inverse widths of the two-pion correlation function in out- and side- directions,  $R_{out}/R_{side}$ , as a function of  $\epsilon_0$  for the Bjorken expansion<sup>2</sup>. Note that this ratio mirrors closely the dependence of the lifetime on initial conditions in Figs. 3 (a,b). The effect is maximized around initial energy densities expected to be reached at the RHIC collider [18]. The enhancement over the ideal gas case is of the order of 40–100% (for  $\Delta T = 0.1 T_c$  to  $\Delta T = 0$ ) and should therefore be in principle experimentally observable.

## V. DIS- AND REAPPEARANCE OF TRANSVERSE DIRECTED FLOW

The softening of the EoS and the delay in the expansion has an interesting consequence for semi-peripheral heavy-ion collisions at AGS energies. If the hot, compressed (baryon-rich) matter in the central zone undergoes a transition to the QGP, its tendency to expand is reduced, similarly as discussed above. This prevents the deflection of spectator matter,

<sup>1</sup>Here defined as the intercept of an isotherm in Figs. 2 (b,d,f) with the  $t$ -axis.

<sup>2</sup>Details on how to calculate this quantity can be found in Ref. [8].



as it would occur for a stiff EoS with a stronger tendency to expand, for instance a purely hadronic EoS without phase transition [11]. As shown in Fig. 4, this effect is observable in the excitation function of the transverse directed flow per baryon,

$$\langle p_x/N \rangle^{dir} = \frac{1}{N} \int_{-y_{CM}}^{y_{CM}} dy \langle p_x/N \rangle(y) \frac{dN}{dy} \text{sgn}(y). \quad (5)$$

The overall decrease of this quantity above  $E_{Lab}^{kin} \sim 2$  AGeV observed for both EoS's is simply due to the fact that faster spectators are less easily deflected by the hot, expanding participant matter. One clearly observes a dramatic *drop* between BEVALAC and AGS beam energies and an *increase* beyond  $\sim 10$  AGeV for the EoS with phase transition as compared to the calculation with the pure hadronic EoS. Thus, *there is a local minimum in the excitation function of the directed transverse (in-reaction-plane) collective flow around  $\sim 6$  AGeV*, which is again related to the phase transition to the QGP and the existence of a “soft region” in the nuclear matter EoS. Note that the position of the minimum strongly depends on the EoS. It may easily shift to higher beam energies, if more resonances are included in the hadronic part of the EoS. Also, absolute values for the directed flow cannot yet be compared to experimentally measured ones, since at this stage freeze-out has not been performed. Moreover, viscosity effects are neglected in the ideal hydrodynamic picture, which are known to have a strong influence on flow [19]. The main point is, however, that irrespective of these quantitative uncertainties, the *minimum* is a generic *qualitative* signal for a transition from hadron to quark and gluon degrees of freedom in the nuclear matter EoS.

## ACKNOWLEDGMENTS

This work was supported by the Director, Office of Energy Research, Division of Nuclear Physics of the Office of High Energy and Nuclear Physics of the U.S. Department of Energy under Contract No. DE-FG-02-93ER-40764. I would like to thank the organizers for their invitation to present these results at the RHIC summer study '96 and Brookhaven National Laboratory for support.

## REFERENCES

- [1] For a review, see:  
H. Stöcker and W. Greiner, Phys. Rep. 137 (1986) 277,  
R.B. Clare and D.D. Strottman, Phys. Rep. 141 (1986) 177.
- [2] W. Scheid, H. Müller, W. Greiner, Phys. Rev. Lett. 32 (1974) 741.
- [3] H.A. Gustaffson et al., Phys. Rev. Lett. 52 (1984) 1590,  
H.H. Gutbrod et al., Phys. Lett. B 216 (1989) 267,  
H.G. Ritter and the EOS collaboration, Nucl. Phys. A 583 (1995) 491c,  
M.D. Partlan and the EOS collaboration, Phys. Rev. Lett. 75 (1995) 2100.
- [4] see, for instance: E. Laermann, Proc. of “Quark Matter '96”, May 20 – 24, 1996, Heidelberg, Germany (to appear in Nuclear Physics A).

- [5] C.M. Hung and E.V. Shuryak, Phys. Rev. Lett. 75 (1995) 4003.
- [6] D.H. Rischke, S. Bernard, J.A. Maruhn, Nucl. Phys. A 595 (1995) 346.
- [7] D.H. Rischke and M. Gyulassy, Nucl. Phys. A 597 (1996) 701.
- [8] D.H. Rischke and M. Gyulassy, Columbia University preprint CU-TP-756 (submitted to Nucl. Phys. A).
- [9] S. Pratt, Phys. Rev. C 49 (1994) 2722, Phys. Rev. D 33 (1986) 1314,  
G. Bertsch, Nucl. Phys. A 498 (1989) 173c.
- [10] L.V. Bravina, N.S. Amelin, L.P. Csernai, P. Levai, D. Strottman, Nucl. Phys. A 566 (1994) 461c.
- [11] D.H. Rischke, Y. Pürsün, J.A. Maruhn, H. Stöcker, W. Greiner, preprint CU-TP-695, nucl-th/9505014 (to be published in Heavy Ion Phys.).
- [12] J. Barrette et al. (E877 collaboration), Phys. Rev. Lett. 73 (1994) 2532, Nucl. Phys. A 590 (1995) 259c,  
Y. Zhang and J.P. Wessels (E877 collaboration), Nucl. Phys. A 590 (1995) 557c,  
G. Rai and the E895 collaboration, LBL PUB-5399 (1993).
- [13] J.P. Blaizot and J.Y. Ollitrault, Phys. Rev. D 36 (1987) 916.
- [14] A. Chodos, R.L. Jaffe, K. Johnson, C.B. Thorn, V.F. Weisskopf, Phys. Rev. D 9 (1974) 3471.
- [15] L.D. Landau and E.M. Lifshitz, "Fluid mechanics" (Pergamon, New York, 1959).
- [16] J.D. Bjorken, Phys. Rev. D 27 (1983) 140,  
G. Baym, B.L. Friman, J.P. Blaizot, M. Soyeur, W. Czyż, Nucl. Phys. A 407 (1983) 541.
- [17] X.-N. Wang, M. Gyulassy, M. Plümer, Phys. Rev. D 51 (1995) 3436,  
R. Baier, Yu.L. Dokshitzer, S. Peigné, D. Schiff, Phys. Lett. B 345 (1995) 277.
- [18] E. Shuryak, Phys. Rev. Lett. 68 (1992) 3270,  
K.J. Eskola and M. Gyulassy, Phys. Rev. C 47 (1993) 2329.
- [19] W. Schmidt, U. Katscher, B. Waldhauser, J.A. Maruhn, H. Stöcker, W. Greiner, Phys. Rev. C 47 (1993) 2782.

# Wilson Fermions at Finite Temperature

Michael Creutz  
*Physics Department*  
*Brookhaven National Laboratory, Upton, NY 11973*  
creutz@bnl.gov

## Abstract

I conjecture on the phase structure expected for lattice gauge theory with two flavors of Wilson fermions, concentrating on large values of the hopping parameter. Numerous phases are expected, including the conventional confinement and deconfinement phases, as well as an Aoki phase with spontaneous breaking of flavor and parity and a large hopping phase corresponding to negative quark masses.

In this talk I conjecture on the rather rich phase structure expected for lattice gauge theory with Wilson fermions, paying particular attention to what happens for large hopping parameter. I consider both zero and non-zero temperature. I restrict myself to the standard hadronic gauge theory of quarks interacting with non-Abelian gluons. I leave aside issues related to electromagnetism and weak interactions, both of which also raise fascinating issues for lattice field theory.

The parameters of the strong interactions are the quark masses. I implicitly include here the strong CP violating parameter  $\theta$ , as this can generally be rotated into the mass matrix [1]. The quark masses are in fact the only parameters of hadronic physics, the strong coupling being absorbed into the units of measurement via the phenomenon of dimensional transmutation [2].

For the purposes of this talk, I take degenerate quarks at  $\theta = 0$ ; so, I can consider only a single mass parameter  $m$ . I discuss only the two flavor case, as this will make some of the chiral symmetry issues simpler. I also will treat the theory at finite temperature,  $T$ , introducing another variable. Finally, as this is a lattice talk, I introduce the lattice spacing  $a$  as a third parameter.

On the lattice with Wilson fermions the three parameters  $(m, T, a)$  are usually replaced with  $\beta$ , representing the inverse bare lattice coupling squared, the fermion hopping parameter  $K$ , and the number of time slices  $N_t$ . The mapping between  $(m, T, a)$  and  $(\beta, K, N_t)$  is non-linear, well known, and not the subject of this talk.

Note that in considering the structure of the theory in either of these sets of variables, I am inherently talking about finite lattice spacing  $a$ . Thus this entire talk is about lattice artifacts.

I start with the  $(\beta, K)$  plane at zero temperature, and defer how this is modified at finite temperature. The  $\beta$  axis with  $K = 0$  represents the pure gauge theory of glueballs. This is expected to be confining without any singularities at finite  $\beta$ . The line of varying  $K$  with  $\beta = \infty$  represents free Wilson fermions [3]. Here, with conventional normalizations, the

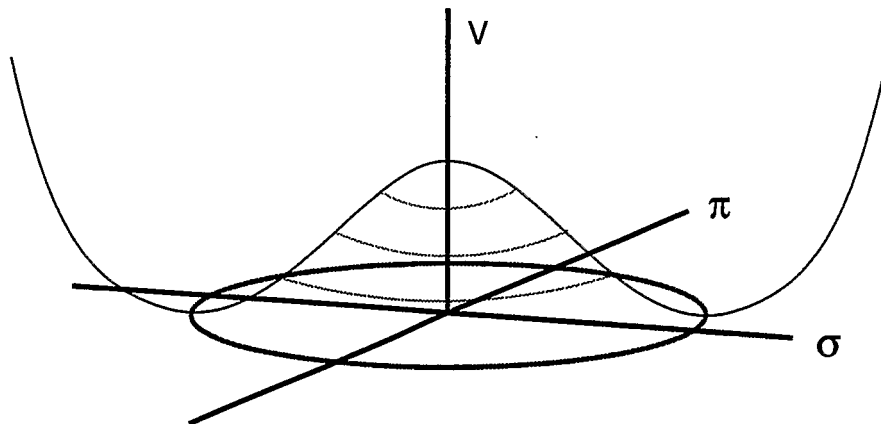


Fig. (1) The effective potential in the canonical sigma model.

point  $K = \frac{1}{8}$  is where the mass gap vanishes and a massless fermion should appear in the continuum limit. The full interacting continuum limit should be obtained by approaching this point from the interior of the  $(\beta, K)$  plane.

While receiving the most attention, this point  $K = \frac{1}{8}$  is not the only place where free Wilson fermions lose their mass gap. At  $K = \frac{1}{4}$  four doubler species become massless. Also formally at  $K = \infty$  six more doublers lose their mass. (Actually, a more natural variable is  $\frac{1}{K}$ .) The remaining doublers occur at negative  $K$ .

The  $K$  axis at vanishing  $\beta$  also has a critical point where the confining spectrum appears to develop massless states. Strong coupling arguments as well as numerical experiments place this point somewhere near  $K = \frac{1}{4}$ , but this is probably not exact. The conventional picture connects this point to  $(\beta = \infty, K = \frac{1}{8})$  by a phase transition line representing the lattice version of the chiral limit.

Now I move ever so slightly inside the  $(\beta, K)$  plane from the point  $(\infty, \frac{1}{8})$ . This should take us from free quarks to a confining theory, with mesons, baryons, and glueballs being the physical states. Furthermore, when the quark is massless, we should have chiral symmetry. Considering here the two flavor case, this symmetry is nicely exemplified in a so called “sigma” model, with three pion fields and one sigma field rotating amongst themselves. Defining the fields

$$\begin{aligned}\sigma &= \bar{\psi}\psi \\ \vec{\pi} &= i\bar{\psi}\gamma_5\vec{\tau}\psi\end{aligned}\tag{1}$$

I consider constructing an effective potential. For massless quarks this is expected to have the canonical sombrero shape stereotyped by

$$V \sim \lambda (\sigma^2 + \vec{\pi}^2 - v^2)^2\tag{2}$$

and illustrated schematically in Fig. (1). The normal æther is taken with an expectation value for the sigma field  $\langle\sigma\rangle \sim v$ . The physical pions are massless goldstone bosons associated with slow fluctuations of the æther along the degenerate minima of this potential.

As I move up and down in  $K$  from the massless case near  $\frac{1}{8}$ , this effective potential will tilt in the standard way, with the sign of  $\langle\sigma\rangle$  being appropriately determined. The role of the quark mass is played by the distance from the critical hopping,  $m_q \sim K_c - K$

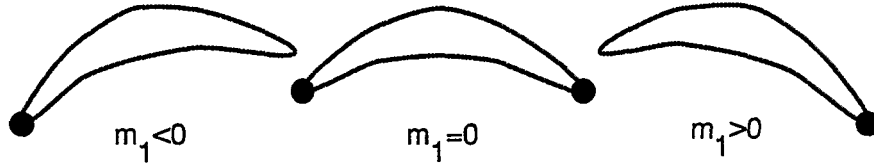


Fig. (2) The effect of a downward warping of the effective potential. The curve represents the warped bottom of the sombrero potential. Here  $m_1$  represents the distance from the critical point. The solid circles represent possible states of the æther. The phase transition now occurs without a diverging correlation length.

with  $K_c \sim \frac{1}{8}$ . At the chiral point there occurs a phase transition, of first order because the sign of  $\langle \sigma \rangle$  jumps discontinuously. At the transition point there are massless goldstone pions representing the spontaneous symmetry breaking. With an even number of flavors the basic physics on each side of the transition is the same, since the sign of the mass term is a convention reversible via a chiral rotation. For an odd number of flavors the sign of the mass is significant because the required rotation involves the  $U(1)$  anomaly and is not a good symmetry. This is discussed in some detail in my recent paper, Ref. [1]. For the present discussion I stick with two flavors.

A similar picture should also occur near  $K = \frac{1}{4}$ , representing the point where a subset of the fermion doublers become massless. Thus another phase transition should enter the diagram at  $K = \frac{1}{8}$ . Similar lines will enter at negative  $K$  and further complexity occurs at  $K = \infty$ . For simplicity, let me concentrate only on the lines from  $K = \frac{1}{8}$  and  $\frac{1}{4}$ .

Now I delve a bit deeper into the  $(\beta, K)$  plane. The next observation is that the Wilson term separating the doublers is explicitly not chiral invariant. This should damage the beautiful symmetry of our sombrero. The first effect expected is a general tilting of the potential. This represents an additive renormalization of the fermion mass, and appears as a beta dependent motion of the critical hopping away from  $\frac{1}{8}$ . Define  $K_c(\beta)$  as the first singular place in the phase diagram for increasing  $K$  at given  $\beta$ . This gives a curve which presumably starts near  $K = \frac{1}{4}$  at  $\beta = 0$  and ends up at  $\frac{1}{8}$  for infinite  $\beta$ .

Up to this point I have only reviewed standard lore. Now I continue to delve yet further away from the continuum chiral point at  $(\beta, K) = (\infty, \frac{1}{8})$ . Then I expect the chiral symmetry breaking of the Wilson term to increase and become more than a simple tilting of the Mexican hat. I'm not sure to what extent a multipole analysis of this breaking makes sense, but let me presume that the next effect is a quadratic warping of our sombrero, i.e. a term something like  $\alpha\sigma^2$  appearing in the effective sigma model potential. This warping cannot be removed by a simple mass renormalization.

There are two possibilities. This warping could be upward or downward in the  $\sigma$  direction. Indeed, which possibility occurs can depend on the value of  $\beta$ .

Consider first the case where the warping is downward, stabilizing the sigma direction for the æther. At the first order chiral transition, this distortion gives the pions a small mass. The transition then occurs without a diverging correlation length. As before, the condensate  $\langle \sigma \rangle$  jumps discontinuously, changing its sign. However, the conventional approach of extrapolating the pion mass to zero from measurements at smaller hopping parameter will no longer yield the correct critical line. The effect of this warping on the potential is illustrated in Fig. (2).

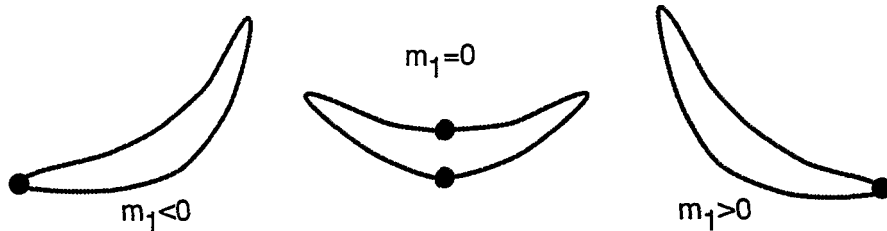


Fig. (3) The effect of an upward warping of the effective potential. Here  $m_1$  represents the distance from  $K_c(\beta)$ . Now there are two phase transitions, with the intermediate phase having an expectation for the pion field.

A second possibility is for the warping to be in the opposite direction, destabilizing the  $\sigma$  direction. In this case we expect two distinct phase transitions to occur as  $K$  passes through the critical region. For small hopping we have our tilted potential with  $\sigma$  having a positive expectation. As  $K$  increases, this tilting will eventually be insufficient to overcome the destabilizing influence of the warping. At a critical point, most likely second order, it will become energetically favorable for the pion field to acquire an expectation value, such a case being stabilized by the upward warping in the sigma direction. As  $K$  continues to increase, a second transition should appear where the tilting of the potential is again sufficiently strong to give only sigma an expectation, but now in the negative direction. The effect of this upward warping on the effective potential is illustrated in Fig. (3).

Thus we expect our critical line to split into two, with a rather interesting phase between them. This phase has a non-vanishing expectation value for the pion field. As the latter carries flavor and odd parity, both are spontaneously broken. Furthermore, since flavor is still an exact continuous global symmetry, when it is broken Goldstone bosons will appear. In this two flavor case, there are precisely two such massless excitations. If the transitions are indeed second order, a third massless particle appears just at the transition lines, and these three particles are the remnants of the three pions from the continuum theory. This picture of a parity and flavor breaking phase was proposed some time ago by Aoki [4], who presented evidence for its existence in the strong coupling regime. This phase should be “pinched” between the two transitions, and become of less importance as  $\beta$  increases. Whether the phase might be squeezed out at a finite  $\beta$  to the above first order case, or whether it only disappears in the infinite  $\beta$  limit is a dynamical question as yet unresolved.

A similar critical line splitting to give a broken flavor phase should also enter our phase diagram from  $(\beta, K) = (\infty, \frac{1}{4})$ , representing the first set of doublers. Evidence from toy models [5] is that after this line splits, the lower half joins up with the upper curve from the  $(\beta, K) = (\infty, \frac{1}{8})$  point. In these models, there appears to be only one broken parity phase at strong coupling.

Now let me go to finite temperature, or more precisely, finite  $N_t$ , the number of sites in the temporal direction. Along the  $\beta$  axis, representing the pure glue theory, a deconfinement transition is expected [6]. For an  $SU(3)$  gauge group, this transition is expected to be first order. Turning on the fermion hopping, this transition should begin to move in  $\beta$ , the first effect being an effective renormalization of  $\beta$  down toward stronger couplings. In the process, the transition may soften, and perhaps eventually turn into a rapid crossover rather than a true singularity. In any case, the numerical evidence is for a single transition

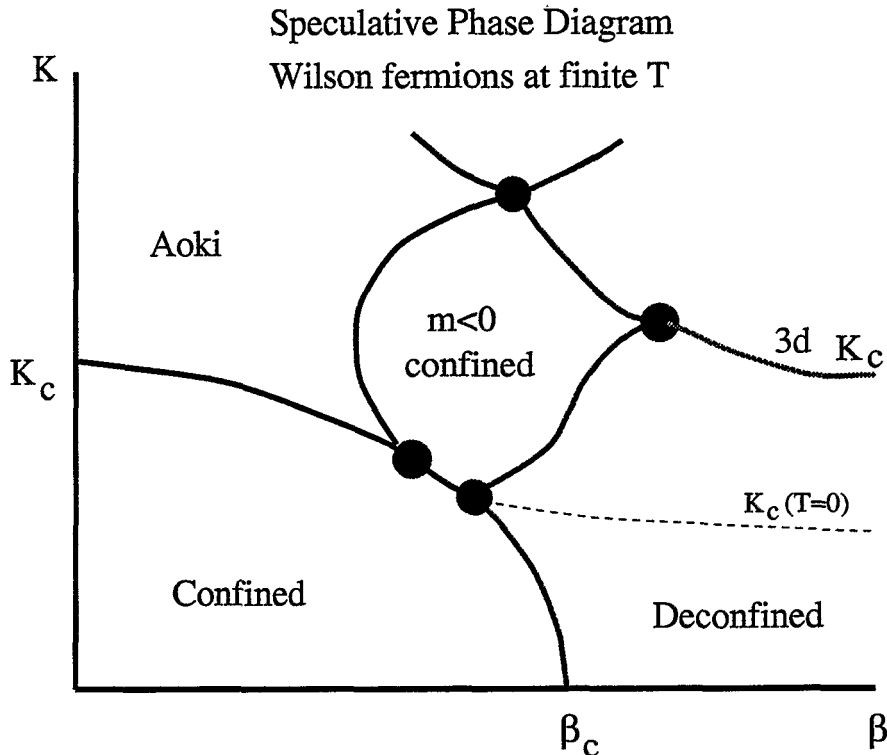


Fig. (4) The conjectured  $(\beta, K)$  phase diagram for finite  $N_t$ .

where both the Polyakov line and the chiral symmetry order parameter undergo a rapid change. The transition region should continue into the  $(\beta, K)$  plane to eventually meet the bulk transition line near  $K_c(\beta)$  coming in from strong coupling.

On the weak coupling side of the deconfinement transition, physics is dramatically different. Here as the quark mass goes to zero, we expect chiral symmetry restoration in the thermal æther. In terms of the effective potential, we expect only a single simple minimum. Most importantly, we do not expect any singularity around zero quark mass, with physics depending smoothly around the  $(\beta, K) = (\infty, \frac{1}{8})$  point. In other words, we expect the chiral transition at small quark masses to be absorbed into the finite temperature transition. As the hopping continues to increase, the  $m \leftrightarrow -m$  symmetry of the continuum theory will play a role, bouncing the deconfinement transition back towards larger  $\beta$  after  $K$  passes  $K_c$ .

What is less clear is what happens to the finite temperature line as we continue further toward the chiral transitions of the doublers. Here I conjecture that another transition line enters the picture. For small  $N_t$  the theory is effectively a three dimensional one, which should have its own chiral transition, possibly somewhere between  $K = \frac{1}{8}$  and  $K = \frac{1}{4}$ . Speculating that the deconfinement transition bounces as well off of this line, but on the opposite side, I arrive at the qualitative finite temperature phase diagram sketched in Fig. (4).

To summarize the picture, at small  $\beta$  and small  $K$  we have the usual low temperature confined phase. Increasing  $K$ , we enter the Aoki phase with spontaneous breaking of flavor and parity. As  $\beta$  increases, the Aoki phase pinches down into either a narrow point or a single first order line, leading towards the free fermion point at  $(\beta, K) = (\infty, \frac{1}{8})$ . Before

reaching that point, this line collides with and is absorbed in the deconfinement transition line. The latter then bounces back towards larger  $\beta$ . Above the chiral line is a phase nearly equivalent physically with the usual confined phase, just differing in the sign of the light quark masses. Indeed, the only physical difference is via the lattice artifacts of the doublers. Finally, and most speculatively, there may be a three dimensional chiral line coming in from large  $\beta$  which reflects the deconfinement transition back to meet the doubler chiral line heading towards  $(\beta, K) = (\infty, \frac{1}{4})$ .

This diagram is wonderfully complex, probably incomplete, and may take some time to map out. Given the results presented by Ukawa at this meeting [7], it appears that we may as yet be at too small a value of  $N_t$  for the negative mass confined phase to have appeared. As a final reminder, this entire discussion is of lattice artifacts, and other lattice actions, perhaps including various “improvements,” will look dramatically different.

## ACKNOWLEDGMENT

This manuscript has been authored under contract number DE-AC02-76CH00016 with the U.S. Department of Energy. Accordingly, the U.S. Government retains a non-exclusive, royalty-free license to publish or reproduce the published form of this contribution, or allow others to do so, for U.S. Government purposes.

## REFERENCES

1. For a recent discussion of this old topic, see M. Creutz, Phys. Rev. D52, 2951 (1995).
2. S. Coleman and E. Weinberg, Phys. Rev. D7 1888 (1973).
3. K. Wilson, in *New Phenomena in Subnuclear Physics*, Edited by A. Zichichi (Plenum Press, NY, 1977), p. 24.
4. S. Aoki, Nucl. Phys. B314, 79 (1989); S. Aoki and A. Gocksch, Phys. Rev. D45, 3845 (1992).
5. S. Aoki, S. Boetcher, and A. Gocksch, Phys. Lett. B331, 157 (1994); K. Bitar and P. Vranas, Phys. Rev. D50, 3406 (1994); Nucl. Phys. B, Proc. Suppl. 34, 661 (1994).
6. For a review see R. Gaii, in *Quantum Fields on the Computer*, M. Creutz, ed., p. 51 (World Scientific, 1992).
7. S. Aoki, A. Ukawa, and T. Umemura, Phys. Rev. Lett. 76, 873 (1996).



# Tensor Charge of the Nucleon on the Lattice

T. Hatsuda

*Institute of Physics, University of Tsukuba, Tsukuba, Ibaraki 305, Japan*

## Abstract

First results of lattice QCD simulation on the nucleon tensor-charge  $\delta q$  are presented. From the quenched QCD simulations with the Wilson quark action at  $\beta = 5.7, 6.0$  on a  $16^3 \times 20$  lattice and at  $\beta = 5.7$  on a  $12^3 \times 20$  lattice, we find (i) the connected part  $\delta q_{con.}$  is determined with small statistical error, (ii) the disconnected part  $\delta q_{dis.}$ , which violates the OZI rule, is consistent with zero, and (iii) the flavor-singlet tensor charge  $\delta\Sigma(\mu^2 = 2\text{GeV}^2) = \delta u + \delta d + \delta s$  takes 0.562(88) at  $\beta = 5.7$ , which is in contrast with the flavor-singlet axial charge  $\Delta\Sigma = 0.1 - 0.3$ .

The parton structure of the nucleon at the twist two level is known to be characterized by three structure functions  $f_1(x, \mu)$ ,  $g_1(x, \mu)$  and  $h_1(x, \mu)$  with  $x$  being the Bjorken variable and  $\mu$  being the renormalization scale (see, [1]).  $f_1$  and  $g_1$ , which represent the quark-momentum distribution and the quark-spin distribution in the nucleon respectively, can be measured by the deep inelastic lepton-hadron scattering. On the other hand,  $h_1(x)$ , which represents the quark-transversity distribution, could be measured in the polarized Drell-Yan processes, since it is related to the matrix element of the chiral-odd quark operator. Such experiment is planned using the relativistic heavy ion collider (RHIC) at BNL. Therefore, theoretical prediction of  $h_1$  is of great importance. Also, whether there is a large OZI violation in the first moment of  $h_1(x)$  has particular interest since the first moment of  $g_1(x)$  and that of the twist three structure function  $e(x)$  have been argued to have large OZI violation from experimental and/or theoretical point of view [2]. In this paper, we will report first results on the first moment of  $h_1(x)$  in lattice QCD simulations [3].

The tensor charge of the nucleon is defined as  $\delta q(\mu) = \int_0^1 [h_1(x, \mu) - \bar{h}_1(x, \mu)] dx$ , where  $h_1(x)$  and  $\bar{h}_1(x)$  are the quark and anti-quark distributions respectively. One can also write  $\delta q$  as a matrix element of the tensor operator

$$\langle ps | \bar{q} i \sigma_{\mu\nu} \gamma_5 q | ps \rangle = 2(s_\mu p_\nu - s_\nu p_\mu) \delta q, \quad (1)$$

where  $p_\mu$  is the nucleon's four momentum, and  $s_\mu$  is the nucleon's covariant spin-vector normalized as  $s_\mu^2 = -1$  [4]. In the nucleon light-cone frame,  $\delta q$  is interpreted as the "transversity" of quarks in a transversely polarized nucleon [1]. On the other hand, in the nucleon rest frame with  $\mu = 0$  and  $\nu = 3$ ,  $\delta q \sim \langle ps | \bar{q} \text{diag.}(\sigma_3, \sigma_3) q | ps \rangle$ . This implies that  $\delta q$  gives an independent information on the spin structure of the nucleon from the axial charge  $\Delta q \sim \langle ps | \bar{q} \gamma_3 \gamma_5 q | ps \rangle \sim \langle ps | \bar{q} \text{diag.}(\sigma_3, -\sigma_3) q | ps \rangle$ .

As for  $\delta q$ , approximate but model-independent inequalities such as  $|\delta u| < 3/2$  and  $|\delta d| < 1/3$  are known [5]. The non-relativistic quark model predicts  $\delta u = \Delta u = 4/3$  and  $\delta d = \Delta d = -1/3$ , while the relativistic quark wave functions with non-vanishing lower components lead to  $\delta u = 1.17$  and  $\delta d = -0.29$  together with the inequality  $|\delta q| > |\Delta q|$  [6]. There also exist estimates of  $\delta q$  using QCD sum rules [6,7] and a chiral quark model [8], but the uncertainties of the results are either large or uncontrollable.

In lattice QCD simulations, one can treat both the connected (OZI preserving) and disconnected (OZI violating) contributions even in the quenched approximation as has been demonstrated in [9,10]. Also, one can estimate systematic errors due to the lattice approximation by combining simulations with different lattice spacing and/or lattice size.

On the lattice, the matrix element of the tensor operator  $O(t, \mathbf{x}) = \bar{q} \text{diag.}(\sigma_3, \sigma_3) q$  is extracted as

$$R(t) \equiv \frac{\sum_{s=\pm} s \langle N_s(t) \sum_{t' \neq 0, x} O(t', \mathbf{x}) \bar{N}_s(0) \rangle}{\sum_{s=\pm} \langle N_s(t) \bar{N}_s(0) \rangle} \rightarrow \text{const.} + Z_T^{-1} \delta q t \quad (\text{large } t), \quad (2)$$

where  $Z_T$  is the lattice renormalization factor for the tensor operator and  $N(t)$  is the nucleon operator projected to zero momentum.

Following the works in ref. [9] where similar simulations have been done, we have taken into account the points below.

(i) We adopt the Wilson quark action and take  $N = (q^t C^{-1} \gamma_5 q)$  as a nucleon interpolating field. To enhance the nucleon signal, we use a wall source at initial time slice  $t = 0$  with the Coulomb gauge fixing at  $t = 0$ . Other time slices are not gauge-fixed. (ii) To avoid the contribution of the negative-parity nucleon propagating backward in time, the Dirichlet boundary condition for the quark propagator in the temporal direction is adopted. (iii) The connected amplitude is calculated by the conventional source method. To obtain the disconnected amplitude, the quark propagator with space-time unit source without gauge fixing is adopted. By this procedure, only the gauge invariant closed-loop is automatically selected after the average over the gauge configurations [9]. Note that  $t' = 0$  must be excluded in the sum in eq.(2) to make the procedure consistent. (iv) To compare the matrix element on the lattice with that in the  $\overline{MS}$  scheme, we employ the tadpole-improved renormalization factor  $Z_T(\mu a)$ . At  $\mu = 1/a$  with  $a$  being the lattice spacing,  $Z_T$  in the Wilson quark action reads [11]  $Z_T = (1 - 0.44 \alpha_{\overline{MS}}(1/a)) (1 - (3K/4K_c))$ , where  $K$  is the hopping parameter.

We carry out the quenched QCD simulation with the Wilson quark action at  $\beta = 5.7$  on a  $16^3 \times 20$  lattice with 1053 gauge configurations. In order to estimate the scaling behavior and the finite size effect, simulations at  $\beta = 6.0$  on a  $16^3 \times 20$  lattice with 420 configurations and at  $\beta = 5.7$  on a  $12^3 \times 20$  lattice with 306 configurations are also performed. Gauge configurations, which are generated with a single plaquette action separated by 1000 pseudo heat bath sweeps, are analyzed for three hopping parameters. The  $u$  and  $d$  quarks are assumed to be degenerate with  $K_u = K_d = K_q$ , while the strange quark is assigned a different hopping parameter  $K_s$ . The statistical errors of the data points are estimated by the single elimination jackknife procedure, and final fit of the hadron masses and  $R(t)$  are done by the  $\chi^2$ -fitting. The lattice spacing  $a$  is extracted from  $m_\rho a$  in the chiral limit.

The connected and disconnected parts of  $R(t)$  at  $\beta = 5.7$  on a  $16^3 \times 20$  lattice are shown in Fig.1 at  $K = 0.164$ . Clear linear behaviors are seen for the  $u$  and  $d$  connected contributions  $\delta q_{con.}$  in the interval up to  $t \sim 11$  even for the smallest quark mass  $K = 0.1665$ . For  $t > 11$ ,

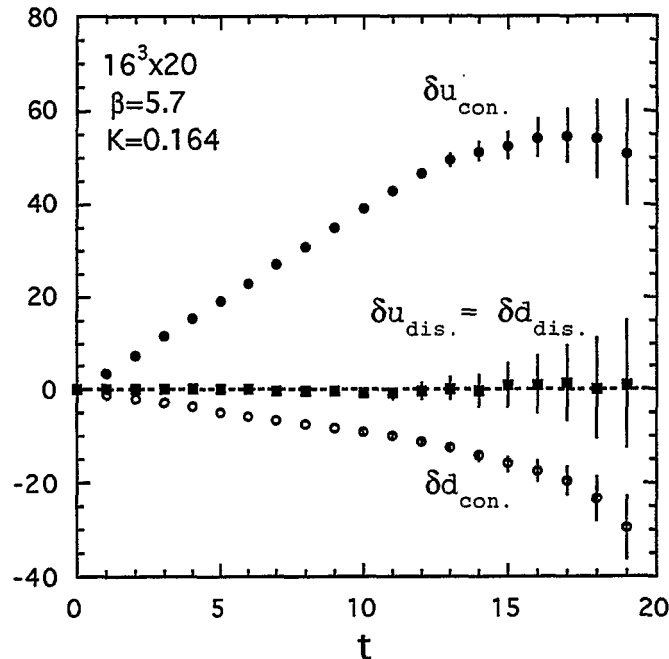


FIG. 1.  $R(t)$  as a function of  $t$  at  $K = 0.164$  and  $\beta = 5.7$  on a  $16^3 \times 20$  lattice.

errors grow rapidly. The disconnected contribution  $\delta q_{dis.}$  are concentrating around zero with errors comparable to the signal below  $t = 11$ . Since the disconnected part of  $R(t)$  does not show clear signal of a linear slope and we find no other sensible criterion, we take the same interval to extract  $\delta q_{dis.}$  in our linear fit. We adopt the same interval also for the fit of hadron masses. The linear fit of the connected part, the disconnected part and their sum are done separately.

For u and d quarks the fitted values are linearly extrapolated to the chiral limit  $m_q a = (1/K_q - 1/K_c)/2 = 0$ . For the strange disconnected contribution, we first make linear interpolation to the physical strange quark mass  $m_s a = (1/K_s - 1/K_c)/2$  at each fixed value of  $K_q$  for nucleon, and then the results are again linearly extrapolated to the chiral limit  $m_q a = (1/K_q - 1/K_c)/2 = 0$ . The physical strange quark mass  $m_s a$  is estimated by generalizing the relation  $m_\pi^2 a^2 = A m_q a$ , obtained from the hadron mass results, to  $m_K^2 a^2 = A(m_q a + m_s a)/2$  and using the experimental ratio  $m_K/m_\rho = 0.64$ .

Our final results extrapolated to the chiral limit at  $\beta = 5.7$  on a  $16^3 \times 20$  lattice are summarized in Table 1. The results for  $L = 12$  ( $\beta = 5.7$ ) and for  $L = 16$  ( $\beta = 6.0$ ), which are done to estimate the finite size effect and the scaling behavior, are also shown in the table. To compare our data on  $\delta q$  with that of  $\Delta q$ , results of a previous simulation for  $\Delta q$  in ref. [9] at  $\beta = 5.7$  on a  $16^3 \times 20$  lattice are presented.

From Table 1, one finds the following features.

1. Both the connected and total tensor charges at  $\beta = 5.7$  on a  $16^3 \times 20$  lattice satisfy the inequalities  $|\delta u| > |\Delta u|$  and  $|\delta d| < |\Delta d|$ . This is different from the prediction of naive quark models  $|\delta q| > |\Delta q|$  mentioned before.
2. We did not see clear linear slope for the disconnected parts and we could not make

tensor charge				axial charge (ref. [9])	
$\beta$	5.7		6.0	$\beta$	5.7
size	$16^3 \times 20$	$12^3 \times 20$	$16^3 \times 20$	size	$16^3 \times 20$
$\delta u$	0.839(60)	0.822(83)	0.805(30)	$\Delta u$	0.638(54)
$\delta u_{con.}$	0.893(22)	0.760(39)	0.811(18)	$\Delta u_{con.}$	0.763(35)
$\delta d$	-0.231(55)	-0.159(75)	-0.202(25)	$\Delta d$	-0.347(46)
$\delta d_{con.}$	-0.180(10)	-0.220(17)	-0.199(7)	$\Delta d_{con.}$	-0.226(17)
$\delta(u, d)_{dis.}$	-0.054(54)	0.076(71)	-0.0024(232)	$\Delta(u, d)_{dis.}$	-0.119(44)
$\delta s_{dis.}$	-0.046(34)	0.071(46)	-0.0017(147)	$\Delta s_{dis.}$	-0.109(30)
$\delta\Sigma$	0.562(88)	0.733(121)	0.601(42)	$\Delta\Sigma$	0.18(10)

TABLE I. Tensor charges extrapolated to the chiral limit together with the axial charge in ref. [9]. The flavor singlet tensor charge is defined as  $\delta\Sigma = \delta u + \delta d + \delta s$ . The matrix elements are evaluated at  $\mu = 1/a$ .

definite conclusion of its precise value from our simulation. Nevertheless, rather small error bars ( $\sim 0.05$ ) for  $\delta q_{dis.}$  in our main simulation ( $L = 16$  at  $\beta = 5.7$ ) indicate that the OZI violation in  $\delta q$  is small with a conservative upper bound  $|\delta q_{dis.}| < 0.1$ . Also, one notices that the disconnected part suffers a large finite volume effect. This is seen by comparing the data with smaller lattice sizes ( $L=12$  at  $\beta = 5.7$ ). The smallness of  $\delta q_{dis.}$  could be related to the C (charge conjugation)-odd and chiral-odd nature of the tensor operator  $\bar{q}\sigma_{\mu\nu}\gamma_5 q$  [12].

3. Due to the small disconnected contributions, the flavor singlet tensor charge  $\delta\Sigma = \delta u + \delta d + \delta s$  is not much suppressed from its quark model value. This is in contrast to the flavor singlet axial charge  $\Delta\Sigma$  which is known to be largely suppressed [2].

In the future, simulations on a larger volume at  $\beta = 6.0$  should be done to extract a definite value of the connected and disconnected tensor charges in the continuum limit as well as to reduce the finite size errors.

## ACKNOWLEDGEMENTS

This report is based on the work done in collaboration with S. Aoki, M. Doui and Y. Kuramashi. T.H. was supported in part by Univ. of Tsukuba Research Projects and in part by the Grants-in-Aid of the Japanese Ministry of Education, Science and Culture (No. 06102004).

## REFERENCES

- [1] R. L. Jaffe and X. Ji, Nucl. Phys. **B375**, 527 (1992) and references therein.
- [2] T. Hatsuda and T. Kunihiro, Phys. Rep. **247**, 221 (1994); G. Altarelli and G. Ridolfi, Nucl. Phys. B (Proc. Suppl.) **39B,C**, 106 (1995); M. Okawa, Nucl. Phys. B (Proc. Suppl.) **47**, 160 (1996).
- [3] Preliminary report of the this study was presented at Australia-Japan workshop on Quarks, Hadrons and Nuclei (Nov. 15-24, 1995, Adelaide, Australia) and at RIKEN

symposium on *Spin Structure of the Nucleon* (RIKEN, Japan, Dec. 18-19, 1995): report-no. Univ. of Tsukuba report UTHEP-337.

- [4] Here we use Minkowski notation with the Bjorken-Drell convention.
- [5] J. Soffer, Phys. Rev. Lett. **74**, 1292 (1995).
- [6] H. He and X. Ji, Phys. Rev. **D52**, 2960 (1995).
- [7] B. L. Ioffe and A. Khodjamiraian, Phys. Rev. **D51**, 3373 (1995).
- [8] H.-C. Kim, M. Polyakov and K. Goeke, Phys. Rev. **D53**, R4715 (1996).
- [9] M. Fukugita, Y. Kuramashi, M. Okawa and A. Ukawa, Phys. Rev. **D51** (1995) 5319; Phys. Rev. Lett. **75**, 2092 (1995).
- [10] S. J. Dong, J.-F. Lagae and K. F. Liu, Phys. Rev. Lett. **75**, 2096 (1995).
- [11] G. P. Lepage and P. B. Mackenzie, Phys. Rev. **D48**, 2250 (1993).
- [12] X. Ji and J. Tang, Phys. Lett. **B362**, 182 (1995).

# The Critical Points of Lattice QCD with a Non-Zero Quark Density

Maria-Paola Lombardo

*Zentrum für interdisziplinäre Forschung, Universität Bielefeld, D-33615 Bielefeld, Germany*

## Abstract

We study the interplay of quark number density and chiral symmetry in lattice QCD. We suggest that both are controlled by the eigenvalue spectrum of the fermionic propagator matrix, which shapes the pattern of zeros of the partition functions. The onset in the quark current would be triggered by the lowest lying eigenvalue, the chiral transition by the density of zeros, the two critical points being distinct in full QCD, and coincident in the quenched approximation. Our preliminary estimate for the critical point in full QCD in the infinite coupling limit compares favourably with the predictions of the strong coupling expansions and of numerical simulations based on exact, alternative representations of the partition function. Several reasons of perplexity however remains, which are briefly discussed.

Lattice QCD at non-zero quark number[1] is a poorly understood subject, despite the success of numerous calculations exploiting approximation schemes or simpler models. Many of the difficulties come from the particular structure of the Lagrangean: as the building blocks of the lattice QCD Lagrangean are quarks fields, a finite density on the lattice is realized by a coupling to a quark density, as opposed to a nucleon density of nuclear physics models. In practical numerical work, this induces several technical problems, which are described in detail in past publications. From a phenomenological point of view, it is not obvious that an excess of  $3N$  quarks would produce the same physical effects as an excess of  $N$  baryons and it might be useful to keep this in mind, especially when facing unexpected results[2].

This warning issued, the rest of this note will only deal with the current formulation of lattice QCD at non-zero quark number. The numerical analysis poses specific problems, since the action is complex. The only method which at the moment has the potential to deal with it, proposed by Barbour some years ago, is based on the representation of the partition function  $Z$  as  $Z = \langle \text{Det}(P - \exp(\mu)) \rangle$  where  $P$  is the fermionic propagator matrix[3].

The quark number density is an interesting observable which can be easily computed within this approach. The common feature of the results for the number density [4,5], as reviewed by Ukawa at this meeting, is a rather early onset  $\mu_o$ , definitively smaller than the critical point for chiral symmetry restoration expected around  $m_N/3$  and a saturation threshold, beyond which the particle density is one.  $\mu_o$  can be rather accurately measured in the strong coupling limit, where we find  $\mu_o \simeq m_\pi/2$ . High statistics simulations confirm that also at intermediate coupling the number density is sensitive to the pion mass [5].

In the following we only discuss the subcritical region at zero temperature in the infinite coupling limit, where the results they can be contrasted with the predictions of the strong

coupling expansions [6] and of an alternative, exact representation of the partition function [7].

We do not discuss here the problems connected with the saturation threshold, which hampers the observation of the Stefan-Boltzmann behaviour deep in the hot and dense phase, we just mention that possible solutions might be found in the framework of the lattice improved/perfect actions discussed here by Karsch, Wiese and T. D. Lee.

*The early onset : the density of states of the fermionic operator and the pion mass.* Gibbs proved that the onset of the number density on isolated configurations is controlled by the lowest eigenvalue of the fermion propagator matrix, and argued that the lowest eigenvalues is half the pion mass [8]. The results reviewed above suggest that this holds true also in the ensemble average. Alternative scenarios can be proposed and we postpone their discussion to a lengthier presentation. Here we merely sketch an argument which suggests that the persistency of this result in the statistical ensemble at zero temperature is compatible with the symmetries of the system, so ergodicity problems, if any, are not obviously manifest.

Consider the determinant on a isolated configuration, and the partition function after averaging over the statistical ensemble:  $Det = \prod_{i=1,6V}(z - \lambda_i)$ ,  $Z = \prod_{i=1,6V}(z - \alpha_i)$ . The  $\lambda_i$ 's are the eigenvalues of the fermionic propagator matrix,  $z$  is the fugacity  $e^\mu$  and the  $\alpha_i$ 's the zeros of the partition function in the complex fugacity plane: the zeros of the partition function can be seen as the "proper" ensemble average of the eigenmodes of the fermionic propagator matrix. From the determinant we obtain the number density on isolated configurations at zero temperature [8]:  $J_0 = 1/V \sum_{1 < |\lambda_i| < e^\mu} 1$ , and we note that an analogous expression holds true in the ensemble average as well, provided that we trade the eigenvalues with the zeros of the partition function. To know the fate of the onset of the current in the statistical ensemble we only need to monitor  $\min \{|\lambda|'s\}$ , the contribution of each pole to the current being, configuration by configuration, constant. Consider now that the Z3 symmetry, well verified in high statistics simulations [5], imposes  $Z = \prod_{i=1,2V}(z^3 - \beta_i)$ , i.e. the Z3 symmetry constraints the arguments of the zeros, but not their modulus. We have indeed checked that, configuration by configuration,  $\min \{\ln |\lambda|\} \simeq m_\pi/2$ : it may well be that the onset in the current in the full ensemble is the same as the onset on isolated configurations, whose origin is clear.

In a sense, this is a straightforward result: it says that the signal in the fermion number density is triggered by the lowest eigenmode in the spectrum of the fermionic propagator matrix. This result is the one expected for non confining theories, like Gross Neveu, where the lowest state defines indeed the dynamical fermion mass [9]. In *this formulation and within this approach* to lattice QCD the lowest eigenvalue gives half the pion mass.

*The chiral transition, and random matrix models* The possibility of observing another phase transition at  $\mu_c > \mu_o$ , and a non trivial distribution of zeros of the partition function are closely related, as we can read off the expression for the number density. How would these transitions at  $\mu_o$  and  $\mu_c$  relate with chiral symmetry restoration?

A very useful laboratory for the study of chiral symmetry is offered by random matrix models. In the case of QCD at finite density, we learnt from the work of Stephanov that the transition would show at a physical  $\mu_c$  in the full model, but at half the pion mass in the quenched approximation [10]. The applications of these results to QCD would suggest

that the onset for the quark number at half the pion mass would also restore the chiral symmetry in the quenched model, because of the simultaneous occurrence of quarks and conjugate quarks in the system, while in full QCD the chiral symmetry, would be restored at the “correct”  $\mu_c$  [6,7] thanks to the rearrangements of the eigenvalues produced by the richer dynamics— this relates also to the different nature of critical phenomena in quenched and full models. <sup>1</sup>

This discussion suggests a natural numerical strategy, whose preliminary outcome is shown in Figure 1. These results, obtained on a  $6^4$  and  $8^4$  lattice with a bare quark mass = .1, are preliminary, and are just meant as an illustration of the simple idea presented above. We see that the two statistical ensembles (quenched and full) show the same extrema, which defines a common critical region for the quenched and the full model. This agrees with the results of [13], where the “forbidden” region of quenched QCD was found to be coincident with the metastable region of full QCD, as computed in strong coupling expansion. However, contrary to the expectations of [13], it seems impossible to measure the real chiral transition point in the quenched approximation, while in the full model a peak in the eigenvalues distribution shows up in correspondence with the expected critical point. <sup>2</sup> Needless to say, it would be very interesting to study the relation of the spectrum of the fermionic propagator matrix with the fermion matrix spectrum, which is naturally related with chiral symmetry.

*Summary* The picture suggested by the above discussions is as follows : on isolated configurations the analysis of the fermionic propagator matrix gives a signal for the current in correspondence to its lowest state. This seems to survive the statistical ensemble average: there are two main reasons for this, first, that the real part of the pole is stable, second, that for each pole the amplitude of the contribution to the current is constant, and equal 1, so no cancellation occurs. Thus the onset for the quark number is the lowest real part of the zero of the partition function, or, equivalently, the real part of the logarithm of the lowest eigenmode of the fermionic propagator matrix. This a straightforward result in non-confining models, while in QCD the result  $\mu_o \simeq m_\pi/2$ , and the nature of the region  $\mu_o < \mu < \mu_c$ , deserve further investigation.

We haven't found any indication of systematic errors associated with the method or lack of ergodicity in the algorithm which can offer an alternative explanations of these observations. Still, they cannot be excluded. The best way to address this issue, in our opinion, is to cross check with the results of alternative formulations<sup>12</sup>.

Within this formulation quenched and full QCD share the same critical region. However, the simple dynamics of the quenched model cannot build up any structure in the density of

---

<sup>1</sup>Given the prominent role of the density of states evaluated at zero  $\mu$ , the suggestion would naturally arise to give a second try to various partial quenched schemes [11]. These approximations were dismissed in the past because of the threshold at half the pion mass, but, as we have shown, this threshold is not necessarily related with the chiral transition. Particularly interesting could be their application to the recent proposal by Kogut and collaborators [12].

<sup>2</sup>The is reminiscent of other observations: quenched and full model can be completely different, but even dramatic qualitative differences are realized by subtle numerical effects.



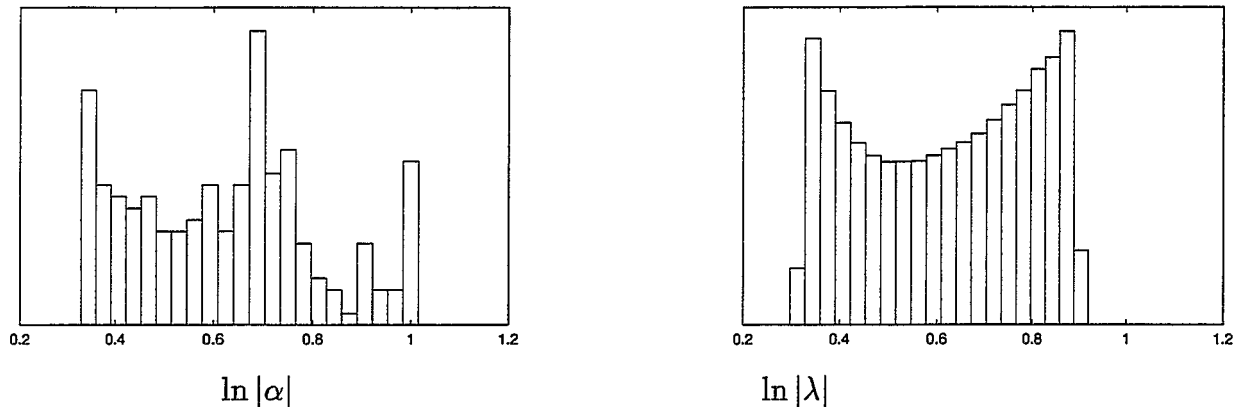


FIG. 1. Density of states for the grand canonical partition function (left) and the fermionic propagator matrix, which is its quenched counterpart: the threshold, compatible with  $m_\pi/2 = .31$ [13] induces a non zero number density in the quenched and full model alike; one appealing scenario could be that this threshold induces the restoration of chiral symmetry in the quenched model, but not in the full model where the chiral transition point, estimated from the position of the peak, is consistent with  $\mu_c = .69(1)$ [7]

modes, so no new transition appears after statistical averaging, and the results from random matrix models suggest that the onset of the current restores chiral symmetry. The structure in the spectrum is instead apparent in full QCD, where we attempted, not unsuccessfully, an estimate of the chiral transition point.

These observations would predict a non-zero critical density at the zero temperature chiral transition, and might be related with the presence of diquarks in the region  $\mu_o < \mu < \mu_c$ . But, again, cross checks with other formulations are mandatory in order to disentangle possible numerical artifacts from predictions amenable to an experimental verification.

This note reports on work in progress with I. Barbour, S. E. Morrison, E. G. Klepfish and J. B. Kogut. I wish to thank my collaborators and acknowledge valuable discussions with F. Karsch. I would like to thank the Physics Department of the University of Bielefeld for its hospitality, and the High Energy Group of HLRZ/Jülich, particularly K. Schilling, for support during the initial stages of this project. The calculations were done at HLRZ/KFA Jülich. This work was partially supported by Nato grant no. CRG 950896.

## REFERENCES

1. J. B. Kogut, H. Matsuoka, M. Stone, H. W. Wyld, S. Shenker, J. Shigemitsu, D. K. Sinclair, Nucl. Phys. **B225** [FS9], (1983) 93; P. Hasenfratz and F. Karsch, Phys. Lett. **125B** (1983) 308.
2. An interesting criticism of the current formulation can be inferred from the paper by D. Kharzeev, Phys. Lett. **B378** (1996) 238.
3. I. Barbour, Nucl. Phys. **B** (Proc. Suppl.) 29 (1992) 22.
4. A. Hasenfratz and D. Toussaint, Nucl. Phys. **B371** (1992) 539.
5. I. Barbour, J. Kogut and S. E. Morrison *Phase structure of lattice QCD at finite density with dynamical fermion*, talk given by S. E. Morrison at Lattice96, 14th International Sym-

- posium on Lattice Field Theory, St. Louis, MO, 4-8 June 1996, hep-lat/ 9608057.
6. N. Bilić, K. Demeterfi and B. Petersson, Nucl. Phys. **B377** (1992) 615.
  7. F. Karsch and K.H. Mütter, Nucl. Phys. **B313** (1989) 541.
  8. P.E. Gibbs, Phys. Lett. **172B** (1986) 53.
  9. S. Hands, S. Kim and J.B. Kogut, Nucl.Phys. **B442** (1995) 364.
  10. M. I. Stephanov, Phys. Rev. Lett. 76 (1996) 4472.
  11. J. Engels and H. Satz, Phys. Lett. **159B** (1985) 151.
  12. J. B. Kogut and D. K. Sinclair, *QCD with chiral 4-fermion interaction*, talk given by D. K. Sinclair at Lattice96, hep-lat/9607083; I. Barbour, J. B. Kogut and S. E. Morrison, *QCD at finite density*, talk given by I. Barbour at the International Conference *Multi Scale Phenomena and their Simulation*, Zentrum für interdisziplinäre Forschung, Bielefeld, Germany, 30 September– 4 October 1996.
  13. M.-P. Lombardo, J. B. Kogut and D. K. Sinclair, Phys. Rev. **D54** (1996) 2303.

# Hadronic Ratios and the Number of Projectile Participants

Jean Cleymans and Azwinndini Muronga  
*Department of Physics, University of Cape Town,  
Rondebosch 7700, South Africa*

## Abstract

We investigate the dependence of hadronic ratios on the number of projectile participants using a thermal model incorporating exact baryon number and strangeness conservation. A comparison is made with results from  $Au - Au$  collisions obtained at the BNL-AGS.

Preliminary results on the dependence of hadronic ratios on the number of projectile participants have recently been presented by the E866 collaboration [1] for relativistic  $Au - Au$  collisions at the BNL-AGS. These results give insight into the behaviour of the produced hadronic system as a function of the baryon number and of the size of the interaction volume.

It is the purpose of the present paper to analyze these results using a thermal resonance gas model at a fixed temperature and a fixed baryon density. Our treatment differs from previous [2,3] ones in that we consider the baryon content exactly. This means that we do not introduce chemical potentials for the baryon number (nor for strangeness). Chemical potentials are usually introduced to enforce the right quantum numbers of the system in an average sense. This is a correct treatment for a large system, however, for a small system the production of e.g. an extra proton - anti-proton pair will clearly be more suppressed than in a large system. These extra corrections were first pointed out by Hagedorn [4] and subsequently a complete treatment was presented by many people [5-8]. We emphasize that these corrections do not contain any information about the dynamics. They simply follow from baryon number conservation. These corrections must be taken into account before considering more involved models. It is also worth emphasizing that they do not involve any new parameters.

As an example we analyze the (preliminary) data recently presented by the E866 collaboration [1] at BNL.

The exact treatment of quantum numbers in statistical mechanics is obtained by projecting the partition function onto the desired values of  $B$  and  $S$

$$Z_{B,S} = \frac{1}{2\pi} \int_0^{2\pi} d\phi e^{-iB\phi} \frac{1}{2\pi} \int_0^{2\pi} d\psi e^{-iS\psi} Z(T, \lambda_B, \lambda_S) \quad (1)$$

where the usual fugacity factors  $\lambda_B$  and  $\lambda_S$  have been replaced by :

$$\lambda_B = e^{i\phi} \quad \lambda_S = e^{i\psi}. \quad (2)$$

We will use

$$B = 2N_{pp} \quad (3)$$

where  $N_{pp}$  is the number of projectile participants with the factor 2 reflecting the symmetry of the  $Au - Au$  collision system. As the contributions always come pairwise for particle and anti-particle the fugacity factors will give rise to the cosine of the angle. In the further treatment it is useful to group all particles appearing in the Particle Data Booklet [10] into four categories depending on their quantum numbers (we leave out charm and bottom).  $Z_K$  is the sum (given below) of all mesons having strangeness  $\pm 1$  ( $K, \bar{K}, K^*, \dots$ ), similarly  $Z_N$  is the sum of all baryons and anti-baryons having zero strangeness,  $Z_Y$  is the sum of all hyperons and anti-hyperons while  $Z_0$  is the sum of all non-strange mesons, and so on :

$$\begin{aligned} Z_K &= \sum_{j \in |S|=1, |B|=0} V \int \frac{d^3 p}{(2\pi)^3} e^{-E_j/T}, \\ Z_N &= \sum_{j \in |S|=0, |B|=1} V \int \frac{d^3 p}{(2\pi)^3} e^{-E_j/T}, \\ Z_Y &= \sum_{j \in |S|=1, |B|=1} V \int \frac{d^3 p}{(2\pi)^3} e^{-E_j/T}, \\ Z_0 &= \sum_{j \in |S|=0, |B|=0} V \int \frac{d^3 p}{(2\pi)^3} e^{-E_j/T}. \end{aligned} \quad (4)$$

We do not include cascade particles as their contribution is unimportant for the energy range under consideration and their inclusion considerably complicates the formalism. Each term will be multiplied by the cosine of an angle, either  $\phi$  or  $\psi$ , in the case where two angles are needed (e.g. for the hyperons) one introduces a new one,  $\alpha$ , using

$$\delta(\phi - \psi - \alpha) = \sum_{n=-\infty}^{\infty} e^{in(\phi - \psi - \alpha)}. \quad (5)$$

Using the integral representation of the modified Bessel functions

$$I_n(z) = \frac{1}{\pi} \int_0^\pi e^{z \cos \theta} \cos n\theta \, d\theta \quad (6)$$

one can write the partition function as

$$Z_{B,S} = Z_0 \sum_{n=-\infty}^{\infty} I_n(2Z_Y) I_{n+B}(2Z_N) I_n(2Z_K) \quad (7)$$

In order to discuss the particle abundances it is useful to introduce the following quantities [8]

$$\begin{aligned} R_K &= \sum_{n=-\infty}^{\infty} I_n(2Z_Y) I_{n+B}(2Z_N) I_{n+1}(2Z_K), \\ R_N &= \sum_{n=-\infty}^{\infty} I_{n+1}(2Z_Y) I_{n+B-1}(2Z_N) I_n(2Z_K), \\ R_Y &= \sum_{n=-\infty}^{\infty} I_{n+1}(2Z_Y) I_{n+B}(2Z_N) I_n(2Z_K), \end{aligned}$$

$$\begin{aligned}
R_{\bar{K}} &= \sum_{n=-\infty}^{\infty} I_n(2Z_Y)I_{n+B}(2Z_N)I_{n-1}(2Z_K), \\
R_{\bar{N}} &= \sum_{n=-\infty}^{\infty} I_{n+1}(2Z_Y)I_{n+B+1}(2Z_N)I_n(2Z_K), \\
R_{\bar{Y}} &= \sum_{n=-\infty}^{\infty} I_{n-1}(2Z_Y)I_{n+B}(2Z_N)I_n(2Z_K).
\end{aligned} \tag{8}$$

If a particle,  $i$ , has strangeness 1 and baryon number 0, it's density will be given by

$$n_i = \left[ Z_0 \frac{R_K}{Z_{B,S}} \right] \int \frac{d^3 p}{(2\pi)^3} e^{-E_i/T}. \tag{9}$$

while a particle with strangeness 0 and baryon number 1, will have a density given by

$$n_i = \left[ Z_0 \frac{R_N}{Z_{B,S}} \right] \int \frac{d^3 p}{(2\pi)^3} e^{-E_i/T} \tag{10}$$

All other particle densities are obtained by using the appropriate  $R$  factor given in equation (8). The factor in square brackets replaces the fugacity in the usual grand canonical ensemble treatment [2,3]. Having thus determined all particle densities, we consider the behaviour at freeze-out time. In this case all the resonances in the gas are allowed to decay into lighter stable particles. This means that each particle density is multiplied with its appropriate branching ratio (indicated by  $Br$  below). The abundances of particles in the final state are thus determined by :

$$\begin{aligned}
n_{\pi^+} &= \sum n_i Br(i \rightarrow \pi^+), \\
n_{K^+} &= \sum n_i Br(i \rightarrow K^+), \\
n_{\pi^-} &= \sum n_i Br(i \rightarrow \pi^-), \\
n_{K^-} &= \sum n_i Br(i \rightarrow K^-), \\
n_p &= \sum n_i Br(i \rightarrow p), \\
n_{\bar{p}} &= \sum n_i Br(i \rightarrow \bar{p}).
\end{aligned} \tag{11}$$

where each sum runs over all particles contained in the hadronic gas.

The comparison with experimental results is shown in figures 1 to 4. To compare with earlier calculations [2,3] we keep the temperature  $T$  and the baryon density  $B/V$  fixed. This corresponds to keeping the baryon chemical potential fixed in the standard hadronic gas calculations using the grand canonical ensemble.

In figure 1 we compare our results with recent data from the AGS [1,11]. Figure 1 shows the  $K^+/\pi^+$  ratio. As one can see the results obtained from our calculation show a steep rise with  $N_{pp}$  before leveling off. The dependence on the baryon density is minimal in this case. This result is confirmed by calculations done in the grand canonical ensemble which also show that this ratio is almost independent of the baryon density [3]. We note that the experimental data indicate a slower rise than the model calculation.

In figures 2, 3 and 4 we show the  $K^-/\pi^+$ , the  $K^+/K^-$  and the  $p/\pi^+$  ratios. In each case good agreement is obtained with the results of the E866 collaboration [1]. The relevant

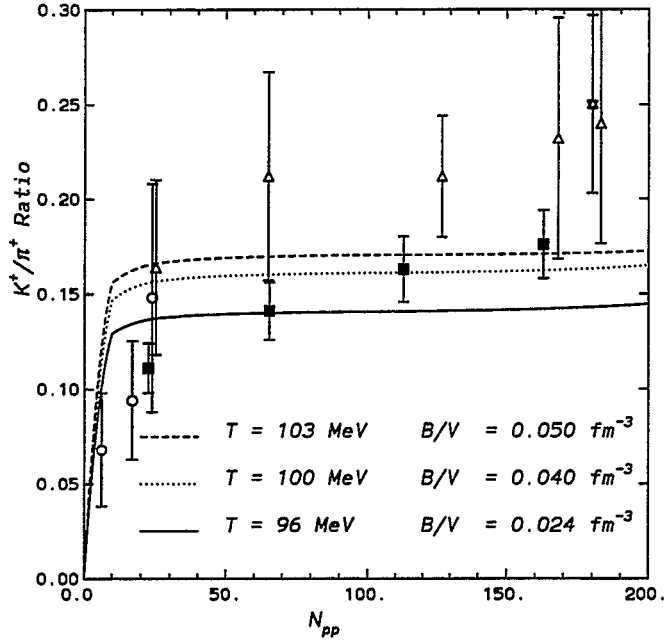


Figure 1

FIG. 1. The  $K^+/\pi^+$  ratio as a function of the number of projectile participants  $N_{pp}$ . The solid line is obtained for  $T = 96$  MeV and  $B/V = 0.024$   $\text{fm}^{-3}$ , the dashed line corresponds to  $T = 103$  MeV and  $B/V = 0.050$   $\text{fm}^{-3}$  while the dotted line corresponds to  $T = 100$  MeV and  $B/V = 0.04$   $\text{fm}^{-3}$ .

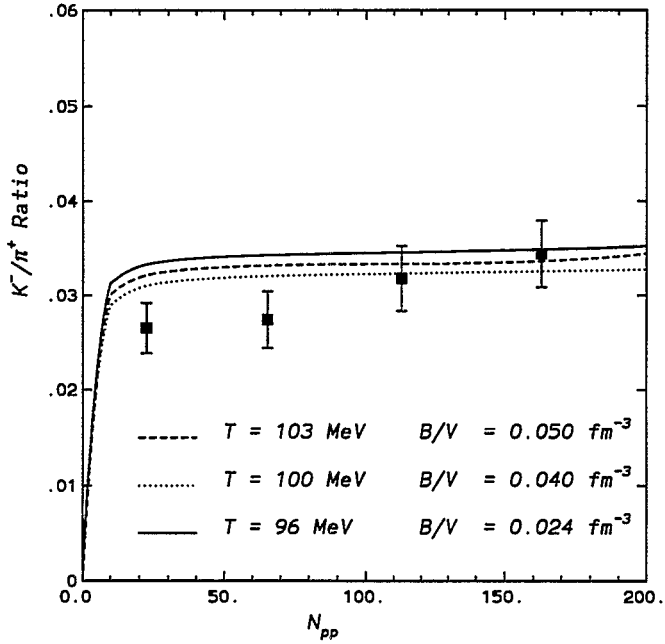


Figure 2

FIG. 2. The  $K^-/\pi^+$  ratio as a function of the number of projectile participants  $N_{pp}$ . The notation is the same as in figure 1.

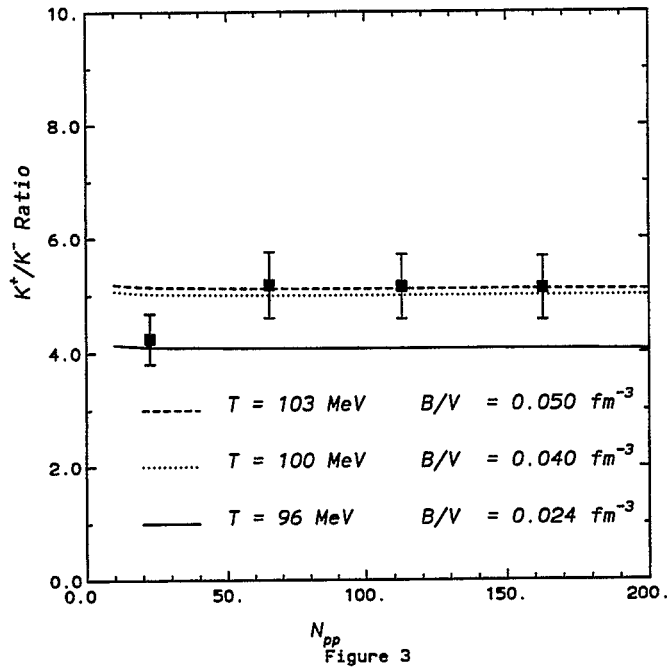


FIG. 3. The  $K^+/K^-$  ratio as a function of the number of projectile participants  $N_{pp}$ . The notation is the same as in figure 1.

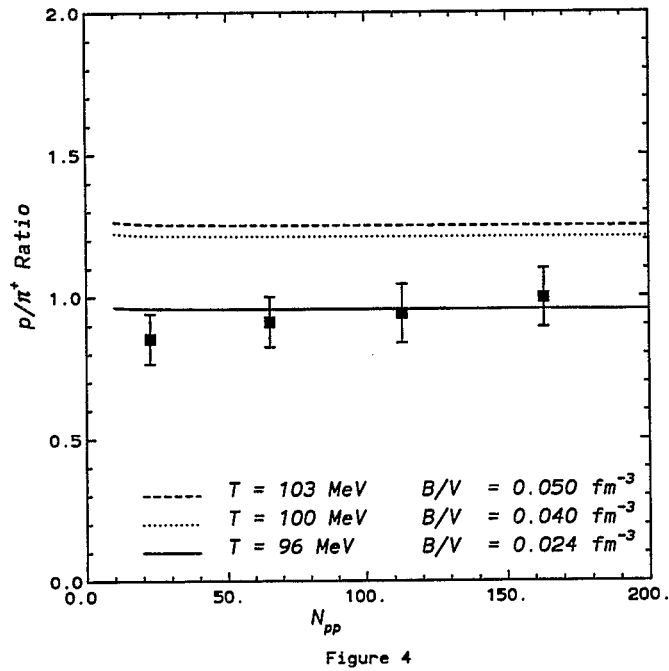


FIG. 4. The  $p/\pi^+$  ratio as a function of the number of projectile participants  $N_{pp}$ . The notation is the same as in figure 1.

temperature is around  $T \approx 100\text{MeV}$ , the baryon density is in the range  $B/V \approx 0.02 - 0.05 \text{ fm}^{-3}$ . In the grand canonical ensemble this corresponds to a baryon chemical potential of  $\mu_B \approx 540 \text{ MeV}$ .

## ACKNOWLEDGMENTS

We gratefully acknowledge the financial support of the University of Cape Town (URC) and of the Foundation for Research development(Pretoria). We acknowledge the help of Duncan Elliott for his analysis of the data in the grand canonical ensemble.

## REFERENCES

- [1] E866 Collaboration, Y. Akiba, Talk presented at Quark Matter '96, Heidelberg May 1996.
- [2] P. Braun-Munzinger, J. Stachel, J. P. Wessels and N. Xu, *Phys. Lett.* B344 (1995) 43.
- [3] J. Cleymans, D. Elliott, H. Satz and R.L. Thews CERN preprint CERN-TH/95-298, *Z. Phys.* C(to be published).
- [4] R. Hagedorn, CERN yellow report 71-12 (1971).
- [5] R. Hagedorn, K. Redlich, *Z. Phys.* C27 (1985) 541.
- [6] C. Derreth, W. Greiner, H.-Th. Elze and J. Rafelski, *Phys. Rev.* C31 (1985) 360.
- [7] M. Gorenstein, V.K. Petrov and G.M. Zinovjev, *Phys. Lett.* B106 (1981) 327.
- [8] J. Cleymans, E. Suhonen, G.M. Weber, *Z. Phys.* C53 (1992)485.
- [9] J. Cleymans and H. Satz, *Z. Phys.* C57 (1993) 135.
- [10] Review of Particle Properties, *Phys. Rev.* D50 (1994) 1177.
- [11] G.S.F. Stephans, "*Strangeness in Hadronic Matter*", ed. J. Rafelski, AIP Press 1995.



**II.**  
**Hard**  
**Probes**

# Medium-induced QCD

Yu.L. Dokshitzer

*INFN, Sezione di Milano, via G. Celoria 16, 20133 Milan, Italy*

*and*

*St.Petersburg Nuclear Physics Institute, 188350 Gatchina, Russia*

## I. QED LPM EFFECT ON THE BACK OF AN ENVELOPE

It is acceleration of a charge that causes radiation. A fast charged particle, when sent through a medium, experiences multiple small-angle scatterings. Multiple kicks lead to multiple photon bremsstrahlung which can be characterized in terms of the induced radiation intensity per unit length (radiation density). The  $\omega$ -dependence of the radiation intensity can be deduced from the following back-of-an-envelope consideration.

If the scattering centres act as independent sources of bremsstrahlung, the radiation density is simply given by

$$\omega \frac{dI^{(BH)}}{d\omega dz} = \frac{1}{\lambda} \left( \omega \frac{dI}{d\omega} \right)^{(1)} ; \quad \left( \omega \frac{dI}{d\omega} \right)^{(1)} \propto \alpha , \quad (1)$$

with  $\lambda$  the mean free path. This expression corresponds to the so called Bethe-Heitler (BH) limit and is valid when the photon *formation time* is small as compared with the distance  $\lambda$  between the neighboring scatterings:

$$t_{\text{form}} \simeq \frac{\omega}{k_{\perp}^2} \simeq \frac{1}{\Theta^2 \omega} < \lambda . \quad (2)$$

QED bremsstrahlung is restricted into cones of opening angle  $\Theta_s \simeq \mu/E$ , with  $E$  the energy of the projectile and  $\mu$  a typical momentum transfer in a single scattering.

Thus, the BH regime applies to photon energies satisfying

$$\frac{E}{E_{\text{LPM}}} < \frac{\omega}{E} < 1 , \quad E_{\text{LPM}} \equiv \lambda \mu^2 . \quad (3)$$

If  $\omega$  is taken sufficiently small the photon formation length  $ct_{\text{form}}$  may embody few scatterings:  $t_{\text{form}} > n\lambda$ ,  $n > 1$ . In such circumstances quantum mechanics enters the game and radiation due to separate scatterings can no longer be treated independently. The amplitudes add up coherently and a group of  $n$  centres radiates as a single effective scattering centre. The bremsstrahlung density gets suppressed by the factor  $n$  as compared to the BH formula:

$$\omega \frac{dI^{(LPM)}}{d\omega dz} = \frac{1}{n_{\text{coh}} \lambda} \left( \omega \frac{dI}{d\omega} \right)^{(1)} . \quad (4)$$

In a course of  $n$  independent interactions with the medium, the typical total scattering angle of the charge, which enters into the expression for the formation time, increases with

$n$  according to the diffusion law,  $\Theta_s^2 \rightarrow n\Theta_s^2$ . As a result, the coherent (LPM) regime holds for

$$t_{\text{form}} \approx \frac{1}{n\Theta_s^2\omega} > n\lambda \implies n < (\omega\lambda\Theta_s^2)^{-\frac{1}{2}} \equiv n_{\text{coh}}^{\text{QED}}. \quad (5)$$

Thus the coherence number  $n_{\text{coh}}$  (in the QED problem) is

$$n_{\text{coh}}^{\text{QED}} = \frac{E}{\sqrt{\omega E_{\text{LPM}}}}. \quad (6)$$

It increases with  $\omega$  decreasing. When  $n_{\text{coh}}$  becomes so large that the coherence length reaches the longitudinal size of the material,  $n_{\text{coh}}\lambda = L$ , the radiation density hits the minimum. In this (so called ‘‘factorization’’) limit the whole medium acts coherently and the *total* bremsstrahlung amounts to radiation off the incoming and outgoing charge, which is practically independent of the medium:

$$\int_0^L dz \frac{\omega dI^{(\text{fact})}}{d\omega dz} = L \cdot \frac{\omega dI^{(\text{fact})}}{d\omega dz} = \left( \omega \frac{dI}{d\omega} \right)^{(1)}.$$

In the intermediate range of photon energies

$$1 < n_{\text{coh}}^{\text{QED}} < \frac{L}{\lambda} \implies \frac{E}{E_{\text{LPM}}} \left( \frac{\lambda}{L} \right)^2 < \frac{\omega}{E} < \min \left\{ \frac{E}{E_{\text{LPM}}}, 1 \right\} \quad (7)$$

the soft bremsstrahlung spectrum acquires an unusual  $\omega$ -dependence

$$dI^{(\text{LPM})} \propto \frac{d\omega}{\sqrt{\omega}}, \quad \text{to be compared with the standard } dI^{(\text{BH})} \propto \frac{d\omega}{\omega}.$$

This spectacular coherent phenomenon has been predicted quite some time ago by Lev Landau and Isaac Pomeranchuk <sup>[1]</sup>. Their semi-qualitative prediction was elaborated by Arkady Migdal in [2] where a rigorous (and mathematically quite involved) derivation has been given. (Hence, an abbreviation LPM in (3) and thereafter.)

Small QED coupling makes the electron mean free path  $\lambda$  rather large and, as a result, puts the characteristic energy  $E_{\text{LPM}}$  (3) in the ball-park of few TeV for realistic target materials. This may explain why it took 40 years to observe the LPM effect in a recent SLAC experiment <sup>[3]</sup> long after this phenomenon has become a part of classical textbooks on radiation physics <sup>[4]</sup>.

Thus for realistic electron energies,  $E < E_{\text{LPM}}$ , three regimes can be observed:

$$\omega \frac{dI}{d\omega dz} \simeq \begin{cases} \frac{\alpha}{L} & \omega < \omega_{\text{fact}} \equiv E^2\lambda/L^2\mu^2, \\ \frac{\alpha}{\lambda} \sqrt{\frac{\lambda\mu^2\omega}{E^2}} & \omega_{\text{fact}} < \omega < \omega_{\text{BH}} \equiv E^2/\lambda\mu^2, \\ \frac{\alpha}{\lambda} & \omega_{\text{BH}} < \omega < E. \end{cases} \quad (8)$$

The most energetic photons with  $\omega \simeq E$  follow the BH pattern, so that the total *radiative energy loss* becomes

$$\Delta E = \int_0^L dz \int \int_0^E d\omega \omega \frac{dI}{d\omega dz} \propto \alpha \frac{L}{\lambda} E.$$

For  $E > E_{\text{LPM}}$  the third (BH) energy interval in (8) collapses, and the coherent LPM suppression starts to affect hard photons:

$$\Delta E \propto \alpha \frac{L}{\lambda} \sqrt{\lambda \mu^2 E}.$$

Finally, in the extreme limit when  $E > L^2 \mu^2 / \lambda$ , the medium becomes “transparent” and we are back to the linear (medium independent) expression

$$\Delta E \propto \alpha E.$$

A fresh treatment of the QED LPM effect based on describing electron propagation in statistically averaged atomic electric fields was recently given by R. Blankenbecler and S. Drell [5]. Of particular interest are coherent structures (maxima and minima) in the photon spectra off *structured* (multi-layer) targets predicted in [6].

## II. LPM EFFECT IN QCD

A new interest in the LPM effect has arisen because of the corresponding problem in QCD: the energy loss of a high energy quark or gluon due to medium-stimulated gluon radiation, if proved noticeably large, may affect the physics of lepton-nucleus, hadron-nucleus and nucleus-nucleus collisions. It may be also important as a signal for quark-gluon plasma formation in high energy heavy ion collisions.

Till recently, for reasons beyond my comprehension, the energy loss for a QCD projectile (say, a quark passing through quark-gluon plasma) was widely believed to be *independent* of the initial energy [7] (though an attentive searcher would have found a rather broad range of predictions, from  $E^0$  up to  $E^2$ , in the literature).

The first step to the true solution of the LPM problem in QCD was made by M. Gyulassy and X.-N. Wang in [8] where the problem has been formulated most clearly in terms of a simplified but realistic model for multiple scattering of a color charge in a QCD medium. The Gyulassy-Wang model pictures the medium as consisting of static scattering centres interacting via one gluon exchange with the energetic quark (gluon) projectile. The static approximation eliminates *collision* energy loss and thus singles out the *radiation* loss under interest.

Gyulassy and Wang considered gluon radiation caused by multiple interactions of the *projectile* with the target medium. It was found that within this picture interference between elementary bremsstrahlung amplitudes due to remote scattering centres are *color suppressed* (by the factor  $(1/2N)^{n-1}$  for the quark-projectile and by  $(1/2)^{n-1}$  for the initial gluon, with  $n$  the distance between the centres in units of  $\lambda$ ). Therefore only gluons with small formation times  $t_{\text{form}} \lesssim \lambda$  are radiated and, as a result, the radiation spectrum falls off rapidly with  $\omega$  and the density of the mean energy loss amounts to a constant:

$$\left| \frac{dE}{dz} \right| = \int_0^E d\omega \omega \frac{dI}{d\omega dz} \sim \alpha_s \mu^2.$$

R. Baier et al. (BDPS) have noticed another set of contributions, disregarded in [8], in which the secondary gluon gets rescattered rather than the projectile color charge, as shown by the second graph in Fig. 1 for the double scattering case.



FIG. 1. Rescattering at  $t_2$  of the initial quark and of the secondary gluon produced at  $t_1$ .

These contributions bring back gluons with large formation times,  $t_{\text{form}} \lesssim \lambda n_{\text{coh}}$ ,  $n_{\text{coh}} \gg 1$ . The coherence number  $n_{\text{coh}}$  differs from  $n_{\text{coh}}^{\text{QED}}$  (6) because of the difference in the accompanying radiation in QED and QCD.

In QED the elementary amplitude for radiation of a soft photon with 4-momentum  $k$  due to scattering  $p_i \rightarrow p_{i+1}$  at a centre  $\#i$  reads

$$A_i^\mu \propto \frac{p_{i+1}^\mu}{(p_{i+1}k)} - \frac{p_i^\mu}{(p_i k)}. \quad (9)$$

As it can be shown making use of the gauge invariance, it may be rewritten in the form of the 2-dimensional current built up of relative “transverse angles” between the photon direction and the directions of the incoming and scattered electrons:

$$\vec{A}_i \propto \frac{\vec{\Theta} - \vec{\Theta}_{i+1}}{(\vec{\Theta} - \vec{\Theta}_{i+1})^2} - \frac{\vec{\Theta} - \vec{\Theta}_i}{(\vec{\Theta} - \vec{\Theta}_i)^2}. \quad (10)$$

Here

$$\vec{\Theta} \equiv \frac{\vec{k}_\perp}{\beta} E, \quad \vec{\Theta}_i \equiv \frac{\vec{p}_{i\perp}}{\beta_i E},$$

with  $\beta$  and  $\beta_i$  the longitudinal light-cone (Sudakov) components of the photon and electron momenta correspondingly. Elastic scattering does not affect the electron energy, so that  $p_{i+1}^{(0)} \approx p_i^{(0)} = E$ ,  $\beta_{i+1} = \beta_i = 1$ ,  $\beta = \omega/E \ll 1$ . Transverse momentum of the projectile changes,  $\vec{p}_{i+1\perp} = \vec{p}_{i\perp} + \vec{q}_{i\perp}$ , and so does the relative angle:

$$\vec{\theta}_i = \vec{\Theta} - \vec{\Theta}_i \implies \vec{\theta}_{i+1} \vec{\Theta} - \vec{\Theta}_{i+1} = \vec{\theta}_i - \vec{\theta}_{si}, \quad \vec{\theta}_{si} \equiv \vec{q}_i/E.$$

So we may represent the elementary QED radiation current as

$$\vec{A}_i \propto \frac{\vec{\theta}_i - \vec{\theta}_{si}}{(\vec{\theta}_i - \vec{\theta}_{si})^2} - \frac{\vec{\theta}_i}{\theta_i^2}. \quad (11)$$

In the QCD case the situation is different. Now the two terms of the basic amplitude (9) corresponding to emission off the outgoing and incoming lines acquires the color generator factors in a different order:

$$A_i^\mu \propto T^a T^b \frac{p_{i+1}^\mu}{(p_{i+1}k)} - T^b T^a \frac{p_i^\mu}{(p_i k)} = \frac{1}{2} \{T^a T^b\} A_i^{(\text{Abelian})} + \frac{1}{2} [T^a T^b] \left( \frac{p_{i+1}^\mu}{(p_{i+1}k)} + \frac{p_i^\mu}{(p_i k)} \right), \quad (12)$$

where  $a$  and  $b$  are the octet color indices of the emitted and exchanged gluons respectively. The *color symmetric* piece of the amplitude (12) has abelian structure and is negligible at high energies as compared with its *color antisymmetric* piece. Indeed, in the limit  $E \rightarrow \infty$  we have  $|\vec{\theta}_{si}| \simeq \mu/E \rightarrow 0$  and the radiation current (11) vanishes. In this limit we can treat our projectile (quark) as moving along the  $z$ -axis, so that  $\Theta_i = 0$  ( $\beta E = \omega$  = fixed,  $\beta_i E \rightarrow \infty$ ). Gluon emission off the incoming and outgoing quark lines combines into the current proportional to the QCD structure constant:

$$\vec{A}_i \propto if_{abc} T^c \frac{\vec{\Theta}_\perp}{\Theta_\perp^2} \propto if_{abc} T^c \frac{\vec{k}_\perp}{k_\perp^2}.$$

Taken together with the specific QCD contribution due to radiation from the  $t$ -channel gluon exchange this results in the effective radiation current (shown by the black blob in Fig. 1)

$$\vec{A}_i \propto if_{abc} T^c \left( \frac{\vec{k}_\perp - \vec{q}_{i\perp}}{(\vec{k}_\perp - \vec{q}_{i\perp})^2} - \frac{\vec{k}_\perp}{k_\perp^2} \right). \quad (13)$$

### III. ENERGY SPECTRUM OF INDUCED GLUON RADIATION

There is a nice correspondence [9] between the effective radiation currents in QED (11) and in QCD (13): the latter we get by substituting *transverse momenta* for the *transverse angles* in the former one! Moreover, QED and QCD multiple scattering patterns also respect such a substitution. Indeed, in the QED case, as it was already mentioned above, it is the photon-electron angle  $\theta_i$  which gets additive independent kicks resulting in a random walk (diffusion) in angle:  $\theta^2 \rightarrow \theta^2 + n(\mu/E)^2$ . At the same time, in QCD it is a gluon, rather than a quark, that receives the kicks, which leads to diffusion in its transverse momentum:  $k_\perp^2 \rightarrow k_\perp^2 + n\mu^2$ .

Given this symmetry, we can simply find the coherence number  $n_{\text{coh}}^{\text{QCD}}$  by repeating the previous estimates based on the formation time (2) now expressed in terms of  $k_\perp$ .

For the BH regime we have

$$t_{\text{form}} = \frac{\omega}{k_\perp^2} < \lambda \implies \omega < \omega_{\text{BH}} = \lambda\mu^2 \equiv E_{\text{LPM}}, \quad (14)$$

where we have used the fact that in a single scattering the gluon is emitted with a typical transverse momentum  $k_\perp \lesssim \langle q_\perp \rangle \simeq \mu$ . The coherence number follows from the inequality (cf. (5))

$$t_{\text{form}} \approx \frac{\omega}{n\mu^2} > n\lambda \implies n < \left( \frac{\omega}{\lambda\mu^2} \right)^{\frac{1}{2}} \equiv n_{\text{coh}}^{\text{QCD}}. \quad (15)$$

Finally, the factorization regime applies to

$$n_{\text{coh}}^{\text{QCD}} \lambda > L \implies \omega > \omega_{\text{fact}} = \mu^2 L^2 / \lambda = \omega_{\text{BH}} (L/\lambda)^2. \quad (16)$$

As expected, neither  $\omega_{\text{BH}}$ ,  $\omega_{\text{fact}}$  nor the differential energy spectrum depend explicitly on the initial energy:

$$\omega \frac{dI}{d\omega dz} \simeq \begin{cases} \frac{\alpha_s}{\lambda} & \omega < \omega_{\text{BH}} = \lambda\mu^2, \\ \frac{\alpha_s}{\lambda} \sqrt{\frac{\lambda\mu^2}{\omega}} & \omega_{\text{BH}} < \omega < \min\{\omega_{\text{fact}}, E\}, \\ \frac{\alpha_s}{L} & \omega_{\text{fact}} < \omega < E; \quad \omega_{\text{fact}} = \lambda\mu^2(L/\lambda)^2. \end{cases} \quad (17)$$

It is interesting to notice that the BH and factorization regimes in (17) are interchanged compared to the QED photon energy spectrum (8). Qualitatively, the LPM gluon spectrum can be obtained from the QED result by substituting  $\omega/E \rightarrow E/\omega$ .

Written in full, the radiation density per unit length in the LPM regime for a projectile in a color representation  $R$  reads <sup>[10]</sup>

$$\omega \frac{dI}{d\omega dz} \simeq \frac{3\alpha_s}{2\pi} C_R \sqrt{\frac{\mu^2}{\lambda_g \omega} \ln\left(\frac{\omega}{\mu^2 \lambda_g}\right)}, \quad (18)$$

with  $\lambda_g$  the gluon mean free path in the medium. After taking into full account both rescattering of the secondary gluon and of the projectile  $R$ , the dependence of the radiative spectrum on the ‘‘color charge’’  $C_R$  proves to be trivial <sup>[9]</sup>. This is natural because, as we have discussed above, at high energies bremsstrahlung is mainly determined by the color of the exchange gluon rather than that of a projectile.

An extra logarithmic enhancement factor in (18) is a peculiar property of the Coulomb scattering off a point-like centre. The normalized scattering cross section

$$V(q^2) = \frac{1}{\sigma} \frac{d^2\sigma}{d^2\vec{q}_\perp}, \quad \int_0^\infty d^2\vec{q} V(q^2) = 1$$

can be written in this case as

$$V(q^2) = \frac{1}{\pi} \frac{\mu^2}{(q^2 + \mu^2)^2}. \quad (19)$$

This is the Rutherford scattering cross section with  $\mu^2$  the infra-red cutoff parameter (the Debye screening parameter for hot plasma). Radiation intensity is determined by the quantity

$$\mu^2 \tilde{v}(b^2) = \int_0^{1/b^2} d^2q q^2 V(q^2), \quad (20)$$

where  $b$  is the characteristic small (*sic!*) impact parameter of the problem,

$$b^{-2} \simeq \mu^2 \cdot n_{\text{coh}}; \quad \mu^2 \cdot n_{\text{coh}}^{\text{QCD}} = \sqrt{\frac{\mu^2}{\lambda} \omega} \gg \mu^2. \quad (21)$$

If the integral in (20) was convergent in the ultraviolet, we could put  $b^2 = 0$  and express the answer in terms of the mean squared momentum transfer in a single scattering,  $\langle q^2 \rangle = \mu^2 \tilde{v}(0)$ .

(Original Migdal derivation based on the classical random walk treatment of the electron propagation <sup>[2]</sup> corresponds to exactly this situation.) However, this is not the case for the Rutherford scattering (19): the region of *large* momentum transfer  $\mu^2 \ll q^2 \ll \mu^2 n_{\text{coh}}$  gives rise to the logarithmic enhancement in (18)

$$\mu^2 \implies \mu^2 \ln n_{\text{coh}}.$$

The LPM problem has been reduced in [10] to analyzing the solution of the Schrödinger equation in impact parameter space, with the potential which (for the Rutherford case) has a logarithmic singularity in the origin. Mathematical aspects of this problem have been studied by Chadan, Martin and Stubbe in [11]. The expression (18) for the induced spectrum has been derived within logarithmic approximation in  $\ln n_{\text{coh}}$ .

#### IV. QCD ENERGY LOSS AND JET BROADENING

In QCD applications (hot plasma, cold nuclear matter) one expects the LPM energy parameter  $E_{\text{LPM}} = \lambda\mu^2 = \omega_{\text{BH}}$  to be on the order of GeV. Only such soft gluons will be radiated independently by each scattering centre, while more energetic gluons are subject to the coherent LPM suppression. For a sufficiently thick target,  $L > L_{\text{cr}} = \sqrt{E\lambda/\mu^2}$ , we have  $E < \omega_{\text{fact}}$  and the total energy loss becomes <sup>[9]</sup>

$$\Delta E \sim L \cdot \alpha_s \sqrt{\frac{\mu^2}{\lambda}} E. \quad (22)$$

For initial energies as high as  $E > E_{\text{cr}} = \mu^2 L^2/\lambda$  the factorization contribution takes over in the energy loss. However, on top of this (dominant) medium-independent piece one can try to see the medium-dependent piece coming from the gluon energies  $\omega \lesssim \omega_{\text{fact}}$ . The latter contribution is *quadratic* in the longitudinal size of the medium <sup>[12]</sup>

$$\Delta E \sim \alpha_s \frac{\mu^2}{\lambda} L^2. \quad (23)$$

This qualitative expectation is supported by the analysis of LPM radiation in a finite length medium, which has been carried out in [13]. With logarithmic accuracy we have

$$\Delta E = \frac{\alpha_s N_c}{8} \frac{\mu^2}{\lambda_R} \tilde{v}(b^2) L^2 \simeq \frac{\alpha_s N_c}{8} \frac{\mu^2}{\lambda_R} L^2 \ln \frac{L}{\lambda_g}. \quad (24)$$

Any estimate of energy loss in possibly realistic circumstances in heavy ion collisions based on semi-quantitative approximate theoretical predictions is hazardous and should be received with caution and scepticism. Nevertheless, let us mention that an energetic quark traversing hot QCD matter with temperature  $T = 250$  MeV is expected to lose <sup>[14]</sup>

$$\Delta E \simeq 80 \text{ GeV} \cdot \alpha_s \left( \frac{L}{10 \text{ fm}} \right)^2, \quad (25)$$

which is rather large a number for  $\alpha_s \sim 1/3$ – $1/2$  or so.



For cold nuclear matter both the infra-red cutoff  $\mu^2$  and the gluon mean free path  $\lambda_g$  are obviously ill-defined quantities. It is remarkable, however, that they enter in the combination which not only is well defined but, moreover, determined by small-distance physics. Indeed, in the characteristic ratio

$$\frac{\mu^2}{\lambda_R} \tilde{v}(b^2) = \rho \int_0^{1/b^2} dq^2 q^2 \frac{d\sigma_R}{dq^2}, \quad \lambda_R = (\rho\sigma_R)^{-1}, \quad (26)$$

dependence on the infra-red-sensitive *total* gluon scattering cross section  $\sigma_g$  cancels, and the answer is expressed in terms of the physical matter density  $\rho$  and large-momentum-dominated integral of the differential cross section.

We conclude that in spite of the fact that each scattering act may be dangerously “soft”,  $q_i^2 \sim \mu^2$ , induced radiation of sufficiently energetic gluons with  $\omega \gg \mu^2 \lambda \sim 1 \text{ GeV}$  stays well enough under jurisdiction of the perturbative QCD. In the finite- $L$  problem the characteristic transverse distance  $b^2$  in (24) and (26) decreases with  $L$  as

$$b^{-2} \simeq \frac{\mu^2}{\lambda_g} L \gg \mu^2. \quad (27)$$

In time of the Brookhaven workshop the last of BDMPS papers [15] was completed which deals with cold matter. By allowing for inelastic breakup of target nucleons, the characteristic parameter of the problem (26) was related, in certain approximation, with small- $x$  behavior of the nucleus gluon distribution [16,15]:

$$\frac{\mu^2}{\lambda_R} \tilde{v}(b^2) = \frac{4\pi^2 \alpha_s C_R}{N_c^2 - 1} \rho xG(x, b^{-2}). \quad (28)$$

Since  $xG(x)$  depends on  $x$  slowly (logarithmically) for  $x \ll 1$ , it suffices to state that  $x$  in (28) should be chosen in the range

$$\frac{1}{ML} \leq x \leq \frac{1}{M\lambda_R}, \quad (29)$$

with  $M$  the nucleon mass. Let us stress again that the gluon distribution is probed at a *large* momentum scale (27). The same argument applies to the  $\alpha_s$  factor in (28).

Using  $\rho = 0.15 \text{ fm}^{-3}$  and  $C_R = C_F = 4/3$  one finds

$$\Delta E \simeq 8 \text{ GeV} \cdot \alpha_s^2 \cdot [xG(x)] \left( \frac{L}{10 \text{ fm}} \right)^2, \quad (30)$$

which is much smaller compared with (25) for hot plasma (for the sake of estimate one may take  $\alpha_s \simeq \frac{1}{2}$ ,  $xG(x) \simeq 1$ ).

However, it would be premature to conclude from this comparison that the energy loss seems to give a reasonable signal for the quark-gluon plasma phase, the reason being a contradictory experimental situation with *jet broadening* in nuclei.

The left-hand side of (28) may be related with another, nonperturbative but measurable, quantity such as the transverse momentum which a jet produced in a hard interaction with a nucleus receives as it passes through.

Luo, Qiu and Sterman (LQS) have studied <sup>[17]</sup>  $p_{\perp}$ -broadening of dijets produced in photon-nucleus collisions at Fermilab. They expressed the transverse momentum squared given to the quark jet by rescatterings in the nucleus in terms of a dimensional parameter  $\lambda_{LQS}^2$  which characterizes the momentum transfer squared in a single collision:

$$p_{\perp W}^2 = \frac{4}{3}\pi^2\alpha_s(Q^2) A^{1/3} \lambda_{LQS}^2. \quad (31)$$

Here  $Q$  is the hardness of the production process (the relative transverse momentum of the two jets making up the Drell-Yan dijet) and  $A$  is the atomic number of the nucleus. An expression for  $\lambda_{LQS}^2$  is given in [17] in terms of a new QCD nuclear matrix element, but the actual determination of  $\lambda_{LQS}^2 \approx 0.05 - 0.1 \text{ GeV}^2$  is made by comparing (31) to experiment <sup>[18]</sup>.

The width of the transverse momentum distribution (31) growth linearly with the longitudinal size of the medium  $L \propto A^{1/3}$  as expected. An interesting relationship between jet broadening and energy loss was found in [15]:

$$\left| \frac{dE}{dz} \right| = \frac{\alpha_s N_c}{8} p_{\perp W}^2. \quad (32)$$

It is completely independent of the dynamics of the multiple scattering and holds equally well in finite length hot matter as well as cold matter. Perhaps even more surprising the coefficient relating  $p_{\perp W}^2$  to  $dE/dz$  is independent of the nature of the high energy parton passing through the matter. Equation (32) makes more precise the bound  $|dE/dz| \leq \frac{1}{2} p_{\perp W}^2$  suggested sometime ago by Brodsky and Hoyer [19] on the basis of the uncertainty relation.

Coming back to numbers, it is straightforward to see that the experimental value  $\lambda_{LQS}^2 = 0.05 - 0.1 \text{ GeV}^2$  when used in (31) and (32) overshoots by an order of magnitude the previous estimate for the energy loss in nuclei, unless an unreasonably large gluon density  $xG(x) \sim 20$  is used in (30).

The problem here is that present experiments find a large  $p_{\perp}$ -broadening (and energy loss) for outgoing partons giving  $\lambda_{LQS}^2 \approx 0.05 - 0.1 \text{ GeV}^2$  (*final state* interaction with medium) while much smaller numbers are found for the broadening of the  $\mu$ -pair spectrum <sup>[20]</sup> (*initial state* parton interaction) the latter numbers being consistent with (30). This puzzle remains unsolved at present.

Very recently an elegant and economic way of reproducing the (infinite medium) BDMPS results for QED and QCD <sup>[10]</sup> was found B. Zakharov. Technology developed in [21] is based on the notion of the (complex) “optical potential” and may prove efficient for future studies.

From the theoretical side, the study of the QCD LPM phenomenon has scarcely begun. There is still a long way to go towards improving theoretical understanding of the problem, especially in “cold matter” applications, and developing rough semi-qualitative expectations into reliable numerical estimates.

Wellcome to the club.

## REFERENCES

- [1] L.D. Landau and I.Ya. Pomeranchuk, *Dokl. Akad. Nauk SSSR* 92 (1953) 535, 735.

- [2] A.B. Migdal, *Phys. Rev.* **103** (1956) 1811 ; and references therein.
- [3] P.L. Anthony et al., *Phys.Rev.Lett.* **75** (1995) 1949;  
S. Klein et al., preprint SLAC-PUB-6378 T/E (November 1993).
- [4] see e.g. M.L. Ter-Mikaelian, *High Energy Electromagnetic Processes in Condensed Media*, John Wiley & Sons, NY, 1972;  
A.I. Akhiezer and N.F. Shul'ga, *Phys.Rep.* **234** (1993) 297 and references therein.
- [5] R. Blankenbecler and S.D. Drell, *Phys. Rev.* **D53** (1996) 6265.
- [6] R. Blankenbecler, SLAC-PUB-96-7156 (April 1996), to appear in *Phys. Rev. D*.
- [7] colleagues worldwide (private communication).
- [8] M. Gyulassy and X.-N. Wang, *Nucl. Phys.* **B420** (1994) 583;  
M. Gyulassy, X.-N. Wang and M. Plümer, *Phys. Rev.* **D51** (1995) 3236.
- [9] R. Baier, Yu.L. Dokshitzer, S. Peigné and D. Schiff, *Phys. Lett.* **345B** (1995) 277.
- [10] R. Baier, Yu.L. Dokshitzer, A.H. Mueller, S. Peigné and D. Schiff, LPTHE-Orsay 95-84 (February 1996), hep-ph 9604327, to appear in *Nucl. Phys. B*.
- [11] K. Chadan, A. Martin, and J. Stubbe, preprint CERN-TH.96/01, to appear in *Nucl. Phys. B*.
- [12] A. H. Mueller, in Proceedings of Workshop on Deep Inelastic Scattering and QCD, Paris, April 1995, Eds. J.-F. Laporte and Y. Sirois, p. 29.
- [13] R. Baier, Yu.L. Dokshitzer, A.H. Mueller, S. Peigné and D. Schiff, preprint LPTHE-Orsay 96-34 (May 1996), hep-ph 9607355, to appear in *Nucl. Phys. B*.
- [14] S. Peigné, Ph. D. thesis, Paris-Sud University, May 1995.
- [15] R. Baier, Yu.L. Dokshitzer, A.H. Mueller, S. Peigné and D. Schiff, preprint LPTHE-Orsay 96-61, hep-ph 9608322, to appear in *Nucl. Phys. B*.
- [16] E.M. Levin, hep-ph 9508414 (August 1995).
- [17] M. Luo, J. Qiu and G. Sterman, *Phys. Rev.* **D49** (1994) 4493.
- [18] T. Fields and M.D. Corcoran, in the EPS Conference proceedings, Marseille, France, July 22–28, 1993; *Phys.Rev.Lett.* **70** (1993) 143;  
R.C. Moore, et al., *Phys. Lett.* **244B** (1990) 347;  
M.D. Corcoran, et al., *Phys. Lett.* **259B** (1991) 209.
- [19] S.J. Brodsky and P. Hoyer, *Phys. Lett.* **298B** (1993) 165.
- [20] D.M. Alde, et al., *Phys.Rev.Lett.* **66** (1991) 2285, and references therein.
- [21] B.G. Zakharov, *JETP Lett.* **63** (1996) 952; hep-ph 9607440.

# PQCD Analysis of Hard Scattering in Nuclei

Jianwei Qiu<sup>a</sup> and George Sterman<sup>b</sup>

<sup>a</sup> *Department of Physics and Astronomy, Iowa State University  
Ames, Iowa 50011*

<sup>b</sup> *Institute for Theoretical Physics, State University of New York  
Stony Brook, NY 11794-3840*

## Abstract

We review the extension of the factorization formalism for perturbative QCD to soft initial- and final-state scattering associated with hard processes in nuclei.

## I. INTRODUCTION

In this talk, we would like to review a few results from a perturbative QCD (pQCD) treatment of the scattering of hadrons and leptons in nuclei, based on factorization, work in collaboration with Ma Luo [1–3] and, more recently, Xiaofeng Guo [4]. At the outset, it may be useful to clarify the relation of this work to the recent papers of Baier *et al.* (BDMPS), described by Dokshitzer at this workshop [5]. We have tried to illustrate this relation schematically in Fig. 1. The BDMPS analysis begins (Fig. 1a) with the classic treatment of radiation induced when a charged particle passes through a large target, due originally to Landau, Pomeranchuk and Migdal (LPM). This analysis does not require the presence of a hard scattering, but describes the coherent results of many soft scatterings. Its primary subject has traditionally been induced energy loss. Our analysis (GLQS) begins with the perturbative QCD treatment of hard-scattering in a small target (Fig. 1b), in which the primary subject of interest is momentum transfer. A complete analysis (Fig. 1c) of hard scattering in a large target, involves both energy loss and the transverse momenta due to initial- and final-state soft scatterings. Our work is a step in this direction, attempting to stay as close as possible to the pQCD formalism, in which we may readily quantify corrections. To be specific, we consider only a single soft initial- or final-state interaction in addition to the hard scattering. Our central observation is that for suitably-defined jet and related inclusive cross sections this is the first order in an expansion in the quantity

$$\frac{A^{1/3} \times \lambda^2}{Q^2}, \tag{1}$$

where  $\lambda$  represents a nonperturbative scale, which we shall identify with a higher-twist parton distribution below. That additional scatterings are suppressed by factors of  $1/Q^2$  is perhaps surprising. Let us review why this is the case, at least for certain cross sections.

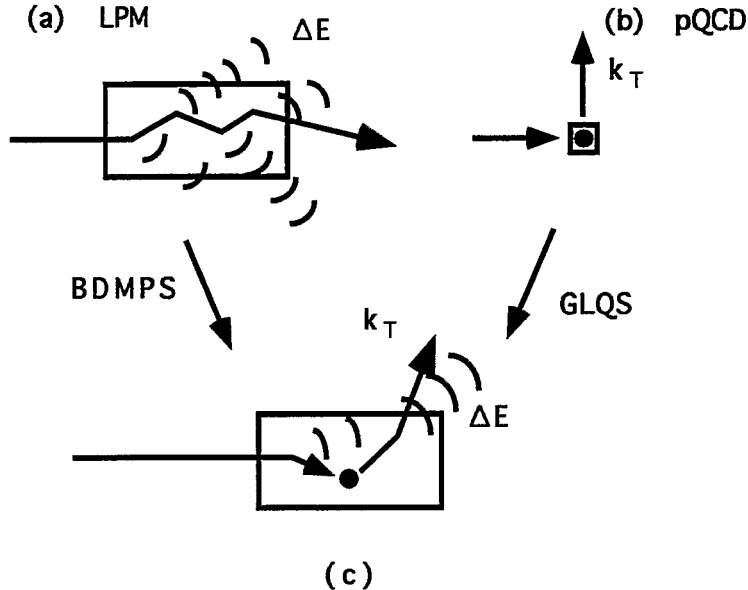


FIG. 1. Alternate approaches to hard scattering in nuclei. (a) Landau-Pomeranchuk-Migdal analysis treats energy loss due to many soft scatterings. (b) Perturbative QCD analysis treats momentum transfer due to hard scattering. (c) For scattering in nuclei, both must be combined.

The basic analysis of hard-scattering in nuclear matter (cold or hot) [6] is quite simple. To be specific, consider the scattering of a quark. A hard-scattering with momentum transfer  $Q$  can resolve states whose lifetimes are as short as  $1/Q$ , for instance quarks off-shell by order  $Q$ , but still less than  $Q$ . The off-shellness of the scattered quark increases with the momentum transfer simply because *the number of available states increases with increasing momentum*. Similarly, the scattered quark, of momentum  $p'$  is typically off-shell by order  $m_J \leq Q$ . We may think of  $m_J$  as the momentum of the jet into which quark fragments. If we are to recognize the jet, we must have  $m_J \ll E_J = p'_0$ . On the other hand, the counting of available states ensures that  $m_J \gg \Lambda_{\text{QCD}}$ .

Now the scattered quark has a lifetime in its own rest frame  $\Delta t^{(p')} \sim \frac{1}{m_J}$  with  $m_J \ll E_J$ . In the target rest frame, however, this becomes, for large enough  $E_J/m_J$ ,  $\Delta t^{(\text{target})} \sim \frac{1}{m_J} \left( \frac{E_J}{m_J} \right) > R_A$ , where  $R_A$  is the (fixed) target size. Thus, at high enough energy the lifetime of the scattered quark will exceed the target size, even though the quark itself is far off the mass shell, typically by a scale that grows with the momentum transfer  $Q$ .

Further couplings of the off-shell quark are suppressed, first of all by the strong coupling evaluated at scale  $m_J$ , and, more importantly, by an overall factor of  $1/m_J^2 \sim 1/Q^2$ , since the effective size of the scattered quark decreases with momentum transfer in this manner.

In summary, for inclusive processes such as jet production, high- $Q$  implies that process-dependent multiple scattering is power-suppressed compared to single scattering. Initial-state interactions internal to the nucleus are leading-power, but factorize. Thus the ‘‘Cronin effect’’,  $A^\alpha$ -dependence with  $\alpha > 1$ , due to multiple scattering, is higher-twist for inclusive distributions, while the ‘‘EMC’’ effect for parton distributions in nuclei is (almost by definition) leading-twist.

The most important point here is that the scattered particle remains off-shell for its entire transit of the target. Thus, its interactions with the target may be treated by the

formalism of perturbative QCD, which, however, must be extended to include corrections that decrease with extra powers of momentum transfer. Up to the first such “higher-twist” contribution, a general cross section has the representation [7]

$$\sigma(Q) = H^0 \otimes f_2 \otimes f_2 + \left(\frac{1}{Q^2}\right) H^1 \otimes f_2 \otimes f_4 + O\left(\frac{1}{Q^4}\right), \quad (2)$$

where  $\otimes$  represents convolutions in fractional momenta carried by partons, and  $f_n$  represents a parton distribution of twist  $n$ . Target-size dependence due to multiple scattering can only appear in the second term in this expansion.

## II. PARTON-NUCLEUS SCATTERING IN PERTURBATIVE QCD

### A. Factorization at Leading and Nonleading Powers

Let us review some of the details of a factorized cross section like (2). The first term, consisting of only twist-two matrix elements has the detailed form,

$$\omega \frac{d\sigma_2}{d^3p'} = \sum_{ij} \int dy f_{j/p_2}(y, Q) \int dx f_{i/p_1}(x, Q) \hat{\sigma}_{ij}(xp_1, yp_2, p'), \quad (3)$$

where we may take  $p'$  as the momentum of an observed jet. The fragmentation of a jet, suitably defined, is calculable in perturbation theory, and may be absorbed into the “hard scattering function”  $\hat{\sigma}$ . The  $f_{a/p}$  are distributions of parton type  $a$  in hadron  $p$ . They have the interpretation of expectation values in the hadronic state of products of fields on the light cone, for instance, for a quark distribution

$$f_{q/p}(x, Q) = \int \frac{dy^-}{2\pi} e^{ixp^+y^-} \langle p | \bar{q}(0) \frac{\gamma^+}{2} q(y^-) | p \rangle, \quad (4)$$

where for simplicity we choose the  $A^+ = 0$  gauge, assuming  $\vec{p}$  is in the plus direction. Eq. (3) is illustrated by Fig. 2a. As shown, the convolution in eq. (3) is in terms of the momentum

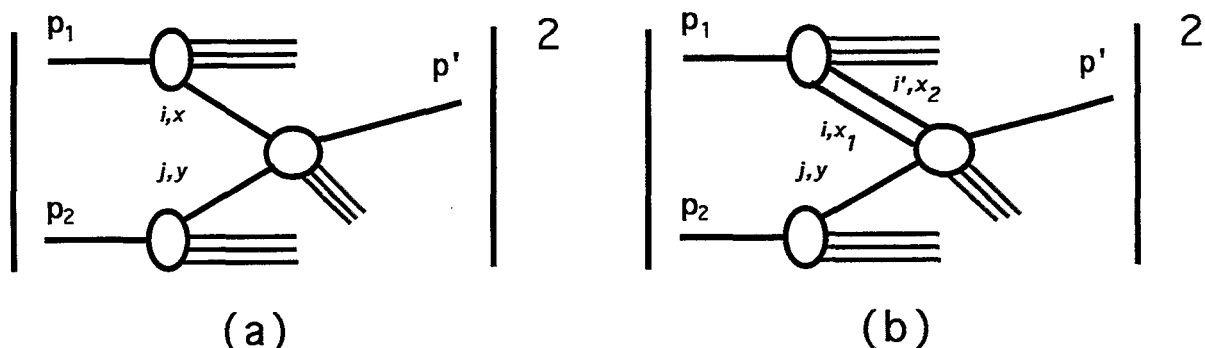


FIG. 2. Perturbative QCD at leading twist (a), and higher twist (b).

fractions  $x$  and  $y$  carried by partons  $i$  and  $j$ , from hadrons  $p_1$  and  $p_2$ , respectively, into the hard scattering.

Fig. 2b is the corresponding picture for a higher-twist contribution to hard scattering. In this case *two* partons  $i$  and  $i'$  with momenta  $x_1 p_1$  and  $x_2 p_1$  from the target (the “nucleus”) collide with a single parton  $j$  of momentum  $y p_2$  (from the “projectile”),

$$\omega \frac{d\sigma_4}{d^3 p'} = \sum_{(ii')_j} \int dy f_{j/p_2}(y, Q) \int dx_1 dx_2 dx_3 T_{(ii')/p_1}(x_1 x_2 x_3, Q) \hat{\sigma}_{(ii')_j}^{(4)}(x_i p_1, y p_2, p'). \quad (5)$$

The expectation value  $T$  corresponding to this multiparton contribution from the target is typically of the form [7],

$$T_{(ii')/p}(x_1 x_2 x_3, Q) = \int \frac{dy_1^- dy_2^- dy_3^-}{(2\pi)^3} e^{ip^+(x_1 y_1^- + x_2 y_2^- + x_3 y_3^-)} \langle p | B_i^\dagger(0) B_{i'}^\dagger(y_3^-) B_{j'}(y_2^-) B_j(y_1^-) | p \rangle, \quad (6)$$

where  $B_i$  is the field corresponding to a parton of type  $i = q, \bar{q}, G$ . In eq. (5), the hard part  $\hat{\sigma}_{(ii')_j}^{(4)}$  depends on the identities and momentum fractions of the incoming partons, but is otherwise independent of the structure – in particular the size – of the target (and projectile). To find  $A$ -enhancement due to multiple scattering, we must look elsewhere.

## B. A-Enhancement from Matrix Elements

For definiteness, we consider photoproduction or deeply inelastic scattering on a nucleus [1,3]. In this case, the additional soft scattering is always a final-state interaction. The structure of the target is manifest only in the matrix element  $T$  in eq. (5). Each pair of fields in the matrix element (6) represents a parton that participates in the hard scattering. The  $y_i^-$  integrals parameterize the distance between the positions of these particles along the path of the outgoing scattered quark. In eq. (6), integrals over the distances  $y_i^-$  generally cannot grow with the size of the target because of oscillations of the exponential factors  $e^{ip^+ x_i y_i^-}$ . Poles from  $\hat{\sigma}$  in the  $x_i$  integrals, associated with the scattered particle, however, can result in finite contributions from points where two of the  $x_i$  vanish [1-3]. An example is shown in Fig. 3. It is important to emphasize that using a pole in the complex  $x_i$

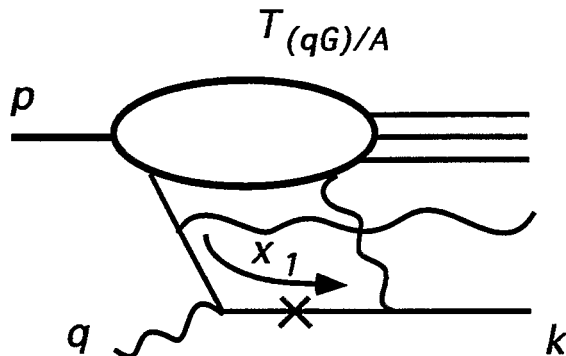


FIG. 3. Pole that gives rise to an  $A$ -enhanced cross section.

(longitudinal momentum) space to do the integral does not correspond to assuming on-shell propagation for the scattered quark. Indeed, the  $x_i$  integrals are not pinched between coalescing singularities at that point, and the same results could be derived by performing the  $x_i$  integrals without ever going through the  $x_i = 0$  points.

The result of this reasoning is that matrix elements that depend on three fractional momenta, as in (6) above, simplify to a form like

$$T_q(x, A) = \int \frac{dy_1^-}{2\pi} e^{ip^+ x y_1^-} \int \frac{dy^- dy_2^-}{2\pi} \theta(y^- - y_1^-) \theta(y_2^-) \\ \times \frac{1}{2} \langle p_A | \bar{q}(0) \gamma^+ F^{\alpha+}(y_2^-) F^+_{\alpha}(y^-) q(y_1^-) | p_A \rangle, \quad (7)$$

where  $|p_A\rangle$  is the relevant nuclear state. In this form, integrals over the  $y_i^-$  can grow with the nuclear radius as fast as  $A^{1/3}$ , once local color confinement is taken into account. The variable  $x$  here is the fractional momentum associated with the hard parton from the target that initiates the process. The soft scattering contributes a negligible longitudinal fractional momentum. Details of the reasoning and calculation for deeply inelastic scattering are given in Ref. [3].

### III. APPLICATIONS

In Refs. [1] and [3], we have applied the formalism sketched above to single-particle inclusive and single-jet production for deeply inelastic scattering and photoproduction. These cases involve final-state interactions only. In each case, the leading  $1/Q^2$  correction is proportional to the matrix element in eq. (7), or to a corresponding matrix element  $T_G$  with four gluon fields. Of course, the value of the correction cannot be estimated without an idea of the magnitudes of the  $T$ 's. Since these magnitudes are nonperturbative they must be taken from experiment. At the same time, we expect the  $x$ -dependence of the probability to detect the hard parton to be essentially unaffected by the presence or absence of an additional soft scattering. Thus, we choose ansatz

$$T_q(x, Q) = \lambda^2 A^{1/3} f_{q/p_A}(x, Q) \quad (8)$$

for  $T_q$ , in terms of the corresponding twist-two parton distribution  $f$ , with  $\lambda$  a constant with dimensions of mass (see eq. (1)). This assumption facilitates the comparison to data.

A quantity that is sensitive to final-state rescattering in a particularly direct way is the momentum imbalance of di-jets in photoproduction in nuclei. The  $A^{4/3}$  dependence of this quantity is related to the matrix elements  $T_q$  and  $T_G$  by the simple formula [2]

$$\langle k_T^2 E_\ell \frac{d\sigma}{d^3\ell} \rangle_{4/3} = \sum_{a=q,g} \int dx T_a(x, A) H^{\gamma a}(xp, p_\gamma, \ell) \\ = \lambda^2 A^{4/3} \sum_{a=q,g} \int dx f_a(x, A) H^{\gamma a}(xp, p_\gamma, \ell), \quad (9)$$

where  $H^{\gamma a}$  is a hard-scattering function that we have computed to lowest order and where in the second equality we have used (8). The momentum  $\ell$  may be identified as the momentum of the more energetic jet. By comparing eq. (9) to data, [8] we found  $\lambda^2 \sim 0.05 - 0.1 \text{ GeV}^2$  [2]. This value may be used to predict anomalous  $A$ -enhancement for other processes.

One such process is direct photon production at measured transverse momentum, whose very moderate  $A$ -dependence has been measured by the E706 experiment at Fermilab. In Ref. [4], it was found that the value of  $\lambda^2$  above, which produces a relatively large enhancement in dijet momentum imbalance, due to final-state interactions, produces a quite small



A-enhancement in photoproduction, due to initial-state interactions, consistent with experiment. This may shed some light on the long-standing observation that (initial-state) transverse momentum effects in Drell-Yan cross sections are also surprisingly small [9]. Clearly, further study of this and related questions is in order.

## REFERENCES

- [1] M. Luo, J. Qiu and G. Sterman, Phys. Lett. B279 (1992) 377.
- [2] M. Luo, J. Qiu and G. Sterman, Phys. Rev. D49 (1994) 4493.
- [3] M. Luo, J. Qiu and G. Sterman, Phys. Rev. D50 (1994) 1951.
- [4] X. Guo and J. Qiu, Phys. Rev. D53 (1996) 6144.
- [5] R. Baier, Yu.L. Dokshitzer, A.H. Mueller, S. Peigné and D. Schiff, hep-ph/9607355 and 9608322.
- [6] A.H. Mueller, in *Proceedings of the XVII Rencontre de Moriond, Vol. 1*, ed. J. Tran Thanh Van, (Editions Frontieres, Gif-sur-Yvette, France, 1982).
- [7] J. Qiu and G. Sterman, Nuc. Phys. B353 (1991) 105, 137.
- [8] D. Naples *et al.* (E683 Collaboration) Phys. Rev. Lett. 72 (1994) 2341.
- [9] M.L. Swartz *et al.* Phys. Rev. Lett. 53 (1984) 32; D.M. Alde *et al. ibid* 66 (1991) 2285.

# Self-Screened Parton Cascades

Kari J. Eskola

*Theory Division, CERN, CH-1211 Geneva23, Switzerland*

Berndt Müller

*Department of Physics, Duke University, Durham, NC 27708*

Xin-Nian Wang

*Nuclear Science Division, Lawrence Berkeley Laboratory, Berkeley, CA 94720*

## Abstract

The high density of scattered partons predicted in nuclear collisions at very high energy makes color screening effects significant. We explain how these screening mechanisms may suppress nonperturbative, soft QCD processes, permitting a consistent calculation of quark-gluon plasma formation within the framework of perturbative QCD. We present results of a model calculation of these effects including predictions for the initial thermalized state for heavy nuclei colliding at RHIC and LHC.

Most recent theoretical predictions for the initial conditions at which a thermalized quark-gluon plasma will be produced at heavy ion colliders are based on the concept of perturbative partonic cascades. The parton cascade model [1] starts from a relativistic transport equation of the form

$$p^\mu \frac{\partial}{\partial x^\mu} F_i(x, p) = C_i(x, p | F_k) \quad i = q, g, \quad (1)$$

where  $F_i(x, p)$  denote the phase space distributions of quarks and gluons. The collision terms  $C_i$  are obtained in the framework of perturbative QCD from elementary  $2 \rightarrow 2$  scattering amplitudes allowing for additional initial- and final state radiation due to scale evolution of the perturbative quanta. To regulate infrared divergences, the parton cascade model requires a momentum cut-off for the  $2 \rightarrow 2$  scattering amplitudes (usually  $p_T^{\min} = 1.5 - 2$  GeV/c) and a virtuality cut-off for time-like branchings ( $\mu_0^2 = 0.5 - 1$  GeV<sup>2</sup>/c<sup>2</sup>).

Numerical simulations of such cascades for heavy nuclei provide a scenario where a dense plasma of gluons and quarks develops in the central rapidity region between the two colliding nuclei shortly after the impact [2]. Detailed studies [3] indicate that the momentum spectrum of partons becomes isotropic and exponential, i.e. practically thermal, at a time  $\tau \approx 0.7\Delta z$  in the rest frame of a slab of width  $\Delta z$  at central rapidity. To permit a hydrodynamic

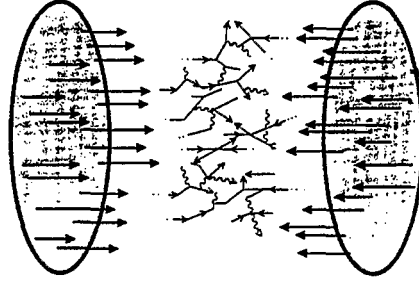


FIG. 1. Schematic representation of a nuclear parton cascade.

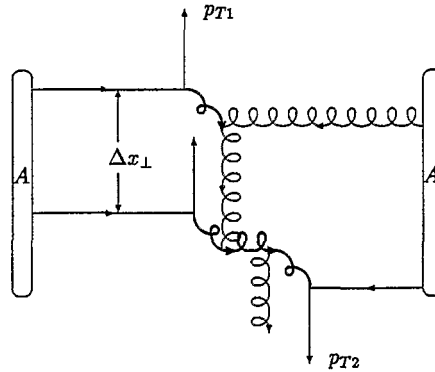


FIG. 2. An example of the processes contributing to color screening.

description, the width of the slab should exceed the mean free path of a parton. Including color screening effects, one finds that the mean free path of a gluon in a thermalized plasma is  $\lambda_f \approx (3\alpha_s T)^{-1}$  where  $T$  is the thermal slope of the parton spectrum. For the predicted very high initial values of  $T$  ( $\geq 0.7$  GeV) one infers that a thermal hydrodynamic description applies after  $\tau_i \approx 0.3$  fm/ $c$ .

The high density of scattered partons in A+A collisions makes it possible to replace the arbitrary infrared cut-off parameters  $p_T^{\text{min}}$  and  $\mu_0^2$  by dynamically calculated medium-induced cut-offs [4]. The dynamical screening of color forces eliminates the need for introduction of the momentum cut-off  $p_T^{\text{min}}$ , and the suppression of radiative processes provided by the Landau-Pomeranchuk-Migdal effect makes the virtuality cut-off  $\mu_0^2$  unnecessary. Note that the viability of this concept crucially depends on the high parton density achieved in nuclear collisions. The dynamical cut-off parameters must lie in the range of applicability of perturbative QCD. Since the density of initially scattered partons grows as  $(A_1 A_2)^{1/3} (\ln s)^2$ , this condition requires both large nuclei and high collision energy. The calculations indicate that this criterion will be met at RHIC and LHC but not at the presently accessible energies of the SPS and AGS. The framework is also not applicable to  $pp$  or  $p\bar{p}$  collisions at current energies because the parton density remains too low.

The dynamic screening of parton cascades can be implemented as follows [5]. Consider an example of two hard processes as illustrated in Fig. 2. Let us assume that jets from the first hard scattering are produced at a large angle and carry a high transverse momentum  $p_{T1}$ . The interaction point is well localized transversely on a distance of  $\hbar/p_{T1}$ . As these

two jets travel in the transverse direction, they will experience secondary interactions, which can give rise to many nuclear effects of hard scatterings, e.g. energy loss and Cronin effects. Here the interactions of the produced hard partons with the propagating partons originating from other perturbative scatterings nearby as shown in Fig. 2 are of interest.

A semiclassical estimate of the screening requires that different scattering events can be treated as incoherent. This condition is satisfied if the produced partons, which screen other softer interactions, can be treated as on-shell particles. This requires that the transverse distance  $\Delta x_{\perp}$  between the two scatterings must be larger than the interaction range of the two hard scatterings which are determined by the off-shellness of the exchanged gluons. If this condition is not satisfied, the propagating parton between two scatterings cannot be treated as real and consequently one cannot treat the multiple scatterings as incoherent. We are thus led to consider

$$\tau_f(p_T) = \frac{a\hbar}{p_T} \quad (2)$$

as the formation time of the produced partons in the mid-rapidity region from the hard or semihard scattering after which they can be treated as real (on-shell) particles and can screen other interactions with smaller transverse momentum transfer. The dimensionless coefficient  $a$  of order unity parametrizes our uncertainty of the precise formation time.

In the framework of the inside-outside cascade, the incoming nuclei being highly Lorentz-contracted, the primary semihard parton-parton collisions all start at  $t = 0$  and the evolving dense system at central rapidity is longitudinally boost invariant. In the space-time evolution of the collision the partons with larger  $p_T$  are produced earlier, as implied by (2). These hard partons will then screen production of partons with smaller  $p_T$  later in time and space. Since, for fixed  $p_T$ , partons with larger rapidities form later in the chosen reference frame, only partons in the same rapidity range are relevant for screening. For the central region around  $y = 0$  we consider the screening effect of partons within a unit rapidity interval,  $\Delta y = 1$ .

We now estimate the static electric screening mass generated by the produced minijets. The number distribution of minijets produced in an  $AA$  collision at an impact parameter  $b = 0$  can be written as [6]

$$\frac{dN_{AA}}{dp_T^2 dy} = T_{AA}(b) \frac{d\sigma_{\text{jet}}}{dp_T^2 dy}, \quad (3)$$

where  $T_{AA}(b)$  is the nuclear overlap function and

$$\frac{d\sigma_{\text{jet}}}{dp_T^2 dy} = K \sum_{ijkl=q,\bar{q}g} \int dy_2 x_1 f_i(x_1, p_T^2) x_2 f_j(x_2, p_T^2) \frac{d\hat{\sigma}^{ij \rightarrow k\ell}}{d\hat{t}}(\hat{s}, \hat{t}, \hat{u}) \quad (4)$$

is the minijet cross section. The hats refer to the kinematical variables of the partonic sub-processes,  $x_i$  is the momentum fraction of the initial state parton  $i$ ,  $p_T$  is the transverse momentum, and  $y$  is the rapidity of the final state parton. The  $f_i$  are the parton distribution functions, and  $K = 2$  is a factor accounting for the contribution from higher-order terms in the cross section [7]. For the purpose of screening we treat all the minijets as gluons. This should again be a good approximation, since gluons clearly dominate the minijet production [8].

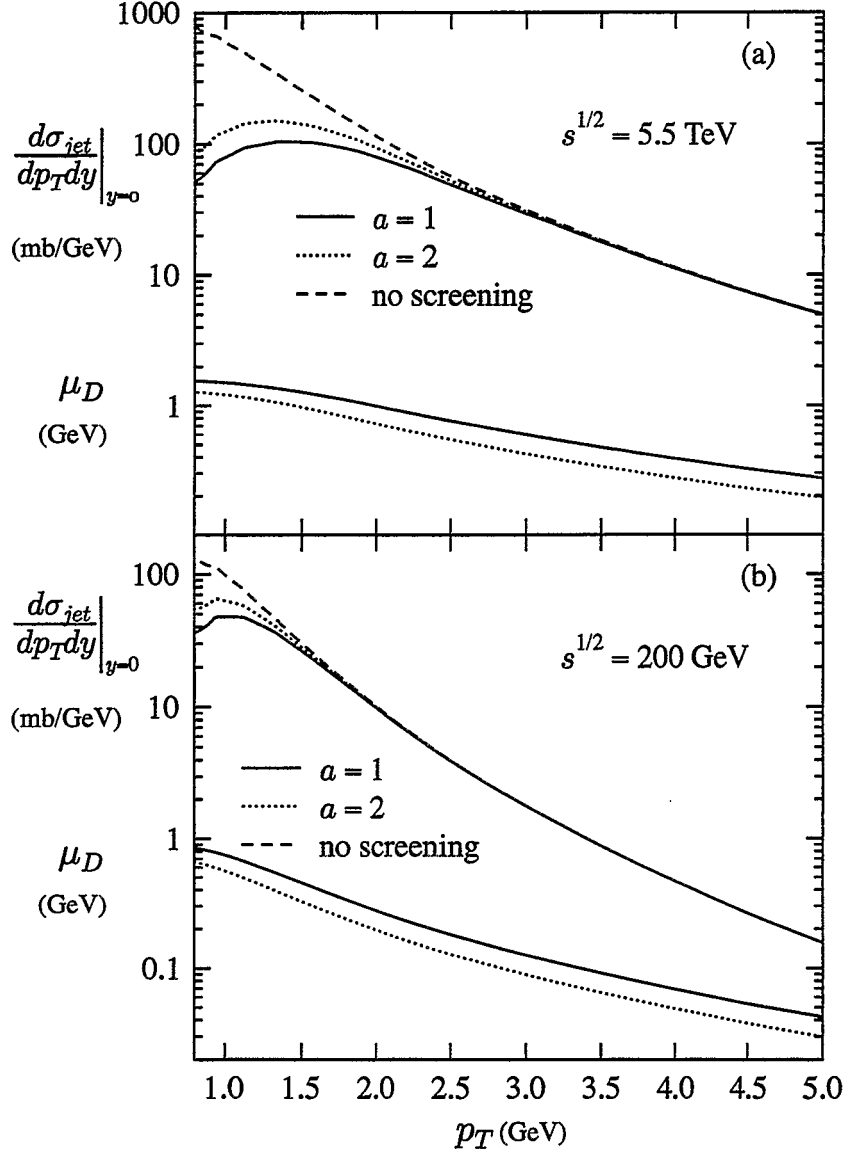


FIG. 3. Differential minijet cross section at  $y = 0$  and screening mass  $\mu_D$  as functions of transverse momentum  $p_T$ . (a) LHC energy, (b) RHIC energy. Dashed line: without screening; solid and dotted lines: with screening.

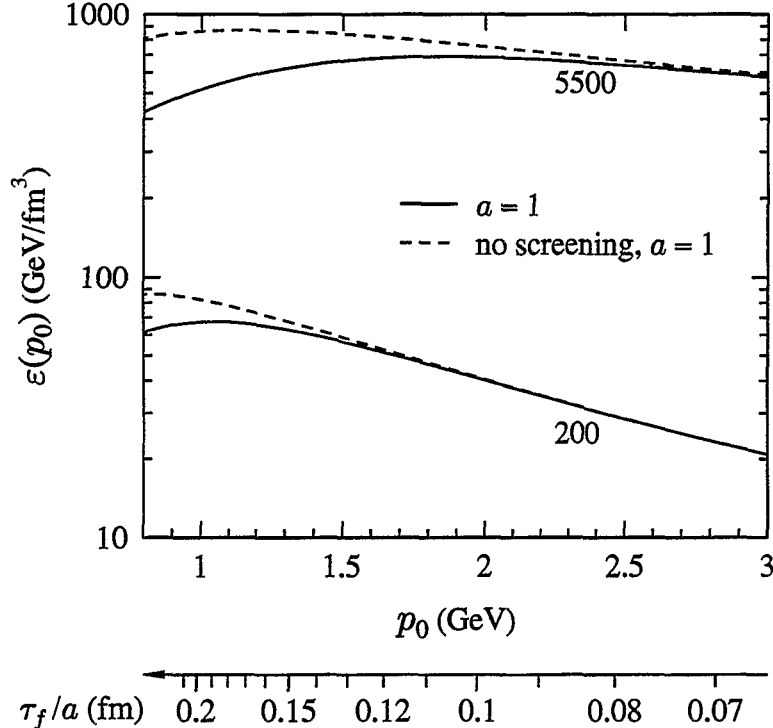


FIG. 4. Transverse energy density  $\epsilon$  of produced minijets as a function of the lowest momentum transfer  $p_0$  or the formation time  $\tau_f(p_0)$ , respectively. The solid and dashed lines show the estimate with and without color screening.

To obtain an estimate of the average parton number density in the central region at a given time  $\tau_f(p_T)$ , we divide (3) by the approximate volume  $V = \pi R_A^2 \Delta z \approx \pi R_A^2 \tau_f \Delta y$  of the produced system. Then the static color screening mass becomes [6]

$$\mu_D^2(p_T) \approx \frac{3\alpha_s(p_T^2)}{R_A^2 \tau_f(p_T) \Delta y} 2 \arcsin[\tanh(\Delta y/2)] \int_{p_T}^{\infty} dk_T \frac{dN_{AA}}{dk_T^2 dy} \Big|_{y=0}, \quad (5)$$

assuming that all the quanta with transverse momenta  $k_T \geq p_T$  screen the formation of partons at transverse momenta  $k_T < p_T$ . Only the quanta within the rapidity window  $\Delta y$  are assumed to contribute to the screening mass.

In order to estimate the effect of this screening on the parton scatterings with smaller  $p_T$ , we use the computed electric screening mass as a regulator for the divergent  $\hat{t}$ - and  $\hat{u}$ -channel sub-processes. We will simply make a replacement  $\hat{t}(\hat{u}) \rightarrow \hat{t}(\hat{u}) - \mu_D^2$  in the minijet cross sections used in (4). In this way, by feeding the  $p_T$ -dependent screening mass back into the equation that defines it, we obtain self-consistent equations for the screening mass and the differential minijet cross section. These equations can be solved numerically by starting at a large  $p_T$  with no screening and then integrating down to smaller  $p_T$ .

In Fig. 3 we show the screening mass  $\mu_D$  and the screened one-jet cross section as functions of  $p_T$ . In the upper panel the results are shown for the LHC energy  $\sqrt{s} = 5.5$  TeV (per nucleon pair) and in the lower panel for the RHIC energy  $\sqrt{s} = 200$  GeV. The jet cross sections are based on MRSA structure functions without nuclear shadowing. The figure clearly supports our self-consistent picture of color screening: as the jet cross section

$\tau_i = 0.25 \text{ fm}/c$	RHIC	LHC
$\epsilon_i \text{ (GeV/fm}^3\text{)}$	61.4	425
$T_i \text{ (GeV)}$	0.668	1.02
$\lambda_g^{(i)}$	0.34	0.43

TABLE I. Initial conditions for the hydrodynamical expansion phase at RHIC and LHC. The initial time is taken as  $\tau_i = 0.25 \text{ fm}/c$ ;  $\epsilon_i$  is the initial transverse energy density, and the effective number of flavors is assumed as  $N_f = 2.5$ .

grows, the parton medium becomes denser and generates a large screening mass, slowing down the rise of the cross section towards smaller  $p_T$ . In this way, the medium of produced minijets regulates the rapid growth of the jet cross section. Finally, at  $\mu_D \sim p_T$ , the cross section saturates.

To study the lack of sensitivity of the results to details of the uncertainty relation (2), we show curves corresponding to  $a = 1$  and  $a = 2$ . For  $A = 200$  collisions at RHIC energy, the screening mass saturates at slightly below 1 GeV, and at 1.5 GeV for collisions at the LHC. Both these values are comfortably within the range of applicability of perturbative QCD, demonstrating that there is no need for an artificial infrared cut-off. The screening of parton scattering by already scattered partons is analogous to the interaction among ladders in the traditional picture of soft hadronic interactions [10]. It would be interesting to rederive our results from this alternative point of view.

In order to study the further evolution of the dense parton plasma created in the first generation of interactions, one can calculate the energy density carried by the scattered partons. The energy density is obtained by dividing the total transverse energy produced by the minijets with momentum transfer  $p_T$  exceeding  $p_0$  by the volume corresponding to the formation time  $\tau_f(p_0)$ :

$$\epsilon(p_0) = \frac{E_T^{AA}(p_0)}{\pi R_A^2 \tau_f(p_0) \Delta y} \equiv \epsilon(\tau_f). \quad (6)$$

The result is shown in Figure 4. As a function of  $\tau_f$  the energy density first rises as more and more parton scatterings are completed, but later starts to fall on account of the longitudinal expansion when the saturation of minijet production due to color screening sets in.

Since earlier studies [3,4] have shown that the conditions for a hydrodynamic description of the expansion are satisfied at a time of order  $\tau_i = 0.25 \text{ fm}/c$ , for the energy densities predicted by (6). The full set of initial conditions is listed in Table 1. The initial temperature is predicted to be very high in nuclear collisions both at RHIC and the LHC, but only about one-third of the gluonic phase space is populated by the initial parton interactions. We assumed here that the parton distributions become isotropic due to free-streaming, and no additional transverse energy is produced in the kinetic equilibration. (We emphasize that the assumptions necessary for the conversion of our results into initial conditions for the hydrodynamic evolution introduce considerable uncertainties into the values listed in Table 1. These uncertainties could be eliminated by a microscopic transport calculation of the kinetic equilibration processes.)

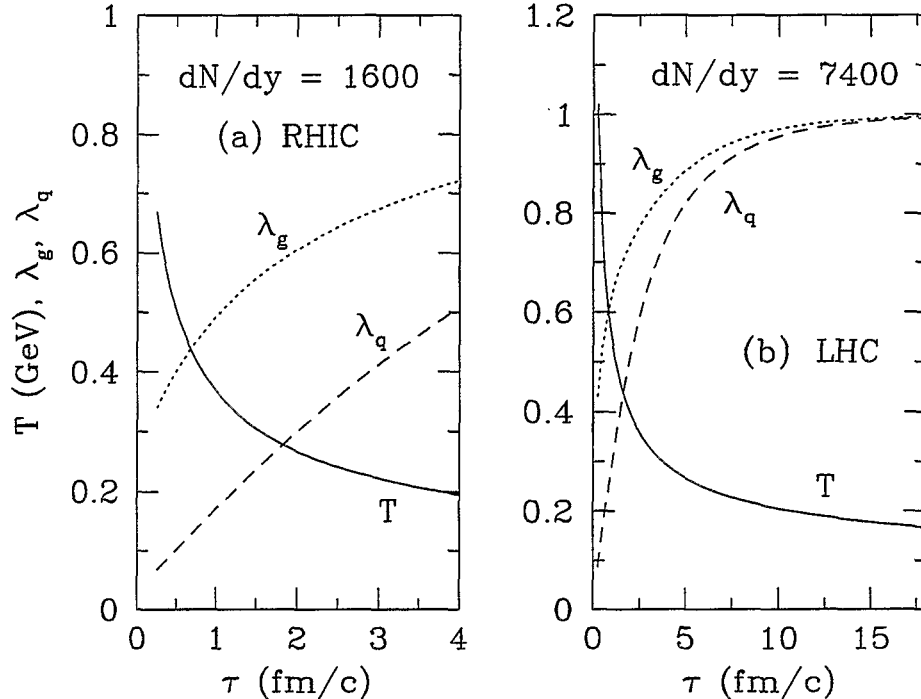


FIG. 5. Evolution of the temperature  $T$  and parton saturation factors  $\lambda_g, \lambda_q$  for the initial conditions given in Table 1 in the longitudinal expansion model.

Figure 5 shows the evolution of the temperature  $T$ , as well as the gluon and quark phase space occupation ratios,  $\lambda_g$  and  $\lambda_q$ , as obtained from a longitudinal hydrodynamical expansion with chemical equilibration [4]. The equilibration only accounts for the processes  $gg \rightarrow ggg$  and  $gg \rightarrow q\bar{q}$ ; it may proceed faster if more complex reactions are also included [12]. We have assumed that  $\lambda_q^{(i)} = \frac{1}{5}\lambda_g^{(i)}$ . The evolution is stopped when the energy density reaches  $1.6 \text{ GeV}/\text{fm}^3$ , where the transition to a mixed phase is assumed to occur. The lifetime of the pure plasma is found to be about  $4 \text{ fm}/c$  at RHIC and  $18 \text{ fm}/c$  at the LHC. For such a long life-time transverse expansion is expected to significantly reduce the plasma life-time at LHC energies and to produce large collective transverse flow [13].

Although many quantitative issues need to be resolved (e.g. the influence of shadowing, the precise formation time, the correct value for  $\Delta y$ ) a well-defined picture of a parton cascade in nuclear collisions, which screens its own infrared divergences, is emerging. The screening mass  $\mu_D(p_T)$  sets a scale which permits a perturbative description of QCD interactions even in the limit  $p_T \rightarrow 0$  as the parton density becomes high. This concept is akin to the picture of random classical color fields proposed in [14] for the small- $x$  gluon structure of large nuclei. It is quite likely that the two approaches can be connected.

## ACKNOWLEDGEMENTS

This work was supported in part by the U.S. Department of Energy (grants DE-FG02-96ER40945 and DE-AC03-76SF00098).



## REFERENCES

- [1] K. Geiger and B. Müller, *Nucl. Phys.* **B369**, 600 (1992).
- [2] K. Geiger, *Phys. Rep.* **258**, 237 (1995).
- [3] K.J. Eskola and X.N. Wang, *Phys. Rev.* **D49**, 1284 (1994).
- [4] T.S. Biró, et al., *Phys. Rev.* **C48**, 1275 (1993).
- [5] K.J. Eskola, B. Müller, and X.N. Wang, *Phys. Lett.* **B374**, 20 (1996).
- [6] T.S. Biró, B. Müller, and X.N. Wang, *Phys. Lett.* **283**, 171 (1992).
- [7] S.D. Ellis, Z. Kunszt and D.E. Soper, *Phys. Rev. Lett.* **62**, 726 (1989); *Phys. Rev.* **D40**, 2188 (1989); *Phys. Rev. Lett.* **69**, 1496 (1992); Z. Kunszt and D.E. Soper, *Phys. Rev.* **D46**, 192 (1992).
- [8] K.J. Eskola, K. Kajantie and P.V. Ruuskanen, *Phys. Lett.* **B332**, 191 (1994).
- [9] B.M. McCoy and T.T. Wu, *Phys. Rev.* **D12**, 546 and 578 (1975).
- [10] S.G. Matinyan and A.G. Sedrakyan, *Sov. J. Nucl. Phys.* **24**, 440 (1976).
- [11] A.D. Martin, W.J. Stirling and R.G. Roberts, *Phys. Rev.* **D51**, 4756 (1995).
- [12] L. Xiong and E.V. Shuryak, *Phys. Rev.* **C49**, 2207 (1994).
- [13] D.K. Srivastava, private communication; B. Kämpfer, private communication.
- [14] L. McLerran and R. Venugopalan, *Phys. Rev.* **D49**, 2233 (1994), *ibid.* **D50** 2225 (1994).

# Minijets in Ultrarelativistic Heavy Ion Collisions at RHIC and LHC

K.J.Eskola\*

CERN/TH, CH-1211 Geneve 23, Switzerland

## Abstract

Recent results on minijet production in nuclear collisions at the RHIC and LHC energies are reviewed. Initial conditions of the QGP at  $\tau = 0.1$  fm/c, especially parton chemistry, thermalization and net baryon number-to-entropy ratio are discussed. Also, contribution of minijets from a hard BFKL-pomeron ladder will be estimated.

## I. INTRODUCTION

Particle and transverse energy production in the central rapidity region of heavy ion collisions can be treated as a combination of hard/semihard parton production and soft particle production. With increasing energies, the semihard QCD-processes are expected to become increasingly important. This is due to two reasons: firstly, already in  $p\bar{p}(p)$  collisions the rapid rise of the total and inelastic cross sections can be explained by copious production of semihard partons, *minijets*, with transverse momenta  $p_T \geq p_0 \sim 1...2$  GeV [1]. This is also expected to happen in  $AA$  collisions at very high energies. Secondly, the semihard particle production scales as  $A^{4/3}$ , so that for large nuclei the importance of semihard partons is increased further [2–4]. The soft, non-perturbative, particle production in ultrarelativistic heavy ion collisions can be modelled *e.g.* through strings [5–7] or through a decaying strong background colour field [8].

The time scale for producing partons and transverse energy into the central rapidity region by semihard collisions is short, typically  $\tau_h \sim 1/p_0 \sim 0.1$  fm/c, where  $p_0 \sim 2$  GeV is the smallest transverse momentum included in the computation. The soft processes are completed at later stages of the collision, at  $\tau_s \sim 1/\Lambda_{\text{QCD}} \sim 1$  fm/c. If the density of partons produced in the hard and semihard stages of the heavy ion collision becomes high enough - as will be the case - a saturation in the initial parton production can occur [2,9–11], and softer particle production will be screened. The fortunate consequence of this is that a larger part of parton production in the central rapidities can be *computed* from perturbative QCD (pQCD) at higher energies and the relative contribution from soft collisions with  $p_T \lesssim 2$  GeV becomes smaller. Typically, the expectation is that at the SPS (Pb+Pb at  $\sqrt{s} = 17$  AGeV),

---

\*On leave of absence from: *Laboratory of High Energy Physics, Department of Physics, P.O.Box 9, 00014 University of Helsinki, Finland*

the soft component dominates, and at the LHC (Pb+Pb at  $\sqrt{s} = 5.5$  ATeV) the semihard component is the dominant one. At the RHIC (Au+Au at  $\sqrt{s} = 200$  AGeV) one will be in the intermediate region, and both components should be taken into account.

A lot of effort has also been devoted for building event generators [7,12] addressing the dominance of semihard processes in nuclear collisions at high energies. These have generated also new insight and very useful discussion during the recent years. Also recently, a promising novel approach to minijet production has been developed [13].

I have divided this talk basically into two halves. In the first one, I will recapitulate the basic features of semihard parton production and review our latest results [4,10,11]. The main goal of these studies is to find out the initial conditions for early QGP-formation at  $\tau \sim 0.1$  fm/c, including the transverse energy deposited into the mid-rapidity region, chemical composition of the parton plasma, and, to study the possibility of a very rapid thermalization and estimate the initial net baryon-to-entropy ratio. It is vitally important to study the early formation of strongly interacting partonic matter, since the later evolution of the QGP, the final state global observables, and the suggested signals of the plasma will strongly depend on the initial conditions. The second half I will devote for discussion of an additional mechanism for parton and transverse energy production: minijets from a BFKL-ladder [14]. Especially, I will estimate the maximum amount of transverse energy one should expect from the BFKL-minijets in heavy ion collisions.

## II. INITIAL CONDITIONS FOR QGP AT $\tau \sim 0.1$ fm/C

Hadronic jets originating from high  $p_T$  quarks and gluons are clearly observed experimentally but when the partons have  $p_T \lesssim 5$  GeV the jets become very difficult to distinguish [15] from the underlying event. In heavy ion collisions, where we expect hundreds (RHIC) or thousands (LHC) of minijets with  $p_T \sim 2$  GeV be produced, detection of individual minijets will be impossible. However, the semihard partons are expected to contribute dramatically to the early formation of QGP. The idea of multiple production of semihard gluons and quarks in  $pp$  and  $AA$  collisions is based on a picture of independent binary parton-parton collisions. The key quantity is the integrated jet cross section,

$$\sigma_{\text{jet}}(\sqrt{s}, p_0) = \frac{1}{2} \int_{p_0^2} dp_T^2 dy_1 dy_2 \sum_{\substack{ijkl= \\ q, \bar{q}, g}} \int dy_2 x_1 f_{i/N}(x_1, Q) x_2 f_{j/N}(x_2, Q) \frac{d\hat{\sigma}^{ij \rightarrow kl}}{d\hat{t}}(\hat{s}, \hat{t}, \hat{u}), \quad (1)$$

where  $x_{1,2}$  are the fractional momenta of the incoming partons  $i$  and  $j$ , and  $f_{i/N}(x, Q)$  are the parton distributions in  $N$  ( $= p, A$ ). The factor 2 comes from the fact that, in the lowest order (LO) pQCD, there are two partons produced in each semihard subcollision. In the eikonal models for  $pp$  collisions [1] the ratio  $\sigma_{\text{jet}}/\sigma_{\text{inelastic}}$  can be interpreted as the average number of semihard events in one inelastic collision. The results I will be quoting in the following [4] are obtained with the MRSH [16] and MRSD-' [17] parton distributions with a scale choice  $Q = p_T$ . More detailed formulation can be found in Refs. [3,11], and numerical evaluation of Eq. (1) in Ref. [4].

The formula above is defined in the lowest order (LO),  $d\hat{\sigma}/d\hat{t} \sim \alpha_s^2$ . Often a constant factor  $K \sim 2$  is used to simulate the effects of NLO terms. Studies of the NLO jet cross section  $d\sigma/(dp_T dy)$  [19] show that (with a scale choice  $Q = p_T$  and with a jet size  $R \sim 1$ )

this is a reasonable approximation [18]. Strictly speaking, however, a theoretical  $K$ -factor can only be defined for quantities where a well-defined, infrared-safe measurement function can be applied [19]. For  $E_T$ -production in nuclear collisions, an acceptance window in the whole central rapidity unit defines such a function but for this acceptance criteria and for  $p_T \sim 2$  GeV the exact NLO contribution has not been computed yet.

The first estimate of the average number of produced semihard partons with  $p_T \geq p_0$  in an  $AA$  collision at a fixed impact parameter  $\mathbf{b}$  can be obtained as [3]

$$\bar{N}_{AA}(\mathbf{b}, \sqrt{s}, p_0) = 2T_{AA}(\mathbf{b})\sigma_{\text{jet}}(\sqrt{s}, p_0), \quad (2)$$

and the average transverse energy carried by these partons as [3]

$$\bar{E}_T^{AA}(\mathbf{b}, \sqrt{s}, p_0) = T_{AA}(\mathbf{b})\sigma_{\text{jet}}(\sqrt{s}, p_0)\langle E_T \rangle, \quad (3)$$

where  $T_{AA}(\mathbf{b})$  is the nuclear overlap function [3] which scales  $T_{AA} \sim A^{4/3}$ , describing thus the typical scaling of hard processes in nuclear collisions. The normalization is  $\int d^2\mathbf{b}T_{AA}(\mathbf{b}) = A^2$  and, for large nuclei with Woods-Saxon nuclear densities,  $T_{AA}(\mathbf{0}) \approx A^2/(\pi R_A^2)$ . The acceptance criteria imposed for the quantities  $\sigma_{\text{jet}}(\sqrt{s}, p_0)$  and for  $\sigma_{\text{jet}}(\sqrt{s}, p_0)\langle E_T \rangle$  will be  $|y| \leq 0.5$ , and the corresponding cuts will be made in  $y_1$  and  $y_2$ . In Eqs. (2) and (3) above,  $T_{AA}(\mathbf{b})\sigma_{\text{jet}}$  is the average number of semihard collisions and  $\langle E_T \rangle$  is the average transverse energy carried by the partons produced in each of these collisions. We fix  $p_0 = 2$  GeV, *i.e.* we describe the initial conditions at  $\tau \sim 1/p_0 = 0.1$  fm/c. The predictions for the central rapidity unit in Pb-Pb collisions at the RHIC and LHC energies are summarized in Tables 1. Also, contributions from gluon, quark and antiquark production are shown separately [4].<sup>1</sup>

In the results given, we have neglected nuclear effects in parton distributions:  $f_{i/A} = Af_{i/p}$ . In reality, however, in the typical  $x$ -region  $x \sim 2p_0/\sqrt{s}$  there are quite strong shadowing corrections [20], especially for the LHC nuclear collisions. Also, the scale evolution of nuclear gluon shadowing was shown to be potentially important in the analysis in Ref. [21]. However, a re-analysis with the input from HERA at small- $x$  [22] has to be performed before getting a solid quantitative prediction of the shadowing effects on minijet production.

The rapid rise of the structure function  $F_2(x, Q)$  at small values of  $x$  observed at HERA [22] does not affect the bulk of the 2 GeV minijets at RHIC energies very much but obviously has quite dramatic consequences at the LHC energies. As demonstrated in [4], there is a clear enhancement of minijet production due to the new parton distributions. However, the more rapidly the gluon distributions rise, the more there should be nuclear shadowing due to the GLRMQ-fusions [9,23,24]. Again, a more quantitative prediction depends on the scale evolution of nuclear gluon shadowing as well.

Let us now have a closer look at the results in Table 1. There are four important observations. Firstly, the gluons clearly dominate both the initial parton and transverse energy production: the initial parton system is about 80 % glue.

Secondly, the effective transverse area of the produced semihard partons is  $\bar{N}_{AA}\pi/p_0^2$ . Comparing this with the effective nuclear transverse area,  $\pi R_A^2$ , we notice that

---

<sup>1</sup>Results for  $d\sigma/(dp_T dy)$  at  $y = 0$  can be found in Ref. [10].

(a)

$\bar{N}_{\text{PbPb}}$	total	$g$	$q$	$\bar{q}$
LHC:	3252	2710	276	266
	5978	5220	385	373
RHIC:	200	156	26.3	17.4
	199	157	25.7	16.6

(b)

$\bar{E}_{\text{T}}^{\text{PbPb}}$	total	$g$	$q$	$\bar{q}$
LHC	10310	8640	854	816
	17580	15330	1150	1100
RHIC	547	426	73.6	47.0
	539	422	71.7	44.8

TABLE I. (a) The average numbers of semihard partons at  $\tau = 0.1$  fm/c with  $|y| \leq 0.5$  and  $p_{\text{T}} \geq 2$  GeV in central Pb-Pb collisions, as given by Eq. (2). Shadowing is not included and  $K = 2$ . The upper values are obtained with MRSB and the lower ones with MRSD-' parton distributions. (b) The average transverse energy carried by these partons, as predicted by Eq. (3).

$$\xi_A \equiv \frac{\bar{N}_{AA}\pi/p_0^2}{\pi R_A^2} \sim 1 \text{ for LHC} \quad \text{and} \quad \xi_A \ll 1 \text{ for RHIC}, \quad (4)$$

*i.e.* the parton system at the LHC at 0.1 fm/c is already dense enough so that a saturation of parton production can take place [2,9,11]. In this way, the scale  $p_0$  acquires also *dynamical* significance. At RHIC, since  $\xi_A < 1$ , saturation occurs at smaller values of  $p_{\text{T}}$  (at  $\tau > 0.1$  fm/c), possibly in the region where pQCD cannot be trusted. This qualitative argumentation is supported by a more quantitative, although still phenomenological, analysis of Ref. [10], where we suggested that at sufficiently large energies (LHC) and large nuclei ( $A \sim 200$ ), a dynamical screening mass is generated, causing a saturation in the minijet cross sections [10] at a perturbative scale like  $p_0 \sim 2 \text{ GeV} \gg \Lambda_{\text{QCD}}$ . The consequence is that the softer parton production is screened and its relative importance becomes smaller.<sup>2</sup>

The third interesting observation is that the gluonic subsystem in the central rapidity unit  $\Delta y = 1$  may thermalize very fast, at least in the LHC nuclear collisions. In the perturbatively produced system the (transverse) energy per gluon is  $\bar{E}_{\text{T}}^g/\bar{N}_{\text{PbPb}}^g = \epsilon_g^{\text{pQCD}}/n_g^{\text{pQCD}} \approx 3 \text{ GeV}$  and the energy density of the system at  $\tau_h = 0.1$  fm/c is  $\epsilon_g^{\text{pQCD}} = \bar{E}_{\text{T}}^g/(\pi R_A^2 \tau_h \Delta y)$ . The temperature  $T_{\text{eq}}$  of an ideal (massless boson) gas in a complete thermal (= both kinetic and chemical) equilibrium with this energy density can be computed from  $\epsilon_g^{\text{ideal}} = 3\pi^2/90 \cdot 16T_{\text{eq}}^4 = \epsilon_g^{\text{pQCD}}$ , and we get  $T_{\text{eq}} = 0.988$  (1.14) GeV with the MRSB (MRSD-' ) densities. Especially, we find [4]

$$\frac{\epsilon_g^{\text{pQCD}}}{n_g^{\text{pQCD}}} \sim \frac{\epsilon_g^{\text{ideal}}}{n_g^{\text{ideal}}} \text{ for LHC} \quad \text{and} \quad \frac{\epsilon_g^{\text{pQCD}}}{n_g^{\text{pQCD}}} > \frac{\epsilon_g^{\text{ideal}}}{n_g^{\text{ideal}}} \text{ for RHIC}, \quad (5)$$

<sup>2</sup>A similar saturation effect is also expected in the approach by McLerran *et al.* [13].

so that at the LHC the average energy of gluons is already as in an ideal gas in thermal equilibrium. Only isotropization is needed, and a rapid thermalization is indeed possible. An instant thermalization would in turn have profound consequences on *e.g.* thermal dileptons, for which a high initial temperature plays a crucial role [25].<sup>3</sup>

Note that our conclusion of the possibility of an almost instant thermalization is due to the small- $x$  enhancement in the HERA gluon densities. From the energy/gluon viewpoint it also seems that thermalization for RHIC is going to happen somewhat later. Note however, that above I did not consider isotropization of the system at all. In the simplified picture presented here, the transit time of the colliding nuclei,  $\tau_{\text{tr}} \sim 2R_A/\gamma$ , and the initial parton spread,  $\Delta z \sim 1/(xp) \sim 1/p_0$  for the partons which will be produced in the mid-rapidity, are neglected. Then a Bjorken-like boost-invariant picture is possible, and in the central rapidities a proper time  $\tau$  is a relevant variable. For a more thorough discussion of isotropization, a more detailed microscopic space-time picture has to be specified, as done in Refs. [12,26] (see also the discussion in [11,10]).

The fourth observation [11] is that initially, at  $\tau \sim 0.1$  fm/c, the net baryon number density in the central rapidity unit is very small as compared to the gluon density but *larger* than the nuclear matter density ( $0.17 \text{ fm}^{-3}$ ), even though the colliding nuclei are practically already far apart, especially at the LHC where  $\tau_{\text{tr}} \ll \tau_{\text{h}}$ . More precisely, we estimate

$$n_{B-\bar{B}} \equiv \frac{1}{3}(n_q - n_{\bar{q}}) = \frac{\frac{1}{3}(\bar{N}_q - \bar{N}_{\bar{q}})}{\pi R_A^2 \Delta y / p_0} = \begin{cases} 0.25 (0.30) \text{ fm}^{-3}, & \text{for LHC} \\ 0.22 (0.23) \text{ fm}^{-3}, & \text{for RHIC} \end{cases} \quad (6)$$

with the MRSB (MRSD-') parton distributions. Computing the net baryon-to-entropy ratio by using  $s_g = 3.6n_g$  for a thermal boson gas gives *initially*, at  $\tau = 0.1$  fm/c:  $(B - \bar{B})/S_g \sim 2 \cdot 10^{-4}$  for LHC, and  $\sim 2 \cdot 10^{-3}$  for RHIC. We conclude that at the future colliders we are still relatively far away from the extreme conditions of the Early Universe, where the inverse of the specific entropy is  $\sim 10^{-9}$  [27]. For the LHC, assuming an instant thermalization of the gluon system at  $\tau = 0.1$  fm/c, and an adiabatic evolution thereafter, the final entropy can be approximated by the initial entropy of gluons [4,11]. The non-perturbative mechanism for particle production will not increase the entropy much but does increase the net baryon number. If the non-perturbative contribution to the net baryon number production is assumed to be of the same order of magnitude as in the current P-b+Pb collisions at SPS, the *final* baryon-to-entropy ratio for the LHC will be  $\sim 10^{-3}$ . For the RHIC nuclear collisions, thermalization is most likely not as instantaneous, but following nevertheless the same line of arguments, and taking into account that the non-perturbative component becomes important also for entropy production, we estimate  $\sim 10^{-2}$  for the final net baryon-to-entropy ratio.

### III. MINIJETS IN THE BFKL-APPROACH

Minijet production I have considered above is based on collinear factorization, where the perturbative partonic cross sections are factorized at a momentum scale  $Q \sim p_T$  from

---

<sup>3</sup>On the other hand, for the thermal dileptons the trouble is the small out-of-equilibrium quark-antiquark component of the early parton system.

the parton distributions with nonperturbative input. Next, I will discuss an additional mechanism for minijet and transverse energy production, where factorization is not used.

The small- $x$  rise in the structure function  $F_2(x, Q^2)$  observed at HERA  $Q^2 > 1.5 \text{ GeV}^2$  [22] can be explained by the leading  $\log(Q^2)$  DGLAP-evolution [28] and also by the leading  $\log(Q^2)\log(1/x)$  evolution [29]. Also a power-like behaviour,  $F_2 \sim x^{-\delta}$ , expected in the leading  $\log(1/x)$  BFKL-approach [30], does not contradict the data. In the following, let us assume that the small- $x$  increase is entirely due to the BFKL-physics. Then, with this assumption, we will study what is the *maximum* transverse energy deposit in the central rapidity unit due to the minijets emitted from a BFKL-ladder in the LHC nuclear collisions. At RHIC the BFKL-minijets are not expected to contribute in any significant manner because the BFKL-enhancement takes place only at  $x \lesssim 0.01$ . Therefore, this latter part of my talk, which is based on Ref. [14], will be relevant only for the LHC.

It is instructive to start from a case of fully inclusive minijets with two tagging jets separated by a wide rapidity gap, as studied by Mueller and Navelet [31]. The (summed) subprocess is also shown Fig. 1a, where the incoming partons have momentum fractions  $x_a$  and  $x_b$ , the tagging jets rapidities  $y_a$  and  $y_b$  ( $y_a \gg y_b$ ) and transverse momenta  $\mathbf{k}_{aT}$  and  $\mathbf{k}_{bT}$ , respectively. Between the tagging jets there are  $n$  gluons emitted, labeled by  $1 \dots n$ . Thus each final state is described by a Feynman graph with 2 incoming and  $n+2$  outgoing on-shell gluons. The colour singlet hard BFKL-pomeron ladder arises when these Feynman graphs are squared and summed. In the kinematic region we will be interested in, the rapidities are strongly ordered,  $y_a \gg y_1 \gg \dots \gg y_n \gg y_b$ , but the transverse momenta are not,  $\mathbf{k}_{Ti} \sim \mathbf{k}_{Tj}$ . Then only the transverse degrees of freedom of the momenta of the virtual legs become important. The tagging jets of Fig. 1a have transverse momenta at a perturbative scale, so that one may use collinear factorization to write the cross section down as:

$$\frac{d\sigma}{d^2\mathbf{k}_{aT}d^2\mathbf{k}_{bT}dy_a dy_b} = \sum_{n=0}^{\infty} x_a g(x_a, \mu^2) x_b g(x_b, \mu^2) \int \prod_{i=1}^n \frac{dy_i d^2\mathbf{k}_{iT}}{4\pi (2\pi)^2} \frac{|\overline{M_{a1\dots nb}}|^2}{16\pi^2 \hat{s}^2} \delta^{(2)}\left(\sum_{j=0}^{n+1} \mathbf{k}_{jT}\right), \quad (7)$$

where only gluons are considered. The strong rapidity ordering simplifies the momentum fractions to  $x_a \approx \frac{k_{aT}}{\sqrt{s}} e^{y_a}$  and  $x_b \approx \frac{k_{bT}}{\sqrt{s}} e^{-y_b}$ , and the parton densities factor out of the sum.

For the process  $gg \rightarrow gg$  the leading contribution in the large  $\hat{s}/\hat{t}$  limit comes from the  $t$ -channel amplitude. In a physical gauge, this amplitude is also gauge invariant up to the subleading terms. The matrix element  $M_{a1\dots nb}$  consists then of the following building blocks: In the leading  $\hat{s}/\hat{t}$  approximation, in a physical gauge and with the strong rapidity ordering, each gluon can be regarded as emitted from an effective non-local Lipatov-vertex, where bremsstrahlung from initial and final legs and emission from the exchanged gluon are summed. These are described by the black blobs in Fig 1. Also the propagators are effective ones since they are exponentiated (Reggeized) after computing the leading virtual corrections to the  $t$ -channel gluon exchange. The effective propagators are drawn by thicker (vertical) lines in Fig. 1. Original references, detailed discussion and derivation of these concepts can be found in the useful lecture notes by Del Duca [32].

Next, we square each matrix element  $M_{a1\dots nb}$ , and due to the strong ordering in rapidities, colour singlet ladders with  $n+2$  rungs are formed. The colour algebra can be performed by summing (averaging) over the final (initial) state colours, and the polarization sums can be done. With help of *e.g.* Laplace-transformation (in  $y_a - y_b$ ), the rapidity integrals can be disentangled. Finally, by summing over  $n$ , one obtains an iterative integral equation,

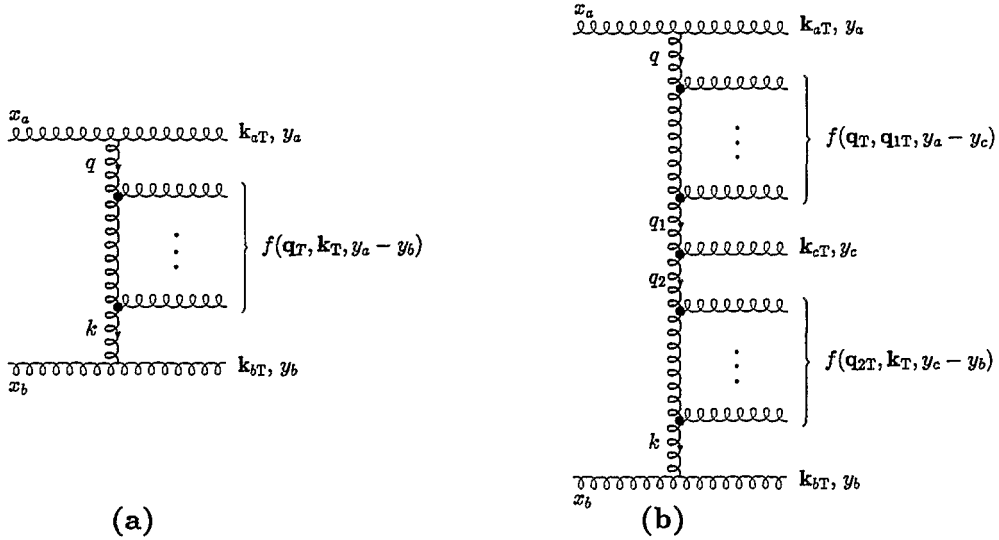


FIG. 1. (a) The BFKL ladder in fully inclusive minijet production between the two tagging jets  $a$  and  $b$  [31,9,33]. (b) Fixing one step of the ladder (c) creates a ladder on each side of the minijet  $c$  [34].

the inhomogeneous BFKL-equation [30,31] (see also [32]), which describes an addition of one rung into the colour-singlet hard pomeron ladder. The BFKL-ladder is denoted by  $f(\mathbf{q}_T, \mathbf{k}_T, y_a - y_b)$  in Fig 1a. The cross section (7) then becomes:

$$\frac{d\sigma}{d^2\mathbf{k}_{aT}d^2\mathbf{k}_{bT}dy_a dy_b} = x_a g(x_a, \mu^2) x_b g(x_b, \mu^2) \frac{4N_c^2 \alpha_s^2}{N_c^2 - 1} \frac{1}{k_{aT}^2} 2f(\mathbf{q}_T, \mathbf{k}_T, y_a - y_b) \frac{1}{k_{bT}^2}, \quad (8)$$

where  $\mathbf{q}_T = -\mathbf{k}_{aT}$  and  $\mathbf{k}_T = \mathbf{k}_{bT}$ . If all the virtual corrections and the real emissions are neglected, the ladder reduces into  $2f(\mathbf{q}_T, \mathbf{k}_T, y) \rightarrow \delta^{(2)}(\mathbf{q}_T - \mathbf{k}_T)$ , and the Born limit for the two jets separated by a large rapidity interval is recovered [32].

Let us then study the case with tagging jets further by fixing one step of the ladder, as shown in Fig. 1b. It is straightforward to sum the graphs with gluon emissions between the tagging jet  $a$  and the fixed minijet  $c$ , and, between the minijet  $c$  and the tagging jet  $b$ . This creates a ladder on each side of the fixed rung. Especially, we learn that a generic factor  $\alpha_s N_c / (\pi^2 k_{cT}^2)$ , which includes the phase-space factor and contraction of the two Lipatov vertices associated with the step  $c$ , arises from fixing the the rung  $c$ . The cross section becomes [34]

$$\frac{d\sigma}{d^2\mathbf{k}_{aT}d^2\mathbf{k}_{bT}d^2\mathbf{k}_{cT}dy_a dy_b dy_c} = x_a g(x_a, \mu^2) x_b g(x_b, \mu^2) \frac{4N_c^2 \alpha_s^2}{N_c^2 - 1} \frac{\alpha_s N_c}{\pi^2} \frac{1}{k_{cT}^2} \int d^2\mathbf{q}_{1T} d^2\mathbf{q}_{2T} \cdot \delta^{(2)}(\mathbf{k}_{cT} - \mathbf{q}_{1T} + \mathbf{q}_{2T}) \frac{2f(\mathbf{k}_{aT}, \mathbf{q}_{1T}, y_a - y_c)}{k_{aT}^2} \frac{2f(\mathbf{q}_{2T}, \mathbf{k}_{bT}, y_c - y_b)}{k_{bT}^2}. \quad (9)$$

Our goal is to study the leading BFKL minijet production mechanism which is  $\sim \alpha_s$ . As illustrated in Fig. 2, we therefore relax the requirement of having tagging jets. Then coupling of the pomeron ladder to the hadron becomes essentially non-perturbative and a form-factor, or, rather, a parton distribution, will be needed. Also, now that we do not require any tagging jets, we have to give up collinear factorization. We do not have any perturbative Born limit to compare with, either. Therefore, the best we can do is to adopt



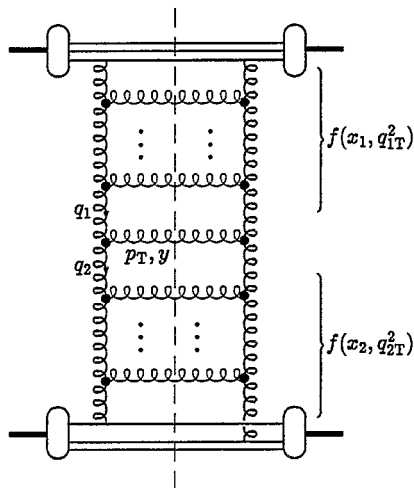


FIG. 2. Minijet production without the tagging jets requires an introduction of unintegrated parton distributions  $f(x, q_T^2)$  [33].

the procedure for deep inelastic scattering (DIS) in [35], where an addition of each rung into the pomeron ladder between the two hadrons or nuclei is expected to be described by the *homogeneous* BFKL equation for the unintegrated gluon density  $f(x, q_T^2)$ ,

$$-x \frac{\partial f(x, q_T^2)}{\partial x} = \frac{\alpha_s N_c}{\pi} q_T^2 \int_0^\infty \frac{dq_{1T}^2}{q_{1T}^2} \left[ \frac{f(x, q_{1T}^2) - f(x, q_T^2)}{|q_T^2 - q_{1T}^2|} + \frac{f(x, q_T^2)}{\sqrt{q_T^4 + 4q_{1T}^4}} \right]. \quad (10)$$

Normalization for this scale-invariant equation is given by the gluon distributions

$$xg(x, Q^2) = \int^{Q^2} \frac{dq_T^2}{q_T^2} f(x, q_T^2), \quad (11)$$

determined from experimental input [35].

By using the knowledge of the factor arising from fixing one rung of the BFKL-pomeron ladder, the inclusive minijet cross section from the BFKL-ladder can now be written down as [33,14]

$$\frac{d\sigma^{\text{jet}}}{d^2\mathbf{p}_T dy} = K_N \frac{\alpha_s N_c}{\pi^2} \frac{1}{p_T^2} \int d^2\mathbf{q}_{1T} d^2\mathbf{q}_{2T} \delta^{(2)}(\mathbf{p}_T - \mathbf{q}_{1T} + \mathbf{q}_{2T}) \frac{f(x_1, q_1^2)}{q_{1T}^2} \frac{f(x_2, q_2^2)}{q_{2T}^2} \quad (12)$$

where  $p_T$  and  $y$  are the transverse momentum and the rapidity (in the hadron CMS) of the minijet. From momentum conservation and multi-Regge kinematics the momentum fractions become  $x_{1(2)} \approx \frac{p_T}{\sqrt{s}} e^{\pm y}$ . Due to the fact that in this case we do not have an “external” hard probe like the virtual photon with an associated quark box as in DIS, nor an on-shell Born cross section to relax into, we cannot determine the overall dimensionless normalization constant  $K_N$  exactly. However, we are able to fix the *slope* of the minijet  $p_T$ -distribution, which will be sufficient for estimating the upper limit of transverse energy production from the BFKL-ladder.

The minijet cross section of Eq. (12) is shown in Fig. 3 [14]. In the BFKL-computation we have used the unintegrated gluon densities compatible with the small- $x$  rise in the set

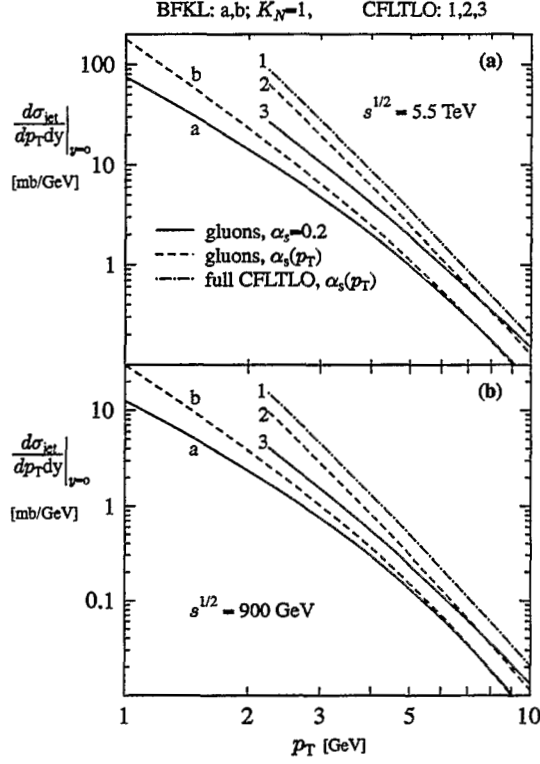


FIG. 3. The minijet cross sections at  $y = 0$  as functions of transverse momentum  $p_T$  at  $\sqrt{s} = 5.5$  TeV from [14]. (panel a) and  $\sqrt{s} = 900$  GeV (panel b) [14]. The curves 1, 2 and 3 are predicted in the approach of collinear factorization, leading twist and lowest order (CFLTLO) pQCD, and MRSD-' parton distributions. The curves a and b are the BFKL-minijets from Eq. (12) with and without running coupling.

MRSD-' [17]. For comparison, the more traditional (CFLTLO) minijet cross sections, discussed in the first half of the talk, are also shown with the MRSD-' parton distributions. The NLO jet analysis [19,18] indicates that LO+NLO calculation with collinear factorization reproduces the measured jet cross sections well. Therefore, at  $p_T \gtrsim 5$  GeV, the BFKL-minijet contribution should be less than the collinearly factorized. We can thus argue that  $K_N \lesssim 1$ .

The transverse energy production due to the minijets from the BFKL-ladders at  $|y| \leq 0.5$  in AA collisions can now be estimated [14] from

$$\left. \frac{d\bar{E}_T^{\text{BFKL}}}{dy} \right|_{y=0} = T_{AA}(\mathbf{b}) \int_{p_0^{\text{BFKL}}} dp_T p_T \left. \frac{d\sigma^{\text{jet}}}{dp_T dy} \right|_{y=0}. \quad (13)$$

The coherence of the BFKL ladder is broken when we fix a rung, and the cross section diverges at  $p_T \rightarrow 0$ . A cut-off is, unfortunately, needed also in the BFKL case. The saturation of the CFLTLO-minijet cross section in the LHC Pb-Pb collisions (as considered in the first half of the talk), implies that the BFKL-cross section should not grow much larger than the curve 2 in Fig. 3. Therefore, we do not trust the BFKL-computation with  $K_N \sim 1$  below  $p_T \leq p_0^{\text{BFKL}} \sim 1$  GeV. With these values, we find for central Pb-Pb collisions at the LHC,  $\bar{E}_T^{\text{BFKL}} = 3060$  GeV with fixed  $\alpha_s = 0.2$ , and, 4940 GeV with (*ad hoc*) running

$\alpha_s(p_T)$ . Comparing these numbers to the value 15330 GeV in Table 1b for gluons, we see that the BFKL-contribution is at most a few 10% correction to the results in [4,11]. On the other hand, one should perhaps compare the results at the same level of approximations, (only LO gluons,  $\alpha_s$  fixed) *i.e.* curves 3 and a in Fig. 3a. Then the two contributions become of similar magnitude. In this case, however, the  $p_0$  in the CFLTLO-computation should be lower than 2 GeV, and the BFKL contribution would again be the smaller one.

We worked under the assumption that the BFKL-evolution is responsible for *all* the small- $x$  rise at HERA, *i.e.* we studied the *maximum* contribution from the kinematical region relevant for the hard BFKL-pomeron. Since the HERA results can be explained by the leading  $\log(Q^2)$  and/or the leading  $\log(Q^2)\log(1/x)$  approximations, the leading  $\log(1/x)$ -contribution is obviously not the dominant mechanism at the present values of  $x$ . Thus, my conclusion is that the BFKL-minijets certainly bridge the way towards softer physics at  $p_T < p_0 \sim 2$  GeV, but the initial conditions relevant for the early QGP-formation in the LHC nuclear collisions are dominantly given by the minijets computed in collinear factorization.

## ACKNOWLEDGEMENTS

The results discussed in this talk are based on Refs. [4,10,11,14]. I would like to thank K. Kajantie, A. Leonidov, B. Müller, V. Ruuskanen and X.-N. Wang for fruitful collaboration. I also owe special thanks to A. Leonidov and V. Ruuskanen for getting our BFKL-study started and finally finished.

## REFERENCES

- [1] X.-N. Wang, Phys. Rev. **D43** (1991) 104, and references therein.
- [2] J.-P. Blaizot and A. Mueller, Nucl. Phys. **B289** (1987) 847.
- [3] K. Kajantie, P. V. Landshoff and J. Lindfors, Phys. Rev. Lett. **59** (1987) 2517;  
K.J. Eskola, K. Kajantie and J. Lindfors, Nucl. Phys. **B323** (1989) 37.
- [4] K.J. Eskola, K. Kajantie and V. Ruuskanen, Phys. Lett. **B332** (1994) 191.
- [5] B. Andersson, G. Gustafson, B. Nilsson-Almqvist, Nucl. Phys. **B281** (1986) 289.
- [6] K. Werner, Phys. Rep. 232 (1993) 87.
- [7] X.-N. Wang and M. Gyulassy, Phys. Rev. **D44** (1991) 3501; *ibid.* **D45**, 844 (1992) 844;  
Phys. Rev. Lett. **68** (1992) 1480; Comput. Phys. Commun. **83** (1994) 307.
- [8] K. Kajantie and T. Matsui, Phys. Lett. **B164**(1985) 373; G. Gattoff, A. K. Kerman and  
T. Matsui, Phys. Rev. **D36** (1987) 114; K.J. Eskola and M. Gyulassy, Phys. Rev. **C47**  
(1993) 2329.
- [9] L. V. Gribov, E. M. Levin and M. G. Ryskin, Phys. Rep. **100** (1983) 1.
- [10] K.J. Eskola, B. Müller and X.-N. Wang, Phys. Lett. **B374** (1996) 20; B. Müller, in this  
workshop.
- [11] K.J. Eskola and K. Kajantie, Preprint CERN-TH/96-259, September 1996.
- [12] K. Geiger and B. Müller, Nucl. Phys. **B369** (1992) 600; K. Geiger, Phys. Rev. **D47**  
(1993) 133.

- [13] A. Kovner, L. Mc Lerran and H. Weigert, Phys. Rev. **D52** (1995) 3809, 6231; R. Venugopalan, Preprint DOE/ER/ 40561-251-INT96-00-120, March 1996.
- [14] K.J. Eskola, A. Leonidov and P.V. Ruuskanen, Preprint CERN-TH/96-124.
- [15] UA1 Collaboration, C. Albajar *et al.*, Nucl. Phys. **B309** (1988) 405.
- [16] A.D. Martin, W.J. Stirling and R.G. Roberts, RAL preprint 93-077 (1993).
- [17] A.D. Martin, W.J. Stirling and R.G. Roberts, Phys. Lett. **B306** (1993) 145.
- [18] K.J. Eskola and X.-N. Wang, Int. J. Mod. Phys. **A10** (1995) 2881.
- [19] S.D. Ellis, Z. Kunszt and D.E. Soper, Phys. Rev. Lett. **69** (1992) 1496; Z. Kunszt and D. E. Soper, Phys. Rev. **D46** (1992) 192.
- [20] NM Collaboration, P. Amaudruz *et al.*, Z. Phys. **C51** (1991) 387.
- [21] K.J. Eskola, Nucl. Phys. **B400** (1993) 240.
- [22] H1 Collaboration, I. Abt *et al.*, Nucl. Phys. **B407** (1993) 515; T. Ahmed *et al.*, Nucl. Phys. **B439** (1995) 471; ZEUS Collaboration, M. Derrick *et al.*, Phys. Lett. **B316** (1993) 412; Z. Phys. **C65** (1995) 379.
- [23] A. Mueller and J. Qiu, Nucl. Phys. **B268** (1986) 427.
- [24] E.M. Levin, in this workshop.
- [25] P.V. Ruuskanen, Proc. *Quark Matter 91*, Nucl. Phys. **A544** (1992) 169c.
- [26] K.J. Eskola and X.-N. Wang, Phys. Rev. **D49** (1994) 1284; T.S. Biró, E. van Doorn, B. Müller, M.H. Thoma and X.-N. Wang, Phys. Rev. **C48** (1993) 1275.
- [27] U. Heinz, "Heavy ion physics at the LHC", in Proc. of *Towards the LHC Experimental Programme*, ECFA meeting, 5-8 March 1992, Evian-les-Bains, France, p. 95.
- [28] Yu. Dokshitzer, Sov. Phys. JETP **46** (1977) 1649; V. N. Gribov and L. N. Lipatov, Sov. Nucl. Phys. **15** (1972) 438, 675; G. Altarelli, G. Parisi, Nucl. Phys. **B126** (1977) 298.
- [29] R. D. Ball and S. Forte, Phys. Lett. **B351** (1995) 313; *ibid* **B359** (1995) 362; *ibid* **B336** (1994) 77.
- [30] E. A. Kuraev, L. N. Lipatov and V. S. Fadin, Sov. Phys. JETP **45** (1977) 199; Ya. Ya. Balitskij and L. N. Lipatov, Sov. J. Nucl. Phys. **28** (1978) 822.
- [31] A. H. Mueller and H. Navelet, Nucl. Phys **B282** (1987) 727.
- [32] V. Del Duca, "An introduction to the perturbative QCD pomeron and to jet physics at large rapidities", DESY 95-023, February 1995.
- [33] L. V. Gribov, E. M. Levin and M. G. Ryskin, Phys Lett. **B100** (1981) 173; Phys Lett. **B121** (1983) 65; E. M. Levin and M. G. Ryskin, Phys. Rep. **189** (1990) 267.
- [34] V. Del Duca, M. E. Peskin and W.-K. Tang, Phys. Lett. **B306** (1993) 151.
- [35] A. J. Askew, J. Kwieciński, A. D. Martin and P. J. Sutton, Phys. Rev. **D49** (1994) 4402.

# Theoretical Overview of Potential of Nuclear beams in HERA and Interface with Heavy Ion Physics. \*

M. Strikman

*Pennsylvania State University, University Park, PA 16802*

## Abstract

Overview is given of the theoretical issues of the physics which can be addressed with nuclear beams circulating in HERA. It is shown that such experiments widen considerably the horizon for probing QCD compared to that from free nucleon targets. They would allow to understand dynamics of nuclear shadowing, the origin of diffraction in deep inelastic scattering. Interplay between the physics to be studied at HERA and in AA collisions at RHIC is also discussed.

## I. INTRODUCTION

The successes of QCD in describing *inclusive* perturbative phenomena have moved the focus of investigations to new frontiers. Three fundamental questions to be resolved are the space-time structure of high-energy strong interactions, the QCD dynamics in the nonlinear, small coupling domain and the QCD dynamics of interactions of fast, compact color singlet systems. The study of electron-nucleus scattering at HERA allows a new regime to be probed experimentally for the first time. This is the regime in which the virtual photon interacts coherently with all the nucleons at a given impact parameter. In the rest frame of the nucleus this can be visualized in terms of the propagation of a small  $q\bar{q}$  pair in high density gluon fields over much larger distances than is possible with free nucleons. In the Breit frame it corresponds to the fact that small  $x$  partons cannot be localized longitudinally to better than the size of the nucleus. Thus low  $x$  partons from different nucleons overlap spatially creating much larger parton densities than in the free nucleon case. This leads to **a large amplification of the nonlinear effects expected in QCD at small  $x$** . The HERA  $ep$  data have confirmed the rapid increase of the parton densities in the small  $x$  limit predicted by perturbative QCD. However the limited  $x$  range available at HERA makes it difficult to distinguish between the predictions of the DGLAP evolution equations and the BFKL-type dynamics. Moreover, the nonlinear effects expected at small  $x$  are relatively small in  $ep$  scattering in the HERA kinematic domain and it may be necessary to reduce  $x$  by at least one order of magnitude to observe unambiguously such effects. However,

---

\*Based on the report of the conveners of the working group "Light and Heavy Nuclei", in the framework of the study "Future of HERA"<sup>1</sup>

the amplification obtained with heavy nuclear targets **allows an effective reduction of about two orders of magnitude in  $x$**  making it feasible to explore such nonlinear effects at the energies available at HERA. The question of nonlinear effects is one of the most fundamental in QCD. It is crucial for understanding the kind of dynamics which would slow down and eventually stop the rapid growth of  $F_2(x, Q^2)$  at small  $x$ . It is also essential in order to understand down to what values of  $x$  the decomposition of the cross section into terms with different powers of  $\frac{1}{Q^2}$  remains effective. It is important for the understanding of the relationship between hard and soft physics. One can also study the dynamics of QCD at high densities and at zero temperatures raising questions complementary to those addressed in the search for a quark-gluon plasma in high-energy heavy ion collisions.

Deep inelastic scattering from nuclei provides also a number of ways to probe **the dynamics of high-energy interactions of small color singlet systems**. This issue started from the work of Gribov [2] who demonstrated the following paradox. If one makes the natural (in soft physics) assumption that at high energies any hadron interacts with a heavy nucleus with cross section  $2\pi R_A^2$  (corresponding to interaction with a black body), Bjorken scaling at small  $x$  is grossly violated –  $\sigma_{\gamma^*A} \propto \ln Q^2$  instead of  $\frac{1}{Q^2}$ . To preserve scaling, Bjorken suggested, using parton model arguments, that only configurations with small  $p_t \leq p_{t0}$  are involved in the interaction (the Aligned Jet Model) [3]. However, in perturbative QCD Bjorken's assumption does not hold – large  $p_t$  configurations interact with finite though small cross sections (color screening), which however increase rapidly with incident energy due to the increase of the gluon density with decreasing  $x$ . Hence again one is faced with a fundamental question which can only be answered experimentally: *Can small color singlets interact with hadrons with cross sections comparable to that of normal hadrons?* At HERA one can both establish the  $x, Q^2$  range where the cross section of small color singlets is small – *color transparency*, and look for the onset of the new regime of large cross sections, *perturbative color opacity*.

Another fundamental question to be addressed is **the propagation of quarks through nuclear matter**. At large energies perturbative QCD leads to the analogue of the Landau-Migdal-Pomeranchuk effect in quantum electrodynamics. In particular Baier et al. [4] find a highly nontrivial dependence of the energy loss on the distance,  $L$ , traveled by a parton in a nuclear medium: the loss instead of being  $\propto L$  is  $\propto L^2$ . Several manifestations of this phenomenon can be studied at HERA.

There is also an *important connection to heavy ion physics*. Study of  $eA$  scattering at HERA would be important for the analysis of heavy ion collisions at the LHC and RHIC. Measurements of gluon shadowing at small  $x$  are necessary for a reliable interpretation of the high  $p_t$  jet rates at the LHC. In addition, the study of parton propagation in nuclear media is important for the analysis of jet quenching phenomena, which may be one of the most direct global signals of the formation of a quark-gluon plasma.

Current fixed target data on lepton-nucleus scattering only touch the surface of all these effects due to the limited  $Q^2$  range of the data at small  $x$ . Indeed the  $Q^2$  range of these data is too small to distinguish the contribution of the vector meson dominance behavior of the photon from its hard QCD behavior at small  $x$ . The range of  $x$  and  $Q^2$  in experiments with nuclei at HERA compared to the fixed target experiments is shown extends a factor of 100 down in  $x$ . The primary experimental program for nuclei in HERA includes: (i) *Study of the  $x$  and  $Q^2$  dependence of nuclear shadowing over a wide  $Q^2$  range*. This will

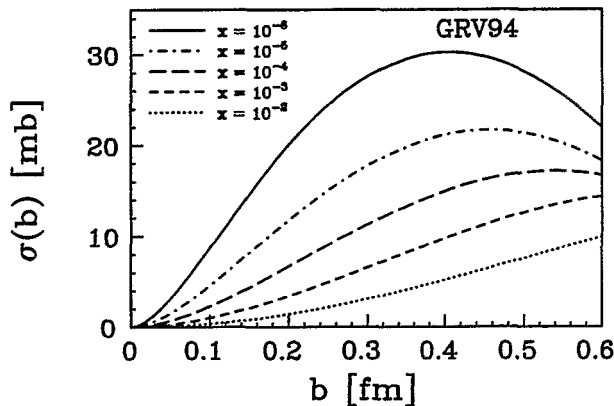


FIG. 1. Color-dipole cross section,  $\sigma_{q\bar{q}N}(x, b)$  of Eq. (1), as a function of the transverse size of the  $q\bar{q}$  pair for various values of  $x$  and for the GRV94 parameterization of  $g_N(x, Q^2)$ .

allow the processes limiting the growth of  $F_2$  as  $x$  tends to zero to be studied in detail. (ii) *To establish the difference between the gluon distributions in nuclei and free nucleons.* This would allow direct access to nonlinear phenomena. (iii) *Study of diffractive processes:* to see if the pomeron generated by nuclei shows any difference from that generated by free nucleons. Processes such as vector meson production can also be used to search for color transparency. (iv) *Study of hadronic final states.* This allows the propagation of partons in the nuclear medium to be studied as well as the multiplicity fluctuations discussed later.

## II. SPACE-TIME PICTURE OF DIS OFF NUCLEI AT SMALL $x$ IN THE NUCLEUS REST FRAME

At small  $x$  it is convenient to consider the process in the rest frame of the target nucleus. In the language of noncovariant diagrams the process corresponds to the virtual photon fluctuating into a quark-antiquark pair at a longitudinal distance  $l_c \sim 1/2m_N x$  from the nucleus which far exceeds the nuclear radius. The distance  $l_c$  is referred to as the “coherence length”. The pair propagates essentially without transverse expansion until it reaches the target. QCD evolution leads to a logarithmic decrease of  $l_c(x)$  with increasing  $Q^2$ . At HERA coherence lengths of up to 1000 fm are possible, so that the interaction of the  $q\bar{q}$  pair with nuclear matter can be studied in detail – notably its transparency to small size pairs - *color transparency*. In the case of transversely polarized photons both configurations with small  $k_t$  and highly asymmetric fractions  $z$  and configurations with comparable  $z$  and  $1 - z$  contribute to the cross section. For the case of the longitudinal photons the asymmetric contribution is strongly suppressed.

At HERA new features of color transparency should emerge: the incident small size  $q\bar{q}$  pair resolves small  $x$  gluon fields with virtualities  $\sim Q^2$ . If the transverse size of the  $q\bar{q}$  pair

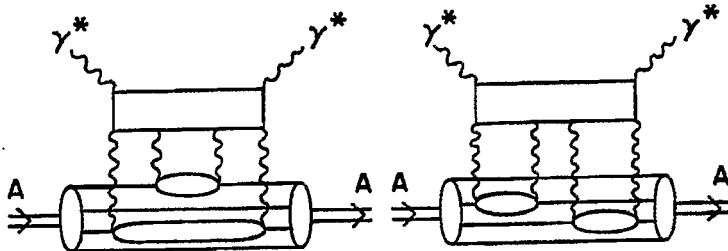


FIG. 2. Typical fan diagrams leading to nonlinear evolution of  $g_A(x, Q^2)$ .

is  $r_t = b_q - b_{\bar{q}}$ , the cross section for interaction with a nucleon is [5]

$$\sigma_{q\bar{q},N}(E_{inc}) = \frac{\pi^2}{3} r_t^2 \alpha_s(Q^2) x g_N(x, Q^2), \quad (1)$$

where  $Q^2 \approx \frac{\lambda(x)}{r_t^2}$ ,  $\lambda(x \approx 10^{-3}) \approx 9$ ,  $x = \frac{Q^2}{2m_N E_{inc}}$ . Since the gluon density increases rapidly with decreasing  $x$ , even small size pairs may interact strongly, leading to some sort of *perturbative color opacity* – the interaction of a small object with a large object with a cross section comparable to the geometric size of the larger object (Fig. 1).

Unitarity considerations for the scattering of a small size system [6] – i.e. the requirement that  $\sigma_{inel}(q\bar{q}, target) \leq \pi R_{target}^2$  – indicate that nonlinear effects (i.e. effects not accounted for by the standard evolution equations) should become significant at much larger values of  $x$  in  $eA$  scattering than in  $ep$  scattering.

In the simplest model of nonlinear effects corresponding to the fan diagrams of Fig. 2, the additional contribution  $\delta g_A(x, Q^2)$  to  $g_A(x, Q^2)$  due to the nonlinear term in the equation for the  $Q^2, x$  evolution of the gluon density is [7]:

$$Q^2 \frac{\partial}{\partial Q^2} \frac{\delta x g_A(x, Q^2)}{A} = -\frac{81}{16} \frac{A^{1/3}}{Q^2 r_0^2} \alpha_s^2(Q^2) \int_x^1 \frac{du}{u} [u g_N(u, Q^2)]^2. \quad (2)$$

The analogous equation for the gluon density in the nucleon has a much smaller coefficient – approximately by a factor  $r_0^2/r_N^2 A^{1/3}$ , where  $r_N \sim 0.8$  fm is the nucleon radius. Once again one can see then that the  $x$ -range where nonlinear effects become significant differs for a heavy nucleus and for a nucleon by more than two orders of magnitude, assuming  $x g_N(x, Q^2) \propto x^n$  with  $n \sim -0.2$ . Thus electron-nucleus collisions at HERA can be seen as efficient amplifiers of nonlinear QCD effects.

### III. PERTURBATIVE AND NONPERTURBATIVE SHADOWING

At small  $x$  the DIS cross section per nucleon in a nucleus is smaller than for a free one, the so called shadowing phenomenon. Shadowing is determined by a combination of non-perturbative and perturbative effects. In the DGLAP evolution equations one can express shadowing at large  $Q^2$  through the shadowing at the normalization point  $Q_0^2$ . This type of shadowing is connected to the soft physics. It can be visualized e.g. in the aligned jet model of Bjorken [3], extended to account for QCD evolution effects [8]. A virtual photon converts to a  $q\bar{q}$  pair with small transverse momenta (large transverse size) which interacts



with the nucleus with a hadronic cross section, leading to shadowing. The effective small phase volume of these configurations ( $\propto \frac{\lambda}{Q^2}$ ) leads to Bjorken scaling and it is due to color transparency [8].

At large  $Q^2$ , these  $q\bar{q}$  pairs evolve into systems with gluons, leading to a shift of shadowing to smaller  $x$ , which is equivalent to the standard  $Q^2$  evolution of parton distributions. These  $q\bar{q}$  pairs, which interact with the target nonperturbatively, seem to be responsible for most of the shadowing at intermediate  $Q^2$  and  $x \sim 10^{-2}$  which has been studied at fixed target energies. This mechanism of shadowing is effective for  $\sigma_T$  only since for  $\sigma_L$  the aligned jet contribution is strongly suppressed. For  $\sigma_L$  (as well as for the production of heavy quarks) one is more sensitive to the shadowing due to the interaction of small size  $q\bar{q}$  pairs with the nuclear gluon field which can be shadowed.

At smaller  $x$  the situation may change rather dramatically because, as the recent HERA data indicate, already for  $Q^2 \sim 1.5 \text{ GeV}^2$  at  $x \sim 10^{-4}$  perturbative contributions to  $F_{2p}(x, Q^2)$  appear to become important, leading to a rapid increase of the structure functions with decreasing  $x$ . Hence contributions of various perturbative mechanisms which may generate shadowing for configurations of a size smaller than the hadronic size may become important. Perturbative QCD may be applicable to those small size pairs. Typical contributions involve diagrams of the eikonal type, various enhanced diagrams, etc.

#### IV. SHADOWING AND DIFFRACTION

In practically all models it is assumed that nuclei are built of nucleons. So the condition that the matrix element  $\langle A|T[J_\mu(y), J_\nu(0)]|A \rangle$  involves only nucleonic initial and final states is implemented<sup>1</sup>. Under these natural assumptions one is essentially not sensitive to any details of the nuclear structure, such as short-range correlations etc.

In the case of scattering off the deuteron and light nuclei the same diagrams contribute to the cross section for diffraction in  $ep$  scattering and the cross section for shadowing – hence similar nonlinear phenomena like those described by eq.(2) are involved in each case. For example for the deuteron [2]:

$$\sigma_{shad} = \frac{\sigma_{tot}(eD) - 2\sigma_{tot}(eN)}{\sigma(eN)} = \frac{d\sigma_{diff}(ep)}{dt}|_{t=0} \frac{1}{\sigma_{tot}(ep)} \frac{1}{8\pi R_D^2} R, \quad (3)$$

where  $R = \frac{(1-\lambda^2)}{(1+\lambda^2)}$ ,  $\lambda = ReA/ImA \approx \frac{\pi}{2} \frac{\partial \ln A}{\partial \ln s}$  for the amplitude  $A$  of  $\gamma^*p$  scattering and  $R_D$  is the deuteron radius. For small  $x$ ,  $\lambda$  may be as large as 0.5, leading to  $R \sim 0.5$  especially for the case of the longitudinal cross section. So already for light nuclei the study of the total cross sections of scattering from nuclei would allow to establish a fundamental connection between the two seemingly unrelated phenomena of diffraction at small  $t$  in  $ep$  scattering and nuclear shadowing. With the increase of  $A$  more complicated nonlinear interactions with several nucleons become important.

---

<sup>1</sup>The condition that nuclei are built of nucleons is not so obvious in the fast frame picture. However it is implemented in most of the models [7,9].

Nuclear shadowing for the total cross sections has a simple physical meaning - it corresponds to a reduction of cross section due to screening of one nucleon by another ( as well as by several nucleons for  $A > 2$ ). If one treats the deuteron as a two nucleon system it is possible to apply the Abramovskii, Gribov, Kancheli (AGK) cutting rules [10] to elucidate **the connection between nuclear shadowing, diffraction and fluctuations of multiplicity**. One observes that the simultaneous interaction of the  $\gamma^*$  with the two nucleons of the deuteron modifies not only the total cross section but also the composition of the produced final states. It increases the cross section for diffractive scattering off the deuteron due to diffractive scattering off both nucleons by  $\delta\sigma_{diff} = \sigma_{shad}$ . At the same time the probability to interact inelastically with one nucleon only is reduced since the second nucleon screens the first one:  $\delta\sigma_{single} = -4\sigma_{shad}$ . In addition, a new process emerges in the case of the deuteron which was absent in the case of the free nucleon - *simultaneous* inelastic interaction with both nucleons which leads to a factor of two larger multiplicity densities for rapidities away from the current fragmentation region:  $\sigma_{double} = 2\sigma_{shad}$ . Altogether these contributions constitute  $-\sigma_{shad}$ , the amount by which the total cross section is reduced <sup>2</sup>.

To summarize, *there is a deep connection between the phenomena of diffraction observed at HERA in ep scattering and nuclear shadowing as well as the A-dependence of diffraction and the distribution of the multiplicities in DIS.*

Using current information from HERA on diffractive production in ep scattering it is straightforward to estimate the amount of nuclear shadowing at small  $x$  taking into account interactions with 3 or more nucleons using the eikonal approximation with an effective cross section,  $\sigma_{eff}$ , determined from diffractive data, see discussion in section V. The result of the calculation [11] is shown in Fig. 3 for  $Re/Im = 0$ ; for  $A \geq 12$  it weakly depends on the value of  $Re/Im$ . Since the data on diffraction indicate that the fraction of diffractive events in DIS weakly depends on  $x, Q^2$  these considerations show that significant shadowing effects should be present for  $F_2^A(x, Q^2)$  in the wide small  $x$  range of HERA. Note that the shadowing effect in DIS is expected to be much smaller than for the case of real photon scattering since the effective cross section for interaction of the hadron component of quasi-real photon at HERA is a factor of  $\sim 3$  larger than for a highly virtual photon (we use here the HERA data on diffraction for real photons).

Since the interaction of the octet color dipole  $gg$  is a factor of 9/4 stronger than for the  $q\bar{q}$  dipole, nonlinear effects are expected to be more important for gluons. So gluon shadowing would provide even more direct access to nonlinear phenomena. Note that in this case there is no simple relation of shadowing with diffraction in  $\gamma^* + p$  DIS, so any information about gluon shadowing would be complementary to the information from ep DIS. Comparison of different determinations of shadowing of gluons and measurements of the scaling violation for the  $F_2^A/F_2^D$  ratios will allow to determine the range of applicability of the DGLAP evolution equations and hence provide unique clues to the role of nonlinear effects.

---

<sup>2</sup>For simplicity we give here relations for the case of purely imaginary  $\gamma^*N$  amplitude  $\frac{ReA}{ImA} = 0$ .

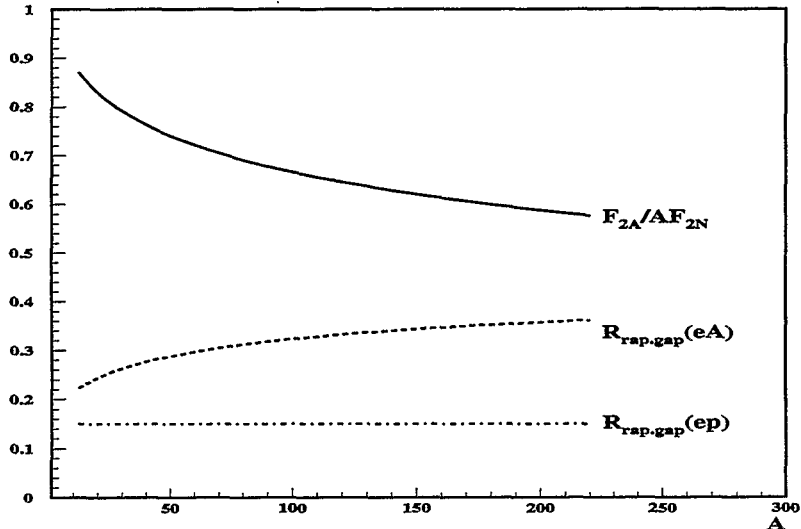


FIG. 3.  $A$ -dependence of nuclear shadowing and probability of rapidity gap events in the color screening model of shadowing; dot-dashed curve assumes  $A$ -independent probability of rapidity gap events.

## V. DIFFRACTION OFF NUCLEI

Diffraction studies have been defined as one of the primary goals of nuclear beams in HERA. Such processes can be interpreted as the diffractive interaction of different hadronic components of the virtual photon with the target via vacuum exchange. Diffraction predominantly selects the  $\gamma^*$  components which interact with sufficiently large cross sections such as large transverse size  $q\bar{q}$ ,  $q\bar{q}g$  color dipoles. Therefore the study of diffraction plays a very important role in determining the relative importance of small and large size configurations and addressing the question whether small white objects interact weakly or not. Indeed if the interaction with a target becomes sufficiently strong at small impact parameters the cross section for diffraction (which includes both elastic scattering and inelastic diffractive dissociation) would reach the black body limit of 50% of the total cross section.

Diffraction off a nucleon (including dissociation of the nucleon) constitutes about 15-20% of the deep inelastic events. Therefore the interaction is definitely far from being close to the scattering off a black body. Even this number came a surprise in view of the large  $Q^2$  value involved. Using the generalized optical theorem as formulated by Miettinen and Pumplin, one can estimate the effective total cross section for the interaction of the hadronic components of the  $\gamma^*$  as  $\sigma_{eff} = 16\pi \frac{d\sigma_{diff}^{\gamma^*+p \rightarrow X+p}}{dt} \Big|_{t=0} / \sigma_{tot}(\gamma^*N) \approx 12 \div 15$  mb. This cross section is significantly smaller than the  $\rho N$  cross section which at the HERA energies can be estimated to be close to 40 mb. However it is sufficiently large to result in a substantial cross section of diffraction for small  $x$  – it can reach 30-40% for large  $A$  (Fig. 3) [11]. For

large  $A$  the coherent diffraction dominates when the incoming wave is sufficiently absorbed at small impact parameters which, by virtue of Babinet's principle, corresponds to scattering beyond the nucleus. In such processes the nucleus remains intact and the average momentum transfer is very small ( $\langle t \rangle \propto A^{-2/3}$ ).

One expects that hadronic configurations interacting with different strength contribute to diffraction (cf. Fig. 1). The parameter  $\sigma_{eff}$  characterizes just the average strength of this interaction, while the distribution over the strengths is expected to be quite broad. The study of diffraction off nuclei allows to separate contributions to diffraction of large and small size configurations due to **the filtering phenomenon**: with the increase of  $A$  the relative contribution of more weakly interacting (smaller size) configurations should increase since they are less shadowed, leading to a relative enhancement of the color transparent subprocesses. Examples of promising processes are: diffractive production of charm, diffractive production of two high  $p_t$  jets as well as related phenomena of multiplicity fluctuations in inelastic  $\gamma^*A$  interactions e [11].

## VI. COLOR TRANSPARENCY PHENOMENA

An important property of QCD is that small objects are expected to interact with hadrons with small cross section [12]. This implies that in the processes dominated by the scattering/production of hadrons in "point-like" (small size) configurations (PLC) when embedded in the nuclei, the projectile or the outgoing hadron essentially does not interact with the nuclear environment. A quantitative formulation of color transparency for high-energy processes can be based on eq.(1). For the case of nuclear targets it implies that for a small enough color dipole, the cross section of its interaction with nuclei is proportional to  $A$  up to the gluon shadowing factor. As a result the color transparency prediction for 2 jet and vector meson diffractive production is [13,14]<sup>3</sup>:

$$\frac{\frac{d\sigma}{dt}(\gamma^*A \rightarrow 2jets + A)|_{t=0}}{\frac{d\sigma}{dt}(\gamma^*N \rightarrow 2jets + N)|_{t=0}} = \frac{\frac{d\sigma}{dt}(\gamma^*A \rightarrow VA)|_{t=0}}{\frac{d\sigma}{dt}(\gamma^*N \rightarrow VN)|_{t=0}} = \left[ \frac{F_A^L(x, Q^2)}{F_N^L(x, Q^2)} \right]^2 = \frac{G_A^2(x, Q^2)}{G_N^2(x, Q^2)}. \quad (4)$$

Gluon shadowing constitutes a rather small effect for  $x \sim 10^{-2}$ . For smaller  $x$  it increases but it is in any case much smaller than the screening effect expected in the case of lack of color transparency if the produced system interacts with cross section comparable to  $\sigma_{\rho N} \sim 30\text{-}40$  mb. For such values of  $\sigma$  one expects the cross section to behave as  $\propto A^{4/3}$  for  $t = 0$  which would be possible to test using diffractive production by quasi-real photons.

### *Coherent diffractive $\rho, J/\psi$ -meson production*

The most straightforward test of color transparency can be made using coherent production of  $\rho$  or  $J/\psi$ -mesons at small  $t$  using nuclei with  $A \geq 12$ . The  $p_t$  resolution of the current detectors is good enough to single out the diffractive peak which is concentrated at  $p_t \leq 0.1$  GeV. In the higher  $x$  end of the range which could be studied at HERA for vector

---

<sup>3</sup>In writing eq.(4) we neglect the difference of  $Q^2$  scales for different processes which is reflected in a different dependence of the essential transverse size of the  $q\bar{q}$  state on the process (see Fig. 4). For a discussion of the appropriate scale for dijet production see [15].

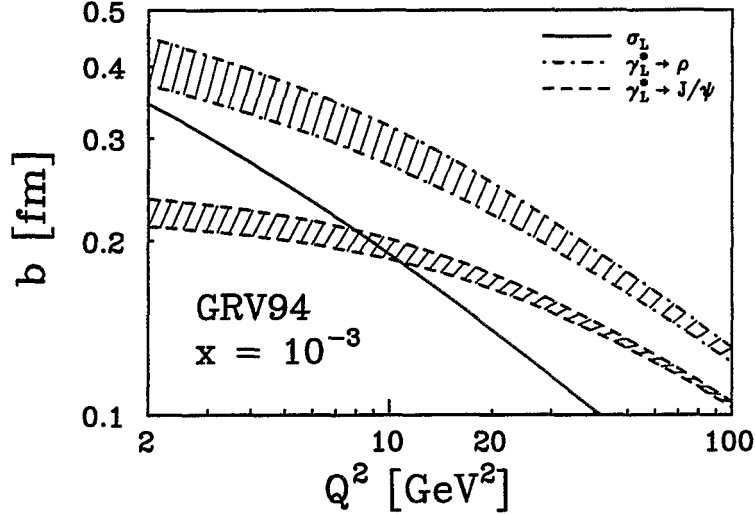


FIG. 4. Average transverse size of the  $q\bar{q}$  components effective in  $\mathcal{A}_{\gamma_L^* N \rightarrow VN}$  for  $\rho$ - and  $J/\psi$ -meson production and  $\sigma_L$ . The probed  $Q^2$  scale is inversely proportional to  $b^2$ .

meson production,  $x \sim 10^{-2}$ , one expects at large  $Q^2$  nearly complete color transparency since gluon shadowing effects are rather small and decrease rapidly with increase of  $Q^2$ , while the transverse separation,  $b$ , between  $q$  and  $\bar{q}$  is of the order of 0.4 fm for  $Q^2 \sim 10$   $\text{GeV}^2$  and further decreases with increase of  $Q^2$  (Fig. 4 [6]). Study of coherent  $J/\psi$  meson production would allow to probe color transparency for propagation of even smaller dipoles since  $\langle b_{c\bar{c}}(Q^2 = 0) \rangle \sim 0.2$  fm.

On the other hand as discussed earlier at the smallest values of  $x$  of the HERA range, screening effects should start to play a role even at large  $Q^2$  so a gradual disappearance of color transparency is expected – the emergence of color opacity. Noticeable screening is expected already on the basis of unitarity constraints. Qualitatively one may expect that the rise of the cross section for vector meson production with increasing energy at fixed  $Q^2$  will slow down at significantly lower energies than for the case of the  $\gamma^* + p$  reaction. Currently theoretical calculations of vector meson production by transversely polarized photons are difficult because the nonperturbative large distance contribution is not as strongly suppressed in this case as in the longitudinal case. If contribution of pairs with large transverse size is indeed important for  $\sigma_T$ , it would be filtered out with increasing  $A$  leading to larger values of  $\sigma_L/\sigma_T$  for large  $A$ .

Several other effects of Color Transparency (CT) in diffractive production can be studied in (i) Production of excited vector meson states  $\rho', \phi'$ . (ii) Production of high  $p_t$  dijets. (iii) Coherent diffractive production at  $-t \geq 0.1$   $\text{GeV}^2$  for  $A = 2, 4$ . An important question here is the possibility to observe the “disappearance” of color transparency for  $\rho$ -meson production and the emergence of “color opacity” – due to nonlinear screening effects at  $x \sim 10^{-4}$ . Manifestations of CT would be the increase of the differential cross section  $\frac{d\sigma}{dt}$  below the diffractive minimum ( $|t_{min}(^4He)| \approx 0.2$   $\text{GeV}^2$ ) and suppression of the cross section in the region of the secondary maximum. (iv)  $A$ -dependence of rapidity gaps between jets in photoproduction which would allow recent interpretation of the HERA  $\gamma p$  rapidity gap data as manifestation of CT [16].

## VII. CONNECTION TO HEAVY-ION COLLISIONS AT HIGH ENERGIES

The interplay between the physics which can be studied in high-energy  $eA$  collisions at HERA and that to be studied in the heavy ion physics was discussed at the dedicated workshop “Nuclei at HERA and Heavy Ion Physics” which was held at BNL in 1995. It was concluded that the measurements of  $eA$  collisions at HERA can provide crucial information necessary for unambiguous interpretation of the heavy ion collisions at RHIC and LHC for establishing whether a quark-gluon plasma is formed in these collisions.

Three major links are

- *Nuclear gluon shadowing.* One needs  $xg_A(x, Q^2)$  for  $x \sim 10^{-2}$ ,  $Q^2 \sim 1 - 10\text{GeV}^2$  and  $x \sim 10^{-3}$ ,  $Q^2 \sim 10\text{GeV}^2$  to fix the initial conditions at RHIC and LHC respectively. This is especially important for the LHC since mini-jet production determines the initial conditions for  $\sqrt{s} \geq 100\text{GeV}$ . The bulk of the particles produced at central rapidities in  $AA$  collisions at the LHC is expected to be generated due to this mechanism [18]. Currently uncertainties in nuclear shadowing transform into at least a factor 2-4 differences in the final transverse energy flow [17].

- *Jet quenching.* Recent QCD studies [19] have demonstrated that the medium induced energy losses and  $p_t$  broadening of a high energy parton traversing a hot QCD medium are much larger than in the case of a cold medium. This provides a unique new set of global probes of the properties of the state formed during  $AA$  collisions [17]. To interpret unambiguously this effect it is necessary both to measure the nuclear gluon shadowing and to study the parton propagation in cold matter in DIS to confirm that the energy losses ( $p_t$ -broadening) remain small at energies comparable to those to be studied at RHIC and LHC.

- *Testing of soft dynamics of interactions with nuclei.* Study of  $eA$  interactions at HERA in the **same energy range** as that to be studied in  $pA$  and  $AA$  collisions at RHIC ( $\sqrt{s} \sim 200\text{ GeV}$ ) will provide a unique testing ground for the modern models of interactions with nuclei which aim at describing on the same footing  $ep$ ,  $eA$ ,  $pp$ ,  $pA$ ,  $AA$  collisions [20]. It would allow to be established whether or not the same dynamics determines hadroproduction in  $eA$  collisions and in central  $AA$  collisions. One of the key questions here is how effective AGK cancellations of the screening effects would work leading to predictions of  $\frac{d\sigma^{h(\gamma)+A \rightarrow h+X}}{dy} = A \frac{d\sigma^{h(\gamma)+N \rightarrow h+X}}{dy}$  and  $\frac{d\sigma^{A_1+A_2 \rightarrow h+X}}{dy} = A_1 A_2 \frac{d\sigma^{N+N \rightarrow h+X}}{dy}$  for the central rapidity range. If these relations would work for heavy ion collisions hard minijet mechanism would be suppressed (due to screening of parton densities) rather than enhanced in  $AA$  collisions as compared to the  $NN$  collisions.

## VIII. ACKNOWLEDGEMENTS

I would like to thank all my colleagues in working group 8 of the workshop “Future of HERA” for their invaluable assistance and for numerous discussions. I thank the U.S. Department of Energy for financial support under grant number DE-FG02-93ER-40771.

## REFERENCES

- [1] M.Arneodo, A.Bialas, W.Krasny, T.Sloan, M.Strikman, Report of conveners of the working group "Light and Heavy Nuclei", Proceedings of workshop "Future of HERA" in press; <http://www.desy.de/heraws96/proceedings>.
- [2] V. N. Gribov, Sov. Phys. JETP **30** 709 (1969).
- [3] J. D. Bjorken in Proceedings of the International Symposium on Electron and Photon Interactions at High Energies, p. 281–297, Cornell (1971).
- [4] R. Baier, Yu.L. Dokshitzer, A.H. Mueller, S. Peigné, D. Schiff, hep-ph 9608322.
- [5] B. Blättel, G. Baym, L.L. Frankfurt and M. Strikman, Phys. Rev. Lett. **71** (1993) 896.
- [6] L. Frankfurt, W. Koepf and M. Strikman, Phys.Rev. **D54** (1996) 3194.
- [7] A.H.Mueller and J-W.Qiu, Nucl. Phys. **B268** (1986) 427.
- [8] L. L. Frankfurt and M. Strikman, Phys. Rep. **160** (1988) 235.
- [9] L.M Lerran and R.Venugopalan, Phys.Rev. **D50** (1994) 225.
- [10] V.Abramovskii, V. N. Gribov and O. V. Kancheli, Sov. J. Nucl. Phys. **18**, 308 (1974).
- [11] L.Frankfurt and M.Strikman, Phys.Lett. **B382** (1996) 6.
- [12] F. E. Low, Phys. Rev. **D12** (1975) 163.
- [13] L. Frankfurt, G.A. Miller and M. Strikman, Phys. Lett. **B304** (1993) 1.
- [14] S.J.Brodsky, L.Frankfurt, J.F.Gunion, A.H.Mueller and M.Strikman, Phys.Rev. **D50** (1994) 3134.
- [15] J.Bartels,H.Lotter and M. Wusthoff, Phys.Lett. **B379** (1996) 239.
- [16] L.Frankfurt and M.Strikman,hep-ph 9609456.
- [17] M.Gyulassy, Proc. 'Nuclei at HERA and Heavy Ion Physics', BNL-62634, 1995.
- [18] X-N.Wang and M.Gyulassy, Phys.Rev.Lett. **68** (1992) 1480.
- [19] R. Baier, Yu.L. Dokshitzer, A.H. Mueller, S. Peigné and D. Schiff hep-ph 9607355.
- [20] J.Ellis, K. Geiger and H. Kowalski, Phys.Rev.D in press, hep-ph/9605425.

# Study Parton Energy Loss in High-energy Heavy-ion Collisions\*

Xin-Nian Wang<sup>a</sup> and Zheng Huang<sup>b</sup>

<sup>a</sup>*Nuclear Science Division, Mailstop 70A-3307, Lawrence Berkeley National Laboratory  
University of California, Berkeley, CA 94720 USA*

<sup>b</sup>*Department of Physics, University of Arizona, Tucson, AZ 85721, USA*

## Abstract

Jet quenching due to parton energy loss in dense matter will suppress leading particles from jet fragmentation in high-energy heavy-ion collisions. We study the effect of jet quenching on inclusive particle  $p_T$  distributions and investigate how one can improve the measurement of parton energy loss in direct photon events. We demonstrate that  $\gamma/\pi^0$  ratio at large  $p_T$  will be significantly increased due to jet quenching. We point out that the medium-induced  $p_T$  broadening of a propagating jet can be studied through the effective jet profile in the opposite direction of the direct photon.

## I. INTRODUCTION

Medium-induced radiative energy loss of a high-energy parton traversing a dense QCD medium is interesting not only because it illustrates the importance of quantum interference effects in QCD, but also because it depends sensitively on the density of the medium and thus can be used as a probe of the dense matter formed in ultrarelativistic heavy-ion collisions. As recent studies demonstrated [1–3], it is very important to take into account the destructive interference effect in the calculation of radiation spectrum from a fast parton induced by multiple scatterings. The so-called Landau-Pomeranchuk-Migdal effect can lead to very interesting, and sometimes nonintuitive results for the energy loss of a fast parton in a QCD medium. For example, Baier *et al.* recent showed [3] that the energy loss per distance,  $dE/dx$ , is proportional to the total length that the parton has traveled. Because of the unique interference effect, the parton somehow knows its history of propagation. Another feature of the induced energy loss is that it depends on the parton density of the medium it is traversing via the final transverse momentum broadening that the parton receives during its propagation. One can therefore determine the parton density of the produced dense matter by measuring the energy loss of a fast parton when it propagates through the medium.

Unlike in the QED case, where one can measure directly the radiative energy loss of a fast electron, one cannot measure directly the energy loss of a fast leading parton in QCD.

---

\*Talk presented by X.-N. Wang



Since a parton is normally studied via a jet, a cluster of hadrons in the phase space, an identified jet can contain particles both from the fragmentation of the leading parton and from the radiated partons. If we neglect the  $p_T$  broadening effect, the total energy of the jet should not change even if the leading parton suffers radiative energy loss. What should be changed by the energy loss are the particle distributions inside the jet or the fragmentation function and the jet profile. Therefore, one can only measure parton energy loss indirectly via the modification of the jet fragmentation function and jet profile.

In principle, one can measure the parton energy loss by directly measuring the fragmentation function and profile of a jet with a determined transverse energy. However, because of the huge background and its fluctuation in high-energy heavy-ion collisions [4], the conventional calorimetric study of a jet cannot determine the jet energy thus the energy loss very well. In Ref. [5], Gyulassy and I proposed that single-particle spectrum can be used to study the effect of jet energy loss, since the suppression of large  $E_T$  jets naturally leads to the suppression of large  $p_T$  particles. However, since the single-particle spectrum is a convolution of the jet cross section and jet fragmentation function, the suppression of produced particles with a given  $p_T$  results from jet quenching with a wide range of initial transverse energies. One, therefore, cannot measure directly, from the single-particle  $p_T$  spectrum, the energy loss of a jet with known initial transverse energy. Recently, Huang, Sarcevic and I proposed to study the jet quenching by measuring the  $p_T$  distribution of charged hadrons in the opposite direction of a tagged direct photon [6]. Since a direct photon in the central rapidity region ( $y = 0$ ) is always accompanied by a jet in the opposite transverse direction with roughly equal transverse energy, the  $p_T$  distribution of charged hadrons in the opposite direction of the tagged direct photon is directly related to the jet fragmentation function with known initial energy. One can thus directly measure the modification of the jet fragmentation and then determine the energy loss suffered by the leading parton.

In this talk, I will review the effects of energy loss on single-particle distributions both in the normal central  $A + A$  collisions and in events with a tagged direct photon with known transverse energy. I will discuss the energy and  $A$  dependences of the energy loss and jet quenching. In the case of jet quenching in  $\gamma + \text{jet}$  events, the  $E_T$  smearing of jet due to initial state radiation will be included. The change of jet profile function in the azimuthal angle due to  $p_T$  broadening of the jet will also be discussed. Finally, discussions will be given on the feasibility of measuring the energy loss in  $\gamma + \text{jet}$  events at RHIC.

## II. MODIFIED JET FRAGMENTATION FUNCTIONS

Jet fragmentation functions have been studied extensively in  $e^+e^-$ ,  $ep$  and  $p\bar{p}$  collisions [7]. These functions describe the particle distributions in the fractional energy,  $z = E_h/E_{jet}$ , in the direction of a jet. The measured dependence of the fragmentation functions on the momentum scale is shown to satisfy the QCD evolution equations very well. We will use the parametrizations of the most recent analysis [8] in both  $z$  and  $Q^2$  for jet fragmentation functions  $D_{h/a}^0(z, Q^2)$  to describe jet ( $a$ ) fragmentation into hadrons ( $h$ ) in the vacuum.

In principle, one should study the modification of jet fragmentation functions in a perturbative QCD calculation in which induced radiation of a propagating parton in a medium and Landau-Pomeranchuk-Migdal interference effect can be dynamically taken into account. However, for the purpose of our current study, we can use a phenomenological model

to describe the modification of the jet fragmentation function due to an effective energy loss  $dE/dx$  of the parton. In this model we assume: (1) A quark-gluon plasma (QGP) is formed with a transverse size of the colliding nuclei,  $R_A$ . A parton with a reduced energy will only hadronize outside the deconfined phase and the fragmentation can be described as in  $e^+e^-$  collisions. (2) The inelastic scattering mean-free-path for the parton  $a$  inside the QGP is  $\lambda_a$ . The radiative energy loss per scattering is  $\epsilon_a$ . The energy loss per distance is thus  $dE_a/dx = \epsilon_a/\lambda_a$ . The probability for a parton to scatter  $n$  times within a distance  $\Delta L$  is given by a Poisson distribution,

$$P_a(n, \Delta L) = \frac{(\Delta L/\lambda_a)^n}{n!} e^{-\Delta L/\lambda_a}. \quad (1)$$

We also assume that the mean-free-path of a gluon is half that of a quark, and the energy loss  $dE/dx$  is twice that of a quark. (3) The emitted gluons, each carrying energy  $\epsilon_a$  on the average, will also hadronize according to the fragmentation function with the minimum scale  $Q_0^2 = 2.0 \text{ GeV}^2$ . We will also neglect the energy fluctuation given by the radiation spectrum for the emitted gluons. Since the emitted gluons only produce hadrons with very small fractional energy, the final modified fragmentation functions in the moderately large  $z$  region are not very sensitive to the actual radiation spectrum and the scale dependence of the fragmentation functions for the emitted gluons.

We will consider the central rapidity region of high-energy heavy-ion collisions. We assume that a parton with initial transverse energy  $E_T$  will travel in the transverse direction in a cylindrical system. With the above assumptions, the modified fragmentation functions for a parton traveling a distance  $\Delta L$  can be approximated as,

$$D_{h/a}(z, Q^2, \Delta L) = \frac{1}{C_N^a} \sum_{n=0}^N P_a(n, \Delta L) \frac{z_n^a}{z} D_{h/a}^0(z_n^a, Q^2) + \langle n_a \rangle \frac{z'_a}{z} D_{h/g}^0(z'_a, Q_0^2), \quad (2)$$

where  $z_n^a = z/(1 - n\epsilon_a/E_T)$ ,  $z'_a = zE_T/\epsilon_a$  and  $C_N^a = \sum_{n=0}^N P_a(n)$ . We limit the number of inelastic scatterings to  $N = E_T/\epsilon_a$  by energy conservation. For large values of  $N$ , the average number of scatterings within a distance  $\Delta L$  is approximately  $\langle n_a \rangle \approx \Delta L/\lambda_a$ . The first term corresponds to the fragmentation of the leading partons with reduced energy  $E_T - n\epsilon_a$  and the second term comes from the emitted gluons each having energy  $\epsilon_a$  on the average.

### III. ENERGY LOSS AND SINGLE-PARTICLE $P_T$ SPECTRUM

To calculate the  $p_T$  distribution of particles from jet fragmentation in a normal central heavy-ion collision, one simply convolutes the fragmentation functions with the jet cross section [9],

$$\frac{dN_{hard}^{AA}}{dy d^2p_T} = K \int d^2r \sum_{abcdh} \int_{x_{amin}}^1 dx_a \int_{x_{bmin}}^1 dx_b f_{a/A}(x_a, Q^2, r) f_{b/A}(x_b, Q^2, r) \frac{D_{h/c}(z_c, Q^2, \Delta L)}{\pi z_c} \frac{d\sigma}{d\hat{t}}(ab \rightarrow cd), \quad (3)$$

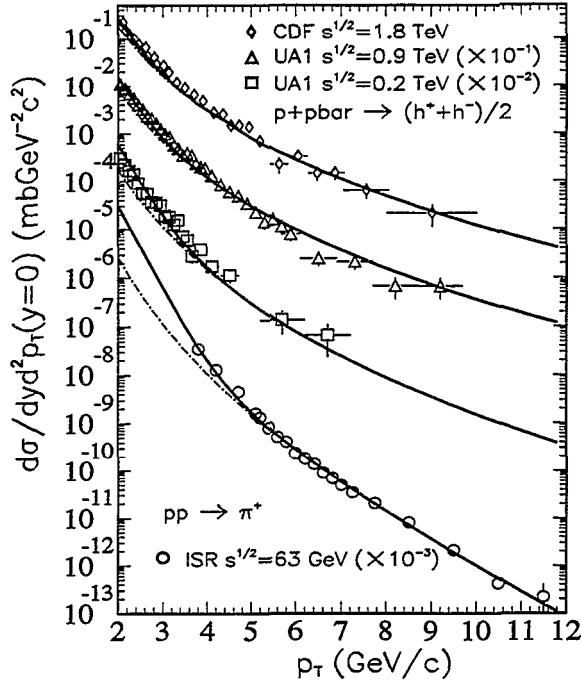


FIG. 1. The charged particle  $p_T$  spectra in  $pp$  and  $p\bar{p}$  collisions. The dot-dashed lines are from jet fragmentation only and solid lines include also soft production parametrized in an exponential form. The experimental data are from Ref. [13–15].

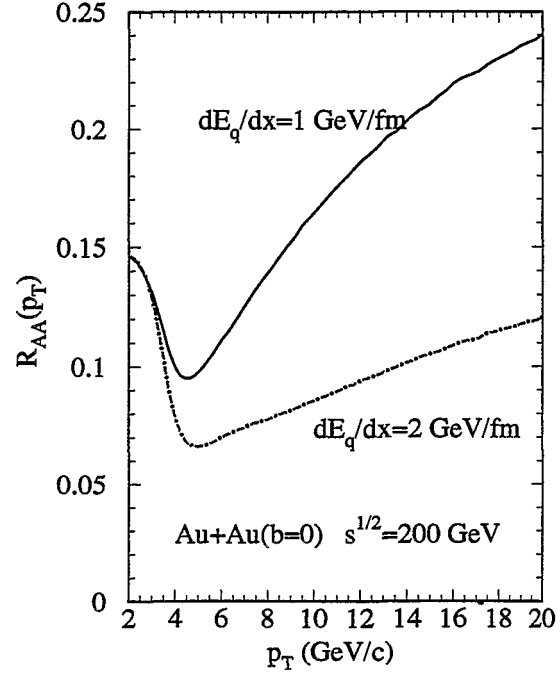


FIG. 2. The ratio of charged particle  $p_T$  spectrum in central  $Au + Au$  collisions at  $\sqrt{s} = 200$  GeV over that of  $pp$  collisions, normalized by the total binary nucleon-nucleon collisions in central  $Au + Au$  collisions. The mean-free-path of a quark inside the medium is assumed to be 1 fm.

where  $z_c = x_T(e^y/x_a + e^{-y}/x_b)/2$ ,  $x_{bmin} = x_a x_T e^{-y}/(2x_a - x_T e^y)$ ,  $x_{amin} = x_T e^y/(2 - x_T e^{-y})$ , and  $x_T = 2p_T/\sqrt{s}$ . The  $K \approx 2$  factor accounts for higher order corrections [10]. The parton distribution density in a nucleus,  $f_{a/A}(x, Q^2, r) = t_A(r) S_{a/A}(x, r) f_{a/N}(x, Q^2)$ , is assumed to be factorizable into the nuclear thickness function  $t_A(r)$  (with normalization  $\int d^2r t_A(r) = A$ ), parton distribution in a nucleon  $f_{a/N}(x, Q^2)$  and the parton shadowing factor  $S_{a/A}(x, r)$  which we take the parametrization used in HIJING model [11]. Neglecting the transverse expansion, the transverse distance a parton produced at  $(r, \phi)$  will travel is  $\Delta L(r, \phi) = \sqrt{R_A^2 - r^2(1 - \cos^2 \phi)} - r \cos \phi$ .

We will use the MRS D-1 parametrization of the parton distributions [12] in a nucleon. The resultant  $p_T$ -spectra of charged hadrons ( $\pi^\pm, K^\pm$ ) for  $pp$  and  $p\bar{p}$  collisions are shown in Fig. III together with the experimental data [13–15] for  $\sqrt{s} = 63, 200, 900$  and  $1800$  GeV. The calculations (dot-dashed line) from Eq. (3) with the jet fragmentation functions given by Ref. [8] agree with the experimental data remarkably well, especially at large  $p_T$ . However, the calculations are consistently below the experimental data at low  $p_T$ , where we believe particle production from soft processes is very important. To account for particle production at small  $p_T$ , we introduce a soft component to the particle spectra in an exponential form whose parameters are fixed by total  $dN/dy$  [16]. The total  $p_T$  spectra including both soft and hard component are shown in Fig. III as solid lines.

To calculate the  $p_T$  spectrum in  $AA$  collisions, one has to take into account both the parton shadowing effect and the modification of the jet fragmentation functions due to parton energy loss inside a medium. In addition, one has to know the  $A$  scaling of the soft particle spectrum in central  $AA$  collisions with respect to  $pp$  collisions. Here we simply assume a linear scaling as in a wounded nucleon model. One can then calculate the ratio,

$$R_{AA}(p_T) = \frac{dN_{AA}/dy/d^2p_T}{\sigma_{pp}T_{AA}(0)dN_{pp}/dy/d^2p_T}, \quad (4)$$

between the spectrum in central  $AA$  and  $pp$  collisions. The ratio is normalized to the effective total number of binary  $pp$  collisions in a central  $AA$  collision. If none of the nuclear effects (shadowing and jet quenching) are taken into account, this ratio should be unity at large transverse momentum. Shown in Fig. III are the results for central  $Au + Au$  collisions at the RHIC energy with  $dE/dx = 1, 2$  GeV/fm, respectively. As we have argued before, jet energy loss will result in the suppression of high  $p_T$  particles as compared to  $pp$  collisions. Therefore, the ratio at large  $p_T$  in Fig. III is smaller than one due to the energy loss suffered by the jet partons. It, however, increases with  $p_T$  because of the constant energy loss (or even some weak energy dependent energy loss). At hypothetically large  $p_T$  when the total energy loss is negligible compared to the initial jet energy, the ratio should approach to one.

At small  $p_T$ , particles from soft interaction (or from hadronization of QGP) dominate. The ratio  $R_{AA}(p_T)$  is very sensitive to the  $A$ -scaling behavior of the soft particle production. Since we assumed a linear scaling for the soft particle production, the ratio should approach to  $A/\sigma_{pp}T_{AA}(0) = 0.149$  at small  $p_T$  for central  $Au + Au$  at the RHIC energy, as shown in Fig. III.

In this framework, one can also study the effect of energy and  $A$  dependence of the energy loss and the effect of energy loss on particle production of different flavors [16].

#### IV. JET QUENCHING IN $\gamma$ +JET EVENTS

Since hadron production at a fixed large  $p_T$  comes from fragmentation of jets with different transverse energies, the suppression factor in Eq. (4) only provides the information about the effect of energy loss on jet fragmentation at an averaged value of  $z = p_T/E_T^{\text{jet}}$ . In order to study the modification of the fragmentation function due to energy loss, one might in principle measure the inclusive  $p_T$  spectrum in the direction of a triggered jet. However, with the large background and its fluctuation due to hadrons from many other minijets and soft processes, the determination of the jet energy is almost impossible. To overcome this difficulty, we proposed the study of high  $p_T$  particle spectrum in the opposite direction of a tagged direct photon [6]. Direct photons are always accompanied by a jet in the opposite transverse direction. Even though taking into account of the initial state radiation, the average energy of the jet is approximately that of the tagged photon. One can therefore relate the  $p_T$  distribution of hadrons in the opposite direction of a tagged photon to the fragmentation function of a jet with known initial energy and study the modification of the fragmentation function due to parton energy loss.

Let us select events which has a direct photon with transverse energy  $E_T^\gamma$  in the central rapidity region,  $|y| \leq \Delta y/2$ ,  $\Delta y = 1$ . For sufficiently large  $E_T^\gamma$  of the photon, the rapidity distribution of the associated jet is also centered around zero rapidity with a comparable

width. If the azimuthal angle of the photon is  $\phi_\gamma$  and  $\bar{\phi}_\gamma = \phi_\gamma + \pi$ , most of the hadrons from the jet fragmentation will fall into the kinematic region, ( $|y| \leq \Delta y/2, |\phi - \bar{\phi}_\gamma| \leq \Delta\phi/2$ ), where one can take  $\Delta\phi = 2$  according to the jet profile as measured in high-energy  $p\bar{p}$  collisions [17]. Given the jet fragmentation functions  $D_{h/a}(z)$ , with  $z$  the fractions of momenta of the jet carried by hadrons, one can calculate the differential  $p_T$  distribution of hadrons from jet fragmentation in the kinematical region  $(\Delta y, \Delta\phi)$ ,

$$\frac{dN_{pp}^{\gamma-jet}}{dyd^2p_T} = \sum_{a,h} r_a(E_T^\gamma) \int dE_T^{jet} g(E_T^{jet}, E_T^\gamma) \frac{D_{h/a}(p_T/E_T^{jet})}{p_T E_T^{jet}} \frac{C(\Delta y, \Delta\phi)}{\Delta y \Delta\phi}, \quad (5)$$

where  $C(\Delta y, \Delta\phi) = \int_{|y| \leq \Delta y/2} dy \int_{|\phi - \bar{\phi}_\gamma| \leq \Delta\phi/2} d\phi f(y, \phi - \bar{\phi}_\gamma)$  is an overall acceptance factor and  $f(y, \phi)$  is the normalized hadron profile around the jet axis. The summation is over both jet ( $a$ ) and hadron species ( $h$ ), and  $r_a(E_T^\gamma)$  is the fractional production cross section of  $a$ -type jet associated with the direct photon.  $C(\Delta y, \Delta\phi)$  is the acceptance factor for finding the jet fragments in the given kinematic range. We find  $C(\Delta y, \Delta\phi) \approx 0.5$  at  $\sqrt{s} = 200$  GeV, independent of the photon energy  $E_T^\gamma$ , using HIJING [11] Monte Carlo simulations for the given kinematic cuts. The normalized function,

$$g(E_T^{jet}, E_T^\gamma) = \frac{1}{N_{\gamma-jet}} \frac{dN_{\gamma-jet}}{dE_T^{jet}}, \quad (6)$$

as shown in Fig. 3, is the  $E_T$  distribution of the jet with a given  $E_T^\gamma$  of the tagged direct photon. As we can see that the transverse energy of the jet has a wide smearing around  $E_T^\gamma$  due to the initial state radiation associated with the hard processes. Because of the rapidly decrease in  $E_T$  of the cross section of direct photon production, the distribution is biased toward smaller  $E_T^{jet}$  than  $E_T^\gamma$ . The average  $E_T^{jet}$  is thus smaller than  $E_T^\gamma$ . Since one only triggers a direct photon with a given  $E_T^\gamma$ , one should average over the  $E_T$  smearing of the jet. Such a smearing is important especially for hadrons with  $p_T$  comparable or larger than  $E_T^\gamma$ .

If we define the inclusive fragmentation function associated with a direct photon as,

$$D^\gamma(z, E_T^\gamma) = \sum_{ah} r_a(E_T^\gamma) \int dE_T^{jet} g(E_T^{jet}, E_T^\gamma) \frac{E_T^\gamma}{E_T^{jet}} D_{h/a}\left(z \frac{E_T^\gamma}{E_T^{jet}}\right), \quad (7)$$

we can rewrite the  $p_T$  spectrum [Eq. (5)] in the opposite direction of a tagged photon as

$$\frac{dN_{pp}^{\gamma-jet}}{dyd^2p_T} = \frac{D^\gamma(p_T/E_T^\gamma, E_T^\gamma) C(\Delta y, \Delta\phi)}{p_T E_T^\gamma \Delta y \Delta\phi}. \quad (8)$$

Using this equation, one can extract the inclusive jet fragmentation function,  $D^\gamma(z, E_T^\gamma)$ , from the measured spectrum. Shown in Fig. 4 are the calculated  $p_T$  distributions from the fragmentation of photon-tagged jets with  $E_T^\gamma = 10, 15$  GeV and the underlying background from the rest of a central  $Au + Au$  collisions at the RHIC energy. The points are HIJING simulations of 10K events and solid lines are numerical results from Eqs. (3) and (5) with the fragmentation functions given by the parametrization of  $e^+e^-$  data [8]. The effect of parton energy loss is not included yet. As we can see, the spectra from jet fragmentation are significantly higher than the background at large transverse momenta. One can therefore easily extract the fragmentation function from the experimental data without much

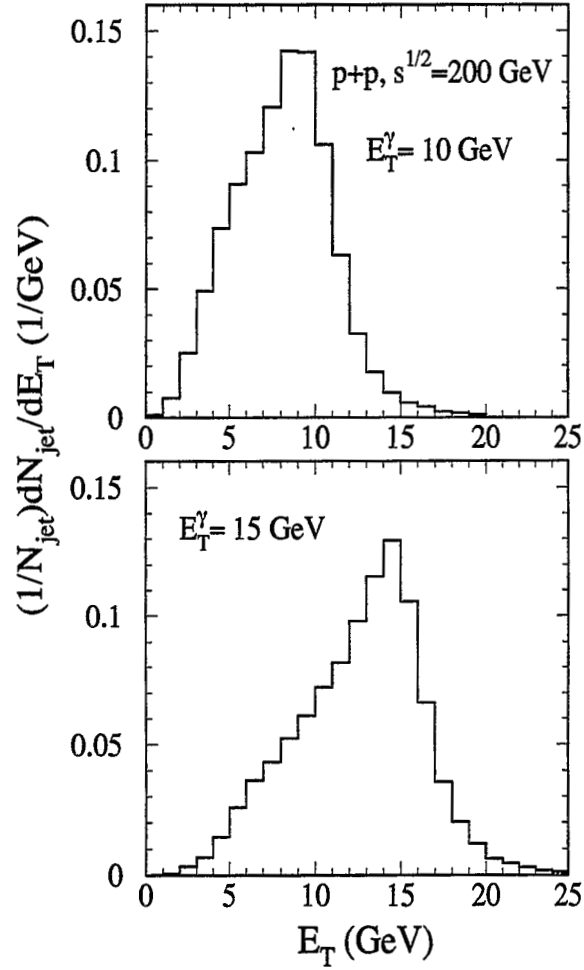


FIG. 3. The  $E_T$  distributions of the jet, caused by the initial state radiations, accompanying a triggered direct photon with  $E_T^\gamma = 10, 15$  GeV, respectively at  $\sqrt{s} = 200$  GeV.

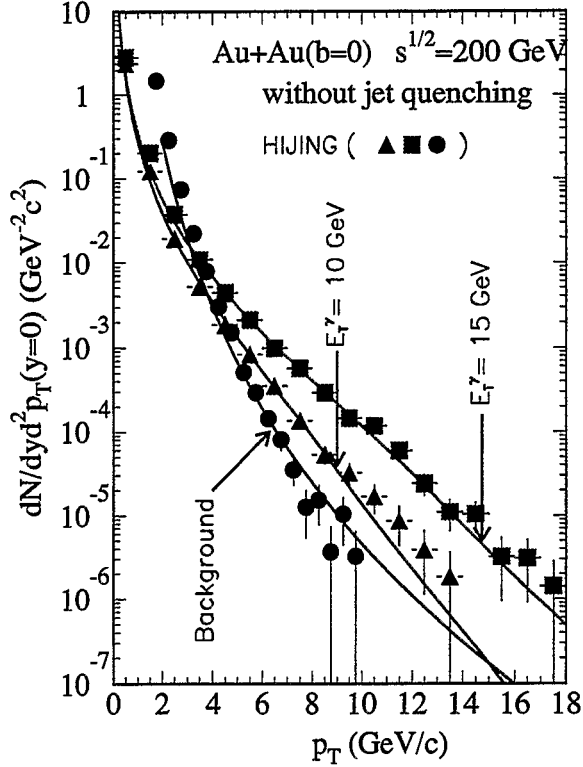


FIG. 4. The differential  $p_T$  spectrum of charged particles from the fragmentation of a photon-tagged jet with  $E_T^\gamma = 10, 15$  GeV and the underlying background in central  $Au + Au$  collisions at  $\sqrt{s} = 200$  GeV. The direct photon is restricted to  $|y| \leq \Delta y/2 = 0.5$ . Charged particles are limited to the same rapidity range and in the opposite direction of the photon,  $|\phi - \phi_\gamma - \pi| \leq \Delta\phi/2 = 1.0$ . Solid lines are from the jet fragmentation function and points are HIJING simulations of 10K events. Parton energy loss is not included yet.

statistical errors from the subtraction of the background. One also notice that there are significant number of particles with  $p_T$  larger than the triggered photon,  $E_T^\gamma$ , because of the  $E_T$  smearing of the jet caused by initial state radiations.

Consider parton energy loss in central  $AA$  collisions, we model the jet fragmentation functions as given by Eq. (2). Including the  $E_T$  smearing and averaging over the  $\gamma$ -jet production position in the transverse direction, the inclusive fragmentation function of a photon-tagged jet is,

$$D_{AA}^\gamma(z) = \int \frac{d^2 r t_A^2(r)}{T_{AA}(0)} \sum_{ah} r_a(E_T^\gamma) \int dE_T^{jet} g(E_T^{jet}, E_T^\gamma) \frac{E_T^\gamma}{E_T^{jet}} D_{h/a}(z \frac{E_T^\gamma}{E_T^{jet}}, \Delta L), \quad (9)$$

where  $T_{AA}(0) = \int d^2 r t_A^2(r)$  is the overlap function of  $AA$  collisions at zero impact-parameter. We assume that jet production rate is proportional to the number of binary nucleon-nucleon collisions.

Shown in Fig. 5 are the ratios of the inclusive fragmentation function in a central  $Au + Au$  collisions with energy loss  $dE_q/dx = 1$  GeV/fm, over the ones in  $pp$  collisions without energy loss. The enhancement of soft particle production due to induced emissions is important only at small fractional energy  $z$ . The fragmentation function is suppressed for large and intermediate  $z$  due to parton energy loss. For a fixed  $dE/dx$ , the suppression becomes less

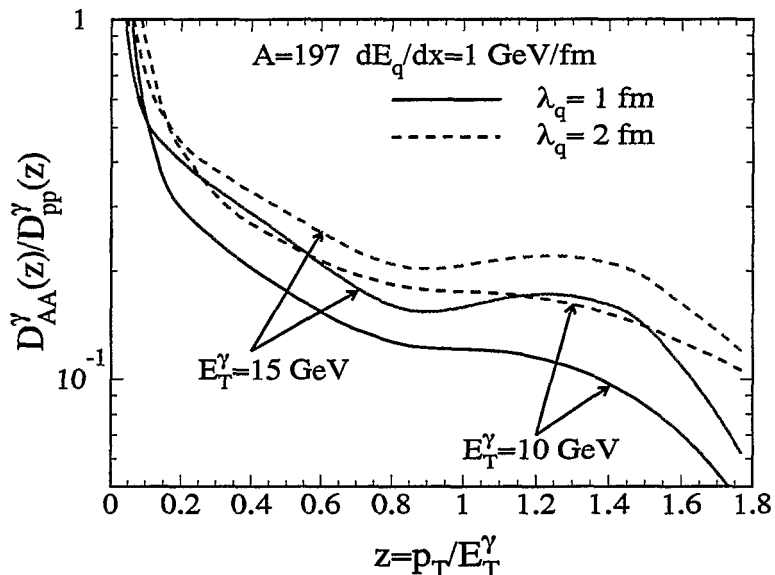


FIG. 5. Ratio of the inclusive fragmentation function of a photon-tagged jet with and without energy loss in central  $Au + Au$  collisions for a fixed  $dE_q/dx = 1$  GeV/fm.

as  $E_T^{\gamma}$  increases. The optimal case is when the average total energy loss is significant as compared to the initial jet energy, and yet the  $p_T$  spectrum from jet fragmentation is still much larger than the underlying background. Notice that we now define  $z$  as the hadron's fractional energy of the triggered photon. Because of the  $E_T$  smearing of the jet caused by initial state radiations, hadrons can have  $p_T$  larger than  $E_T^{\gamma}$ . Therefore, the effective inclusive jet fragmentation function does not vanish at  $z = p_T/E_T^{\gamma} > 1$ .

As compared to our earlier results [6] where we did not take into account the  $E_T$  smearing of the jet, the modification of the averaged fragmentation function due to energy loss is quite sensitive to the value of the mean-free-path for  $dE_q/dx = 1$  GeV. To study the sensitivity of the suppression to the energy loss, we plot in Fig. 6 the same ratio at a fixed value of  $z = 0.4$  as functions of  $dE_q/dx$ . The ratio in general decreases with  $dE_q/dx$  as more large  $p_T$  particles are suppressed when leading partons loss more energy. For small values of  $dE_q/dx$ , the suppression factor is more or less independent of the mean-free-path. However, for large values of  $dE_q/dx \geq 1$  GeV/fm, the ratio is sensitive to the mean-free-path. One thus needs additional information or a global fit to determine both the energy loss  $dE/dx$  and the mean-free-path from the experimental data.

As we discussed in the introduction, recent studies [3] of energy loss in a dense medium indicate that the energy loss per distance  $dE/dx$  might be proportional to the total distance that the parton has traveled since it was produced. One way to test this experimentally is to study the suppression factor at any given  $z$  value for different nucleus-nucleus collisions or for different centrality (impact parameter). Shown in Fig. 7, are the suppression factor for the jet fragmentation function at  $z = 0.4$  as functions of  $A^{1/3}$ . In one case (dashed lines), we assume a constant energy loss  $dE/dx = 0.5$  GeV/fm. The suppression factor decreases almost linearly with  $A^{1/3}$ . In another case (solid lines), we assume  $dE_q/dx = 0.2(L/\text{fm})$  GeV/fm. The average distance a parton travels in a cylindrical system with transverse size  $R_A$  is  $\langle L \rangle = 0.905R_A$ . We assume  $R_A = 1.2A^{1/3}$  fm. We choose the coefficient in  $dE_q/dx$  such that it roughly equals to 0.5 GeV/fm for  $A = 20$ . As we can see, the suppression



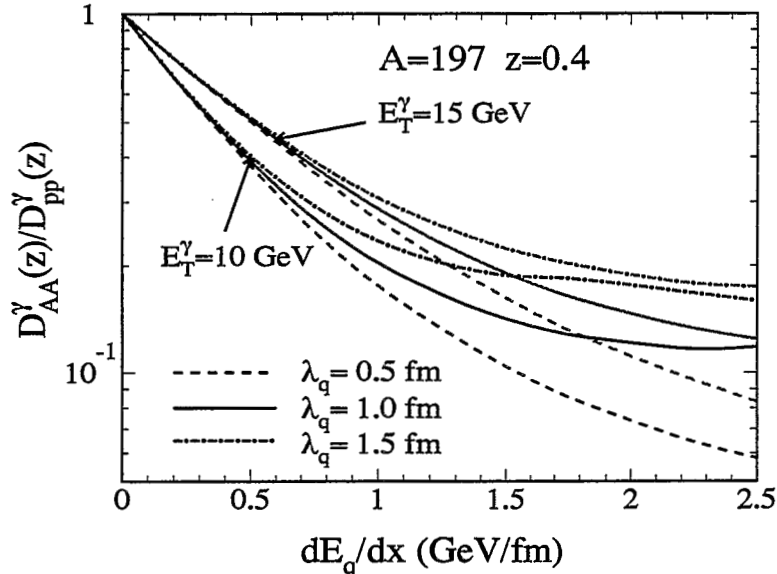


FIG. 6. Ratio of the inclusive fragmentation function of a photon-tagged jet with and without energy loss in central  $Au + Au$  collisions at  $z = 0.4$  as a function of  $dE_q/dx$ .

factor for a distance-dependent  $dE/dx$  decreases faster than the one with constant  $dE/dx$ . Unfortunately, we have not found a unique way to extract the average total energy loss so that we can show it is proportional to  $A^{2/3}$  for the distance-dependent  $dE/dx$ .

## V. $p_T$ BROADENING AND JET PROFILE

In the above calculation, we have assumed that the jet profile in the opposite direction of the tagged photon remains the same in  $AA$  collisions, since we used the same acceptance factor  $C(\Delta y, \Delta\phi)$ . However, due to multiple scatterings suffered by the leading parton, the final jet must acquire additional acoplanarity with respect to its original transverse direction. Such a change to the jet profile could affect the acceptance factor, which will be an overall factor to the measured jet fragmentation function if we assume the jet profile to be the same for particles with different fractional energies.

To demonstrate this, we plot in Fig. 8 as the solid line the azimuthal angle distribution of  $E_T$  (within  $|y| < 0.5$ ) with respect to the opposite direction of the tagged photon with  $E_T^{\gamma} = 10$  GeV. We have subtracted the background so that  $dE_T/d\phi = 0$  at  $\phi = \pi$ . The profile distribution includes both the intrinsic distribution from jet fragmentation and the effect of initial state radiation. The acceptance factor is simply the fractional area within  $|\phi| < \Delta\phi/2$  region. The  $p_T$  broadening of jets due to multiple scatterings will broaden the profile function. Shown as the dashed line is the profile function for an average  $\Delta p_T^2 = 4$   $(\text{GeV}/c)^2$  with a Gaussian distribution. It is clear that with a modest value of the  $p_T$  broadening, the acceptance factor only changes by around 10% [18].

In addition, since the change of the jet profile function is related to the average  $p_T$  broadening, one can combine the measurement with the measured energy loss to verify the relationship between  $dE/dx$  and  $\Delta p_T^2$  as suggested by recent theoretical studies [3].

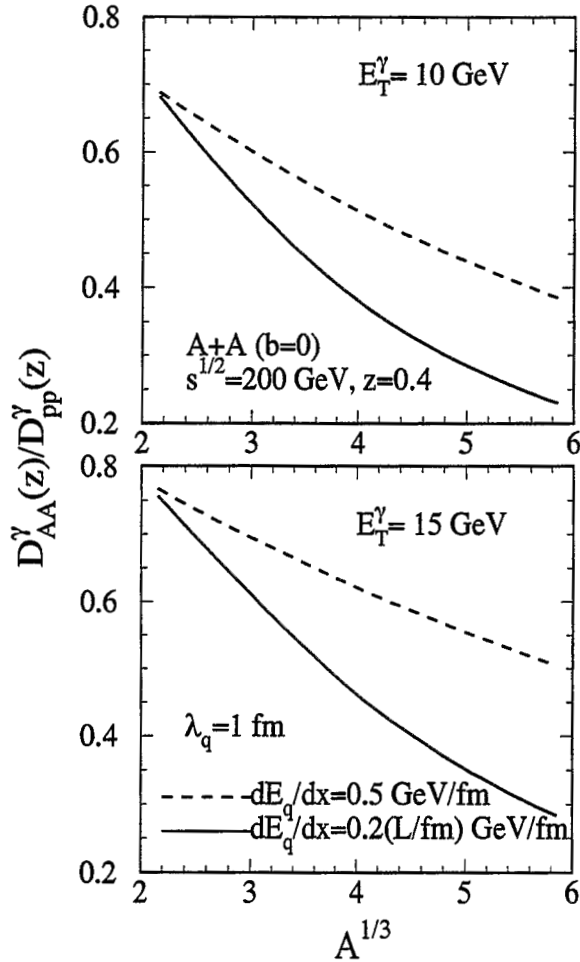


FIG. 7. Ratio of the inclusive fragmentation function of a photon-tagged jet with and without energy loss in central  $Au + Au$  collisions at  $z = 0.4$  as a function of  $A^{1/3}$ . A constant energy loss,  $dE_q/dx = 0.5$  GeV/fm (dashed lines) and  $dE_q/dx = 0.2(L/\text{fm})$  GeV/fm (solid lines), which is linear in the total distance the jet has traveled, are assumed.

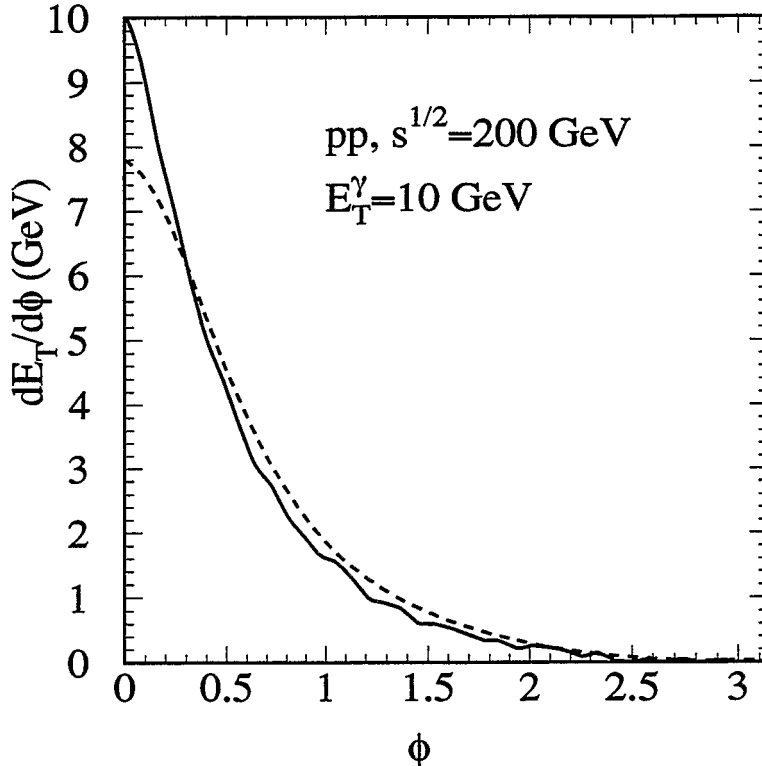


FIG. 8. The effective profile function of the photon-tagged jet, defined as the  $E_T$  distribution in azimuthal angle respect to the opposite direction of a photon with  $E_T^\gamma = 10$  GeV. The dashed line assumes a Gaussian form of  $p_T$  broadening for the jet with an average  $\Delta p_T^2 = 4$  (GeV/c) $^2$ .

$E_T^\gamma$ (GeV)	10	15	20
$dN^{\gamma\text{-jet}}/dydE_T/\text{year}$	3500	400	70

TABLE I. Rate of direct photon production in central  $Au + Au$  collisions at  $\sqrt{s} = 200$  GeV, with luminosity  $\mathcal{L} = 2 \times 10^{26}$  cm $^{-2}$ s $^{-1}$  and 100 operation day per year.

## VI. DISCUSSIONS

To have a feeling of the experimental feasibility of the proposed  $\gamma$ -jet measurement, we list in Table 1 the number of  $\gamma$ -jet events per year per unit rapidity and unit (GeV)  $E_T$ . We assume a central  $Au + Au$  cross section of 125 mb with impact-parameters  $b < 2$  fm. We have taken the designed luminosity of  $\mathcal{L} = 2 \times 10^{26}$  cm $^{-2}$ s $^{-1}$  with 100 operation days per year. As we can see, the rate for  $E_T^\gamma = 15, 20$  GeV is too small to give any statistically significant measurement of the fragmentation function and its modification in  $AA$  collisions. If one can increase the luminosity by a factor of 10, the numbers of events for both  $E_T^\gamma = 10$  and 15 GeV are significant enough for a reasonable determination of the fragmentation function of the photon-tagged jets.

Given increased luminosity and enough number of events, one still has to overcome the large background of  $\pi^0$ 's to identify the direct photons. Plotted in Fig. 9, are the production

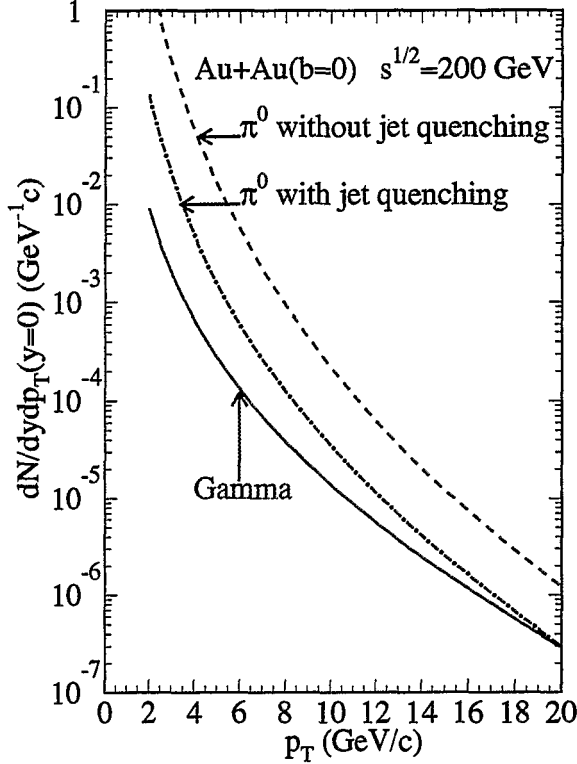


FIG. 9. The inclusive  $p_T$  distribution for direct photons as compared to that of  $\pi^0$ 's with and without parton energy loss in central  $Au + Au$  collisions at  $\sqrt{s} = 200$  GeV.  $dE_q/dx = 1$  GeV/fm and mean-free-path  $\lambda_q = 1$  fm are assumed.

rates of direct photons (solid line) and  $\pi^0$ 's (dashed and dot-dashed lines). We can see that without parton energy loss,  $\pi^0$  production rate is about 20 times larger than the direct photons at  $p_T = 10$  GeV/c. Fortunately, jet quenching due to parton energy loss can significantly reduce  $\pi^0$  rate at large  $p_T$  as shown by the dot-dashed line. However, one still has to face  $\pi^0$ 's about 4 times higher than the direct photons at  $p_T = 10$  GeV/c. At larger  $p_T$ , the situation improves, but one loses the production rate. Since the isolation cut method normally employed in  $pp$  collisions to reduce the background to direct photons does not work anymore, the only way one can identify them has to be through improvement of detector hardwares.

## VII. ACKNOWLEDGEMENTS

We thank I. Sarcevic for discussions and her early collaboration. X.N.W would like to thank J. Carroll, M. Gyulassy and J. W. Harris for helpful discussions. This work was supported by the Director, Office of Energy Research, Office of High Energy and Nuclear Physics, Divisions of Nuclear Physics, of the U.S. Department of Energy under Contract

## REFERENCES

- [1] M. Gyulassy and X.-N. Wang, Nucl. Phys. **B420**, 583 (1994); X.-N. Wang, M. Gyulassy and M. Plümer, Phys. Rev. **D 51**, 3436 (1995).
- [2] R. Baier, Yu. L. Dokshitzer, S. Peigné and D. Schiff, Phys. Lett. **B345**, 277 (1995).
- [3] R. Baier, Yu. L. Dokshitzer, A. Mueller, S. Peigné and D. Schiff, hep-ph/9608322; also see Dokshitzer's contribution in this proceedings.
- [4] X.-N. Wang and M. Gyulassy, proceedings of the Fourth Workshop on Experiments and Detectors for RHIC, July 2-7, 1990, Brookhaven National Laboratory, Eds. M. Fatyga and B. Moskowitz, p.79, BNL-52262.
- [5] X.-N. Wang and M. Gyulassy, Phys. Rev. Lett. **68**, 1480 (1992).
- [6] X.-N. Wang, Z. Huang and I. Sarcevic, Phys. Rev. Lett. **77**, 231 (1996)..
- [7] P. Mättig, Phys. Rep. **177**, 141 (1989).
- [8] J. Binnewies, B. A. Kniehl and G. Kramer, Z. Phys. **C65**, 471 (1995).
- [9] J. F. Owens, Rev. Mod. Phys. **59**, 465 (1987).
- [10] K. J. Eskola and X.-N. Wang, Int. J. Mod. Phys. A **10**, 3071 (1995).
- [11] X.-N. Wang and M. Gyulassy, Phys. Rev. D **44**, 3501 (1991); Comp. Phys. Comm. **83**, 307 (1994).
- [12] A. D. Martin, W. J. Stirling and R. G. Roberts, Phys. Lett. **B306**, 145 (1993).
- [13] British-Scandinavian Collab., B. Alper, *et al.*, Nucl. Phys. **B87**, 19 (1975).
- [14] UA1 Collab., C. Albajar, *et al.*, Nucl. Phys. **B335**, 261 (1990).
- [15] F. Abe, *et al.*, Phys. Rev. Lett. **61**, 1819 (1988).
- [16] X.-N. Wang, in preparation.
- [17] UA1 Collab., G. Arnison *et al.*, Phys. Lett. **B 172**, 461 (1986); C. Albajar *et al.*, Nucl. Phys. **B309**, 405 (1988).
- [18] X.-N. Wang and Z. Huang, in preparation.

# Gluon Density in Nuclei\*

A. L. Ayala <sup>F<sup>e</sup> a)b)\*</sup>, M. B. Gay Ducati <sup>a)\*\*</sup> and E. M. Levin <sup>c)d)†</sup>

<sup>a)</sup>*Instituto de Física, Univ. Federal do Rio Grande do Sul  
Caixa Postal 15051, 91501-970 Porto Alegre, RS, BRAZIL*

<sup>b)</sup>*Instituto de Física e Matemática, Univ. Federal de Pelotas  
Campus Universitário, Caixa Postal 354, 96010-900, Pelotas, RS, BRAZIL*

<sup>c)</sup>*Theory Division, Fermi National Accelerator Laboratory  
Batavia, IL 60510 - 0500, USA*

<sup>d)</sup>*Theory Department, Petersburg Nuclear Physics Institute  
188350, Gatchina, St. Petersburg, RUSSIA*

## Abstract

In this talk we present a detailed study on the shadowing corrections to the gluon structure functions for nuclei. Starting from the present status of the HERA data, we develop the Glauber - Mueller approach for the gluon density in a nucleus and estimate the shadowing corrections in the small  $x$  region which turns out to be big. Based on this observation we suggest and solve the new evolution equation for gluon density in a nucleus, which could be used to provide a reliable initial conditions for the time evolution of the nucleus-nucleus cascade. The extended version of the talk is published in Ref. [1].

## I. INTRODUCTION

In this talk we present our new results concerning the whole issue of the shadowing corrections ( SC ) to the gluon density in nuclei [2]. We show that SC for the gluon distribution in a nucleus can be treated theoretically in the framework of perturbative QCD (pQCD) and can be calculated from the gluon structure function for the nucleon. We choose the gluon distribution in nucleus because the nucleus DIS is easier to handle theoretically, and we expect larger SC for a nucleus since the analysis of the SC shown that it is a density effect in the parton cascade ( see review [3] for example ). We consider also that gluon

---

\*Talk given by E.M. Levin

\*\* E-mail: ayala@if.ufrgs.br

\*\*\* E-mail: gay@if.ufrgs.br

† E-mail: levin@hep.anl.gov; leving@ccsg.tau.ac.il

density in nuclei will provide the initial condition for any phenomenological cascades for high energy nucleus - nucleus interaction at RHIC.

Our motivation comes from some inconsistency on the interpretation of the HERA present results. In HERA [4] data for DIS the structure function  $F_2(x, Q^2)$  increases in the region of small  $x$  ( at high energies) as  $F_2(x, Q^2) \propto \frac{1}{x^{0.2}}$  for  $10^{-2} > x > 10^{-5}$  at large and small ( $Q^2 \approx 1 - 2 GeV^2$ ) values of the photon virtualities  $Q^2$ . This steep behavior is well fitted by the perturbative QCD evolution given by the Dokshitzer-Gribov-Lipatov-Altareli-Parisi equation [5], even for the small values of  $Q^2$ . Thus we can conclude that the parton cascade which describes the DGLAP evolution is a dilute system of partons, and there is no need of SC to describe the DIS data.

On the other hand, from HERA data we can evaluate also the parameter  $\kappa$  which characterizes the amount of the SC [6]  $\kappa = \frac{\sigma(GG)}{\pi R^2} xG(x, Q^2) = \frac{3\pi\alpha_s}{Q^2 R^2} xG(x, Q^2)$ , where  $xG(x, Q^2)$  is the gluon structure function and  $R$  is the radius of the area populated by gluons in a nucleon.  $\sigma(GG)$  is the cross section of two gluon interaction in the parton cascade calculated in [7]. The physical meaning of this formula is the probability of the gluon - gluon interaction inside the parton cascade. From HERA data on photoproduction of  $J/\Psi$  meson [8],  $R^2 = 5.0 GeV^{-2}$  and the values of  $\kappa$  are bigger than one in substantial part of HERA kinematic region.

We can conclude that the situation looks very controversial and the statement that the DGLAP evolution works is first but not the last outcome of the HERA data.

## II. THE GLAUBER APPROACH IN QCD .

The idea of how to write the Glauber formula in QCD was originally formulated in Ref. [9,10]. Let us consider that the gluon distribution is probed by a high energy particle with virtuality  $Q^2$ . In the space-time description of the process, the probe decays in a gluon-gluon pair with transverse separation  $r_\perp$  ( corresponding transverse momentum  $k_\perp$  ). This pair interacts with the nucleon due to the exchange of a gluon ladder diagram. In Double Log Approximation (DLA), the transverse momentum of the gluon in the ladder,  $l_\perp$ , is much smaller than the transverse momentum of the gluon in the pair ( $l_\perp \ll k_\perp$ ). Also,  $r_\perp$  is almost constant during the  $GG$ -nucleus interaction ( see Ref. [1] for details).

In the above framework, the  $GG$  pair cross section with the nucleon can be written (for  $N_c = 3$ ) as [10]

$$\sigma_{GG}(r_\perp^2) = \frac{3\alpha_s(\frac{4}{r_\perp^2})}{4} \pi^2 r_\perp^2 \left( xG_N^{GLAP}(x, \frac{4}{r_\perp^2}) \right), \quad (1)$$

and the nuclear gluon distribution is given by the Mueller ( Glauber) formula [10]

$$xG_A(x, Q^2) = \frac{4}{\pi^2} \int_x^1 \frac{dx'}{x'} \int_{\frac{4}{Q^2}}^\infty \frac{d^2 r_\perp}{\pi r_\perp^4} \int_0^\infty \frac{d^2 b_\perp}{\pi} 2 \left\{ 1 - e^{-\frac{1}{2} \sigma_N^{GG}(x', r_\perp^2) S(b_\perp^2)} \right\}. \quad (2)$$

The term in curly brackets is the total cross section of the interaction of the gluon pair with the nucleus in the eikonal approach. This term is the solution of the  $s$ -channel unitarity constraint if the elastic amplitude of the gluon nuclei scattering is purely imaginary at high

energy and the structure of the final state is mostly the uniform distribution of the produced gluons ( see Ref. [1] for more detail explanation). The first term in the expansion of eq. (2) with respect to  $\sigma$  gives the DGLAP equation in the region of small  $x$ . Using a Gaussian parameterization for the profile function  $S(b_t)$  we can take the integral over the impact parameter  $b_t$  which gives

$$xG_A(x, Q^2) = \frac{2R_A^2}{\pi^2} \int_x^1 \frac{dx'}{x'} \int_{\frac{1}{Q_0^2}}^{\frac{1}{Q^2}} \frac{dr_t^2}{r_t^4} \left\{ C + \ln(\kappa_G(x', r_t^2)) + E_1(\kappa_G(x', r_t^2)) \right\} \quad (3)$$

where  $C$  is the Euler constant and  $E_1$  is the exponential integral (see Ref. [11] Eq. 5.1.11) and

$$\kappa_G(x', r_t^2) = \frac{3\alpha_S A \pi r_t^2}{2R_A^2} x' G_N^{DGLAP}(x', \frac{1}{r_t^2}) \quad (4)$$

In order to estimate of the SC predicted by the Mueller formula we will use the GRV [12] parameterization for the gluon distribution in a nucleon. This parameterization is a solution of GLAP equation evolved from a very small virtuality and its most essential contribution comes from the region  $\alpha_S \ln Q^2 \approx 1$  and  $\alpha_S \ln 1/x \approx 1$ . This allows to estimate the SC from large distances and use the DLA, where Mueller formula is proven.

However, in spite of the fact that the GLAP evolution in the GRV parameterization starts from very low virtuality ( $Q_0^2 \sim 0.25 \text{ GeV}^2$ ) it turns out that the DLA still does not work quite well in the accessible kinematic region ( $Q^2 > 1 \text{ GeV}^2$ ,  $x > 10^{-5}$ ). In order to develop a more realistic approach in the region of not ultra small  $x$  ( $x > 10^{-4}$ ), we suggest to substitute the small  $x$  kernel in the Born term in the expression (2) by the full DGLAP kernel. This procedure gives

$$xG_A(x, Q^2) = xG_A(x, Q^2)(eq. (2)) + AxG_N^{GRV}(x, Q^2) - A \frac{\alpha_S N_c}{\pi} \int_x^1 \int_{Q_0^2}^{Q^2} \frac{dx'}{x'} \frac{dQ'^2}{Q'^2} x' G_N^{GRV}(x', Q'^2) . \quad (5)$$

The above equation includes also  $AxG_N^{GRV}(x, Q_0^2)$  as the initial condition for the gluon distribution and gives  $AxG_N^{GRV}(x, Q^2)$  as the first term of the expansion with respect to  $\kappa_G$ . Therefore, this equation is an attempt to include the full expression for the anomalous dimension for the scattering off each nucleon, while we use the DLA to take into account all SC.

In order to investigate the general features of the nuclear gluon distribution we compare  $xG_A$  with the solution of the DGLAP evolution equations in the GRV parameterization using the following three functions:

$$R_1^N = \frac{xG^A(x, Q^2)(eq. (5))}{xG_N^{GRV}(x, Q^2)} , \quad \langle \omega \rangle = \frac{\partial \ln(xG^A(x, Q^2))}{\partial \ln(1/x)} , \quad \langle \gamma \rangle = \frac{\partial \ln(xG^A(x, Q^2))}{\partial \ln(Q^2/Q_0^2)} ; \quad (6)$$

The reason why we chose these functions is that in the semiclassical approach (see [6]), the nucleon structure function is equal to  $xG^A(x, Q^2) = C \{Q^2\}^{\langle \gamma \rangle} \{1/x\}^{\langle \omega \rangle}$ . The results of



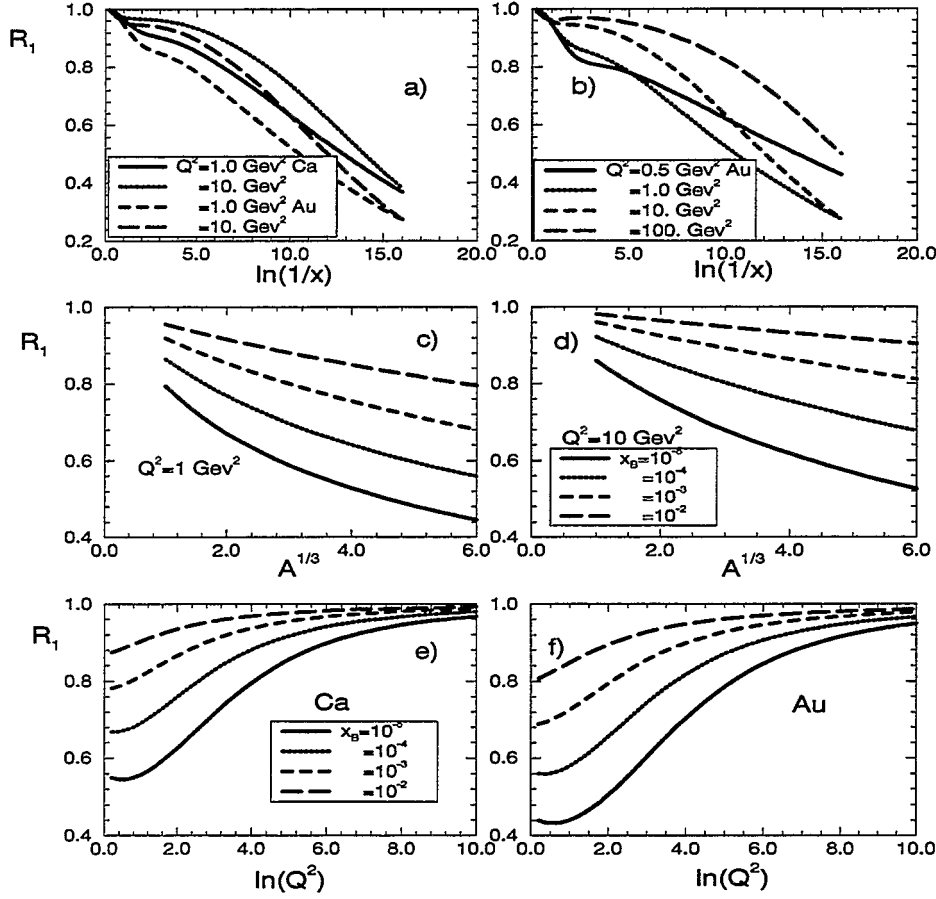


FIG. 1.  $R_1$  as a function of  $\ln(1/x)$ ,  $\ln Q^2$  and  $A^{1/3}$ : a)  $R_1$  as a function of  $\ln(1/x)$  for different nucleus and different values of  $A$ ; b)  $R_1$  as a function of  $\ln Q^2$  for different values of  $x_B$  for Au; c) and d)  $R_1$  as a function of  $A^{1/3}$  for different  $Q^2$ ; e) and f)  $R_1$  dependence on  $Q^2$  for Ca and Au.

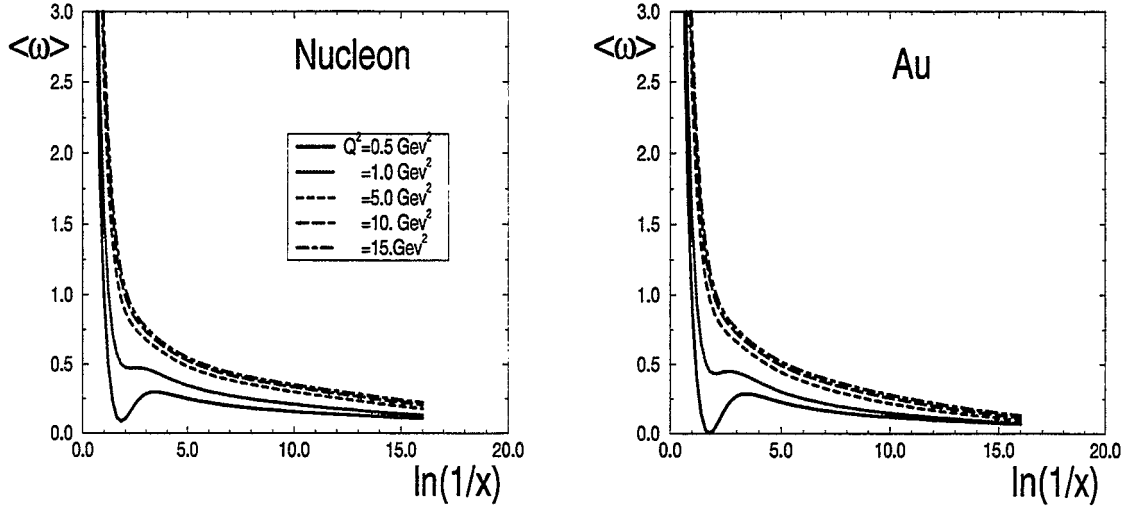


FIG. 2. The effective power  $\langle \omega \rangle$  calculated for  $xG^A$  (Au) and the Nucleon distribution  $xG^A$  ( $A = 1$ ).

our calculation are shown in Fig.1 for  $R_1$  as a function of  $\ln(1/x)$ ,  $\ln Q^2$  and  $A^{1/3}$  and in Figs. 2 and 3 for Ca and Au for different  $Q^2$  as function of  $x$ .

The main message that one can read from these figures is that the SC turn out to be considerable and they change the  $x$  and  $Q^2$  dependence of the gluon structure function.

However it should be stressed that the effective power of  $x$  remains bigger than the intercept of the so called "soft" Pomeron [13], even in the case of a sufficiently heavy nucleus (Au), for  $Q^2 > 1 \text{ GeV}^2$ . At small values of  $x$ , the anomalous dimension  $\langle \gamma \rangle$  shows a sizeable reduction, which increases with  $A$  and  $\langle \gamma \rangle$  is smaller than  $\frac{1}{2}$  for all  $Q^2 > 2 \text{ GeV}^2$ .

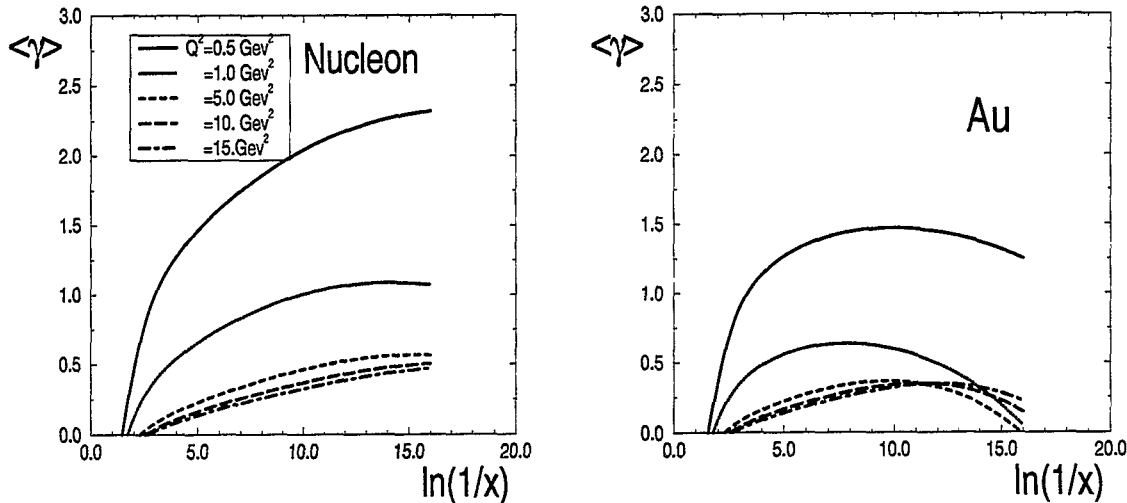


FIG. 3. The effective value of the anomalous dimension calculated for Nucleon and Au.

### III. CORRECTIONS TO THE GLAUBER ( MUELLER) APPROACH.

The Mueller ( Glauber ) formula (3) is not an evolution equation and it gives the possibility to calculate  $xG_A(x, Q^2)$  and the SC for nucleus from the solution of GLAP equations. In order to evaluate the corrections to the Glauber approach we calculate the second iteration of the Mueller formula of eq. (2). The Mueller formula describes the rescattering of the fastest gluon in the pair during the passage through a nucleus. The second iteration takes into account also the rescattering of the next to the fastest gluon. This is a well defined task due to the strong ordering in the parton fractions of energy in the parton cascade in leading  $\ln(1/x)$  approximation of pQCD that we are dealing with.

One can see in Figs.4 that the second iteration gives a big effect and changes crucially  $R_1$ ,  $\langle \omega \rangle$ , and  $\langle \gamma \rangle$ . The most remarkable feature is the crucial change of the value of the effective power  $\omega(Q^2)$  for the "Pomeron" intercept which tends to zero at HERA kinematic region. The main conclusions from Figs.4 are: (i) the second iteration gives a sizeable contribution in the region  $x < 10^{-2}$  and for  $x \leq 10^{-3}$  it becomes of the order of the first iteration;(ii) It occurs because the second iteration gives correction of the order of  $\alpha_S \ln(Q^2/Q_0^2) \ln(1/x) \approx 1$  for the DLA. (iii) for  $x < 10^{-3}$  we have to calculate the next iteration.

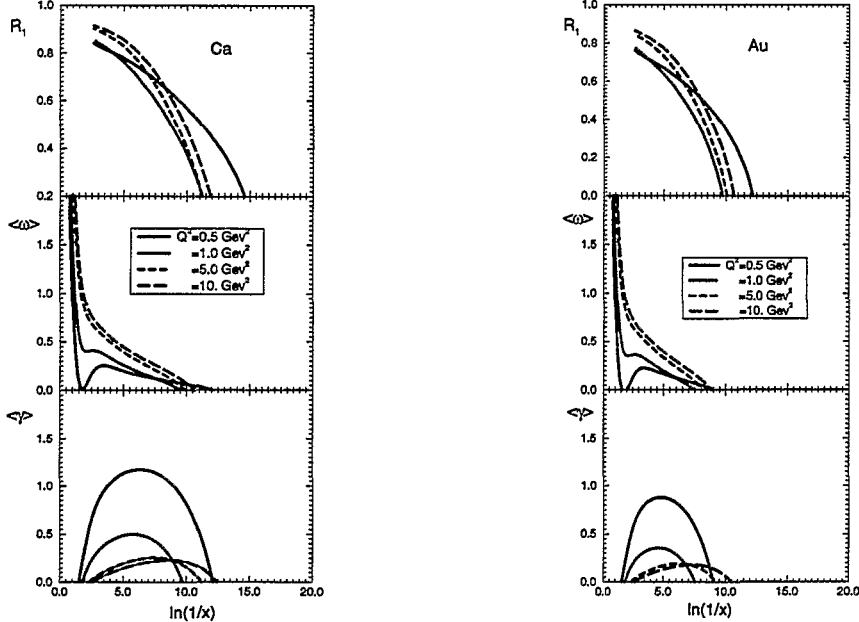


FIG. 4. Second iteration calculations for  $R_1$ ,  $\langle \omega \rangle$ , and  $\langle \gamma \rangle$  for Ca and Au.

#### IV. THE GENERAL APPROACH.

In order to improve the calculation of the SC to the nuclear distribution  $xG_A(x, Q^2)$ , we suggest a new approach, which will take into account the interaction of all partons in a parton cascade with the target. Let us differentiate the Mueller formula over  $y = \ln(1/x)$  and  $\xi = \ln(Q^2/Q_0^2)$ , and write it as an equation for  $\kappa$  ( see Ref. [1] for more discussions). The result reads

$$\frac{\partial^2 \kappa(y, \xi)}{\partial y \partial \xi} + \frac{\partial \kappa(y, \xi)}{\partial y} = \frac{N_c \alpha_S}{\pi} \{ C + \ln \kappa(y, \xi) + E_1(\kappa(y, \xi)) \} \equiv F(\kappa). \quad (7)$$

where  $\kappa$  is given by  $\kappa = \frac{N_c \alpha_S \pi}{2Q^2 R_A^2} xG_A(x, Q^2)$ . This is a generalized nonlinear evolution equation for the nuclear gluon distribution. This equation sums all contributions of the order  $(\alpha_S y \xi)^n$  absorbing them in  $xG_A(y, \xi)$ , as well as all contributions of the order of  $\kappa^n$  in the kinematic region where  $\alpha_S \kappa < 1$ .

This equation has the following nice features: (i) for  $\kappa \ll 1$  this equation provides the correct matching with the DGLAP equations; (ii) for  $\kappa \approx \alpha_S$  this equation gives the GLR equation ; (iii) in the region  $\alpha_S y \xi \leq 1$  it gives the Glauber ( Mueller ) formula and (iv) it coincides with the equation that L.McLerran with collaborators [14] derived from different approach and with different technique .

We solve the above equation in semiclassical approach for  $\alpha_S$  constant using the method of characteristics ( see ref [2] for a detailed discussion ). This method has been adjusted to the solution of the nonlinear equation of eq.(7)-type in Refs. [6,15] In semiclassical approach, we write  $\kappa$  in the form  $\kappa = e^S$ , where the partial derivatives  $\partial S / \partial y = \omega$  and  $\partial S / \partial \xi = \gamma$  are supposed to be smooth functions of  $y$  and  $\xi$ . The set of equations which describe the characteristics is

$$\frac{d\xi}{dy} = \frac{\Phi(S)}{(\gamma+1)^2}; \quad \frac{dS}{dy} = \frac{2\gamma+1}{(\gamma+1)^2}\Phi(S); \quad \frac{d\gamma}{dy} = \Phi'_S \frac{\gamma}{\gamma+1}, \quad (8)$$

where  $\Phi = e^{-S}F(e^S)$  and  $\Phi'_S = \frac{\partial\Phi}{\partial S}$ . The initial condition for the characteristics is given by

$$\begin{aligned} S_0 &= \ln \kappa_{in}(y_0, \xi_0) \\ \gamma_0 &= \left. \frac{\partial \ln \kappa_{in}(y_0, \xi)}{\partial \xi} \right|_{\xi=\xi_0} = \langle \gamma \rangle_{Glauber} - 1. \end{aligned} \quad (9)$$

where  $\kappa_{in}$  is

$$\kappa \rightarrow \kappa_{in} = \frac{N_c \alpha_S \pi}{2 Q^2 R_A} x G_A(x, Q^2), \quad (10)$$

and  $xG_A$  is given by the Mueller formula. The GLAP equation for  $\kappa$  is obtained taking the term in the curly in r.h.s of eq. (7) equal to  $\kappa$ .

We set the initial condition  $y = y_0 = 4.6$  ( $x_B = 10^{-2}$ ), where the shadowing correction is not big and the evolution starts from  $\gamma < 0$ . In this case  $d\gamma/dy > 0$  and the value of  $\gamma$  increases. At the same time  $dS/dy < 0$  and  $S$  decreases if  $\gamma_0 < -1/2$ . With the decrease of  $S$ , the value of  $\Phi'_S$  becomes smaller and after short evolution the trajectories of the nonlinear equation start to approach the trajectories of the DGLAP equations. We face this situation for any trajectory with  $\gamma_0$  close to -1. If the value of  $\gamma_0$  is smaller than  $-\frac{1}{2}$  but the value of  $S_0$  is sufficiently big, the decrease of  $S$  due to evolution cannot provide a small value for  $\Phi'(S)$  and  $\gamma$  increases until its value becomes bigger than  $-\frac{1}{2}$  at some value of  $y = y_c$ . In this case, for  $y > y_c$  the trajectories behave as in the case with  $\gamma_0 > -\frac{1}{2}$ . For  $\gamma_0 > -1/2$ , the picture changes crucially. In this case,  $dS/dy > 0$ ,  $d\gamma/dy > 0$  and both increase. Such trajectories go apart from the trajectories of the DGLAP equation and nonlinear effects play more and more important role with increasing  $y$ . These trajectories approach the asymptotic solution very quickly, which is  $\xi$  independent and satisfies the equation:  $\frac{d\kappa_{asympt}(y)}{dy} = F(\kappa)$  ( see [2] for details). In Figs. 5 and 6 we plot also the lines with definite value of the ratio  $R = \frac{xG(x, Q^2)(generalized\ equation)}{xG(x, Q^2)(GLAP)}$  (horizontal lines). These lines estimate that the SC are big.

## V. AND WHAT?

We presented here our approach to the SC and a natural question arises: and what? What and how we can do for the RHIC physics. How our approach can help in creating a reliable Monte Carlo code for nucleus - nucleus interaction at high energies?

Considering the space time structure of the nucleus - nucleus interaction we can set four stages ( see Ref. [1] ): (i)  $t < t_0$ , being  $t_0$ , the time of the first parton - parton interaction, the system behaves as a very coherent system of partons, confined in both nuclei, and it's physics is almost unknown; (ii) at time  $t_0$  the coherence of the parton system is destroyed; (ii)  $t_0 < t < t_h$ ,  $t_h$  being the hadronization time, there is a quark - gluon stage of the process, where QCD applies, and also new collective phenomena (e.g. Quark - Gluon Plasma) could be created. This stage could be described by known the Monte Carlo codes, lattice calculations and ideas, presented at this conference; (iv)  $t > t_h$  there is a hadronization stage which is a black box.

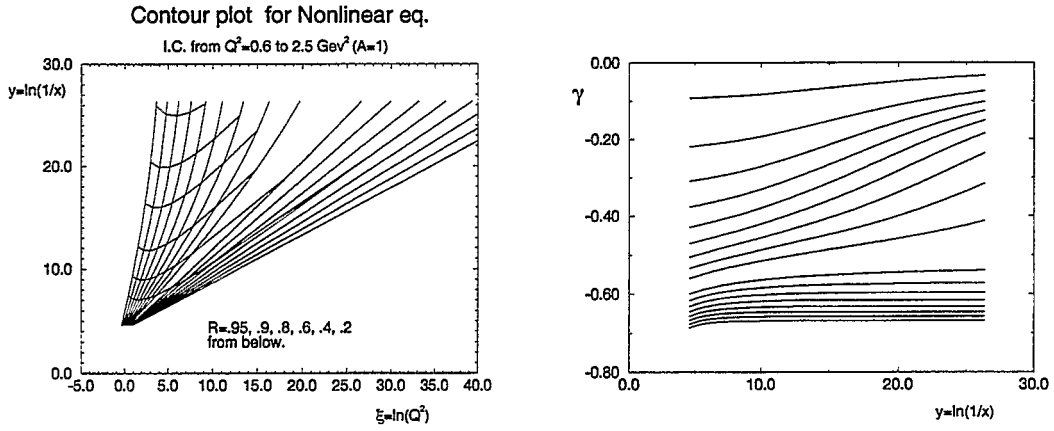


FIG. 5. *The trajectories and contour plot for the solution of the generalized evolution equation for N.  $R = \frac{xG(x, Q^2)(generalized\ equation)}{xG(x, Q^2)(GLAP)}$ .*

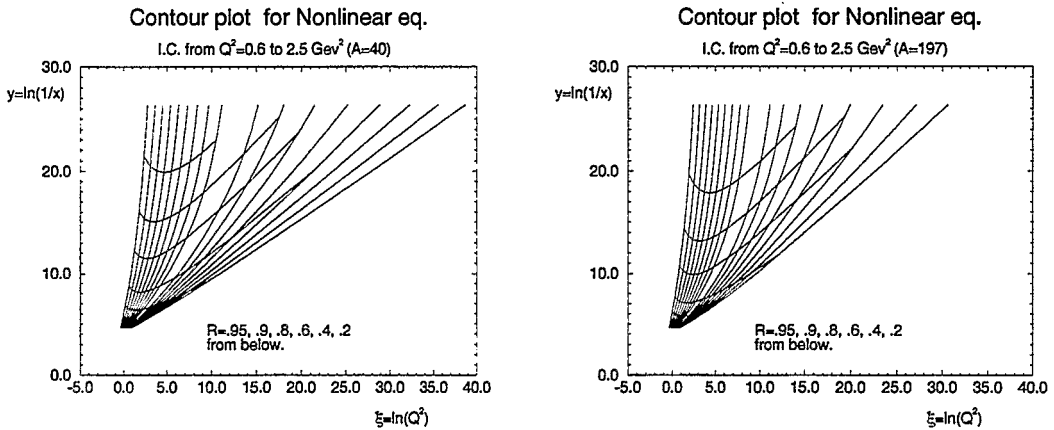


FIG. 6. *The trajectories and contour plot for the solution of the generalized evolution equation for Ca and Au.  $R = \frac{xG(x, Q^2)(generalized\ equation)}{xG(x, Q^2)(GLAP)}$ .*

In our approach we are able to calculate the inclusive cross section for gluons at  $t = t_0$ , providing a natural cutoff for the divergence at small transverse momentum.

We can calculate also the double inclusive cross section which gives the two gluon correlation function at  $t = t_0$ . We expect that this correlation is big for nucleus - nucleus collisions since it includes the production of two gluons from two parton cascade as well as from one. We hope that these two observables: gluon distribution and two gluon correlation will be enough to define the initial condition for the QCD motivated cascade during the third stage of the process. However, before providing a reliable QCD motivated Monte Carlo code we have to understand how to write it in correct degrees of freedom which are colorless quark - antiquark dipoles [16] but not quarks and gluons. We intend to do this in the nearest future.

The important question for the future Monte Carlo code is also the mixing of "soft" and "hard" processes. We firmly believe that the correct way of including them is to use the Glauber formula with the replacement  $\sigma(r_{\perp}^2) \rightarrow \sigma_{soft} + \sigma_{hard}$ . More detail discussion you can find in Ref. [1].

## VI. CONCLUSIONS.

Several aspects are being addressed to progress in our study of the SC: calculation of  $F_2^A(x, Q^2)$ ; use of other parameterization for  $S(b_t)$ ; calculation with  $\alpha_s$  running; introduction of the life-time gluon effect; introduction of the parton interaction inside the  $GG + N$  scattering, and the generalization of the approach to the BFKL dynamics.

We can conclude also:

1. We hope to have convinced you that we are on the way from our Really Highly Inefficient Calculation to your RHIC. Much work is needed to clarify the initial condition for the QCD phase of nucleus - nucleus interaction and this is the first and the most important task which we need to attack, since it will determine the correct degrees of freedom for further evolution of QCD cascades.

2. Everything that we have talked about satisfies the third law of theoretical physics: *Any model is a theory which we apply to a kinematic region, where we cannot prove that this theory is wrong.* We firmly believe that correct SC will provide the picture of the nucleus - nucleus interaction in which hard and semihard processes will play a crucial role with only small if any contamination of the soft contribution.

## ACKNOWLEDGEMENTS:

One of us (E.M.L.) is very grateful to Sid Kahana for creating a stimulating atmosphere of discussion at RHIC'96 Workshop and for enlightening discussions of the difficult theoretical problems in the modeling of heavy ion collisions. E.M.L. thanks all participant of the hard working group and especially Yu. Dokshitzer, C. Eskola, A. Mueller and M. Strikman for fruitful discussions on the subject of the talk and related topics. MBGD thanks A. Capella and D. Schiff for enlightening discussions. Work partially financed by CNPq, CAPES and FINEP, Brazil.

## REFERENCES

- [1] A.L.Ayala, M.B. Gay Ducati and E.M.Levin: FERMILAB-CONF-96-224-T, hep-ph 9608304.
- [2] A.L.Ayala, M.B.Gay Ducati and E.M. Levin: CBPF-FN-020/96,hep-ph 9604383.
- [3] E. Laenen and E. Levin: *Ann. Rev. Nucl. Part.* **44** (1994) 199.
- [4] H1 collaboration, T. Ahmed et al.: *Nucl. Phys.* **B439** (1995) 471;  
ZEUS collaboration, M. Derrick et al.: *Z. Phys. C* **69** (1995) 607; H1 collaboration, S. Aid et al.: DESY 96 - 039 (1996).
- [5] V.N. Gribov and L.N. Lipatov: *Sov. J. Nucl. Phys.* **15** (1972) 438; L.N. Lipatov: *Yad. Fiz.* **20** (1974) 181; G. Altarelli and G. Parisi: *Nucl. Phys. B* **126** (1977) 298; Yu.L.Dokshitzer: *Sov.Phys. JETP* **46** (1977) 641.
- [6] L. V. Gribov, E. M. Levin and M. G. Ryskin: *Phys.Rep.* **100** (1983) 1.
- [7] A.H. Mueller and J. Qiu: *Nucl. Phys.* **B268** (1986) 427.
- [8] H1 collaboration, S. Aid et al.: DESY 96 - 037, March 1996.
- [9] E.M. Levin and M.G.Ryskin: *Sov. J. Nucl. Phys.* **45** (1987) 150.
- [10] A.H. Mueller: *Nucl. Phys.* **B335** (1990) 115;
- [11] M. Abramowitz and I.A. Stegun: "*Handbook of Mathematical Functions*", Dover Publication, INC, NY 1970.
- [12] M. Glück, E. Reya and A. Vogt: *Z. Phys C* **67** (1995) 433.
- [13] A. Donnachie and P.V. Landshoff: *Phys. Lett.* **B185** (1987) 403, *Nucl. Phys.* **B311** (1989) 509; E. Gotsman, E. Levin and U. Maor: *Phys. Lett.* **B353** (1995) 526.
- [14] Jamal Jullian-Marian, Alex Kovner, Larry McLerran and Herbert Wiegert: HEP-MINN-96-1429.
- [15] J.C. Collins and J. Kwiecinski: *Nucl. Phys.* **B335** (1990) 89. J. Bartels, J. Blumlein and G. Shuler: *Z. Phys. C* **50** (1991) 91.
- [16] A.H. Mueller: *Nucl. Phys.* **B415** (1994) 373.

# Review of $J/\psi$ Production Data at Fixed-Target Energies

R. Vogt\*

*Lawrence Berkeley National Laboratory, Berkeley, California  
and*

*Physics Department, University of California, Davis, California*

## Abstract

The interpretation of the recent NA50 data depends crucially on the understanding of  $J/\psi$  production in  $pp$  interactions. I briefly review the existing data and discuss how well the production cross section can be known. I also give some simple parameterizations of data that can be used in event generators simulating  $J/\psi$  production and suppression and outline their range of validity.

Inclusive  $J/\psi$  production,  $AB \rightarrow J/\psi X$ , can be characterized by the transverse momentum,  $p_T$ , or transverse mass,  $m_T = \sqrt{M^2 + p_T^2}$ , and either the Feynman  $x$ ,  $x_F = p_L/p_{L,\max}$ , or the rapidity,  $y = 0.5 \ln((E + p_L)/(E - p_L))$ , of the  $J/\psi$ . The maximum momentum of the  $J/\psi$  depends on the minimum invariant mass of the unobserved particles,  $m_{X,\min} > 2m_p$ , in  $pp$  interactions. When  $m_{X,\min} \ll M$ ,  $p_{\max} \approx (s - M^2)/2\sqrt{s} \approx \sqrt{s}/2$  at high energy. In the center of mass system,  $-1 < x_F < 1$ .

The  $J/\psi$  invariant cross section is usually assumed to be factorizable with the data fit to separate functional forms describing the  $x_F$  and  $p_T$  distributions,

$$E \frac{d\sigma}{d^3p} = \frac{1}{\pi} \frac{E}{p_{\max}} \frac{d\sigma}{dx_F dp_T^2} = \frac{1}{\pi} \frac{d\sigma}{dy dp_T^2} \quad (1)$$

$$= f(x_F)g(p_T) . \quad (2)$$

Assuming that the  $x_F$  distribution is symmetric about  $x_F = y = 0$  in  $pp$  (and  $pA$ ) interactions, the data is usually fit to either the invariant form,

$$E \frac{d\sigma}{dx_F} = (1 - |x_F|)^d \quad (3)$$

or the noninvariant

$$\frac{d\sigma}{dx_F} = (1 - |x_F|)^c . \quad (4)$$

---

\*Supported by the U. S. Department of Energy under Contract No. DE-AC03-76SF00515.



The  $p_T$  distribution is usually parameterized as

$$g(p_T) \propto \exp(-bp_T) \text{ or } \exp(-ap_T^2), \quad (5)$$

appropriately normalized. Note that, in principal, the  $x_F$  and  $p_T$  distributions are not easy to separate because  $x_F$  is a function of  $p_T$ ,

$$x_F = \frac{2m_T}{\sqrt{s}} \sinh y. \quad (6)$$

The total cross section is never measured since no experiment covers all the phase space. Extrapolations to unmeasured regions of phase space are very sensitive to the parameterization of the cross section, perhaps leading to significant errors in the extracted total cross section. In fixed-target experiments, most of the forward  $x_F$  range is available. The  $x_F$  distributions narrow with increasing energy so that, at high energies, the exponents,  $d$  and  $c$ , used to characterize the distributions can become large. To expand information in the limited  $x_F$  range available, the rapidity variable is often used in collider experiments. In fact, most of these experiments only cover a central region of rapidity, around  $y = 0$ .

The  $J/\psi$  cross section data is given in Table 1, essentially taken from Ref. [1]. Most of the data are gathered by measuring the  $J/\psi$  through its decay to leptons, thus at central rapidity,  $Bd\sigma/dy|_{y=0}$  has not been corrected for the branching ratio to lepton pairs. The forward,  $x_F > 0$ , cross section data has been adjusted so that the same branching ratio  $B(J/\psi \rightarrow \mu^+ \mu^-) = (5.97 \pm 0.25)\%$  is used for all the data. Most of the ISR experiments provide only  $Bd\sigma/dy|_{y=0}$  rather than attempting to extrapolate to unknown regions. Note also that, for reasons of statistics, the fixed-target measurements generally use a nuclear target. Some of these experiments used more than one target and reported a nuclear dependence [2–6]. Only the cross section from the light target is given in the table. Since several of these experiments showed that the  $x_F$  distribution is modified in the nuclear target, the assumption that the  $x_F$  distribution is symmetric about  $x_F = 0$  may not hold for the light nuclear targets. Recent data from E772 [7] on the target dependence is not shown in the table because their acceptance was such that it was not possible to extract absolute cross sections. In Ref. [1] all the nuclear target data has been “corrected” to  $pp$  by assuming  $\sigma_{pA} = \sigma_{pp}A^\alpha$  where  $\alpha = 0.9$ . This value is actually somewhat smaller than the  $A$  dependence fit by most experiments,  $\alpha = 0.94$  from NA3 [3] and  $\alpha = 0.91$  from E772 [7] and NA38/NA50 [8], so that one must be careful with the treatment of the nuclear data. From the table, it is clear that  $\langle p_T \rangle$  and  $\langle p_T^2 \rangle$  increase slowly with energy. However, nuclear effects have been observed to broaden the  $p_T$  distributions, attributed to initial-state elastic scattering with the nucleons, see *e.g.* [9] and references therein.

The energy dependence of the cross section has been parameterized in two different forms, depending on whether one concentrates on the central rapidity value or the total cross section. Both assume that the cross sections scale as a universal function of  $\tau = M/\sqrt{s}$ . In the 1978 review in Ref. [10] a compilation of available data showed that the  $J/\psi$  and  $\psi'$  production cross sections in  $pp$  collisions obeyed the relation

$$B \frac{d\sigma}{dy} \Big|_{y=0} = A \exp(-14.7\tau), \quad (7)$$

where  $B \equiv B(\psi \rightarrow \mu^+ \mu^-)$  is the branching ratio of the meson decays to muon pairs and  $A_{J/\psi} = 40$  nb and  $A_{\psi'} = 0.018 A_{J/\psi}$  [10]. The normalization has been adjusted to take into

Exp.	$A^{(a)}$	$\sqrt{s}$ (GeV)	$\sigma(x_F > 0)$ (nb)	$B \frac{d\sigma}{dy}  _{y=0}$ (nb)	$\langle p_T \rangle$ (GeV)	$\langle p_T^2 \rangle$ (GeV <sup>2</sup> )
MIT-BNL [11]	Be	6.1	$0.1^{+0.10}_{-0.05}$ (b)	$\sim 0.01$	-	-
PS [2]	$p$	6.7	$0.31 \pm 0.09$ (c)	$0.055 \pm 0.02$	-	$0.62$ (d,e)
MIT-BNL [12]	Be	7.3	$1^{+1.0}_{-0.5}$ (b)	$\sim 0.1$	$\sim 0.33$ (f)	$\sim 0.62$ (e)
WA39 [13]	$p$	8.6	$1.2 \pm 0.6$	$0.2 \pm 0.1$ (g)	-	-
IHEP [14]	Be	11.5	$11 \pm 3$ (c)	$1.2 \pm 0.4$	-	$0.55 \pm 0.09$ (e)
FNAL [15]	Be	16.8	-	$5.6 \pm 1.5$	-	$\sim 1$ (e)
FNAL [16]	Be	16.8	$69 \pm 23$	$7.2 \pm 2.5$ (h)	$0.96 \pm 0.12$ (f)	-
NA3 [3]	$p$	16.8	$47 \pm 10$ (i)	-	-	-
NA3 [3]	$p$	19.4	$61 \pm 11$	$4.1 \pm 0.3$	$0.95 \pm 0.02$	$1.23 \pm 0.05$
FNAL [4] (j)	C	20.5	$147 \pm 7$	$14.3 \pm 1.5$ (h)	$0.98 \pm 0.04$ (f)	-
FNAL [5] (j)	C	20.5	$95 \pm 13$	$9.5 \pm 1.0$	$0.97 \pm 0.10$	$1.25 \pm 0.10$
E705 [17]	Li	23.8	$162 \pm 22$	-	-	-
UA6 [18]	$p$	24.3	$71.8 \pm 9.3$	$6.2 \pm 1.1$	$1.1 \pm 0.2$	-
FNAL [19]	Be	27.4	$110 \pm 27$ (c)	$8.9 \pm 2.2$	$1.25 \pm 0.27$ (f)	$0.91 \pm 0.29$ (e)
ISR [20]	$p$	30	-	$9.1 \pm 2.5$	$1.14 \pm 0.12$	-
ISR [21]	$p$	30.6	-	$6.6 \pm 1.8$	-	-
E672/706 [6]	Be	31.5	$161 \pm 35$	$8 \pm 2$	$1.06 \pm 0.05$	$1.55 \pm 0.11$
ISR [22]	$p$	52	-	$7.5 \pm 2.5$	$\geq 0.67$ (k)	-
ISR [23]	$p$	52	$350 \pm 160$ (c)	$12 \pm 5$	$1.0 \pm 0.2$	$1.2 \pm 0.3$
ISR [24]	$p$	52	-	$12.8 \pm 3.2$	$1.25 \pm 0.27$ (d)	-
ISR [21]	$p$	52.7	-	$11.0 \pm 0.4$	$1.57 \pm 0.07$ (f)	$1.92 \pm 0.15$ (e)
ISR [20]	$p$	53	-	$13.6 \pm 3.1$	$1.39 \pm 0.05$	-
ISR [21]	$p$	62.4	-	$10.2 \pm 0.7$	$1.5 \pm 0.1$ (f)	$1.7 \pm 0.2$ (e)
ISR [20]	$p$	63	-	$14.8 \pm 3.3$	$1.29 \pm 0.05$	-

TABLE I. The  $J/\psi$  cross section for  $x_F > 0$  with the branching ratio to leptons,  $B(J/\psi \rightarrow \mu^+ \mu^-) = (5.97 \pm 0.25)\%$  divided out and  $B d\sigma/dy|_{y=0}$ . All cross sections are per nucleon. (a) Target mass dependence is accounted for assuming  $A^{0.9}$  [1]. (b) Assuming  $d\sigma/dx_F \sim (1 - |x_F|)^c$  and  $c = 1^{+2}_{-1}$ . (c) Forward cross section obtained by assuming  $x_F$  distribution symmetric about  $x_F = 0$ . (d) Assumed, not measured. (e) From  $d\sigma/dp_T^2 \sim \exp(-ap_T^2)$  with  $\langle p_T^2 \rangle = 1/a$ . (f) From  $d\sigma/dp_T^2 \sim \exp(-bp_T)$  with  $\langle p_T \rangle = 2/b$ . (g) Assuming  $d\sigma/dx_F \sim (1 - |x_F|)^c$  with  $c \sim 2$  and  $\langle p_T \rangle \sim 1$  GeV. (h) A  $\sim 3\%$  background not subtracted. (i) Extracted from  $\sigma(\bar{p})/\sigma(p)$ . (j) Same experiment, [5] claimed to be more reliable. (k) Changing  $\langle p_T \rangle$  to 1 GeV increases cross section 60%.

account the most recent measurement of the branching ratios. The  $J/\psi$  and  $\psi'$  branching ratios are the same for muon and electron pair decays. The forward cross section and the noninvariant  $x_F$  distribution were parameterized by the E672 collaboration [6] as

$$\sigma(x_F > 0) = \sigma_0(1 - \tau)^n \quad (8)$$

$$\frac{d\sigma}{dx_F} = (1 - |x_F|)^c \quad (9)$$

$$c = \frac{a}{1 + b/\sqrt{s}} \quad (10)$$

where  $n = 12.0 \pm 0.9$ ,  $a = 13.5 \pm 4.5$  and  $b = 44.9 \pm 21.9$  GeV. The cross section  $\sigma_0$  fit by E762 for their Be target was adjusted to a proton target assuming an  $A$  dependence of  $A^{0.9}$  in [1]. This parameterization of the cross section, called the Schuler parameterization by NA50 and used by them to adjust their  $pA$  and Pb+Pb data to  $p_{\text{beam}} = 200$  GeV, is applicable for  $\sqrt{s} \leq 31$  GeV.

The cross section may also be calculated from perturbative methods up to next-to-leading order (NLO) and compared to the data. This was done in the spirit of the color evaporation model [25] which assumes that *e.g.* the  $J/\psi$  cross section is proportional to the free spin and color averaged open  $c\bar{c}$  pair cross section integrated between  $2m_c \leq M_{c\bar{c}} < 2m_D$  so that

$$\sigma = F \int_{2m_c}^{2m_D} dM_{c\bar{c}} \frac{d\sigma[c\bar{c}]}{dM_{c\bar{c}}} . \quad (11)$$

The model is based on two ingredients. The quarkonium dynamics are assumed to be identical to those of low mass  $Q\bar{Q}$  pairs. All perturbative QCD corrections apply to the short-distance cross section and are therefore identical for open pair and bound state production. Additionally, although the  $Q\bar{Q}$  pair is produced at short distances in different color, angular momentum and relative momentum states and the relative production rates of these states may be different for different high-energy collisions. The average of many nonperturbative matrix elements are combined into the universal factor  $F$  which determines the probability to form a bound state. Once  $F$  has been fixed, the model predicts the shape of the energy dependence and the absolute normalization. The model was shown to describe the energy and  $x_F$  dependence [25] and, more recently, the  $p_T$  dependence [29] of  $J/\psi$  and  $\Upsilon$  production up to high energies where both of the previously discussed parameterizations break down. Note that  $\chi$  production is also in agreement with these results [25].

The quarkonium production cross section to NLO was obtained using the  $Q\bar{Q}$  pair production code developed in Ref. [26] with a mass cut of  $M_{c\bar{c}} < 2m_D = 3.74$  GeV for charmonium. The calculations were performed with two recent sets of parton densities, MRS D-' [27] and GRV HO [28]. Equivalent results were found at presently available energies for the two sets. Similar results on  $\Upsilon$  production were shown to agree with the total cross sections reported by CDF [31] and UA1 [32]. Although these data were taken in  $p\bar{p}$  colliders, at high energies  $\sigma(\bar{p})/\sigma(p) \approx 1$  because of the dominance of gluon fusion. Total cross sections have not yet been reported for the  $J/\psi$  at high energies because  $J/\psi$ 's with  $p_T < 5$  GeV have not been measured.

In fig. 1 we compare the  $Bd\sigma/dy|_{y=0}$  data to the Craigie parameterization and the NLO calculation. Figure 2 shows the comparison between the Schuler parameterization of the forward cross section and the NLO result. At low energies, the comparison is rather good

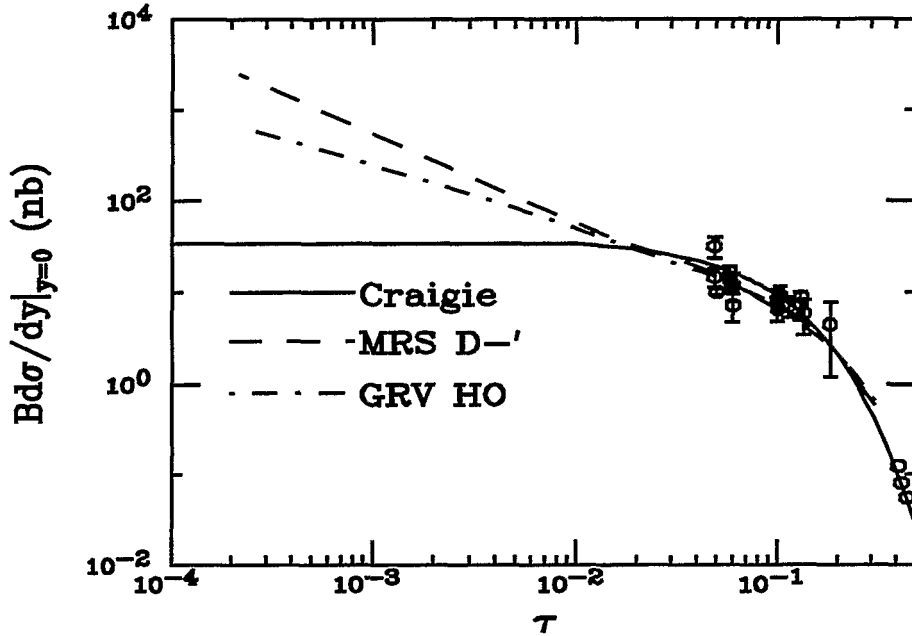


FIG. 1. The calculated central cross section is compared to the Craigie parameterization and data from Table 1.

for both parameterizations. The relative production cross sections for different energies may be satisfactorily scaled with the Schuler parameterization, as done by NA50 [8]. However, the differences at high energy,  $\tau = 0.0155$  at RHIC Au+Au energies and  $\tau = 0.00056$  at LHC Pb+Pb energies, are significant.

The data shown here can constrain the mass and scale parameters in the calculation of the  $pp$  cross section, but only up to the 20-30% level, especially if the fit of  $F$  is skewed by an overestimate of the  $A$  dependence. In fact, when a comparison is made between  $pA$  fits to the NA50 data with  $\alpha = 0.94$ , corresponding to  $\sigma_{\psi N} = 4.8$  mb, and  $\alpha = 0.91$  where  $\sigma_{\psi N} = 7$  mb, neither can be ruled out by the precision of the  $pp$  production cross section. Near the NA50 energy, 200 GeV/nucleon for S+U and 160 GeV/nucleon for Pb+Pb, the  $x_F$  distributions have been parameterized using the invariant form of eq. (3) with  $d = 2.94 \pm 0.32$  at  $\sqrt{s} = 16.8$  GeV [16] and  $d = 3.55 \pm 0.11$  at  $\sqrt{s} = 20.5$  GeV [5]. Either these values or those estimated by eq. (10) for the noninvariant form,  $c = 3.7 \pm 1.9$  at  $\sqrt{s} = 16.8$  GeV or  $c = 4.1 \pm 2.0$  at  $\sqrt{s} = 19.4$  GeV, can be used for longitudinal momentum distributions in event generators. The NA3 experiment [3] has information at the appropriate NA38 energy to obtain the  $p_T$  distributions for  $pp$  and  $pPt$  interactions. A similar increase in the average  $p_T$  may be seen in the  $AB$  data [9]. Since the shapes of the distributions rather than the absolute normalization are most important in the event generators, these distributions can be used to model  $J/\psi$  production before subsequent interactions with nucleons and secondaries in simulations of  $J/\psi$  suppression. However, one should keep in mind that the data is so far not precise enough to draw definitive conclusions concerning the origin of the observed  $J/\psi$  suppression. Until the  $pp$  production cross section can be known precisely, the interpretation of the suppression can remain open. We also point out that the interpretation of the  $\psi$ -to-continuum data will still be subject to debate unless the Drell-Yan or continuum cross section is also known precisely.

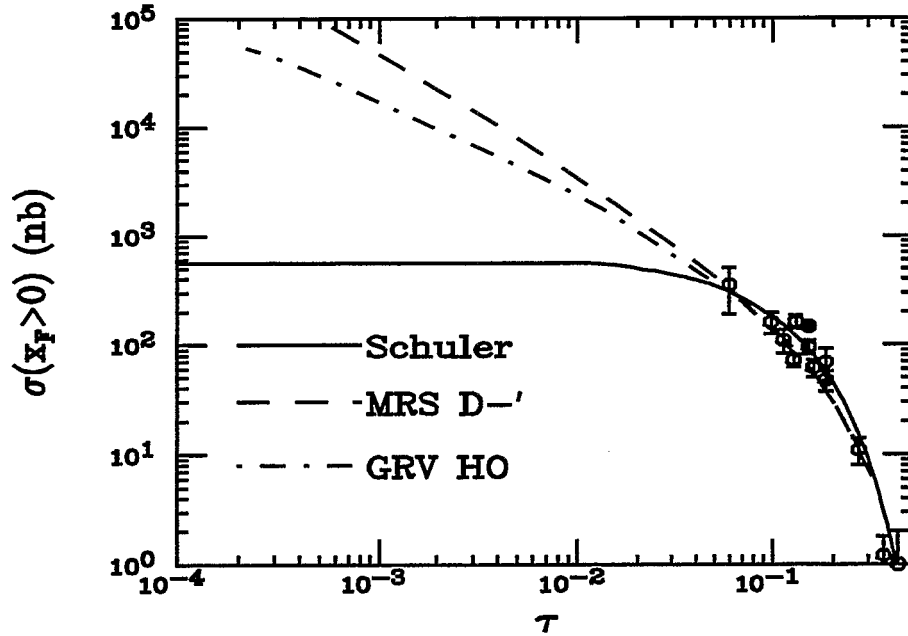


FIG. 2. The calculated forward cross section is compared to the Schuler parameterization and data from Table 1.

## REFERENCES

- [1] G.A. Schuler, CERN Preprint, CERN-TH.7170/94.
- [2] A. Bamberger *et al.*, Nucl. Phys. **B134** (1978) 1.
- [3] J. Badier *et al.*, Z. Phys. **C20** (1983) 101.
- [4] J.G. Branson *et al.*, Phys. Rev. Lett. **38** (1977) 1331.
- [5] K.J. Anderson *et al.*, Phys. Rev. Lett. **42** (1979) 944.
- [6] V. Abramov *et al.*, Fermilab-PUB-91/62-E, March 1991.
- [7] D.M. Alde *et al.*, Phys. Rev. Lett. **66** (1991) 133.
- [8] M. Gonin, in proceedings of *Quark Matter '96*, Heidelberg, Germany, May 1996.
- [9] S. Gavin and M. Gyulassy, Phys. Lett. **B214** (1988) 241.
- [10] N.S. Craigie, Phys. Rep. **47** (1978) 1.
- [11] S.C.C. Ting, in proceedings of the *Int. Symp. on Lepton and Photon Int. at High Energies*, W.T. Kirk, ed., Stanford University, USA, 1975, p. 155.
- [12] J.J. Aubert *et al.*, Phys. Rev. Lett. **33** (1974) 1404.
- [13] M.J. Corden *et al.*, Phys. Lett. **B98** (1981) 220.
- [14] Yu.M. Antipov *et al.*, Phys. Lett. **B60** (1976) 309.
- [15] K.J. Anderson *et al.*, Phys. Rev. Lett. **36** (1976) 237.
- [16] K.J. Anderson *et al.*, Phys. Rev. Lett. **37** (1976) 799.
- [17] L. Antoniazzi *et al.*, Phys. Rev. Lett. **70** (1993) 383.
- [18] C. Morel *et al.*, Phys. Lett. **B252** (1990) 505.
- [19] H.D. Snyder *et al.*, Phys. Rev. Lett. **36** (1976) 1415.
- [20] C. Kourkoumelis *et al.*, Phys. Lett. **B91** (1980) 481.
- [21] A.G. Clark *et al.*, Nucl. Phys. **B142** (1978) 29.
- [22] F.W. Büsser *et al.*, Phys. Lett. **B56** (1975) 482.

- [23] E. Nagy *et al.*, Phys. Lett. **B60** (1975) 96.
- [24] E. Amaldi *et al.*, Lett. Nuovo Cim. **19** (1977) 152.
- [25] R.V. Gvai *et al.*, Int. J. Mod. Phys. **A10** 3043.
- [26] M.L. Mangano, P. Nason and G. Ridolfi, Nucl. Phys. **B405** (1993) 507.
- [27] A.D. Martin, R.G. Roberts and W.J. Stirling, Phys. Lett. **B306** (1993) 145.
- [28] M. Glück, E. Reya and A. Vogt, Z. Phys. **C53** (1993) 127.
- [29] G.A. Schuler and R. Vogt, CERN-TH/96-157, LBL-39012, Phys. Lett. **B**, in press.
- [30] Review of Particle Properties, Phys. Lett. **B204** (1988) 1.
- [31] F. Abe *et al.*, Phys. Rev. Lett. **75** (1995) 4358.
- [32] K. Eggert and A. Morsch (UA1) private communication.



### **III.**

## **Phenomenology**



# Non-Equilibrium QCD of High-Energy Multi-Gluon Dynamics

Klaus Geiger

*Brookhaven National Laboratory, Upton, N.Y. 11973, U.S.A.*

## Abstract

I discuss an approach to derive from first principles, a real-time formalism to study the dynamical interplay of quantum and statistical-kinetic properties of non-equilibrium multi-parton systems produced in high-energy QCD processes. The ultimate goal (from which one is still far away) is to have a practically applicable description of the space-time evolution of a general initial system of gluons and quarks, characterized by some large energy or momentum scale, that expands, diffuses and dissipates according to the self- and mutual-interactions, and eventually converts dynamically into final state hadrons. For example, the evolution of parton showers in the mechanism of parton-hadron conversion in high-energy hadronic collisions, or, the description of formation, evolution and freezeout of a quark-gluon plasma, in ultra-relativistic heavy-ion collisions.

## I. INTRODUCTION

In general, the study of a high-energy multi-particle system and its quantum dynamics involves three essential aspects: first, the aspect of space-time, geometry and the structure of the vacuum; second, the quantum field aspect of the particle excitations; and third, the statistical aspect of their interactions. These three elements are generally interconnected in a non-trivial way by their overall dynamical dependence. Therefore, in order to formulate a quantum description of the complex non-equilibrium dynamics, one needs to find a quantum-statistical and kinetic formulation of QCD that unifies the three aspects self-consistently. The main tools to achieve this are: the *closed-time-path* (CTP) formalism [1,2] (for treating initial value problems of irreversible systems), and (ii) *transport theory* based on Wigner function techniques [3] (for a kinetic description of inhomogenous non-equilibrium systems).

The common feature of high-energy particle collisions is that they allow a distinction between a short-distance quantum field theoretical scale and a larger distance statistical-kinetic scale, which is essentially an effect of ultra-relativistic kinematics. This advantageous property facilitates the passage from *exact QCD field theory* of coherent non-abelian gauge fields to an *approximate quantum kinetic theory* of an ensemble of incoherent gluons. When described in a reference frame, in which the particles move close to the speed of light, the effects of time dilation and Lorentz contraction separate the intrinsic quantum motion of the individual particles from the statistical correlations among them. On the one hand, the quantum dynamics is determined by the self-interactions of the bare quanta, which dresses

them up to quasi-particles with a substructure of quantum fluctuations. This requires a fully quantum theoretical analysis including renormalization. On the other hand, the kinetic dynamics can well be described statistically-mechanically by the motion of the quasi-particles that is, by binary interactions between these quasi-particles, and by the possible presence of a coherent mean color field that may be induced by the collective motion of the partons. Such a distinct description of quantum and kinetic dynamics is possible, because the quantum fluctuations are highly concentrated around the light cone, occurring at very short distances, and decouple to very good approximation from the kinetic evolution which is dictated by comparably large space-time scales. As mentioned, the natural two-scale separation is just the consequence of time dilation and Lorentz contraction, and is true for any lightcone dominated process. In fact, at asymptotic energies the quantum fluctuations are exactly localized on the lightcone, and so the decoupling becomes perfect. This observation is the key to formulate a quantum kinetic description in terms of particle phase-space densities, involving a simultaneous specification of momentum space and space-time, because at sufficiently high energy, the momentum scale  $\Delta p$  of the individual particles' quantum fluctuations and the scale  $\Delta r$  of space-time variations of the system of particles satisfy  $\Delta p \Delta r \gg 1$ , consistent with the uncertainty principle.

In what follows, I am guided by the recent paper [4] and the related literature discussed therein, plus on preliminary results of work in progress [5]. For purpose of lucidity, I will henceforth confine myself to pure Yang-Mills theory, i.e. consider gluons only and ignore the quark degrees of freedom. The latter are straightforward to include.

## II. NON-EQUILIBRIUM TECHNIQUES FOR QCD

### A. Basics of the closed-time-path formalism

As proclaimed, the goal is to describe the time evolution of a non-equilibrium quantum system consisting of an initial ensemble of high-energy gluons at starting time  $t_0$ . In this context, the starting point of non-equilibrium field theory is to write down the CTP *in-in amplitude*  $Z_P$  for the evolution of the initial quantum state  $|in\rangle$  forward in time into the remote future, in the presence of a medium which described by the density matrix. The amplitude  $Z_P$  is formally given by [2]:

$$Z_P[\mathcal{J}, \hat{\rho}] = \langle in | in \rangle_{\mathcal{J}} = \text{Tr} \left\{ U^\dagger(t_0, t) U(t, t_0) \hat{\rho}(t_0) \right\}_{\mathcal{J}}, \quad (1)$$

where  $\mathcal{J} = (\mathcal{J}^+, \mathcal{J}^-)$  is an external source with components on the + and - time branch.  $\hat{\rho}(t_0)$  denotes the The initial state density matrix is denoted  $\hat{\rho}(t_0)$ ,  $U$  is the time evolution operator, and  $T$  ( $T^\dagger$ ) denotes the time (anti-time) ordering. Within the CTP formalism the amplitude  $Z_P$  can be evaluated by time integration over the *closed-time-path*  $P$  in the complex  $t$ -plane. This closed-time path extends from  $t = t_0$  to  $t = t_\infty$  in the remote future along the positive (+) branch and back to  $t = t_0$  along the negative (-) branch. where any point on the + branch is understood at an earlier instant than any point on the - branch. With  $Z_P$  defined on this closed-time-path, one may then, as in standard field theory, derive from it the Green functions and their equations of motion. The differences between the CTP

and the standard field theory, which are briefly summarized below, arise then solely from the different time contour.

The interpretation of this formal apparatus for the evolution along the closed-time path  $P$  is rather simple: If the initial state is the vacuum itself, that is, the absence of a medium generated by other particles, then the density matrix  $\hat{\rho}$  is diagonal and in (1), one has  $|in\rangle \rightarrow |0\rangle$ . In this case the evolution along the  $+$  branch is identical to the anti-time ordered evolution along the  $-$  branch (modulo an irrelevant phase), and space-time points on different branches cannot cross-talk. In the presence of a medium however, the density matrix contains off-diagonal elements, and there are statistical correlations between the quantum system and the medium particles (e.g. scatterings) that lead to correlations between space-time points on the  $+$  branch with space-time points on the  $-$  branch. Hence, when addressing the evolution of a multi-particle system, both the deterministic self-interaction of the quanta, i.e. the time (anti-time) ordered evolution along the  $+$  ( $-$ ) branch, *and* the statistical mutual interaction with each other, i.e. the cross-talk between  $+$  and  $-$  branch, must be included in a self-consistent manner. The CTP method achieves this through the time integration along the contour  $P$ . Although for physical observables the time values are on the  $+$  branch, both  $+$  and  $-$  branches will come into play at intermediate steps in a self-consistent calculation.

The convenient feature of this Green function formalism on the closed-time path is that it is formally completely analogous to standard quantum field theory, except for the fact that the fields have contributions from both time branches, and the path-integral representation of the *in-in* amplitude (1), contains as usual the classical action  $I[\mathcal{A}$  and source terms  $\mathcal{J} \circ \mathcal{A}$ , but now for both time branches,

$$Z_P[\mathcal{J}^+, \mathcal{J}^-, \hat{\rho}] = \int \mathcal{D}\mathcal{A}^+ \mathcal{D}\mathcal{A}^- \exp \left[ i \left( I[\mathcal{A}^+] + \mathcal{J}^+ \cdot \mathcal{A}^+ \right) - i \left( I^*[\mathcal{A}^-] + \mathcal{J}^- \cdot \mathcal{A}^- \right) \right] \mathcal{M}[\hat{\rho}]. \quad (2)$$

From this path-integral representation one obtains the  $n$ -point Green functions  $G^{(n)}(x_1, \dots, x_n)$ , which are now

$$G^{\alpha_1 \alpha_2 \dots \alpha_n}(x_1, \dots, x_n), \quad \alpha_i = \pm,$$

depending on whether the space-time points  $x_i$  lie on the  $+$  or  $-$  time branch, and it is possible to construct a perturbative expansion of the non-equilibrium Green functions in terms of modified Feynman rules (as compared to standard field theory),

- (i) The number of elementary vertices is doubled, because each propagator line of a Feynman diagram can be either of the four components of the Green functions. The interaction vertices in which all the fields are on the  $+$  branch are the usual ones, while the vertices in which the fields are on the  $-$  branch have the opposite sign. On the other hand, combinatoric factors, rules for loop integrals, etc., remain exactly the same as in usual field theory.
- (ii) All local 1-point functions, such as the gauge-field or the color current, are ‘vectors’ with 2 components,

$$\mathcal{A}(x) \equiv \begin{pmatrix} \mathcal{A}^+ \\ \mathcal{A}^- \end{pmatrix} \quad \mathcal{J}(x) \equiv \begin{pmatrix} \mathcal{J}^+ \\ \mathcal{J}^- \end{pmatrix} \quad (3)$$

Similarly, all 2-point functions, as the gluon propagator  $\Delta_{\mu\nu}$  and the polarization tensor  $\Pi_{\mu\nu}$ , are  $2 \times 2$  matrices with components

$$\Delta(x_1, x_2) \equiv \begin{pmatrix} \Delta^{++} & \Delta^{+-} \\ \Delta^{-+} & \Delta^{--} \end{pmatrix} \quad \Pi(x_1, x_2) \equiv \begin{pmatrix} \Pi^{++} & \Pi^{+-} \\ \Pi^{-+} & \Pi^{--} \end{pmatrix}. \quad (4)$$

Explicitely, the components of the propagator are

$$\begin{aligned} \Delta_{\mu\nu}^F(x, y) &\equiv \Delta_{\mu\nu}^{++}(x, y) = -i \langle T \mathcal{A}_\mu^+(x) \mathcal{A}_\nu^+(y) \rangle \\ \Delta_{\mu\nu}^<(x, y) &\equiv \Delta_{\mu\nu}^{+-}(x, y) = -i \langle \mathcal{A}_\nu^+(y) \mathcal{A}_\mu^-(x) \rangle \\ \Delta_{\mu\nu}^>(x, y) &\equiv \Delta_{\mu\nu}^{-+}(x, y) = -i \langle \mathcal{A}_\mu^-(x) \mathcal{A}_\nu^+(y) \rangle \\ \Delta_{\mu\nu}^{\bar{F}}(x, y) &\equiv \Delta_{\mu\nu}^{--}(x, y) = -i \langle \bar{T} \mathcal{A}_\mu^-(x) \mathcal{A}_\nu^-(y) \rangle, \end{aligned} \quad (5)$$

where  $\Delta^F$  is the usual time-ordered Feynman propagator,  $\Delta^{\bar{F}}$  is the corresponding anti-time-ordered propagator, and  $\Delta^>$  ( $\Delta^<$ ) is the unordered correlation function for  $x_0 > y_0$  ( $x_0 < y_0$ ). In compact notation,

$$\Delta_{\mu\nu}(x, y) = -i \langle T_P \mathcal{A}(x) \mathcal{A}(y) \rangle, \quad (6)$$

where the generalized time-ordering operator  $T_P$  is defined as

$$T_P A(x) B(y) := \theta_P(x_0, y_0) A(x) B(y) + \theta_P(y_0, x_0) B(y) A(x), \quad (7)$$

with the  $\theta_P$ -function defined as

$$\theta_P(x_0, y_0) = \begin{cases} 1 & \text{if } x_0 \text{ succeeds } y_0 \text{ on the contour } P \\ 0 & \text{if } x_0 \text{ precedes } y_0 \text{ on the contour } P \end{cases}. \quad (8)$$

Higher order products  $A(x)B(y)C(z)\dots$  are ordered analogously. Finally, for later use, let me also introduce the generalized  $\delta_P$ -function defined on the closed-time path  $P$ :

$$\delta_P^4(x, y) := \begin{cases} +\delta^4(x - y) & \text{if } x_0 \text{ and } y_0 \text{ from positive branch} \\ -\delta^4(x - y) & \text{if } x_0 \text{ and } y_0 \text{ from negative branch} \\ 0 & \text{otherwise} \end{cases}. \quad (9)$$

Henceforth I will not explicitly label the  $+$ ,  $-$  components, unless it is necessary. Instead a compressed notation is used, in which it is understood that, e.g., 1-point functions such as  $\mathcal{A}(x)$  or  $\mathcal{J}(x)$ , 2-point functions such as  $\Delta_\mu(x, y)$  or  $\Pi_{\mu\nu}(x, y)$ , receive contributions from both  $+$  and  $-$  time branches.

## B. The generating functional for the non-equilibrium Green functions

The amplitude  $Z_P$  introduced in (1) admits a path-integral representation which gives the *generating functional for the CTP Green functions* defined on closed-time-path  $P$  [5]:

$$Z_P[\mathcal{J}, \hat{\rho}] = \mathcal{N} \int \mathcal{D}\mathcal{A} \det \mathcal{F} \delta(f[\mathcal{A}]) \exp \left\{ i \left( I[\mathcal{A}, \mathcal{J}] \right) \right\} \mathcal{M}(\hat{\rho}), \quad (10)$$

where  $\mathcal{A} = (\mathcal{A}^+, \mathcal{A}^-)$  and  $\mathcal{J} = (\mathcal{J}^+, \mathcal{J}^-)$  have two components, living on the  $+$  and  $-$  time branches.

The structure of the functional  $Z_P$  in (10) is the following:

- (i) The functional integral (with normalization  $\mathcal{N}$ ) is over all gauge field configurations with measure  $\mathcal{D}\mathcal{A} \equiv \prod_{\mu,a} \mathcal{D}\mathcal{A}_\mu^a$ , subject to the condition of gauge fixing, here for the *class of non-covariant gauges* defined by

$$f^a[\mathcal{A}] := \hat{n} \cdot \mathcal{A}^a(x) - B^a(x) \quad \Longrightarrow \quad \langle \hat{n}^\mu \mathcal{A}_\mu^a(x) \rangle = 0, \quad (11)$$

where  $\hat{n}^\mu \equiv \frac{n^\mu}{\sqrt{|n^2|}}$  and  $n^\mu$  is a constant 4-vector, being either space-like ( $n^2 < 0$ ), time-like ( $n^2 > 0$ ), or light-like ( $n^2 = 0$ ). With this choice of gauge class the *local gauge constraint* on the fields  $\mathcal{A}_\mu^a(x)$  in the path-integral (10) becomes,

$$\begin{aligned} \det \mathcal{F} \delta(\hat{n} \cdot \mathcal{A}^a - B^a) &= \text{const} \times \exp \left\{ -\frac{i}{2\alpha} \int_P d^4x [\hat{n} \cdot \mathcal{A}^a(x)]^2 \right\} \\ &\equiv I_{GF}[\hat{n} \cdot \mathcal{A}], \end{aligned} \quad (12)$$

where  $\det \mathcal{F}$  is the Fadeev-Popov determinant (which in the case of the non-covariant gauges turns out to be a constant factor), and where  $\delta(\hat{n} \cdot \mathcal{A}) \equiv \prod_a \delta(\hat{n} \cdot \mathcal{A}^a)$ . The right side translates this constraint into a the *gauge fixing* functional  $I_{GF}$ . The particular choice of the vector  $\hat{n}^\mu$  and of the real-valued parameter  $\alpha$  is dictated by the physics or computational convenience, and distinguishes further within the class of non-covariant gauges [6,7]:

$$\begin{aligned} \text{homogenous axial gauge :} & \quad n^2 < 0 \quad \alpha = 0 \\ \text{inhomogenous axial gauge :} & \quad n^2 < 0 \quad \alpha = 1 \\ \text{temporal axial gauge :} & \quad n^2 > 0 \quad \alpha = 0 \\ \text{lightcone gauge :} & \quad n^2 = 0 \quad \alpha = 0. \end{aligned} \quad (13)$$

- (ii) The exponential  $I$  is the *effective classical action* with respect to both the  $+$  and the  $-$  time contour,  $I[\mathcal{A}, \mathcal{J}] \equiv I[\mathcal{A}^+, \mathcal{J}^+] - I^*[\mathcal{A}^-, \mathcal{J}^-]$ , including the usual Yang-Mills action  $I_{YM} = \int d^4x \mathcal{L}_{YM}$ , plus the source  $\mathcal{J}$  coupled to the gauge field  $\mathcal{A}$ :

$$\begin{aligned} I[\mathcal{A}, \mathcal{J}] &= -\frac{1}{4} \int_P d^4x \mathcal{F}_{\mu\nu}^a(x) \mathcal{F}^{\mu\nu,a}(x) + \int_P d^4x \mathcal{J}_\mu^a(x) \mathcal{A}^{\mu,a}(x) \\ &\equiv I_{YM}[\mathcal{A}] + \mathcal{J} \circ \mathcal{A}, \end{aligned} \quad (14)$$

where  $\mathcal{F}_{\mu\nu}^a = \partial_\mu^x \mathcal{A}_\nu^a - \partial_\nu^x \mathcal{A}_\mu^a + g f^{abc} \mathcal{A}_\mu^b \mathcal{A}_\nu^c$ .

(iii) The form of the initial state at  $t = t_0$  as described by the density matrix  $\hat{\rho}$  is embodied in the function  $\mathcal{M}(\hat{\rho})$  which is the density-matrix element of the gauge fields at initial time  $t_0$ ,

$$\mathcal{M}(\hat{\rho}) = \langle \mathcal{A}^+(t_0) | \hat{\rho} | \mathcal{A}^-(t_0) \rangle \equiv \exp(i \mathcal{K}[\mathcal{A}]) , \quad (15)$$

where  $\mathcal{A}^\pm$  refers to the  $+$  and  $-$  time branch at  $t_0$ , respectively. The functional  $\mathcal{K}$  may be expanded in a series of non-local kernels corresponding to multi-point correlations concentrated at  $t = t_0$ ,

$$\begin{aligned} \mathcal{K}[\mathcal{A}] = & \mathcal{K}^{(0)} + \int_P d^4x \mathcal{K}_{\mu}^{(1)a}(x) \mathcal{A}^{\mu,a}(x) \\ & + \frac{1}{2} \int_P d^4x d^4y \mathcal{K}_{\mu\nu}^{(2)ab}(x,y) \mathcal{A}^{\mu,a}(x) \mathcal{A}^{\nu,b}(y) \dots \end{aligned} \quad (16)$$

Clearly, the sequence of kernels  $\mathcal{K}^{(n)}$  contains as much information as the original density matrix. In the special case that  $\hat{\rho}$  is diagonal, the kernels  $\mathcal{K}^{(n)} = 0$  for all  $n$ , and the usual ‘vacuum field theory’ is recovered.

The path-integral representation (10) can be rewritten in a form more convenient for the following: First, the gauge-fixing functional  $I_{GF}[\hat{n} \cdot \mathcal{A}]$  is implemented by using (12). Second, the series representation (16) is inserted into the initial state functional  $\mathcal{M}(\hat{\rho})$ . Third,  $\mathcal{K}^{(0)}$  is absorbed in the overall normalization  $\mathcal{N}$  of  $Z_P$  (henceforth set to unity), and the external source  $\mathcal{J}$  in the 1-point kernel  $\mathcal{K}^{(1)}$ :

$$\mathcal{K}^{(0)} := i \ln \mathcal{N} , \quad \mathcal{K}^{(1)} := \mathcal{K}^{(1)} + \mathcal{J} . \quad (17)$$

Then (10) becomes,

$$Z_P[\mathcal{J}, \hat{\rho}] \implies Z_P[\mathcal{K}] = \int \mathcal{D}\mathcal{A} \exp \left\{ i \left( I[\mathcal{A}, \mathcal{K}] \right) \right\} , \quad (18)$$

where, instead of (14),

$$I[\mathcal{A}, \mathcal{K}] \equiv I_{YM}[\mathcal{A}] + I_{GF}[\hat{n} \cdot \mathcal{A}] + \mathcal{K}^{(1)} \circ \mathcal{A} + \frac{1}{2} \mathcal{K}^{(2)} \circ (\mathcal{A} \mathcal{A}) + \frac{1}{6} \mathcal{K}^{(3)} \circ (\mathcal{A} \mathcal{A} \mathcal{A}) + \dots \quad (19)$$

### III. SEPARATING SOFT AND HARD DYNAMICS AND THE EQUATIONS OF MOTION

The first step in the strategy is a separation of soft and hard physics in the path-integral formalism with Green functions of both the soft and hard quanta in the presence of the soft classical field is induced by and feeding back to the quantum dynamics. The basic idea to

split up the gauge field  $\mathcal{A}_\mu$  appearing in the classical action  $I_{YM}[\mathcal{A}]$  into a soft (long-range) part  $A_\mu$ , and a hard (short-range) quantum field  $a_\mu$ :

$$\begin{aligned} \mathcal{A}_\mu^a(x) &= \int \frac{d^4k}{(2\pi)^4} e^{+ik \cdot x} \mathcal{A}_\mu^a(k) \theta(\mu - k^0) \\ &+ \int \frac{d^4k}{(2\pi)^4} e^{+ik \cdot x} \mathcal{A}_\mu^a(k) \theta(k^0 - \mu) \equiv A_\mu^a(x) + a_\mu^a(x). \end{aligned} \quad (20)$$

This is the formal definition of the terms ‘soft’ and ‘hard’. The soft and hard physics are separated by a (at this point arbitrary) space-time scale  $\lambda \equiv 1/\mu$ , so that one may associate the soft field  $A_\mu$  being responsible for long range color collective effects, and the hard field  $a_\mu$  embodying the short-range quantum dynamics. Consequently, the field strength tensor receives a soft, a hard part, a mixed contribution,

$$\mathcal{F}_{\mu\nu}^a(x) \equiv \left( F_{\mu\nu}^a[A] + f_{\mu\nu}^a[a] + \phi_{\mu\nu}^a[A, a] \right)(x). \quad (21)$$

Now comes physics input. Consider the following *physics scenario*: The initial state is a (dilute) ensemble of hard gluons of very small spatial extent  $\ll \lambda$ , corresponding to transverse momenta  $k_\perp^2 \gg \mu^2$ . By definition of  $\lambda$ , or  $\mu$ , the short-range character of these quantum fluctuations implies that the expectation value  $\langle a_\mu \rangle$  vanishes at all times. However, the long-range correlations of the eventually populated soft modes with very small momenta  $k_\perp^2 \ll \mu^2$  may lead to a collective mean field with non-vanishing  $\langle A \rangle$ . Accordingly, the following condition on the expectation values of the fields is imposed:

$$\langle A_\mu^a(x) \rangle \begin{cases} = 0 & \text{for } t \leq t_0 \\ \geq 0 & \text{for } t > t_0 \end{cases} \quad \langle a_\mu^a(x) \rangle \stackrel{!}{=} 0 \quad \text{for all } t. \quad (22)$$

Furthermore, for simplicity the quantum fluctuations of the soft field are ignored, assuming any multi-point correlations of soft fields to be small,

$$\langle A_{\mu_1}^{a_1}(x_1) \dots A_{\mu_n}^{a_n}(x_n) \rangle \ll \langle A_{\mu_1}^{a_1}(x_1) \rangle \dots \langle A_{\mu_n}^{a_n}(x_n) \rangle, \quad (23)$$

i.e. take  $A_\mu$  as a non-propagating and non-fluctuating, classical field.

When quantizing this decomposed theory by writing down the appropriate *in-in* amplitude  $Z_P$ , one must be consistent with the gauge field decomposition (20) into soft and hard components and with the classical character of the former.  $M_\mu^{(1)} = 0$ ,  $M_{\mu\nu}^{(2)} \geq 0$ . That is, I restrict in the following to a class of non-equilibrium initial states of Gaussian form (i.e. quadratic in the  $a_\mu$  fields) and do not consider possible linear force terms.

Substituting the soft-hard mode decomposition (20) with the condition (22) into (18), the functional integral of the *in-in* amplitude (18) becomes:

$$Z_P[\mathcal{K}] = \int \mathcal{D}A \mathcal{D}a \exp \left\{ i \left( I[A] + I[a] + I[A, a] \right) \right\}, \quad (24)$$

with a soft, hard, and mixed contribution, respectively [5].

Introducing the *connected* generating functional for the *connected* Green functions, denoted by  $\mathcal{G}^{(n)}$ ,

$$W_P[\mathcal{K}] = -i \ln Z_P[\mathcal{K}] , \quad (25)$$

from which one obtains the *connected* Green functions  $\mathcal{G}^{(n)}$  by functional differentiation, in terms of mixed products of  $a_\mu$  and  $A_\mu$  fields

$$(-i) \mathcal{G}^{(n) a_1 \dots a_n}_{\mu_1 \dots \mu_n}(x_1, \dots, x_n) \equiv \frac{\delta}{i \delta \mathcal{K}^{(n)}} W_P[\mathcal{K}] \Big|_{\mathcal{K}=0} , \quad (26)$$

where the superscript (c) indicates the ‘connected parts’. Specifically, one finds

$$\begin{aligned} \mathcal{G}^{(1) a}_{\mu}(x) &= \langle A_{\mu}^a(x) \rangle_P^{(c)} \equiv \bar{A}_{\mu}^a(x) \\ \mathcal{G}^{(2) ab}_{\mu\nu}(x, y) &= \langle a_{\mu}^a(x) a_{\nu}^b(y) \rangle_P^{(c)} \equiv i \hat{\Delta}_{\mu\nu}^{ab}(x, y) . \end{aligned} \quad (27)$$

These relations define the soft mean field  $\bar{A}$  and the hard propagators  $\hat{\Delta}$ .

The equations of motions for  $\bar{A}$  and  $\hat{\Delta}$  follow now as in usual field theory by functional differentiation of the effective action,

$$\Gamma_P[\bar{A}, \hat{\Delta}] = W_P[\mathcal{K}] - \mathcal{K}^{(1)} \circ \bar{A} - \frac{1}{2} \mathcal{K}^{(2)} \circ (i \hat{\Delta} + \bar{A}^2) . \quad (28)$$

Note that the main approximation at this point is the truncation of the infinite hierarchy of equations for the  $n$ -point Green functions of the exact theory, to the 1-point function (the soft mean field  $\bar{A}(x)$ ) and the 2-point function (the hard propagator  $\hat{\Delta}(x, y)$ ), with all higher-point functions being combinations of these and connected by the 3-gluon and 4-gluon vertices.

### A. Yang-Mills equation for the ‘soft’ mean field

The equation of motion for the soft field  $\bar{A}_{\mu}^a(x)$ , is given by  $\delta \Gamma_P / \delta \bar{A} = -\mathcal{K}^{(1)} - \mathcal{K}^{(2)} \circ \bar{A}$ , from which one obtains, upon taking into account the initial condition  $\mathcal{K}^{(1)} = 0$ , the *Yang-Mills equation for  $\bar{A}$* :

$$\left[ \bar{D}^{\lambda, ab}, \bar{F}_{\lambda\mu}^b \right] (x) = -\hat{j}_{\mu}^a(x) - \int_P d^4 y \mathcal{K}_{\mu\lambda}^{(2)ab}(x, y) \bar{A}^{\lambda, b}(y) , \quad (29)$$

where  $[\bar{D}, \bar{F}] = \bar{D} \bar{F} - \bar{F} \bar{D}$  with the covariant derivative defined as  $\bar{D}^{\lambda} \equiv D^{\lambda}[\bar{A}] = \partial_x^{\lambda} - ig \bar{A}^{\lambda}$ , and  $\bar{F}_{\lambda\mu} \equiv F_{\lambda\mu}[\bar{A}] = [\bar{D}_{\lambda}, \bar{D}_{\mu}] / (-ig)$ . The left hand side of (29) may be written as

$$\left[ \bar{D}^{\lambda, ab}, \bar{F}_{\lambda\mu}^b \right] (x) = \mathcal{D}_{(0) \mu\nu}^{-1 ab} \bar{A}^{\lambda, b}(x) + \bar{\Xi}_{\mu}^a(x) \quad (30)$$

$$\mathcal{D}_{(0) \mu\nu}^{-1 ab} \equiv \delta^{ab} \left( g_{\mu\lambda} \partial_x^2 - \partial_{\mu}^x \partial_{\lambda}^x - \hat{n}_{\mu} \hat{n}_{\lambda} \right) , \quad (31)$$

where, upon taking into account the gauge constraint (11), the  $-\hat{n}_{\mu} \hat{n}_{\lambda} \bar{A}^{\lambda}$  does not contribute, because  $0 = \langle \hat{n} \cdot A \rangle = \hat{n}^{\nu} \bar{A}_{\nu}$ , and where



$$\bar{\Xi}_\mu^a(x) = \bar{\Xi}_{(1)\mu}^a(x) + \bar{\Xi}_{(2)\mu}^a(x) \quad (32)$$

$$\bar{\Xi}_{(1)\mu}^a(x) = -\frac{g}{2} \int_P \prod_{i=1}^2 d^4 x_i V_{(0)\mu\nu\lambda}^{abc}(x, x_1, x_2) \bar{A}^{\nu,b}(x_1) \bar{A}^{\lambda,c}(x_2) \quad (33)$$

$$\begin{aligned} \bar{\Xi}_{(2)\mu}^a(x) = & + \frac{ig^2}{6} \int_P \prod_{i=1}^3 d^4 x_i W_{(0)\mu\nu\lambda\sigma}^{abcd}(x, x_1, x_2, x_3) \\ & \times \bar{A}^{\nu,b}(x_1) \bar{A}^{\lambda,c}(x_2) \bar{A}^{\sigma,d}(x_3). \end{aligned} \quad (34)$$

On the right hand side of (29), the current  $\hat{j}$  is the *induced current* due to the ‘hard’ quantum dynamics in the presence of the ‘soft’ field  $\bar{A}$ :

$$\hat{j}_\mu^a(x) = \hat{j}_{(1)\mu}^a(x) + \hat{j}_{(2)\mu}^a(x) + \hat{j}_{(3)\mu}^a(x) \quad (35)$$

$$\hat{j}_{(1)\mu}^a(x) = -\frac{ig}{2} \int_P \prod_{i=1}^2 d^4 x_i V_{(0)\mu\nu\lambda}^{abc}(x, x_1, x_2) \hat{\Delta}^{\nu\lambda,bc}(x_1, x_2) \quad (36)$$

$$\begin{aligned} \hat{j}_{(2)\mu}^a(x) = & -\frac{g^2}{2} \int_P \prod_{i=1}^3 d^4 x_i W_{(0)\mu\nu\lambda\sigma}^{abcd}(x, x_1, x_2, x_3) \\ & \times \bar{A}^{\nu,b}(x_1) \hat{\Delta}^{\lambda\sigma,cd}(x_2, x_3) \end{aligned} \quad (37)$$

$$\begin{aligned} \hat{j}_{(3)\mu}^a(x) = & -\frac{ig^3}{6} \int_P \prod_{i=1}^3 d^4 x_i d^4 y_i W_{(0)\mu\nu\lambda\sigma}^{abcd}(x, x_1, x_2, x_3) \hat{\Delta}^{\nu\nu',bb'}(x_1, y_1) \\ & \times \hat{\Delta}^{\lambda\lambda',cc'}(x_2, y_2) \hat{\Delta}^{\sigma\sigma',dd'}(x_3, y_3) V_{(0)\mu'\nu'\lambda'\sigma'}^{abcd}(y_1, y_2, y_3). \end{aligned} \quad (38)$$

Finally, the second term on the right side of (29) is the initial state contribution to the current, which vanishes for  $t = x^0 > t_0$ .

Notice that the function  $\bar{\Xi}$  on the left hand side of (29) contains the non-linear self-coupling of the soft field  $\bar{A}$  alone, whereas the induced current  $\hat{j}$  on the right hand side is determined by the hard propagator  $\hat{\Delta}$ , thereby generating the soft field.

## B. Dyson-Schwinger equation for the ‘hard’ Green function

The equation of motion for the ‘hard’ propagator,  $\hat{\Delta}_{\mu\nu}^{ab}(x, y)$ , is  $\delta\Gamma_P/\delta\hat{\Delta} = \mathcal{K}^{(2)}/(2i)$ , from which one finds after incorporating the initial condition  $\mathcal{K}^{(1)} = 0$ , the *Dyson-Schwinger equation for  $\hat{\Delta}$* :

$$\left[ \left(\hat{\Delta}_{\mu\nu}^{ab}\right)^{-1} - \left(\Delta_{(0)\mu\nu}^{ab}\right)^{-1} + \bar{\Pi}_{\mu\nu}^{ab} + \hat{\Pi}_{\mu\nu}^{ab} \right] (x, y) = \mathcal{K}_{\mu\nu}^{(2)ab}(x, y), \quad (39)$$

where  $\hat{\Delta} \equiv \hat{\Delta}_{[\bar{A}]}$  is the *fully dressed propagator* of the ‘hard’ quantum fluctuations in the presence of the ‘soft’ mean field, whereas  $\Delta_{(0)}$  is the *free propagator*. The polarization tensor  $\Pi$  has been decomposed in two parts, a mean-field part, and a quantum fluctuation part. The *mean-field polarization tensor*  $\bar{\Pi}$  incorporates the *local* interaction between the ‘hard’ quanta and the ‘soft’ mean field,

$$\bar{\Pi}_{\mu\nu}^{ab}(x, y) = \bar{\Pi}_{(1)\mu\nu}^{ab}(x, y) + \bar{\Pi}_{(2)\mu\nu}^{ab}(x, y) \quad (40)$$

$$\bar{\Pi}_{(1)\mu\nu}^{ab}(x, y) = \frac{ig}{2} \delta_P^4(x, y) \int_P d^4z V_{(0)\mu\nu\lambda}^{abc}(x, y, z) \bar{A}^{\lambda,c}(z) \quad (41)$$

$$\begin{aligned} \bar{\Pi}_{(2)\mu\nu}^{ab}(x, y) = \frac{g^2}{6} \delta_P^4(x, y) \int_P d^4z d^4w W_{(0)\mu\nu\lambda\sigma}^{abcd}(x, y, z, w) \\ \times \bar{A}^{\lambda,c}(z) \bar{A}^{\sigma,d}(w). \end{aligned} \quad (42)$$

plus terms of order  $g^3 \bar{A}^3$  which one may safely ignore within the present approximation scheme. The *fluctuation polarization tensor*  $\hat{\Pi}$  contains the quantum self-interaction among the ‘hard’ quanta in the presence of  $\bar{A}$ , and is given by the variation of 2-loop part  $\Gamma_P^{(2)}$ , of the effective action,  $2i\delta\Gamma_P^{(2)}/\delta\hat{\Delta}$ ,

$$\hat{\Pi}_{\mu\nu}^{ab}(x, y) = \left( \hat{\Pi}_{(1)} + \hat{\Pi}_{(2)} + \hat{\Pi}_{(3)} + \hat{\Pi}_{(4)} \right)_{\mu\nu}^{ab}(x, y), \quad (43)$$

$$\hat{\Pi}_{(1)\mu\nu}^{ab}(x, y) = -\frac{g^2}{2} \int_P d^4x_1 d^4y_1 W_{(0)\mu\nu\lambda\sigma}^{abcd}(x, y, x_1, y_1) \hat{\Delta}^{\lambda\sigma, cd}(y_1, x_1) \quad (44)$$

$$\begin{aligned} \hat{\Pi}_{(2)\mu\nu}^{ab}(x, y) = -\frac{ig^2}{2} \int_P \prod_{i=1}^2 d^4x_i d^4y_i V_{(0)\mu\lambda\sigma}^{acd}(x, x_1, x_2) \\ \times \hat{\Delta}^{\lambda\lambda', cc'}(x_1, y_1) \hat{\Delta}^{\sigma\sigma', dd'}(x_2, y_2) \hat{V}_{\sigma'\lambda'\nu}^{d'c'b}(y_2, y_1, y) \end{aligned} \quad (45)$$

$$\begin{aligned} \hat{\Pi}_{(3)\mu\nu}^{ab}(x, y) = -\frac{g^4}{6} \int_P \prod_{i=1}^3 d^4x_i d^4y_i W_{(0)\mu\lambda\sigma\tau}^{acde}(x, x_1, x_2, x_3) \\ \times \hat{\Delta}^{\lambda\lambda', cc'}(x_1, y_1) \hat{\Delta}^{\sigma\sigma', dd'}(x_2, y_2) \\ \times \hat{\Delta}^{\tau\tau', ee'}(x_3, y_3) \widehat{W}_{\tau'\sigma'\lambda'\nu}^{e'd'c'b}(y_3, y_2, y_1, y) \end{aligned} \quad (46)$$

$$\begin{aligned} \hat{\Pi}_{(4)\mu\nu}^{ab}(x, y) = -\frac{ig^4}{24} \int_P \prod_{i=1}^2 d^4x_i d^4y_i d^4z_i W_{(0)\mu\lambda\sigma\tau}^{acde}(x, x_1, x_2, x_3) \\ \times \hat{\Delta}^{\sigma\rho', df'}(x_2, z_2) \hat{\Delta}^{\tau\rho'', ef''}(x_3, z_3) \hat{V}_{\rho''\rho'\rho}^{f''f'f}(z_3, z_2, z_1) \\ \times \hat{\Delta}^{\rho\lambda', fc'}(z_1, y_1) \hat{\Delta}^{\lambda\sigma', cd'}(x_1, y_2) \hat{V}_{\lambda'\sigma'}^{c'd'}(y_1, y_2, y). \end{aligned} \quad (47)$$

Note that the usual Dyson-Schwinger equation in *vacuum* is contained in (39) -(47) as the special case when the mean field vanishes,  $\bar{A}(x) = 0$ , and initial state correlations are absent,  $\mathcal{K}^{(2)}(x, y) = 0$ . In this case, the propagator becomes the usual vacuum propagator, since the mean-field contribution  $\bar{\Pi}$  is identically zero, and the quantum part  $\hat{\Pi}$  reduces to the vacuum contribution.

#### IV. TRANSITION TO QANTUM KINETICS

The equations of motion (29) and (39) are non-linear integro-differential equations and clearly not solvable in all their generality. To make progress, one must be more specific and employ now the details of the proclaimed physics scenario, described above.

## A. Quantum and kinetic space-time regimes

The key assumption is the separability of hard and soft dynamics in terms of the space-time scale  $r(\mu) \propto 1/\mu \approx 1 \text{ fm}$ . This implies that one may characterize the dynamical evolution of the gluon system by a short-range *quantum scale*  $r_{qua} \ll r(\mu)$ , and a comparably long-range *kinetic scale*  $r_{kin} \gtrsim r(\mu)$ . Low-momentum collective excitations that may develop at the particular momentum scale  $g\mu$  are thus well separated from the typical hard gluon momenta of the order  $\mu$ , if  $g \ll 1$ . Therefore, collectivity can arise, because the wavelength of the soft oscillations  $\sim 1/g\mu$  is much larger than the typical extension of the hard quantum fluctuations  $\sim 1/\mu$ . Notice that this separation of scales is not an academic construction, but rather is a general property of quantum field theory. A simple example is a freely propagating electron: In this case, the quantum scale is given its the Compton wavelength  $\sim 1/m_e$  in the restframe of the charge, and measures the size of the radiative vacuum polarization cloud around the bare charge. The kinetic scale, on the other hand, is determined by the mean-free-path of the charge, which is infinite in vacuum, and in medium is inversely proportional to the local density times the interaction cross-section,  $\sim 1/(n_g \sigma_{int})$ . Adopting this notion to the present case of gluon dynamics, let me define  $r_{qua}$  and  $r_{kin}$  as follows:

**quantum scale  $r_{qua}$ :** Measures the spatial extension of quantum fluctuations associated with virtual and real radiative emission and re-absorption off a given hard gluon, described by the hard propagator  $\hat{\Delta}$ . It can thus be interpreted as its Compton wavelength, corresponding to the typical transverse extension of the fluctuations and thus inversely proportional to the average transverse momentum,

$$r_{qua} \equiv \hat{\lambda} \simeq \frac{1}{\langle k_{\perp} \rangle}, \quad \langle k_{\perp} \rangle \geq \mu, \quad (48)$$

where the second relation is imposed by means of the definition (20) of hard and soft modes. Note that  $\hat{\lambda}_C$  is a space-time dependent quantity, because the magnitude of  $\langle k_{\perp} \rangle$  is determined by both the radiative self-interactions of the hard gluons and their interactions with the soft field.

**kinetic scale  $r_{kin}$ :** Measures the range of the long-wavelength correlations, described by the soft mean-field  $\bar{A}$ , and may be parametrized in terms of the average momentum of soft modes  $\langle q \rangle$ , such that

$$r_{kin} \equiv \bar{\lambda} \simeq \frac{1}{\langle q_{\perp} \rangle}, \quad \langle q_{\perp} \rangle \lesssim g\mu, \quad (49)$$

where  $\bar{\lambda}$  may vary from one space-time point to another, because the population of soft modes  $\bar{A}(q)$  is determined locally by the hard current  $\hat{j}$  with dominant contribution from gluons with transverse momentum  $\simeq \mu$ .

The above classification of quantum- (kinetic-) scales specifies in space-time the relevant regime for the hard (soft) dynamics, and the separability of the two scales  $r_{qua}$  and  $r_{kin}$  imposes the following condition on the relation between space-time and momentum:

$$\hat{\lambda} \ll \bar{\lambda}, \quad \text{or} \quad \langle k_{\perp} \rangle \approx \mu \gg g\mu \approx \langle q_{\perp} \rangle. \quad (50)$$

The physical interpretation of (50) is simple: At short distances  $r_{qua} \ll 1/(g\mu)$  a hard gluon can be considered as an *incoherent quantum* which emits and partly reabsorbs other hard gluons corresponding to the combination of real bremsstrahlung and virtual radiative fluctuations. Only a hard probe with a short wavelength  $\leq r_{qua}$  can resolve this quantum dynamics. On the other hand, at larger distances  $r_{kin} \approx 1/(g\mu)$ , a gluon appears as a *coherent quasi-particle*, that is, as an extended object with a changing transverse size corresponding to the extent of its intrinsic quantum fluctuations. This dynamical substructure is however not resolvable by long-wavelength modes  $\geq r_{kin}$  of the soft field  $\bar{A}$ .

Accordingly, one may classify the quantum and kinetic regimes, respectively, by associating with two distinct space-time points  $x^{\mu}$  and  $y^{\mu}$  the following characteristic scales:

$$\begin{aligned} s^{\mu} &\equiv x^{\mu} - y^{\mu} \sim \hat{\lambda} = \frac{1}{g\mu}, & \partial_s^{\mu} &= \frac{1}{2} (\partial_x^{\mu} - \partial_y^{\mu}) \sim g\mu \\ r^{\mu} &\equiv \frac{1}{2} (x^{\mu} + y^{\mu}) \sim \bar{\lambda} = \frac{1}{\mu}, & \partial_r^{\mu} &= \partial_x^{\mu} + \partial_y^{\mu} \sim \mu. \end{aligned} \quad (51)$$

The *kinetic scale* is therefore  $g^2\mu^2$ : The effect of the soft field modes of  $\bar{A}$  on the hard quanta involves the coupling  $g\bar{A}$  to the hard propagator and is of the order of the soft wavelength  $\bar{\lambda} = 1/(g\mu)$ , so that one may characterize the soft field strength by

$$g\bar{A}_{\mu}(r) \sim g\mu, \quad g\bar{F}_{\mu\nu}(r) \sim g^2\mu^2, \quad (52)$$

plus corrections of order  $g^2\mu^2$  and  $g^3\mu^3$ , respectively, which are assumed to be small.

The *quantum scale* on the other hand is  $\mu^2$ , because

$$\hat{\Delta}_{\mu\nu}^{-1} \sim k_{\perp}^2 \gtrsim \mu^2 \gg g^2\mu^2 \sim g\bar{F}_{\mu\nu}, \quad (53)$$

and one expects that that the short-distance fluctuations corresponding to emission and reabsorption of gluons with momenta  $k_{\perp} \geq \mu$ , are little affected by the long-range, soft mean field, because the color force  $\sim g\bar{F}$  acting on a gluon with momentum  $k_{\perp} \sim \mu$  produces only a very small change in its momentum.

Concerning the Yang-Mills equation (29), one finds then immediately from the above scale relations that both the derivative terms  $\partial^2\bar{A}$  and the self-coupling terms  $\bar{\Xi}$  are of the same order and need to be included consistently in order to preserve the gauge symmetry when performing a perturbative analysis. Of course, if the field is weak,  $\bar{F}_{\mu\nu} \ll g\mu^2$ , the nonlinear effects contained in the function  $\bar{\Xi}$  of (29) are be subdominant, so that in leading order of  $g$ , the color fields would then behave like abelian fields.

## B. The kinetic approximation

The realization of the two space-time scales, short-distance quantum and quasi-classical kinetic, allows to reformulate the quantum field theoretical problem as a relativistic many-body problem within kinetic theory. The key element is to establish the connection between the preceding quantum-theoretical description in terms of Green functions and a probabilistic

kinetic description in terms of so-called Wigner functions [8]. Whereas the 2-point functions, such as the propagator or the polarization tensor, depend on two separate space-time points  $x$  and  $y$ , their Wigner transform utilizes a mixed space-time/momentum representation, which is particularly convenient for implementing the assumption of well separated quantum and kinetic scales, i.e., that the long-wavelength field  $\bar{A}$  is slowly varying in space-time on the scale of short-range quantum fluctuations. Moreover, the trace of the Wigner transformed propagator is the quantum analogue of the single particle phase-space distribution of gluons, and therefore provides the basic quantity to make the connection with kinetic theory of multi-particle dynamics.

In terms of the center-of-mass coordinate,  $r = \frac{1}{2}(x+y)$ , and relative coordinate  $s = x-y$ , of two space-time points  $x$  and  $y$ , eq. (51), one can express any 2-point function  $\mathcal{G}(x, y)$ , such as  $\hat{\Delta}, \Pi$ , in terms of these coordinates,

$$\mathcal{G}_{\mu\nu}^{ab}(x, y) = \mathcal{G}_{\mu\nu}^{ab}\left(r + \frac{s}{2}, r - \frac{s}{2}\right) \equiv \mathcal{G}_{\mu\nu}^{ab}(r, s), \quad (54)$$

The *Wigner transform*  $\mathcal{G}(r, k)$  is then defined as the Fourier transform with respect to the relative coordinate  $s$ , being the canonical conjugate to the momentum  $k$ . In general, the necessary preservation of local gauge symmetry leads to additional constraint, but for the specific choice of gauge (11), the Wigner transform is simply

$$\mathcal{G}(r, s) = \int \frac{d^4 k}{(2\pi)^4} e^{-ik \cdot s} \mathcal{G}(r, k), \quad \mathcal{G}(r, k) = \int d^4 s e^{ik \cdot s} \mathcal{G}(r, s). \quad (55)$$

The Wigner representation (55) will facilitate a systematic identification of the dominant contributions of the soft field  $\bar{A}$  to the hard propagator  $\hat{\Delta}$ : First one expands both  $\bar{A}$  and  $\hat{\Delta}_{[\bar{A}]}$  in terms of the long-range variation with the kinetic scale  $r$  (gradient expansion), then one makes an additional expansion in powers of the soft field  $\bar{A}$  and of the induced perturbations  $\hat{\Delta}_{[\bar{A}]} \sim g \hat{\Delta}_{[0]}$ . On this basis, one isolates and keep consistently terms up to order  $g^2 \mu^2 \hat{\Delta}_{[0]}$ .

To proceed, recall that the coordinate  $r^\mu$  describes the kinetic space-time dependence  $O(\Delta r_{kin})$ , whereas  $s$  measures the quantum space-time distance  $O(\Delta r_{qua})$ . In translational invariant situations, e.g. in vacuum or thermal equilibrium,  $W(r, s)$  is independent of  $r^\mu$  and sharply peaked about  $s^\mu = 0$ . Here the range of the variation is fixed by  $\hat{\lambda} = 1/\mu$ , eq. (48), corresponding to the confinement length  $\approx 0.3 \text{ fm}$  in the case of vacuum, or to the thermal wavelength  $\approx 1/T$  in equilibrium. On the other hand, in the presence of a slowly varying soft field  $\bar{A}$  with a wavelength  $\bar{\lambda} = 1/(g\mu)$ , eq. (49), the  $s^\mu$  dependence is little affected, while the acquired  $r^\mu$  dependence will have a long-wavelength variation. This suggests therefore to neglect the derivatives of  $\mathcal{G}(r, k)$  with respect to  $r^\mu$  of order  $g\mu$ , relative to those with respect to  $s^\mu$  of order  $\mu$ .

Hence one can perform an expansion of the soft field and the hard propagator and polarization tensor in terms of gradients, and keep only terms up to first order, i.e.,

$$\begin{aligned} \bar{A}_\mu(x) &= \bar{A}_\mu\left(r + \frac{s}{2}\right) \simeq \bar{A}_\mu(r) + \frac{s}{2} \cdot \partial_r \bar{A}_\mu(r) \\ \bar{A}_\mu(y) &= \bar{A}_\mu\left(r - \frac{s}{2}\right) \simeq \bar{A}_\mu(r) - \frac{s}{2} \cdot \partial_r \bar{A}_\mu(r) \\ \Delta_{(0)\mu\nu}(x, y) &= \Delta_{(0)\mu\nu}(0, s) \end{aligned}$$

$$\begin{aligned}
\widehat{\Delta}_{\mu\nu}(x, y) &= \widehat{\Delta}_{\mu\nu}(r, s) \simeq \widehat{\Delta}_{\mu\nu}(0, s) + s \cdot \partial_r \widehat{\Delta}_{\mu\nu}(r, s) \\
\overline{\Pi}_{\mu\nu}(x, x) &= \overline{\Pi}_{\mu\nu}(r) + \frac{s}{2} \cdot \partial_r \overline{\Pi}_{\mu\nu}(r) \\
\widehat{\Pi}_{\mu\nu}(x, y) &= \widehat{\Pi}_{\mu\nu}(r, s) \simeq \widehat{\Pi}_{\mu\nu}(0, s) + s \cdot \partial_r \widehat{\Pi}_{\mu\nu}(r, s) ,
\end{aligned} \tag{56}$$

and furthermore, in order to isolate the leading effects of the soft mean field  $\overline{A}$  on the hard quantum propagator  $\widehat{\Delta}$ , one separates the mean field contribution from the quantum contribution by writing

$$\widehat{\Delta}(r, k) \equiv \widehat{\Delta}_{[\overline{A}]}(r, k) = \widehat{\Delta}_{[\emptyset]}(k) + \delta\widehat{\Delta}_{[\overline{A}]}(r, k) \tag{57}$$

with a translation-invariant vacuum quantum contribution and a  $r$ -dependent mean field part, respectively,

$$\widehat{\Delta}_{[\emptyset]}^{-1} = \widehat{\Delta}^{-1}|_{\overline{A}=0} = \Delta_{(0)}^{-1} - \widehat{\Pi}|_{\overline{A}=0} \qquad \delta\widehat{\Delta}_{[\overline{A}]}^{-1} = \overline{\Delta}^{-1} - \Delta_{(0)}^{-1} = -\overline{\Pi} . \tag{58}$$

where  $\Delta_{(0)}$  denotes the *free* propagator, and the  $\overline{\Delta}$  the mean-field propagator, that is, the free propagator in the presence of the mean field, but in the absence of quantum fluctuations.

Given the ansatz (57), with the feedback of the induced soft field to the hard propagator being contained in  $\delta\widehat{\Delta}_{[\overline{A}]}$ , one can expand the latter in powers of the soft field coupling  $g\overline{A}$ , and anticipate that it is *at most  $g$  times* the vacuum piece  $\widehat{\Delta}_{[\emptyset]}$ , that is,

$$\delta\widehat{\Delta}_{[\overline{A}]}(r, k) = \sum_{n=1, \infty} \frac{1}{n!} (g\overline{A}(r) \cdot \partial_k)^n \widehat{\Delta}_{[\emptyset]}(k) \simeq g\overline{A}(r) \cdot \partial_k \widehat{\Delta}_{[\emptyset]}(k) , \tag{59}$$

and, to the same order of approximation,  $\partial_r^\mu \delta\widehat{\Delta}_{[\overline{A}]}{}_{\mu\nu}(r, k) \simeq g(\partial_r^\mu \overline{A}^\lambda) \partial_k^\lambda \widehat{\Delta}_{[\emptyset]}{}_{\mu\nu}$ .

Inserting now into eqs. (29) and (39) the decomposition (57) with the approximation (59), and keeping consistently all terms up to order  $g^2\mu^2\widehat{\Delta}_{[\emptyset]}$ , one arrives (after quite some journey [5]) at a set of equations that can be compactly expressed in terms of the *kinetic* momentum  $K_\mu$  rather than the *canonical* momentum  $k_\mu$  (as always in the context of interactions with a gauge field). For the class of gauges gauge (13) amounts to the replacements

$$k_\mu \longrightarrow K_\mu = k_\mu - g\overline{A}_\mu(r) , \qquad \partial_\mu^r \longrightarrow \overline{D}_\mu^r = \partial_\mu^r - g\partial_\mu^r \overline{A}^\nu(r) \partial_\nu^k . \tag{60}$$

and, within the present approximation scheme, one has  $K^2\widehat{\Delta} \gg \overline{D}_r^2\widehat{\Delta}$ . The result of this procedure is:

$$\begin{aligned}
\left[ \overline{D}_r^\lambda, \overline{F}_{\lambda\mu}^b \right] (r) &= -\widehat{j}_\mu(r) \\
&= -g \int \frac{d^4 K}{(2\pi)^2} \text{Tr} \left\{ -K_\mu \widehat{\Delta}_{[\overline{A}]}{}^\nu{}_\nu(r, K) + \widehat{\Delta}_{[\overline{A}]}{}^\nu{}_\mu(r, K) K_\nu \right\}
\end{aligned} \tag{61}$$

$$\left\{ K^2, \widehat{\Delta}_{[\emptyset]}^{\mu\nu} \right\} (K) = d^{\mu\nu}(K) + \frac{1}{2} \left\{ \widehat{\Pi}_{[\emptyset]}{}^\mu{}_\sigma(K), \widehat{\Delta}_{[\emptyset]}^{\sigma\nu}(K) \right\} \tag{62}$$

$$\begin{aligned}
\left[ K \cdot \overline{D}_r, \widehat{\Delta}_{[\overline{A}]}^{\mu\nu} \right] (r, K) &= -\frac{i}{2} \left[ \overline{\Pi}_\sigma^\mu(r, K), \widehat{\Delta}_{[\emptyset]}^{\sigma\nu}(K) \right] \\
&\quad - \frac{i}{2} \left[ \widehat{\Pi}_{[\emptyset]}{}^\mu{}_\sigma(K), \widehat{\Delta}_{[\emptyset]}^{\sigma\nu}(K) \right] .
\end{aligned} \tag{63}$$

One sees that the original Dyson-Schwinger equation reduces in the kinetic approximation to a coupled set of algebraic equations. Recall that (62) and (63) are still  $2 \times 2$  matrix equations mix the four different components of  $\hat{\Delta} = (\hat{\Delta}^F, \hat{\Delta}^>, \hat{\Delta}^<, \hat{\Delta}^{\bar{F}})$  and of  $\hat{\Pi} = (\hat{\Pi}^F, \hat{\Pi}^>, \hat{\Pi}^<, \hat{\Pi}^{\bar{F}})$ . For the following it is more convenient to employ instead an equivalent set of independent functions, namely, the *retarded* and *advanced functions*  $\hat{\Delta}^{ret}$ ,  $\hat{\Delta}^{adv}$ , plus the *correlation function*  $\hat{\Delta}^{cor}$ , and analogously  $\hat{\Pi}$ . This latter set is more directly connected with physical, observable quantities, and is commonly referred to as *physical representation* [2]:

$$\hat{\Delta}^{ret} = \hat{\Delta}^F - \hat{\Delta}^> \quad \hat{\Delta}^{adv} = \hat{\Delta}^F - \hat{\Delta}^< \quad \hat{\Delta}^{cor} = \hat{\Delta}^> + \hat{\Delta}^< \quad (64)$$

Similarly, for the polarization tensor the retarded, advanced and correlation functions are defined as (note the subtle difference to (64)):

$$\hat{\Pi}^{ret} = \hat{\Pi}^F + \hat{\Pi}^< \quad \hat{\Pi}^{adv} = \hat{\Pi}^F + \hat{\Pi}^> \quad \hat{\Pi}^{cor} = -\hat{\Pi}^> - \hat{\Pi}^< \quad (65)$$

Loosely speaking, the retarded and advanced functions characterize the intrinsic quantum nature of a ‘dressed’ gluon, describing its substructural state of emitted and reabsorbed gluons, whereas the correlation function describes the kinetic correlations among different such ‘dressed’ gluons. The great advantage [2] of this physical representation is that in general the dependence on the phase-space occupation of gluon states (the local density) is essentially carried by the correlation functions  $\hat{\Delta}^>$ ,  $\hat{\Delta}^<$ , whereas the dependence of the retarded and advanced functions,  $\hat{\Delta}^{ret}$ ,  $\hat{\Delta}^{adv}$ , on the local density is weak. More precisely, the retarded and advanced propagators and the imaginary parts of the self-energies embody the renormalization effects and dissipative quantum dynamics that is associated with short-distance emission and absorption of quantum fluctuations, whereas the correlation function contains both the effect of interactions with the soft mean field and of statistical binary scatterings among the hard gluons. In going over to the physical representation, one arrives at the set of master equations: The Yang-Mills equation (61) reads

$$\left[ \bar{D}_r^\lambda, \bar{F}_{\lambda\mu} \right] = -g \int \frac{d^4k}{(2\pi)^2} \text{Tr} \left\{ \left( -K_\mu \hat{\Delta}_{[\bar{A}]\nu}^{cor} + \hat{\Delta}_{[\bar{A}]\mu}^{cor} K_\nu \right) \right\} \quad (66)$$

and the renormalization (62) and transport equations (63), become [4]

$$\left\{ K^2, \hat{\Delta}_{[\bar{0}]}^{ret} - \hat{\Delta}_{[\bar{0}]}^{adv} \right\}_{\mu\nu} = -\frac{1}{2} \left\{ \mathcal{M}^2, \text{Im} \hat{\Delta}_{[\bar{0}]} \right\}_{\mu\nu} - \frac{1}{2} \left\{ \Gamma, \text{Re} \hat{\Delta}_{[\bar{0}]} \right\}_{\mu\nu} \quad (67)$$

$$\begin{aligned} \left[ K \cdot \bar{D}_r, \hat{\Delta}_{[\bar{A}]}^{cor} \right]_{\mu\nu} &= +\frac{i}{2} \left[ \Pi^{cor}, \text{Re} \hat{\Delta}_{[\bar{0}]} \right]_{\mu\nu} - \frac{1}{4} \left\{ \Pi^{cor}, \text{Im} \hat{\Delta}_{[\bar{0}]} \right\}_{\mu\nu} \\ &+ \frac{i}{2} \left[ \mathcal{M}^2, \hat{\Delta}_{[\bar{0}]}^{cor} \right]_{\mu\nu} - \frac{1}{4} \left\{ \Gamma, \hat{\Delta}_{[\bar{0}]}^{cor} \right\}_{\mu\nu}, \end{aligned} \quad (68)$$

where  $\Pi = \bar{\Pi} + \hat{\Pi}$ , and the real and imaginary components of the polarization tensor are denoted by

$$\mathcal{M}_{\mu\nu}^2 \equiv \text{Re} \Pi_{\mu\nu} = \frac{1}{2} \left( \Pi^{ret} + \Pi^{adv} \right)_{\mu\nu} \quad \Gamma_{\mu\nu} \equiv \text{Im} \Pi_{\mu\nu} = i \left( \Pi^{ret} - \Pi^{adv} \right)_{\mu\nu} \quad (69)$$

Note also, that the real and imaginary components of the Hard propagator are given by the sum and difference of the retarded and advanced contributions, respectively,

$$\text{Re}\hat{\Delta}_{\mu\nu} = \frac{1}{2} (\hat{\Delta}^{ret} + \hat{\Delta}^{adv})_{\mu\nu} \quad \text{Im}\hat{\Delta} = i (\hat{\Delta}^{ret} - \hat{\Delta}^{adv})_{\mu\nu} . \quad (70)$$

The physical significance of the (67) and (68) is the following: Eq. (67) determines the state of a dressed parton with respect to their virtual fluctuations and real emission (absorption) processes, corresponding to the real and imaginary parts of the retarded and advanced self-energies. Eq. (68), on the other hand characterizes the correlations among different dressed parton states, and the self-energies appear here in two distinct ways. The first two terms on the right hand side account for scatterings between quasi-particle states, i.e. dressed partons, whereas the last two terms incorporate the renormalization effects which result from the fact that the dressed partons between collisions do not behave as free particles, but change their dynamical structure due to virtual fluctuations, as well as real emission and absorption of quanta. For this reason  $\Pi_{adv}^{ret}$  is called *radiative* self-energy, and  $\Pi^{cor}$  is termed *collisional* self-energy. It is well known [2], that the imaginary parts of the retarded and advanced Green functions and self-energies are just the spectral density  $\rho = \text{Im}\hat{\Delta}$ , giving the probability for finding an intermediate multi-particle state in the dressed parton, respectively the decay width  $\Gamma$ , describing the dissipation of the dressed parton. The formal solution of (67) and (68) for the spectral density  $\rho$  is

$$\rho(r, k) = \frac{\Gamma}{k^2 - \mathcal{M}^2 + (\Gamma/2)^2} \equiv \rho_{\mathcal{M}^2} + \rho_{\Gamma} , \quad (71)$$

describing the particle density in terms of the finite width  $\Gamma$  and the dynamical ‘mass term’  $\mathcal{M}^2$  (which in the ‘free-field’ case are  $\Gamma = \mathcal{M}^2 = 0$ , corresponding to an on-shell, classically stable particle). On the right hand side of (71), the second form exhibits the physical meaning more suggestively in terms of the ‘wavefunction’-renormalization ( $\rho_{\mathcal{M}^2} = \rho_{\Gamma=0}$ ) due to virtual fluctuations, and the dissipative parts ( $\rho_{\Gamma} = \rho_{\mathcal{M}^2=0}$ ) due to real emission (absorption) processes.

## V. OUTLOOK

What remains to be done is to solve the set of equations (66)-(68) which is the hardest part. For the case of  $\bar{A}_\mu = 0 = \bar{F}_{\mu\nu}$ , this was discussed in Ref. [4]. For the present general case, the coupling between hard gluons ( $\hat{\Delta}$ ) and the soft field ( $\bar{A}$ ), complicates things considerably. A possible iterative scheme of solution, which is currently under study [5], may be as follows:

- a) Specify initial condition in terms of a phase-space density of hard gluons at time  $t = t_0$ . This initial gluon distribution determines  $\hat{\Delta}_{[\bar{0}]}(t = t_0, \vec{r}, k)$ .
- b) Solve the renormalization equation (62) with  $\bar{A}(t_0, \vec{r}) = 0$ , i.e. just as in the case of vacuum [4], except that now  $K = k - g\bar{A}$  contains the soft field. Substitute the resulting form of  $\hat{\Delta}_{[\bar{0}]}^{ret}$  and  $\hat{\Delta}_{[\bar{0}]}^{adv}$  into the transport equation (63) to get the solution for  $\hat{\Delta}_{[\bar{0}]}^{cor}$ .



- c) Insert  $\widehat{\Delta}_{[\partial]}^{cor}$  into the right hand side of the Yang-Mills equation (66), and solve for  $\overline{A}$ .
- d) Repeat from a) but now include the finite contribution from the coupling between  $\widehat{\Delta}_{[\partial]}$  and  $\overline{A}$ .

## REFERENCES

- [1] J. Schwinger, J. Math. Phys. **2**, 407 (1961), L. V. Keldysh, Sov. Phys. JETP **20**, 1018 (1965), L. P. Kadanoff and G. Baym, *Quantum Statistical Mechanics* (Benjamin, New York 1962).
- [2] K. C. Chou, Z.-B. Su, B.-L. Hao, and L. Yu, Phys. Rep. **118**, 1 (1985).
- [3] S. de Groot, W. A. van Leuwen and C. G. van Weert, *Relativistic Kinetic Theory* (North Holland, Amsterdam 1980).
- [4] K. Geiger, Phys. Rev. **D54**, 949 (1996).
- [5] K. Geiger, in preparation.
- [6] G. Leibbrandt, Rev. Mod. Phys. **59**, 1067 (1987).
- [7] A. Bassetto, G. Nardelli and R. Soldati, *Yang-Mills theories in algebraic non-covariant gauges* (World Scientific, Singapore 1991).
- [8] E. P. Wigner, Phys. Rev. **40**, 749 (1932); M. Hillery, R. F. O'Connell, M. O. Scully, and E. P. Wigner, Phys. Rep. **106**, 121 (1984).

# Simulation of Heavy Ion Collisions at $\sqrt{s} = 20\text{-}200$ GeV

D. E. Kahana

*Physics Department, State University of New York  
Stony Brook, NY 11791*

## Abstract

A new hadronic cascade code (LUCIFER) is introduced, for simulation of relativistic heavy ion collisions at CERN energies and up to RHIC. It is based on a simple, experimentally and theoretically motivated picture of  $hh$  interactions. Final state hadrons are produced by decay of intermediate state clusters, or lumps of excited hadronic matter. These are similar to resonances, but have a continuous mass distribution. Clusters are the objects that re-interact in the cascade. Single diffractive dissociation is used to fix the cluster properties. The model has just two parameters:  $\tau_d$ , the decay time of the clusters, and  $\tau_f$  the formation time of the clusters. Comparison is made with recent CERN data in the Pb+Pb system. The first consistent cascade simulation, of  $J/\psi$  production/suppression is presented. It appears likely that a purely hadronic interpretation can be given to recent CERN data on apparently anomalous  $J/\psi$  suppression in Pb+Pb.

## I. INTRODUCTION

The hadronic cascade ARC [1] has been remarkably successful in describing nucleus-nucleus collisions at AGS energies,  $\sqrt{s} = 5.0\text{-}5.4$  GeV/A. Such energies, of course, are very low in comparison to the highest energy considered in this talk, so perhaps one cannot borrow directly from this previous experience. Surely, for example, it must be the eventual aim of any viable simulation at SPS to RHIC energies to include both quark and gluon degrees of freedom explicitly. Such an outcome is in fact being actively pursued here with Klaus Geiger. The program, LUCIFER, considered here is intended to serve as the hadronic component in a mixed hadronic/partonic cascade. Nevertheless, it is of considerable interest to elaborate the hadronic aspects and to push this approach as far as is possible on its own. Even if one accepts what we are being told about RHIC collisions [2], namely that as much as 50% of the energy flow involves semi-hard 'minijets' or the like, there remains half of the total energy in essentially soft QCD processes. The 50% labelled hard presumably also contributes appreciably to low  $p_t$  spectra *via* eventual hadronisation of partons. However energy flow beginning and remaining at low  $p_t$  is by no means all non-interacting, since large multiplicities are also observed for example, in  $pp$  events with no obvious hard scattering. These soft interactions must also be addressed.

In this workshop, Al Mueller [3] has called, as a starting point, for a simulation initialized by instantaneously converting all hadrons into partons. This is after all the Bjorken [4]

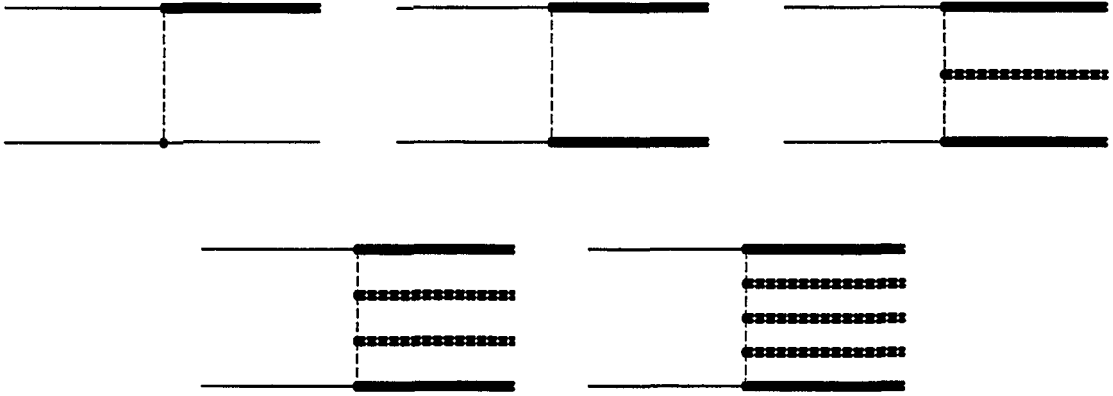


FIG. 1. Underlying cluster model for  $hh$  collisions in LUCIFER. Diagrams represent production of  $N$  intermediate state clusters. Leading clusters always have quantum numbers consistent with the incoming hadrons, *e.g* for a  $pp$  collision they would be baryonic. Internal additional clusters are always mesonic.

approach. It has been carried out in the past [5], and will no doubt continue to be redone in the future [6]. Although, in a RHIC nucleus-nucleus event, the time over which the totality of baryon-baryon collisions takes place is extremely short, nevertheless there may be a very rich structure: multiple coherent soft interactions may take place contemporaneously with incoherent parton cascading. If this structure is ignored it may deny one the chance to produce realistic initial conditions for the ensuing parton cascade. In particular, since the larger RHIC detectors are concentrated heavily on mid-rapidity, one should have an accurate count of the mesons produced there in the absence of interesting high energy-density mechanisms such as plasma, before believing such effects truly are present. It is just at such rapidities that soft processes may produce ambiguities. Despite what has been said in the workshop summaries, what gets to mid-rapidity does not *always* start at mid-rapidity. This is a minimum lesson to learned from what follows here.

The purpose of this presentation is to seek an efficient means of dealing with soft interactions, a means which, unlike strings [8,9], can mesh naturally with the parton cascade already implemented in VNI [10]. There are undoubtedly formidable problems facing a cascade of any sort at ultra high energies, including a partonic cascade, not the least of which may be the relativistic covariance of its output. I will discuss the latter in light of the useful points raised by T. D. Lee [7], and discussions held during the workshop. However a more fundamental difficulty, in my point of view, is to characterise the nature of the soft interactions, the interactions of matter which remains at low  $p_t$ .

## II. PHYSICS OF THE CASCADE

The essential features of the code LUCIFER can be summarised quickly. Basic hadron-hadron interactions are assumed to proceed through the production of intermediate state clusters or lumps of *hadronic* matter (see Fig 1). Clusters then produce the final state hadrons by a sequential decay mechanism, which is not necessarily isotropic. These clusters are the objects which re-interact in the cascade. Two types of cluster are posited, mesonic and baryonic, corresponding to  $(q\bar{q}$  / multi- $g$ ) or  $(qqq)$  valence parton content of the cluster.

Both are imagined to be color singlets, consistent with only a soft interaction having taken place between the incoming hadrons. The interaction cross-section is chosen universally, in the spirit of the additive quark model, to be one of:  $\sigma_{pp}$ ,  $\sigma_{\pi p}$ , or  $\sigma_{\pi\pi}$ , evaluated at the appropriate energy. With that picture in mind we can proceed to a more extensive discussion of the underlying physics.

In the low energy cascade ARC, it had already become apparent that energy-momentum released in the initial nucleon-nucleon collisions re-interacted through resonances and stable hadrons, dominantly the  $\Delta$ ,  $N^*$  and  $\rho$ . Special properties of the particular resonant states involved had apparently little effect on the overall behaviour of the system. Indeed, one could just as well have used a single generic baryon resonance and a single generic meson resonance, both having average widths. The essential point was that energy flow was retained in the resonances, as was required by the proper treatment of relativistic time evolution. This played a central role in ion-ion dynamics at the AGS [1], and indeed led simultaneously to the enhancement of strangeness production and broadening of  $p_t$  spectra which had been initially proposed as signals of plasma formation. For these energies the formation times for produced particles were often included in the resonance lifetimes, which of course for rapidly moving resonances considerably delay the production of pions, and hence reduce their rescattering. Despite dire warnings voiced by detractors, this early approach gives very useful hints on how to proceed at the highest energies. One can also borrow from previous research to justify a possible route to high energy; particularly instructive are the works of Berger and coworkers [11], Quigg and coworkers [12], Beusch *et al.* [13], on the existence of ‘clustering’ in  $pA$  data. This clustering also naturally arises in the multiperipheral models.

Above all, Gottfried, in (1974), put forth a very simple exposition [14] of a scheme for  $pA$  collisions (see Fig. 2), anticipating the approach taken in LUCIFER and ARC by many years, which provides a phenomenological paradigm for extending the cascade to higher energies. Contemporaneously, Koplik and Mueller [15] considered the  $pA$  collisions at high energy, formalising some of Gottfried’s phenomenology within a multiperipheral, Regge-Gribov [16] framework. I present some of this development here, for the moment limited to the context of  $pA$  collisions. This restriction is made, because it is conceptually simpler to track one hadron through a target.

Gottfried noted that although a hadron-nucleon collision within a nucleus cannot immediately produce the final state hadrons one would see in free space, it might still be possible to extrapolate this final state backwards in time and use this information to guide the time evolution of the ‘leading’ hadron through its subsequent collisions with other target nucleons. He proposed that what mattered most for the reinteraction was the flux of energy-momentum through the nucleus. The experimental evidence [14,17] from  $pA$  is that high energy, forward pions, accompanying the leading proton, are suppressed, the pion multiplicity not being enhanced much over  $pp$ . Additionally, only a weak dependence on  $A$  is observed. In LUCIFER, this behaviour is accounted for at least partly by grouping the final particles into clusters, and introducing a formation time  $\tau_f$  for the non-leading clusters. The relativistic dilation  $\gamma\tau_f$  then makes it unlikely for fast produced particles to materialise inside the nucleus, interact, and add to the multiplicity.

Secondary collisions in the target by the leading proton must still be dealt with, and I propose doing this, like Gottfried, essentially by introducing an energy-momentum tensor to describe the energy flux associated with the leading baryon after its first collision. In

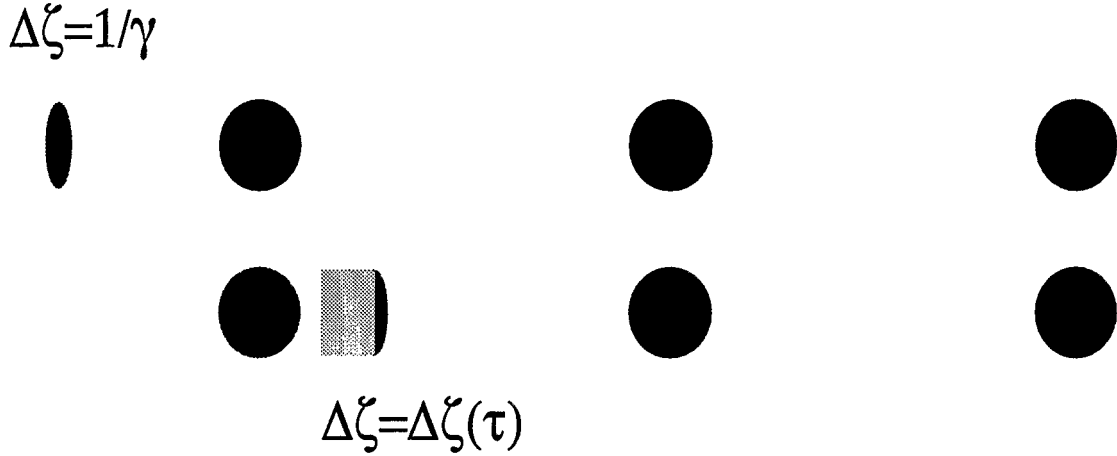


FIG. 2. Gottfried's model for  $pA$  collisions. The incoming proton is Lorentz contracted to size  $\Delta\zeta \sim 1/\gamma$  fm in the lab frame before its first collision. Afterwards its energy density is in an expanding cylinder of length  $\Delta\zeta(t)$ . This model is essentially implemented in LUCIFER by means of cluster production and formation times.

In his picture, the entire energy density is initially contained in the volume occupied by the original incoming proton (a sphere, highly Lorentz contracted longitudinally in the lab frame, so essentially a disk, or cylinder). The real questions now come with ensuing collisions, for which Gottfried enunciated two guidelines:

- (I) *After the initial proton-nucleon collision the incoming (leading) baryon exists in an expanding cylinder, with initial longitudinal width  $\Delta z_0 \sim s^{-1/2} \sim \frac{1}{\gamma}$  fm. This cylinder already contains the expected final produced particles of the  $pp$  collision, though these are as yet unformed. The initial velocities are obtained from the final state rapidity distributions and the cylinder grows by classical propagation of the final particles.*
- (II) *This energy flux scatters from further target nucleons in its path 'as if it were a set of hadrons'  $\{h_i(t)\}$ . The division into separately existing hadrons is made by slicing the cylinder into pieces  $\Delta z_0$ : a first non-leading hadron (meson-like) to be allowed, for example, when the cylinder reaches twice its original width.*

Gottfried [14] terms rule (II) a *universality* hypotheses: a hadronic state occupying the same volume and travelling with the same rapidity as a nucleon or pion, has collisions close in character to those of the corresponding ordinary hadrons. This is precisely the approach taken in LUCIFER and ARC for cluster or resonance cross-sections. The volume occupied, and the nature of constituent partons contained therein, determine the character of the cluster cross-sections. One can also invoke the additive quark model for support of such cross-sections. The detail-insensitivity of the excited hadron-hadron interactions is in keeping with the multi-gluon exchange nature of soft, confining QCD interactions. Those who believe the present approach to be laden with adjustable parameters should study this point very carefully. Rule (II) defines the interaction of an excited nucleon or excited hadron (cluster) very narrowly, making an initial *ad hoc*, but reasonable, hypothesis and thenceforth allowing no further freedom of adjustment.

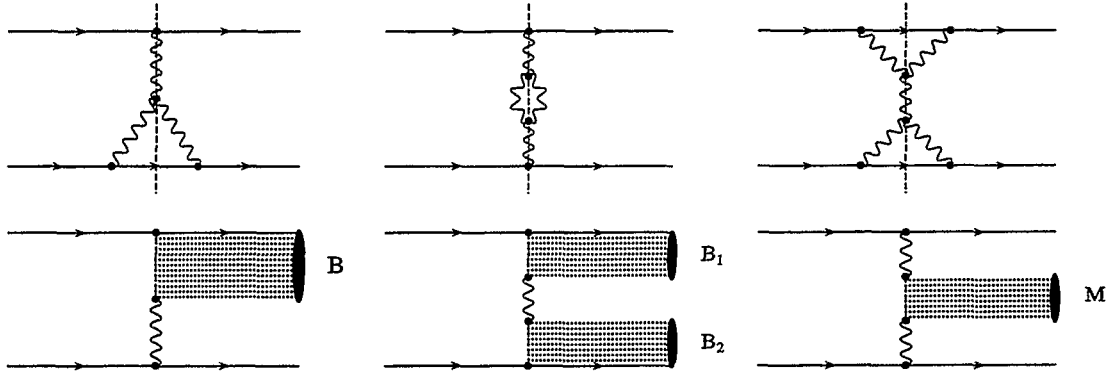


FIG. 3. Pomeron exchange diagrams leading to various types of cluster production in  $pp$  scattering. The cut triple pomeron diagram is prototypical and leads to single diffractive scattering. The forward proton is separated by a rapidity gap from the diffractive baryonic cluster. In LUCIFER, the multiperipheral dynamics is simulated by the decay of the baryonic cluster. Diagrams are shown for double diffractive scattering with the production of a purely mesonic cluster, and for double diffractive dissociation. More general pomeron exchanges lead to the multi-cluster production model used in LUCIFER. The dominant process is taken to be  $pp \rightarrow B_1 + B_2 + M$ .

In Gottfried's model, the energy-momentum tensor was used to decide at what point the flux arising some previous collision should be divided into two parts and so forth. This procedure was then iterated and he was able to obtain a closed analytic treatment of the problem in one dimension. The cascade can do this automatically, producing the set  $h_i(t)$ , and making each constituent available for interaction at the appropriate time. Nor is it restricted to one dimension. Gottfried uses, as do all cascade practitioners, classical motion, rule (I), between collisions. He presents what he calls 'alibis' for this with which we concur, the main excuse being the high energy and short wave lengths involved in the longitudinal motion.

Produced hadrons may begin to reinteract, for high incoming energy, well before they materialise into final state mesons. However, prior to expansion to  $2\Delta z_0$  the energy momentum is retained in the original proton. Extrapolation to further collisions, or for that matter to  $AB$  events is straightforward. LUCIFER incorporates the above principles but adds a cluster model of the  $pp$  intermediate state, introduced to include and build upon existing experimental and theoretical descriptions of  $pp$  scattering. The cluster properties are taken from the data on single diffractive scattering. This can be considered the prototypical soft process.

In constructing LUCIFER then, the following rules are added to (I) and (II):

- (III) *The  $pp$  collision proceeds to the final baryon + meson final state through a choice of excited states depicted in Fig(3). The existence of such new excited entities, both baryonic and mesonic, was suggested, from data, by many authors [11–13]. Beusch [13] cites  $hA$  data at quite low energy ( $\sim 15\text{--}20$  GeV) for  $3\pi$  and even  $5\pi$  clusters which appear to have interacted surprisingly little in the nucleus, perhaps propagating throughout as a compact  $q\bar{q}$  pair.*
- (IV) *The decay of the clusters sequentially, one at a time, into low mass mesons*

produces the final  $pp$  state. The lifetime in the cluster rest frame, is taken as

$$\tau_d = \alpha M_{cl}^{-1} \quad (1)$$

*That is, the highly excited clusters decay rapidly, while the low mass clusters emit final hadrons more slowly.*

To rules (III) and (IV), must be added rules for the longitudinal and transverse phase space and cluster mass distributions. I emphasize that almost all of the apparent freedom in building the model, including of course these distributions, is to be constrained by  $pp$ ,  $p\bar{p}$ , and  $\pi p$  measurements. The only model parameters, at this stage, left to be determined in  $h + A$  collisions concern the time structure of  $pp$ , for example, the cluster formation time  $\tau_f$  and the proportionality constant  $\alpha$ , which at low mass ought to produce a decay time in the range of low mass resonance lifetimes such as  $\tau_\Delta$  or  $\tau_\rho$ . I note that following Gottfried's prescription for the separation of the energy flux obviates to some extent the need for a cluster formation time  $\tau_f$ .

For the cluster mass distributions in LUCIFER is added a fifth rule:

- (V) *The mass distribution of the clusters in Fig 3, whether for simple single diffractive scattering or for multiple cluster production, is taken from theoretical (pomeron exchange) and experimental knowledge of single diffractive scattering. When  $N$  clusters are produced, the **maximum** energy available for internal excitation of any particular cluster is taken to be  $\sqrt{s}/N$ .*

This rule will be expanded upon in the next section.

Much grumbling was directed at the clusters during the workshop, as though very high mass clusters dominated the NN interaction. Nothing could be further from the truth. The spectrum of diffractive cluster masses falls roughly as  $M_{cl}^{-2}$  and high masses are improbable. Most of the action for clusters lies in mass ranges generally attributed to minijets. **Moreover, in actual measurements of single diffractive scattering, by definition and notably a low  $p_t$  process, such high mass objects really are produced.** At least momentarily then, the concomitant high energy densities must exist, and their consequences cannot be ignored or avoided. Possibly, however, since (IV) leads to high  $p_t$  tails for decay of the largest  $M_{cl}$ , the fusion of partonic to hadronic cascades will quickly shunt the energy in the highest masses to the partonic side. Anticipating this eventuality, I have not retained the roughly constant high mass tail seen experimentally in the diffraction dissociation distributions, which are selected below as prototypical of the cluster behaviour, but instead allowed the cluster mass spectrum to be cut off as  $1/M_{cl}^2$ .

One might also relate this modelling to the dual string approaches [8,9]. The energy-momentum flow created at initial proton-proton collisions within a nucleus has been alternatively described as residing in colourless strings. Such a picture however is not easily meshed with partonic cascading and any prescription for reinteracting strings tends to be cumbersome. In the remainder of this article I will detail the specific choices in rapidity and transverse momentum distributions made for  $pp$ , guided by the existing  $pp$  and  $p\bar{p}$  data and theoretical analyses, and first apply this to  $pA$  at FNAL and CERN energies, and then to S+S and Pb+Pb at CERN. Subsequently, some minimal predictions are presented for  $s^{1/2} = 200$ , i.e. at RHIC. It is also tempting to include essentially the first complete

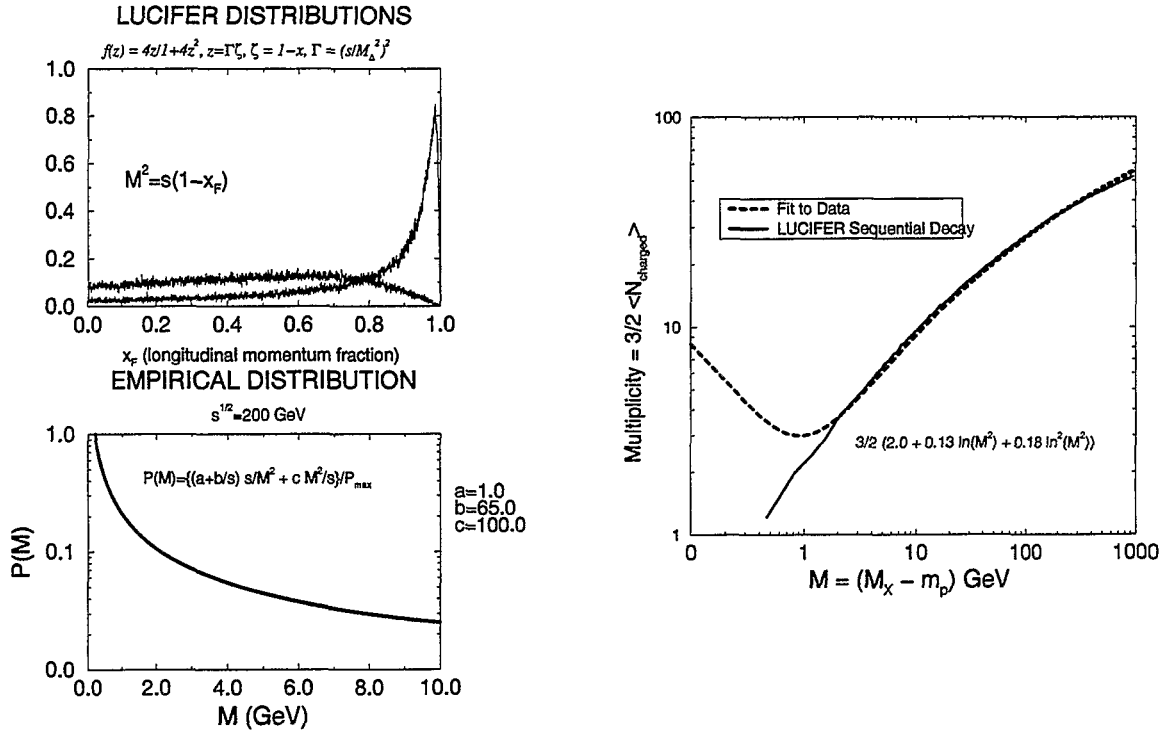


FIG. 4.

(a) Top: Feynman  $x$  distributions for the undisturbed proton in single diffractive scattering:  $x_F$  is related to the diffractive cluster mass by  $M^2 = s(1 - x_F)$ . The distribution falls off rapidly,  $\sim 1/M^2$ , for large cluster masses, and peaks at the  $\Delta$  mass. Bottom: Empirical diffractive cluster mass distribution for  $\sqrt{s} = 200$  GeV. (b) Multiplicity vs mass for diffractive clusters. LUCIFER sequential decay is adjusted to agree with the charge multiplicity in single diffractive  $pp$  scattering.

hadronic cascade estimates of  $J/\psi$  production at CERN energies. The work of Gavin and Vogt [18], based on the Glauber formalism, also relies on only hadronic processes but has no real internal means of calculating the important transverse energy. I also discuss the frame dependence of calculated results for  $pA$  and  $S+S$  at the highest, here RHIC, energies.

### III. NUCLEON-NUCLEON INTERACTION FROM DIFFRACTION

As a first guess I have tried to construct the entire intermediate cluster structure of NN (and for that matter  $hh$ ) from the properties of states observed experimentally in single diffractive scattering, which in our modeling arises from the triple pomeron diagram (Fig. 3). This diagram with appropriate kinematic constraints, produces a final state like that seen in experimental  $hh$  diffractive scattering. Such a method of fixing the cluster properties is not mandated. Any scheme for NN, consistent with the data and not doing violent damage to widely held theoretical concepts, would be acceptable. The parametrisation of  $pp$  and  $\pi p$  data constitute the input to LUCIFER, are fixed by elementary data, and then are frozen.



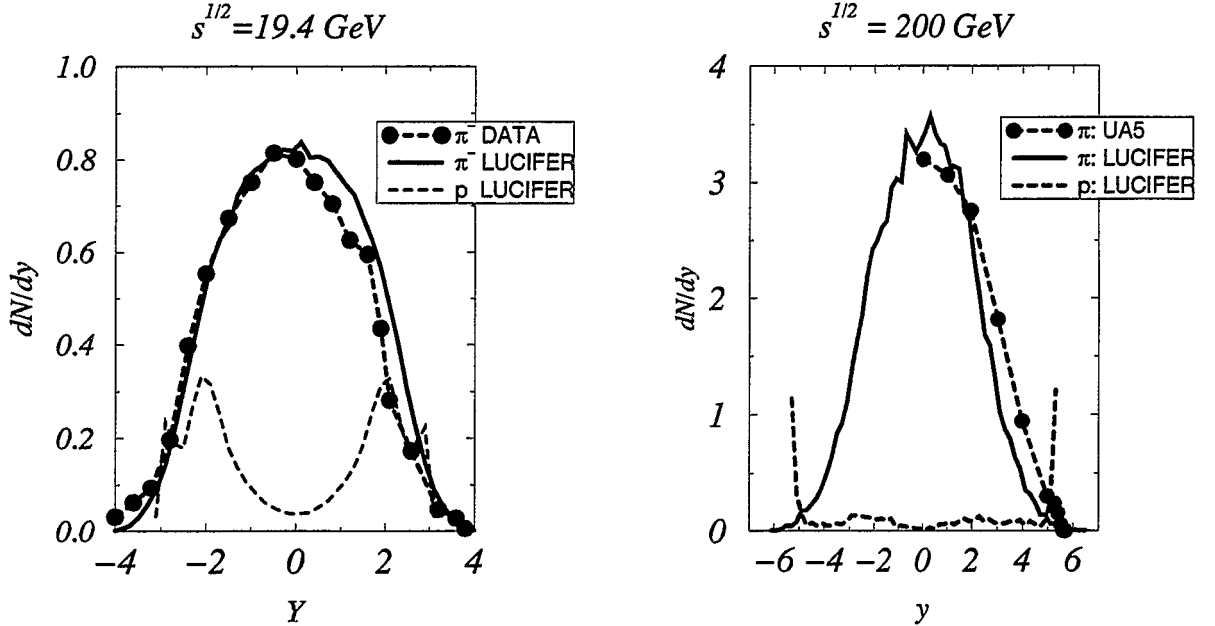


FIG. 5. LUCIFER fits to  $pn$  data from FNAL and  $p\bar{p}$  data from UA5 obtained using the cluster production model. The high energy data is a prediction, using the same model parameters as the low energy data.

The purpose of the cascade is to gain information about the many body system from the two body system. In the process of accomplishing this, data for

$$pp \rightarrow pX, \quad pp \rightarrow \pi X, \quad \pi p \rightarrow \pi X, \quad (2)$$

from  $\sqrt{s} = 20 \rightarrow 900$  GeV and for  $p\bar{p}$  to  $\sqrt{s} = 1.8$  TeV [19–21], are considered.

The experimental [19–22] mass and multiplicity distributions for diffraction are exhibited in Fig 4. Using these measurements the mass distributions for clusters are fixed. The mass distribution may be deduced from the differential cross-section  $d\sigma/dtd(M_x^2)$  for the diffractive process  $pp \rightarrow pX$ , for which we take the form:

$$P(z) = \frac{4z}{1 + 4z^2}, \quad z = (s/M_\Delta^2)^2(1 - x), \quad M_x^2 \sim s(1 - x), \quad (3)$$

a formula essentially derived from pomeron exchange analysis of diffraction, in this instance involving the triple pomeron exchange [22,23,16]. The variable  $x$  is the usual Feynman variable  $x_F = p_{||}/p_{max}$ . The crucial features of the spectrum are a  $1/M_x^2$  dependence of the cluster mass at large masses, and a peak adjusted to be near the  $\Delta$  mass, independent of  $s$ . The  $\rho$  mass is used for mesonic clusters. This form is roughly observed in the data, where real resonant states are seen for forward enough  $x \sim 1$  values of the undisturbed arm. The excitation mass in the ‘dissociated’ arm is given by simple kinematics:

$$M_x^2 - m_p^2 \cong (1 - x)s \quad (4)$$

If one takes the minimum, in this case longitudinal, momentum transfer to be

$$q_{||} = (1 - x)m_p \cong m_p(M_x^2 - m_p^2/s), \quad (5)$$

$S+S$  at  $s^{1/2} = 19.4$  Gev  
NA35 (1994) Central ( $b < 2$ )

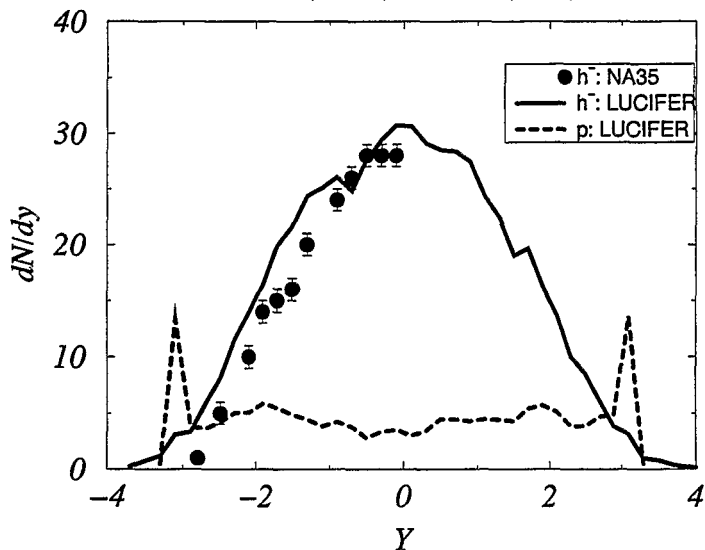


FIG. 6. Sulfur + Sulfur data from NA35 compared with LUCIFER calculation (fitted) for negative hadron production. Strangeness production is not yet included in LUCIFER.

then diffraction becomes increasingly evident when  $q_{\parallel}^{-1}$  is less than the approximate interaction radius  $m_{\pi}^{-1}$ , i.e. for  $(1-x) \sim (m_{\pi}/M_p) \sim 0.15$ . The proper quantum context, tying elastic and diffractive scattering (closely) together and both to the total cross-section is well described in many places, [16,23] but I have relied particularly on Goullianos [22]. The rapidity gap between the unexcited proton and the diffractive cluster  $M_x$  implies that the relevant pomeron graph to be cut involves a triple exchange. The quantum dynamics of high energy  $pp$  ( $hh$ ) collisions is contained in the cascade within the two body processes and then by the Gottfried rules to the interaction of cylinders of rapidity-unseparated leading clusters. The high energy leading  $s$ -dependence is exploited wherever possible to simplify the underlying structure of  $hh$ .

In dealing with a multi-cluster diagram in Fig 3 the longitudinal phase space is obtained by assigning the mid-rapidity clusters first, and then using energy-momentum conservation to specify the outer two. One parameter freedom exploited, but again I emphasise, for  $hh$  only, is the ratio of outer to inner cluster masses. This can be used to help ensure that the leading particle behaviour matches that seen in experiment. The final ratio selected, which could be  $s$ -dependent, is close to unity. The *maximum* energy available to any cluster for internal excitation, is near  $\sqrt{s}/N$ ,  $N$  being the number of clusters in an event. This lower energy, not the full  $s$ , is used in Eqn. 3 to fix the mass distribution for the sub-clusters. Once again I remind the reader  $\sqrt{s}/N$  is the maximum mass available for cluster excitation, not a typical mass. Since large masses are much less probable, most of the cluster energy-momentum is kinematic at any stage of a hadron-nucleus collision. Moreover, the meson-like clusters or any produced clusters will, given the formation time assigned to them, rarely decay or reinteract within the nuclear medium. Their energy-momentum

## *Pb+Pb at $s^{1/2} = 17.2$ Gev*

*NA49 (1995) Central*

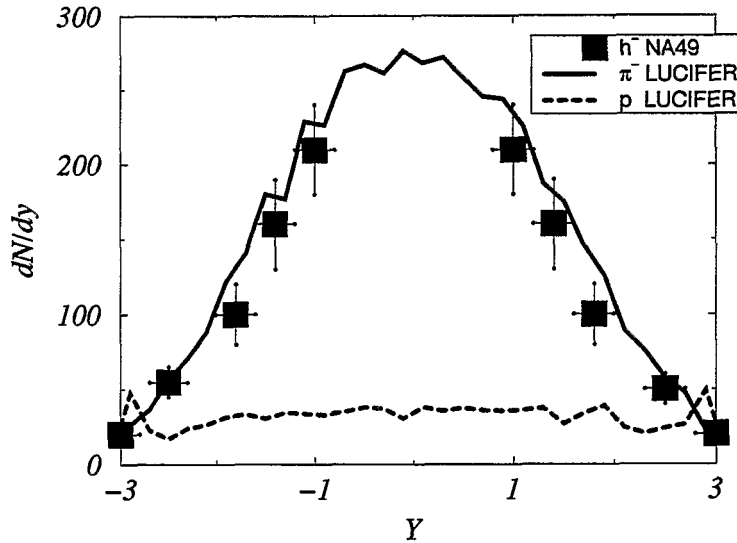


FIG. 7. LUCIFER Prediction for Pb+Pb, obtained using parameters determined by the fits to  $pp$  and S+S.

will also only separate from the hadrons which produced them according to rule (I), which generally severely restricts the energy available for excitation and eventual production. To ensure leading particle behaviour, the rapidity of produced particles in  $hh$  is restricted to lie within the range defined by the final values for the two initial hadrons.

### Cluster Decay

The decay of clusters in LUCIFER is also, consistently controlled by diffractive processes taken as prototypical. Clusters decay sequentially, for the moment into  $\pi$ 's, eventually into strange mesons, antibaryon pairs, etc.,

$$\begin{aligned} B &\rightarrow B_1 + \pi_1 \rightarrow B_2 + \pi_1 + \pi_2 \rightarrow \dots \\ M &\rightarrow M_1 + \pi_1 \rightarrow M_2 + \pi_1 + \pi_2 \rightarrow \dots \end{aligned} \quad (6)$$

The mass step  $\delta m$  in these chains,

$$\delta m \sim m^\beta, \quad \beta(m) = 0.5 + \beta_0 \ln(m), \quad (7)$$

is selected to reproduce the observed average multiplicity  $N(m)$  produced from a diffractive excitation of mass  $M_x = m$ , as is shown in Fig. 4. In practice, the step  $\delta m$  is multiplied by a random number, so that the multiplicity fluctuation is also approximately reproduced.

The decay constant  $\tau_d = \alpha M_x^{-1}$ , essentially the only parameter left to be determined in either  $pA$  or light heavy ion reactions, is in fact fixed here using S+S data at  $\sqrt{s} = 20$  [25] as  $\alpha = 0.07$ , only slightly lower than the value  $\sim 0.10$  which would reproduce the  $\Delta$ ,  $N^*$ , or  $\rho$  lifetimes.

## 1 Au+Au Event @ RHIC

Central Au+Au  $s^{1/2} = 200$  GeV

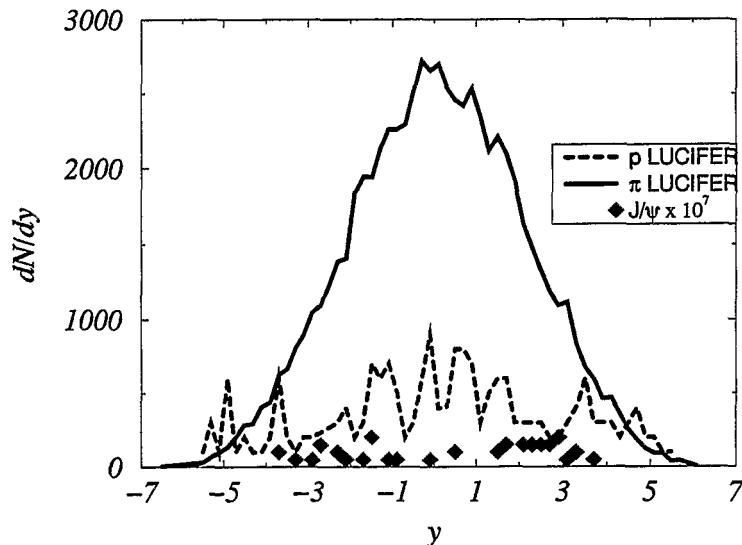


FIG. 8. LUCIFER Prediction for Au+Au at RHIC, using the same parameters for  $pp$  and the decay lifetimes as described in the text.

### IV. LUCIFER RESULTS AT CERN AND RHIC

The level of accuracy of the fits to charged pion production in nucleon-nucleon scattering is displayed in Fig. 5(a,b). All ‘parameters’ of the fit were fixed from the lower energy data, so the results in Fig 5(b) can be viewed as ‘predictions’ of the model for  $pp$  outlined here. It can be seen that not much  $s$  dependence of the parameters is required to get a good description at both energies. For this preliminary workshop version of LUCIFER, only production of  $\pi$ -mesons was considered. Strangeness and other heavy quark production processes can be straightforwardly included in the cluster scheme for  $pp$ .

Finally then the results in Fig. 7 and Fig. 8 represent LUCIFER predictions for  $\pi$  production in Pb+Pb [26] at CERN energies, and for Au+Au at RHIC where of course data doesn’t exist. The Pb+Pb [26] measurements are described quite well, having been constructed from the  $pp$  input and from experimental knowledge of the negative hadrons in S+S. The RHIC numbers are taken from a single simulated event and certainly must be viewed as highly preliminary. Since one expects appreciable strangeness production  $\sim 30\%$ , the number of  $\pi$ ’s must be reduced by at least this amount. Careful implementation of the Gottfried rules could cut down production further, so for the moment Fig. 8 should be regarded as an appreciable upper limit.

CERN  $\sqrt{s} = 20$  GeV pion production [25] data were used to determine  $\alpha$ , and hence the decay rate of the LUCIFER clusters. The matching of the LUCIFER calculation to S+S data at  $\sqrt{s} \cong 20$  GeV is shown in Fig. 6. In principle, a full implementation of rules (I), and (II) would eliminate the need for a formation time, here taken as  $\tau_f \sim 1$  fm, replacing it instead by the hadronic scale,  $\sim 1$  fm in the collision center of momentum frame, governing

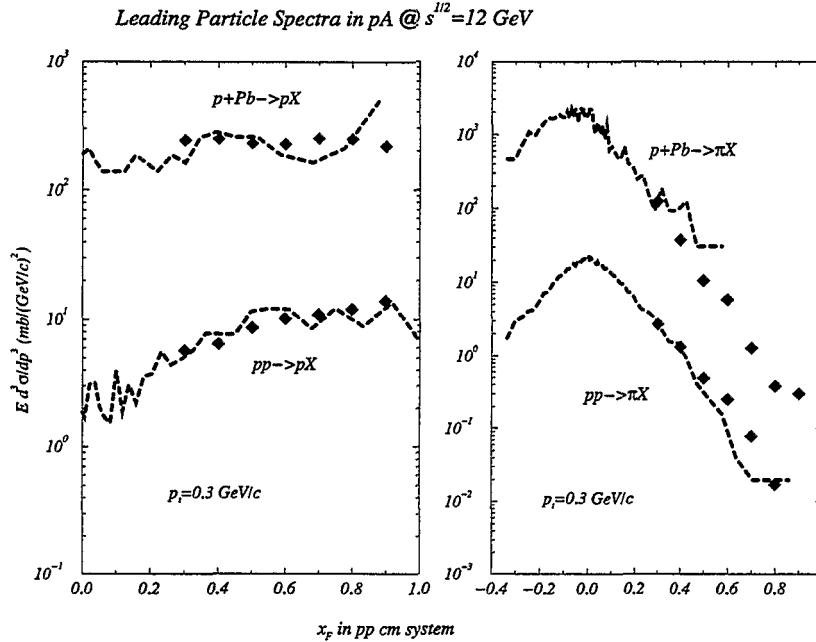


FIG. 9. LUCIFER leading particle spectra in  $p+A$  collisions. In general there is no great difficulty in fitting the results for  $p+Pb$ . Note that the pion data are extremely forward, and constitute only a very small fraction of the total produced pions.

separation of the clusters from the leading hadron. The number of pions produced in  $S+S$  is highly sensitive, as one might expect, to the one truly free parameter,  $\alpha$ , but the value settled on  $\sim 0.07$  is eminently reasonable for the typical cluster masses.

Since much of the introductory structure for LUCIFER was laid out for  $pA$ , I include results for inclusive proton production for this exemplary case in Fig. 9, the data taken from 100 GeV/c FNAL experiments [17]. There seems in the main, to be no trouble in reproducing these, but rules (I), and (II) are especially important for the most forward, though very few,  $\pi$ 's.

## V. FRAME DEPENDENCE OF THE CASCADE.

All cascade models attempt to construct the time evolution of a complex many particle system from elementary interactions (collisions) of the constituent particles. Therefore, some method must be found for triggering these elementary collisions, and determining when they occur. The method most generally used in relativistic cascades, and which is used in LUCIFER and ARC, is to trigger a collision when two particles approach to a distance less than the geometrical interaction cross-section, all distances being evaluated in the collision center of momentum frame. When a collision occurs, several outgoing particles may be produced. One must then decide where in detail they materialise, but locality of the underlying interactions demands that produced particles emerge near to the collision point. Additionally, the cascade is always imagined to proceed in some global frame. This might

Frame Dependence at RHIC  $s^{1/2}=200$  GeV

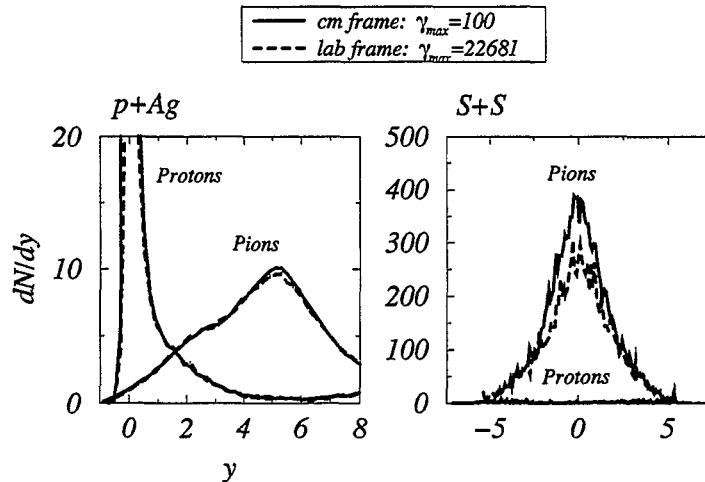


FIG. 10. Frame dependence of LUCIFER results in p+Ag and S+S collisions at RHIC energies. For pA results there is virtually no frame dependence, while S+S exhibits about a 25% effect. Even for the heavier Ag+Ag system, the effect increases only moderately. One expects that screening of the in medium cross-section, and implementation of the Gottfried approach will considerably reduce this dependence.

be, for instance, the equal velocity frame of the two incoming nuclei, or the lab frame.

Obviously, such a procedure can never be made completely frame independent. This is because the interaction between two incoming particles occurs at a spacelike separation. A signal propagates between the particles faster than the speed of light, and the collision ‘time’ is frame dependent. In any frame besides the collision center of momentum frame, there are at least two times at which one might say the collision occurred:  $t_1$ , when one of the incoming particles feels the interaction, and  $t_2$ , when the other particle feels it.

If we view the cascade from the global frame it seems reasonable to demand that we see no apparent violation of causality in that frame during the cascade. Particles should not appear before the collision in which they are produced, nor should produced particles be allowed to collide with the original particles that produced them. Neither should particles be influenced by collisions that have not yet occurred. This legislation against first order causality violations might be called an *anti-grandfather clause*:

- *The grandfather paradox is not allowed in the cascade. The time order of collisions is strictly causal in any global frame.*

If we accept the anti-grandfather clause, then there is only one possibility for the collision time: the earlier of  $t_1$  and  $t_2$  must be taken.

However, it is then clear that in some other global frame we may have to take the opposite choice. In that frame, the collision in question may occur before some other collision rather than after it. In general, if many particles collide, and a list is drawn up of the times of all the possible collisions, we find that the time-order of the list is not the same in different global frames. So the time evolution of the cascade is different, and the results are dependent on the choice of global frame. The special relativistic constraint  $v < c$  for physical signals,

disallowing *action at a distance*, has been violated, and this is the penalty. The question is only: how frame dependent are the results? Any method short of a fully consistent field theoretical, or perhaps string-theoretical, treatment of the ion-ion collision will suffer from this defect to some extent. It may nevertheless be that the frame dependence is not so serious, and even if so, it is not logically ruled out that it can be reduced by a clever choice of algorithm.

The case of  $pA$  collisions is again illustrative. It turns out that such a cascading system can in practice be rendered virtually frame independent (Fig.10), i.e. relativistically covariant, by a production scheme which places emitted particles on a hyperboloid of constant proper time, and eliminating some acausalities originally present in ARC cascading, which did not obey the anti-grandfather clause. In this figure I considered the results obtained in two external frames for  $pA$  collisions, the laboratory and the equal velocity frame.

The frame dependencies in  $S + S$  collisions at RHIC energies are on the order of 25% for the lightest mesons, the pions, (Fig.10), and only moderately higher for the more massive  $Ag + Ag$  pair. One can trace the frame dependence to a slight readjustment of the cluster formation time with changes in the global frame, slowly varying with the combined mass of the system considered. The frame dependence might thus be considerably tamed by a simple global tuning, based on knowledge of data in some low mass nuclear collision at the higher energies.

## VI. $J/\psi$ PRODUCTION

It is tempting to turn LUCIFER to the currently, experimentally, interesting topic of  $J/\psi$  production near  $\sqrt{s} = 20$  GeV. The recent data of Gonin *et al.* [27] for Pb+Au has been widely interpreted as heralding presence of QCD plasma [28,29]. This is eminently a case for test use of a pure hadronic simulation, like LUCIFER. Gavin and Vogt [18] have made a model calculation within a Glauber-like framework which normalizes the elementary  $J/\psi$  production from  $pA$  measurements [27] and produces breakup hadronically, against nucleons and co-movers. Presumably, if the purely hadronic description, reasonably parametrised, describes the increased suppression measured in Pb+Au, then it is difficult to argue plasma has been created. Aside from quibbling over S+Pb vs Pb+Au the Glauber estimates would seem to describe the data adequately. One major problem with Glauber theory is its inability internally and consistently to calculate the abscissa in Fig. 11, the all important  $E_t$ . A clear second problem is the use of the ‘co-mover’ density as a free parameter. The cascade can eliminate both of these problems, providing the relationship of suppression to  $E_t$  directly, and calculating the co-moving density dynamically. The calculation presented here is surprisingly, I believe, the first self-consistent hadronic simulation of  $J/\psi$  to be done with relativistic ions. H. Stoecker, at this workshop [30] has presented a simulation in which  $J/\psi$ 's were injected rather arbitrarily *in medias res*, at some ‘zero’ of time in an event: a quick and dirty first step towards a more consistent treatment.

Borrowing the  $J/\psi$  elementary production cross-sections  $\sigma_{pp \rightarrow J/\psi}$ , and  $\sigma_{\pi p \rightarrow J/\psi}$  from data [31], and choosing the  $J/\psi$  breakup cross-section  $\sigma_{br} \sim 5$  mb against either baryons, or hadronic comovers, the results in Fig 11 were obtained. These results are built on the same assumptions as in Ref 18. Such a breakup cross-section appears to be consistent in the Glauber picture with  $pA$  data on  $J/\psi$ . Another critical parameter is the  $J/\psi$  formation

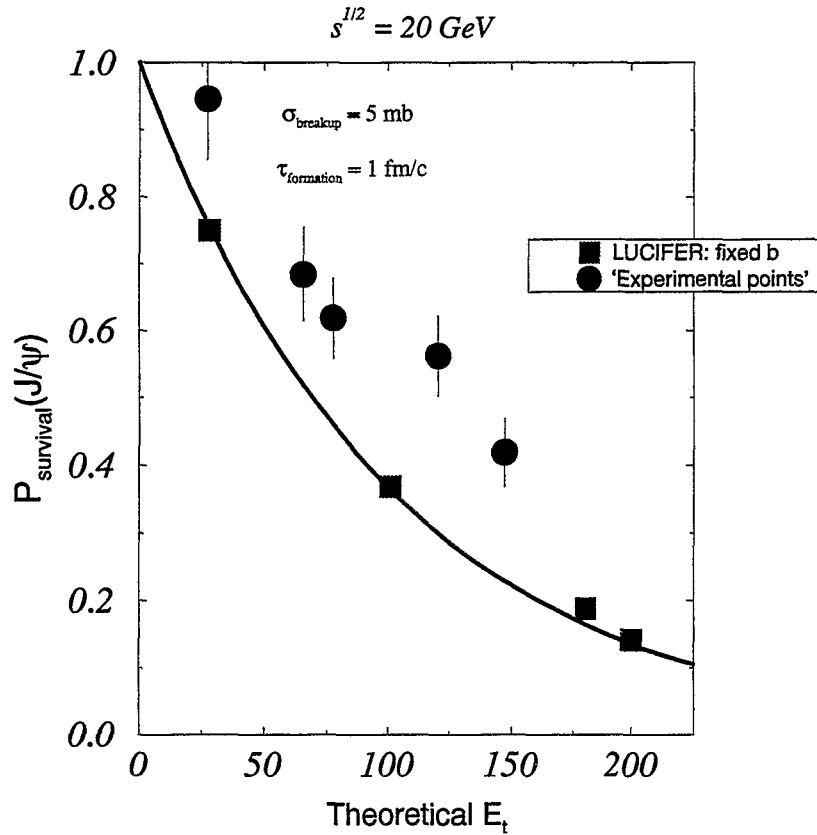


FIG. 11. The survival probability of the  $J/\psi$  in a Pb+Pb collision at CERN energy plotted against the ‘theoretical’  $E_t$  produced in the collision. Data points have been translated from ‘ $b$ ’ to the more physical  $E_t$  scale by S. Gavin [18].

time  $\tau_{J/\psi} \sim 1\text{fm}$ . Both of these parameters, it should be noted, are *a priori* unknown, from the point of view of a hadronic simulation. The conclusion, reinforcing Gavin and Vogt, is that reasonable assumptions for input and breakup cross-sections can perfectly well accommodate the latest NA50 data. One would have to establish unambiguously that, for example, the  $J/\psi$  breakup cross-sections were well below the 3-5 mb range for alternative explanations of the suppression to be viable. There are of course also relevant data on dilepton and direct photon production which should be examined with LUCIFER. No single signal for plasma formation is likely to be probative. Summarising, one can also conclude the  $J/\psi$  measurements are explainable by hadronic cascade only if most breakup is on final state mesons, light ones at that, and if the formation time is within a tight range near 1 fm/c. Since the cascade indicates breakup is dominantly at late stages in the simulations, the introduction of a mass threshold for the annihilation biases against  $\pi$ 's and in favour of  $\rho$ 's as the important comovers. Such points merit further study, and of course could also argue against a conventional hadronic explanation of the data. For the moment there would appear to be too much theoretical freedom to draw absolute conclusions, and certainly not in favour of QCD plasma.



## VII. THE IMMEDIATE FUTURE

The first task is to expand the scope of the hadronic cascade, and establish its adherence to the obvious principles which determine the space-time structure of high energy collisions. Relativistic invariance has been demonstrated for  $pA$  reactions (see Fig. 9); placing the produced hadrons on a 4-d hyperboloid of constant proper time in the cm frame of the two colliding hadrons reduces frame dependence virtually to nil, even at RHIC energies. S+S collisions at RHIC still exhibit  $\sim 25\%$  frame variation, for extreme choices of frame. At high particle densities one may have to introduce classical screening [32] of the two-body interactions, which will cut down relativistic effects by limiting the two-body cross-section to be no larger than one corresponding to the interparticle separation. As a byproduct overall production rates may further drop, another reason Fig. 8 is probably an overestimate at RHIC. In any case cross-sections in general should not exceed  $\pi d^2$ , where  $d$  is the average distance between interacting particles, be these hadrons or partons, if a two-body picture is to be retained.

The second major task, already undertaken, is to merge LUCIFER and VNI, K. Kinder-Geiger's partonic cascade. Hadron-hadron collisions leading to transverse momentum  $p_t$  higher than some preselected cutoff will be moved from the hadronic to the partonic cascade. The obvious theoretical experiment to perform, is to compare the results of the pure hadronic and mixed hadronic/partonic models. Beside these, of course, will also be placed Al Mueller's desired pure partonic cascade followed by eventual hadronisation and pure hadronic cascading. Energy loss formulae for high energy partons appropriate to the high density environment [33,34] can be introduced and studied for their possible effects in the high density medium produced by the cascade. Differences between the three pictures should guide experiments where to look for unusual effects at RHIC.

## VIII. ACKNOWLEDGEMENTS

I would like to thank my collaborators, S.H. Kahana for encouragement and crucial discussions and Y. Pang for help with some of the early cluster programming, and of course both for their generosity in having allowed me to build on the original ARC architecture.

This manuscript has been authored under DOE supported research Contract No. DE-FG02-93ER40768.

## REFERENCES

- [1] Y. Pang, T. J. Schlagel, and S. H. Kahana, *et al*, *Phys. Rev. Lett* **68**, 2743 (1992); S. H. Kahana, D. E. Kahana, Y. Pang, and T. J. Schlagel, *Annual Reviews Of Nuclear and Particle Science*, **46**, 1996, ( ed C. Quigg)
- [2] K. Eskola, *Proceedings, RHIC Summer Study'96*
- [3] A. H. Mueller *Proceedings, RHIC Summer Study'96*
- [4] J. D. Bjorken, *et al*, *Phys. Rev.* **D27**, 140 (1983)
- [5] D. Boal, *Proceedings of the RHIC Workshop I*, (1985) and , *Phys. Rev.* **C33**,2206 (1986); K. J. Eskola, K. Kajantie and J. Lindfors, *Nucl. Phys.* **B323**, 37 (1989); X. N. Wang and M. Gyulassy,, *Phys. Rev.* **D44**, 3501 (1991); K. Geiger and B. Mueller *Nucl. Phys.* **B369**, 600 (1992); K. Geiger *Phys. Rev.* **D46**, 4965, and 4986 (1992).
- [6] K. Geiger, These proceedings.
- [7] T. D. Lee, These proceedings.
- [8] B. Andersson, G. Gustafson, G. Ingelman, and T. Sjostrand, *Phys. Rep* **97**, 31 (1983); B. Andersson, G. Gustafson, and B. Nilsson-Almqvist, *Nucl. Phys* **B281**, 289 (1987)
- [9] J. Ranft and S. Ritter, *Z. Phys.***C27**, 413 (1985); J. Ranft *Nucl. Phys.* **A498**, 111c (1989); A. Capella and J. Tran Van, *Phys. Lett.***93B**, 146 (1980) and *Nucl. Phys***A461**, 501c (1987); K. Werner, *Z. Phys. C* **42**, 85 (1989)
- [10] K. Geiger, *Proceedings of Quark Matter'83*, *Nucl. Phys.* **A418**, 257c (1984); K. Geiger, *Phys. Rev.***D51**, 2345 (1995)
- [11] E. L. Berger and G. C. Fox, *Phys. Lett* **47B**, 162 (1973)
- [12] A. Wu. Chao and C. Quigg, *Phys. Rev.***D9**, 2016 (1974)
- [13] W. Beusch, *Acta. Phys. Pol***B3**, 1679 (1972)
- [14] K. Gottfried *Phys. Rev. Lett.* **32**, 957 (1974); and *Acta. Phys. Pol***B3**, 769 (1972)
- [15] J. Koplik and A. H. Mueller *Phys. Rev.* **D12**, 3638 (1975)
- [16] V. N. Gribov, B. L. Joffe and I. Ya. Pomeranchuk, *Sov. J. Nucl. Phys.***2**, 549(1966); V. N. Gribov, *JETP***26**, 414 (1968); J. Kogut and L. Susskind, *Phys. Rep***8C**, No. 2 (1973); H. D. Abarbanel, J. D. Bronzan, R. L. Sugar and A. L. White, *Phys. Rep***21C**, No. 3 (1975); H. Chen and T. T. Wu *Phys. Rev. Lett***24**, 1456 (1970).
- [17] D. S. Barton *et al*, *Phys. Rev.***D27**, 2580 (1983); W. Busza *et al*, *Phys. Rev. Lett.***34**, 836 (1975); W. Busza *Proceedings of Quark Matter'83*, *Nucl. Phys.* **A418**, 635c (1984)
- [18] S. Gavin, *Proceedings, RHIC Summer Study'96*; S. Gavin and R. Vogt *Proceedings of Quark Matter '96*, Heidelberg, May 1996
- [19] CHLM Collaboration, *Nucl. Phys.***B108**, 1 (1976); J. W. Chapman *et al* *Phys. Rev. Lett.***32**, 257 (1973); T. Kafka *et al* *Phys. Rev.***D16**, 1261 (1977)
- [20] G. Ekspong for the UA5 Collaboration, *Nucl. Phys.***A461**, 145c (1987); G. J. Alner for the UA5 Collaboration, *Nucl. Phys.***B291**, 445 (1987)
- [21] Y. Eisenberg *et al* *Nucl. phys.***B154**, 239 (1979)
- [22] K. Goullianos, *Phys. Rep***101**, No. 3, (1983), 169-219
- [23] G. Alberi and G. Goggi, *Phys. Rep***74**, No. 1, (1981), 1-207; P. V. Landshoff and O. Nachtmann, *Z. Phys.***C35**, 405 (1987)
- [24] A. Schwimmer *Nucl. Phys.* **B94**, 44 (1975)
- [25] J. Baechler for the NA35 Collaboration, *Phys. Rev. Lett.***A461**, 72 (1994); S. Margetis for the NA35 Collaboration, *Snowbird 1994, Proceedings, Advances in Nuclear Dynamics*, 128-135

- [26] S. Margetis for the NA49 Collaboration *Proceedings of Quark Matter '95*, , Edited by A. M. Poskanzer, J. W. Harris and L. S. Schroeder, (North Holland, 1995), 355c ; and *Phy. Rev. Lett***75**, 3814 (1995)
- [27] M. Gonin, for the NA50 Collaboration, *Proceedings of Quark Matter '96*, Heidelberg, May 1996
- [28] D. Kharzeev and H. Satz, *Proceedings of Quark Matter '96*, Heidelberg. May 1996
- [29] J. -P Blaizot and J. -Y Ollitrault, *Proceedings of Quark Matter '96*, Heidelberg, May 1996
- [30] H. Stoecker, These proceedings.
- [31] R. Gavai *et al*, *Int. J. Mod. Phys***A10**, 3043 (1995); S. Gavin *et al*, *Int. J. Mod. Phys***A10**, 2961 (1995)
- [32] S. H. Kahana, Y. Pang, T. J. Schlagel, *Phys. Rev.***C47**, R1356 (1993)
- [33] Y. Dokshitzer, these Proceedings.
- [34] Y. Dokshitzer, these Proceedings.

# General Cascade Program

Yang Pang

*Department of Physics, Brookhaven National Laboratory, Upton, NY 11973  
and*

*Department of Physics, Columbia University, New York, NY 10027*

## Abstract

In order to compare various microscopic models of nucleus-nucleus collisions at RHIC, one must have easy access to all physics input and assumptions in the model. The General Cascade Program, developed during this workshop, achieves this by making physics input literally as an input rather than a complex part of the code. As the very first application of this model, the question of Lorentz invariance in cascades is studied.

## I. INTRODUCTION

Cascade models have been quite successful in reproducing experimental spectra of nucleus-nucleus collisions at all available energies. This is rather remarkable, since the physical processes in these models can be quite different. For most cascade based models, it is often difficult to identify the key physics ingredient without having to go over the entire source code. So we can not readily compare various models, even when good agreement among the models and the experiments in the observed spectra is reached.

The General Cascade Program is developed in an attempt to overcome this difficulty. Section II briefly describes the program and its current status. Section III explores the problem of Lorentz noninvariance in cascades, and a solution to this problem is presented in Section IV.

## II. GENERAL CASCADE PROGRAM

The aim of this program differs from most other similar cascade programs. Our goal is to develop a useful tool for studying various physical models instead of building a model. To achieve this goal, we do need a fast and reliable cascade.

There are at least three components in each cascade: computer algorithms, kinematics, and dynamics. These three components are not necessarily distinguished or written in separately parts of the code. This is the main reason for the difficulty of comparing different models.

Computer codes are by nature unforgiving about errors and mistakes. The only way to ensure its quality is to have a large number of people examine it and using it. The

source code and related documentations for the General Cascade Program described below are available from anonymous FTP at `rhic.phys.columbia.edu/gcp` and WWW at `'http://rhic.phys.columbia.edu/gcp/''`.

## A. Basic Cascade Algorithm

Although most event generators based on cascade algorithm are rather long and seemingly complicated, the cascade algorithm itself are usually quite simple. The following is a complete cascade program in C language. Translating it to any other programming language, such as Fortran, should be straightforward.

```
main ()
{
    do_initialization ();
    while (find_next_collision () == next_collision_found)
        do_next_collision ();
    write_output ();
}
```

As we can see, the above cascade is done in four steps:

1. Create a list of cascading objects and assign each object an initial coordinate and momentum.
2. For each pair of objects, find the distance  $d$  and the times of their closest approach. If  $\pi d^2$  is less than the total cross-section, a possible collision is found. The next collision is chosen to be the earliest of all possible collisions.
3. A collision converts the incoming objects to a set of outgoing objects. The list of objects is then updated by deleting the incoming objects and adding the outgoing objects. Steps 2 and 3 are repeated until there are no more collisions.
4. Writing the result to an output file.

For this writeup, we will limit our discussions to include only binary collisions and decays. The General Cascade Program are constructed with more general interactions in mind. The step 2 above is the most critical part in the cascade algorithm. When the number of objects becomes large, if a cascade code is not well optimized, almost all CPU time is spent on deciding which pair shall collide next. There is another more serious problem in step 2, that is the collisions are decided by the distance of closest approach; as we shall see, this leads to the violation of Lorentz invariance.

Let us consider two objects  $O_1$  and  $O_2$ , and they are created at

$$x_1 = (t_1, \vec{x}_1) \quad \text{and} \quad x_2 = (t_2, \vec{x}_2),$$

where the coordinates are given in some global frame. Their four momenta in the same frame are

$$p_1 = (E_1, \vec{p}_1) \quad \text{and} \quad p_2 = (E_2, \vec{p}_2).$$

The distance of closest approach can be calculated from the following Lorentz invariant formula (valid even when the times  $t_1$  and  $t_2$  are not equal)

$$d^2 = -(\Delta x)^2 - \frac{(\Delta x p_1)^2 p_2^2 + (\Delta x p_2)^2 p_1^2 - 2(\Delta x p_1)(\Delta x p_2)(p_1 p_2)}{(p_1 p_2)^2 - p_1^2 p_2^2},$$

where

$$\Delta x \equiv x_2 - x_1$$

is the four vector difference between  $x_2$  and  $x_1$ , and the sign convention is  $p^2 = m^2$ .

In the center of mass of these two objects, there is a well defined time when the objects reach the distance of closest approach. The time is also well defined in a reference frame where one of the object is at rest. However, because the particles are distance  $d$  apart, in an arbitrary global frame the event in general has two different times. The general formula is

$$t_{12} - t_1 = -\frac{E_1[(\Delta x p_1)p_2^2 - (\Delta x p_2)p_1 p_2]}{(p_1 p_2)^2 - p_1^2 p_2^2}$$

where  $t_{12}$  is the time of closest approach for  $O_1$  with  $O_2$  in the global frame, similarly the time of closest approach for  $O_2$  with  $O_1$  is

$$t_{21} - t_2 = \frac{E_2[(\Delta x p_2)p_1^2 - (\Delta x p_1)p_1 p_2]}{(p_1 p_2)^2 - p_1^2 p_2^2}$$

If  $t_{12} < t_1$ ,  $O_2$  is moving away from  $O_1$  at the time  $t_1$ .

The distance of closest approach is defined in the center of mass of the incoming objects, so we can have a manifestly invariant formula for  $d^2$ . If  $O_1$  and  $O_2$  are the only two objects in our system, we would have a Lorentz invariant collision rate. In general, each object will have a set of possible collision times. For  $O_1$ , one might have  $t_{12}, t_{14}, t_{17}, \dots$ , and for  $O_2$ ,  $t_{21}, t_{23}, t_{25}, \dots$ . When  $t_{12}$  and  $t_{21}$  are not the two earliest times, e.g.  $t_{12} < t_{23} < t_{21} < \dots$ , one has to introduce another criterion in order to select the next collision. The common recipe is to define the average of the two times,  $(t_{12} + t_{21})/2$ , as the “real” collision time for  $O_1$  and  $O_2$ . On the other hand, one could very well choose either the earliest or the latest of the two times. The final result does depend on these choices.

## B. Basic Data Structure

In cascades, each object travels on a straight line trajectory. To get a complete history of an object, one only need to specify the object’s initial and final locations. Alternatively, if one can provide an initial location  $x^i = (t^i, \vec{x}^i)$ , a four momentum  $p = (E, \vec{p})$ , and a final time  $t^f$ . From the programming point of view, cascade is a procedure for updating a list of objects. The structure for each entry on the list is

```

struct list
{
    object_ptr object;
    double x[5];
    double p[4];
};

```

One can regard `object` as an object id. Five double precision numbers for  $x$  are  $t^i, \vec{x}^i$  and  $t^f$ . The total size of the above structure is 76 bytes, so 1MB of memory could hold well over ten thousand such entries. This list is in fact the largest data structure in a cascade. From computer memory consideration alone, one could do rather large cascade simulations on practically any computer.

The properties of each types of objects and their interactions are input to the cascade. In the General Cascade Program, this information is explicitly treated as external input. The cascade algorithm and the physics input are separate entities. The physics are read in at the beginning of each run. Several utilities are constructed for converting readable text tables into the internal table in the code.

The minimal amount of input to define an object is a symbol and a mass. For example, one could define a nucleon, in the General Cascade Program, by

```

specie
{
    symbol      N
    mass       0.938
}

```

To define an interaction, we need to provide a formula for evaluating the total cross-section, a formula for the partial cross-sections, and a description of the outgoing momentum distribution. The format for these tables are still evolving, but the basic ideas will remain the same, i.e. the physics input and assumptions should be specified outside of the source code. This way one achieves the separation of algorithms and physics, a necessary first step for any serious comparisons of various physical models.

Since the program itself does not have specific information on the objects or details of the interactions, the program is not only more versatile and potentially more robust, but also gives user access to all physics input and assumptions without having to go through any part of the source code.

### C. Efficient Cascade Algorithms

As mentioned in section II A, if the code is not properly optimized, most of the CPU times are used in search of the next collision. It is easy to see why this is the case, since the amount of computation for finding *all* binary collision is proportional to the square of the number of objects in the system. The most straightforward approach requires  $n^2$  computations for each collision. The result would be an extremely slow cascade for any system of interest.

A better way is to do the  $n^2$  search once and save the result. After each collision, we only need to search the collisions between newly produced particles and the existing particles. This operation is proportional to  $mn$ , where  $m$  is the number of outgoing particles in a binary collision. This is the method employed in ARC [1]. If the number of objects is very large, one could end up with a very long list of potential collisions, which not only occupies more memory space, its maintenance would also slow things down. We can improve this method by noting that it is sufficient to save the first few potential collisions for each object. Tests show that in most cases the optimal number is between 2 and 3.

The improved algorithm would still require  $mn$  computations for each collision. Just as there is no need to keep all possible collisions, it is not necessary to check all particles. In a relativistic cascade, all particles travel at the speed of light or slower. If we intend to save only 2 to 3 potential collisions, there is no need to check particles beyond 2 to 3 mean free path away. The parallel cascade algorithm [4] does this by dividing the space into regions. The linear size of each region is chosen to be several times the average mean free path. The boundary of these regions does not have to be fixed in space. For example, in the later stages of a nucleus-nucleus collision, natural boundaries along the beam axis would be those traveling at constant rapidities. In the parallel cascade, the amount of computation for each collision is proportional to  $mn'$ , where  $n'$  is the average number of objects in each box. Thus the amount of computation per collision no longer depends on the total number of objects.

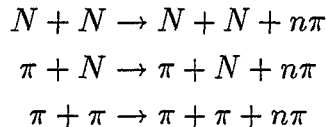
### III. LORENTZ NONINVARIANCE IN CASCADE

#### A. A Simple Model

In building a cascade model for nucleus-nucleus collisions, it is often convenient and instructive to build up the physics step by step. For example in ARC [1], the first physical ingredients are simply uncharged nucleons and pions, next we put charge in, and then the strangeness is included. There is a vast amount of experimental data on cross-sections, branching ratios and momentum spectra for these particles. We were able to demonstrate with confidence that the model based solely on these ingredients can not describe the experimental data.

In the same spirit, let me introduce the following model.

1. Objects: Nucleons ( $N$ ) and pions ( $\pi$ ).
2. Interactions:



where

$$n = 0.80 + 0.47 \ln(\sqrt{s}) + 0.112 \ln^2(\sqrt{s}).$$



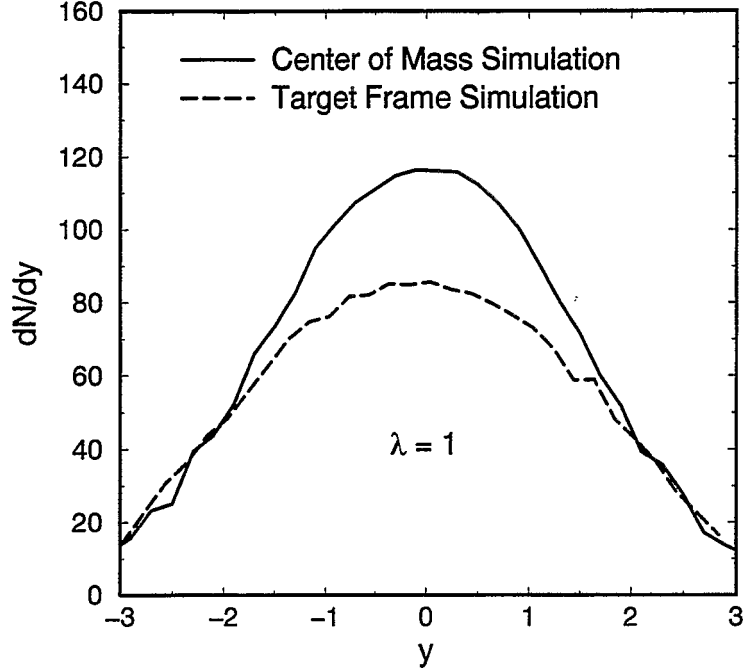


FIG. 1. Pion rapidity distribution in the simple model for  $S+S$  at 200 GeV/c. The simulations are carried out in two different global frames, center of mass (solid line) and target frame (dashed line). The spectra is very sensitive to the choice of the global frame.

3. Momentum distribution: uniform in phase space

$$\int \prod_{j=1}^m \frac{d^3 \vec{p}_j}{(2\pi)^3 2E_j} W_t W_l \delta^4$$

with the additional weights

$$W_t = e^{-p_t^2/\beta^2}$$

$$W_l = e^{-\alpha(1 \pm p_l/p_{max})}$$

The parameter  $\beta$  is adjusted to get the correct average transverse momentum, and  $\alpha$  is chosen to ensure the leading particles loose only 50% of its incoming energy.

## B. Tests of Lorentz Noninvariance

We can now do a nucleus-nucleus collision. Figure 1 shows the final pion rapidity spectra from  $S+S$  collisions at 200 GeV/c per nucleon laboratory momentum. The solid line is a simulation done in the center of mass frame, and the dashed line in lab frame. The difference in spectra from two different frames is certainly significant in this model.

To understand such large differences let us examine the collisions in detail. As mentioned in the previous section, in the global frame, each collision has two times. In the simulations, the collisions are ordered using the average of these two times. In a different frame the

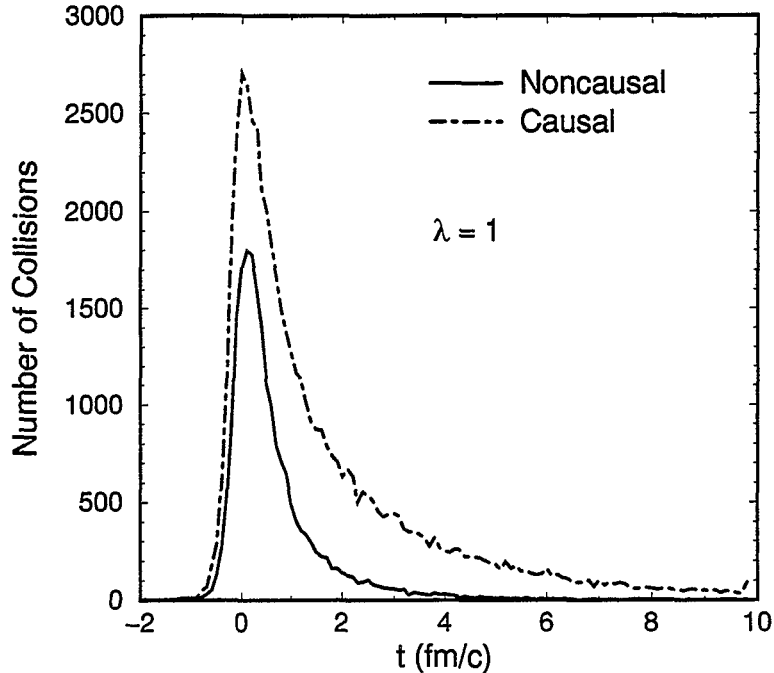


FIG. 2. Number of collisions as a function of time for simulations carried out in the center of mass frame. Solid line are noncausal collisions and the dashed lines are causal collisions.

average time will give us a different collision ordering. Suppose we have three particles  $O_1$ ,  $O_2$  and  $O_3$ , and their collisions satisfy the following inequality

$$\begin{aligned}
 t_{12} &< t_{13}, \\
 t_{23} &< t_{21}, \\
 t_{31} &< t_{32},
 \end{aligned}
 \tag{1}$$

these three inequalities are frame independent. So no matter in what frame, one has to impose other conditions to decide which of the three collisions should happen first. This additional condition will introduce a Lorentz noninvariance. On the other hand, if the collisions times satisfy

$$\begin{aligned}
 t_{12} &< t_{13}, \\
 t_{21} &< t_{23}, \\
 t_{31} &< t_{32},
 \end{aligned}
 \tag{2}$$

then clearly  $O_1$  and  $O_2$  should collide first. Since the inequalities are frame independent, the ordering for these three collisions would be the same in all frames. We call the first kind of collision, (1), non-causal collision and the second kind, (2), causal collision. Figure 2 shows these two types of collisions as a function of time. The ratio non-causal to causal collisions is comparable to the frame dependence observed in the pion rapidity spectra.

When a cascade violates Lorentz invariance, the result is certainly frame dependent. This does not mean that certain frames are better than others. The solution is not simply the one of choosing a “good” frame, because the amount of violation, as defined in (1), is actually frame independent.

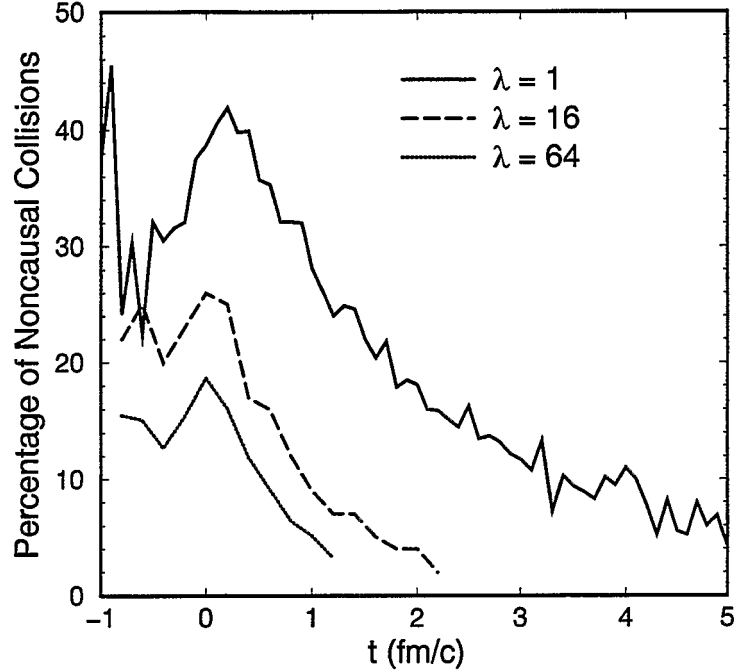


FIG. 3. Ratio of non-causal to causal collisions for three values of the  $\lambda$  parameter :  $\lambda = 1$ ,  $\lambda = 16$ , and  $\lambda = 64$ .

The problem of Lorentz noninvariance in cascade does depend strongly on the details of the model. The problem is quite severe in this particular model. We suggest that the following test on Lorentz invariance or noninvariance should be done for all event generators for RHIC:

1. Test the dependence of physical observable on the choice global frame .
2. Test different recipes for collision time ordering: average time, earliest time and the latest time.
3. Find out the amount of causal and noncausal collisions.

#### IV. RESTORATION OF LORENTZ INVARIANCE IN CASCADE

Under certain limit, cascade is the solution of the following relativistic Boltzmann equation [2]

$$\begin{aligned}
p^\mu \partial_\mu \mathcal{W}_a(\vec{x}, t, \vec{p}) &= \sum_n \sum_{b_1, b_2, \dots, b_n} \int \prod_{i=1}^n \frac{d^3 \vec{p}_{b_i}}{(2\pi)^3 2E_{b_i}} \mathcal{W}_{b_i}(\vec{x}, t, \vec{p}_{b_i}) \\
&\sum_m \sum_{c_1, c_2, \dots, c_m} \int \prod_{j=1}^m \frac{d^3 \vec{p}_{c_j}}{(2\pi)^3 2E_{c_j}} |A_{n \rightarrow m}|^2 \\
&(2\pi)^4 \delta^4 \left( \sum_{l=1}^n p_{b_l} - \sum_{k=1}^m p_{c_k} \right) \\
&\left[ - \sum_{i=1}^n \delta_{ab_i} \delta^3(\vec{p} - \vec{p}_{b_i}) + \sum_{j=1}^m \delta_{ac_j} \delta^3(\vec{p} - \vec{p}_{c_j}) \right],
\end{aligned}$$

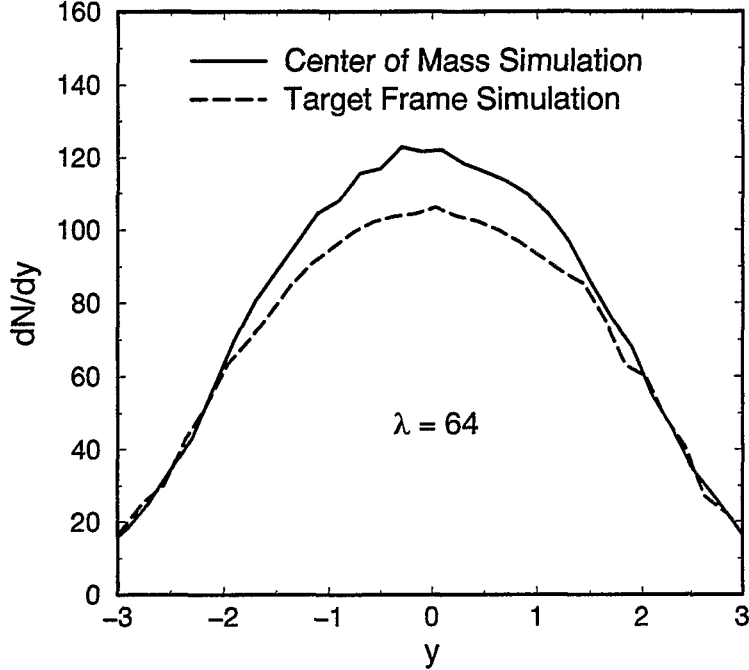


FIG. 4. The pion rapidity spectra from simulations in two different frames at  $\lambda = 64$ . The frame dependences are much reduced.

where  $\mathcal{W}_a(\vec{x}, t, \vec{p})$  is the probability of finding an on-shell particle  $a$ , with momentum  $\vec{p}$ , at position  $x^\mu = (\vec{x}, t)$ , and  $b_1, b_2, \dots, b_n$  and  $c_1, c_2, \dots, c_m$  are the incoming and outgoing particles of a local interaction

$$\begin{aligned} & \langle c_1, c_2, \dots, c_m | S | b_1, b_2, \dots, b_n \rangle \\ & = A_{n \rightarrow m} (2\pi)^4 \delta^4 \left( \sum_{i=1}^n p_{b_i} - \sum_{j=1}^m p_{c_j} \right). \end{aligned}$$

Although the relativistic Boltzmann equation is local and therefore is Lorentz invariant, the cascade breaks this invariance by allowing particles to collide at a distance  $d = \sqrt{\sigma/\pi}$  apart. This invariance can be restored. Let us observe that the Boltzmann equation is invariant under a scale transformation

$$\mathcal{W}_a \rightarrow \lambda \mathcal{W}_a, \quad \text{and} \quad |A_{n \rightarrow m}|^2 \rightarrow |A_{n \rightarrow m}|^2 / \lambda^{n-1}$$

For two-body collisions, the above transformation scales the cross-section by  $1/\lambda$ , but keeps the mean free path constant. In the limit  $\lambda \rightarrow \infty$ , the ratio between the  $d$  and the mean free path goes to zero. This removes the ambiguity in collision ordering and thus restores the Lorentz invariance in the cascade. Figure 3 and 4 shows such scaling and the reduction in frame dependence when  $\lambda$  is increased from the usual value of 1 to 64. When the code is further optimized for speed, by implementing the parallel cascade algorithm, we will be able to choose a sufficiently large  $\lambda$  to have a frame independent result.

There is a major difference between cascades and the Boltzmann equations. While Boltzmann equations give us single particle distributions, cascades potentially could contain additional fluctuations and correlations [5]. The above procedure for the restoration of

the Lorentz invariance would lose these fluctuations. However, if the effect due to Lorentz noninvariance in a cascade is large, whether that cascade can give us any meaningful fluctuations is still an open question, and noncausal collisions in the cascade could also introduce artificial correlations.

## ACKNOWLEDGMENTS

I would like to thank A. Baltz, W. Q. Chao, C. Dover, S. Gavin, M. Gyulassy, D. E. Kahana, S. H. Kahana, K. Kinder-Geiger, T. D. Lee, R. Mattiello, J. Randrup, T. J. Schlagel, and B. Zhang for many helpful discussions. This research is supported in part by DOE and Alfred P. Sloan Foundation.

## REFERENCES

- [1] Y. Pang, T. J. Schlagel and S. H. Kahana, *Phys. Rev. Lett.* **68**, 2743 (1992).
- [2] Y. Pang, in *Proceedings of CCAST Symposium/Workshop on Particle Physics at Fermi Scale*, Beijing, May 1993, Edited by Y. Pang, J. Qiu, and Z. Qiu, (Gordon Breach, New York, 1993), p451.
- [3] T.D. Lee, *Proceedings of International Symposium in Honour of Boltzmann's 150th Birthday*, February 1994. (CU-TP-626).
- [4] Bin Zhang implemented this parallel cascade algorithm in his parton cascade code, and demonstrated significant improvement over other cascades in speed.
- [5] J. Randrup, private communication.

# A Realistic Model for Nuclear Collisions at RHIC

S. Ostapchenko

*Moscow State University, Institute of Nuclear Physics, Moscow, Russia*

T. Thouw

*Forschungszentrum Karlsruhe, IK III, D-76021 Karlsruhe, Germany*

K. Werner

*SUBATECH, Université de Nantes – IN2P3/CNRS – EMN, Nantes, France*

## Abstract

We develop a consistent formalism to treat soft and semihard processes to describe ultrarelativistic nuclear scatterings. At low energies (CERN-SPS), the approach is just the string model, whereas at extremely high energies, we recover the purely perturbative domain (elementary parton interactions and parton cascading). At intermediate energies, represented by the future colliders RHIC and LHC, both aspects contribute.

## I. INTRODUCTION

In the energy range  $10 \text{ GeV} < \sqrt{s} < 50 \text{ GeV}$ , hadronic interactions are well described in the framework of Gribov-Regge theory (GRT). Here, the elementary “exchange object” is the so-called Pomeron, and the theory is formulated entirely in terms of Pomeron exchanges.

At high energies, say  $\sqrt{s} > 50 \text{ GeV}$ , the soft Pomeron is not sufficient, the theory has to be generalized. It is well known that perturbative QCD (PQCD) comes into play, in particular, in case of large momentum transfer  $t$ , one may write inclusive cross sections as

$$\sigma(s) = \sum_{ij} \int dx_1 dx_2 dt f_i(x_1, t) f_j(x_2, t) \frac{d\sigma_{ij}}{dt}(x_1 x_2 s, t), \quad (1)$$

with  $f_1, f_2$  representing the momentum distributions of partons in nucleons, and where  $d\sigma_{ij}/dt$  represents parton-parton scattering according to an elementary QCD diagram.

Any formalism aiming at describing hadronic interactions in an energy range from 10 GeV up to several TeV should therefore have the following objectives:

- provide GRT for small energies ;
- reproduce PQCD results at high energies.

We are going to present such a formalism in this paper.

## II. THE SOFT POMERON

In the following, we sketch the basic features of Gribov-Regge theory based on the soft Pomeron.

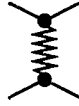
The elastic amplitude  $A^{h_1 h_2}(s, t)$  for the scattering of hadron  $h_1$  and hadron  $h_2$  is given as

$$A^{h_1 h_2}(s, t) = \sum_n A_n^{h_1 h_2}(s, t), \quad (2)$$

where

$$A_n^{h_1 h_2}(s, t) = \frac{i^{n-1} \pi^{1-n} C^{n-1}}{n!} \int \prod_{i=1}^n d^2 k_i \delta(k - \sum k_i) \prod_{j=1}^n G^{h_1 h_2}(s, k_j^2) \quad (3)$$

represents  $n$  Pomeron exchanges. As usual, the Mandelstam variables  $s$  and  $t$  are used. Actually,  $s$  is meant to be in units of some scale  $s_0 = 1$  GeV and is therefore a dimensionless quantity. The function  $G$  is the Pomeron propagator, representing the exchange of a soft Pomeron, graphically expressed by a zigzag line:



The Pomeron propagator is given as

$$G^{h_1 h_2}(s, k^2) = i \gamma_{h_1 h_2} e^{-(R_{h_1}^2 + R_{h_2}^2) k^2} s^{\Delta - \alpha' k^2}, \quad (4)$$

with

$$\Delta = \alpha(0) - 1, \quad (5)$$

with the so-called “intercept”  $\alpha(0)$ , the “slope”  $\alpha'$ , and the “Regge radii”  $R_h^2$ . Using the above parametrization for the Pomeron propagator, we obtain

$$A(s, t) = \frac{i}{4\pi C} \int d^2 b \exp(i \vec{k} \vec{b}) \left\{ 1 - \exp \left[ -C \chi_{\text{soft}}^{h_1 h_2}(s, b) \right] \right\}, \quad (6)$$

with the so-called “soft eikonal”  $\chi_{\text{soft}}^{h_1 h_2}(s, b)$  being the Fourier transform of the Pomeron propagator,

$$\chi_{\text{soft}}^{h_1 h_2}(s, b) = \frac{1}{i\pi} \int d^2 k G(s, k^2) \exp(-i \vec{k} \vec{b}), \quad (7)$$

which leads to

$$\chi_{\text{soft}}^{h_1 h_2}(s, b) = \frac{\gamma_{h_1 h_2} s^{\Delta}}{\lambda_{h_1 h_2}(s)} \exp \left\{ -\frac{b^2}{4\lambda_{h_1 h_2}(s)} \right\}. \quad (8)$$

$\lambda$  is defined as

$$\lambda_{h_1 h_2}(s) = R_{h_1}^2 + R_{h_2}^2 + \alpha'(0) \ln s. \quad (9)$$

The total cross section is then

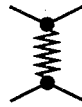
$$\sigma_{\text{tot}}^{h_1 h_2}(s) = \frac{2}{C_{h_1 h_2}} \int d^2 b [1 - e^{-C_{h_1 h_2} \chi_{h_1 h_2}^{\text{soft}}(s, b)}], \quad (10)$$

We use essentially the same symbols as used in ref. [1], apart of using  $\gamma$  instead of  $N_0$ . We also consider here different hadron types and correspondingly different parameters for different hadron classes (this concerns  $\gamma$ ,  $R^2$ , and  $C$ ), see table II.

symbol	in [1]	meaning
$\Delta$	$\Delta$	overcriticality
$\alpha'(0)$	$\alpha'(0)$	slope of Regge trajectory
$\gamma_{h_1 h_2}$	$N_0$	vertex constant
$R_h^2$	$R^2$	Regge radius
$C_{h_1 h_2}$	$C$	shower enhancement coeff.

### III. THE SEMIHARD POMERON

We are now going to generalize the formalism discussed in the preceding section to high energies. The basic idea [2] is to replace the soft Pomeron



by a so-called “semihard Pomeron”, which is defined to be an ordinary soft Pomeron with the middle piece replaced by a “QCD parton ladder”. In other words, we have a parton ladder sandwiched between two soft Pomerons:



Here, we use the symbol for the ladder diagram and zigzag symbol for the soft Pomeron. It is assumed that the ladder and the soft Pomeron may only be connected via gluons, i.e. the external legs of the ladder are necessarily gluons. Therefore the semihard Pomeron is said to be of  $gg$ -type (for gluon-gluon). Ladders with external quark lines can only couple directly to the hadron, on the projectile side, on the target side, or on both sides. Correspondingly



we introduce  $qg$ -type,  $gq$ -type, and  $qq$ -type Pomerons (quark–gluon, gluon–quark, quark–quark):

$$(12)$$

Here, the lines connecting ladder and soft Pomeron, are, as before, gluons, whereas the other external lines of the ladder are quarks. Associated with the four types of semihard Pomerons, we have four contributions to the semihard eikonal, which are discussed in the following, one after the other. In all cases, the eikonals are written as

$$\chi_t^{h_1 h_2}(s, b) = \int dx^+ dx^- \tilde{\chi}_t^{h_1 h_2}(s, b, x^+, x^-), \quad (13)$$

where  $t$  refers to the type ( $gg$  or  $qg$  or  $gq$  or  $qq$ ). The integrand of the semihard  $gg$ -type eikonal is defined to be

$$\begin{aligned} \tilde{\chi}_{gg}^{h_1 h_2}(s, b, x^+, x^-) &= \frac{1}{2} f_e^{h_1}(x^+) f_e^{h_2}(x^-) \int \frac{dz^+}{z^+} \frac{dz^-}{z^-} r(z^+) r(z^-) \\ &\chi^{\text{soft}}\left(\frac{1}{z^+ z^-}, b\right) \sigma_{\text{jet}}^{gg}(z^+ z^- x^+ x^- s) \Theta(z^+ z^- x^+ x^- s - 4q_0^2) \end{aligned} \quad (14)$$

with  $f_e^{h_1}(x)$  representing the momentum fraction distribution of the partons in the hadron representing the soft Pomeron end, parametrized as

$$f_e(x) = c_e x^{\alpha_e} (1-x)^{\beta_e}. \quad (15)$$

The function

$$r(z) = r_0 (1-z)^{\beta_{\text{cut}}} \quad (16)$$

provides a large  $z^+$  ( $z^-$ ) cutoff. The integrand of the semihard  $qg$ -type eikonal is

$$\begin{aligned} \tilde{\chi}_{qg}^{h_1 h_2}(s, b, x^+, x^-) &= \frac{1}{2} f_q^{h_1}(x^+) f_e^{h_2}(x^-) \int \frac{dz^-}{z^-} r(z^-) \\ &\chi^{\text{soft}}\left(\frac{1}{z^-}, b\right) \sigma_{\text{jet}}^{qg}(z^- x^+ x^- s) \Theta(z^- x^+ x^- s - 4q_0^2), \end{aligned} \quad (17)$$

and the integrand of the semihard  $gq$ -type eikonal correspondingly as

$$\begin{aligned} \tilde{\chi}_{gq}^{h_1 h_2}(s, b, x^+, x^-) &= \frac{1}{2} f_e^{h_1}(x^+) f_q^{h_2}(x^-) \int \frac{dz^+}{z^+} r(z^+) \\ &\chi^{\text{soft}}\left(\frac{1}{z^+}, b\right) \sigma_{\text{jet}}^{gq}(z^+ x^+ x^- s) \Theta(z^+ x^+ x^- s - 4q_0^2), \end{aligned} \quad (18)$$

with  $f_q^{h_1}(x)$  representing the momentum fraction distribution of quarks in the hadron, parametrized as

$$f_q(x) = c_q x^{\alpha_q} (1-x)^{\beta_q}. \quad (19)$$

Finally, the integrand of the semihard  $qq$ -type eikonal may be written as

$$\begin{aligned} \tilde{\chi}_{qq}^{h_1 h_2}(s, b, x^+, x^-) &= \frac{1}{2} f_q^{h_1}(x^+) f_q^{h_2}(x^-) \\ &\sigma_{\text{jet}}^{gg}(x^+ x^- s) \Theta(x^+ x^- s - 4q_0^2) \frac{1}{R_{qq}^2(0)} \exp\left\{-\frac{b^2}{4R_{qq}^2(0)}\right\}. \end{aligned} \quad (20)$$

#### IV. THE POMERON CONFIGURATION

Now we are going to discuss, how to determine the ‘‘Pomeron configuration’’, i.e. the precise specification of the type of interaction for all possible pairs of projectile and target nucleons. These specifications are based on the eikonals, determined earlier. We define the total eikonal to be

$$\chi_{\text{tot}}^{h_1 h_2}(s, b) = \chi_{\text{soft}}^{h_1 h_2}(s, b) + \chi_{\text{semi}}^{h_1 h_2}(s, b), \quad (21)$$

with the soft eikonal  $\chi_{\text{soft}}$  given in eq. (8), and with the semihard eikonal  $\chi_{\text{semi}}$  being the sum of the semihard eikonals of types  $gg$ ,  $qg$ ,  $gq$ ,  $qq$ ,

$$\chi_{\text{semi}}^{h_1 h_2}(s, b) = \chi_{gg}^{h_1 h_2}(s, b) + \chi_q^{h_1 h_2}(s, b), \quad (22)$$

with

$$\chi_q^{h_1 h_2}(s, b) = \chi_{qg}^{h_1 h_2}(s, b) + \chi_{gq}^{h_1 h_2}(s, b) + \chi_{qq}^{h_1 h_2}(s, b). \quad (23)$$

In case of nucleus–nucleus, nucleon–nucleus, or nucleon–nucleon scattering, we have obviously  $h_i = p$  or  $n$ . However, the following considerations also apply to hadron–nucleus and hadron–hadron scattering in general, for arbitrary hadrons. We nevertheless refer to ‘‘nucleons of the projectile nucleus’’ or ‘‘nucleons of the target nucleus’’, which have to be understood as ‘‘projectile hadron’’ and/or ‘‘target hadron’’ in case.

The strategy to determine the configuration is as follows: for given projectile and target nucleus, incident energy, and impact parameter, the distance between some projectile nucleon  $i$  and some target nucleon  $j$  is

$$b_{ij} = b + b_i - b_j \quad (24)$$

with  $b_i$  and  $b_j$  being the transverse coordinates of the two nucleons. In the following, we use the abbreviations

$$\chi_{\text{tot}} = \chi_{\text{tot}}^{h_1 h_2}(s, b_{ij}) \quad (25)$$

$$\chi_{\text{soft}} = \chi_{\text{soft}}^{h_1 h_2}(s, b_{ij}) \quad (26)$$

$$\chi_{\text{semi}} = \chi_{\text{semi}}^{h_1 h_2}(s, b_{ij}) \quad (27)$$

and corresponding abbreviations for  $\chi_{gg}$ ,  $\chi_{qg}$ ,  $\chi_{gq}$ ,  $\chi_{qq}$ , and for  $\chi_q$ .

The probability for an inelastic interaction (at least one cut Pomeron) is given as

$$\sigma_{\text{inel}} = \left\{ 1 - e^{-2\chi_{\text{tot}}} \right\}, \quad (28)$$

In case of an inelastic interaction, we have at least one cut Pomeron, and we have to determine the number of cut Pomerons and their types. We expand

$$\sigma_{\text{inel}} = 1 - e^{-2\chi_{\text{tot}}} \quad (29)$$

as

$$\sigma_{\text{inel}} = \sum_{m \geq 1} \sigma_{\text{inel}}^{(m)}, \quad (30)$$

with

$$\sigma_{\text{inel}}^{(m)} = \frac{(2\chi_{\text{tot}})^m}{m!} e^{-2\chi_{\text{tot}}}, \quad (31)$$

where  $\sigma_{\text{inel}}^{(m)}$  represents the probability of  $m$  cut Pomerons. In the Monte Carlo procedure, we generate  $m$  according to the distribution  $\sigma_{\text{inel}}^{(m)}$ . A particular cut Pomeron is soft or hard with probabilities

$$\frac{\chi_{\text{soft}}}{\chi_{\text{tot}}} \quad (32)$$

and

$$\frac{\chi_{\text{semi}}}{\chi_{\text{tot}}} = 1 - \frac{\chi_{\text{soft}}}{\chi_{\text{tot}}}. \quad (33)$$

In case of a semihard Pomeron, a particular type  $t$  ( $gg$ ,  $qg$ ,  $gq$ ,  $qq$ ) occurs with probability

$$\frac{\chi_t}{\chi_{\text{semi}}}. \quad (34)$$

As a summary of this section, we list in the following the algorithm to determine the Pomeron configuration.

- determine impact parameter  $b$
- loop over all projectile–target pairs  $i, j$
- determine the distance  $b_{ij} = b + b_i - b_j$  between the nucleons
- calculate the eikonals

$$\chi_{\text{tot}} = \chi_{\text{tot}}^{h_1 h_2}(s, b_{ij}) \quad (35)$$

$$\chi_{\text{soft}} = \chi_{\text{soft}}^{h_1 h_2}(s, b_{ij}) \quad (36)$$

$$\chi_{\text{semi}} = \chi_{\text{semi}}^{h_1 h_2}(s, b_{ij}) \quad (37)$$

and

$$\chi_{gg} = \chi_{gg}^{h_1 h_2}(s, b_{ij}) \quad (38)$$

$$\chi_{qg} = \chi_{qg}^{h_1 h_2}(s, b_{ij}) \quad (39)$$

$$\chi_{gq} = \chi_{gq}^{h_1 h_2}(s, b_{ij}) \quad (40)$$

$$\chi_{qq} = \chi_{qq}^{h_1 h_2}(s, b_{ij}) \quad (41)$$

$$(42)$$

- calculate the cross sections (probabilities)

$$\sigma_{\text{tot}} = \frac{2}{C} \{1 - e^{-C \chi_{\text{tot}}}\}, \quad (43)$$

$$\sigma_{\text{inel}} = \frac{1}{C} \{1 - e^{-2C \chi_{\text{tot}}}\}, \quad (44)$$

$$\sigma_{\text{dif}} = \left(1 - \frac{1}{C}\right) (\sigma_{\text{tot}} - \sigma_{\text{inel}}) \quad (45)$$

- realize an interaction with probability

$$\sigma_{\text{inel}} + \sigma_{\text{dif}} \quad (46)$$

- in case of an interaction, consider it to be diffractive or nondiffractive with probabilities

$$\frac{\sigma_{\text{dif}}}{\sigma_{\text{inel}} + \sigma_{\text{dif}}} \quad (47)$$

and

$$\frac{\sigma_{\text{inel}}}{\sigma_{\text{inel}} + \sigma_{\text{dif}}} \quad (48)$$

- in case of a nondiffractive interaction, determine number  $m$  of cut Pomerons according to the distribution  $\sigma_{\text{inel}}^{(m)}$  see eq. (31)
- loop over cut Pomerons  $m$
- determine the nature of the Pomeron. Take it to be soft with probability

$$\frac{\chi_{\text{soft}}}{\chi_{\text{tot}}} \quad (49)$$

and to be semihard with probability

$$\frac{\chi_{\text{semi}}}{\chi_{\text{tot}}} \quad (50)$$

- In case of a semihard Pomeron, determine its type  $t$  ( $gg, qg, gq, qq$ ) according to the probabilities

$$\frac{\chi_t}{\chi_{\text{semi}}} \quad (51)$$

## V. OUTLOOK

Having determined the configuration, one calculates the energy sharing among the Pomerons, for the semihard Pomerons also the energy sharing among the soft and the hard pieces. In case of semihard Pomerons, the parton ladders have to be generated explicitly. Finally, partons and remnants constitute kinky strings. The details of these different procedures will be explained in a future publication.

## REFERENCES

- [1] K. Werner, Physics Reports 232 (1993) 87-299
- [2] N.N. Kalmykov, S.S. Ostapchenko, Phys. At. Nucl. (USA), 56 (1993) N3 346

# Signatures of Dense Hadronic Matter in Ultrarelativistic Heavy Ion Reactions\*

L.A. Winckelmann<sup>d</sup>, C. Ernst<sup>b,d</sup>, L. Gerland<sup>d</sup>, J. Konopka<sup>d</sup>, S. Soff<sup>e</sup>, S.A. Bass<sup>d</sup>, M. Bleicher<sup>d</sup>, M. Brandstetter<sup>d</sup>, A. Dumitru<sup>d</sup>, C. Spieles<sup>d</sup>, H. Weber<sup>d</sup>, C. Hartnack<sup>f</sup>, J. Aichelin<sup>f</sup>, N. Amelin<sup>g</sup>, H. Stöcker<sup>cd</sup> and W. Greiner<sup>d</sup>

<sup>d</sup>*Institut für Theoretische Physik, Johann Wolfgang Goethe-Universität, Frankfurt, Germany*

<sup>e</sup>*Gesellschaft für Schwerionenforschung, Darmstadt, Germany*

<sup>f</sup>*SUBATECH, Ecole des Mines, Nantes, France*

<sup>g</sup>*Joint Institute for Nuclear Research (JINR), Dubna, Russia*

## Abstract

The behavior of hadronic matter at high baryon densities is studied within Ultrarelativistic Quantum Molecular Dynamics (URQMD). Baryonic stopping is observed for Au+Au collisions from SIS up to SPS energies. The excitation function of flow shows strong sensitivities to the underlying equation of state (EOS), allowing for systematic studies of the EOS. Dilepton spectra are calculated with and without shifting the  $\rho$  pole. Except for S+Au collisions our calculations reproduce the CERES data.

## I. INTRODUCTION

The only possibility to probe excited nuclear matter in the laboratory are nucleus-nucleus reactions [1]. In particular when two heavy ions like Au or Pb collide most centrally, the combined system forms a zone of high (energy) density and high excitation of the involved constituents. The transient pressure at high density has specific dynamic implications, such as collective sideward flow. Hence, fundamental properties like the repulsion of the nuclear equation of state (EOS) are studied via event shape analysis of nucleons and clusters [2–4]. The EOS at fixed temperature yields a density dependent potential and a modified nucleon mass. At low densities these effects are proposed by chiral lagrangians [5]. [7]. Since the chiral condensate  $\langle \bar{q}q \rangle$  relates closely to hadron masses, the decay of short lived vector mesons, observed through the dilepton channel, is suggested as a promising experimental signal to investigate the gradual restoration of chiral symmetry.

---

\*Supported by BMBF, DFG and GSI, <sup>b</sup>E-mail: ernst@th.physik.uni-frankfurt.de, <sup>c</sup>Invited speaker

N	$\Delta$	$\Lambda$	$\Sigma$	$\Xi$	$\Omega$	
938	1232	1116	1192	1317	1672	
1440	1600	1405	1385	1530		$1^-$
1520	1620	1520	1660	1690		$\rho(1450)$
1535	1700	1600	1670	1820		$\rho(1700)$
1650	1900	1670	1790	1950		$\omega(1420)$
1675	1905	1690	1775			$\omega(1600)$
1680	1910	1800	1915			
1700	1920	1810	1940			$0^-$ $1^-$ $0^+$ $1^+$ $2^+$
1710	1930	1820	2030			$\pi$ $\rho$ $a_0$ $a_1$ $a_2$
1720	1950	1830				$K$ $K^*$ $K_0^*$ $K_1^*$ $K_2^*$
1990		2100				$\eta$ $\omega$ $f_0$ $f_1$ $f_2$
		2110				$\eta'$ $\phi$ $\sigma$ $f_1'$ $f_2'$

Table 1: List of implemented baryons, mesons and their resonances. In addition *all* charge conjugate and iso-spin projected states (and photons) are taken in and treated on the same footing.

## II. ULTRARELATIVISTIC QUANTUM MOLECULAR DYNAMICS

Since many important aspects of nuclear matter are not observable, numerical transport models are suited to test which assumptions are compatible to nature. The present model (URQMD) [8,9] includes explicitly 50 different baryon species (nucleon, delta, hyperon and their resonances up to masses of 2.11 GeV) and 25 different meson species (including strange meson resonances), which are supplemented by all isospin-projected states (see Table 1). Symmetries regarding time inversion, iso-spin, charge conjugation, etc. are implemented in a general manner, e.g. all corresponding antiparticles are included and treated on the very same (charge-conjugate) footing. For excitations of higher masses a newly developed string model is invoked. It consistently allows for the population of *all* included hadrons from a decaying string. At low energies the dominant part of MM and MB interactions is modeled via *s*-channel reactions (formation and decays of resonances), whereas BB interactions are designed as exchange of charge, strangeness and four momentum in the *t*-channel. For all resonances we use mass-dependent decay widths as illustrated in Fig.1 for the  $a_2$  meson. The lifetime of resonances is calculated as their inverse width. There exist, however, recent theoretical ansatzes which yield a different mass dependence for the life-times of resonances [10]. The real part of the baryon optical potential is modeled according to the simple Skyrme ansatz, including Yukawa and Coulomb forces.

## III. CREATION OF DENSE NUCLEAR MATTER: STOPPING

Baryonic stopping is a necessary condition for the creation of hot and dense nuclear matter. The key observable is the rapidity distribution of baryons. It is displayed in Fig.2

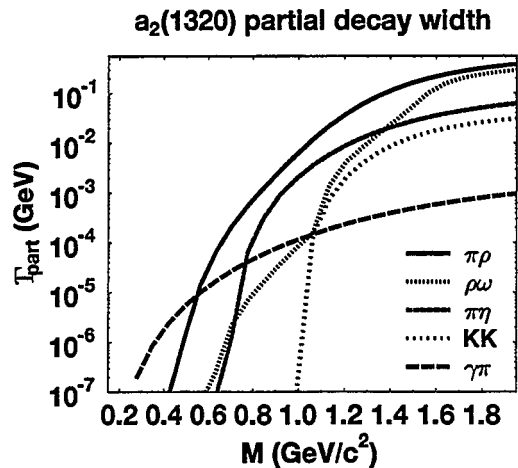


FIG. 1.  $a_2$  partial decay rates into specific channels. The average lifetime is given by the inverse of the sum. Hence, in URQMD particles below resonance mass live longer, due to shrinking phase space.

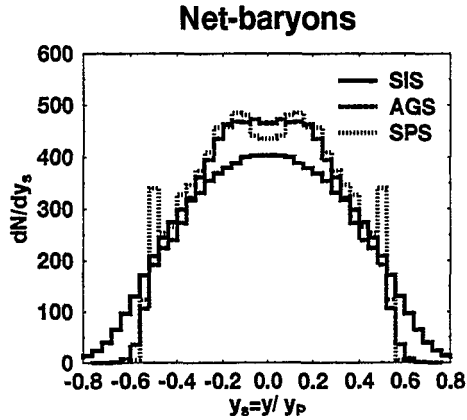


Fig.2. Rapidity distributions for Au+Au collisions at SIS (1 AGeV), AGS (10.6 AGeV) and Pb+Pb at CERN/SPS energies (160 AGeV).

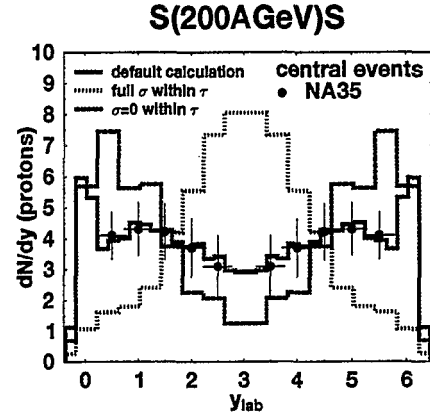


Fig.3. Rapidity distribution for S(200 AGeV)S for various treatments of the constituent (di-)quark cross section (see text).

and 4 for heavy systems such as Au+Au and Pb+Pb at energies referring to three presently used heavy ion accelerators. In all cases gaussian rapidity distributions with peak around midrapidity are found. However, the physical processes associated show characteristic differences: The average longitudinal momentum loss in the SIS energy regime is mainly due to the creation of transverse momentum, whereas at AGS/SPS energies abundant particle production consumes a considerable amount of the incident beam energy.

At CERN/SPS energies baryon stopping is influenced also by the formation time of strings which are excited in hard collisions. In URQMD baryons originating from a leading constituent (di-)quark at the string edges interact with  $(2/3)1/3$  and mesons with  $1/2$  of their full cross sections during their formation time  $\tau$ . The sensitivity on this reduction is shown in Fig.3 for the system S+S at 200 AGeV. The default calculation (including formation time) reproduces the data [11] fairly well whereas the calculation with zero formation time (dotted line) exhibits strongest stopping. A calculation with zero cross section within the formation time gives transparency.

In order to study the influence of this effect more closely the  $\sqrt{s}$  distributions for Au+Au collisions at AGS and S+S collisions at SPS energies are analyzed. Fig.5 (right) shows the respective distribution for Au+Au. The collision spectrum is dominated by BB collisions with full cross sections and exhibits a maximum at low energies. Approximately 20% of the collisions involve a diquark, i.e. a baryon originating from a string decay whose cross section is reduced to  $2/3$  of its full cross section.

In Fig.5 (left) the same analysis is performed for S+S at 200 AGeV. In contrast to the heavy system at AGS the collision spectrum exhibits two pronounced peaks dominated by full BB collisions, one in the beam energy range and one in the low (thermal) energy range. Now approximately 50% of the collisions, most of them at intermediate  $\sqrt{s}$  values, involve baryons stemming from string excitations whose cross sections are reduced by factors of  $2/3$  (referred to as *diquarks*) or  $1/3$  (referred to as *quarks*). The peak at high  $\sqrt{s}$  values stems from the initial hard collisions whereas the peak at low energies is related to the late, thermal stages of the reaction.



## IV. PROBING THE REPULSION OF THE EOS: FLOW

The creation of transverse flow is strongly correlated to the underlying EOS [1]. In particular it is believed that secondary minima as well as the quark-hadron phase transition lead to a weakening of the collective sideward flow. The occurrence of a phase transition should therefore be observable through abnormal behaviour (e.g. jumps) of the strength of collective motion of the matter [13]. Note that URQMD in its present form does not include any phase transition explicitly. In Fig.6 the averaged in plane transverse momentum is displayed for Au+Au from 0.1 to 4 AGeV incident kinetic energy. Calculations employing a hard EOS (full squares) are compared to cascade simulations (full circles). In the latter case only a slight energy dependence is observed. In contrast, the calculation with a hard EOS shows strong sensitivity. Here, the integrated directed transverse momentum per nucleon is more than twice as high as for the cascade calculation. This indicates the importance of a non-trivial equation of state of hadronic matter.

The amount of directed transverse momentum scales in the same way as the total transverse momentum produced in the course of the reaction. Hence, the directivity depends only on the reaction geometry but not on the incident energy. This is demonstrated in Fig.7, where the mean  $p_x$  as a function of the rapidity divided by the average transverse momentum of all particles is plotted.

## V. TEMPERATURE DEPENDENCE OF THE EOS: PHOTONS

Semiclassical cascade models in terms of scattering hadrons have proven to be rather accurate in explaining experimental data. Therefore it is of fundamental interest to extract the equation of state from such a microscopic model, i.e. to investigate the equilibrium limits and bulk properties, which are not an explicit input to the non-equilibrium transport approach with its complicated collision term (unlike e.g. in hydrodynamics [13,14]). In Fig.8 the thermodynamic properties of infinite nuclear matter are studied within URQMD.

Infinite hadronic matter is simulated in URQMD by constructing a box of 250 fm<sup>3</sup> volume with periodic boundary conditions. According to the saturation density, nucleons are initialized randomly in phase space, such that a given energy density is reproduced. After the system has equilibrated according to the simulation with URQMD the temperature is extracted by fitting the particles' momentum spectra. Alternatively, the temperature can be extracted from the relative abundances of different hadrons, e.g. the  $\Delta/N$  ratio.

In Fig.8 the result of this procedure is compared to various analytic forms of the EOS. While the EOS of a Hagedorn gas and a QGP yields energy densities  $\epsilon \sim 1\text{GeV}/\text{fm}^3$  at  $T = 150\text{ MeV}$  the temperature dependence is much smaller in URQMD. It yields about 4-5 times less energy density, being in fair agreement with a gas composed of nonrelativistic nucleons and ultrarelativistic pions. It remains to be seen whether a reparametrization of the resonance continuum in the Hagedorn model as suggested in Ref. [17] would resolve the deviation as compared to URQMD. On the other hand, beyond  $T \sim 200\text{ MeV}$  the energy density rises much faster than  $T^4$  approaching even the QGP value of  $\epsilon \sim 10\text{ GeV}/\text{fm}^3$  around  $T = 300\text{ MeV}$ . This indicates an increase in the number of degrees of freedom. It may be interpreted as a consequence of the numerous high mass resonances and string excitations, which seem to release constituent quark degrees of freedom (but, of course, no

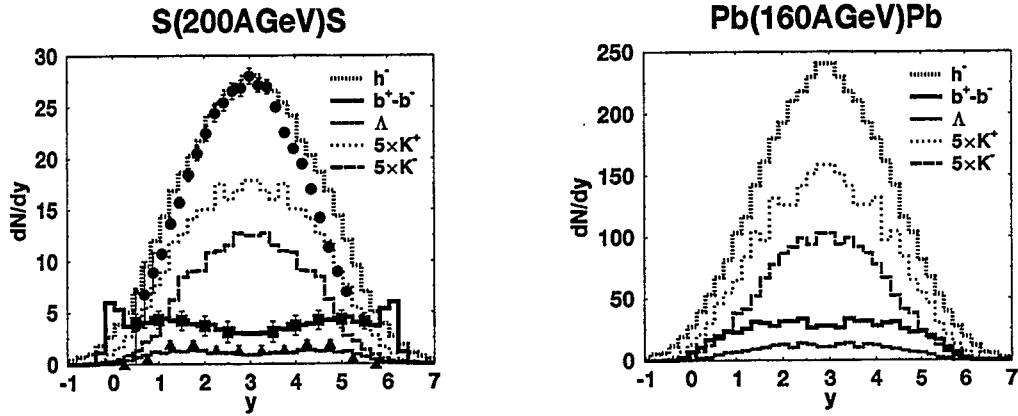


Fig.4. Rapidity distributions for S+S at 200 AGeV (left) and Pb+Pb at 160 AGeV (right). The histograms label from top to bottom: negative hadrons ( $h^-$ ), kaons ( $K^-, K^+$ ), protons ( $b^+ - b^-$ ) and lambdas ( $\Lambda$ ). The kaons are multiplied by five. The symbols show data from NA35 [11].

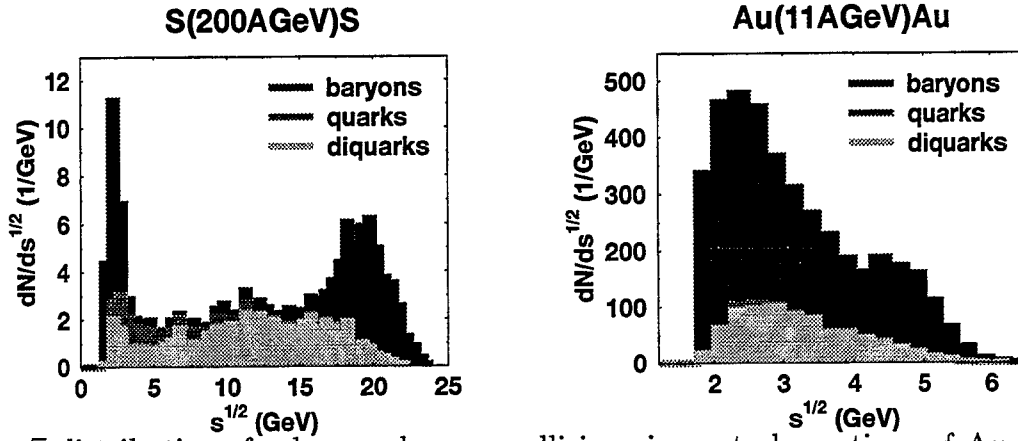


Fig.5.  $\sqrt{s}$  distributions for baryon baryon collisions in central reactions of Au+Au (left) and S+S (right) at AGS and SPS energies respectively.

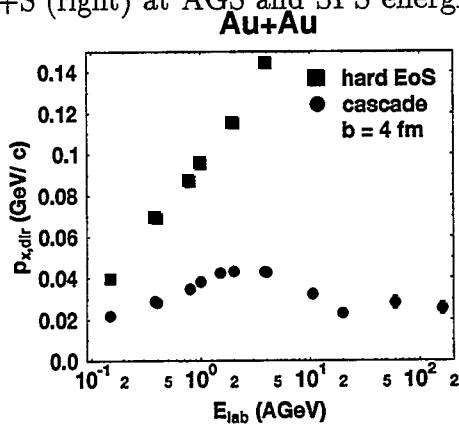


Fig.6. Excitation function of the total directed transverse momentum transfer  $p_{x,dir}$  for Au+Au. URQMD calculations including a hard EOS (full squares) are compared to the predictions of cascade calculations (full circles).

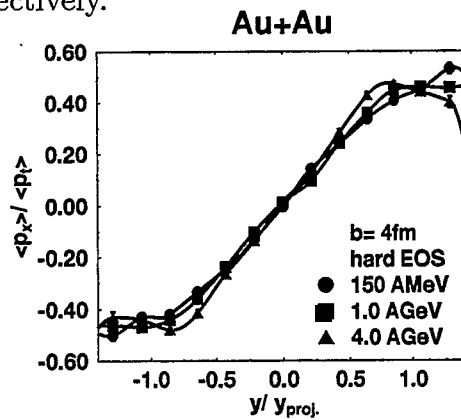


Fig.7. Mean directed transverse momentum as a function of the scaled rapidity. The transverse flow  $\langle p_x \rangle (y/y_{proj.})$   $s$ -scales with the mean transverse momentum  $\langle p_t \rangle$ , i.e. directivity does not depend on the bombarding energy.

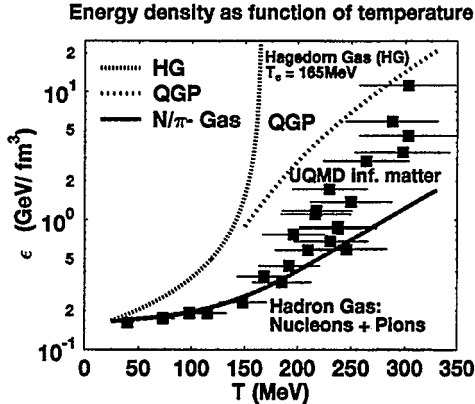


Fig.8. 'EOS' of infinite nuclear matter as a function of the energy density versus temperature at fixed net-baryon density of  $\rho_B = 0.16/\text{fm}^3$  in URQMD (symbols). The curves refer to analytical forms of the EOS, i.e. a Hagedorn-gas (top), a quark-gluon plasma (middle), and an ideal gas of nucleons and ultrarelativistic pions (bottom).

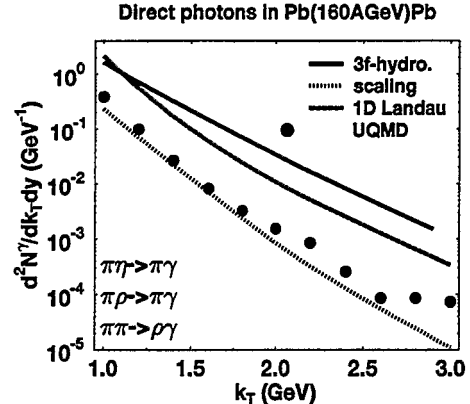


Fig.9. Transverse momentum spectrum of directly produced photons in Pb+Pb collisions at 160 AGeV calculated with URQMD. The resulting spectrum is compared with hydrodynamical calculations. In all models the processes  $\pi\eta \mapsto \pi\gamma$ ,  $\pi\rho \mapsto \pi\gamma$  and  $\pi\pi \mapsto \rho\gamma$  are considered as photon sources.

free current quarks as in an ideal QGP). Investigations of equilibration times and relative particle and cluster abundances are in progress. Moreover, the admittedly poor statistics have to be improved, in order to study the high temperature behavior.

Experimentally, the EOS can be accessed by measuring electromagnetic radiation [15]. In Fig.9 the direct photon production from meson+meson collisions in Pb+Pb collisions at 160 AGeV is shown. Here, only mesons stemming from string decays are included. Elastic meson-meson scattering with  $\sigma_{el} = 15\text{mb}$  (independent of  $\sqrt{s}$ ) was allowed. The result is compared to calculations within the 3-fluid model [14], scaling and Landau expansion with  $T_i = 300$  MeV.

## VI. IN MEDIUM MASSES: DILEPTONS

In Fig.10 and 11 calculations of dilepton spectra with URQMD are shown for  $p+\text{Be}$  and  $\text{S}+\text{Au}$ . Dilepton sources considered here are Dalitz decays ( $\pi^0$ ,  $\eta$  and  $\omega$ ) and vector meson decays ( $\rho$ ,  $\omega$  and  $\phi$ ). Dalitz decays of heavier meson and baryon resonances are included explicitly via their emission of  $\rho$  mesons (assuming vector meson dominance). In order to avoid double counting, the  $\rho$  mesons from  $\eta$ 's, and  $\omega$ 's are excluded from the  $\rho$  contribution. Pion annihilation is included dynamically into the contribution of decaying  $\rho$  mesons ( $\pi^+\pi^- \mapsto \rho \mapsto e^+e^-$ ).

While the result for  $p+\text{Be}$  agrees well with the published data from CERES/SPS [18], two points around  $M \sim 400$  MeV are missed by about two standard deviations for  $\text{S}+\text{Au}$ . Speculations about the origin of this deviation include electromagnetic bremsstrahlung, annihilations of pions and a modification of the  $\rho$  meson propagator due to a gradual restoration

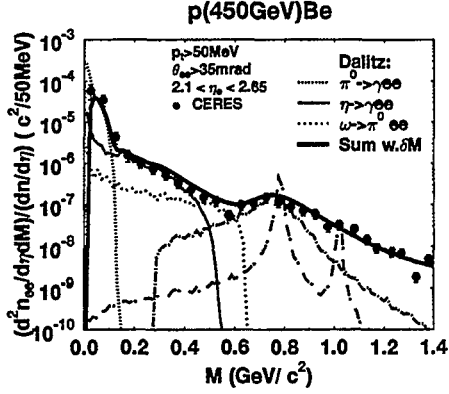


Fig.10. Dilepton mass spectrum for  $p+\text{Be}$  at 450 GeV. The calculation includes Dalitz decays and conversion of vector mesons (see also legend for S+Au). The sum of all contributions (solid curve) is folded with the CERES mass resolution.

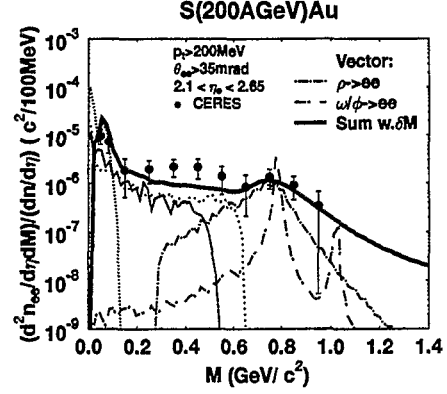


Fig.11. Dilepton mass spectrum for S+Au at 200 AGeV (see also legend for  $p+\text{Be}$ ). Here no in-medium modifications of the  $\rho$  propagator is considered. Around  $M \sim 400$  MeV two points are missed by  $< 2\sigma$ .

of the chiral symmetry.

In URQMD the contribution of pion annihilation to the  $\rho$ -peak ( $\pi^+\pi^- \mapsto \rho$ ) is only 40% for S+Au. Major additional sources are decays of heavy baryons ( $\Delta^*/N^* \mapsto N\rho$ ) as proposed in Ref. [19] and meson resonances (see also Fig.1):

$$\begin{pmatrix} \eta, \omega, \eta', \phi \\ a_1, f_1, a_2, f_2 \\ \omega(1420), \rho(1450) \\ \omega(1600), \rho(1700) \end{pmatrix} \mapsto \begin{pmatrix} \rho\gamma \\ \rho\pi \\ \rho\sigma \\ \rho\rho \end{pmatrix}. \quad (1)$$

In Ref. [5,7] a linear dependence of the  $\rho^0/\omega$  pole position as a function of the nuclear density  $\rho$  has been suggested:  $m_{\rho^0}(\rho/\rho_0) = m_{\rho^0}(0)(1 - \lambda\rho/\rho_0)$ . Here  $\rho_0$  denotes the ground state density of nuclear matter, and  $\lambda = 0.18$ , in agreement with various other calculations. Since the restriction to low densities may not be suitable for heavy ion collisions, the following extrapolation towards higher densities is taken:

$$m_{\rho^0}(\rho/\rho_0) = \frac{m_{\rho^0}(0)}{1 + \lambda \rho/\rho_0}. \quad (2)$$

In Fig.12 an application of Eq.(2) is made to calculate a dielectron mass spectrum for a density dependent vector meson pole. This result yields only a small enhancement around  $M \sim 500$  MeV as compared to the calculation without pole shift (bottom curve). On the other hand, the data can nicely be reproduced, if the strong (unphysical) assumption is made, that the pole at the decay point ( $\rho \mapsto e^+e^-$ ) is shifted according to the creation density (upper curve). This would be a neglect of the finite decay length. The discrepancy of a calculation without decay length ( $\lambda_{\text{dec}} = 0$  fm) as compared to the result including the decay length is driven by two reasons: i) The increase of the  $\rho$  lifetime ( $\sim 7$  fm/c) below its resonance mass in the region  $M \sim 0.3-0.5$  GeV (where a dilepton excess in S+Au is reported [18]) lowers the decay density down to  $\langle \rho \rangle \sim 0.2\rho_0$  for S+Au (or  $0.3\rho_0$  for Pb+Au). ii) An

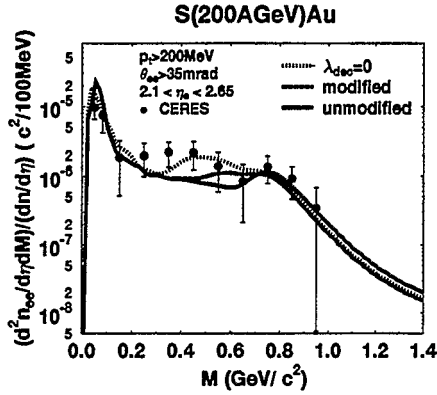


Fig.12. Dilepton mass spectrum for S+Au at 200 AGeV. The curves label simulations with pole shift according to the creation density (top), the decay density (middle) and without pole shift (bottom).

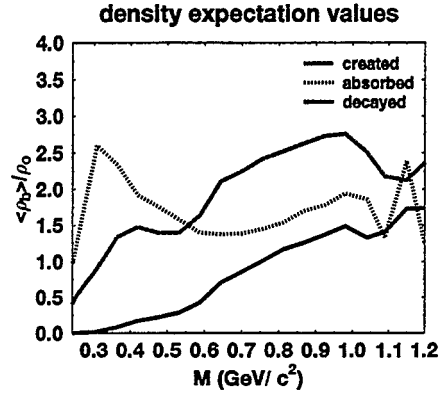


Fig.13. Dependency of  $\rho$ -interactions on the density expectation values. The curves show the values for the creation, absorption and decay of  $\rho$  mesons. Note that  $\langle \rho_b \rangle < 0.5 \rho_0$  around  $M \simeq 0.4$  GeV.

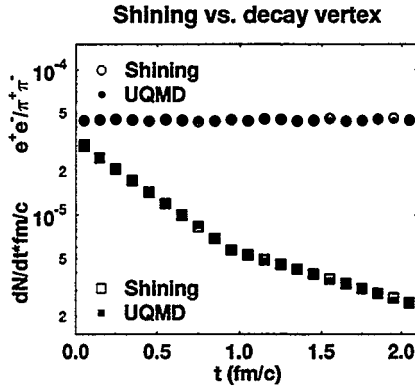


Fig.14 Comparison of the treatment of shining  $\rho$ -sources to the URQMD approach, where the dileptons are created at the  $\rho$  decay vertex. For  $t < 1$  fm/c a constant  $\rho$  absorption is considered. Both methods show the same time dependence.

enhancement of the decay length leads to an increase of reabsorption. Hence, the radiation path for  $\rho \mapsto e^+e^-$  is substantially truncated. This fact is further investigated in Fig.13, where the effect of the mass dependent  $\rho$ -width is depicted by the course of the density dependence for  $\rho$  mesons with invariant masses  $M$ . The decreasing width (i.e. increasing lifetime) of low-mass-resonances leads to higher mean decay times where the baryon density is already dilute. Thus in-medium-corrections can only yield small enhancements when treated this way. However, the interpretation of the experimental data gives the following impression: The data for light systems such as  $p$ +Be and  $p$ +Au (see also Ref. [21,22]) as well as the data for the heavy Pb+Au system both for inclusive and central reactions are reproducible without mass shifts. In contrast, the central data for S+Au exceed the URQMD calculation around  $M \sim 0.4$  GeV by about two standard deviations.

In URQMD the  $\rho$  meson pole position is shifted according to the density at which the  $\rho$  meson decays, i.e. eventually converts into  $e^+e^-$ . Note that this procedure is equivalent to a "shining" description, where the  $\rho$  constantly emits  $e^+e^-$  pairs according to the rate  $dN^{ee}/dt = \Gamma(\rho \mapsto e^+e^-)$ . In Fig.14 the shining description is compared to the treatment in URQMD for a  $\rho$  source at rest including a time dependent reabsorption probability. Both methods yield - within the statistical limits - the same average emission times. Furthermore

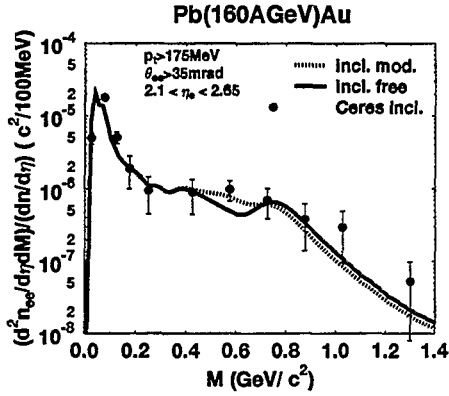


Fig.15. Dilepton mass spectra for Pb+Au at 160 AGeV. The curves label calculations for inclusive reactions with (mod.) and without a pole shift (free). The symbols refer to preliminary data for peripheral events from CERES.

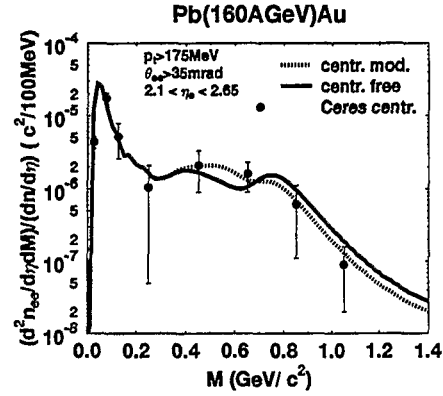


Fig.16. Dilepton mass spectra for Pb+Au at 160 AGeV. The curves label calculations for central reactions with (mod.) and without a pole shift (free). The symbols refer to preliminary data for high multiplicity events from CERES.

a simple time dependent density profile is used to calculate the mean  $e^+e^-$  emission density. Again, both methods yield the same values.

The results for Pb+Au are shown in Figs.15 and 16. Both calculations for inclusive reactions are in fair agreement with the preliminary observation from CERES [20]. The result for central events is given in Fig.16. Note that the calculations without modifications are well compatible for  $p+Be$  and Pb+Au for both centralities. Only in S+Au reactions two datapoints are missed by the default calculation by about two standard deviations.

## VII. SUMMARY

Studies of the equation of state and consequences of gradual restoration of the chiral symmetry are presented using a novel microscopic phase space model, URQMD, including 75 hadron species and strings. The directed transverse momentum shows strong sensitivities to the underlying EOS: It is small in the cascade calculation, whereas it scales linearly with the average transverse momentum for a hard equation of state. Hence, measuring the excitation function of the transverse directed flow allows for a systematic study of the EOS. The calculation of dilepton yields without modifications of the  $\rho$  mass pole is well compatible with the CERES-data for  $p+Be$  and Pb+Au. Only in S+Au reactions two datapoints at 0.3 – 0.5 GeV are missed by the default URQMD-calculation by about two standard deviations.

## REFERENCES

- [1] H. Stöcker and W. Greiner, Phys. Rep. **137**(1986)277
- [2] K. G. R. Doss et al., Phys. Rev. Lett. **57**(1986)302 and **59**(1987)2270

- [3] R. Mattiello, A. Jahns, H. Sorge, H. Stoecker and W. Greiner, *Phys. Rev. Lett.* **74**(1995)2180
- [4] M. D. Partlan et al., *Phys. Rev. Lett.* **75**, 2100 (1995).
- [5] G. E. Brown and M. Rho, *Phys. Rev. Lett.* **66**(1991)2720
- [6] K. Kusaka and W. Weise, *Phys. Lett.* **288B**(1992)6
- [7] T. Hatsuda and S. H. Lee, *Phys. Rev. C* **46**(1992)R34
- [8] The URQMD-Collaboration, source code and documentation, to be published
- [9] L. A. Winckelmann, PhD-thesis, Harri Deutsch 1996, ISBN 3-8171-1517-2
- [10] P. Danielewicz and S. Pratt, *Phys. Rev. C* **53**(1996)249
- [11] S. Wenig, PhD-thesis, Frankfurt (1990)
- [12] J. Konopka, S. A. Bass, M. Bleicher, M. Brandstetter, C. Ernst, L. Gerland, W. Greiner, S. Soff, C. Spieles, H. Stocker, H. Weber, L. A. Winckelmann, CRIS '96, e-Print Archive: nucl-th/9607015
- [13] D.H. Rischke et al., *Heavy Ion Physics* **1**(1995)309
- [14] A. Dumitru, U. Katscher, J.A. Maruhn, H. Stöcker, W. Greiner, D.H. Rischke, *Phys. Rev. C* **51**(1995)2166
- [15] J. Kapusta, P. Lichard, D. Seibert, *Phys. Rev.* **D44**(1991)2774
- [16] C. Spieles, A. Dumitru, S. A. Bass, M. Bleicher, J. Brachmann, M. Brandstetter, C. Ernst, L. Gerland, J. Konopka, S. Soff, H. Weber, L. A. Winckelmann, J. Maruhn, H. Stoecker, W. Greiner, PANIC '96, e-Print Archive: nucl-th/9606030
- [17] H. Stöcker, A.A. Ogloblin and W. Greiner, *Z. Phys. A* **303**(1981)259
- [18] G. Agakichev for the CERES collaboration, *Phys. Rev. Lett.* **75**(1995)1272
- [19] L. A. Winckelmann, H. Stöcker, W. Greiner, H. Sorge, *Phys. Rev. C* **51**(1995)9
- [20] T. Ullrich for the CERES collaboration, Proceedings to Quark-Matter '96, *Nucl. Phys. A*(in press)
- [21] C. M. Ko et al., Proceedings to Quark-Matter '96, *Nucl. Phys. A*(in press)
- [22] W. Cassing, W. Ehehalt, C. M. Ko, *Phys. Lett.* **363B**(1995)35

# Charm Production at RHIC

R. Vogt\*

*Lawrence Berkeley National Laboratory, Berkeley, California*

*and*

*Physics Department, University of California, Davis, California*

## Abstract

A study of  $c\bar{c}$  production at next-to-leading order in  $pp$  collisions is presented for RHIC energies. The dependence of the rates on the renormalization and factorization scales is discussed. We also discuss the charm contribution to the dilepton continuum above 2 GeV/ $c^2$ .

Charm production in the initial nucleon-nucleon collisions will be copious in heavy-ion colliders. Semileptonic charm decays represent a significant background to dilepton production [1]. A quantitative knowledge of the production cross section in  $pp$  collisions is a prerequisite for understanding the nuclear dependence and detecting the quark-gluon plasma.

Previous measurements of the  $c\bar{c}$  production cross section suggested that the lowest order (LO),  $\mathcal{O}(\alpha_s^2)$ , results underpredicted the data by a factor of two to three [2,3], called the  $K$  factor as in Drell-Yan production. More generally,

$$K_{\text{exp}} = \frac{\sigma_{\text{data}}(AB \rightarrow c\bar{c})}{\sigma_{\text{theory}}(AB \rightarrow c\bar{c})}. \quad (1)$$

The projectile and target,  $A$  and  $B$ , can be either hadrons or nuclei. From the next-to-leading order (NLO) corrections,  $\mathcal{O}(\alpha_s^3)$ , [4,5], a theoretical  $K$  factor can be defined,

$$K_{\text{th}} = \frac{\sigma_{\text{NLO}}(AB \rightarrow c\bar{c})}{\sigma_{\text{LO}}(AB \rightarrow c\bar{c})}, \quad (2)$$

where  $\sigma_{\text{NLO}}$  is the sum of the LO and NLO corrections. Particularly for the charm quark, the NLO cross section is strongly dependent on the renormalization and factorization scales which determine both  $K_{\text{exp}}$  and  $K_{\text{th}}$ .

We summarize results from several recent papers and only discuss charm production at RHIC. The same arguments apply to other heavy flavors. For full details, see [1,6,7].

The double differential  $c\bar{c}$  pair production cross section is

---

\*Supported by the U. S. Department of Energy under Contract No. DE-AC03-76SF00515.



$$E_c E_{\bar{c}} \frac{d\sigma_{AB}}{d^3 p_c d^3 p_{\bar{c}}} = \sum_{i,j} \int dx_1 dx_2 F_i^A(x_1, \mu_F) F_j^B(x_2, \mu_F) E_c E_{\bar{c}} \frac{d\hat{\sigma}_{ij}(x_1 P_1, x_2 P_2, m_c, \mu_R)}{d^3 p_c d^3 p_{\bar{c}}} \quad (3)$$

where  $i$  and  $j$  are the interacting partons and  $F_i^A$  are the parton densities in the hadron with momentum fraction  $x$  and mass factorization scale  $\mu_F$ . The partonic cross section,  $\hat{\sigma}_{ij}$ , is a perturbation series in  $\alpha_s(\mu_R)$  where  $\mu_R$  is the renormalization scale. Both scales are of order  $m_c$ . At LO,  $\mu_F = \mu_R = \mu$  while at higher orders the scales can be independent.

At LO,  $c\bar{c}$  production proceeds by two basic processes,  $q\bar{q} \rightarrow c\bar{c}$  and  $gg \rightarrow c\bar{c}$ . The invariant cross section for a pair of hadrons is

$$E_D E_{\bar{D}} \frac{d\sigma_{AB}}{d^3 p_D d^3 p_{\bar{D}}} = \int \frac{\hat{s}}{2\pi} dx_1 dx_2 dz_c dz_{\bar{c}} C(x_1, x_2) \frac{E_D E_{\bar{D}}}{E_c E_{\bar{c}}} \frac{D_{D/c}(z_c)}{z_c^3} \frac{D_{\bar{D}/\bar{c}}(z_{\bar{c}})}{z_{\bar{c}}^3} \delta^4(p_1 + p_2 - p_c - p_{\bar{c}}), \quad (4)$$

where  $\sqrt{\hat{s}}$ , the parton-parton center of mass energy, is related to  $\sqrt{s}$ , the hadron-hadron center of mass energy, by  $\hat{s} = x_1 x_2 s$  where  $x_{1,2} = (\widehat{m}_c / \sqrt{s})(e^{\pm y_c} + e^{\pm y_{\bar{c}}})$  and  $\widehat{m}_c = \sqrt{m_c^2 + p_T^2}$ . The sum of the LO subprocess cross sections convoluted with the parton number densities is contained in  $C(x_1, x_2)$  [6,8],

$$C(x_1, x_2) = \sum_q [F_q^A(x_1) F_{\bar{q}}^B(x_2) + F_{\bar{q}}^A(x_1) F_q^B(x_2)] \frac{d\hat{\sigma}_{q\bar{q}}}{d\hat{t}} + F_g^A(x_1) F_g^B(x_2) \frac{d\hat{\sigma}_{gg}}{d\hat{t}}. \quad (5)$$

Only light flavors with  $m < m_c$  are included in the sum. The  $\mu_F$  dependence has been suppressed.

The fragmentation functions,  $D_{D/c}(z)$ , describe the hadronization of the charm quarks where  $z$  is the fraction of the charm momentum in the hadron. Fragmentation affects the charmed hadron distributions, not the total  $c\bar{c}$  production cross section. The  $D$  meson  $x_F$  distribution is harder than the predicted charmed quark distribution in hadron-hadron interactions because at low  $p_T$  the charmed quark can coalesce with comoving light quarks. Fragmentation functions tuned to  $D$  production in  $e^+e^-$  annihilation soften the  $D$  distribution through light  $q\bar{q}$  pair production [9].

At NLO, in addition to virtual corrections to the LO diagrams, real production by  $q\bar{q} \rightarrow c\bar{c}g$ ,  $gg \rightarrow c\bar{c}g$ , and  $q(\bar{q})g \rightarrow c\bar{c}(\bar{q})q$  must also be included. Quark-gluon scattering has been interpreted at LO as flavor excitation [4], small near threshold. The partonic cross section  $\hat{\sigma}_{ij}$  is

$$\hat{\sigma}_{ij}(\hat{s}, m_c, \mu_R) = \frac{\alpha_s^2(\mu_R)}{m_c^2} \left\{ f_{ij}^0(\rho) + \frac{\alpha_s(\mu_R)}{4\pi} [f_{ij}^1(\rho) + \bar{f}_{ij}^1(\rho) \ln(\mu_R^2/m_c^2)] + \mathcal{O}(\alpha_s^2) \right\} \quad (6)$$

where  $\rho = 4m_c^2/\hat{s}$ . At LO,  $f_{qg}^0 = 0$ . Our calculations of the total and differential hadronic cross section are done using a Monte Carlo program developed in Refs. [4,5]. Note that in  $c\bar{c}$  pair production, the cancellation of soft and collinear divergences is performed within the numerical integration. The price paid for this is often a negative cross section near the phase space boundaries, particularly when  $p_T \rightarrow 0$  and  $\phi \rightarrow \pi$  since these distributions are trivial at LO. A positive differential cross section for  $p_T \rightarrow 0$  can only be obtained by resumming the leading logarithms, not yet done for heavy quark production [5].

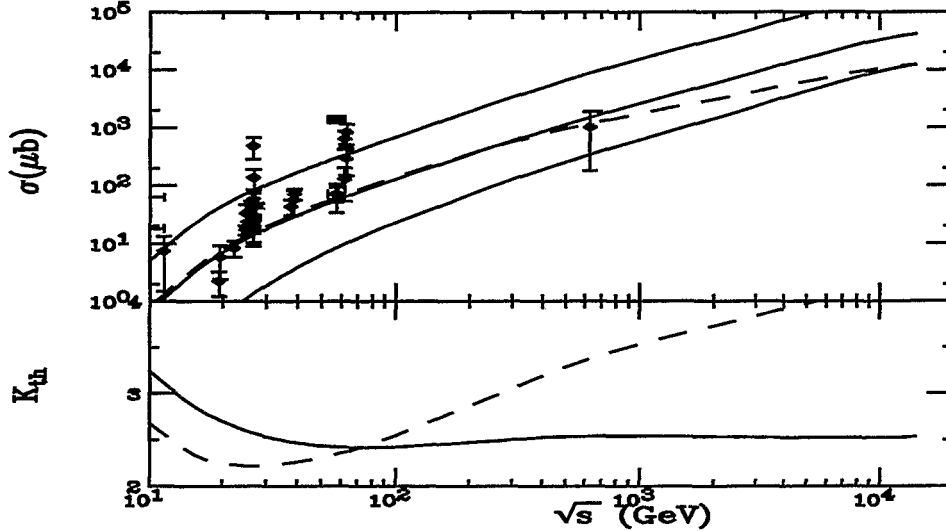


FIG. 1. The variation in  $\sigma_{cc}^{\text{tot}}(s)$  and  $K_{\text{th}}(s)$  with parton density,  $m_c$  and  $\mu$ . In (a) the three solid curves are calculated with MRS D-’ densities and  $m_c = 1.2$  GeV,  $\mu_R = m_c/2$  (upper);  $m_c = 1.2$  GeV,  $\mu_R = 2m_c$  (middle); and  $m_c = 1.8$  GeV,  $\mu_R = 2m_c$  (lower). The other calculations are with the GRV HO densities. The dashed curve, with GRV HO, has  $m_c = 1.3$  GeV,  $\mu = m_c$ .  $K_{\text{th}}$  is shown in (b) for the central MRS D-’ and the GRV HO calculations.

The physical cross section should be independent of the scale. If further higher-order corrections are small, at some scale  $\sigma(\mathcal{O}(\alpha_s^{n+1})) < \sigma(\mathcal{O}(\alpha_s^n))$ . When the scale dependence is strong, as is true for charm, convergence of the expansion is slow [8]. Although the scales are, in principle, independent, we take  $\mu_F = \mu_R = \mu$  unless otherwise noted because this assumption is inherent in global analyses of parton densities.

In fig. 1(a), we show the scale dependence of the NLO calculations with the  $pp$  and  $pA$  data on  $\sigma_{cc}^{\text{tot}}$  [2,3,10] assuming a linear nuclear dependence [11]. The data has been corrected to include  $D_s$  and  $\bar{\Lambda}_c$  contributions as in [10]. We have included a recent upper limit on  $\sigma_{cc}^{\text{tot}}$  from single electron measurements in  $p\bar{p}$  collisions at  $\sqrt{s} = 630$  GeV [12]. At such high energies, charm production in  $pp$  and  $p\bar{p}$  collisions should be nearly identical.

To extrapolate to RHIC energies and beyond [6], the NLO calculations were compared to the data to fix  $m_c$  and  $\mu$  when  $K_{\text{exp}}^{\text{NLO}} \sim 1$ . We have used two sets of recent parton distribution functions (see [13] for all available parton densities) GRV HO [14] and MRS D-’ [15]. Both are compatible with deep-inelastic scattering data from HERA [16]. Since  $m_c < Q_{0,\text{MRS}}$ , we take  $\mu_F = 2m_c$  and  $m_c/2 < \mu_R < 2m_c$  with  $1.2 < m_c < 1.8$  GeV to show the full theoretical uncertainty [4,10]. The  $K_{\text{th}}$  for  $m_c = 1.2$  GeV and  $\mu = 2m_c$  is given in fig. 1(b). Although only one example is shown, the results are nearly identical. Agreement was found for  $m_c = 1.2$  GeV,  $\mu = 2m_c$  for MRS D-’ and  $m_c = 1.3$  GeV,  $\mu = m_c$  for GRV HO<sup>1</sup> which we use in further calculations. The results are shown in the middle curves in fig. 1(a) and in fig. 1(b). For these parameters,  $K_{\text{th}}$  is quite stable. However, at lower scales,

<sup>1</sup>We use  $\mu = m_c$  here because of the low  $Q_{0,\text{GRV}}$ .

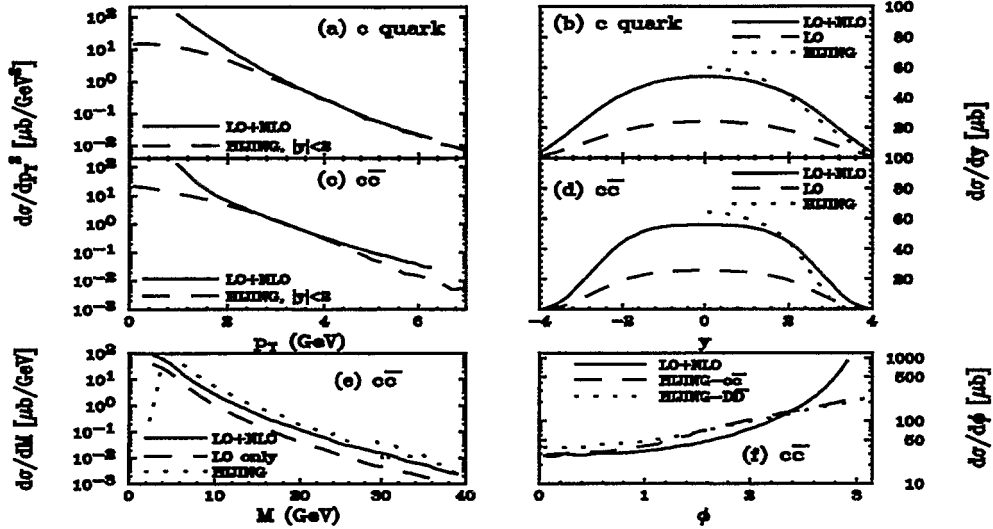


FIG. 2. Predictions for  $c$  and  $c\bar{c}$  production with MRS D-'. The  $c$  quark  $p_T$  distributions at NLO are shown in (a) and the rapidity distributions at LO and NLO are shown in (b). The  $c\bar{c}$  pair distributions are shown in (c)-(f). The LO distributions are shown only for mass and rapidity. Corresponding HIJING distributions are also given.

$K_{\text{th}}$  for the GRV HO set increase with energy [7].

The calculations tend to underestimate  $\sigma_{c\bar{c}}^{\text{tot}}$  with  $K_{\text{exp}}^{\text{NLO}} \sim 1.1 - 2$ . In the range of the parameter space defined by  $m_c$ ,  $\mu_R$  and  $\mu_F$ ,  $K_{\text{exp}}^{\text{NLO}}$  can be reduced to unity. However, it is questionable if the mass and scale values needed for  $K_{\text{exp}}^{\text{NLO}} \sim 1$  are consistent with a perturbative treatment. Since  $K_{\text{th}} \approx 2.5$ , further higher-order corrections may be large. A resummation of the soft and virtual gluon corrections to  $\sigma_{c\bar{c}}^{\text{tot}}$  near threshold, applicable for  $\sqrt{s} \leq 25$  GeV, shows that the perturbative expansion is more convergent for  $m_c = 1.5$  GeV and the GRV HO parton densities [17]. A low  $x$  resummation [18] is more appropriate for RHIC.

We show the predicted heavy quark distributions for RHIC gold beam energies using the MRS D-' densities at LO (where appropriate) and NLO in fig. 2. We take  $\mu = n\hat{m}_c$  for the charm quark and  $\mu = n\sqrt{m_c + (p_{T_c}^2 + p_{T_{\bar{c}}}^2)}/2$  for the  $c\bar{c}$  pair distributions [4,5] to avoid the appearance of large logarithms at high  $p_T$  which can be introduced using a constant scale, as in Ref. [19]. When using MRS distributions,  $n = 2$ , otherwise,  $n = 1$ . There is a rapidity plateau in both the single and pair distributions although the plateau is broader for the single quarks. The average single quark and pair  $p_T$  increases with energy, the  $\langle p_T^2 \rangle$  of the pair is larger than for a single quark. The GRV HO results are similar although the rapidity distributions are somewhat narrower.

While the NLO calculations are needed for the  $p_T$  dependence of  $c\bar{c}$  pair production, it would be convenient if other relevant distributions could be modeled by the LO distributions to within a constant  $K$  factor. In fig. 3 we show  $K_{\text{th}}$  for the nontrivial LO distributions [7]. We see that  $K_{\text{th}}$  is indeed nearly constant for these quantities although  $K_{\text{th}}(p_T^2)$  increases 50%, perhaps indicating the appearance of large logarithms in the  $p_T$  distributions. Some variations occur near the phase space boundaries, see fig. 3(c). Note that  $K_{\text{th}}$  is nearly independent of the parton densities. In general, event generators can scale all nontrivial LO

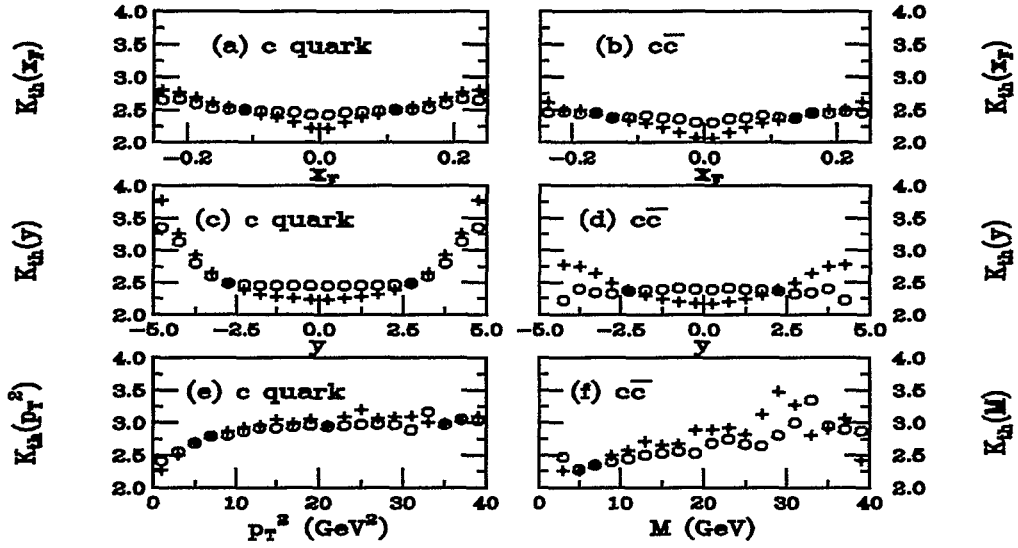


FIG. 3. The differential  $K_{\text{th}}$ . Single charm  $x_F$ , rapidity, and  $p_T^2$  results are shown in (a), (c), and (e) respectively. The  $c\bar{c}$  pair  $x_F$ ,  $y$ , and mass ratios are shown in (b), (d), and (f). The GRV HO results are given by the circles, MRS D-', the diamonds.

results by  $K_{\text{th}}$ .

We finally compare thermal dilepton and thermal charm production from a simple, optimistic thermal model with the hard ‘background’ from  $c\bar{c}$  and  $b\bar{b}$  pair decays and Drell-Yan production at RHIC [1]. The invariant mass distributions of the calculated contributions to the dilepton continuum in central nucleus-nucleus collisions are given in fig. 4. Initial  $c\bar{c}$  production and decay dominates the continuum below the  $\Upsilon$  mass. In particular, the charm signal is more than an order of magnitude above the optimistic thermal rates for  $M > 2$  GeV. Therefore dilepton measurements can be used to extract the low  $x$  gluon density in the nucleus (see also [20] for a discussion of  $pA$  measurements of gluon shadowing). However, the isolation of thermal signals will not be straightforward.

The value of  $\sigma_{c\bar{c}}^{\text{tot}}$  is quite important since it determines the charm background to the thermal signal. If the average number of  $D\bar{D}$  pairs,

$$N_{D\bar{D}} = T_{AB}(0)\sigma_{D\bar{D}}, \quad (7)$$

produced in central collisions is small,  $N_{D\bar{D}} \ll 1$ , the lepton pairs will be correlated with  $N_{ll}^{\text{corr}} = N_{D\bar{D}}B^2(D/\bar{D} \rightarrow l^\pm X)$ . However, if  $N_{D\bar{D}} > 1$ , opposite sign lepton pairs from uncorrelated  $D\bar{D}$  pair decays need to be taken into account. When  $N_{D\bar{D}} \gg 1$ , on average,  $N_{ll}^{\text{uncorr}} = N_{D\bar{D}}(N_{D\bar{D}} - 1)B^2(D\bar{D} \rightarrow l^\pm X)$ . If  $N_{D\bar{D}} \approx 1$ , a distribution in  $N_{D\bar{D}}$  must be considered to calculate the uncorrelated pairs.

The  $c\bar{c}$  production cross sections are large enough for lepton pair production from uncorrelated  $D\bar{D}$  decays to be substantial in nuclear collisions. Given  $\sigma_{c\bar{c}}^{\text{tot}} = 350\mu\text{b}$  and assuming that all  $c\bar{c}$  pairs produce final-state  $D\bar{D}$  pairs, we find 8.7 correlated pairs and 67 uncorrelated pairs, certainly large numbers. Ideally the uncorrelated pairs can be removed by a like-sign subtraction while acceptance cuts can substantially reduce the charm contribution relative to the other sources, especially the uncorrelated pairs. However, this reduction is not enough for the thermal production to shine through [1].

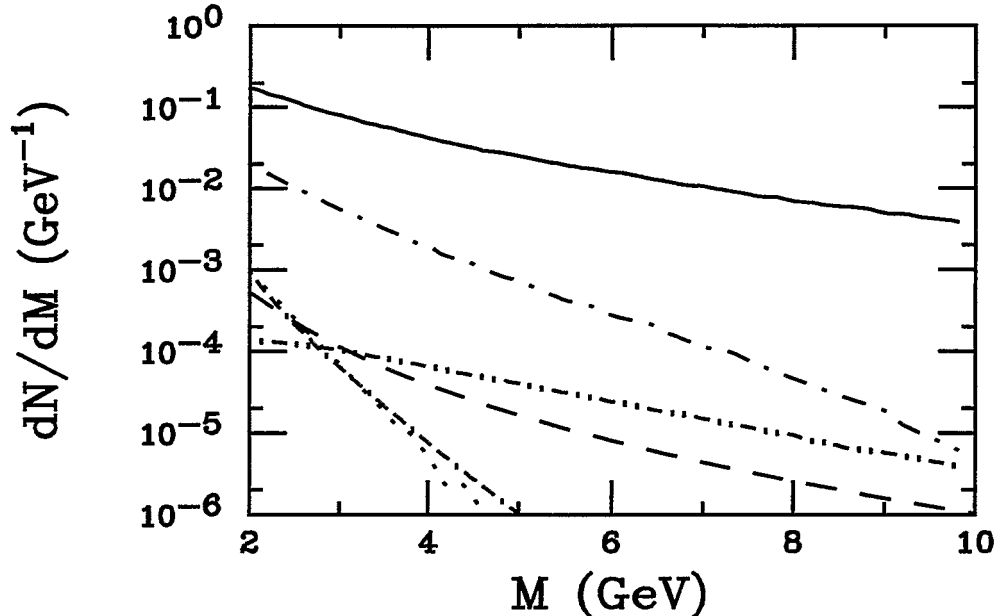


FIG. 4. The lepton pair mass distributions are given for central Au+Au collisions at RHIC. The contributions are: Drell-Yan (dashed) and thermal dilepton (dot-dashed-dashed) production and thermal  $D\bar{D}$  decays (dotted), as well as initial correlated (dot-dashed)  $D\bar{D}$  and  $B\bar{B}$  (dot-dot-dashed) production and decay. Note that lepton pairs from uncorrelated initial  $D\bar{D}$  decays are not shown but are a very large contribution to the continuum.

Charm production is the dominant source of dileptons in heavy-ion collisions, even with acceptance cuts, for  $M < 6 - 8$  GeV. Uncertainties in QCD calculations may change the rates by a factor of two at RHIC, not enough to affect this conclusion. Charm is both signal and background because the multiple  $c\bar{c}$  pair production results in substantial uncorrelated  $D\bar{D}$  contributions to the background. We have only included heavy quark production by first collisions. One uncertainty in these results involves the nuclear dependence of hard processes. We checked two different parameterizations of the nuclear parton densities [21,22] and find that the charm and Drell-Yan yields may be reduced 40-50%. The results depend on the  $x$  region probed and, in the case of the second parameterization, the scale  $Q^2$ . Additionally, multiple hard scattering in  $AB$  collisions can increase the charm yield before equilibration and cascading of the  $c$  and  $\bar{c}$  quarks in the medium can lead to energy loss, perhaps sufficient for the quarks to be equilibrated with the flowing plasma [23,24]. Since it is highly unlikely that all of the  $c\bar{c}$  pairs can annihilate, cascading will not change the number of pairs appreciably. However, it is clear that systematic studies in  $pp$ ,  $pA$  and  $AB$  interactions are needed to fully understand charm production.

## REFERENCES

- [1] S. Gavin, P.L. McGaughey, P.V. Ruuskanen and R. Vogt, LBL-37981, hep-ph/9604369, Phys. Rev. C, in press.
- [2] S.P.K. Tavernier, Rep. Prog. Phys. **50** (1987) 1439.

- [3] J.A. Appel, *Ann. Rev. Nucl. Part. Sci.* **42** (1992) 367.
- [4] P. Nason, S. Dawson, and R.K. Ellis, *Nucl. Phys.* **B303** (1988) 607; *Nucl. Phys.* **B327** (1989) 49.
- [5] M.L. Mangano, P. Nason, and G. Ridolfi, *Nucl. Phys.* **B373** (1992) 295.
- [6] P.L. McGaughey *et al.*, *Int. J. Mod. Phys.* **A10** (1995) 2999.
- [7] R. Vogt, LBL-37105, *Z. Phys. C*, in press.
- [8] R.K. Ellis, in *Physics at the 100 GeV Scale*, Proceedings of the 17<sup>th</sup> SLAC Summer Institute, Stanford, California, 1989, edited by E.C. Brennan (SLAC Report No. 361, Stanford, 1990).
- [9] R. Vogt and S.J. Brodsky, *Nucl. Phys.* **B438** (1995) 261.
- [10] S. Frixione, M.L. Mangano, P. Nason, and G. Ridolfi, *Nucl. Phys.* **B431** (1994) 453.
- [11] G. Alves *et al.*, E769 Collab., *Phys. Rev. Lett.* **70** (1993) 722.
- [12] O. Botner *et al.*, *Phys. Lett.* **B236** (1990) 488.
- [13] H. Plochow-Besch, *Comp. Phys. Comm.* **75**, (1993) 396.
- [14] M. Glück, E. Reya and A. Vogt, *Z. Phys.* **C53** (1992) 127.
- [15] A.D. Martin, R.G. Roberts and W.J. Stirling, *Phys. Lett.* **B306**, 145 (1993).
- [16] M. Derrick *et al.*, ZEUS Collab., *Phys. Lett.* **B316** (1993) 515.
- [17] J. Smith and R. Vogt, LBL-38282, ITP-SB-95-60 and Refs. therein.
- [18] J.C. Collins and R.K. Ellis, *Nucl. Phys.* **B360** (1991) 3.
- [19] I. Sarcevic and P. Valerio, *Phys. Lett.* **B338** (1994) 426; *Phys. Rev.* **C51** (1995) 1433.
- [20] Z. Lin and M. Gyulassy, Columbia University preprint, CU-TP 714.
- [21] K.J. Eskola, J. Qiu and J. Czyzewski, private communication.
- [22] K.J. Eskola, *Nucl. Phys.* **B400** (1993) 240.
- [23] E. Shuryak, nucl-th/9605011.
- [24] R. Vogt and X.-N. Wang, in progress.

# Percolation approach and $J/\psi$ suppression in the String Fusion Model\*

N. Armesto, M. A. Braun<sup>†</sup> E. G. Ferreiro and C. Pajares  
*Departamento de Física de Partículas, Universidade de Santiago de Compostela,  
15706-Santiago de Compostela, Spain*

## Abstract

It is shown that the critical threshold for percolation of the overlapping strings exchanged in heavy ion collisions can naturally explain the sharp strong suppression of  $J/\psi$  shown by the experimental data on central Pb–Pb collisions, which does not occur in central O–U and S–U collisions.

The NA50 collaboration ([1]) has reported a strong suppression of  $J/\psi$  production in central Pb–Pb collisions at 158 AGeV/c. The suppression is much stronger than the expected one due to  $J/\psi$  absorption corresponding to a cross section of 6.3 mb, by which the NA38 data for central O–U and S–U collisions ([2,3]) and the hadron–nucleus data can be explained. The NA50 data show a clear deviation from the previous situation ([4]). The  $J/\psi$  suppression in peripheral Pb–Pb collisions is similar to the one corresponding to central S–U collisions, but a sharp enhancement occurs as the centrality of the Pb–Pb collisions increases.

In this paper we draw attention to the fact that the continuum percolation of colour strings can naturally describe the sharp difference in the  $J/\psi$  suppression at present energies between O–U, S–U and peripheral Pb–Pb collisions on the one side and central Pb–Pb collisions on the other side. Predictions for RHIC and LHC energies are given.

The continuum percolation of colour strings takes place when the density of strings rises above a threshold, which can be calculated on geometrical grounds. In this picture, the region where several strings fuse can be considered a droplet of a non-thermalized Quark Gluon Plasma, in which the  $J/\psi$  is suppressed as predicted by Matsui and Satz ([5]). Percolation means that these droplets overlap and the Quark Gluon Plasma domain becomes comparable to the nuclear size.

In many models of hadronic collisions ([6]–[11]), colour strings are exchanged between projectile and target. The number of strings grows with the energy and with the number of nucleons of the participant nuclei. When the density of strings becomes high the string colour

---

\*Presented by E. G. Ferreiro

<sup>†</sup>Permanent address: Department of High Energy Physics, University of St. Petersburg, 198904 St. Petersburg, Russia.

fields begin to overlap and eventually individual strings may fuse ([12]– [16]), forming a new string which has a higher colour charge at its ends, corresponding to the summation of the colour charges located at the ends of the original strings. The new strings break into hadrons according to their higher colour. As a result, heavy flavour is produced more efficiently and there is a reduction of the total multiplicity ([13]). Also, as the energy–momenta of the original strings are summed to obtain the energy–momentum of the resulting string, the fragmentation of the latter can produce some particles outside the kinematical limits of nucleon–nucleon collisions if the original strings come from different nucleons ([17,18]). Fusion of strings has been incorporated in several Monte Carlo codes. In particular, in the Quark Gluon String Model (QGSM) it is assumed that strings fuse when their transverse positions come within a certain interaction area  $a$  ([13]). The value of  $a$  is determined to reproduce  $\bar{\Lambda}$  rapidity distributions in central S–S and S–Ag collisions at  $p_{lab}= 200$  GeV/c per nucleon.

From the value of  $a$ , the radius  $r$  of the transverse dimension of the string can be obtained,  $a = 2\pi r^2$  ([19]). In our code only fusion of two strings is considered, so the obtained  $r$ –value,  $r=0.36$  fm, is an effective one, somewhat larger than the real transverse radius of the string. Denoting by  $N_j$  the number of strings which fuse into  $j$ –fold strings and  $N'_2$  and  $r_{eff}$  the number of all fused strings and the effective transverse size of the string, respectively, we will have

$$2N'_2\pi r_{eff}^2 = \sum_{j=2} N_j j\pi r^2, \quad (1)$$

$$N'_2 = \sum_{j=2} N_j. \quad (2)$$

The upper limit of the sum in (1) is determined by the constraint (2). The values of  $N'_2$  and  $r_{eff}^2$  were fixed in our calculation by comparing the results of the string fusion model with the experimental data on  $\bar{\Lambda}$  production in central S–S collisions at  $\sqrt{s}=19.4$  AGeV. Computing  $N_j$  in our Monte Carlo code we obtain from (1) the value  $r=0.2$  fm both for Pb–Pb and S–Ag collisions.

In nucleus–nucleus collisions many strings are exchanged. In impact parameter space these strings are seen as circles inside the total collision area. As the number of strings increases, more strings overlap. Several fused strings can be considered as a domain of a non–thermalized Quark Gluon Plasma. Following the arguments of Matsui and Satz ([5]) the  $J/\psi$  can not be formed inside this domain. Also the  $J/\psi$  will be destroyed by interaction with these fused strings. Above a critical density of strings percolation occurs, so that paths of overlapping circles are formed through the whole collision area. Along these paths the medium behaves like a colour conductor. Percolation gives rise to the formation of Quark Gluon Plasma on a nuclear scale. The phenomenon of continuum percolation is well known ([20]). It explains hopping conduction in doped semiconductors and other important physical processes ([21]). The percolation threshold  $\eta_c$  is related to the critical density of circles  $n_c$  by the expression

$$\eta_c = \pi r^2 n_c. \quad (3)$$



$\eta_c$  has been computed using Monte Carlo simulation, direct-connectedness expansion and other different methods. All the results are in the range  $\eta_c = 1.12 - 1.175$  ([22]– [26]). Taking the above mentioned value of  $r$ , these values imply

$$n_c = 8.9 - 9.3 \text{ strings/fm}^2. \quad (4)$$

One may introduce a hard core to model a repulsive interaction between the circles, or to substitute circles by squares. The percolation threshold  $\eta_c$  is only slightly reduced in these cases. This enhances the confidence in its value and the application to our case where we do not know the dynamics of the interaction among strings.

In Table 1 the number of strings exchanged for central p-p, S-S, S-U and Pb-Pb collisions is shown together with their densities. It is seen that at SPS energies only the density reached in central Pb-Pb collisions is above the critical density. In minimum bias Pb-Pb collisions the average number of strings at SPS energies is 227, very similar to the value for central S-U collisions, so the density is lower than the critical one.

**Table 1.** Number of strings (upper numbers) and their densities ( $\text{fm}^{-2}$ ) (lower numbers) in central p-p, S-S, S-U and Pb-Pb collisions at SPS, RHIC and LHC energies.

$\sqrt{s}$ (AGeV)	Collision			
	p-p	S-S	S-U	Pb-Pb
19.4	4.2	123	268	1145
	1.3	3.5	7.6	9.5
200	7.2	215	382	1703
	1.6	6.1	10.9	14.4
5500	13.1	380	645	3071
	2.0	10.9	18.3	25.6

The  $J/\psi$  suppression experimentally observed follows the same pattern. The strong suppression is only observed in central Pb-Pb collisions. According to Table 1, a strong  $J/\psi$  suppression is also expected in S-U collisions at RHIC energies and in S-S and S-U collisions at LHC energies.

Recently ([27]) it has been assumed that the produced  $J/\psi$  is completely destroyed whenever the energy density exceeds a certain value and this energy density is taken proportional to the density of participants. The critical value is chosen to lie between the density of participants of central S-U collisions and Pb-Pb collisions. With this choice a good description of the experimental data is obtained. In our model the density of strings is proportional to the number of collisions, and we obtain similar quantitative results. However, in our approach the critical value is naturally explained on geometrical grounds.

Also it is possible that the percolation process takes place among the produced resonances and particles instead of strings ([28]). The two cases can be distinguished by studying the behaviour of long range correlations and measuring forward-backward correlations ([29]).

The percolation of strings can be considered as a smooth way to Quark Gluon Plasma. Around the percolation threshold, strong fluctuations in the number of strings with a given

colour should appear. This will produce large fluctuations in a number of different observables, like strangeness, in an event by event analysis. Also a large number of  $\Omega^-$  (confirmed by the experimental data ([30])) and a copious production of hadronic particles with  $|x_F|$  much larger than 1, outside the kinematical nucleon–nucleon limits, may serve as clear signatures. The latter would also distinguish our picture from the percolation of resonances and particles.

In conclusion we thank A. Capella, S. Gavin, M. Gyulassy and R. Pisarski for useful comments and discussions and the Comisión Interministerial de Ciencia y Tecnología (CI-CYT) of Spain for financial support under contract AEN96-1673. Also M. A. Braun thanks IBERDROLA and E. G. Ferreiro the Xunta de Galicia for financial support. Finally we thank S. H. Kahana and T. W. Ludlam for organizing such a nice meeting.

## REFERENCES

- [1] NA50 Collaboration, M. Gonin, Proceedings of Quark Matter '96, Eds. P. Braun–Munzinger *et al*, to appear in Nucl. Phys. **A**.
- [2] J. Hüfner and C. Gerschel, Z. Phys. **C56**, 171 (1992).
- [3] A. Capella, J. Casado, C. Pajares, A. V. Ramallo and J. Tran Thanh Van, Phys. Lett. **B206**, 354 (1988); C. Gerschel and J. Hüfner, Phys. Lett. **B207**, 253 (1988); J. P. Blaizot and J. Y. Ollitrault, Phys. Lett. **B199**, 499 (1987); A. Capella, C. Merino, C. Pajares, A. V. Ramallo and J. Tran Thanh Van, Phys. Lett. **B243**, 144 (1990).
- [4] NA38 Collaboration, C. Baglin *et al*, Phys. Lett. **B220**, 471 (1989); Phys. Lett. **B272**, 449 (1991).
- [5] T. Matsui and H. Satz, Phys. Lett. **B178**, 416 (1986).
- [6] B. Andersson, G. Gustafson and B. Nilsson–Almqvist, Nucl. Phys. **B281**, 289 (1987).
- [7] M. Gyulassy, CERN report CERN–TH 4794 (1987).
- [8] H. Sorge, H. Stöcker and W. Greiner, Nucl. Phys. **A498**, 567c (1989).
- [9] A. Capella, U. P. Sukhatme, C.–I. Tan and J. Tran Thanh Van, Phys. Rep. **236**, 225 (1994).
- [10] K. Werner, Phys. Rep. **232**, 87 (1993).
- [11] A. B. Kaidalov and K. A. Martirosyan, Phys. Lett. **B117**, 247 (1982).
- [12] M. A. Braun and C. Pajares, Phys. Lett. **B287**, 154 (1992).
- [13] N. S. Amelin, M. A. Braun and C. Pajares, Phys. Lett. **B306**, 312 (1993); Z. Phys. **C63**, 507 (1994).
- [14] H.–J. Möhring, J. Ranft, C. Merino and C. Pajares, Phys. Rev. **D47**, 4142 (1993); C. Merino, C. Pajares and J. Ranft, Phys. Lett. **B276**, 168 (1992).
- [15] H. Sorge, M. Berenguer, H. Stöcker and W. Greiner, Phys. Lett. **B289**, 6 (1992).
- [16] A. Capella, A. B. Kaidalov, A. Kouider Akil, C. Merino and J. Tran Thanh Van, Z. Phys. **C70**, 507 (1996).
- [17] N. Armesto, M. A. Braun, E. G. Ferreiro, C. Pajares and Yu. M. Shabelski, Santiago preprint US–FT/6–96, hep–ph/9606333 (1996).
- [18] B. Andersson and P. Henning, Nucl. Phys. **B355**, 82 (1991).
- [19] N. Armesto, M. A. Braun, E. G. Ferreiro and C. Pajares, Phys. Lett. **B344**, 301 (1995).
- [20] M. B. Isichenko, Rev. Mod. Phys. **64**, 961 (1992).

- [21] B. I. Shklovskii and A. L. Efros, *Electronic Properties Of Doped Semiconductors*, Springer-Verlag, New York 1984.
- [22] G. E. Pike and C. H. Seager, Phys. Rev. **B10**, 1421 (1974); E. T. Gawlinski and H. E. Stanley, J. Phys. **A10**, 205 (1977); S. B. Lee, Phys. Rev. **B42**, 4877 (1990).
- [23] U. Alon, A. Drory and I. Balberg, Phys. Rev. **A42**, 4634 (1990).
- [24] T. Vicsek and J. Kertesz, J. Phys. **A14**, L31 (1981).
- [25] E. T. Gawlinski and S. Redner, J. Phys. **A16**, 1063 (1983); I. Balberg, Philos. Mag. **B56**, 991 (1987).
- [26] C. Domb and N. F. Sykes, Phys. Rev. **122**, 77 (1960).
- [27] J. P. Blaizot and J. I. Ollitrault, Phys. Rev. Lett. **77**, 1703 (1996).
- [28] K. Werner and J. Aichelin, Phys. Lett. **B308**, 372 (1993); K. Werner, Phys. Rev. Lett. **73**, 1594 (1994).
- [29] N. S. Amelin, N. Armesto, M. A. Braun, E. G. Ferreira and C. Pajares, Phys. Rev. Lett. **73**, 2013 (1994).
- [30] WA97 Collaboration, Proceedings of Quark Matter '96, Eds. P. Braun-Munzinger *et al*, to appear in Nucl. Phys. **A**.

# Charmonium Suppression in Nuclear Collisions

Sean Gavin\*

*Physics Department, Brookhaven National Laboratory, Upton, NY<sup>†</sup>*

*and*

*Department of Physics, Columbia University, New York, NY.*

## Abstract

Measurements of  $\psi$  and  $\psi'$  production from experiment NA50 at the CERN SPS are compared to calculations based on a hadronic model of charmonium suppression developed previously. Data on centrality dependence and total cross sections are in good accord with these predictions. Uncertainties in theoretical quantities such as NA50's  $L$  parameter are discussed.

## I. INTRODUCTION

Has the quark gluon plasma been discovered at the CERN SPS? Experiment NA50 has reported an abrupt decrease in  $\psi$  production in Pb+Pb collisions at 158 GeV per nucleon [1]. Specifically, the collaboration presented a striking 'threshold effect' in the  $\psi$ -to-continuum ratio by plotting it as a function of a calculated quantity, the mean path length of the  $\psi$  through the nuclear medium,  $L$ , as shown in fig. 1a. This apparent threshold has sparked considerable excitement as it may signal deconfinement in the heavy Pb+Pb system [2].

In this talk I report on work with Ramona Vogt in ref. [3] comparing Pb results to predictions [4,5] using a hadronic model of charmonium suppression. We first demonstrate that the behavior in the NA50 plot, fig. 1a, is not a threshold effect but, rather, reflects the approach to the geometrical limit of  $L$  as the collisions become increasingly central. When plotted as a function of the *measured* neutral transverse energy  $E_T$  as in fig. 1b, the data varies smoothly as in S+U measurements in fig. 3b below [1,6-9]. The difference between S+U and Pb+Pb data lies strictly in the relative magnitude. To assess this magnitude, we compare  $\psi$  and  $\psi'$  data to expectations based on the hadronic comover model [4,5]. The curves in fig. 1 represent our calculations using parameters fixed earlier in Ref. [5]. Our result is essentially the same as the Pb+Pb prediction in [4].

Our primary intention is to demonstrate that there is no evidence for a strong discontinuity between pA, S+U and Pb+Pb data. However, to quote Maurice Goldhaber, "... absence of evidence is *not* evidence of absence." Our secondary goal is to show that our

---

\*This work was supported in part by US-DOE contracts DE-FG02-93ER40764 and DE-AC02-76CH00016.

<sup>†</sup>Mailing address.

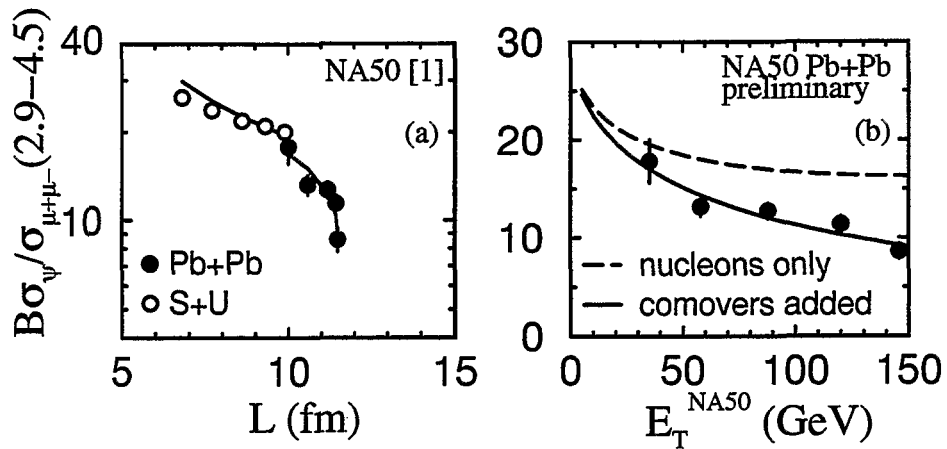


FIG. 1. (a) The NA50 [1] comparison of  $\psi$  production in Pb+Pb and S+U collisions as a function of the average path length  $L$ , see eq. (3).  $B$  is the  $\psi \rightarrow \mu^+\mu^-$  branching ratio. (b) Transverse energy dependence of Pb+Pb data. Curves in (a) and (b) are computed using eqs. (4-6).

model predictions agree with the new Pb+Pb data. The consistency of these predictions is evident from the agreement of our old  $pA$  and S+U calculations with more recent NA38 and NA51 data. Nevertheless, the significance of this result must be weighted by the fact that all  $pA$  and AB data are preliminary and at different beam energies.

In this work, we do not attempt to show that our comover interpretation of the data is unambiguous – this is certainly impossible at present.

## II. NUCLEONS AND COMOVERS

The hadronic contribution to charmonium suppression arises from scattering of the nascent  $\psi$  with produced particles – the comovers – and nucleons [4,5]. To determine the suppression from nucleon absorption of the  $\psi$ , we calculate the probability that a  $c\bar{c}$  pair produced at a point  $(b, z)$  in a nucleus survives scattering with nucleons to form a  $\psi$ . The standard [5,10] result is

$$S_A = \exp\left\{-\int_z^\infty dz \rho_A(b, z) \sigma_{\psi N}\right\} \quad (1)$$

where  $\rho_A$  is the nuclear density,  $b$  the impact parameter and  $\sigma_{\psi N}$  the absorption cross section for  $\psi$ -nucleon interactions. One can estimate  $S_A \sim \exp\{-\sigma_{\psi N} \rho_0 L_A\}$ , where  $L_A$  is the path length traversed by the  $c\bar{c}$  pair.

Suppression can also be caused by scattering with mesons that happen to travel along with the  $c\bar{c}$  pair (see refs. in [4]). The density of such comovers scales roughly as  $E_T$ . The corresponding survival probability is

$$S_{co} = \exp\left\{-\int d\tau n \sigma_{co} v_{rel}\right\}, \quad (2)$$

where  $n$  is the comover density and  $\tau$  is the time in the  $\psi$  rest frame. We write  $S_{co} \sim \exp\{-\beta E_T\}$ , where  $\beta$  depends on the scattering frequency, the formation time of the comovers and the transverse size of the central region,  $R_T$ , cf. eq. (8).

To understand the saturation of the Pb data with  $L$  in fig. 1a, we apply the schematic approximation of Ref. [10] for the moment to write

$$\frac{\sigma_{\psi}^{AB}(E_T)}{\sigma_{\mu^+\mu^-}^{AB}(E_T)} \propto \langle S_A S_B S_{co} \rangle \sim e^{-\sigma_{\psi NN} \rho_0 L} e^{-\beta E_T}, \quad (3)$$

where the brackets imply an average over the collision geometry for fixed  $E_T$  and  $\sigma(E_T) \equiv d\sigma/dE_T$ . The path length  $L \equiv \langle L_A + L_B \rangle$  and transverse size  $R_T$  depend on the collision geometry. The path length grows with  $E_T$ , asymptotically approaching the geometric limit  $R_A + R_B$ . Explicit calculations show that nucleon absorption begins to *saturate* for  $b < R_A$ , where  $R_A$  is the smaller of the two nuclei, see fig. 4 below. On the other hand,  $E_T$  continues to grow for  $b < R_A$  due, *e.g.*, to fluctuations in the number of  $NN$  collisions. Equation (2) falls exponentially in this regime because  $\beta$ , like  $L$ , saturates.

In fig. 1b, we compare the Pb data to calculations of the  $\psi$ -to-continuum ratio that incorporate nucleon and comover scattering. The contribution due to nucleon absorption indeed levels off for small values of  $b$ , as expected from eq. (3). Comover scattering accounts for the remaining suppression.

These results are *predictions* obtained using the computer code of Ref. [4] with parameters determined in Ref. [5]. However, to confront the present NA50 analysis [1], we account for changes in the experimental coverage as follows:

- Calculate the continuum dimuon yield in the new mass range  $2.9 < M < 4.5$  GeV.
- Adjust the  $E_T$  scale to the pseudorapidity acceptance of the NA50 calorimeter,  $1.1 < \eta < 2.3$ .

The agreement in fig. 1 depends on these updates.

### III. $J/\psi$ SUPPRESSION

We now review the details of our calculations, highlighting the adjustments as we go. For collisions at a fixed  $b$ , the  $\psi$ -production cross section is

$$\sigma_{\psi}^{AB}(b) = \sigma_{\psi}^{NN} \int d^2 s dz dz' \rho_A(s, z) \rho_B(b - s, z') S, \quad (4)$$

where  $S \equiv S_A S_B S_{co}$  is the product of the survival probabilities in the projectile  $A$ , target  $B$  and comover matter. The continuum cross section is

$$\sigma_{\mu^+\mu^-}^{AB}(b) = \sigma_{\mu^+\mu^-}^{NN} \int d^2 s dz dz' \rho_A(s, z) \rho_B(b - s, z'). \quad (5)$$

The magnitude of (4,5) and their ratio are fixed by the elementary cross sections  $\sigma_{\psi}^{NN}$  and  $\sigma_{\mu^+\mu^-}^{NN}$ . We calculate  $\sigma_{\psi}^{NN}$  using the phenomenologically-successful color evaporation model [11]. The continuum in the mass range used by NA50,  $2.9 < M < 4.5$  GeV, is described by the Drell-Yan process. To confront NA50 and NA38 data in the appropriate kinematic regime, we compute these cross sections at leading order following [11,12] using GRV LO parton distributions with a charm  $K$ -factor  $K_c = 2.7$  and a color evaporation coefficient

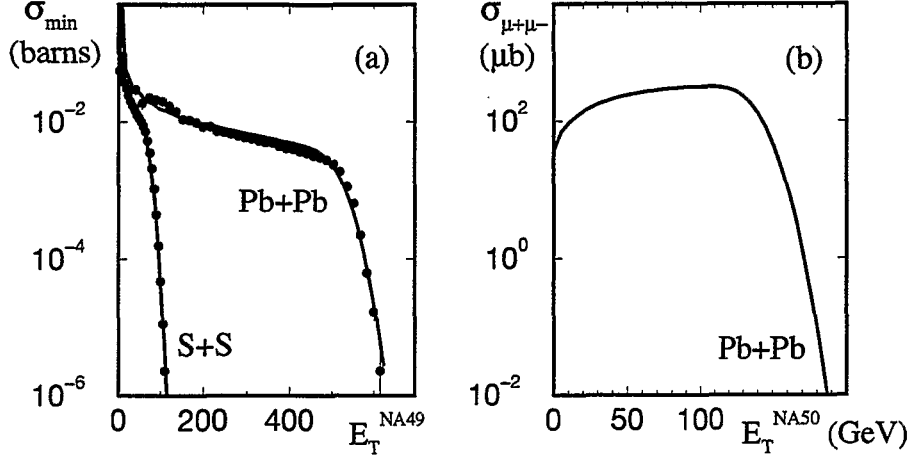


FIG. 2. Transverse energy distributions from eq. (7). The S–Pb comparison (a) employs the same parameters.

$F_\psi = 2.54\%$  and a Drell–Yan  $K$ -factor  $K_{DY} = 2.4$ . Observe that these choices were fixed by fitting  $pp$  data at all available energies [11]. Computing  $\sigma_{\mu^+\mu^-}^{NN}$  for  $2.9 < M < 4.5$  GeV corresponds to the first update.

To obtain  $E_T$  dependent cross sections from eqs. (4) and (5), we write

$$\sigma^{AB}(E_T) = \int d^2b P(E_T, b) \sigma^{AB}(b). \quad (6)$$

The probability  $P(E_T, b)$  that a collision at impact parameter  $b$  produces transverse energy  $E_T$  is related to the minimum–bias distribution by

$$\sigma_{\min}(E_T) = \int d^2b P(E_T, b). \quad (7)$$

We parametrize  $P(E_T, b) = C \exp\{-(E_T - \bar{E}_T)^2/2\Delta\}$ , where  $\bar{E}_T(b) = \epsilon \mathcal{N}(b)$ ,  $\Delta(b) = \omega \epsilon \bar{E}_T(b)$ ,  $C(b) = (2\pi\Delta(b))^{-1}$  and  $\mathcal{N}(b)$  is the number of participants (see, *e.g.*, Ref. [4]). We take  $\epsilon$  and  $\omega$  to be phenomenological calorimeter–dependent constants.

We compare the minimum bias distributions for total hadronic  $E_T$  calculated using eq. (7) for  $\epsilon = 1.3$  GeV and  $\omega = 2.0$  to NA35 S+S and NA49 Pb+Pb data [13]. The agreement in fig. 2a builds our confidence that eq. (7) applies to the heavy Pb+Pb system. Figure 2b shows the distribution of neutral transverse energy calculated using eqs. (5) and (6) to simulate the NA50 dimuon trigger. We take  $\epsilon = 0.35$  GeV,  $\omega = 3.2$ , and  $\sigma_{\mu^+\mu^-}^{NN} \approx 37.2$  pb as appropriate for the dimuon–mass range  $2.9 < M < 4.5$  GeV. The  $E_T$  distribution for  $S+U \rightarrow \mu^+\mu^- + X$  from NA38 was described [5] using  $\epsilon = 0.64$  GeV and  $\omega = 3.2$  – the change in  $\epsilon$  corresponds roughly to the shift in particle production when the pseudorapidity coverage is changed from  $1.7 < \eta < 4.1$  (NA38) to  $1.1 < \eta < 2.3$  (NA50). Taking  $\epsilon = 0.35$  GeV for the NA50 acceptance is the second update listed earlier. We now apply eqs. (1,2,4) and (5) to charmonium suppression in Pb+Pb collisions. To determine nucleon absorption, we used  $pA$  data to fix  $\sigma_{\psi N} \approx 4.8$  mb in Ref. [5]. This choice is in accord with the latest NA38 and NA51  $pA$  data, see fig. 3a. To specify comover scattering [5], we assumed that the dominant contribution to  $\psi$  dissociation comes from exothermic hadronic reactions such as

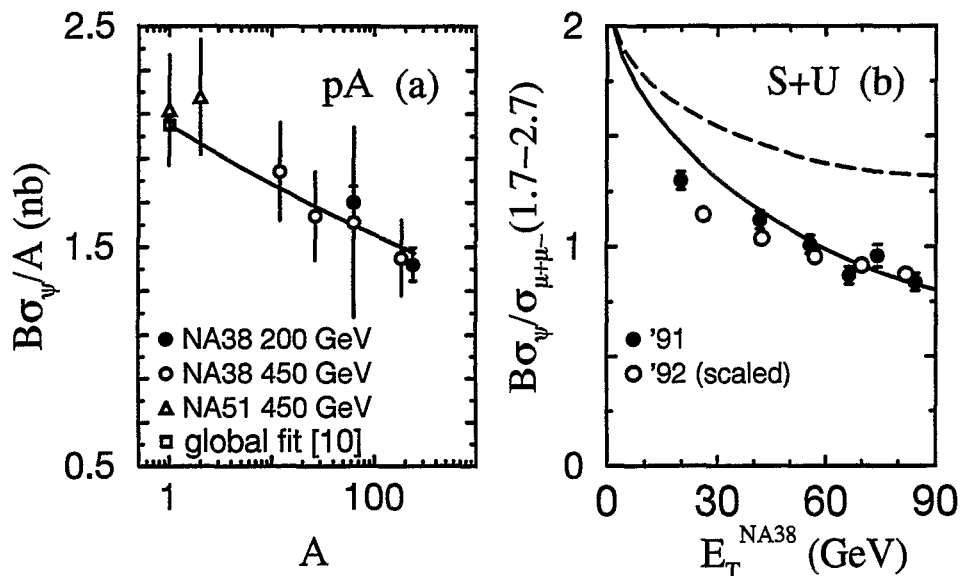


FIG. 3. (a)  $pA$  cross sections [1] in the NA50 acceptance and (b) S+U ratios from '91 [7] and '92 [1] runs. The '92 data are scaled to the '91 continuum. The dashed line indicates the suppression from nucleons alone. The  $pp$  cross section in (a) is constrained by the global fit to  $pp$  data in ref. [11].

$\rho + \psi \rightarrow D + \bar{D}$ . We further took the comovers to evolve from a formation time  $\tau_0 \sim 2$  fm to a freezeout time  $\tau_F \sim R_T/v_{\text{rel}}$  following Bjorken scaling, where  $v_{\text{rel}} \sim 0.6$  is roughly the average  $\psi - \rho$  relative velocity. The survival probability, eq. (2), is then

$$S_{\text{co}} = \exp\{-\sigma_{\text{co}}v_{\text{rel}}n_0\tau_0 \ln(R_T/v_{\text{rel}}\tau_0)\} \quad (8)$$

where  $\sigma_{\text{co}} \approx 2\sigma_{\psi N}/3$ ,  $R_T \approx R_A$  and  $n_0$  is the initial density of sufficiently massive  $\rho, \omega$  and  $\eta$  mesons. To account for the variation of density with  $E_T$ , we take  $n_0 = \bar{n}_0 E_T/\bar{E}_T(0)$  [4]. A value  $\bar{n}_0 = 0.8 \text{ fm}^{-3}$  was chosen to fit the central S+U datum. Since we fix the density in central collisions, this simple *ansatz* for  $S_{\text{co}}$  may be inaccurate for peripheral collisions. [Densities  $\sim 1 \text{ fm}^{-3}$  typically arise in hadronic models of ion collisions, e.g., refs. [15]. The internal consistency of hadronic models at such densities demands further study.]

We expect the comover contribution to the suppression to increase in Pb+Pb relative to S+U for central collisions because both the initial density and lifetime of the system can increase. To be conservative, we assumed that Pb and S beams achieve the same mean initial density. Even so, the lifetime of the system essentially doubles in Pb+Pb because  $R_T \sim R_A$  increases to 6.6 fm from 3.6 fm in S+U. The increase in the comover contribution evident in comparing figs. 1b and 3b is described by the seemingly innocuous logarithm in eq. (8), which increases by  $\approx 60\%$  in the larger Pb system.

In Ref. [5], we pointed out that comovers were necessary to explain S+U data from the NA38 1991 run [6]. Data just released [1] from their 1992 run support this conclusion. The '91  $\psi$  data were presented as a ratio to the dimuon continuum in the low mass range  $1.7 < M < 2.7$  GeV, where charm decays are an important source of dileptons. On the other hand, the '92  $\psi$  data [1,9] are given as ratios to the Drell-Yan cross section in the range  $1.5 < M < 5.0$  GeV. That cross section is extracted from the continuum by fixing the  $K$ -factor in the high mass region [14]. To compare our result from Ref. [5] to these



data, we scale the '92 data by an empirical factor. This factor is  $\approx 10\%$  larger than our calculated factor  $\sigma_{DY}^{NN}(92)/\sigma_{cont.}^{NN}(91) \approx 0.4$ ; these values agree within the NA38 systematic errors. [NA50 similarly scaled the '92 data to the high-mass continuum to produce fig. 1a.] Because our fit is driven by the highest  $E_T$  datum, we see from fig. 3b that a fit to the '92 data would not appreciably change our result. Note that a uniform decrease of the ratio would increase the comover contribution needed to explain S+U collisions.

NA50 and NA38 have also measured the total  $\psi$ -production cross section in Pb+Pb [1] and S+U reactions [7]. To compare to that data, we integrate eqs. (4, 6) to obtain the total  $(\sigma/AB)_\psi = 0.95$  nb in S+U at 200 GeV and 0.54 nb for Pb+Pb at 158 GeV in the NA50 spectrometer acceptance,  $0.4 > x_F > 0$  and  $-0.5 < \cos \theta < 0.5$  (to correct to the full angular range and  $1 > x_F > 0$ , multiply these cross sections by  $\approx 2.07$ ). The experimental results in this range are  $1.03 \pm 0.04 \pm 0.10$  nb for S+U collisions [6] and  $0.44 \pm 0.005 \pm 0.032$  nb for Pb+Pb reactions [1]. Interestingly, in the Pb system we find a Drell-Yan cross section  $(\sigma/AB)_{DY} = 37.2$  pb while NA50 finds  $(\sigma/AB)_{DY} = 32.8 \pm 0.9 \pm 2.3$  pb. Both the  $\psi$  and Drell-Yan cross sections in Pb+Pb collisions are somewhat above the data, suggesting that the calculated rates at the  $NN$  level may be  $\sim 20 - 30\%$  too large at 158 GeV. This discrepancy is within ambiguities in current  $pp$  data near that low energy [11]. Moreover, nuclear effects on the parton densities omitted in eqs. (4,5) can affect the total S and Pb cross sections at this level.

We remark that if one were to neglect comovers and take  $\sigma_{\psi N} = 6.2$  mb, one would find  $(\sigma/AB)_\psi = 1.03$  nb in S+U at 200 GeV and 0.62 nb for Pb+Pb at 158 GeV. The agreement with S+U data is possible because comovers only contribute to the total cross section at the  $\sim 18\%$  level in the light system. This is expected, since the impact-parameter integrated cross section is dominated by large  $b$  and the distinction between central and peripheral interactions is more striking for the asymmetric S+U system. As in Ref. [5], the need for comovers is evident for the  $E_T$ -dependent ratios, where central collisions are singled out.

#### IV. SATURATION AND THE DEFINITION OF $L$

To see why saturation occurs in Pb+Pb collisions but not in S+U, we compare the NA50  $L(E_T)$  [1] to the average impact parameter  $\langle b \rangle(E_T)$  in fig. 4. To best understand fig. 1a, we show the values of  $L(E_T)$  computed by NA50 for this figure. We use our model to compute  $\langle b \rangle = \langle b T_{AB} \rangle / \langle T_{AB} \rangle$ , where  $\langle f(b) \rangle \equiv \int d^2 b P(E_T, b) f(b)$  and  $T_{AB} = \int d^2 s dz dz' \rho_A(s, z) \rho_B(b - s, z')$ . [Note that NA50 reports similar values of  $\langle b \rangle(E_T)$  [1].] In the  $E_T$  range covered by the S experiments, we see that  $\langle b \rangle$  is near  $\sim R_S = 3.6$  fm or larger. In this range, increasing  $b$  dramatically reduces the collision volume and, consequently,  $L$ . In contrast, in Pb+Pb collisions  $\langle b \rangle \ll R_{Pb} = 6.6$  fm for all but the lowest  $E_T$  bin, so that  $L$  does not vary appreciably.

To understand the sensitivity of fig. 1a to the definition of the path length, we now estimate  $L(E_T)$  [16]. We identify (3) with the exact expression formed from the ratio of (4) and (5). Expanding in  $\sigma_{\psi N}$  and neglecting comovers, we find:

$$L(E_T) = \{2\rho_0 \langle T_{AB} \rangle\}^{-1} \left\langle \int d^2 s [T_A(s)]^2 T_B(b-s) + [T_B(b-s)]^2 T_A(s) \right\rangle, \quad (9)$$

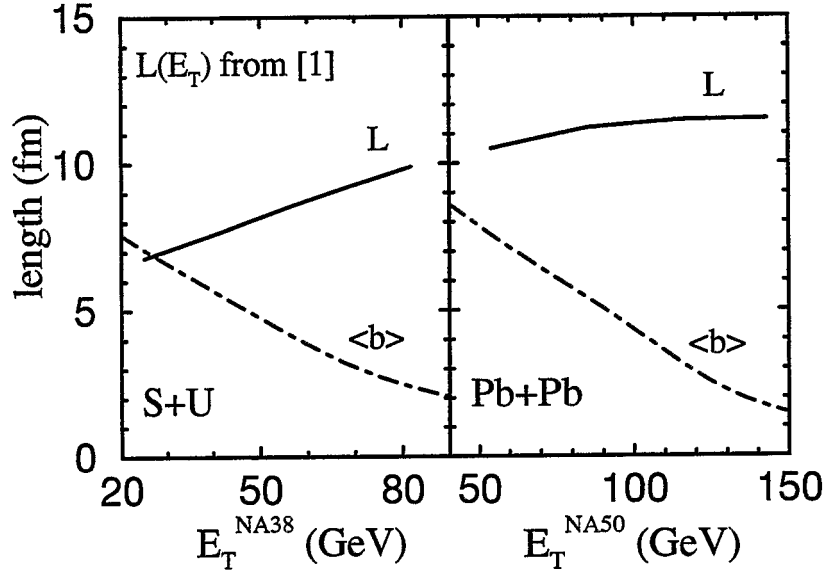


FIG. 4.  $E_T$  dependence of  $L$  (solid) used by NA50 [1] (see fig. 1a) and the average impact parameter  $\langle b \rangle$  (dot-dashed). The solid line covers the measured  $E_T$  range.

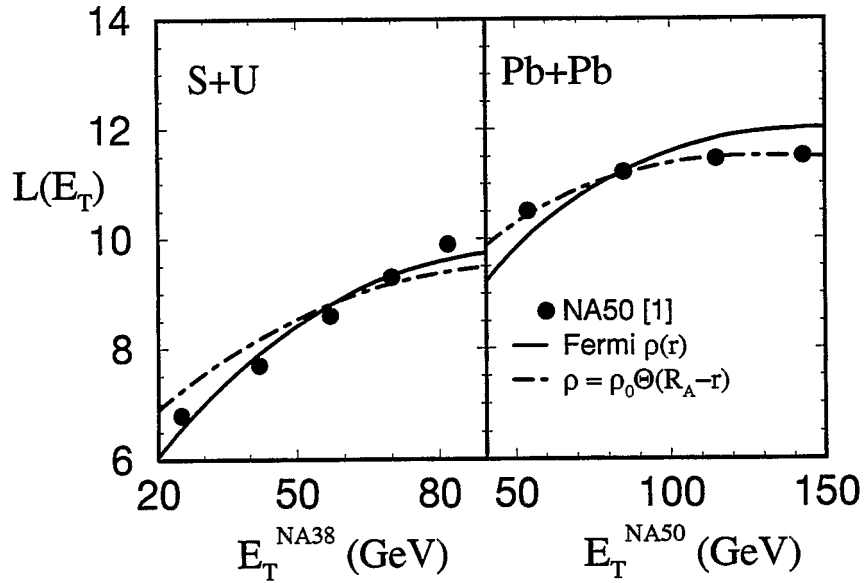


FIG. 5. NA50  $L(E_T)$  [1] (points) compared to calculations for realistic nuclear densities (solid), as used here, and for a sharp-surface approximation (dot-dashed).

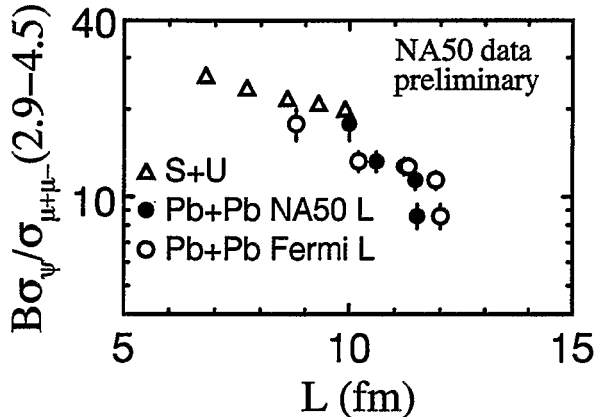


FIG. 6. NA50 data replotted with a realistic  $L(E_T)$  from (9).

where  $T_A(s) = \int \rho_A(s, z) dz$ . In fig. 5 we compare the NA50  $L(E_T)$  to the path length calculated using two assumptions for the nuclear density profile: our realistic three-parameter Fermi distribution and the sharp-surface approximation  $\rho = \rho_0 \Theta(R_A - r)$ . NA38 [17] obtained  $L$  for S+U using the empirical prescription of ref. [10], while NA50 calculated  $L$  assuming the sharp-surface approximation [18]. Indeed, we see that the NA50 Pb+Pb values agree with our sharp-surface result, while the NA38 S+U values are nearer to the realistic distribution.

To see how the value of the path length can affect the appearance of fig. 1a, we replot in fig. 6 the NA50 data using  $L(E_T)$  from (9) with the realistic density. We learn that the appearance of fig. 1a is very sensitive to the definition of  $L$ . Furthermore, with a realistic  $L$ , one no longer gets the impression given by the NA50 figure [1] of Pb+Pb data “departing from a universal curve.” Nevertheless, the saturation phenomena evident in fig. 1a does not vanish. Saturation is a real effect of geometry.

## V. $\psi'$ SUPPRESSION

To apply eqs. (4-6) to calculate the  $\psi'$ -to- $\psi$  ratio as a function of  $E_T$ , we must specify  $\sigma_{\psi'N}$ ,  $\sigma_{\psi'co}$ , and  $\sigma_{\psi'co}$ . Following Ref. [11], we use  $pp$  data to fix  $B\sigma_{\psi'N}^{NN}/B\sigma_{\psi}^{NN} = 0.02$  (this determines  $F_{\psi'}$ ). The value of  $\sigma_{\psi'N}$  depends on whether the nascent  $\psi'$  is a color singlet hadron or color octet  $c\bar{c}$  as it traverses the nucleus. In the singlet case, one expects the absorption cross sections to scale with the square of the charmonium radius. Taking this *ansatz* and assuming that the  $\psi'$  forms directly while radiative  $\chi$  decays account for 40% of  $\psi$  production, one expects  $\sigma_{\psi'} \sim 2.1\sigma_{\psi}$  for interactions with either nucleons or comovers [5]. For the octet case, we take  $\sigma_{\psi'N} \approx \sigma_{\psi N}$  and fix  $\sigma_{\psi'co} \approx 12$  mb to fit the S+U data. In fig. 7a, we show that the singlet and octet extrapolations describe  $pA$  data equally well.

Our predictions for Pb+Pb collisions are shown in fig. 8. In the octet model, the entire suppression of the  $\psi'$ -to- $\psi$  ratio is due to comover interactions. In view of the schematic nature of our approximation to  $S_{co}$  in eq. (8), we regard the agreement with data of singlet and octet extrapolations as equivalent.

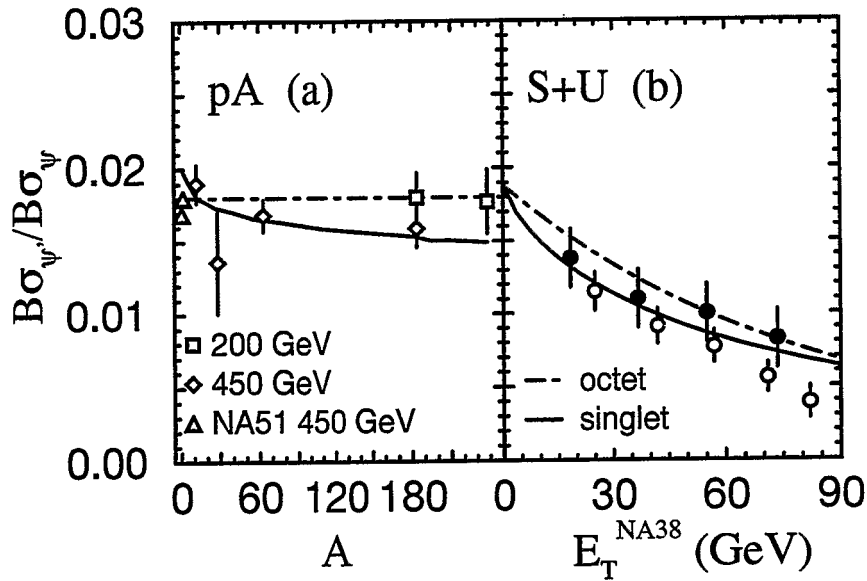


FIG. 7. Comover suppression of  $\psi'$  compared to (a) NA38 and NA51 pA data [1,9] and (b) NA38 S+U data [8] (filled points) and preliminary data [1].

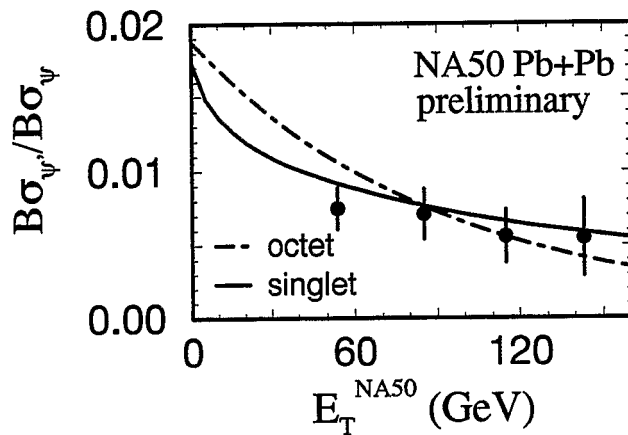


FIG. 8. Comover suppression in  $\text{Pb}+\text{Pb} \rightarrow \psi' + X$ .

## VI. SUMMARY

In summary, the Pb data [1] cannot be described by nucleon absorption alone. This is seen in the NA50 plot, fig. 1a, and confirmed by our results. The saturation with  $L$  but not  $E_T$  suggests an additional density-dependent suppression mechanism. Earlier studies pointed out that additional suppression was already needed to describe the S+U results [5]; recent data [1] support that conclusion (see, however, [2]). Comover scattering explains the additional suppression. Nevertheless, it is unlikely that this explanation is unique. SPS inverse-kinematics experiments ( $B < A$ ) and AGS  $pA$  studies near the  $\psi$  threshold can help pin down model uncertainties.

After the completion of [3], several cascade calculations [15] have essentially confirmed our conclusions. This confirmation is important, because such calculations do not employ the simplifications (*e.g.*  $n_0 \propto E_T$ ) needed to derive (8). In particular, these models calculate  $E_T$  and the comover density consistently. Some of these authors took  $\sigma_{\psi N} \sim 6$  mb (instead of  $\sim 5$  mb) to fit the NA51 data in fig. 3a somewhat better.

I am grateful to Ramona Vogt for her collaboration in this work. I also thank C. Gerschel and M. Gonin for discussions of the NA50 data, and M. Gyulassy, R. Pisarski and M. Tytgat for insightful comments.

## REFERENCES

- [1] M. Gonin *et al.* (NA50), Proc. Quark Matter '96, Heidelberg, Germany, P. Braun-Munzinger *et al.*, eds. (1996).
- [2] J.-P. Blaizot and J.-Y. Ollitrault, Phys. Rev. Lett. 77 (1996) 1703; D. Kharzeev, hep-ph/9609260 (1996).
- [3] S. Gavin and R. Vogt, LBL-37980 (1996), hep-ph/9606460.
- [4] S. Gavin and R. Vogt, Nucl. Phys. B345 (1990) 104.
- [5] S. Gavin, H. Satz, R. L. Thews, and R. Vogt, Z. Phys. C61 (1994) 351; S. Gavin, Nucl. Phys. A566 (1994) 383c.
- [6] O. Drapier *et al.* (NA38) Nucl. Phys. A544 (1992) 209c.
- [7] C. Baglin *et al.* (NA38) Phys. Lett. B270 (1991) 105.
- [8] C. Baglin *et al.* (NA38) Phys. Lett. B345 (1995) 617; S. Ramos *et al.* Nucl. Phys. A590 (1995) 117c.
- [9] C. Lourenco (NA38/NA50), Europhysics Conf. on High Energy Physics - EPS-HEP, Brussels (1995).
- [10] C. Gerschel and J. Hüfner, Z. Phys. C56 (1992) 171.
- [11] R. Gavai *et al.*, Int. J. Mod. Phys. A10 (1995) 3043.
- [12] S. Gavin *et al.*, Int. J. Mod. Phys. A10 (1995) 2961.
- [13] S. Margetis *et al.* (NA49), Phys. Rev. Lett. 75 (1995) 3814.
- [14] M. C. Abreu *et al.*, Nucl. Phys. A566 (1994) 77c.
- [15] W. Cassing and C. M. Ko, nucl-th/9609025 (1996); D. Kahana, S. H. Kahana and Y. Pang, in progress; L. Gerland *et al.*, in progress.
- [16] S. Gavin and R. Vogt, in progress.
- [17] A. Borhani, NA38, Ph. D. Thesis, l'Ecole Polytechnique (1996).
- [18] C. Gerschel, NA50, private communications.

**IV.**  
**Chiral**  
**Symmetry**

# Formation of DCCs with the Linear Sigma Model

Jørgen Randrup

*Nuclear Science Division, Lawrence Berkeley Laboratory, Berkeley, California 94720*

## Abstract

A simple approximate treatment of statistical equilibrium is developed within the linear  $\sigma$  sigma model by means of the Hartree factorization technique, providing a simple means for sampling initial configurations of the chiral field. These are then subjected to pseudo-expansions and their non-equilibrium relaxation towards the normal vacuum is studied.

## I. INTRODUCTION

The possibility of forming disoriented chiral condensates in high-energy hadron and heavy-ion collisions, such as those anticipated at *RHIC*, has generated considerable interest in the past few years. The underlying assumption is that the collision produces an extended hot region within which approximate chiral symmetry is temporarily restored. The rapid disassembly of the system then induces a non-equilibrium relaxation of the chiral field which may lead to the formation of large coherent sources of correspondingly soft pions [1-5]. Since these disoriented chiral ‘domains’ have well-defined orientations in isospace the associated pion multiplicity distributions display anomalous features. The occurrence of the phenomenon may thus provide an observational opportunity for testing our understanding of chiral symmetry. Recent reviews of the topic may be found in refs. [6-8].

In order to elucidate the conditions for the occurrence of *DCC* phenomena and the prospects for their experimental detection, it is necessary to carry out dynamical simulations of the non-equilibrium evolution experienced by the chiral field as it relaxes from an initially very excited state, in which chiral symmetry is approximately restored, towards the normal vacuum in which the symmetry is significantly broken. The most popular tool for such dynamical studies has been the linear  $\sigma$  model [9] in which the chiral degrees of freedom are described by an  $O(4)$  real classical field with a simple non-linear self-interaction [10-20]. Even though this description is relatively simple, ignoring all other degrees of freedom (such as those represented by other mesonic species or individual partons), it still presents a significant computational challenge. It is therefore of practical interest to develop useful approximate methods for solving the equation of motion for the chiral fields and for understanding their complicated non-linear dynamics.

We first describe how it is possible to make a simple approximate treatment of statistical equilibrium by employing the Hartree factorization technique. We here largely follow the developments made in ref. [21]. Subsequently, following ref. [22], we employ that framework for understanding the non-equilibrium relaxation of chiral matter subjected to pseudo-expansions, with particular emphasis on the conditions for achieving an amplification of the

low-energy pion modes. A more comprehensive study of *DCC* observables, and the utility of the mean-field approximation for their calculation, is being reported elsewhere [23].

## II. HARTREE APPROXIMATION IN EQUILIBRIUM

Most dynamical studies of disoriented chiral condensates have been based on the linear  $\sigma$  model in which the chiral degrees of freedom are described by the real  $O(4)$  field  $\phi = (\sigma, \boldsymbol{\pi})$  having the equation of motion

$$\left[ \square + \lambda(\phi^2 - v^2) \right] \phi = H \hat{\sigma}, \quad \phi(\mathbf{r}, t) = (\sigma(\mathbf{r}, t), \boldsymbol{\pi}(\mathbf{r}, t)). \quad (1)$$

The three parameters in the model can be fixed by specifying the pion decay constant,  $f_\pi = 92$  MeV, and the meson masses,  $m_\pi = 138$  MeV and  $m_\sigma = 600$  MeV, leading to the values  $\lambda = (m_\sigma^2 - m_\pi^2)/2f_\pi^2 = 20.14$ ,  $v = [(m_\sigma^2 - 3m_\pi^2)/(m_\sigma^2 - m_\pi^2)]^{1/2} f_\pi = 86.71$  MeV, and  $H = m_\pi^2 f_\pi = (120.55 \text{ MeV})^3$ , with  $\hbar, c=1$  [21].

As is apparent from eq. (1), the vacuum configuration is aligned with the  $\sigma$  direction,  $\phi_{\text{vac}} = (f_\pi, \mathbf{0})$ , and at low temperature the fluctuations represent nearly free  $\sigma$  and  $\pi$  mesons. In the other extreme, at temperatures well above  $v$ , the field fluctuations are centered near zero and approximate  $O(4)$  symmetry prevails.

In the present discussion, we limit the considerations to macroscopically uniform configurations (chiral matter) and therefore enclose the system in a box with periodic boundary conditions. It is then possible to uniquely decompose the chiral field,

$$\phi(\mathbf{r}, t) = \underline{\phi}(t) + \delta\phi(\mathbf{r}, t), \quad \underline{\phi} = \langle \phi \rangle. \quad (2)$$

The first term,  $\underline{\phi}$ , is the spatial average of the chiral field and may be identified with the order parameter, while the fluctuations,  $\delta\phi(\mathbf{r})$ , represent elementary quasi-particle excitations relative to the constant field.

By taking the spatial average of the full equation of motion (1), it is possible to derive an equation of motion for the order parameter [24]. If we subsequently subtract that from (1) and apply a Hartree-type factorization [16,21], we obtain a corresponding equation for the field fluctuations. The resulting equations of motion are of mean-field form,

$$\left[ \square + \mu_0^2 \right] \underline{\phi} = H \hat{\sigma}, \quad \mu_0^2 = \lambda \left[ \phi_0^2 + \langle \delta\phi^2 \rangle + 2 \langle \delta\phi_{\parallel}^2 \rangle - v^2 \right], \quad (3)$$

$$\left[ \square + \mu_{\parallel}^2 \right] \delta\phi_{\parallel} = 0, \quad \mu_{\parallel}^2 = \lambda \left[ 3\phi_0^2 + \langle \delta\phi^2 \rangle + 2 \langle \delta\phi_{\parallel}^2 \rangle - v^2 \right], \quad (4)$$

$$\left[ \square + \mu_{\perp}^2 \right] \delta\phi_{\perp} = \mathbf{0}, \quad \mu_{\perp}^2 = \lambda \left[ \phi_0^2 + \langle \delta\phi^2 \rangle + 2 \langle \delta\phi_{\perp}^2 \rangle - v^2 \right]. \quad (5)$$

Here  $\delta\phi_{\parallel} = \delta\phi \circ \hat{\phi}$  is the fluctuation along the order parameter and  $\delta\phi_{\perp}$  is the fluctuation perpendicular to  $\hat{\phi}$ . Furthermore, the spatial averages  $\langle \cdot \rangle$  have been replaced by the corresponding thermal average  $\langle \cdot \rangle$ , evaluated at the given temperature  $T$ . We note that the effective masses increase with the magnitude of the order parameter  $\phi_0$  as well as with the field fluctuations. They are degenerate for  $\phi_0=0$  and vanish at the temperature  $T_c = \sqrt{2}v$ . Moreover, we always have  $\mu_0^2 \leq \mu_{\perp}^2 \leq \mu_{\parallel}^2$ . Since the quasi-particles are thus governed by a Klein-Gordon equation, it is simple to obtain the thermal averages self-consistently,



$$\langle \delta\phi_{\parallel}^2 \rangle = \frac{1}{\Omega} \sum_{\mathbf{k} \neq 0} \frac{1}{\epsilon_{\mathbf{k}} e^{\epsilon_{\mathbf{k}}/T} - 1}, \quad \epsilon_{\mathbf{k}}^2 = k^2 + \mu_{\parallel}^2, \quad (6)$$

$$\langle \delta\phi_{\perp}^2 \rangle = \frac{1}{\Omega} \sum_{\mathbf{k} \neq 0} \frac{1}{\epsilon_{\mathbf{k}} e^{\epsilon_{\mathbf{k}}/T} - 1}, \quad \epsilon_{\mathbf{k}}^2 = k^2 + \mu_{\perp}^2. \quad (7)$$

The volume of the box is given by  $\Omega$  and  $\mathbf{k}$  denotes the wave vector of the individual modes in the cavity. The corresponding dispersion relations are indicated as well and the resulting effective masses are shown in Fig. 1.

Eq. (3) was first derived in ref. [24] and the Hartree treatment is in accordance with ref. [16]. Furthermore, we note that the terms  $\langle \delta\phi^2 \rangle$  in eqs. (3-5) are sums of the field fluctuations in each of the  $N=4$  chiral directions and thus constitute the leading-order fluctuation contribution in a  $1/N$  expansion. These are the ‘direct’ terms that have been included in a number of previous *DCC* treatments or discussions in terms of effective masses [10-11,16-19,25-27]. The additional fluctuation terms are the ‘exchange’ terms and each is twice the fluctuation along the particular chiral direction considered (either parallel or perpendicular to the order parameter). Although these terms are only of next-to-leading order in  $1/N$ , they increase the fluctuation contributions by  $2/N = 50\%$  and their effect may thus be significant. Recent analyses suggest that the mean-field treatment with all the fluctuation terms included is in fact a quite good approximation for both the equilibrium properties [21] and for the calculation of *DCC* observables [23].

The statistical properties of chiral matter are most naturally derived on the basis of the partition function,

$$\mathcal{Z}_T = \int \mathcal{D}[\psi, \phi] e^{-\frac{\Omega}{T} E[\psi, \phi]} = \int d^4\underline{\psi} d^4\underline{\phi} W_T(\underline{\psi}, \underline{\phi}), \quad W_T(\underline{\psi}, \underline{\phi}) \approx e^{-\frac{\Omega}{T}(K_0 + V_T - TS_T)}, \quad (8)$$

where  $K_0 = \psi_0^2/2$  is the kinetic energy density of the order parameter  $\underline{\phi}$ . The statistical weight  $W_T$  gives the relative probability for finding the system with a specified value of the order parameter  $\underline{\phi}$  and its time derivative  $\underline{\psi}$ . Its simple approximate form contains the effective potential energy density  $V_T$ , which is shown in Fig. 2, and the entropy density  $S_T$  associated with the quasi-particle degrees of freedom for a given value of  $\phi_0$ .

The corresponding free energy density  $F_T = V_T - TS_T$  governs the distribution of the order parameter  $\underline{\phi}$ . It depends only on the magnitude  $\phi_0$  and the disorientation angle  $\chi_0$  (the angle between  $\underline{\phi}$  and the  $\sigma$  direction) and it is easy to calculate in the mean-field approximation. Figure 3 shows its appearance along the  $\sigma$  axis where its minima are situated. For high temperatures, the free energy has its minimum near the origin, a reflection of the approximate  $O(4)$  symmetry restoration, and as  $T$  is decreased, the minimum moves smoothly outwards and finally settles at the vacuum value  $f_{\pi}$ .

The location of the minimum in  $F_T$  gives the most probable value of the order parameter. For the relatively small volumes of relevance in collision experiments, there are significant statistical fluctuations around the preferred value and the corresponding thermal distribution is determined by the statistical weight  $W_T$  in (8).

The resulting behavior of the magnitude of the order parameter is shown in Fig. 4. As  $T$  is increased from zero, the fluctuations grow steadily and the equilibrium value of  $\phi_0$  begins to decrease from  $f_{\pi}$ . The most rapid change occurs at  $T \approx 220$  MeV, above which  $\phi_0$  keeps decreasing at an ever slower rate. Correspondingly,  $\mu_{\perp}$  increases monotonically with

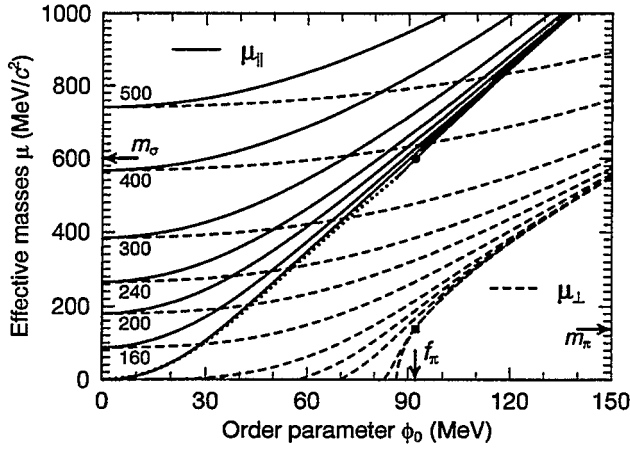


FIG. 1. Effective masses.

The effective masses  $\mu_{\parallel}$  and  $\mu_{\perp}$  as functions of  $\phi_0$  for a range of temperatures, calculated in the thermodynamic limit,  $L \rightarrow \infty$ . For temperatures above  $T_c$ , the curves start at  $\phi_0 = 0$  with degenerate values, whereas below  $T_c$  they only exist if  $\phi_0$  is sufficiently large. The corresponding starting points for  $\mu_{\parallel}$  are connected by the dotted curve and, since  $\mu_{\parallel}$  is then nearly independent of  $T$ , only the curve for  $T=0$  is shown. The locations of the vacuum values  $m_{\sigma}$ ,  $m_{\pi}$  are also shown.

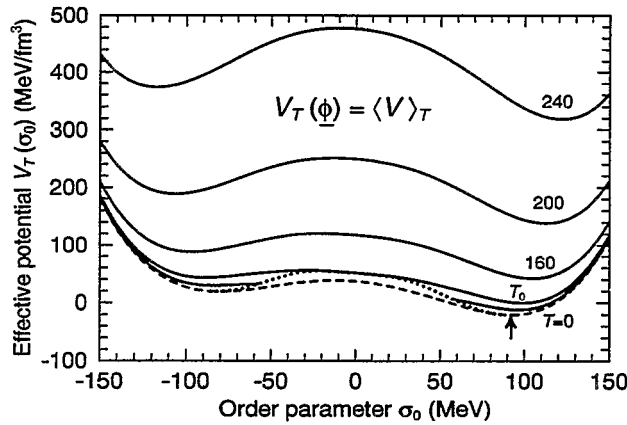


FIG. 2. Effective potential.

The effective potential energy density along the  $\sigma$  axis for a range of temperatures. For  $T < T_c$  the curve starts at a minimum value between 0 and  $v$ ; these starting points are connected by the dotted curve, while the dashed curve shows the bare potential  $V_0$  for which  $\delta\phi \equiv \mathbf{o}$ . The potential for other orientations of the order parameter can be obtained from  $V_T(\phi_0, \chi_0) = V_T(\phi_0, 0) + H\phi_0(1 - \cos\chi_0)$ .

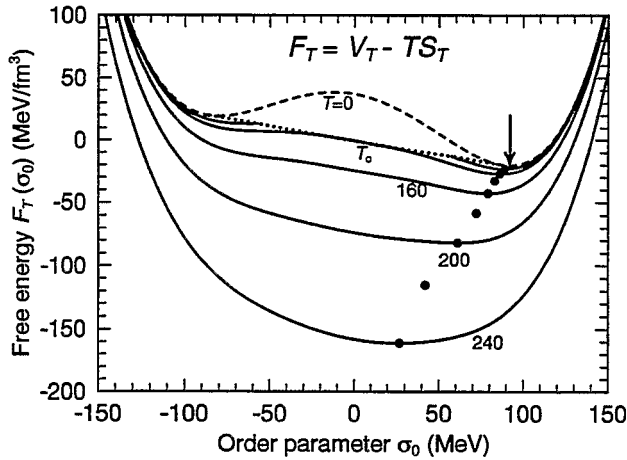


FIG. 3. Free energy.

The free energy density along the  $\sigma$  axis for a range of temperatures. The solid curves show the results for a number of temperatures. For  $T < T_c$  the curve starts at a minimum value of  $\phi_0$  and these starting points are connected by the dotted curve, while the dashed curve shows the result obtained when the temperature is neglected. The arrow points to the vacuum value  $F_{T=0}$  and the location of the minima for finite temperatures are indicated by the solid dots.

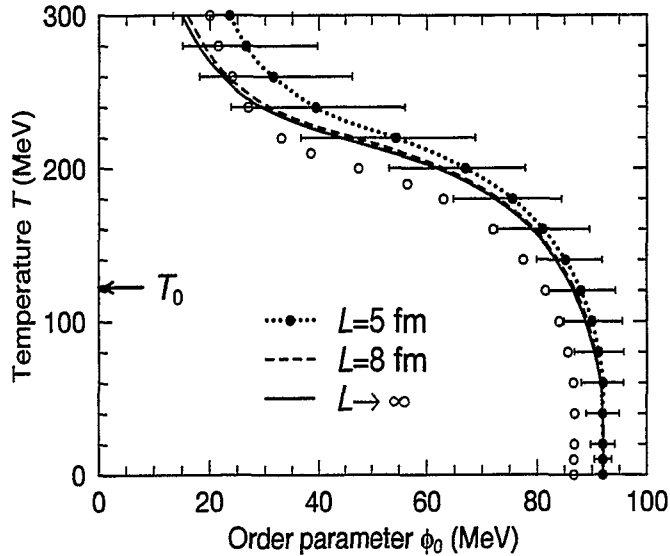


FIG. 4. Temperature dependence of the order parameter.

The most probable value of  $\phi_0$ , the magnitude of the order parameter, in the standard case where  $H > 0$ . In the thermodynamics where  $L \rightarrow \infty$  (solid curve)  $\phi_0$  is constrained to the value for which the free energy density has its minimum (see Fig. 3). The bars show the full width at half maximum of the thermal distribution of  $\phi_0$  in the system with  $L = 5$  fm; those for  $L = 8$  fm are about half that size. The open dots show the centroids for the idealized case having  $H = 0$ , for the box with  $L = 5$  fm; the behavior is qualitatively similar even though the nature of the phase transition changes.

$T$  from its free value  $m_\pi$  towards  $\approx 1.6T$  for  $T \gg T_c$ , while  $\mu_{\parallel}$  first decreases, then displays a minimum at  $T \approx 240$  MeV, and finally becomes degenerate with  $\mu_{\perp}$  [21].

### III. SAMPLING OF THERMAL FIELD CONFIGURATIONS

The simple description resulting from the Hartree factorization makes it possible to develop a convenient approximate manner for sampling chiral field configurations describing macroscopically uniform matter in thermal equilibrium [21]. Since this method is generally applicable, it may be of broad interest and we therefore briefly summarize it here.

The first task is to sample the order parameter  $(\underline{\psi}, \phi)$  on the basis of the statistical weight  $W_T(\psi_0, \phi_0, \chi_0)$  given in eq. (8). This quantity factorizes, due to the additive form of the exponent. The time derivative  $\psi_0$  is then governed by a four-dimensional normal distribution,  $P_{\psi}(\psi) \sim \exp(-\Omega\psi_0^2/2T)$ . Furthermore, since the distribution of the magnitude  $\phi_0$  can be pretabulated (ignoring at first the  $H$  term), the associated sampling task is computationally simple. Once  $\phi_0$  has been picked, the disorientation angle  $\chi_0$  is easy to sample from its conditional distribution,  $P_{\chi}(\chi_0) \sim \exp(-H\phi_0 \cos \chi_0)$ , and the  $O(3)$  direction  $(\vartheta_0, \varphi_0)$  of  $\underline{\pi}$  is uniform on  $4\pi$ .

Once the magnitude of the order parameter is known, the thermal quasiparticle distributions are fully determined and the number of quanta in each elementary mode is readily sampled, using  $P(n_{\mathbf{k}}) \sim \exp(-n_{\mathbf{k}}\epsilon_{\mathbf{k}}/T)$  for each of the four principal chiral directions. Since the quasi-particle mass tensor is aligned with the  $O(4)$  direction of the order parameter,  $(\chi_0, \vartheta_0, \varphi_0)$ , a subsequent  $O(4)$  rotation of  $\phi(\mathbf{r})$  and  $\psi(\mathbf{r})$  must then be performed in order to express the sampled field configuration in the usual  $(\sigma, \boldsymbol{\pi})$  reference system.

#### IV. EXPANSION DYNAMICS

We have shown above how thermal equilibrium can be treated approximately in the mean-field approximation. However, it is expected that the early collision dynamics causes the chiral field to be formed in a state of rapid expansion. The subsequent evolution may then lead to a supercooled configuration situated inside the unstable region, thus effectively producing a “quench”. Several quenched scenarios have been considered [10-12,15-18] but they were largely imposed by *fiat*, thereby reducing the predictive power of the dynamical calculations - essentially any degree of magnification can be achieved by suitable adjustment of the initial conditions. The degree of arbitrariness can be reduced by examining under which conditions a quench-like early scenario may develop dynamically from various possible types of initial scenarios.

Simple Bjorken-like pictures can be invoked to emulate expansion in  $D$  dimensions, either longitudinal ( $D=1$ ) [12,17-18], transverse ( $D=2$ ), or isotropic ( $D=3$ ) [13,27]. We have studied such scenarios in an approximate manner by augmenting the equation of motion (1) with a Rayleigh dissipation term [22],

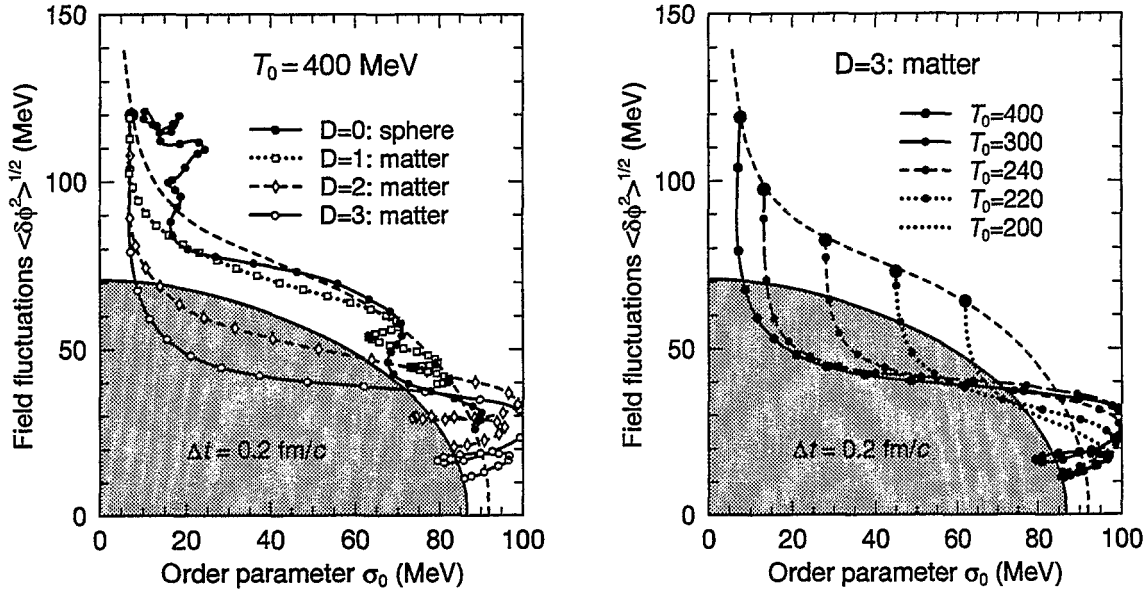
$$\left[ \square + \lambda(\phi^2 - v^2) \right] \phi - H\dot{\phi} = -\frac{D}{t}\psi, \quad \psi = \partial_t \phi. \quad (9)$$

The cooling term causes the field fluctuations to decay in the course of time and the associated decrease of the energy density is given by  $\dot{E} = -(D/t) \langle \psi^2 \rangle$ . At sufficiently large times, the quasiparticle number density decreases as  $\sim t^{-D}$  as  $t \rightarrow \infty$ , as is characteristic of an expansion in  $D$  dimensions. The time variable should now be reinterpreted as the elapsed proper time in a comoving frame (starting at  $t_0 = 1$  fm/c, usually). The corresponding Lorentz transformation of the (scaled) spatial coordinates is less essential for our present discussion and has therefore been ignored.

Figures 5a-b depict dynamical trajectories for a variety of instructive scenarios. In order to make a display that does not rely on any assumption with regard to the degree of equilibrium, we adopt the field dispersion as a measure of the degree of agitation; it can be visualized as a model-independent replacement of the temperature variable. In Fig. 5a is shown the dynamical trajectory of the central part of a Ni-sized spherical source prepared at  $T_0=400$  MeV without any initial expansion. The system keeps away from the unstable regime, exhibiting an approximately adiabatic evolution. This behavior is rather robust, as it occurs for a wide range of initial temperatures and for rod or slab geometries as well. It thus appears that initially static field configurations in local equilibrium do not develop any instabilities during their subsequent expansion.

The other trajectories in Fig. 5a illustrate the effect of endowing the system with an initial expansion. The effect increases with  $D$ , since the dimensionality of the pseudo-expansion effectively acts as the strength of the damping term. The isotropic expansion leads to a significant incursion into the unstable region, while the longitudinal one is too slow for that and appears to be closer to the self-generated near-adiabatic expansion.

The approximate equations (3-5) provide a convenient framework for developing an understanding of the dynamics generated by the pseudo-expansion (9). Imagine that the system is initially created in thermal equilibrium at a temperature  $T_0$  well above  $T_c$ . The field fluctuations are then sufficiently large to ensure  $\mu^2 > 0$  in all three eqs. (3-5). The system is



The combined dynamical evolution of the order parameter  $\phi_0 \approx \langle \sigma \rangle$  and the fluctuations  $\langle \delta\phi^2 \rangle^{1/2}$ . The dashed curve connects the equilibria from  $T=0$  to above 500 MeV and the unstable region where  $\mu_1^2 < 0$  is shown by the shaded region; its border intersects the  $\sigma$  axis at  $f_\pi$  and extends up to  $T_c/\sqrt{3}$  at  $\phi_0=0$ . Each system has been prepared in thermal equilibrium at  $T_0 = 400$  MeV, using a periodic box (20 fm side length). The irregular solid trajectory (labelled  $D=0$ ) was obtained by solving the standard eq. (1) after applying a spherical Saxon-Woods modulation factor (5 fm radius and 0.5 fm width) to the hot matter, thereby producing a hot Ni-sizes sphere embedded in vacuum; the field was sampled only in the interior ( $r < 2.5$ ). The other three trajectories have been obtained by solving the pseudo-expansion equation of motion (9) without applying a spatial modulation, thus emulating uniform expansions in  $D = 1, 2, 3$  dimensions. The marks along the trajectories are positioned at time intervals of  $\Delta t = 0.2$  fm/c.

FIG. 5. Dynamical trajectories.

expected to experience a cooling resulting from expansion and radiation, so the fluctuations decrease in the course of time. This reduces  $\mu^2$  which allows the order parameter to grow larger, thus counteracting the decrease of the effective masses. The resulting behavior of  $\mu^2$  is then a delicate balance: for slow cooling the induced growth of  $\phi_0$  is approximately adiabatic and the system relaxes towards the vacuum through metastable configurations; however, if the fluctuations diminish rapidly a compensating growth of the order parameter can no longer occur quickly enough and one or more of the effective masses may turn imaginary,  $\mu^2 < 0$ , indicating that the system has entered an unstable regime where some modes grow exponentially.

Figure 5b shows trajectories for  $D=3$  starting from various temperatures. If the initial temperature is lower than 200 MeV or so, the initial value of  $\phi_0$  is already fairly large (over 60 MeV) and the dynamical trajectories will miss the unstable region. A wide range of higher temperatures lead into the unstable region, provided the supercooling occurs sufficiently fast. Ultimately, at very high temperatures (above those shown) the system will again stay stable throughout, because it takes so long to reduce the fluctuations down to critical size that the order parameter has meanwhile had time to start its growth.

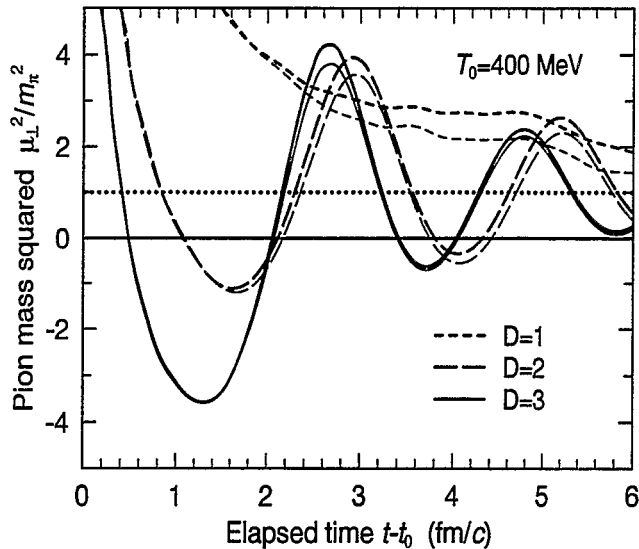


FIG. 6. Time evolution of the pion mass.

In order to quantify the analysis, it is useful to consider the time evolution of the effective masses. Since  $\mu_{\parallel}^2 > \mu_{\perp}^2$  we concentrate on the latter which is illustrated in Fig. 6. It is noteworthy that  $\mu_0 \approx \mu_{\perp}$  throughout the evolution, implying that the amplification of the lowest pionic modes is practically identical to that of the order parameter itself. This simple feature makes it an easier task to analyze more complicated scenarios. It is convenient to express the resulting enhancement of a mode in terms of its amplification coefficient [28],

$$G_k^{\pi} \equiv \int_{\omega_k^2 < 0} dt \sqrt{-\omega_k(t)^2}, \quad \omega_k^2 = k^2 + \mu_{\perp}(t)^2, \quad (10)$$

which expresses approximately the factor by which the amplitude of a pionic mode has been magnified due to incursion(s) into the unstable regime. An upper bound on the magnification is provided by the coefficient for  $k=0$ , shown in Table I. The purely longitudinal expansions largely miss the unstable region, while significant magnification occurs for the transverse and isotropic expansions, amounting to over a factor of ten in the most favorable cases.

TABLE I. Amplification coefficients/correlation lengths.

$T_0$ (MeV)	$D = 1$	$D = 2$	$D = 3$
200	0.00 / 1.4	0.02 / 1.8	0.11 / 2.0
220	0.00 / 1.3	0.50 / 1.9	0.55 / 2.5
240	0.01 / 1.3	1.20 / 2.0	1.19 / 2.7
300	0.00 / 0.9	1.84 / 1.7	2.06 / 2.7
400	0.00 / 0.6	1.67 / 1.3	2.49 / 2.1
500	0.00 / 0.5	1.31 / 1.1	2.61 / 1.6

The maximum enhancement factor,  $G_{k=0}^{\pi}$ , in macroscopically uniform chiral matter and the resulting *FWHM* of the pion correlation function  $C_{\pi}(r_{12}) = \langle \delta\pi(r_1) \cdot \delta\pi(r_2) \rangle$  for pions emerging after pseudo-expansions (9) starting from thermal equilibrium at the temperature  $T_0$  and using  $D = 1, 2, 3$ .

Figure 7 gives an impression of the net effect on the power spectrum of the emerging free pions. As expected, the transient instabilities present for  $D \gtrsim 2$  lead to significant enhancements of the power carried off by soft pions. The effect amounts to about an order

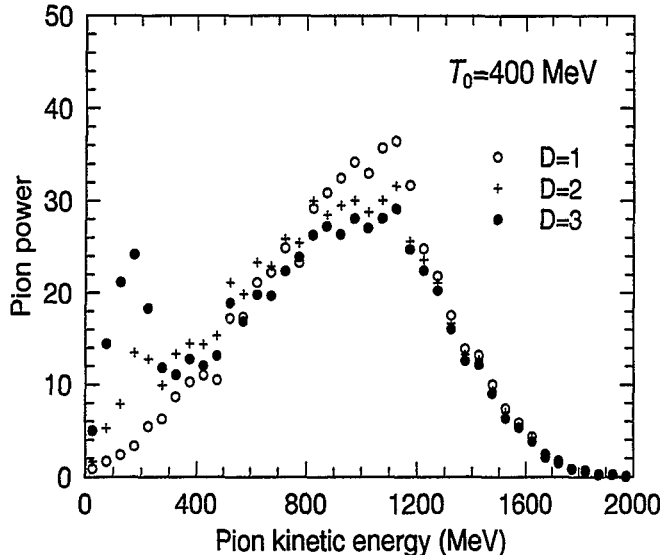


FIG. 7. Pion power spectrum.

The relative power spectrum of the pions,  $\sim \omega_k^2 \pi_k^2$ , where  $\pi_k$  is the Fourier amplitude of the pion field, plotted as a function of the pion kinetic energy  $\omega_k - m_\pi$ . The extraction is made at large times when the asymptotic scenario of free evolution has been reached. The plots are based on samples of 20 field configurations prepared at  $T_0 = 400$  MeV and subjected to idealized expansions with either  $D=1$  (open dots),  $D=2$  (crosses), or  $D=3$  (solid dots). The irregularities are primarily due to the shell structure in the level density of the cube.

of magnitude for  $D=3$  (relative to the smooth spectrum obtained for  $D=1$ ), in accordance with the amplification coefficients given in Table I. Although these results were calculated for idealized expansion scenarios, they do support the suggestion that such enhancements may provide an observable signal of *DCC* formation [7].

## V. CONCLUDING REMARKS

We have discussed some of the key features associated with the formation of disoriented chiral condensates in high-energy collisions, such as those planned at *RHIC*. By application of the Hartree factorization technique, it is possible to develop a simple mean-field treatment which in turn leads to an efficient method for sampling thermal field configurations. Moreover, the mean-field approximation provides a useful conceptual framework for understanding the non-equilibrium dynamics of the chiral field as it relaxes from its initial very excited state towards the normal vacuum. By augmenting the full equation of motion with a cooling term it is possible to emulate chiral matter in uniform Bjorken-like expansion.

With this method, we have studied the conditions for amplification of the soft pionic modes, an important element in the observation of *DCCs*. Our analysis shows that the occurrence of instabilities, and the associated amplification of pionic modes, depends sensitively on the cooling rate, which in turn is intimately related to the character of the expansion. Our idealized scenario for  $D=3$  corresponds closely to the isotropic expansion considered in refs. [13,27] and our results corroborate the conclusion in [13] that such a scenario leads to amplification. Furthermore, our analysis suggest that a longitudinal expansion alone is insufficient to cause a quench, if the initial fluctuations are of thermal magnitude. This is consistent with what was found in refs. [12,18] for effectively one-dimensional expansions.

This qualitative sensitivity to the collision dynamics highlights the importance of employing realistic initial conditions for the dynamical simulations of *DCC* formation. Ultimately, the appropriate initial field configurations must be calculated on the basis of the early par-

tonic evolution, a task which is thus crucial for our ability to assess the prospects of forming disoriented chiral condensates in high-energy collisions.

This work was supported in part by the Director, Office of Energy Research, Office of High Energy and Nuclear Physics, Nuclear Physics Division of the U.S. Department of Energy under Contract No. DE-AC03-76SF00098.

## REFERENCES

- [1] A.A. Anselm, Phys. Lett. B217, 169 (1989).
- [2] A.A. Anselm and M.G. Ryskin, Phys. Lett. B266 (1991) 482
- [3] J.-P. Blaizot and A. Krzywicki, Phys. Rev. D46 (1992) 246
- [4] K. Rajagopal and F. Wilczek, Nucl. Phys. B399 (1993) 395
- [5] J.D. Bjorken, K.L. Kowalski, and C.C. Taylor, Report SLAC-PUB-6109 (1993)
- [6] K. Rajagopal, in *Quark-Gluon Plasma 2*, ed. R. Hwa, World Scientific (1995)
- [7] S. Gavin, Nucl. Phys. A590 (1995) 163c
- [8] J.-P. Blaizot and A. Krzywicki, Acta Physica Polonica B; hep-ph/9606263 (1996)
- [9] M. Gell-Mann and M. Levy, Nuovo Cimento 16 (1960) 705
- [10] K. Rajagopal and F. Wilczek, Nucl. Phys. B404 (1993) 577
- [11] S. Gavin, A. Gocksch, and R.D. Pisarski, Phys. Rev. Lett. 72 (1994) 2143
- [12] Z. Huang and X.-N. Wang, Phys. Rev. D49 (1994) 4335
- [13] S. Gavin and B. Müller, Phys. Lett. B329 (1994) 486
- [14] J.-P. Blaizot and A. Krzywicki, Phys. Rev. D50 (1994) 442
- [15] M. Asakawa, Z. Huang, and X.-N. Wang, Phys. Rev. Lett. 74 (1995) 3126
- [16] D. Boyanovsky, H.J. de Vega, and R. Holman, Phys. Rev. D51 (1995) 734
- [17] F. Cooper, Y. Kluger, E. Mottola, and J.P. Paz, Phys. Rev. D51 (1995) 2377
- [18] Y. Kluger, F. Cooper, E. Mottola, J.P. Paz, A. Kovner, Nucl. Phys. A590 (1995) 581c
- [19] S. Mrówczyński and B. Müller, Phys. Lett. 363B (1995) 1
- [20] L.P. Csernai and I.N. Mishustin, Phys. Rev. Lett. 74 (1995) 5005
- [21] J. Randrup, Phys. Rev. D (submitted); Report LBL-38125 (1996)
- [22] J. Randrup, Phys. Rev. Lett. 77 (1996) 1226
- [23] J. Randrup, Nucl. Phys. A (submitted); Report LBNL-39328 (1996)
- [24] G. Baym and G. Grinstein, Phys. Rev. D15 (1977) 2897
- [25] D. Boyanovsky and D.L. Lee, Phys. Rev. D48 (1993) 800
- [26] R.D. Amado and I.I. Kogan, Phys. Rev. D51 (1995) 190
- [27] M.A. Lampert, J.F. Dawson, and F. Cooper, Preprint hep-th/9603068 (1996)
- [28] H. Heiselberg, C.J. Pethick, and D.G. Ravenhall, Phys. Rev. Lett. 61 (1988) 818



# “Baked Alaska” in Relativistic Heavy Ion Collisions: Formation of Disoriented Chiral Condensate

Masayuki Asakawa

*Department of Physics, School of Science,  
Nagoya University, Nagoya 464-01, Japan*

## Abstract

We demonstrate that the chiral phase transition is automatically incorporated in the numerical simulations of the classical equations of motion in the linear  $\sigma$ -model. We find that domains of disoriented chiral condensate (DCC) with 4–5 fm in size can form through a quench while an annealing leads to domains of smaller sizes. We also demonstrate that quenching cannot be achieved by relaxing a chirally symmetric system through expansion in ultrarelativistic heavy ion collisions. At the end, we discuss the possibility to create DCC in laboratories.

Since Rajagopal and Wilczek [1] proposed a nonequilibrium phase transition through quenching as a possible scenario for the production of large DCC domains, which is one of the explanations for the Centauro events in high energy cosmic ray experiments [2], a lot of investigation has been carried out on the possible size of DCC domains created in ultrarelativistic heavy ion collisions [3–5].

To model a quench, Rajagopal and Wilczek argued that one can evolve the classical fields according to the zero temperature equations of motion from a chirally symmetric initial condition with short correlation lengths. As we shall show, however, fluctuations introduced in the initial configuration actually render the effective potential a non-zero temperature one. The interaction between the mean fields and the fluctuations as well as their evolution can be automatically included in the numerical simulations of the equations of motion. Thus, by choosing different initial conditions, we can study the evolution of the system in both quenching [1] and annealing [6,7] scenarios with the chiral phase transition taken into account.

First let us see how the fluctuations affect chiral symmetry. In the standard linear  $\sigma$ -model, the equations of motion are given by,

$$\square\phi = \lambda(v^2 - \phi^2)\phi + Hn_\sigma, \quad (1)$$

where  $\phi \equiv (\sigma, \boldsymbol{\pi})$  is a vector in internal space,  $n_\sigma = (1, \mathbf{0})$ , and  $Hn_\sigma$  is an explicit chiral symmetry breaking term. In the following, we shall use  $\lambda = 19.97$ ,  $v = 87.4$  MeV, and  $H = (119 \text{ MeV})^3$ , with which  $m_\pi = 135$  MeV and  $m_\sigma = 600$  MeV at  $T = 0$ . We examine the Hartree approximation of Eq. (1). Separating  $\phi$  into the mean fields  $\langle\phi\rangle$  and the

fluctuations  $\delta\phi$  around  $\langle\phi\rangle$ , i.e.,  $\phi = \langle\phi\rangle + \delta\phi$ , and taking average of Eq. (1), we have

$$\begin{aligned}\square\langle\phi\rangle &= \lambda(v^2 - \langle\phi\rangle^2 - 3\langle\delta\phi_{\parallel}^2\rangle - \langle\delta\phi_{\perp}^2\rangle)\langle\phi\rangle + Hn_{\sigma}, \\ &\equiv -\chi\langle\phi\rangle + Hn_{\sigma},\end{aligned}\tag{2}$$

where  $\langle\phi\rangle^2 = \langle\phi_i\rangle\langle\phi_i\rangle$ ,  $\delta\phi_{\parallel}$  is the component of the fluctuation parallel to  $\langle\phi\rangle$ , and  $\delta\phi_{\perp}$  is the orthogonal component. Eq. (2) describes the mean fields moving in an effective potential,

$$V(\langle\phi\rangle) = \frac{\lambda}{4}(\langle\phi\rangle^2 + 3\langle\delta\phi_{\parallel}^2\rangle + \langle\delta\phi_{\perp}^2\rangle - v^2)^2 - H\langle\sigma\rangle,\tag{3}$$

which in the presence of the fluctuations clearly differs from the zero temperature one. According to the level of fluctuations, chiral symmetry can be either restored or spontaneously broken. The above effective potential is very generic since no assumption has been made for the fluctuations except that they are only of a classical nature. If the fluctuation terms in Eq. (3) are replaced by their counterparts in a finite temperature field theory, the well-known one loop effective potential at finite temperature [8] is recovered. Therefore, the classical equations of motion already includes the effect of fluctuations present in the effective potential. This can be easily understood in a thermal equilibrium case. In a finite temperature field theory, the temperature dependence of the effective potential arises from the on-shell part of the propagator. Since no contribution from virtual particles is involved, all thermal corrections at one loop level are purely classical. As a result, the time evolution of the field configuration obtained from Eq. (1) already includes the effect of the time dependence of the effective potential. *The use of the equations of motion does not ensure that the effective potential takes its zero temperature form or that chiral symmetry is spontaneously broken.*

When  $\delta^2 \equiv (3\langle\delta\phi_{\parallel}^2\rangle + \langle\delta\phi_{\perp}^2\rangle)/6$  is large enough, chiral symmetry is restored. If the explicit chiral symmetry breaking term is neglected, the phase transition takes place at the critical fluctuation,  $\delta_c^2 \equiv v^2/6$ . For  $\delta^2 < \delta_c^2$ , the effective potential takes its minimum value at  $\langle\phi\rangle = (\sigma_e, \mathbf{0})$ . When the mean fields are displaced from this equilibrium point to the central lump of the ‘‘Mexican hat’’ ( $\langle\phi_i\rangle \sim 0$ ) and  $\chi$  defined in Eq. (2) becomes negative, modes below the critical momentum,

$$k_c = \sqrt{-\chi},\tag{4}$$

become unstable and thus DCC domains can form. Thus,  $\chi$  characterizes the instability of the system. We note that since smaller momentum modes are amplified more,  $1/k_c$  does not directly give the typical size of DCC domains. *It also depends on the time scale during which these modes are unstable.*

Let us now consider three different scenarios. (i) In a quenching scenario, the initial fluctuation is below the critical value,  $\delta^2 \leq \delta_c^2$ , and  $\langle\phi_i\rangle \sim 0$  in the central region. As the mean fields roll down from the central lump of the potential, pion modes below  $k_c$  will be amplified. In the meantime, as the system cools down and the fluctuation decreases, the effective potential will also change and the equilibrium point of the potential moves towards the zero temperature value. (ii) On the other hand, if we initially choose  $\langle\phi\rangle$  to be very close to the equilibrium point of the effective potential, we refer to the scenario as a cold annealing. (iii) What we shall call a hot annealing scenario is similar to the cold annealing except that the initial fluctuation is much larger than the critical value,  $\delta^2 \gg \delta_c^2$ , so that chiral symmetry is almost restored. For the three scenarios we consider here, we take for

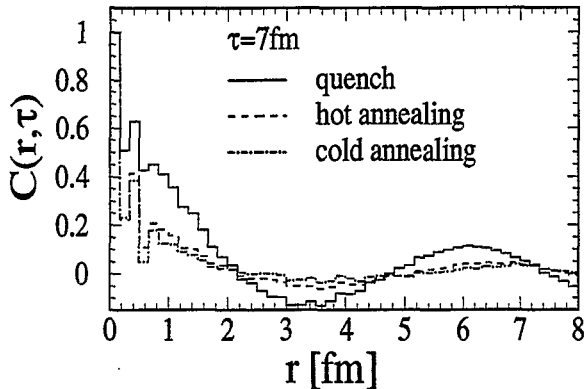


FIG. 1. Correlation functions for the quenching, hot and cold annealing scenarios at  $\tau = 7$  fm.

quenching and cold annealing cases,  $\delta_0^2 = \delta_c^2 = v^2/6$ , with which the system is about to go through a phase transition, and for a hot annealing case,  $\delta_0^2 = v^2/4$ .

We carried out numerical simulations of Eq. (1) including both the longitudinal and transverse expansions [5]. We assume boost invariance in the longitudinal direction so that the longitudinal expansion is automatically included. To consider the transverse expansion, we use a cylindrical boundary condition. The initial  $\phi$  fields are randomly distributed according to a Gaussian form. Inside a disk, whose radius is  $R_0$ , initially fluctuations exist and the mean fields are different from their vacuum expectation values. Outside this region, the vacuum configuration with no fluctuation is imposed. In the following calculations, we take the initial time  $\tau_0 = 1$  fm and transverse radius  $R_0 = 5$  fm to simulate ultrarelativistic heavy ion collisions.

We define a correlation function  $C(r, \tau)$  as

$$C(r, \tau) = \frac{\sum_{i,j} \boldsymbol{\pi}(i) \cdot \boldsymbol{\pi}(j)}{\sum_{i,j} |\boldsymbol{\pi}(i)| |\boldsymbol{\pi}(j)|}, \quad (5)$$

where the sum is taken over those grid points  $i$  and  $j$  such that the distance between  $i$  and  $j$  is  $r$ . In Fig. 1, we compare the results of the quenching, hot and cold annealing scenarios at  $\tau = 7$  fm. We observe that quenching gives the largest correlation among the three cases. The situation does not improve much even if a second order phase transition is assumed ( $H = 0$ ), because the expansion time scale is too short for any long range correlation to develop.

In Fig. 2, we show the time evolution of  $\chi/m_\sigma^2(T = 0)$ . We have generated 100 events and averaged over the central region  $r \leq 3$  fm. In Fig. 2, we have taken very small initial fluctuation,  $\delta_0^2 = v^2/16$  to simulate a very strong quenching case for the solid line. For the dashed line,  $\delta_0^2 = 3v^2/8$ , which is much larger than  $\delta_c^2$ , has been taken to simulate a very hot annealing case. We clearly see that in the quenching case  $\chi$  stays negative longer than the annealing case and that  $\chi$  becomes negative again even after it once became positive. Therefore the DCC formation time in the quenching case is *not* characterized by  $1/m_\sigma$ . This explains the large correlation length in the quenching case as observed in Fig. 1. We note that in a smaller region in a single event the duration when  $\chi$  is negative can be even longer due to fluctuation. On the other hand, in the annealing case,  $\chi$  stays almost always positive. In other words, the mean fields evolve almost synchronously with the effective potential. Thus, the low momentum modes are less amplified. As a result, domains cannot grow out

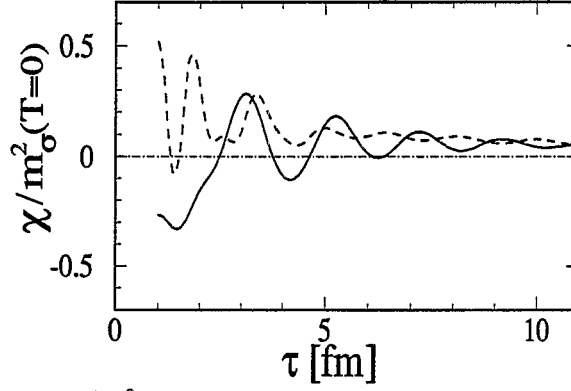


FIG. 2. Time evolution of  $\chi/m_\sigma^2(T=0)$ . The solid and dashed lines are quenching and hot annealing cases, respectively.

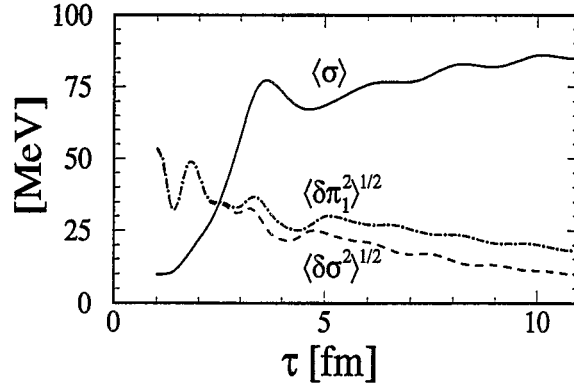


FIG. 3. Time evolution of  $\langle\sigma\rangle$ ,  $\langle\delta\sigma^2\rangle^{1/2}$ , and  $\langle\delta\pi_1^2\rangle^{1/2}$  in a very hot annealing case.

of noise, and they are less visible and smaller than in the quenching case. This shows that a quenching condition can never be realized through a hot annealing in ultrarelativistic heavy ion collisions.

In Fig. 3, we show the time evolution of the average  $\sigma$  field,  $\langle\sigma\rangle$ , and the average fluctuations,  $\langle\delta\sigma^2\rangle^{1/2}$  and  $\langle\delta\pi_1^2\rangle^{1/2}$ , respectively.  $\langle\delta\pi_2^2\rangle^{1/2}$  and  $\langle\delta\pi_3^2\rangle^{1/2}$  are similar to  $\langle\delta\pi_1^2\rangle^{1/2}$ . For this figure, we also generated 100 events and averaged over the central region. We have taken the second parameter set of Fig. 2, i.e., a very hot annealing case. We see that  $\langle\delta\sigma^2\rangle$  and  $\langle\delta\pi_1^2\rangle$  decrease on the average with time due to the longitudinal and transverse expansion. On the other hand,  $\langle\sigma\rangle$  increases, following the equilibrium position of the evolving effective potential. In principle,  $\langle\sigma\rangle$  approaches to its vacuum value,  $f_\pi$ , as  $\delta^2$  goes to zero. However, the most important point here is that  $\langle\delta\sigma^2\rangle$  and  $\langle\delta\pi_1^2\rangle$  decouple from each other at about  $\delta = 35$  MeV, which is about the value of the critical fluctuation  $\delta_c$ . This decoupling is due to nothing but the mass splitting during the chiral phase transition: the pion mass becomes smaller and the sigma mass becomes larger. This clearly demonstrates that the equations of motion already include the effect of the chiral phase transition in the presence of fluctuation.

An important question here is whether there is a way to create DCC experimentally. First, we summarize the requirements for DCC formation.

- i) Spontaneous chiral symmetry breaking, i.e., Mexican hat effective potential.
- ii) Discordance between the minimum of the effective potential and the mean position

of the field configuration.

These ensure the emergence of unstable modes with long wave lengths. In the quenching scenario, these conditions are implemented from the beginning, so DCC formation is observed. On the other hand, we have found that the annealing initial condition does not lead to states where these two are realized in the course of the time evolution, if the  $2 + 1 + 1$  dimensional boost invariant states with the radius of the initial hot region 5 fm are assumed. In order to realize these two conditions, it is necessary to cool the system promptly (this is noting but the literal meaning of quenching!) after chiral symmetry is restored. The motion of the mean of the field configuration is essentially determined by the internal dynamics determined by theory, in the present case the linear sigma model, and cannot be accelerated arbitrarily. On the other hand, the shape of the effective potential is determined by the fluctuation of the field as we have shown, and the fluctuation is related, roughly speaking, to the energy density or the entropy density. As a result, the rate of its decrease can be changed by taking different scenarios for the expansion of the system. This is the reason why it is expected that prompt cooling could lead to DCC formation. At least there are two possible cases where cooling could be fast enough to create the quenching field configuration. One of them is a system with small initial radius and approximate boost invariance such as high energy  $pp$ , or  $\bar{p}p$ , or  $pA$  collisions [9]. In this case, fast cooling is expected because of faster transverse expansion due to less causal constraint. The other is expansion with higher dimensionality such as three dimensional fireball-like expansion [10]. Numerical calculations show that indeed these two can lead to the formation DCC domains. However, the latter scenario is not that realistic in laboratories, since the three dimensional fire balls are not expected to be formed in such high energy heavy ion collisions to restore chiral symmetry initially.

In summary, it is necessary for the system to go through fast cooling after initially chiral symmetry is restored in order to create DCC domains. In this sense, the comparison of DCC formation to “Baked Alaska” is not quite appropriate. Ice cream is cold by nature and it is quite straightforward to create Baked Alaska. On the contrary, states created in heavy ion collisions or hadron collisions are essentially hot and are extremely hard to be cooled to create Baked Alaska-like states.

## ACKNOWLEDGMENT

I would like to thank S. Kahana, T. Ludlam, and R. Pisarski for giving me the opportunity to attend the exciting workshop.

## REFERENCES

- [1] K. Rajagopal and F. Wilczek, Nucl. Phys. **B404** (1993) 577.
- [2] C. M. G. Lattes, Y. Fujimoto, and S. Hasegawa, Phys. Rep. **65** (1980) 151.
- [3] S. Gavin, A. Gocksch, and R. D. Pisarski, Phys. Rev. Lett. **72**, 2143 (1994).
- [4] F. Cooper, Y. Kluger, E. Mottola, and J. P. Paz, Phys. Rev. D **51** (1995) 2377.
- [5] M. Asakawa, Z. Huang, and X.-N. Wang, Phys. Rev. Lett. **74**, 3126 (1995).

- [6] S. Gavin and B. Müller, Phys. Lett. **B329** (1994) 486.
- [7] D. Boyanovsky, H. J. de Vega, and R. Holman, Phys. Rev. D **51** (1995) 734.
- [8] L. Dolan and R. Jackiw, Phys. Rev. D **9** (1974) 3320.
- [9] M. Asakawa and X. N. Wang, in preparation.
- [10] J. Randrup, LBL preprint LBL-38379, hep-ph/9605223.

# Light Vector Mesons at Finite Baryon Density

T. Hatsuda

*Institute of Physics, University of Tsukuba, Tsukuba, Ibaraki 305, Japan*

## Abstract

We summarize the current theoretical and experimental status of the spectral changes of vector mesons ( $\rho$ ,  $\omega$ ,  $\phi$ ) at finite baryon density. Various approaches including QCD sum rules, effective theory of hadrons and bag models show decreasing of the vector meson masses in nuclear matter. Possibility to detect the mass shift through lepton pairs in  $\gamma - A$ ,  $p - A$  and  $A - A$  reactions are also discussed.

## I. INTRODUCTION

At high temperature ( $T$ ) and density ( $\rho$ ), hadronic matter is expected to undergo a phase transition to the quark-gluon plasma. The order parameter characterizing the transition is the chiral quark condensate  $\langle \bar{q}q \rangle$ , the absolute value of which decreases as  $(T, \rho)$  increases. Numerical simulations of quantum chromodynamics (QCD) on the lattice are actively pursued to determine the precise nature of the transition at finite  $T$  [1] and various model calculations have been done to look for the observable signature of the phase transition.

In this talk, I will concentrate on one of the interesting critical phenomena associated with the QCD phase transition, namely the spectral change of hadrons, in particular the mass shift of light vector-mesons ( $\rho$ ,  $\omega$  and  $\phi$ ) in nuclear matter at zero  $T$ . The vector mesons are unique in the sense that they decay into lepton pairs ( $e^+e^-$  and  $\mu^+\mu^-$ ) which can be detected experimentally without much disturbance by complicated hadronic interactions.

In section 2, I will review the current knowledge of the quark condensate in medium. In section 3, various approaches to calculate the vector meson masses in nuclear matter are summarized. Experimental possibilities to detect the spectral change are discussed in section 4. Concluding remarks are given in section 5.

## II. QUARK CONDENSATES IN NUCLEAR MATTER

The medium modification of the quark condensate has been calculated since then by various methods (lattice QCD, chiral perturbation theory, Nambu-Jona-Lasinio model etc). See an overview [2]. By these studies, it turned out that there is one noticeable difference between the behavior of  $\langle \bar{q}q \rangle$  at finite  $T$  (with  $\rho = 0$ ) and that at finite  $\rho$  (with  $T = 0$ ): In the former case, the significant change of the condensate can be seen only near the critical point  $T \sim T_c$  [3]. On the other hand, in the latter case,  $O(30\%)$  change of  $\langle \bar{q}q \rangle$  could be seen even in normal nuclear-matter density. This observation is based on the following formula in the fermi-gas approximation (independent particle approximation) [4]

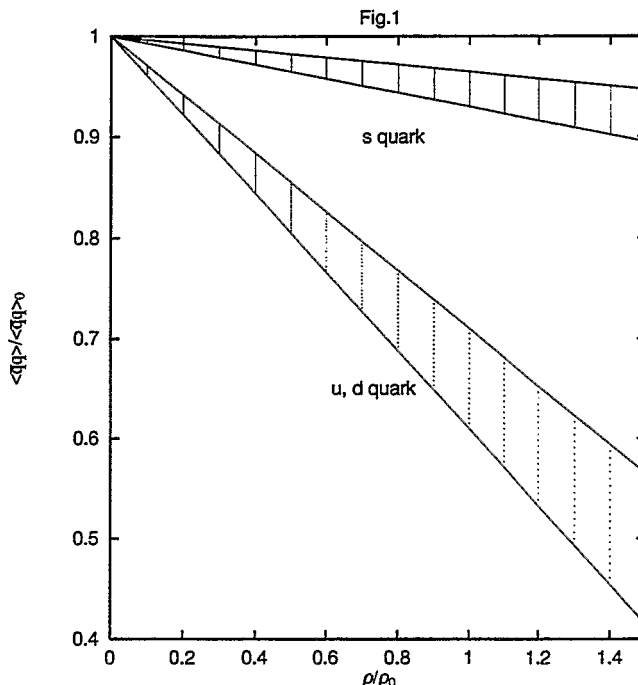


FIG. 1. The light quark condensates in  $N=Z$  nuclear matter in the linear density approximation. Theoretical uncertainty of the  $\pi N$  sigma term is taken into account. We take  $y = 0.12$  for the OZI breaking parameter, where  $y \equiv 2\langle \bar{s}s \rangle_N / \langle \bar{u}u + \bar{d}d \rangle_N$  with  $\langle \cdot \rangle_N$  being the nucleon matrix element.

$$\frac{\langle \bar{u}u \rangle}{\langle \bar{u}u \rangle_0} \simeq 1 - \frac{4\Sigma_{\pi N}}{f_\pi^2 m_\pi^2} \int_0^{p_F} \frac{d^3 p}{(2\pi)^3} \frac{M_N}{E(p)}. \quad (1)$$

Here  $m_N(m_\pi)$  is the nucleon (pion) mass,  $f_\pi$  is the pion decay constant,  $\Sigma_{\pi N} = (45 \pm 10)\text{MeV}$  is the  $\pi N$  sigma term, and  $E(p) \equiv \sqrt{p^2 + M_N^2}$ .  $\langle \cdot \rangle$  and  $\langle \cdot \rangle_0$  denote the expectation value in nuclear matter and that in the vacuum respectively. The integration for the nucleon momentum  $p$  should be taken from 0 to the fermi momentum  $p_F$ . At normal nuclear matter density ( $\rho = \rho_0 = 0.17/\text{fm}^3$ ), the above formula gives  $(34 \pm 8)\%$  reduction of the chiral condensate from the vacuum value. In Fig.1,  $\langle \bar{u}u \rangle / \langle \bar{u}u \rangle_0$  as well as the strangeness condensate  $\langle \bar{s}s \rangle / \langle \bar{s}s \rangle_0$  are shown in the linear density approximation [5], where the uncertainty of  $\Sigma_{\pi N}$  is considered. Estimates taking into account the fermi motion and the nuclear correlators show that these corrections at  $\rho = \rho_0$  are less than the above uncertainty [6].

Unfortunately, the condensate itself is not a direct observable and one has to look for physical quantities which are measurable and simultaneously sensitive to the change of the condensate. The masses of light vector-mesons are the leading candidates of such quantities.

### III. VECTOR MESONS IN NUCLEAR MATTER

Let's consider  $\rho$ ,  $\omega$  and  $\phi$  mesons propagating inside the nuclear matter. Adopting the same fermi-gas approximation with (1) and taking the vector meson at rest ( $\mathbf{q} = 0$ ), one can generally write the mass-squared shift as

$$\delta m_v^2 \equiv m_v^{*2} - m_v^2 = 4 \int_0^{p_F} \frac{d^3 p}{(2\pi)^3} \frac{M_N}{E(p)} f_{vN}(\mathbf{p}), \quad (2)$$



where  $f_{VN}(\mathbf{p})$  denotes the vector-meson (V) – nucleon (N) forward scattering amplitude in the relativistic normalization, and  $m_V^*(m_V)$  denotes the vector meson mass in nuclear matter (vacuum). Here, we took spin-isospin average for the nucleon states in  $f_{VN}$ . If one can calculate  $f_{VN}(\mathbf{p})$  reasonably well in the range  $0 < p < p_F = 270$  MeV (or  $1709$  MeV  $< \sqrt{s} < 1726$  MeV in terms of the  $V - N$  invariant mass), one can predict the mass shift. Unfortunately, this is a difficult task:  $f_{VN}(\mathbf{p})$  is not a constant in the above range since there are at least two s-channel resonances  $N(1710)$ ,  $N(1720)$  in the above interval and two nearby resonances  $N(1700)$  and  $\Delta(1700)$ . They all couple to the  $\rho - N$  system [7] and give variation of  $f_{VN}(\mathbf{p})$  as a function of  $p$  in principle. From this reason, one should develop other methods to estimate  $\delta m_V^2$  without referring to the detailed form of  $f_{VN}(\mathbf{p})$ . We will briefly review two of such approaches in the following subsections, namely the QCD sum rules and effective theories of hadron.

### A. QCD sum rules

The QCD sum rules (QSR) for vector mesons in nuclear matter were first developed by Hatsuda and Lee [8]. In their approach, one starts with the retarded current correlation function in nuclear matter,

$$\Pi_{\mu\nu}(\omega, \mathbf{q}) = i \int d^4x e^{iqx} \langle \text{R}J_\mu(x) J_\nu(0) \rangle, \quad (3)$$

where  $q^\mu \equiv (\omega, \mathbf{q})$  and  $\text{R}J_\mu(x) J_\nu(0) \equiv \theta(x^0) [J_\mu(x), J_\nu(0)]$  with the source currents  $J_\mu$  defined as  $J_\mu^{\rho, \omega} = \frac{1}{2}(\bar{u}\gamma_\mu u \mp \bar{d}\gamma_\mu d)$  ( $-(+)$  is for the  $\rho^0(\omega)$ -meson) and  $J_\mu^\phi = \bar{s}\gamma_\mu s$ . Although there are two independent invariants in medium (transverse and longitudinal polarization), they coincide in the limit  $\mathbf{q} \rightarrow 0$  and reduce to  $\Pi_{\mu\mu}/(-3\omega^2) \equiv \Pi$ .  $\Pi$  satisfies the following dispersion relation,

$$\text{Re}\Pi(\omega^2) = \frac{1}{\pi} \text{P} \int_0^\infty du^2 \frac{\text{Im}\Pi(u)}{u^2 - \omega^2} + (\text{subtraction}). \quad (4)$$

In QSR, the spectral density  $\text{Im}\Pi$  is modeled with several phenomenological parameters, while  $\text{Re}\Pi$  is calculated using the operator product expansion (OPE). The phenomenological parameters are then extracted by matching the left and right hand side of (4) in the asymptotic region  $\omega^2 \rightarrow -\infty$ . The density dependence in the OPE side is solely determined by the density dependent condensates which are evaluated from low energy theorems or from the parton distribution of the nucleon [8].

In the medium, we have three kinds of structure in the spectral density: the resonance poles, the continuum and the Landau damping contribution. For  $\mathbf{q} \rightarrow 0$ , the last contribution is calculable *exactly* and behaves like a pole at  $\omega^2 = 0$  [8,9]. In total, the hadronic spectral function looks as

$$8\pi \text{Im}\Pi(u > 0^-) = \delta(u^2)\rho_{sc} + F^* \delta(u^2 - m_V^{*2}) + (1 + \frac{\alpha_s}{\pi})\theta(u^2 - S_0^*) \equiv \rho_{had.}(u^2), \quad (5)$$

with  $\rho_{sc} = 2\pi^2 \rho / \sqrt{p_F^2 + M_N^2} \simeq 2\pi^2 \rho / M_N$ .  $m_V^*$ ,  $F^*$  and  $S_0^*$  are the three phenomenological parameters in nuclear matter to be determined by the sum rules.

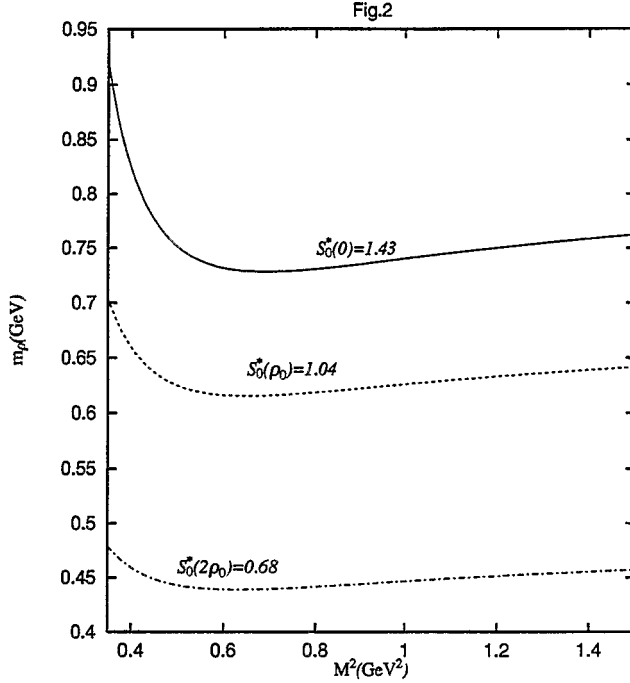


FIG. 2. Borel curve for the  $\rho(\omega)$  meson mass. Solid, dashed and dash-dotted lines correspond to  $\rho/\rho_0 = 0, 1.0$  and  $2.0$  respectively.  $S_0^*(\rho)$  determined by the Borel stability method at each density is also shown in  $\text{GeV}^2$  unit. The Borel window is chosen to be  $0.41\text{GeV}^2 < M^2 < 1.30\text{GeV}^2$ .

Matching the OPE side and the phenomenological side via the dispersion relation in the asymptotic region  $\omega^2 \rightarrow -\infty$ , we can relate the resonance parameters to the density dependent condensates. There are two major procedures for this matching, namely the Borel sum rules (BSR) [10] and the finite energy sum rules (FESR) [11], which can be summarized as

$$\int_0^\infty ds W(s) [\rho_{had.}(s) - \rho_{OPE}(s)] = 0, \quad (6)$$

$$W(s) = s^n \theta(S_0 - s) \quad (\text{FESR}), \quad e^{-s/M^2} \quad (\text{BSR}). \quad (7)$$

Here the spectral function  $\rho_{had.}(s)$  stands for eq.(5).  $\rho_{OPE}(s)$  is a hypothetical imaginary part of  $\Pi$  obtained from OPE.

To make quantitative analyses of spectral parameters, the stability analysis based on the Borel transform is more suitable than FESR. Since the Borel mass  $M$  is a fictitious parameter introduced in the sum rule, the physical quantities should be insensitive to the change of  $M$  within a Borel interval  $M_{\min} < M < M_{\max}$ ; namely the principle of minimum sensitivity (PMS) is used. One can accomplish this insensitivity by choosing  $S_0^*$  suitably at given density. In Fig. 2, the Borel curves for the  $\rho(\omega)$  meson for three different values of baryon density are shown with  $S_0^*$  chosen to make the Borel curve as flat as possible in the interval  $0.41\text{GeV}^2 < M^2 < 1.30\text{GeV}^2$ . The upper (lower) bound of the Borel interval is determined so that the power (continuum) correction after the Borel transform does not exceed 30 % of the lowest order term in OPE.

By making a linear fit of the result, one obtains [8]

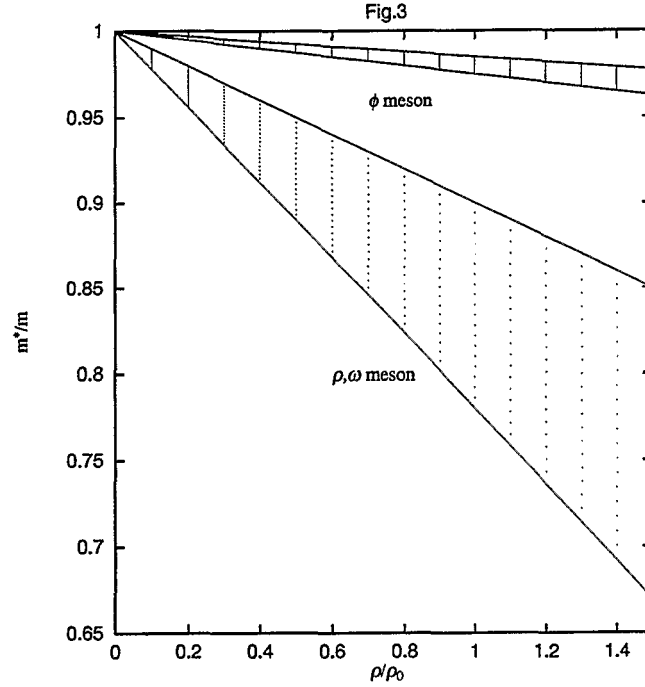


FIG. 3. Masses of  $\rho, \omega$  and  $\phi$  mesons in nuclear matter predicted in the QCD sum rules. The hatched region shows theoretical uncertainty.

$$\frac{m_{\rho, \omega}^*}{m_{\rho, \omega}} = 1 - (0.16 \pm 0.06) \frac{\rho}{\rho_0}, \quad (8)$$

$$\sqrt{\frac{S_0^*}{S_0}} = 1 - (0.15 \pm 0.05) \frac{\rho}{\rho_0}, \quad (9)$$

$$\frac{F^*}{F} = 1 - (0.24 \pm 0.07) \frac{\rho}{\rho_0}, \quad (10)$$

and

$$\frac{m_{\phi}^*}{m_{\phi}} = 1 - (0.15 \pm 0.05) y \frac{\rho}{\rho_0}, \quad (11)$$

where  $y$  is the OZI breaking parameter in QCD defined as  $y = 2\langle \bar{s}s \rangle_N / \langle \bar{u}u + \bar{d}d \rangle_N$  with  $\langle \cdot \rangle_N$  being the nucleon matrix element.  $y$  takes the value 0.1–0.2 [8]. The decrease in eqs. (8,11) is dictated by the density dependent condensates  $\langle \bar{q}q \rangle$ ,  $\langle (\bar{q}q)^2 \rangle$  and  $\langle \bar{q}\gamma_{\mu}D_{\nu}q \rangle$ . The errors in the above formulas are originating from the uncertainties of the density dependence of the these condensates. The contribution of the quark-gluon mixed operator with twist 4, [8] which may possibly weaken the mass shift, is neglected in the above. Shown in Fig.3 is the mass shift given in eqs. (8,11) with possible theoretical uncertainties.

Some sophistications of the QSR analyses by Hatsuda and Lee have been done later by several authors.

(i) Asakawa and Ko have introduced a more realistic spectral function than (5) by taking into account the width of the  $\rho$ -meson and the effect of the collisional broadening due to the  $\pi - N - \Delta - \rho$  dynamics [12]. By doing the similar QSR analysis as above, they found that the negative mass shift persists even in this realistic case. The width of the rho

meson in their calculation decreases as density increases, which implies that the phase space suppression from the  $\rho \rightarrow 2\pi$  process overcomes the collisional broadening at finite density. Further examination of this interplay between the mass shift and the collisional broadening is important in relation to the future experiments. Also, finite temperature generalization of the Asakawa-Ko's calculation should be done.

(ii) Monte Carlo based error analysis was applied to the Borel sum rule by Jin and Leinweber [13] instead of the Borel stability or PMS analysis employed in [8]. They found  $m_{\rho,\omega}^*/m_{\rho,\omega} = 1 - (0.22 \pm 0.08)(\rho/\rho_0)$  and  $m_\phi^*/m_\phi = 1 - (0.01 \pm 0.01)(\rho/\rho_0)$ , which are consistent with eqs. (8,11) within the error bars.

(iii) Koike analysed an *effective* scattering amplitude  $\bar{f}_{VN}$  defined as  $\delta m_V^2 \equiv \bar{f}_{VN} \cdot \rho$  using the QSR in the vacuum [14]. Although his original calculation predicting  $\bar{f}_{VN} > 0$  is in error as was pointed out in ref. [8,13], revised calculation gives a consistent result with eqs. (8,11) within the error bars [15]. Note here that  $\bar{f}_{VN}$  does not have direct relation to the scattering length at zero momentum  $f_{VN}(0)$ .

## B. Effective theories

There have been many attempts so far to calculate the spectral change of the vector mesons using effective theories of QCD. The first attempt by Chin [16] using the quantum hadrodynamics (QHD) shows increasing  $\omega$ -meson mass in medium due to a process analogous to the Compton scattering;

$$\omega + N \rightarrow \omega + N. \quad (12)$$

For the  $\rho$ -meson, similar but more sophisticated calculations taking into account  $\Delta$ -resonance and in-medium pion show a slight increase of the  $\rho$ -meson mass [17]. In these calculations, only the polarization of the Fermi sea (the particle-hole excitations) was considered. Also their predictions are different from the general assertion by Brown and Rho claiming that all the hadron masses except for pion should decrease [18].

On the other hand, Saito, Maruyama and Soutome, and Kurasawa and Suzuki [19] have realized that the mass of the  $\omega$ -meson is affected substantially by the vacuum polarization of the nucleon in medium

$$\omega \rightarrow N^* \bar{N}^* \rightarrow \omega, \quad (13)$$

where  $N^*$  is the nucleon in nuclear matter which has smaller effective mass than that in the vacuum. They show that the vacuum polarization dominates over the Fermi-sea polarization in QHD and leads decreasing vector meson mass. This conclusion was later confirmed by several groups [20] and was generalized for the  $\rho$  and  $\phi$  mesons [21]. Jaminon and Ripka has also reached a similar conclusion by using a model of vector mesons coupled to constituent quarks [22].

Saito and Thomas have examined a rather different but comprehensive model (bag model combined with QHD) and found decreasing vector-meson masses [23];  $m_{\rho,\omega}^*/m_{\rho,\omega} \sim 1 - 0.09(\rho/\rho_0)$ . The spectral shift of the quarks inside the bag induced by the existence of nuclear medium plays a key role in this approach.

Basic idea common in the approaches predicting the decreasing mass may be summarized as follows. In nuclear matter, scalar ( $\sigma$ ) and vector ( $\omega$ ) mean-fields are induced by the nucleon sources. These mean-fields give back-reactions to the nucleon propagation in nuclear matter and modify its self-energy. This is an origin of the effective nucleon mass  $M_N^* < M_N$  in the relativistic models for nuclear matter. The same mean-fields should also affect the propagation of vector mesons in nuclear medium. In QSR, the quark condensates act on the quark propagator as density dependent mean-fields. In QHD, the coupling of the mean-field with the vector mesons are taken into account through the short distant nucleon loop with the effective mass  $M_N^*$ . In the bag-model, the mean fields outside the bag acts on quarks confined in the bag and change their energy spectrum.

Let us show here that one can understand the negative mass shift of the vector mesons in a simple and intuitive way in the context of QHD. More quantitative discussion will be given in the later section. After renormalizing infinities in the vacuum loop, the density-dependent part of the Dirac-sea polarization to the vector-meson propagator is approximately written as

$$D(q) \simeq \frac{1}{Z^{-1}q^2 - m_V^2} = \frac{Z}{q^2 - Zm_V^2}, \quad (14)$$

where  $Z$  being the finite wave-function renormalization constant in medium. The pole position is thus obtained as  $m_V^* = \sqrt{Z}m_V$ . Because of the current conservation, only the wave function part of the propagator is modified in medium. Since the effective mass of the nucleon decreases in medium ( $M_N^*/M_N < 1$ ), physical vector mesons have more probability to be in virtual baryon-anti-baryon pairs compared to that in the vacuum. This means  $Z < 1$ , which leads to  $m_V^*/m_V \equiv Z < 1$  [20,21].

$$M_N^*/M_N < 1 \quad \rightarrow \quad Z < 1 \quad \rightarrow \quad m_V^*/m_V \equiv Z < 1 \quad . \quad (15)$$

#### IV. EXPERIMENTS

How one can detect the spectral change of vector mesons in experiments? One of the promising ideas is to use heavy nuclei and produce vector mesons in  $\gamma - A$  or  $p - A$  reactions. Suppose one could create a vector meson at the center of a heavy nucleus. (It does not matter whether it is created at the nuclear surface or at the center as far as the produced vector mesons run through the nucleus before the hadronic decay). It is easy to see that the number of lepton pairs decaying inside the nucleus  $N_{in}(l^+l^-)$  and that outside the nucleus  $N_{out}(l^+l^-)$  are related as

$$\frac{N_{in}(l^+l^-)}{N_{out}(l^+l^-)} \sim \frac{1 - e^{-\Gamma_{tot}R}}{e^{-\Gamma_{tot}R}}, \quad (16)$$

where  $\Gamma_{tot}$  denotes the total width of vector mesons ( $(1.3\text{fm})^{-1}$ ,  $(23\text{fm})^{-1}$  and  $(45\text{fm})^{-1}$  for  $\rho$ ,  $\omega$  and  $\phi$ , respectively) and  $R$  being the nuclear radius. Eq.(16) shows that even the  $\phi$  meson has considerable fraction of  $N_{in}/N_{out}$  if the target nucleus is big enough.

There exist already some proposals to look for the mass shift of vector mesons in nuclear medium [24]. One is by Shimizu et al. who propose an experiment to create  $\rho$  and  $\omega$  in

heavy nuclei using coherent photon - nucleus reaction and subsequently detect the lepton pairs from  $\rho$  and  $\omega$ . Enyo et al. propose to create  $\phi$  meson in heavy nuclei using the proton-nucleus reaction and to measure kaon pairs as well as the lepton pairs. By doing this, one can study not only the mass shift but also the change of the leptonic vs hadronic branching ratio  $r = \Gamma(\phi \rightarrow e^+e^-)/\Gamma(\phi \rightarrow K^+K^-)$ . Since  $m_\phi$  is very close to  $2m_K$  in the vacuum, any modification of the  $\phi$ -mass or the  $K$ -mass changes the ratio  $r$  substantially as a function of mass number of the target nucleus. Similar kinds of experiments are also planned at GSI.

There are also on-going heavy ion experiments at SPS (CERN) and AGS (BNL) where high density matter is likely to be formed. In particular, CERES/NA45 and HELIOS-3 at CERN reported enhancement of the lepton pairs below the  $\rho$  resonance [25,26], which may not be explained by the conventional sources of lepton pairs. If this phenomena is real, low mass enhancement of the lepton pair spectrum expected by the mass shift of the vector mesons could be a possible explanation [27]. In nuclear collisions at higher energies (RHIC and LHC), hot hadronic matter or possibly the quark-gluon-plasma with low baryon density are expected to be formed. In such cases, double  $\phi$ -peak structure proposed by Asakawa and Ko [28] as well as the spectral change of  $\rho$ ,  $\omega$  and scalar mesons [29] will be a distinct signal of the chiral restoration in QCD.

## V. CONCLUDING REMARKS

The spectral change of the elementary excitations in medium is an exciting new possibility in QCD. By studying such phenomenon, one can learn the structure of the hadrons and the QCD ground state at finite  $(T, \rho)$  simultaneously. Theoretical approaches such as the QCD sum rules and the hadronic effective theories predict that the light vector mesons ( $\rho$ ,  $\omega$  and  $\phi$ ) are sensitive to the partial restoration of chiral symmetry in hot/dense medium. These mesons are good probes experimentally, since they decay into lepton pairs which penetrate the hadronic medium without losing much information. Thus, the lepton pair spectroscopy in QCD will tell us a lot about the detailed structure of the hot/dense matter, which is quite similar to the soft-mode spectroscopy by the photon and neutron scattering experiments in solid state physics.

## ACKNOWLEDGEMENTS

This work was supported by the Grants-in-Aids of the Japanese Ministry of Education, Science and Culture (No. 06102004).

## REFERENCES

- [1] A. Ukawa, in these Proceedings.
- [2] T. Hatsuda and T. Kunihiro, Phys. Rep. **247** (1994) 221.
- [3] P. Gerber and H. Leutwyler, Nucl. Phys. **B321** (1989) 387.

- [4] E. G. Drukarev and E. M. Levin, *Prog. Part. Nucl. Phys.* **A556** (1991) 467;  
T. Hatsuda, H. Hogaasen and M. Prakash, *Phys. Rev. Lett.* **66** (1991) 2851;  
T. D. Cohen, R. J. Furnstahl and D. K. Griegel, *Phys. Rev. Lett.* **67** (1991) 961.
- [5] T. Hatsuda, *Nucl. Phys.* **A544** (1992) 27c.
- [6] G. Q. Li and C. M. Ko, *Phys. Lett.* **B338** (1994) 118.
- [7] Review of Particle Properties, *Phys. Rev.* **D50** (1994) No.3.
- [8] T. Hatsuda and S. H. Lee, *Phys. Rev.* **C46** (1992) R34.  
T. Hatsuda, S. H. Lee and H. Shiomi, *Phys. Rev.* **C52** (1995) 3364 .
- [9] A. L. Bochkarev and M. E. Shaposhnikov, *Nucl. Phys.* **B268** (1986) 220.
- [10] A. Shifman, A. I. Vainshtein and V. I. Zakharov, *Nucl. Phys.* **B147** (1979) 385.
- [11] N. V. Krasnikov, A. A. Pivovarov and N. N. Tavkhelidze, *Z. Phys.* **C19** (1983) 301.
- [12] M. Asakawa and C. M. Ko, *Phys. Rev.* **C48** (1993) 526.
- [13] X. Jin and D. B. Leinweber, *Phys. Rev.* **C52** (1995) 3344.
- [14] Y. Koike, *Phys. Rev.* **C51** (1995) 1488.
- [15] Y. Koike, private communication.
- [16] S. A. Chin, *Ann. Phys.* **108** (1977) 301.
- [17] M. Asakawa, C. M. Ko, P. Levai and X. J. Qiu, *Phys. Rev.* **C46** (1992) R1159.  
M. Herrmann, B. L. Friman and W. Noerenberg, *Nucl. Phys.* **A560** (1993) 411.
- [18] G. E. Brown and M. Rho, *Phys. Rev. Lett.* **66** (1991) 2720.
- [19] K. Saito, T. Maruyama and K. Soutome, *Phys. Rev.* **C40** (1989) 407.  
H. Kurasawa and T. Suzuki, *Prog. Theor. Phys.* **84** (1990) 1030.
- [20] J. C. Caillon and J. Labarsouque, *Phys. Lett.* **B311** (1993) 19;  
H.-C. Jean, J. Piekarewicz and A. G. Williams, *Phys. Rev.* **C49** (1994) 1981.
- [21] H. Shiomi and T. Hatsuda, *Phys. Lett.* **B334** (1994) 281;  
H. Kuwabara and T. Hatsuda, *Prog. Theor. Phys.* **96** (1995) 1163.
- [22] M. Jaminon and G. Ripka, *Nucl. Phys.* **A564** (1993) 505.
- [23] K. Saito and A. W. Thomas, *Phys. Rev.* **C51** (1995) 2757, *ibid.* **C52** (1995) 2789.
- [24] H. Shimizu, private communication.  
H. Enyo, in *Properties and Interactions of Hyperons*, ed. B. Gibson, P. Barnes and K. Nakai (World Scientific, 1994, Singapore); KEK-PS proposal (1994).
- [25] G. Agakichev et al., *Phys. Rev. Lett.* **75** (1995) 1272; CERES Collaboration, J. P. Wurm, *Nucl. Phys.* **A590** (1995) 103c.
- [26] HELIOS-3 Collaboration, M. Maser, *Nucl. Phys.* **A590** (1995) 93c.
- [27] G. Q. Li, C. M. Ko and G. E. Brown, *Phys. Rev. Lett.* **75** (1995) 4007, C. M. Hung and E. V. Shuryak, hep-ph/9608299; J. V. Steele, H. Yamagishi and I. Zahed, hep-ph/9603290.
- [28] M. Asakawa and C. M. Ko, *Phys. Rev.* **C50** (1994) 3064; *Nucl. Phys.* **A572** (1994) 732.
- [29] R. D. Pisarski, *Phys. Lett.* **110B** (1982) 155; *Phys. Lett. Phys. Rev.* **D52** (1995) 3773.  
T. Hatsuda and T. Kunihiro, *Phys. Rev. Lett.* **55** (1985) 158; T. Hatsuda, Y. Koike and S.H. Lee, *Nucl. Phys.* **B394** (1993) 221.

# On the Physics of a Cool Pion Gas <sup>†</sup>

Robert D. Pisarski and Michel Tytgat\*  
*Physics Department, Brookhaven National Laboratory,  
PO Box 5000, Upton, NY 11973-5000, USA*

## Abstract

At finite temperature, the Nambu-Goldstone bosons of a spontaneously broken chiral symmetry travel at a velocity  $v < 1$ . This effect first appears at order  $\sim T^4$  in an expansion about low temperature, and can be related to the appearance of two distinct pion decay constants in a thermal bath. We discuss some consequences on the thermodynamics of a gas of massless pions.

## I. INTRODUCTION

In these proceedings, we extend some previous work of ours [1]. The starting point is very simple. In the vacuum one invokes Lorentz invariance to define the pion decay constant,  $f_\pi \sim 93$  MeV, by

$$\langle 0 | A_\mu^a | \pi^b(P) \rangle = i f_\pi \delta^{ab} P_\mu, \quad (1)$$

where  $A_a^\mu$  is the axial-vector current, and the pion has euclidean momentum  $P^\mu = (p^0, \vec{p})$ . At finite temperature, Lorentz invariance is lost and they are *a priori* two distinct pion “decay constants”: the temporal component has one,

$$\langle 0 | A^{0a} | \pi^b(P) \rangle_T = i f_\pi^t \delta^{ab} p^0, \quad (2)$$

and, assuming O(3) invariance, the spatial part of the current has another,

$$\langle 0 | A^{ia} | \pi^b(P) \rangle_T = i f_\pi^s \delta^{ab} p^i. \quad (3)$$

This is familiar from nonrelativistic systems, such as discussed by Leutwyler [2]; in a similar context, this has been recognized by Kirchbach and Riska [3].

As in the vacuum, the pion mass shell is defined using current conservation,

$$\partial^\mu \langle 0 | A^{\mu a} | \pi^b \rangle = 0 \longrightarrow f_\pi^t \omega^2 = f_\pi^s p^2. \quad (4)$$

---

<sup>†</sup>Talk given by M. Tytgat at the “RHIC Summer Studies ’96”, Brookhaven National Laboratory, New York, USA

\*mtytgat@wind.phy.bnl.gov



Then, quite trivially,  $f_\pi^t \neq f_\pi^s$  implies the velocity  $v$ <sup>3</sup>

$$v^2 = \text{Re}(f_\pi^s/f_\pi^t) < 1. \quad (5)$$

This, again, is familiar from other contexts, like the propagation of light in a medium –  $v < 1$  corresponds to an index of refraction  $n > 1$ . But dealing with Nambu-Goldstone bosons has some non-trivial consequences. For instance, the  $f_\pi$ 's develop an imaginary part at finite temperature. From (4) one can conclude that the damping rate of massless pions vanishes at zero momentum [1], an expression of the Goldstone theorem.<sup>4</sup>

It is easy to extend these considerations to include explicit symmetry breaking [1]. For soft pions,  $p \ll f_\pi$ , at low temperature,  $T \ll f_\pi$  – christened *cool pions* in [1] – the dispersion relation is of the form

$$\omega^2 = v^2 p^2 + m^2 \quad (6)$$

If  $v \neq 1$ , there is both a dynamic (position of the pole in the complex  $\omega$  plane, at  $p = 0$ ) and a static mass (position of the pole in the complex  $p$  plane, at  $\omega = 0$ ), the two being related by

$$m_{dyn} = v \cdot m_{stat} \leq m_{stat} \quad (7)$$

Incidentally, one can define two Gell-Mann - Oakes - Renner relations:

$$(\text{Re}f_\pi^t)^2 m_{dyn}^2 = 2m_q \langle \bar{q}q \rangle_T \quad (8)$$

or

$$\text{Re}f_\pi^t \text{Re}f_\pi^s m_{stat}^2 = 2m_q \langle \bar{q}q \rangle_T \quad (9)$$

A pion dispersion relation like (6) has been particularly advocated by Shuryak [9] (see also Gale and Kapusta [10]), following a different line of thought. Note that  $v < 1$  implies a *flattening* of the dispersion relation at finite temperature. Experimentally such an effect might produce an enhancement of dileptons from  $\pi\pi$  annihilations [10].

## II. QUANTITATIVE RESULTS

To leading order in a low temperature expansion  $\sim T^2/f_\pi^2$ , and in the chiral limit  $m_\pi = 0$ ,

$$f_\pi(T) = f_\pi(1 - T^2/12f_\pi^2) \quad (10)$$

This result was first obtained, in a different context, by Binetruy and Gaillard [4] and subsequently derived by Gasser and Leutwyler [5] using chiral perturbation theory ( $\chi$ PT). Here, (10) implies that  $f_\pi^t = f_\pi^s$  to leading order. This is actually a consequence of chiral symmetry<sup>5</sup>, as made particularly clear by the derivation of Dey, Eletsky and Ioffe [6]. Using

---

<sup>3</sup>That  $v \leq 1$  is required by causality. It is possible that in some background  $v > 1$ , but this is not what our work is about.

<sup>4</sup>In a nonlinear  $\sigma$  model,  $\gamma \sim pT^4/f_\pi^4$ .

<sup>5</sup>This has been checked recently by Bochkarev and Kapusta [7] by comparing the predictions of the  $O(N)$  linear and non-linear (using different parametrizations)  $\sigma$  models.

Current Algebra and PCAC, they showed that

$$\langle A_\mu^a A_\nu^b \rangle_T \sim (1 - T^2/6f_\pi^2) \langle A_\mu^a A_\nu^b \rangle + T^2/6f_\pi^2 \langle V_\mu^a V_\nu^b \rangle. \quad (11)$$

From pion pole dominance, one then extracts (10) from (11). Besides the mixing with the vector-vector correlator, what is remarkable is that Lorentz invariance is manifest – hence that  $v = 1$  – to order  $T^2/f_\pi^2$ .

Thus, the effect discussed here can only appear at next-to-leading order  $\sim T^4$ . In  $\chi$ PT this implies computing to two-loop order. For the sake of the argument, in [1] we instead made use of a weakly coupled linear  $\sigma$  model, *i.e.* with a *light*  $\sigma$  particle:  $m_\sigma^2 = 2\lambda\sigma^2$  and  $f_\pi \equiv \sigma$ , so that  $O(T^4/f_\pi^2 m_\sigma^2)$  corrections dominate over the  $O(T^4/f_\pi^4)$  ones. Expanding in powers of  $T/m_\sigma$ , a one-loop calculation then suffices to verify (5). The result for the  $f_\pi$ 's is

$$f_\pi^t \sim (1 - t_1 + 3t_2 + it_3)f_\pi \quad (12)$$

$$f_\pi^s \sim (1 - t_1 - 5t_2 - it_3)f_\pi \quad (13)$$

with

$$t_1 = T^2/12f_\pi^2, \quad t_2 = \frac{\pi^2 T^4}{45f_\pi^2 m_\sigma^2}, \quad t_3 = \frac{m_\sigma^4}{32\pi f_\pi^2 \omega^2} \exp(-m_\sigma^2/4\omega T) \quad (14)$$

so that

$$v^2 \sim 1 - 8t_2 \quad (15)$$

which agrees with the direct calculation of the dispersion relation, as first carried out by Itoyama and Mueller [8].

There is no calculation of  $f_\pi$  to next-to-leading order in  $\chi$ PT, but that  $v < 1$  in the chiral limit is implicit in [11] where Gerber and Leutwyler computed, among other things, the three-loop corrections to the energy density  $u$  of a massless pion gas:

$$u = \frac{1}{10}\pi^2 T^4 \left[ 1 + \frac{T^4}{108f_\pi^4} \left( 7 \ln \frac{\Lambda_p}{T} - 1 \right) + O(T^6) \right] \quad (16)$$

Apart from the pion decay constant, the energy density depends on another scale in the chiral limit,  $\Lambda_p \sim 275$  MeV [11]. The first term in (16) is the energy density of a non-interacting massless pion gas,

$$u_0 = 3 \int \frac{d^3 p}{(2\pi)^3} \omega(p) n_B(p) = \frac{1}{10}\pi^2 T^4 \quad (17)$$

with  $\omega(p)^2 = p^2$ . Substituting in (17) a modified pion dispersion relation,

$$\omega^2 = v^2 p^2, \quad (18)$$

can mimic the effect of the pion interactions. The energy density of a gas of free quasi-pions,

$$u = \frac{u_0}{v^3}, \quad (19)$$

reproduces (16), provided the following estimate of the quasi-pion mean velocity holds:

$$v \sim 1 - \frac{1}{3} \frac{T^4}{108 f_\pi^4} \left( 7 \ln \frac{\Lambda_p}{T} - 1 \right) \quad (20)$$

In agreement with our previous argument,  $v = 1$  to  $O(T^2)$ . It is equivalent<sup>6</sup> to recognize that there is no  $T^6$  correction to the energy density (16). Also,  $v < 1$  for  $T < \sim 250$  MeV, so that  $u > u_0$ .

What about massive pions ? The most extensive work on the propagation of thermal pions is due to Schenk [12,13]. Apparently, he found no evidence of (6). However, in fig. 5 of ref. [12] and fig. 7 of ref. [13], Schenk plots  $R(p)$ , the ratio of the quasiparticle energy, to the pion energy in free space, as a function of momentum. To two loop order, as  $p$  increases from zero there is a *dip* in  $R(p)$ : it first decreases, and then increases, approaching one from below. This is only possible if the quasiparticle energy  $\omega(p)^2 = v^2(p)p^2 + m_\pi^2(T)$ , with  $v(0) < 1$ . A. Schenk, private communication, estimates that  $v(0) \sim .87$  at  $T \sim 150$  MeV.

### III. OUTLOOK

We conclude with two remarks. The first concerns spin waves in ferromagnets (magnons) and was brought to our attention by R. Brout. The other is on the behavior of  $f_\pi$  near the critical temperature.

In two landmark papers, Dyson [14], improving on earlier ideas of Bloch [15], developed a formalism to describe the motion of magnons, and computed the low temperature corrections to the magnetization. Taking magnon interactions into account, he found

$$M(T)/M(0) \sim 1 - a_0 T^{3/2} - a_1 T^{5/2} - a_2 T^{7/2} - a_3 T^4 + O(T^{9/2}) \quad (21)$$

Given the magnon dispersion relation

$$\omega \sim cp^2 + O(p^4), \quad (22)$$

the  $T^{3/2}$  term is the famous prediction of the simple Bloch theory, in which magnons are treated as non-interacting bosonic particles. The  $a_1$  and  $a_2$  terms are lattice effects (the  $O(p^4)$  terms in (22)), and do not concern us. Only the  $a_3$  term  $\sim T^4$  is due to magnon interactions. What is striking is that there is no  $T^3$  term in (21); this is reminiscent of the absence of  $T^6$  term in (16). In the quasi-particle picture, this means that the parameter  $c$  in (22), is not renormalized to leading order ( $T^{3/2}$  in the present case) but only to next-to-leading order, or  $\sim T^{5/2}$ . Also, in both cases – magnons and massless pions – the correction to the “velocity” is proportional to the energy density.

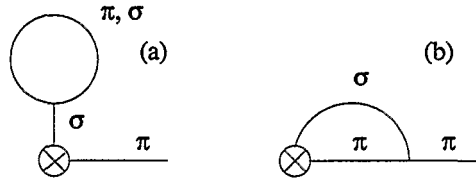
These are precisely the kind of similarities that an effective Lagrangian approach, like  $\chi$ PT, to the dynamical properties of spin waves, both in ferromagnets and antiferromagnets, could shed light on [2,16].

---

<sup>6</sup>This is the argument that lead Shuryak to (6). [9]

Now about  $f_\pi$  near  $T_c$ ? In a recent paper, Jeon and Kapusta [17], computed  $f_\pi$  to  $O(T^2)$ , both at low  $T$  and near the critical temperature  $T_c$ , in an  $O(N)$  non-linear  $\sigma$  model, to next-to-leading order in a large  $N$  expansion. Here, we give a sketch of a linear  $\sigma$  model derivation of their results<sup>7</sup>.

The relevant diagrams are shown below. At low  $T \ll m_\sigma$ ,  $\sigma$  mode propagation is Boltz-



mann suppressed in diagrams (a) and (b). The latter shrinks to a tadpole and both diagrams contribute to order  $\sim T^2$ . The result, taking into account wave function renormalization, is

$$f_\pi(T) = \sigma(1 - T^2/12\sigma^2), \quad (23)$$

to be compared with the low  $T$  dependence of the order parameter

$$\sigma(T) = \sigma(1 - T^2/8\sigma^2) \quad (24)$$

Near  $T_c$ , the  $\sigma$  particle is light,  $m_\sigma \ll T$ , and, in the *high*  $T$  expansion, (b) does not contribute nor is there wave function renormalization to  $O(T^2)$ : hence, only the tadpole (a) contributes and, manifestly,

$$f_\pi(T) = \sigma(T) = \sigma(1 - T^2/4\sigma^2) \quad (25)$$

for  $T$  near and below  $T_c$ . This agrees with Jeon and Kapusta [17]. That  $f_\pi$  and  $\sigma$  vanish at the same temperature is hardly surprising. An interesting question is whether the critical exponents of  $f_\pi$  and  $\sigma$  are the same also in the critical regime, *i.e.* beyond the mean-field result (25).

## REFERENCES

- [1] R. D. Pisarski and M. Tytgat, *Phys. Rev. D* **54**, 2989 (1996), hep-ph/9604404; see also R.D. Pisarski and M. Tytgat, proceedings of the 2nd Workshop on Continuous Advances in QCD '96, Minneapolis, hep-ph/9606459
- [2] H. Leutwyler, *Phys. Rev. D* **49**, 3033 (1994)
- [3] M. Kirchbach and D. O. Riska, *Nucl. Phys. A* **578**, 511 (1994).
- [4] P. Binetruy and M. K. Gaillard, *Phys. Rev. D* **32**, 931 (1985)
- [5] J. Gasser and H. Leutwyler, *Phys. Lett. B* **184**, 83 (1987)
- [6] M. Dey, V. L. Eletsky, and B. L. Ioffe, *Phys. Lett. B* **252**, 620 (1990)

---

<sup>7</sup>The Lagrangian can be found in [1].

- [7] A. Bochkarev and J. Kapusta, *Phys. Rev. D* **54**, 4066 (1996)
- [8] H. Itoyama and A.H. Mueller, *Nucl. Phys. B* **218**, 349 (1983)
- [9] E.V. Shuryak, *Phys. Rev. D* **42**, 1764 (1990)
- [10] C. Gale and J. Kapusta, *Phys. Rev. C* **35**, 2107 (1987)
- [11] P. Gerber and H. Leutwyler, *Nucl. Phys. B* **321**, 387 (1989)
- [12] A. Schenk, *Nucl. Phys. B* **363**, 97 (1991)
- [13] A. Schenk, *Phys. Rev. D* **47**, 5138 (1993)
- [14] F.J. Dyson, *Phys. Rev.* **102**, 1217 (1956); F.J. Dyson, *ibid* **130**, 1230 (1956)
- [15] F. Bloch, *Z. Physik* **61**, 206 (1930)
- [16] C. P. Hofmann, Bern University preprint BUTP-95/40, 1995.
- [17] S. Jeon and J. Kapusta, Univ. of Minnesota preprint NUC-MINN-96/3-T, 1996, hep-ph/9602400

# New Mesons in the Chirally Symmetric Plasma

H. Arthur Weldon

*Department of Physics, West Virginia University, Morgantown, WV 26506-6315*

## Abstract

A nonperturbative proof is given that the chirally-invariant quark propagator contains both particle and hole singularities with different dispersion relations. Mesons made of a quark and a hole will produce dilepton pairs at masses characteristic of the plasma and with a distinct energy dependence.

## I. INTRODUCTION

The central purpose of the experimental program at RHIC is to produce a quark-gluon plasma. Despite a great deal of theoretical effort there is no clear experimental signature of the quark-gluon plasma that will distinguish it from the very complicated hadron phase. The Theory Workshop on Relativistic Heavy Ion Collisions is intended both to refine previous ideas and to initiate discussion of new possibilities. It is in the latter spirit that this paper proposes investigation of a new experimental signal not previously considered. The present analysis of this signal still leaves unanswered questions that require further investigation by other theorists using other techniques.

In the QGP at temperature  $T$ , a typical state  $|\Phi\rangle$  will have almost all the quark and antiquark modes with momentum less than  $T$  occupied and considerably fewer modes occupied that have momentum larger than  $T$ . If a quark or antiquark is added to this background the result is  $b^\dagger|\Phi\rangle$  or  $d^\dagger|\Phi\rangle$ . The new possibility is that removal of a quark gives a state  $b|\Phi\rangle$  and the norm of this quark vacancy state is not small if the momentum is less than  $T$ . Similarly an antiquark vacancy is  $d|\Phi\rangle$ . Chiral symmetry plays an essential role in this argument because the hole states are only important if  $b|\Phi\rangle$  has an energy higher than  $|\Phi\rangle$  and this is only possible when the constituent quark mass is smaller than  $T$ . Thus approximate chiral symmetry is essential. This has two consequences: (1) Only  $u$  and  $d$  quarks are candidates and (2) When chiral symmetry is badly broken, i.e. the hadron phase, there are no hole states.

The proof of hole states in Sec II is entirely non-perturbative. The end of Sec II contains references to perturbative results. Sec III focusses on experimental consequences of the hole states, the most important of which is the annihilation of a quark and hole into a virtual photon that subsequently converts to a lepton pair. If this quark and hole are bound into a meson, there will be a resonance in the dilepton invariant mass spectrum with new features.

## II. QUARK HOLES IN THE EXACT THERMAL PROPAGATOR

### A. Singularities of the exact propagator

It is remarkable that certain simple properties of the exact thermal quark propagator guarantee that the existence of low momentum hole states ( $k < T$ ) in the chirally symmetric plasma. The inverse of the exact time-ordered thermal propagator must be of the form

$$[S(\omega, \vec{k})]^{-1} = \gamma_0 A(\omega, k) - \vec{\gamma} \cdot \hat{k} B(\omega, k) \quad (2.1)$$

because of chiral invariance. The propagator itself is

$$S(\omega, \vec{k}) = \frac{1}{2} \frac{\gamma_0 - \vec{\gamma} \cdot \hat{k}}{A - B} + \frac{1}{2} \frac{\gamma_0 + \vec{\gamma} \cdot \hat{k}}{A + B}. \quad (2.2)$$

At  $k = 0$  the propagator cannot depend on the direction of  $\hat{k}$ . Therefore  $B(\omega, 0) = 0$  and consequently  $S(\omega, 0) = \gamma_0/A(\omega, 0)$ . Now comes the one dynamical input, namely that at  $k = 0$  there is a pole in the propagator at the thermal mass of the quark. Lattice calculations of temporal quark propagators have measured this thermal mass [1]. The thermal mass must have a negative imaginary part because of damping. By dimensional analysis, both the real and imaginary parts are proportional to temperature. Denote this complex mass by  $m_T$ . Then at  $k = 0$ ,  $A(\omega, 0) = (\omega - m_T)a(\omega)$  where  $a(\omega)$  does not have a pole at  $\omega = m_T$ . At non-zero momentum  $A$  has the structure  $A(\omega, k) = (\omega - m_T)a(\omega) + A_1(\omega, k)$  where  $A_1$  is defined to vanish at  $k = 0$ . The first denominator in (2.2) is  $A - B = (\omega - m_T)a(\omega) + A_1(\omega, k) - B(\omega, k)$ . Since  $A_1$  and  $B$  both vanish at  $k = 0$ , they are both small when  $k$  is chosen sufficiently small. Therefore  $A - B$  will vanish at  $\omega = E_p$ , where  $E_p$  is equal to  $m_T$  plus a small,  $k$ -dependent correction:

$$E_p \approx m_T + [-A_1(m_T, k) + B(m_T, k)]/a(m_T) + \dots \quad (k \text{ small}) \quad (2.3)$$

For small  $k$  the other denominator  $A + B$  vanishes at  $\omega = E_h$  where  $E_h$  is equal to  $m_T$  plus a different small  $k$  correction because  $B$  occurs with opposite sign:

$$E_h \approx m_T + [-A_1(m_T, k) - B(m_T, k)]/a(m_T) + \dots \quad (k \text{ small}) \quad (2.4)$$

The first energy will be called the particle energy and the second the hole energy. The justification for these names will come in the next section. It is easy to see that the inclusion of a bare quark mass in the propagator spoils these arguments.

Knowing that  $A - B$  vanishes at  $\omega = E_p$  and  $A + B$  vanishes at  $\omega = E_h$ , one can show that PCT invariance requires  $A - B$  to also vanish at  $\omega = -E_h$  and  $A + B$  to also vanish at  $\omega = -E_p$ . The exact propagator therefore has four singularities and may be written

$$S(\omega, \vec{k}) = \frac{1}{2}(\gamma_0 - \vec{\gamma} \cdot \hat{k}) \left[ \frac{Z_p(\omega, k)}{\omega - E_p} + \frac{Z_h(-\omega, k)}{\omega + E_h} \right] + \frac{1}{2}(\gamma_0 + \vec{\gamma} \cdot \hat{k}) \left[ \frac{Z_p(-\omega, k)}{\omega + E_p} + \frac{Z_h(\omega, k)}{\omega - E_h} \right], \quad (2.5)$$

where  $\text{Im } E_p < 0$  and  $\text{Im } E_h < 0$ . It is difficult to deduce much about the numerator functions  $Z_p$  and  $Z_h$ . They are very complicated functions of  $\omega$  and contain all the branch cuts and any other singularities of the exact propagator. The  $\pm\omega$  in the arguments of these functions are determined by PCT. From the previous argument we know that at zero momentum the residues of the two kinds of poles are equal:  $Z_p(m_T, 0) = Z_h(m_T, 0)$ .

## B. Operator meaning of the hole singularities

The existence of a pole at a  $m_T$  in the zero-momentum propagator led to the distinct poles at  $\pm E_p$  and  $\pm E_h$  in (2.2). The next task is to figure out what these poles mean in terms of quark creation and destruction operators. At time  $t=0$  the exact field operator for massless quarks in a finite volume  $V$  can be expanded as

$$\psi(0, \vec{x}) = \frac{1}{\sqrt{V}} \sum_{\vec{k}, s} (u_\alpha(\vec{k}, s) b_{\vec{k}, s} e^{i\vec{k}\cdot\vec{x}} + v_\alpha(\vec{k}, s) d_{\vec{k}, s}^\dagger e^{-i\vec{k}\cdot\vec{x}}). \quad (2.6)$$

The field operator at any other time can be expressed as  $\psi(t, \vec{x}) = \exp(iHt)\psi(0, \vec{x})\exp(-iHt)$ . The exact time-ordered thermal propagator may be written in terms of two resolvents:

$$S(\omega, \vec{k}) = \frac{1}{2}(\gamma_0 - \vec{\gamma} \cdot \hat{k}) [R_p(\omega, k) - R_h(-\omega, k)] + \frac{1}{2}(\gamma_0 + \vec{\gamma} \cdot \hat{k}) (-R_p(-\omega, k) + R_h(\omega, k)) \quad (2.7)$$

$$R_p(\omega, k) \equiv \langle b_{\vec{k}} \frac{1}{\omega + i\epsilon - \hat{H}} b_{\vec{k}}^\dagger \rangle \quad R_h(\omega, k) \equiv \langle b_{-\vec{k}}^\dagger \frac{1}{\omega + i\epsilon - \hat{H}} b_{-\vec{k}} \rangle, \quad (2.8)$$

where PCT was used to express antiquark resolvents in terms of quark resolvents. For compactness I have used the thermo field dynamics notation  $\hat{H} = H - \hat{H}$  and the brackets denote the expectation value in the TFD ground state [2]. Both resolvents (2.8) are analytic for  $\text{Im } \omega > 0$  and have branch cuts along the real  $\omega$  axis.

The pole in (2.5) at  $\omega = E_p$  is in the lower half  $\omega$  plane and has a characteristic spinor structure. Comparison with (2.7) shows that it must come from  $R_p(\omega, k)$  since  $R_h(-\omega)$  is analytic for  $\text{Im } \omega < 0$ . To understand what this means, recall that each state  $|\Phi\rangle$  in the thermal average is an energy eigenstate. The existence of the pole at  $E_p$  means roughly that the state  $b^\dagger|\Phi\rangle$  has an energy that is higher by  $E_p$ . (More precisely,  $b^\dagger|\Phi\rangle$  is not an energy eigenstate but it has a non-zero overlap with an energy eigenstate that is higher by  $E_p$ .)

The new feature in (2.5) is the pole at  $\omega = E_h$  in the lower-half  $\omega$  plane with the spinor structure  $\gamma_0 + \vec{\gamma} \cdot \hat{k}$ . Comparison with (2.7) shows that it can only come from  $R_h(\omega, k)$  since  $R_p(-\omega)$  is analytic for  $\text{Im } \omega < 0$ . Therefore the state  $b|\Phi\rangle$  with one fewer particle than  $\Phi$  nevertheless has an energy that is higher by  $E_h$ . This state is called a quark hole or quark vacancy.

The residue of the poles requires evaluating the numerator functions  $Z(\omega, k)$  in (2.5) at the energy of the pole. At  $k = 0$  the holes have the same residue as the particles:  $Z_h(m_T, 0) = Z_p(m_T, 0)$ . However at  $k > T$  the residue of the hole  $Z_h(E_h, k)$  becomes very small. This means that high momentum hole states decouple from the field operator  $\psi(x)$ . It does not mean that high momentum hole states disappear, only that  $b|\Phi\rangle$  becomes a poor description. Since gluons couple to color currents  $\bar{\psi}\lambda^a\gamma^\mu\psi$  and photons couple to the electromagnetic current  $\bar{\psi}\gamma^\mu\psi$ , hole states with high momentum propagate have very small coupling to gluons and photons.



### C. Perturbative results on holes

Nothing in the argument presented above is perturbative. However the observation that the thermal quark propagator contains two kinds of poles, one for quarks and one for holes, did arise in one-loop perturbative calculations [3–5]. The quark and hole states have been constructed to one-loop order in [6]. The dependence of the spectrum upon chiral symmetry has been studied in one-loop order [7,8]. The quark and hole states have been used in calculations of dilepton production [9] and of Higgs damping rates [10].

## III. NEW MESONS USING HOLE STATES

### A. Binding of quarks and holes

It is easy to envision how new mesons can arise in the chirally symmetric phase though it is difficult to prove their existence. If  $|\Phi\rangle$  is a color singlet state in the thermal ensemble then  $b_k^\dagger|\Phi\rangle$  is a color triplet with an energy higher by  $E_p(k)$  after all the interactions between the  $b^\dagger$  and the plasma are included. Similarly  $b_{k'}|\Phi\rangle$  is a color antitriplet with an energy higher by  $E_h(k')$  when all its interactions are included. A color singlet state  $b_k^\dagger b_{k'}|\Phi\rangle$  should have an energy of approximately  $E_p(k) + E_h(k')$  minus the color binding energy.

In the chirally symmetric phase the color force is not confining but it is still attractive in color singlet channels. There are two different contributions to this binding: gluon exchange and instantons. The first may be thought of in terms of a Bethe-Salpeter equation with a kernel for the exchanged gluons. Although the numerators of the quark propagator (2.5) have no mass term, it is the denominators that control the kinematics. This leads to differential operators that are approximately Klein-Gordon  $\partial^2 + m_T^2$ , with  $m_T \approx 150$  MeV, acting on the coordinates of the Bethe-Salpeter wave function. This is analogous to the positronium problem and even non-relativistic analysis may be useful.

A second source of color binding comes from non-trivial topologies, specifically the random instanton liquid advocated by Shuryak [11]. Here because of chiral symmetry the field operator satisfies the equation  $\gamma_\mu D^\mu \psi = 0$  with no chiral-symmetry breaking mass term. When  $A^\mu$  is an instanton configuration the classical solutions of this produce a strong attraction in mesonic channels in which the fermions have the opposite chirality, e.g. attractive in the scalar channel but not in the vector channel. The lattice calculations of the Shuryak group confirm this picture. Note that although the thermal mass of the quarks is present, it is irrelevant for the instanton attraction.

### B. Quantum numbers of $QQ_h$ mesons

To determine the possible quantum numbers of the new mesons it is useful to examine the bilinear operators  $J_\Gamma^a(x) = \bar{\psi}_i(x) t_{ij}^a \Gamma \psi_j(x)$ , where  $\Gamma$  is one of the sixteen Dirac matrices and  $t^a$  are one of the four  $2 \times 2$  matrices for isospin 0 or 1. The choice of  $\Gamma$  determines the value of  $J$  for the operator and its behavior under parity and charge conjugation. To determine the quark operator content of each  $J_\Gamma^a$ , we again use the expansion (2.6) of the

exact field operator. Integrating  $J_{\Gamma}^a(0, \vec{x})$  over three dimensional space then gives an operator describing a meson at rest.

For example, if  $\Gamma = i\gamma_5$  then the result is an operator for pseudoscalar  $\pi^a$  and  $\sigma$  mesons:

$$\int d^3x \bar{\psi}_i(\vec{x}) t_{ij}^a i\gamma_5 \psi_j(\vec{x}) = 2i \sum_{\vec{k}, s} [b_i^\dagger(\vec{k}, s) t_{ij}^a d_j^\dagger(-\vec{k}, s) - d_i(-\vec{k}, s) t_{ij}^a b_j(\vec{k}, s)]. \quad (3.1)$$

This operator has the expected structure:  $b^\dagger d^\dagger$  for the creation of a quark-antiquark pair plus its PCT conjugate  $db$ . The pair has no orbital angular momentum,  $L=0$ , and no spin,  $S=0$ . Since the total angular momentum is  $J=0$ , it correctly describes the  $\pi$  and  $\eta$  mesons as  $^1S_0$  state of quark and antiquark.

As an example of a meson operator that gives a quark paired with a hole, let  $\Gamma = \gamma_0$ . Then

$$\int d^3x \bar{\psi}_i(\vec{x}) t_{ij}^a \gamma_0 \psi_j(\vec{x}) = 2 \sum_{\vec{k}, s} [b_i^\dagger(\vec{k}, s) t_{ij}^a b_j(\vec{k}, s) + d_i(\vec{k}, s) t_{ij}^a d_j^\dagger(\vec{k}, s)]. \quad (3.2)$$

If this operator acts on a typical state  $|\Phi\rangle$  containing many quarks and antiquarks it can create a new kind of meson at rest,  $b^\dagger(\vec{k})b(\vec{k})|\Phi\rangle$  (or the PCT conjugate) with an energy approximately  $E_p + E_h$  minus the binding energy.

The chart below tabulates the quantum numbers of the possible mesons for all 16 Dirac matrices. The choice of  $\Gamma$  determines the value of  $J^{PC}$  for that operator. For the last four operators in the chart,  $J_{\Gamma}^a$  contains both ordinary meson combinations  $b^\dagger d^\dagger$  and new combinations  $b^\dagger b$ .

$\Gamma$	$J^{PC}$	$Q\bar{Q}$ MESONS	$QQ_h$ MESONS
$i\gamma_5$	$0^{-+}$	$^1S_0 : \pi$ and $\eta$	--
1	$0^{++}$	$^3P_0 : a_0$ and $\sigma$	--
$\gamma_0$	$0^{+-}$	--	$^1S_0 : I = 1, 0$
$\gamma_5\gamma_0$	$0^{-+}$	--	$^3P_0 : I = 1, 0$
$\vec{\gamma}$	$1^{--}$	$^3S_1 : \rho$ and $\omega$	$^1P_1 : I = 1, 0$
$\gamma_5\vec{\gamma}$	$1^{++}$	$^3P_1 : a_1$ and $f_1$	$^3D_1 : I = 1, 0$
$\gamma_5\gamma_0\vec{\gamma}$	$1^{+-}$	$^1P_1 : b_1$ and $h_1$	$^3S_1 : I = 1, 0$
$\gamma_0\vec{\gamma}$	$1^{--}$	$^3D_1 : \rho'$ and $\omega'$	$^3P_1 : I = 1, 0$

The lightest  $Q\bar{Q}$  mesons are at the top of the chart; the heaviest at the bottom. Isotriplets are listed before isosinglets. The arrows in the chart indicate the opposite parity states that are degenerate in mass because of  $SU(2)_A$  symmetry. The  $SU(2)_A$  multiplets have various dimensions:  $\pi + \sigma$  is four dimensional;  $\rho + a_1$  is six dimensional;  $\omega$  is a chiral singlet. The  $Q\bar{Q}$  mesons automatically have  $P = (-1)^{L+1}$  and  $C = (-1)^{L+S}$ . The  $QQ_h$  mesons in the second column have  $P = (-1)^L$  but  $C$  is not determined by the values of  $L$  and  $S$ .

### C. Decays and experimental signals of $QQ_h$ mesons

In the chirally invariant phase not all the  $Q\bar{Q}$  and  $QQ_h$  mesons will be bound. The combinations that are bound into isosinglets have a Zweig suppressed decay into two or more gluons depending upon  $J^{PC}$ . Their decay into photons might be detectable. The isotriplets cannot decay into gluons but they could break up by collisions with free quarks in the plasma. Most importantly, the holes can only exist in the chirally invariant phase. Thus in a RHIC collision they can exist for a maximum of 5 or 10 fm/c, corresponding to a minimum width of 20 MeV to 40 MeV.

In the random instanton liquid model [11] the combinations that bind are those whose constituents have opposite chirality, viz  $\Gamma = 1, i\gamma_5, \gamma_5\gamma_0\vec{\gamma}, \gamma_0\vec{\gamma}$ . The last two of these would give  $QQ_h$  vector mesons with  $J^{PC} = 1^{+-}$  and  $1^{--}$ . The latter would produce a characteristic dilepton pair signal at its mass. It seems quite unlikely that this thermal meson mass would coincide with that of any known sources of dileptons.

The calculation of meson binding and of decay depends crucially on the residue function  $Z_h(E_h, k)$ . As mentioned earlier it is the same as the quark residue  $k = 0$  but at  $k > T$  it is negligible. This complication helps distinguish the  $QQ_h$  dilepton signal from background. All dilepton rates fall exponentially like  $\exp(-E/T)$  where  $E$  is the energy of the lepton pair. For normal sources such as  $\rho$  and  $\omega$ , the prefactor of this exponential is almost independent of  $E$ . For dileptons produced by  $QQ_h$  mesons the prefactor will fall rapidly with the dilepton energy  $E$  and be negligible at  $E \sim T$ . Thus in a plot of dilepton invariant mass that includes only low energy pairs such as  $E < 50$  MeV or  $E < 100$  MeV, the  $QQ_h$  signal is most likely to stand out.

### ACKNOWLEDGMENTS

It is a pleasure to thank Sid Kahana and the entire BNL theory group for organizing and hosting a very stimulating workshop. This work was supported in part by National Science Foundation grants PHY-9213734 and PHY-9630149.

### REFERENCES

- [1] G. Boyd, S. Gupta, and F. Karsch, Nucl. Phys. **B 385**, 481 (1992).
- [2] N.P. Landsman and Ch. G. van Weert, Phys. Rep. **145**, 141 (1987).
- [3] V.V. Klimov, Sov. J. Nucl. Phys. **33**, 934 (1981).
- [4] H.A. Weldon, Phys. Rev. **D 26**, 1394 (1982); **D 40**, 2410 (1989) and Physica **A 158**, 169 (1989).
- [5] R.D. Pisarski, Phys. Rev. Lett. **63**, 1129 (1989); Nucl. Phys. **A498**, 423c (1989).
- [6] J.P. Blaizot, J.Y. Ollitrault, and E. Iancu, Saclay preprint T95/087, to appear in *Quark Gluon Plasma II*, ed. R.C. Hwa (World Scientific, Singapore).
- [7] G. Baym, J.P. Blaizot, and B. Svetitsky, Phys. Rev. **D 46**, 4043 (1992).
- [8] E. Petitgirard, Z. Phys. **C 54**, 673 (1992).

- [9] E. Braaten, R.D. Pisarski, and T.C.Yuan, Phys. Rev. Lett. **64** 2242 (1990).
- [10] P. Elmfors, K. Enqvist, and I. Vilja, Nucl Phys. **B 412**, 459 (1994).
- [11] E. V Shuryak and J.J.M. Verbaarschot, Nucl. Phys. **B 410**, 37 and 55 (1993); T. Schäfer, E. V Shuryak, and J.J.M. Verbaarschot, Nucl. Phys. **B 412**, 143 (1994).

# Consequences of Partial $U_A(1)$ Restoration\*

Zheng Huang<sup>a</sup> and Xin-Nian Wang<sup>b</sup>

<sup>a</sup>*Department of Physics, University of Arizona, Tucson, AZ 85721*

<sup>b</sup>*Nuclear Science Division, Mailstop 70A-3307, Lawrence Berkeley National Laboratory  
University of California, Berkeley, CA 94720 USA*

## Abstract

We argue that if  $U_A(1)$  symmetry is partially restored at high temperatures,  $\eta$  and  $\eta'$  masses will decrease, leading to enhanced thermal production of  $\eta$  and  $\eta'$  mesons. Such enhancement can survive thermal interaction only if the chemical equilibrium processes for an  $\eta$ - $\pi$  system stop before the thermal freeze-out. We calculate the chemical and thermal freeze-out times in an  $\eta$ - $\pi$  gas, using t' Hooft model, which incorporate explicitly the  $U_A(1)$  anomaly. Assuming an exponential suppression of the  $U_A(1)$  anomaly, we also take into account the partial restoration of  $U_A(1)$  symmetry at high temperatures. We find that the chemical equilibrium between  $\eta$  and  $\pi$  breaks up considerably earlier than the thermal equilibrium.

## I. INTRODUCTION

In the chiral limit with vanishing quark masses, QCD lagrangian has  $U_L(N_f) \times U_R(N_f)$  symmetries, under which all left-handed and right-handed quark fields can be rotated independently. The chiral symmetry  $SU_L(N_f) \times SU_R(N_f)$  is spontaneously broken giving rise to massless Goldstone bosons. While another remaining symmetry  $U_V(1)$  conserves baryon number, the  $U_A(1)$  symmetry is violated by the axial anomaly present at the quantum level and thus cannot give rise to another Goldstone boson. The  $U_A(1)$  particle, known as  $\eta'(958)$  in the  $N_f = 3$  case, acquires an additional mass through interactions with topologically nontrivial vacuum, *e.g.*, instantons [1],

$$\begin{aligned} \lim_{m_q \rightarrow 0} m_{\eta'}^2 &= \frac{2N_f}{f_\pi^2} (-i) \int d^4x \left(\frac{\alpha_s}{16\pi}\right)^2 \langle T[F_{\mu\nu} \tilde{F}^{\mu\nu}(x), F_{\mu\nu} \tilde{F}^{\mu\nu}(0)] \rangle_{\text{YM}} \\ &\equiv \frac{2N_f}{f_\pi^2} \langle \nu^2 \rangle_{\text{YM}} , \end{aligned} \quad (1)$$

thus breaking up the mass degeneracy with pions, kaons and  $\eta$  in the chiral limit, where  $\tilde{F}^{\mu\nu}$  is the dual gluon field strength tensor,  $\langle \nu^2 \rangle$  is the topological susceptibility and  $\langle \dots \rangle$

---

\*talk presented by X.-N. Wang

stands for the vacuum expectation value at zero temperature or the thermal average at finite temperature.

It is believed that at high temperatures the instanton effects are suppressed due to the Debye-type screening [2]. Then one expects a practical restoration of  $U_A(1)$  at high temperatures. If the restoration occurs at a temperature lower than the chiral phase transition temperature  $T_x$ , there may be some interesting phenomenological implications in high-energy heavy-ion collisions, as suggested first by Pisarski and Wilczek [3] and more recently by Shuryak [4]. One of the consequences of  $U_A(1)$  restoration is the enhancement of  $\eta$  particle production at small and intermediate transverse momenta due to the softening of its mass at high temperatures [5]. However, the final yield of the  $\eta$  particles and their  $p_t$  distributions both depend crucially on the chemical and thermal equilibrating processes involving the  $\eta$  [6].

In this talk, we shall examine the rates of various processes relevant for the thermal  $\eta$  particle production, in particular, whether or not the  $\eta$  can decouple early enough from the thermal system expected to be produced in relativistic heavy ion collisions. We shall present a model calculation of the thermal cross sections for the processes  $\eta\eta \leftrightarrow \eta\eta$ ,  $\pi\eta \leftrightarrow \pi\eta$  and  $\eta\eta \leftrightarrow \pi\pi$ , essential to the thermal and chemical equilibration. Our calculations are based on models which explicitly incorporate the  $U_A(1)$  anomaly. We also assume an exponential suppression of the  $U_A(1)$  anomaly due to the Debye-type screening of the instanton effect [2], which leads to the temperature dependence of the  $\eta$  and  $\eta'$  masses. Our results suggest that the chemical equilibrium breaks up for  $\eta$  particles long before the thermal freeze-out. Therefore a modest enhancement of thermal  $\eta$  production could signal the relic of partial  $U_A(1)$  restoration.

## II. TEMPERATURE DEPENDENCE OF $\eta$ AND $\eta'$ MASSES

The standard Di Vecchia-Veneziano model [7,8], which incorporates the explicit  $U_A(1)$  anomaly, reads after integrating out the gluon field

$$\mathcal{L}_{\text{eff}} = \frac{f_\pi^2}{4} \text{Tr}(\partial^\mu U \partial_\mu U^\dagger) + \frac{f_\pi^2}{4} \text{Tr}(MU + MU^\dagger) + \frac{f_\pi^2}{4} \frac{a}{4N_c} (\log \det U - \log \det U^\dagger)^2, \quad (2)$$

where  $U = \exp(i\Phi/f_\pi)$ ,  $f_\pi = 93$  MeV,  $M = \text{diag}(m_\pi^2, m_\pi^2, 2m_K^2 - m_\pi^2)$  and

$$\Phi = \begin{pmatrix} \pi^0 + \eta_8/\sqrt{3} + \sqrt{2}\eta_1/\sqrt{3} & \sqrt{2}\pi^+ & \sqrt{2}K^+ \\ \sqrt{2}\pi^- & -\pi^0 + \eta_8/\sqrt{3} + \sqrt{2}\eta_1/\sqrt{3} & \sqrt{2}K^0 \\ \sqrt{2}K^- & \sqrt{2}K^0 & -2\eta_8/\sqrt{3} + \sqrt{2}\eta_1/\sqrt{3} \end{pmatrix}. \quad (3)$$

The last term in Eq. (2) is the anomaly term which breaks  $U_A(1)$  explicitly. It is easy to check that Eq. (2) satisfies the anomalous Ward identity which is crucial for determining the form of  $U_A(1)$  breaking [9]. In Eq. (2),  $a$  is related to the topological susceptibility in pure Yang-Mills theory

$$a = \frac{2N_f}{f_\pi^2} \langle \nu^2 \rangle_{\text{YM}}. \quad (4)$$

The quadratic terms for the octet  $\eta_8$  and the singlet  $\eta_1$  from the Lagrangian reads

$$\mathcal{L}_{\text{mass}} = -\frac{1}{2} \left[ \left( -\frac{m_\pi^2}{3} + \frac{4m_K^2}{3} \right) \eta_8^2 + \left( \frac{2m_K^2}{3} + \frac{m_\pi^2}{3} + a \right) \eta_1^2 + \frac{2\sqrt{2}}{3} (2m_\pi^2 - 2m_K^2) \eta_8 \eta_1 \right]. \quad (5)$$

We consider the difference between the strange and non-strange quark masses. Therefore, there is a mixing between the octet  $\eta_8$  and the singlet  $\eta_1$ . The physical  $\eta(547)$  and  $\eta'(958)$  are defined by

$$\eta = \eta_8 \cos \theta + \eta_1 \sin \theta \quad ; \quad \eta' = -\eta_8 \sin \theta + \eta_1 \cos \theta \quad (6)$$

to diagonalize the quadratic terms with the mixing angle

$$\tan \theta = \frac{4m_K^2 - m_\pi^2 - 3m_\eta^2}{2\sqrt{2}(m_K^2 - m_\pi^2)}, \quad (7)$$

and the physical masses are

$$m_\eta^2 = (m_K^2 + a/2) - \frac{1}{2} \sqrt{(2m_K^2 - 2m_\pi^2 - a/3)^2 + 8a^2/9}, \quad (8)$$

$$m_{\eta'}^2 = (m_K^2 + a/2) + \frac{1}{2} \sqrt{(2m_K^2 - 2m_\pi^2 - a/3)^2 + 8a^2/9}. \quad (9)$$

The mixing angle  $\theta$  as well as  $m_\eta^2$  and  $m_{\eta'}^2$ , depend on the instanton-induced quantity  $a$  which is a function of temperature. It is known that mixing angle  $\theta$ ,  $m_\eta^2$  and  $m_{\eta'}^2$ , at  $T = 0$  cannot be simultaneously fit to their experimental values by a single parameter  $a(0)$ . The best fit is to use the measured value of  $m_\eta^2 + m_{\eta'}^2$ , as an input to determine  $a(0) = (m_\eta^2 + m_{\eta'}^2) - 2m_K^2$  and use this  $a(0)$  to predict  $\theta$ ,  $m_\eta^2$  and  $m_{\eta'}^2$ , using Eqs. (7) and (8). The predicted values are  $\theta = 18.3^\circ$ ,  $m_\eta = 500$  MeV and  $m_{\eta'} = 984$  MeV, compared to the measured values  $\theta^{\text{exp}} \simeq 20^\circ$  from  $\eta, \eta' \rightarrow \gamma\gamma$ ,  $m_\eta^{\text{exp}} = 547$  MeV and  $m_{\eta'}^{\text{exp}} = 958$  MeV.

We now assume that the temperature dependence of  $m_\eta$  and  $m_{\eta'}$  is completely determined through the temperature dependence of  $a(T)$  or the topological susceptibility. The precise form of  $a(T)$  at a temperature lower than the chiral phase transition temperature ( $T_\chi$ ) is not known. It has been shown by Shuryak and Velkovsky [10], using soft pion approximation, that at a very low  $T < f_\pi$ , the instanton density shows a rather weak dependence on  $T$ . It is also argued by Pisarski and Wilczek [3] and by Shuryak [4] that at  $T_\chi$  the instanton effect should be suppressed at least by a order of magnitude if the instanton is responsible for the spontaneous chiral symmetry breaking. This indicates a rather strong temperature dependence of the instanton effect as  $T$  approaches  $T_\chi$  from below. Recent lattice QCD calculation [11] indeed demonstrated such behavior of the topological susceptibility of the pure Yang-Mills fields as shown in Fig. 1. To model such a dependence, we use a phenomenological parametrization in an exponential form [12–14]

$$a(T) = a(0)e^{-(T/T_0)^2}, \quad (10)$$

where  $T_0 \simeq 100 - 200$  MeV, while keeping the masses of the pion and kaon approximately temperature independent, since they change very slowly with the temperature. Throughout this paper, we take  $T_0 = 150$  MeV in Eq. (10) as shown by the solid line in Fig. 1.

We plot schematically the temperature dependence of  $\eta$  and  $\eta'$  masses in Fig. 2. Clearly, the  $\eta$  becomes soft at high  $T$  and eventually is degenerate with the pions. The mass of  $\eta'$

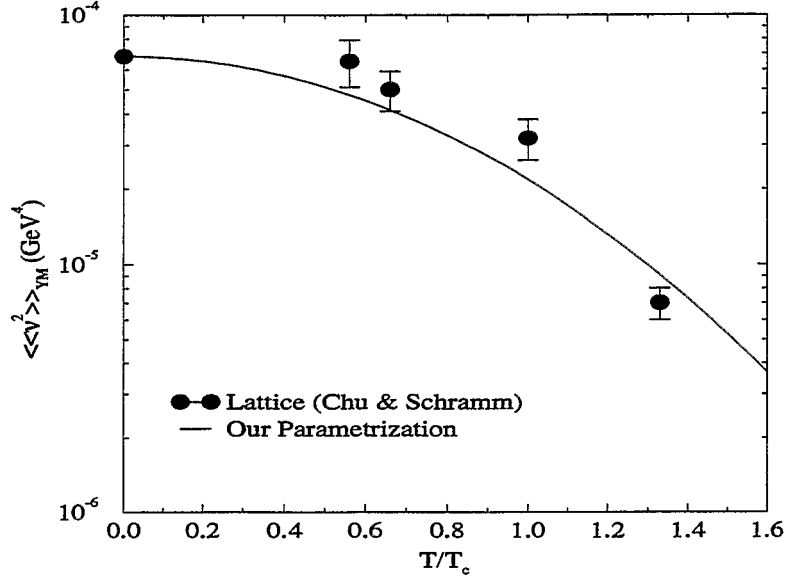


FIG. 1. The temperature dependence of the topological susceptibility of pure Yang-Mills fields from Ref. [11]. The solid line is a exponential fit in Eq. (10) with  $T_0 = 150$  MeV.

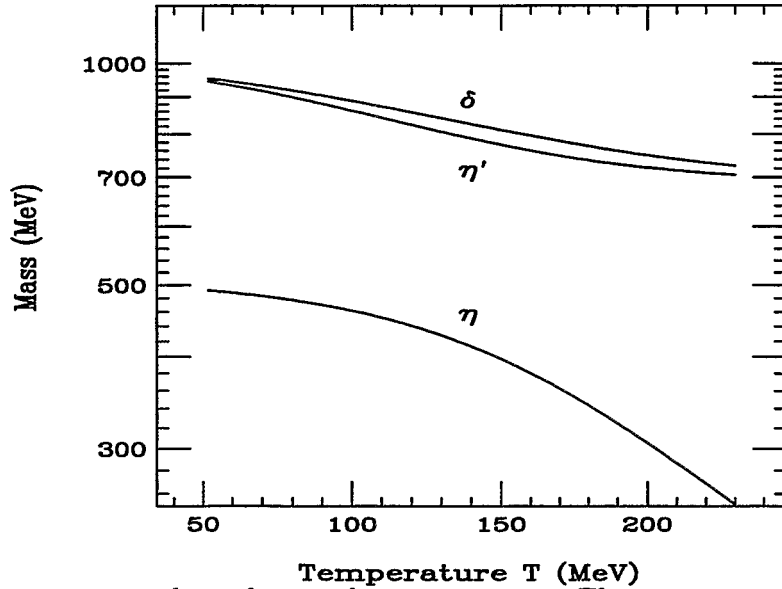


FIG. 2. The temperature dependence of  $m_\eta$ ,  $m_{\eta'}$ ,  $m_\delta$ . The parameter in the exponential suppression of the instanton effect is taken to be  $T_0 = 150$  MeV.



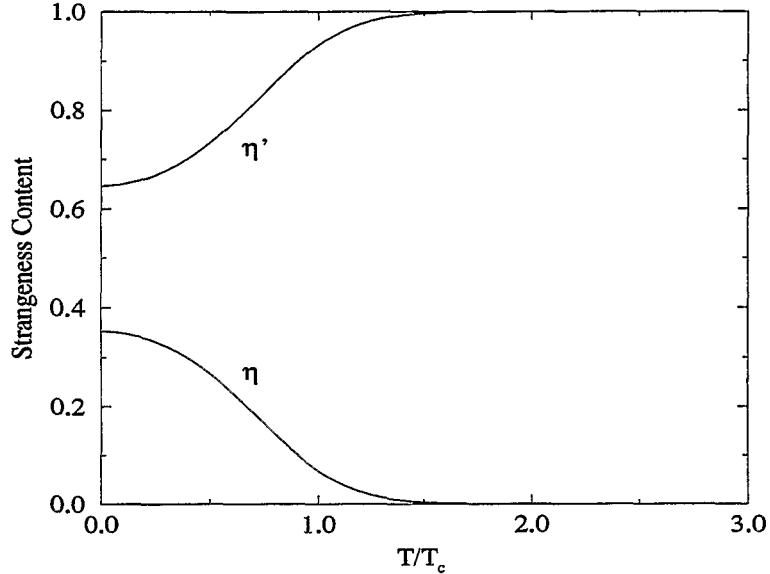


FIG. 3. The temperature dependence of the strangeness contents in  $\eta$  and  $\eta'$

also decreases. However, it does not become degenerate with the pion because of the large strange-quark mass, as is seen from Eq. (9). From Fig. 2 we see that the  $\eta'$  mass at high temperatures is still higher than the  $\eta$  mass at zero temperature. In Fig. 2 we also plot the temperature dependence of the  $\delta$  resonance mass which we will discuss later. At temperatures higher than  $T_x$  when chiral symmetry is restored, the masses of these excitation modes will all rise again.

The temperature dependence of the topological susceptibility can also cause the mixing among  $\eta$  and  $\eta'$  to change. To demonstrate such effects, we plot in Fig. 3 the strangeness contents in  $\eta$  and  $\eta'$  as functions of temperature. We see that as  $U_A(1)$  is practically restored,  $\eta$  becomes completely non-strange while  $\eta'$  becomes a  $s\bar{s}$  state.

### III. CHEMICAL AND THERMAL EQUILIBRIUM TIMES

As we have postulated earlier, when the  $\eta$  mass decreases at high temperature as  $U_A(1)$  is partially restored, its thermal production must be enhanced. However, if chemical equilibrium is maintained when interactions change the  $\eta$  mass all the way until freeze-out, there should not be any enhancement of final  $\eta$  production. In order for the enhancement of thermal  $\eta$  production to survive the interactions that can change  $\eta$  number, such interactions must effectively stop long before the thermal freeze-out. In other words, chemical freeze-out must happen long before the thermal freeze-out.

In order to estimate the chemical and thermal freeze-out time at finite temperature, one should also include resonances. The linear  $\sigma$ -model based on the chiral symmetry is known to satisfy the low-energy theorems, and at the same time to be able to incorporate the resonances. To further reduce the input parameters, we consider the  $\sigma$  and  $\delta(980)$  [now called  $a_0(980)$ ] resonances, which, together with  $\pi$  and the  $\eta_{ns}$  to be defined below, form a complete representation of  $U(2) \times U(2)$ . We shall concentrate on the  $\eta$  particle, since there is no dramatic change of the  $\eta'$  mass with temperature, as shown in Fig. 2. We study

the most relevant processes for the  $\eta$  production:  $\eta\eta \leftrightarrow \pi\pi$ ,  $\pi\eta \leftrightarrow \pi\eta$ , and  $\eta\eta \leftrightarrow \eta\eta$ . In this case,  $U(3) \times U(3)$  reduces to  $U(2) \times U(2)$  except for the mixing effects which we have already calculated. The reactions  $\eta\eta \rightarrow \eta\eta$  and  $\pi\eta \rightarrow \pi\eta$  determine the collision time scale responsible for maintaining the thermal equilibrium while  $\eta\eta \rightarrow \pi\pi$  is responsible for the chemical equilibrium between  $\pi$ 's and  $\eta$ 's.

Let us introduce the nonstrange mode  $\eta_{\text{ns}} = (u\bar{u} + d\bar{d})/\sqrt{2}$  and take  $m_s$  to be heavy. Then  $\eta_{\text{ns}}$  is approximately a mass eigenstate,  $\eta_{\text{ns}} = \eta \sin \chi + \eta' \cos \chi$ , whose mass is determined from Eq. (5) to be  $m_{\text{ns}}^2 \simeq 2a/3 + m_\pi^2$ . At zero temperature,  $m_{\text{ns}} \simeq 709$  MeV. We then define the (2,2) representation multiplet of  $U(2) \times U(2)$  as

$$\Phi = \frac{1}{2}(\sigma + i\eta_{\text{ns}}) + \frac{1}{2}(\delta + i\pi) \cdot \tau. \quad (11)$$

The most general  $U(2) \times U(2)$  invariant potential is

$$V_0 = -\mu^2 \text{Tr}(\Phi^\dagger \Phi) + \frac{1}{2}(\lambda_1 - \lambda_2)(\text{Tr} \Phi^\dagger \Phi)^2 + \lambda_2 \text{Tr}(\Phi^\dagger \Phi)^2 \quad (12)$$

and the mass term is

$$V_m = \frac{m_\pi^2 f_\pi}{4} \text{Tr}(\Phi^\dagger + \Phi), \quad (13)$$

where  $\lambda_1, \lambda_2$  are dimensionless constants. The  $U_A(1)$ -breaking term, consistent with the Ward identity, is introduced by t' Hooft [15] as

$$V_a = \frac{a}{3}(\det \Phi^\dagger + \det \Phi), \quad (14)$$

and the coefficient in  $V_a$  is chosen such that it gives the correct mass for  $\eta_{\text{ns}}$ . The mass spectrum can be derived from Eqs. (12), (13) and (14) by making a shift  $\sigma \rightarrow f_\pi + \sigma$ :

$$m_\sigma^2 = \lambda_1 f_\pi^2 + m_\pi^2 \quad ; \quad m_\delta^2 = \lambda_2 f_\pi^2 + m_{\text{ns}}^2. \quad (15)$$

The decay widths are

$$\Gamma_\sigma = \frac{3}{32\pi}(m_\sigma^2 - 4m_\pi^2)^{1/2} \frac{(m_\sigma^2 - m_\pi^2)^2}{f_\pi^2 m_\sigma^2}, \quad (16)$$

$$\Gamma_\delta = \{[(m_\delta^2 - (m_{\text{ns}} + m_\pi)^2)][(m_\delta^2 - (m_{\text{ns}} - m_\pi)^2)]\}^{1/2} \frac{(m_\delta^2 - m_{\text{ns}}^2)^2}{16\pi f_\pi^2 m_\delta^3}. \quad (17)$$

At zero temperature,  $\Gamma_\sigma \sim 1$  GeV (if  $m_\sigma \sim 700$  MeV) and  $\Gamma_\delta \sim 200$  MeV. In principle, we should also take into account the temperature dependence of  $f_\pi$  and  $m_\sigma$  below  $T_\chi$ . Here, we assume the chiral phase transition is very rapid after which  $f_\pi$  and  $m_\sigma$  have very slow temperature dependences. Furthermore, due to the large width of the  $\sigma$ , the slow temperature dependence of  $m_\sigma$  will not change our results significantly. Under such an assumption, the linear  $\sigma$ -model predicts also some softening of the  $\delta$  resonance as  $T$  increases, because  $\delta$  is the chiral partner of  $\pi$  and acquires some mass from the  $U_A(1)$  anomaly. The temperature dependence of  $m_\delta$  is plotted in Fig. 2.

The interaction terms are

$$\begin{aligned} \mathcal{L}_{\text{int}} = & \frac{\lambda_1 f_\pi}{2} (\sigma^2 + \eta_{\text{ns}}^2 + \delta^2 + \pi^2) \sigma + \frac{\lambda_1}{8} (\sigma^2 + \eta_{\text{ns}}^2 + \delta^2 + \pi^2)^2 \\ & + \lambda_2 f_\pi (\sigma \delta + \eta_{\text{ns}} \pi) \cdot \delta + \frac{\lambda_2}{2} (\sigma \delta + \eta_{\text{ns}} \pi)^2 + \frac{\lambda_2}{2} (\delta \times \pi)^2 . \end{aligned} \quad (18)$$

The coupling constants  $\lambda_1$  and  $\lambda_2$  can be obtained from the mass relations of Eq. (15). It is worth pointing out that the above model should not be used to estimate the pion-pion scattering amplitude, because it does not include the important vector resonances such as  $\rho$  and  $A_1$ . However, since  $\eta\eta$  and  $\pi\eta$  scatterings cannot go through  $J = 1$  channel, they do not directly affect the interaction rates for  $\eta$ . Similarly, we have also neglected the  $\eta$ - $\rho$  interaction.

To calculate the scattering amplitudes at the lowest order, we have to remove a pole singularity encountered when a resonance appears in the  $s$ -channel. A naive introduction of Breit-Wigner resonance width will spoil the delicate cancellation between the contact interaction and the pole exchange at low energy, leading to the violation of the low-energy theorems. We adopt a minimal prescription to save the low-energy limit developed by Chanowitz and Gaillard [16], making the following replacement

$$\lambda_1 + \frac{\lambda_1^2 f_\pi^2}{s - m_\sigma^2 + i m_\sigma \Gamma_\sigma} \rightarrow \lambda_1 (1 - i \Gamma_\sigma / m_\sigma) \frac{s - m_\pi^2}{s - m_\sigma^2 + i m_\sigma \Gamma_\sigma} . \quad (19)$$

Given the interactions, we define the time scales  $\tau_{\text{ther}}$  and  $\tau_{\text{chem}}$  for thermal and chemical equilibrium, respectively, as

$$\begin{aligned} \tau_{\text{ther}}^{-1} &= \langle v \sigma (\eta\eta \rightarrow \eta\eta) \rangle n_\eta + \langle v \sigma (\eta\eta \rightarrow \pi\pi) \rangle n_\eta + \langle v \sigma (\pi\eta \rightarrow \pi\eta) \rangle n_\pi , \\ \tau_{\text{chem}}^{-1} &= \langle v \sigma (\eta\eta \rightarrow \pi\pi) \rangle n_\eta , \end{aligned} \quad (20)$$

where  $n_\pi$  and  $n_\eta$  are the number densities for  $\pi$  and  $\eta$ , and the summation over different pion states is understood. In Fig. 4,  $\tau_{\text{ther}}$  and  $\tau_{\text{chem}}$  are plotted as functions of the temperature. In the calculation, we have explicitly taken into account the temperature dependence of  $m_\eta(T)$ ,  $m_\delta(T)$ ,  $m_{\text{ns}}(T)$  and  $\Gamma_\delta(T)$ . For a typical value  $R = 6$  fm for the transverse freeze-out radius of the system, we define the thermal and chemical freeze-out temperatures  $T_{\text{th}}$  and  $T_{\text{ch}}$  respectively as  $\tau_{\text{ther}}(T_{\text{th}}) = R$  and  $\tau_{\text{chem}}(T_{\text{ch}}) = R$ . One finds from Fig. 4

$$T_{\text{th}} \simeq 139 \text{ MeV} \quad \text{and} \quad T_{\text{ch}} \simeq 168 \text{ MeV} , \quad (21)$$

which are the temperatures at which the thermal and chemical equilibria start to break up, respectively. Therefore, the chemical freeze-out happens considerably earlier than the thermal freeze-out.

#### IV. CONCLUSIONS

After chemical freeze-out,  $T < T_{\text{ch}}$ , the  $\pi$ - $\eta$  conversion process becomes slow and effectively is turned off; the system can no longer maintain the chemical equilibrium. There is an approximate conservation of the total number of  $\eta$ 's since neither  $\eta\eta \rightarrow \eta\eta$  nor  $\pi\eta \rightarrow \pi\eta$  can change the total  $\eta$ -number though thermal equilibrium is still maintained when  $T > T_{\text{th}}$ . During the expansion and cooling afterwards, the  $\eta$  mass continue to increase to its vacuum

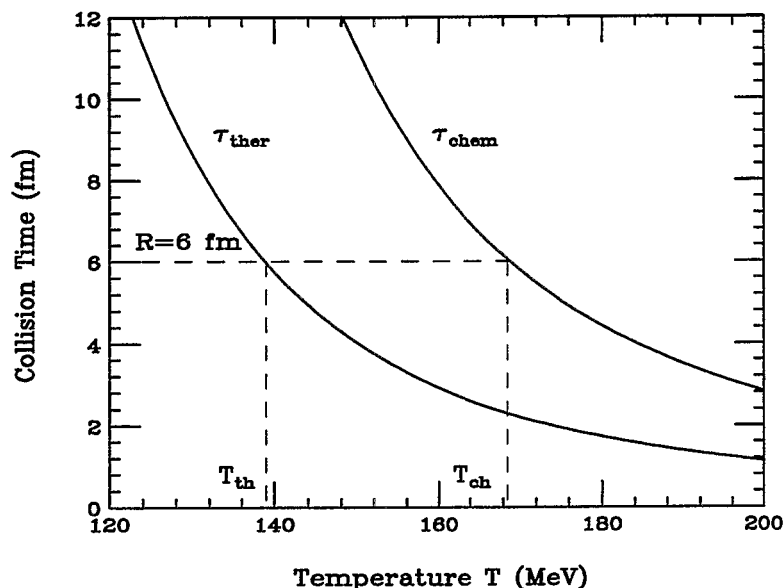


FIG. 4. The characteristic time scales of the thermal and chemical equilibration for the  $\eta$  particle.

value, a finite chemical potential develops from which one can calculate the enhancement of  $\eta$  production. The enhancement depends very sensitively on how the system cools down and break-up.

After the thermal freeze-out, it is clear that there must exist some mechanism for the  $\eta$  to relax from the 'temporary' entity whose mass is smaller than its vacuum value to its true identity at zero temperature with  $m_\eta = 540$  MeV. A possible picture might be that the  $\eta$  particles still feel a negative potential in the fireball. The height of the potential barrier is determined by the mass difference  $\Delta m \approx m_\eta - m_\eta(T_{\text{ch}})$ . The  $\eta$  particles with  $p_t$  smaller than  $\Delta m$  will be trapped in the potential well until the rarefaction wave reaches the center of the interaction volume. Such a picture has been suggested by Shuryak [4]. At this stage, we do not attempt to address this nonequilibrium issue, but just to remark that our calculation here indicates some enhancement effect at small  $p_t \lesssim \Delta m \sim 100 - 200$  MeV.

## ACKNOWLEDGEMENTS

This work was supported by the Director, Office of Energy Research, Office of High Energy and Nuclear Physics, Divisions of Nuclear Physics, of the U.S. Department of Energy under Contract No. DE-AC03-76SF00098, DE-FG03-93ER40792. X.N.W was also supported by the U.S. - Hungary Science and Technology Joint Fund J.F.No.378.

## REFERENCES

- [1] G. 't Hooft, Phys. Rev. **D14**, 3432 (1976).
- [2] D. J. Gross, R.D. Pisarski and L.G. Yaffe, Rev. Mod. Phys. **53**, 43 (1981).
- [3] R. D. Pisarski and F. Wilczek, Phys. Rev. **D29**, 338 (1984).

- [4] E. Shuryak, Comments Nucl. Part. Phys. **21**, 235 (1994).
- [5] J. Kapusta, D. Kharzeev and L. McLerran, Phys. Rev. D **53**, 5028 (1996).
- [6] Z. Huang and X.-N. Wang, Phys. Rev. D **53**, 5034 (1996).
- [7] P. Di Vecchia and G. Veneziano, Nucl. Phys. **B171**, 253 (1980).
- [8] H. Chen, Phys. Rev. **D44**, 166 (1991); A. Pich and E. de Rafael, Nucl. Phys. **B367**, 313 (1991).
- [9] S. Aoki and T. Hatsuda, Phys. Rev. **D45**, 2427 (1992).
- [10] E. Shuryak and M. Velkovsky, Phys. Rev. **D50**, 3323 (1994).
- [11] M. C. Chu and S. Schramm, Phys. Rev. D **51**, 4580 (1995).
- [12] R. D. Pisarski and L. G. Yaffe, Phys. Lett. **B97**, 110 (1980).
- [13] H. Kikuchi and T. Akiba, Phys. Lett. **B200**, 543 (1988).
- [14] T. Kunihiro, Nucl. Phys. **B351**, 593 (1991).
- [15] G. 't Hooft, Phys. Rep. **142**, 357 (1986)
- [16] M. Chanowitz and M. K. Gaillard, Nucl. Phys. **B261**, 379 (1985).



## V. Experimental Developments

# Interesting Aspects of the STAR Detector and Physics Program\*

Timothy J. Hallman  
For the STAR Collaboration  
*Brookhaven National Laboratory, Upton, New York, 11973, USA*

The Solenoidal Tracker At RHIC (STAR) is a large acceptance collider detector scheduled to begin operation at the Relativistic Heavy Ion Collider (RHIC) in the fall of 1999. Simply stated, the physics goals of STAR are,

- to study the behavior of strongly interacting matter at high energy density
- to search for signatures of a deconfined partonic phase of matter, and
- to study the importance of spin as a fundamental property of QCD interactions and measure the spin-dependent parton distributions (gluon, valence quark, sea quark) of the proton.

With regard to the search for a deconfined phase of matter, STAR [1] is designed to search for signatures of QGP formation through the measurement and correlation of global observables on an event-by-event basis and the use of hard scattering of partons to probe the properties of high density matter.

The baseline STAR detector (Fig. 1) utilizes a time projection chamber (TPC) in a solenoidal magnetic field of 0.5T covering approximately 4 units of the central rapidity. An additional element of the detector is a silicon vertex tracker (SVT) to locate the position of the primary vertex to high accuracy, and to locate secondary vertices to an accuracy of 20  $\mu\text{m}$ . A *Pb*-scintillator sampling electromagnetic calorimeter will be used to trigger on transverse energy and measure jets, direct photons and leading  $\pi^0$  production. A portion of the acceptance will be instrumented with a highly segmented TOF array, extending the maximum momentum for  $\pi/K$  separation from 0.6 to 1.5 GeV/c and the corresponding limit for  $K/p$  separation from 1–2.4 GeV/c. Forward TPCs (FTPC) located in the region  $2 < |\eta| \leq 4.5$  will be used to study the transfer of energy from projectile rapidity to midrapidity by following the fate of the incident baryons rescattered in the collision.

An important measure of recent progress in the construction of STAR is the initiation of the first phase of the STAR “system test”. In this effort, all of the key elements of the STAR data taking chain (TPC, front end electronics, DAQ, trigger, and slow controls) are

---

\*This research was supported by the U.S. Department of Energy under Contract Nos. DE-AC02-76CH00016.



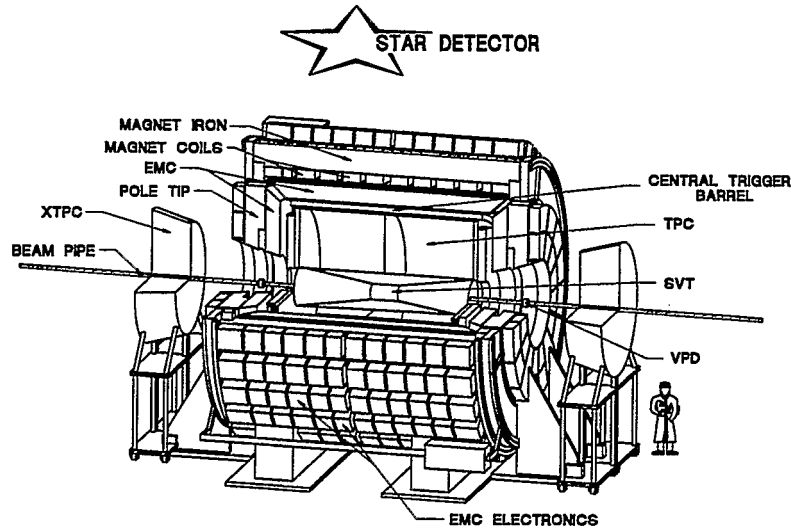


FIG. 1. Schematic layout of the STAR detector.

physically interfaced and made to work together for the first time. Progress in this area is evident in Fig. 2, in which the first cosmic ray data detected in a STAR TPC pad plane are shown. Further work using both cosmic rays and lasers will test the channel to channel uniformity, the position resolution for a single track, and the two-track resolution.

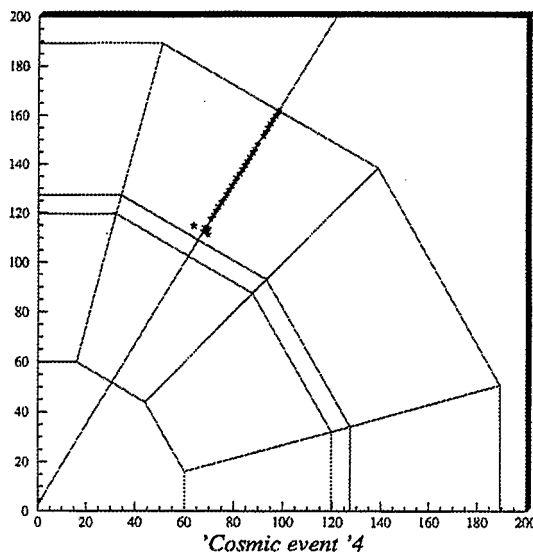


FIG. 2. The first cosmic ray data recorded in a STAR TPC pad plane as part of the STAR system test.

One important aspect of the STAR program will be to search for special events in which the measurement and correlation of event-by-event observables (e.g.  $dn_{\pi}/dy$ ,  $T_{\pi}$ ,  $K/\pi$ ,  $p_{t\pi}$ ,  $dn/dy$ ) indicates the transition to a deconfined phase may have occurred. An event in this category might be characterized, for example, by an unusually high inverse slope parameter

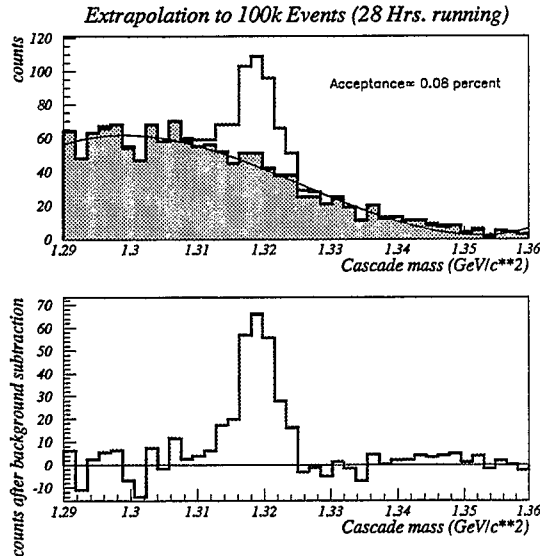


FIG. 3. Simulated invariant mass distribution for the  $\Xi^-$  using the STAR SVT.

for the pion spectrum or large non-statistical fluctuations in the  $dn/dy$  spectra. A second goal will be to measure the thermodynamic observables ( $T$ ,  $\mu_B$ ,  $\mu_s$ ) for an ensemble of events to establish whether a state of thermal and chemical equilibrium has been reached. This state of matter is predicted to occur in the evolution of the system from deconfinement to hadronization, and its observation would be strong evidence that a phase transition to a QGP had taken place. The design of the detector allows for the precise measurement, for example, of particle ratios ( $p/\bar{p}$ ,  $\bar{\Lambda}/\Lambda$ ,  $K/\pi$ ) to determine the strange chemical and baryo-chemical potentials, inverse slope parameters and  $p_t$  to determine the energy density (temperature), and  $dn/dy$  distributions to investigate entropy production. These observables will be measured and correlated to determine if a state in which chemical and thermal equilibrium has been reached can be identified.

Determination of the strangeness density and strangeness “saturation” in relativistic heavy ion collisions have long been recognized [2] as important probes of plasma production primarily because a rapid increase in  $s\bar{s}$  production through gluon-gluon interactions in a QGP would allow saturation of the strangeness degrees of freedom much more quickly than could be achieved in multiple hadronic interactions. The measurement of strange baryons at RHIC however is complicated due to the short lifetime and low mean  $p_t$  which characterize the production. As a consequence, combinatorics pose a significant background, and an inner tracking system capable of accurate determination of secondary vertices is essential.

In STAR, this is accomplished with a new type of detector developed at Brookhaven National Laboratory (BNL) through RHIC R&D – the silicon drift detector (SDD). With careful shaping of the electrostatic potentials, the ionization deposited by a charged particle traversing a fully depleted silicon wafer can be made to drift at a constant velocity the entire length of the wafer. Knowing the time of the drift and determining the position in the anode direction by charge sharing, the position of the charged particle can be determined with great precision. Extensive bench tests at BNL and elsewhere have shown that space point resolutions on the order of a few tens of microns are achievable. The STAR silicon

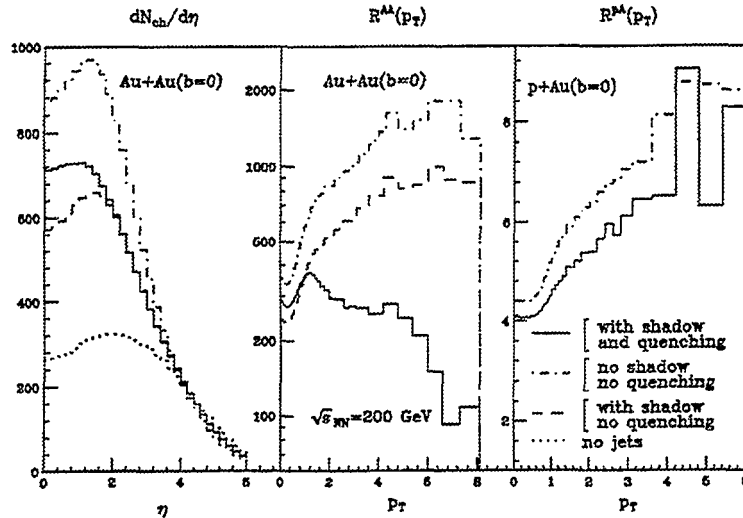


FIG. 4. Results from HIJING calculations on the dependence of the inclusive charged hadron spectra in central  $AuAu$  and  $pAu$  collisions on mini-jet production (dash-dotted), gluon shadowing (dashed) and jet quenching (solid) assuming that gluon shadowing is identical to that of quarks.  $R^{AB}(p_t)$  is the ratio of the inclusive  $p_t$  spectrum of charged hadrons in  $A + B$  collisions to that of  $pp$  [3].

vertex tracker (SVT) is constructed of ladders of SDDs arranged in three concentric cylinders at mean radii of 6.5, 10.5, and 14.5 cm.

The utility of the STAR SVT is demonstrated in Fig. 3. Using the characteristic resolutions demonstrated through R&D for this device, the  $\Xi^-$  yield and signal to noise ratio for approximately 2-3 days of  $AuAu$  running are shown to be quite good. This detector is nearing the beginning of its construction phase, and completion is projected for the end of calendar year 1999.

Two specific aspects of the STAR program which merit a somewhat more detailed discussion are measurement of the gluon distribution in the nucleus, and the detection and interpretation of multiple non-statistical correlations possibly indicative of new physics.

An important element in the ion studies at RHIC and LHC will be the determination of the initial conditions – the parton distributions in the nucleus. RHIC will be the first heavy ion accelerator in which a large part (50%) of the energy transferred into particle production comes directly from partonic processes which are calculable in pQCD. Theoretical guidance as to the evolution of the early stages of the collision is therefore possible if the initial distribution of partons in the nucleus is known. Presently it is expected that gluon-gluon scattering will dominate at early times with chemical equilibration of the quark degrees of freedom proceeding much more slowly. Determination of the gluon distribution in the nucleus in  $pA$  interactions, which is not provided by deep inelastic scattering studies, is therefore of particular interest. One would like to know the distribution down to the smallest values of  $x_{BJ}$  of relevance for particle production in the ion studies. At RHIC this value is  $x_{BJ} \sim .01$ . At LHC it is an order of magnitude lower, and this study may be problematic due to the two-in-one magnet design of the accelerator.

The fact that the quark (valence plus sea) structure function of a nucleon in a nucleus is

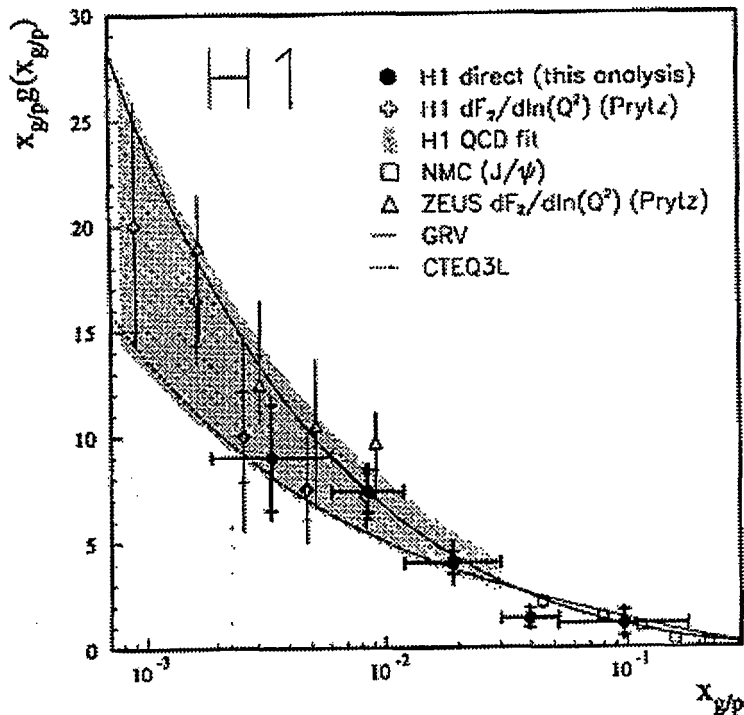


FIG. 5. The measured gluon density at an average  $Q^2$  of  $30 \text{ GeV}^2$  as a function of the fractional gluon momentum compared with indirect determinations by  $H1$  and  $ZEUS$  at  $Q^2 = 20 \text{ GeV}^2$  as well as with a determination from  $J/\Psi$  production by  $NMC$  evolved to  $Q^2 = 30 \text{ GeV}^2$  [4].

modified with respect to that for a free nucleon is well known from deep inelastic scattering. It has also been pointed out for some time [3] that one also expects a similar modification of the gluon structure function. Inspecting the middle panel of Fig. 4, for example, the ratio of single particle inclusive production in  $AA$  to that in  $pp$  varies by a factor of approximately two depending on whether or not such a modification—“gluon shadowing”—is assumed. To reduce this uncertainty in the interpretation of the measured spectra, it would be of great value to have independent knowledge of the gluon structure function in the nucleus.

Experimental effort thus far has focused on measurement of the gluon distribution in the proton with the consequence that significant data on  $xg(x)$  are now available at low  $x_{BJ}$  from  $H1$  and  $Zeus$ , with complementary data closer to the valence region available from  $NMC$  and  $BCDMS$ . The data at low  $x_{BJ}$  come both from direct measurement of photon-gluon fusion, and from examining the scaling violation of the  $F_2$  structure function at low  $x_{BJ}$ , the latter presumably resulting from the production of sea quark pairs in gluon-gluon interactions. A compilation of the available data on  $xg(x)$  normalized at a  $Q^2$  of  $30 \text{ GeV}^2$  is shown in Fig. 5 [4].

It is interesting to note that even at the lowest  $x_{BJ}$  measured, the value of  $xg(x)$  is considerably less than the value one would naively expect if gluons completely filled the transverse size of the proton. In principle, saturation of the gluon density in the proton at low  $x_{BJ}$  could yield important information about the modification of the gluon distribution at higher  $x_{BJ}$  in the nucleus, since both effects result from the same basic gluon recombination

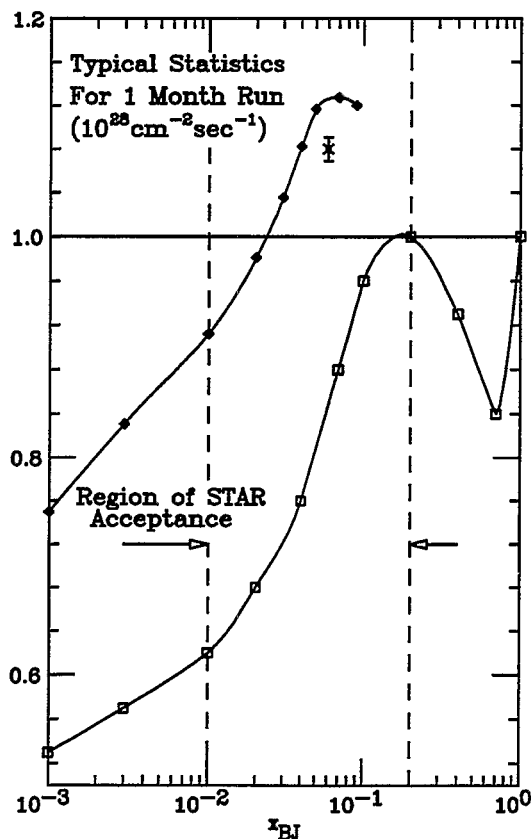


FIG. 6. The range of  $x_{BJ}$  for which the gluon distribution in the nucleus will be investigated in STAR using direct photon + jet coincidences. The statistical accuracy expected for 1 month of running for  $pAu$  interactions at the design luminosity is indicated. The top curve shows a theoretical estimate of gluon shadowing in the nucleus[5]. The quark shadowing in the nucleus expected for  $pAu$  interactions is shown for reference (bottom curve).

processes. What is not obvious thus far in the data of Fig. 5 is the extent to which saturation of the parton distribution may already be present in the data, or indeed how to extract this information. A further technical difficulty is that it is precisely at the point where saturation of the parton density occurs that the assumption of factorization may break down.

In STAR, the intent is to measure the gluon distribution in the nucleus directly in order to determine the initial conditions before the collision. This will be probed using the QCD Compton diagram, detecting the final state jet and direct photon coincidence in the STAR TPC and electromagnetic calorimeter. The contribution to this channel from  $q\bar{q}$  annihilation should be small (of order 10%) at these energies. The region of the STAR acceptance (in  $x_{BJ}$ ) for this measurement as well as the projected sensitivity for a pAu run of 1 month at the design luminosity are indicated in Fig. 6. Work is ongoing within STAR both to refine the design of the EMC to address the measurement of jets and direct photons in AA interactions (in pp and  $pAu$  this capability has already been demonstrated) as well as to perform realistic simulations focused on identifying and understanding potential sources of systematic error in this measurement.

A second effort that has recently become the focus of increased effort and interest is to

develop techniques from information theory on how, beyond simple two dimensional correlation techniques (e.g. scatterplots), to detect and measure non-statistical multi-dimensional correlations [6].

The basic idea underlying this analysis is that there is a unique physical scale associated with correlations of a particular type. This is to some extent familiar from common experience. If viewed from many miles away, the correlation information contained within a city skyline might be hard to distinguish from the surrounding horizon by the naked eye. From several miles away, however, the skyline of the city would be unmistakable and one would be able to make a fairly precise estimation, for example, of the size and outline of the city. If standing then between two tall skyscrapers within the city which subtended most of the field of view, it would be again hard to determine much about the overall dimensions or outline of the city, although it might be much easier to detect a different correlation,—for example, an unusually high probability of finding a delicatessen in the neighborhood. The essence of this technique then is to determine the correlation information content within a given central AuAu interaction by examining the “topological” or “Renyi entropy”—the amount of information available—at a number of different physical scales which relate to the physical size of various elements of the STAR detector system. The goal is to select events based on the level of their information content, rather than on the extent to which they resemble or differ from criteria developed from event generators of unknown reality.

Practically, to make this determination, each event is first examined to determine the “Renyi entropy” at a given scale. In practice this can be as simple, as counting the number of particles or the transverse energy (normalized for convenience) entering a set of bins (scintillator counters, calorimeter towers, etc.) of a given size and determining the logarithm of the moments of the distribution. This procedure is then repeated with a slightly different binning at the same scale, to insure the results are independent of the choice of binning. The results of several trials determine the average “scaled entropy” for that event. The scaled entropy for a given event may then be compared to the scaled entropy for an ensemble of reference events generated either from an event generator, or some a priori notion concerning the nature of the fluctuations for a given type of distribution.

The difference between the average scaled entropy for an event of interest and the reference ensemble is termed the “scaled information” for that event. Having determined the scaled information at a given scale, the process is repeated to determine the scaled information for each event of interest for a range of different physical scales (usually 50-100). Finally the “dimension lowering” —the derivative of the scaled information with respect to scale size—is determined, for example, at 3 different scales, and the result plotted in a Cartesian space to determine if events belonging to distinctly different populations in this space can be identified.

In principle one can generalize this technique to examine events in an n-dimensional space to search for unique non-statistical n-dimensional correlations. Further, this analysis technique may be used either at the trigger level, or in off-line analysis. The power of this technique is illustrated in Figs. 7 and 8, in which several event types which differ in the nature of the energy deposition in the interaction region have been used. What is noted is that essentially all event types exhibit very similar multiplicity distributions (Fig. 7) which do not distinguish one type of event from another. When the dimension lowering for each event at 3 different scales is plotted in a Cartesian space however (Fig. 8), the event types

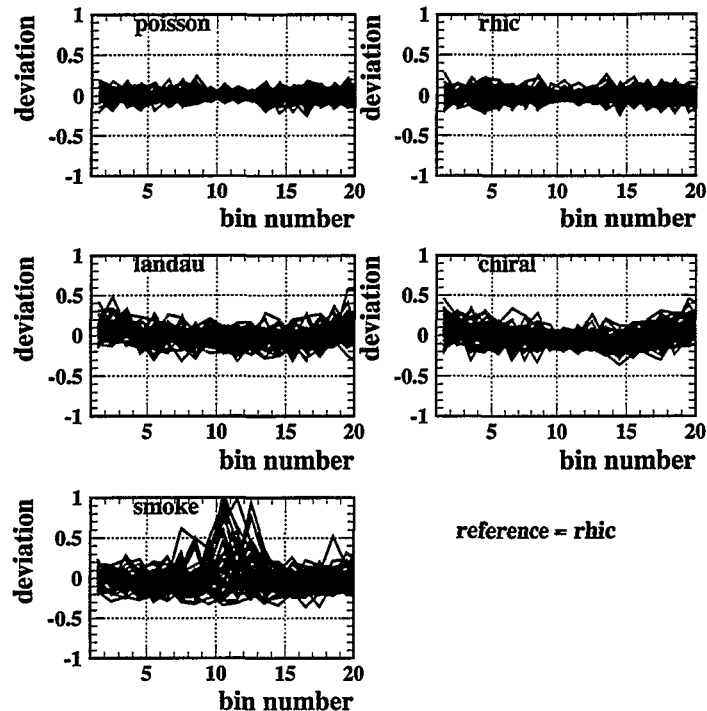


FIG. 7. The relative deviation, as a function of pseudorapidity (bin number) of the charged-particle multiplicity for several hypothetical event samples from the event ensemble average of a standard RHIC event class (except for the POISSON events, which are shown relative to a uniform distribution).

are quite distinct and the events contained in one particular population can be separated out for further analysis with appropriate cuts.

This technique appears to be quite promising, and it would be of significant interest to perform such an analysis, for example, for events with and without mini-jets, the presence of which is in general difficult to isolate. One obvious consequence of this type of analysis technique is the somewhat urgent need for more realistic RHIC event and plasma event generators to assess the physical significance and interpretation of fluctuations and correlations which may be observed.

In conclusion, to search for evidence of a transition to a deconfined phase the STAR detector will measure and correlate a number of global observables on an event-by-event basis. STAR will also provide important information on the initial conditions, using jet-direct photon coincidences to probe the gluon distribution of a nucleon in the nucleus via the QCD Compton process. Work is continuing on refining the STAR capability to use hard-scattered partons as a penetrating probe to provide information on the medium in the

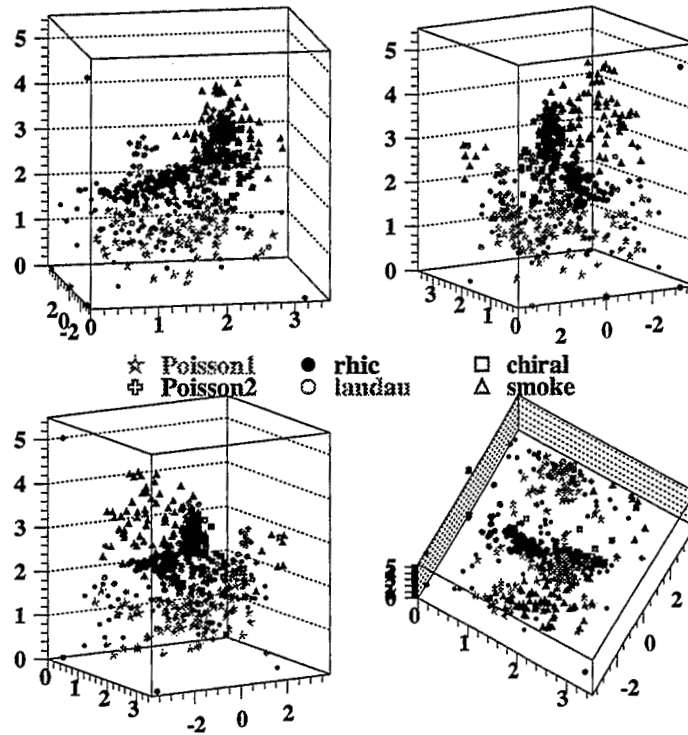


FIG. 8. The distribution in a polar coordinate space, for the same event samples plotted in Fig. 7, of the dimension lowering at three different physical scales. (Each axis locates for a given event the dimension lowering at one physical scale). Close inspection (made easier by the use of color plots not shown here) indicates that, plotted in this manner, the event samples shown in Fig. 7 populate different regions in this space corresponding to differing assumptions regarding the deposition of energy and subsequent hadronization in the interaction.

early stages of relativistic AuAu interactions.

## REFERENCES

- [1] Further details of the STAR experimental program may be found in the STAR Conceptual Design Report, LBL PUB-5347, June 1992.
- [2] J. Rafelski, Phys. Lett. B262 (1991) 333; see also E. Andersen et al., Phys. Lett. B327 (1994) 433, and references therein.
- [3] X.N. Wang and M. Gyulassy, Phys. Rev. Lett., 68 (1992) 1480.



- [4] H1 Collaboration, DESY preprint 95-086, (ISSN 0418-7833).
- [5] K.J. Eskola, Jianwei Qiu, and Xin-Nian Wang, Phys. Rev. Lett. 72 (1994) 36.
- [6] T.A. Trainor and J.G. Reid, STAR Level-2 Trigger Algorithms Simulations and Performance, U. of Washington, unpublished.

# Some Recent Results in Au+Au collisions at AGS

Ziping Chen  
Dept. of Physics  
Brookhaven National Lab.  
Upton NY, 11973

## Abstract

Many interesting results have been obtained for Au+Au reactions at AGS. The basic information about the reaction dynamics comes from the hadronic distribution, and this article reviews the recent progress of these distributions in details. The proton rapidity distribution shows significantly increased stopping compared to lighter systems, implying the formation of a state of high baryon density. Unlike reactions at this energy induced by lighter heavy ions, at low  $m_t - m_0$  the proton invariant spectra deviate from a single exponential shape and become flat, while pion spectra are found to rise in this region, with the  $\pi^-$  spectra rising faster than the  $\pi^+$  spectra. The inverse slope parameter increases faster for particles of larger mass as the number of participant in the reaction increases, an indication of increased effect of radial expansion in central collision. Anti-proton yields have been measured recently, and unfortunately a comparison among current results from different experiments indicates discrepancy.

## I. INTRODUCTION

At AGS energies collisions of heavy ions provide a unique opportunity for studying nuclear matter far from its normal density. This condition is made possible because of the large degree of stopping of the incident nucleons. Hadron spectra which result from collisions of silicon beams with targets ranging from aluminum to gold indicate that the projectile deposits essentially all its incident energies in target larger than copper [1]. It is anticipated that an interaction region of larger volume, longer lifetime, and higher maximum density could be achieved by the collision of two truly heavy ions such as gold. With the installation of the Booster, the Brookhaven Tandem-AGS complex is capable of accelerating Au ions with energies up to 11.6 A·GeV/c. Some of the phenomena which have been considered to be associated with such large degree of stopping include effects of the compression and heating of nuclear matter, the production of a state of very high nucleonic density, and the achievement of thermal and chemical equilibrium. Most speculatively, it has been conjectured that a sufficiently high baryonic density can be attained to effect a phase change from the initial hadronic matter to a quark-gluon plasma. The basic information about the dynamics of these reactions comes from measurements of the transverse momentum and rapidity distributions of hadron spectra. In particular, the proton distributions allow the

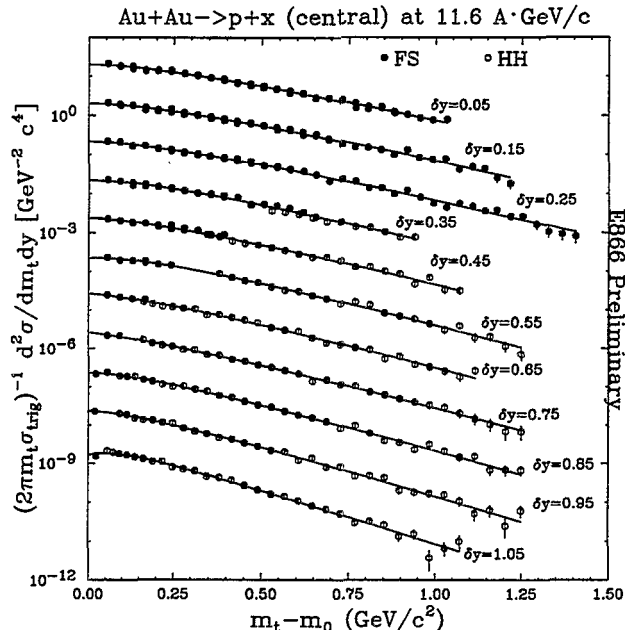


FIG. 1. E866 measured invariant cross-section divided by the trigger cross section for identified protons in different rapidity intervals as a function of transverse kinetic energy  $m_t - m_0$ . The bin width of the rapidity interval is 0.1, and  $\delta y$  is the distance of the measured rapidity of the spectra from the central rapidity  $y_{nn} = 1.6$ . The spectra are scaled down by a factor of 10 successively.

determination of the nucleonic stopping in the reactions. The article does not intend to cover all the topics studied by the heavy ion experiments at AGS, but rather concentrate on hadronic spectra of various particle species.

## II. RESULTS AND DISCUSSION

Figure 1 shows the measured invariant spectra of E866 for protons at different rapidity intervals. On the horizontal axis  $m_t$  is the so-called transverse mass defined as  $m_t = \sqrt{p_t^2 + m_0^2}$ , where  $p_t$  is the transverse momentum and  $m_0$  is the rest mass of the identified particle. On the vertical scale is the invariant cross-section divided by the trigger cross section  $\sigma_{trig}$  where  $\sigma_{trig} = 350$  mb corresponds to 6% of the total interaction cross section. The solid points are the measurement from the Forward Spectrometer while the open ones are from the large aperture spectrometer. Beam rapidity for Au ions at 11.6 A·GeV/c is 3.2. Since projectile and target are identical, the cross-section is therefore symmetric around the mid-rapidity,  $y_{nn} = 1.6$ . This symmetry is used to fold spectra of same  $\delta y$  together, where  $\delta y$  is the distance of the measured rapidity  $y$  from the central rapidity  $\delta y = |y - y_{nn}|$ . This experiment covers a rapidity range up to  $\delta y = 1.05$  with the projectile (or target) rapidity corresponds to  $\delta y = 1.6$ . The curves in the figure are the fits to the spectra with a two exponential function.

Proton spectra are also measured in E877, but in a different kinematic region close to the beam rapidity, as indicated in Figure 2 [2]. The vertical axis is slightly different from Figure. 1, and the spectra are once again displaced by a factor of 10. The inverse slope of

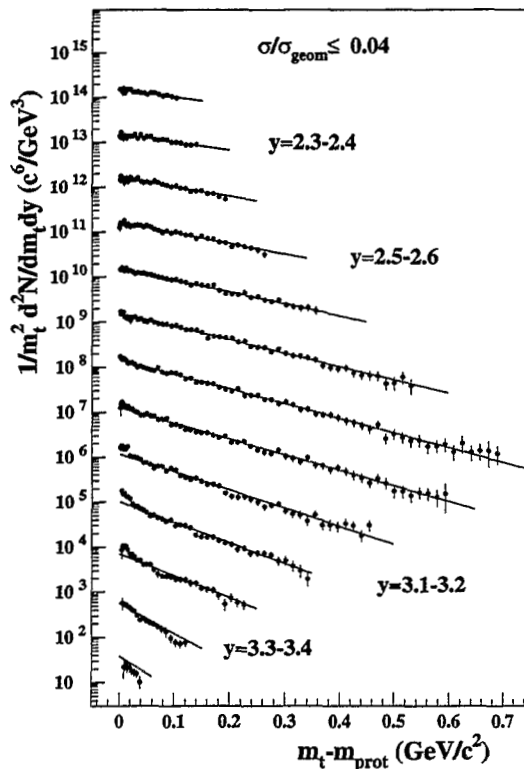


FIG. 2. The preliminary results of E877 measured spectra for identified protons in different rapidity intervals as a function of transverse kinetic energy  $m_t - m_0$ . The bin width of the rapidity interval is 0.1. The spectra are scaled up by a factor of 10 successively.

the spectra decreases as the rapidity increases. Around the beam rapidity,  $y_b = 3.2$ , another component appears in the spectra at low  $m_t$  which is even steeper in slope. These are the nucleons which do not go through any violent collision.

To inspect the shapes of the particle spectra in more detail, the measured particle distributions for  $\pi^+$ ,  $\pi^-$ , and protons are displayed in Figure 3 as a function of  $m_t - m_0$  for the central rapidity interval of  $0 < \delta y < 0.2$ , where the proton spectrum has been multiplied by 0.5 for clarity. Clearly, the proton spectrum is much flatter compared with those for pions, and it tends to bend down at low  $m_t - m_0$ . Hence unlike the proton spectra measured in reactions induced by lighter projectiles at similar incident energy per nucleon, namely p+A [3] and Si+A [4,5], the proton spectrum here cannot be described satisfactorily by a single exponential fit. The spectrum for  $\pi^-$  is also impossible to describe satisfactorily with a single exponential, since it shows a strong rise at low  $m_t - m_0$ . The rise at low  $m_t - m_0$  for  $\pi^+$  is much less. The rise of both pion spectra at the low  $m_t - m_0$  can be explained, in part, by the decay of resonances such as  $\Delta$ 's which tend to produce relatively low momentum pions [6]. Spectra for  $\pi^-$  increase faster than those for  $\pi^+$  in this region, and there are several reasons for this. The weak decay of the lambda produces relatively low momentum  $\pi^-$ , and some of these  $\pi^-$  survive the target position cut and show up in the low  $m_t$  region.

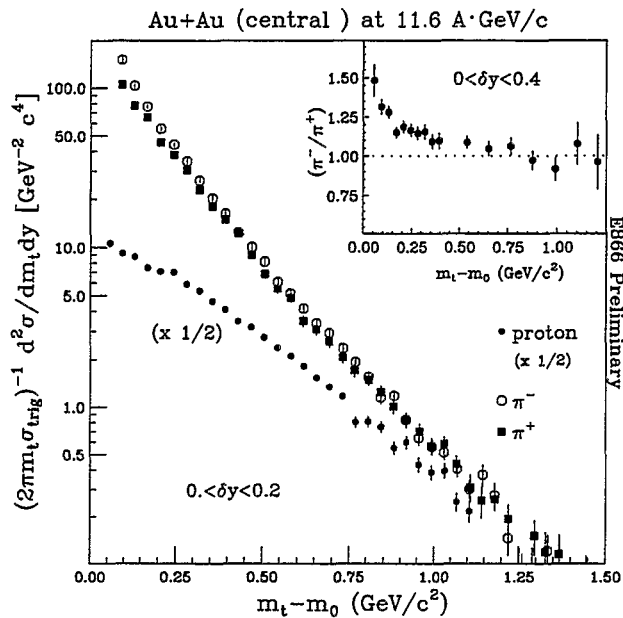


FIG. 3. E866 measured invariant cross-section divided by the trigger cross section for identified pions and protons in the rapidity interval  $0 < \delta y < 0.2$  as a function of transverse kinetic energy  $m_t - m_0$ . The spectra for protons, plotted as solid round points, is scaled down by a factor of 2. The open circles in the figure are the spectra for  $\pi^-$ , and the solid squares are that for  $\pi^+$ . The insert shows the ratio of  $\pi^-/\pi^+$  as a function of  $m_t - m_0$  in a larger rapidity interval,  $0 < \delta y < 0.4$ .

Also the production of low momentum pions through  $\Delta$ 's prefers  $\pi^-$  [7] because there are more neutrons than protons in the projectile/target. However, a major contributor to the difference between the  $\pi^-$  and  $\pi^+$  spectra may well be their Coulomb interaction with the rest of the co-moving media [8-10] which in average is positively charged. In the insert, the ratio  $(\pi^-/\pi^+)$  is plotted with a larger rapidity bin,  $0 < \delta y < 0.4$ , and the normalization is absolute. At high  $m_t - m_0$ , the ratio approaches one.

Figure 4 shows the same ratio,  $\pi^-/\pi^+$ , at the same rapidity in reactions of different centralities. The spectra are scaled up by a factor of 2 successively, and the horizontal lines are the corresponding positions for the ratio 1. In peripheral reactions, the ratio is flat over the entire  $m_t$  range and its value above one. This is consistent with the fact that there are more neutrons than protons in the colliding nuclei. For comparison, the ratio not only rises at low  $m_t$  but also falls down to unity at high  $m_t$  in central collisions. This is what would happen if the positive pions were pushed away and the negative pions were pulled in, for example by Coulomb interaction. So the centrality dependency of the  $\pi^-/\pi^+$  ratio provides support to the picture of pions interacting with the co-moving medium of positive charge in average.

The rapidity dependence of this ratio is also studied by E877, as illustrated in Figure 5 [2]. In this figure,  $\pi^-/\pi^+$  is plotted for events of the 4% most central reactions as a function of  $m_t - m_0$ . The rapidity interval are indicated in each panel. For rapidity interval smaller than the beam rapidity similar trend of the ratio is observed as in E866, and the  $m_t$  dependence of the ratio is weakened around the beam rapidity. Beyond beam rapidity, the

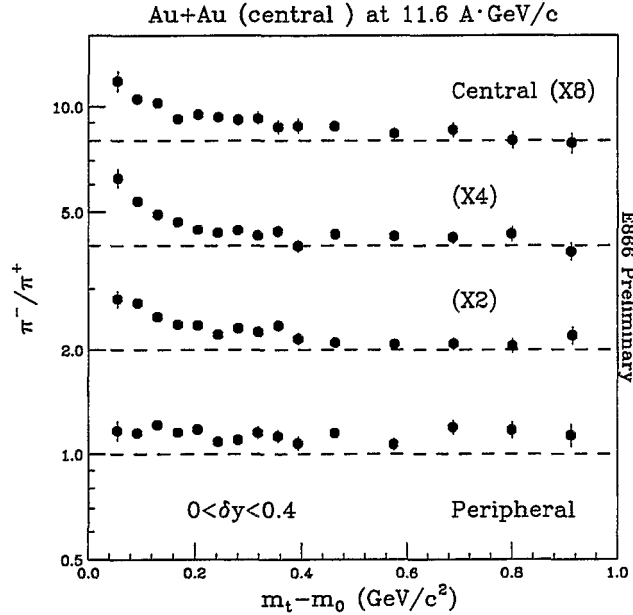


FIG. 4. The centrality dependence of the ratio,  $\pi^-/\pi^+$ , for Au+Au reactions at 11.6 A·GeV/c. The ratio is scaled up successively by a factor of 2 from the peripheral to the central. The data is from E866.

ratio is almost flat. Again, this is consistent with the picture discussed above, since most of the protons which provide the positive charge in the medium reside around the central rapidity as discussed later.

By integrating the parameterization of the spectra over  $m_t - m_0$  in each rapidity bin, one can obtain the distribution of particle yield over rapidity,  $dn/dy$ . The left panel of Figure 6 shows the  $dn/dy$  distribution for pions, kaons, and protons. The error bars shown in the figure are statistical only. The spectrum for protons is scaled up by a factor of 10. As indicated in the figure, the centrality for the different particle species is slightly different: 7% most central events for protons and pions, and 10% most central events for kaons and anti-protons. The overall shapes of the rapidity distribution for all the particles are similar. There are more  $\pi^-$  than  $\pi^+$ , as is expected from the low  $m_t$  rise of the  $\pi^-$ . Roughly there are a factor of 5 more  $K^+$  than  $K^-$ . With a limited statistics for anti-protons, its yield is presented within a big bin. On the right hand side of the figure, the mean transverse momentum is plotted for the various particles. The mean  $p_t$  for protons is very high and peaked around the central rapidity. Anti-protons have similar, though slightly lower, value as protons. The mean  $p_t$  for  $\pi^+$  is a little higher than that for  $\pi^-$ . Both kaons have similar  $p_t$ , and their values are in between of those for protons and pions.

Figure 7 shows the rapidity distributions for protons and pions from the p+p collisions to the central Au+Au reactions. The horizontal axis is the rapidity normalized to the beam rapidity, and the vertical axis is the yield,  $dn/dy$ . For protons, the rapidity distribution for p+p has two peaks around the projectile and target rapidities respectively, indicating that most of the protons keep traveling at almost the same rapidity before and after the collision, little stopping by the reaction. The situation does not change significantly for

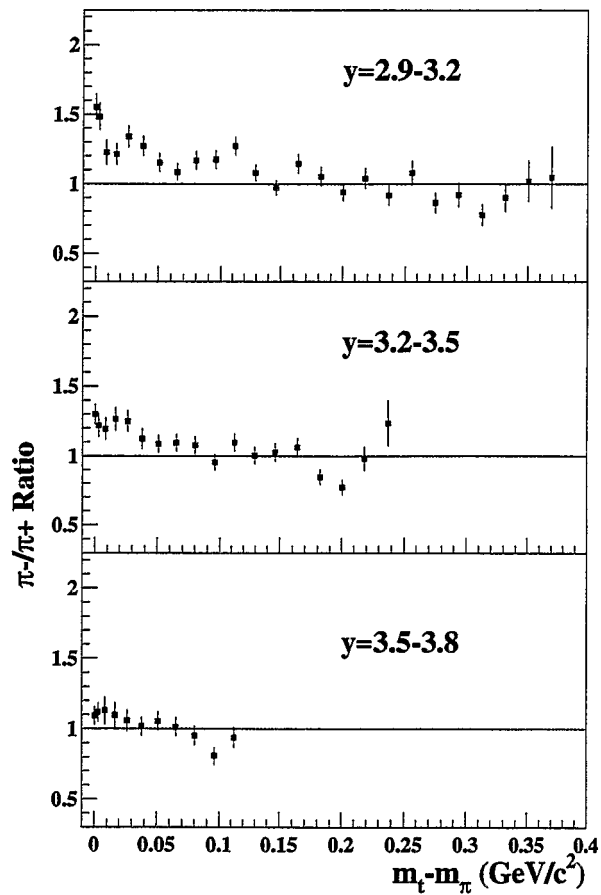


FIG. 5. The  $\pi^-/\pi^+$  ratio as a function of  $m_t - m_0$  in different rapidity bins. The figure is a preliminary result from E877.

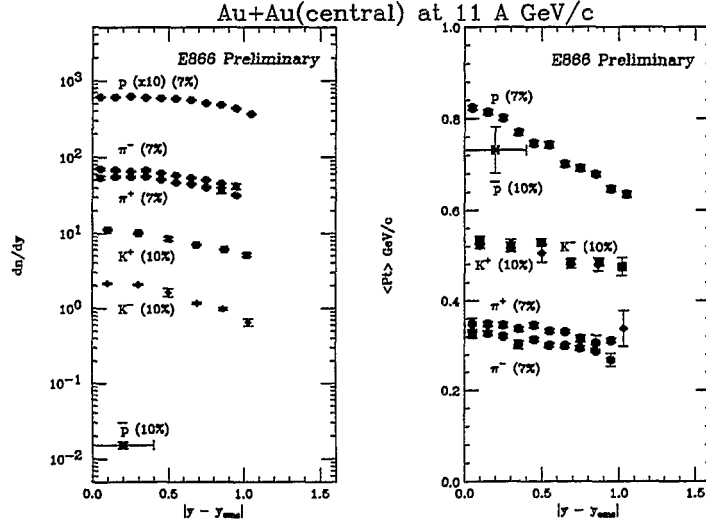


FIG. 6. The rapidity distributions of the yield (left panel) and mean  $p_t$  (right panel) for protons, pions, kaons, and anti-protons.

peripheral collisions of Al+Si, an almost symmetric system, and in central Al+Si there is significant shifting in rapidity away from the projectile and the target, but a hole in the central rapidity still exists. Only in the central Au+Au reactions, due to the large size of the gold ions, protons pile up at mid-rapidity, with the hole in the middle filled up, confirming the expectation of a large amount of stopping and concomitant high baryon density in central Au nuclei collisions.

Figure 8 shows the  $m_t$  spectra for deuterons at  $y=1.3$  for centralities ranging from the peripheral to the central. The spectra again are scaled up by a factor of 2 successively. It is clear that the spectrum in the central reactions is much flatter than that in the peripheral collisions. The straight lines are an attempt to fit the spectra with a single exponential. As discussed before, in general particle spectra deviate from a single exponential parameterization in central Au+Au reactions, so the fit in the figure is intended to be qualitative to discern any systematic trend of the spectrum shape for different centralities and/or reactions. This systematic comparison is summarized in Figure 9, where the inverse slope parameters for pions, protons, and deuterons are plotted for a combination of reactions at various centralities. The horizontal axis is the number of participants estimated from the centrality cut of the reactions. The solid points are from Au+Au reactions at 11.6 A·GeV/c, the open squares are data from p+Au reactions at 14.6 GeV/c, and the open diamond is from central Si+Au reaction at 14.6 A·GeV/c. For pions, there is little change of the inverse slope parameter from the p+Au reactions to that of the central Au+Au reactions. The inverse slope parameter increases for protons as the number of participants in the reactions increases, and the increase is most pronounced for deuterons. This is consistent with the picture that radial expansion exists after the high density stage is reached. In this picture, qualitatively speaking the larger the mass of a particle, the larger the transverse momentum



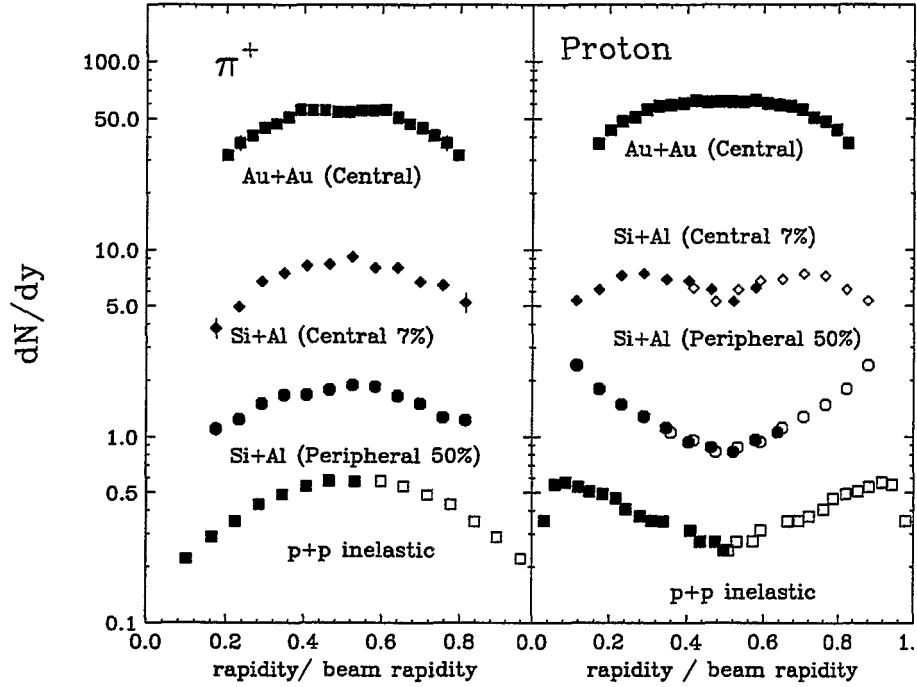


FIG. 7. Rapidity distribution of particle yield for protons and  $\pi^+$  from p+p reactions to the central Au+Au collisions. The rapidity on the x-axis is normalized to the beam rapidity.

it gains from the radial expansion – hence higher inverse slope parameter in its spectrum [11,12].

In the high baryon density environment, the final yield of the anti-proton is sensitive to many factors, both in its production and in its annihilation. The interesting question is whether the high baryon density environment would modify the free-space mechanism of production and annihilation in the absence of the high density. Considerable effort has been put in to the experimental measurement of the anti-protons yield, and now results are available in a large kinematic coverage. E866 is the experiment which covers the central rapidity for anti-proton with a reasonable range in  $m_t - m_0$ . Figure 10 shows the anti-proton spectra around the central rapidity for three centrality ranges. The solid points are from E866 experiment, the open points from E878, and the cross from E864. The yields from E866 increase slowly as more central reaction is selected. As far as the shape is concerned, it is exponential for the peripheral reactions, and the low  $m_t$  end of the spectrum starts to bend down, like protons, for more central reactions. In comparison with models such as ARC [13], a shielding has to be introduced to reduce the annihilation in order to reproduce the final yield [14]. Unfortunately, discrepancy exists among the experimental data, and as an example Figure 10 summarizes the situation. Since data from E878 were taken in 1993 run where the beam momentum was 10.7 A·GeV/c, compared to a beam momentum of 11.6 A·GeV/c for the other two experiments, a scale up factor of 1.4 was introduced to facilitate a direct comparison. The factor 1.4 comes from an interpolation of anti-proton production in p-p reactions. In peripheral reactions, data from E878 is consistent with that of E866, and it gradually becomes somewhat lower in central reactions. One possible explanation for

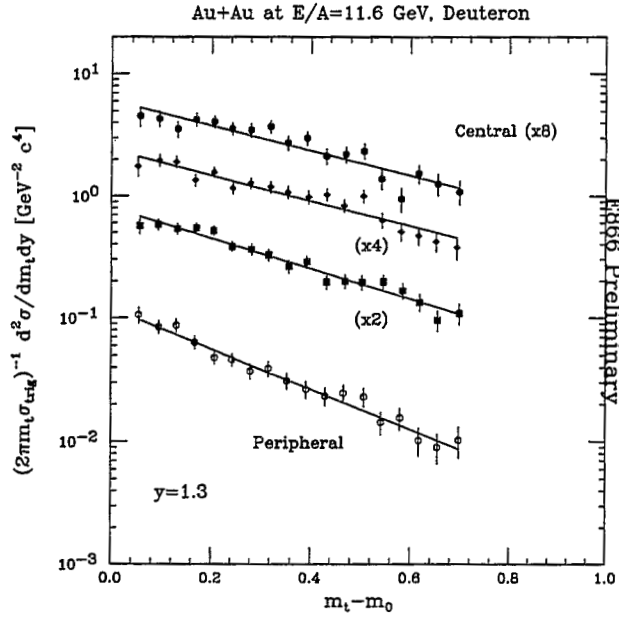


FIG. 8. Centrality dependence of the deuteron  $m_t$  spectra at rapidity  $y=1.3$ . The spectra are scaled up by a factor of 2 successively as more central events are selected.

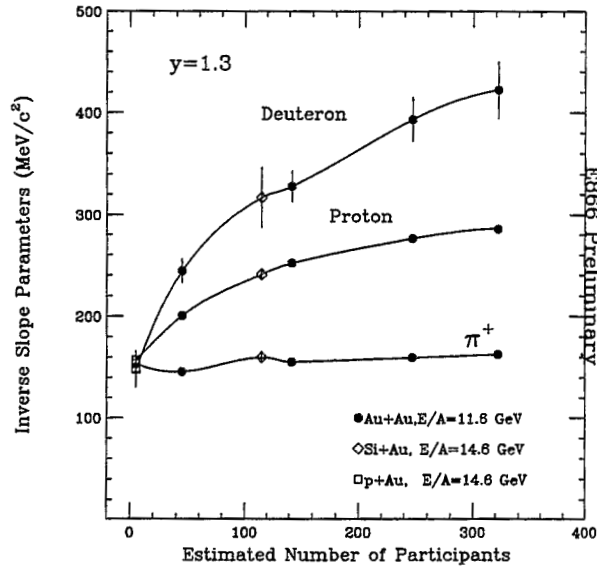


FIG. 9. Inverse slope parameters as a function of the estimated number of participants in the reactions for pions, protons, and deuterons. The data included in the figure are from p+Au reactions at 14.6 GeV/c, Si+Au reactions at 14.6 A-GeV/c, and Au+Au reactions at 11.6 A-GeV/c.

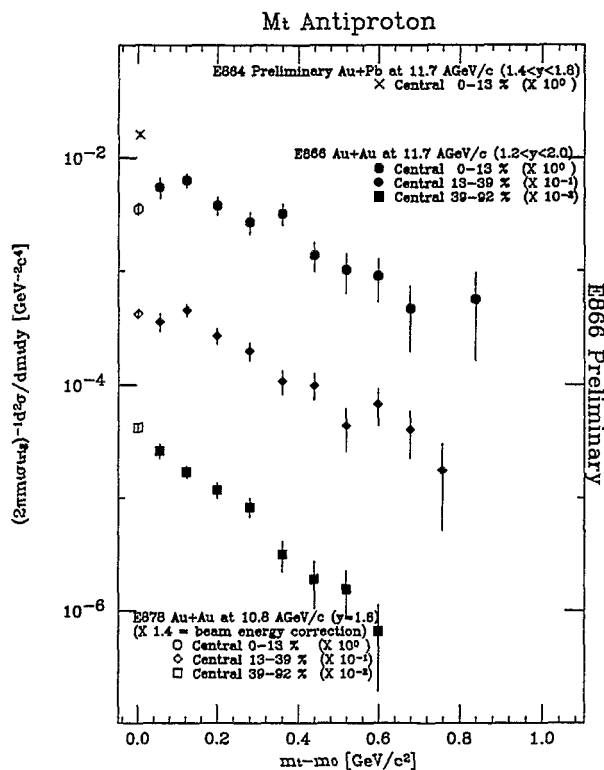


FIG. 10. Comparison of anti-proton yields among E866, E878, and E864 for three selected centralities. The solid points are from E866, the open points from E878, and the cross from E864. In central collision, the discrepancy between E864 and E878 is obvious (see text for more details).

this could be that the centrality device in E878 is not effectively discriminating peripheral collisions from its central events, lowering its anti-proton yields in central collisions as a result. On the other hand, data from E864 seems high compared with that of E866 in the central collisions, but not in contradiction. The contradiction shows up when data from E864 and E878 are brought together for comparison, and there is about a factor of 4 difference between these two measurements. It was pointed out that the difference could be due to the anti-lambda contribution to E864, which accepts essentially all the anti-protons from the decay of anti-lambda while E878 takes none. Based on this assumption, one could estimate the yield of anti-lambda in the reactions, and the anti-lambda to anti-proton ratio was concluded to be  $\bar{\Lambda}/\bar{p} = 5.9 \pm 2.5$  [15] at midrapidity near  $p_t = 0$ . This is a very large ratio, and it is worth to bear in mind that  $K^-$  yield from E864 is also somewhat high in comparison with that of E866.

### III. SUMMARY

In summary, many new results have become available in Au+Au reactions at AGS energies. From the proton rapidity distribution it is concluded that a state of high baryon density has been achieved in central Au+Au reactions. A systematic comparison of inverse slope parameters for different particle species points out that radial expansion exists when

the high density matter starts to disintegrate. More systematic effort on the anti-proton analysis is needed in order to resolve the current discrepancy among results from different experiments.

#### IV. ACKNOWLEDGMENT

This work was supported by the U.S. Department of Energy under contracts with BNL (DE-AC02-76CH00016). The author likes to thank Dr. S. Kahana for the invitation to participate in the workshop. It is the author's pleasure to thank the E802 collaboration for making excellent progresses in data analysis. It is also an appropriate opportunity for the author to thank people in BNL-HIRG group, especially Drs. C. Chasman and F. Videbaek, for help in many ways. At last the author likes to acknowledge Dr. T. Hemmick and Mr. T. Piazza for providing postscript files of E877 results.

#### REFERENCES

- [1] E-802 Collaboration, T. Abbott et al., Phys. Lett. B **197**, 285 (1987).
- [2] T. Piazza, Private communication.
- [3] E-802 Collaboration, T. Abbott et al., Phys. Rev. D **45**, 3906 (1992).
- [4] E-802 Collaboration, T. Abbott et al., Phys. Rev. Lett. **64**, 847 (1990).
- [5] E-802 Collaboration, T. Abbott et al., Phys. Rev. C **50**, 1024 (1994).
- [6] R. Brockmann et al. Phys. Rev. Lett. **53**, 2012 (1984).
- [7] R. Stock, Phys. Rep. **135**, 259 (1986).
- [8] J. P. Sullivan et al. Phys Rev C **24** 1499 (1981).
- [9] H. Böggild et al. Phys. Lett. B **372** 339 (1996).
- [10] M. Gyulassy and S.K. Kauffmann, Nucl. Phys. A **362** 503 (1981).
- [11] P.J. Siemens and J. O. Rasmussen, Phys. Rev. Lett. **42**, 880 (1979).
- [12] R. Mattiello et al., Phys. Rev. Lett. **74**, 2180 (1994).
- [13] S. Kahana et al. Proceedings of HIPAGS '93, page 26, edited by G. Stephans, S. Steadman, and W. Kehoe (MITLNS-2158).
- [14] B.S. Kumar et al. Nucl. Phys. A566 439c-442c (1994).
- [15] J.G. Lajoie et al. Proceedings of HIPAGS'96, edited by S. Bennett and C. Pruneau (to be published).

# The Brahms Experiment at RHIC

Flemming Videbæk

*Physics Department, Brookhaven National Laboratory  
Upton, NY 11973-5000, U.S.A.*

## Abstract

The BRAHMS experiment is designed to measure semi-inclusive spectra of charged hadron over a wide range of rapidity. It will yield information on particle production, both at central rapidity and in the baryon rich fragmentation region. Examples of measurements for soft as well as for hard physics are presented.

## I. INTRODUCTION

The main motivations for the RHIC experiments are the search for and the investigation of the quark-gluon plasma. It is thought that QGP can be created in high energy heavy ion collisions under a broad range of experimental conditions bounded in one direction by high baryon densities and in the other by zero baryon density and temperatures above the critical temperature. At RHIC with energies  $\sqrt{s} = 200 \text{ GeV}/c$  per nucleon pair, which is above the stopping regime presently being explored at AGS and SPS, a baryon poor region with a high energy density is expected to be created at mid-rapidity. The region near the initial nuclei will be baryon rich at relative high temperature. This gives experimental opportunities to study both regimes at RHIC and search for the quark-gluon plasma under several different conditions.

The Broad Range Hadron Magnetic Spectrometers (BRAHMS) experiment has been designed to gather basic information in heavy ion reactions on momentum spectra and yields for various emitted particles as function of transverse momenta,  $p_t$ , and rapidity,  $y$ . These yields as function of rapidity are important indicators of the densities reached in the collisions and of the produced entropy. The spectral shapes and their  $y$ -dependence reveal the reaction dynamics and the degree of thermalisation attained. The high  $p_t$  parts of the spectra carry information from the early times in the reaction. The centrality measurements are an integral part of the experiment, and systematic studies are needed to establish the reaction dynamics.

The BRAHMS spectrometers are small solid-angle devices so the measurements will be semi-inclusive; i.e., the average spectra for given event classes as determined by the centrality detectors will be measured. This contrasts to the large RHIC experiments where event-by-event information can be collected, but BRAHMS has a unique place in the RHIC experimental program with its wide coverage in rapidity and  $p_t$ . The coverage is essentially limited by the accelerator structures, the size of the experimental halls, and the modest budget for BRAHMS.

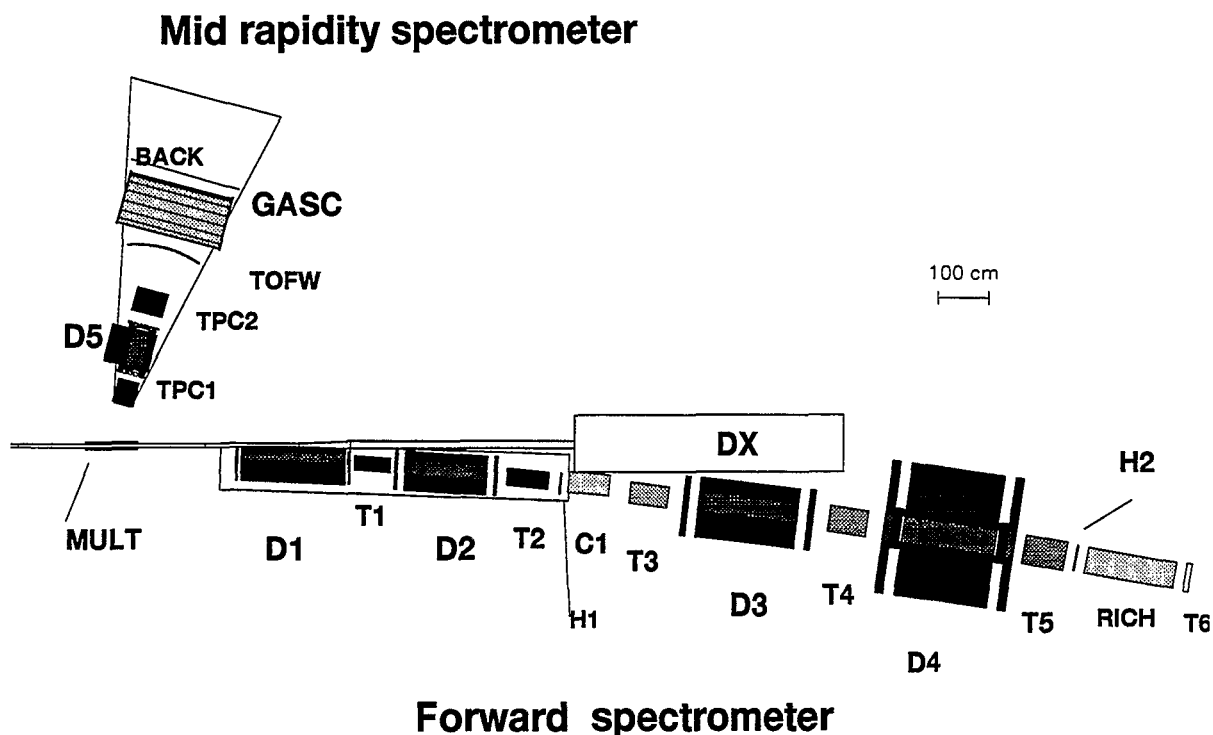


FIG. 1. Top view of spectrometers. The labelled detector elements are described in the text.

## II. THE SPECTROMETERS

This section gives only a very brief description of the BRAHMS detectors. For more detailed information the reader is referred to [1-4]. A top view of the two moveable spectrometers is shown in figure 1.

The BRAHMS experiment is designed to measure well identified charged hadrons ( $\pi^\pm, K^\pm, p^\pm$ ) over a wide range of rapidity and transverse momenta at all energies and beams available at RHIC. The very different experimental conditions, momenta, and particle densities at mid-rapidity and forward angles has lead to the design with two moveable magnetic spectrometers. The Mid-Rapidity Spectrometer (MRS) covers the angular region  $30^\circ \leq \Theta \leq 95^\circ$  ( $-1 \leq \eta \leq 1.3$ ) and the forward spectrometer (FS) the region  $2.3^\circ \leq \Theta \leq 30^\circ$  ( $1.3 \leq \eta \leq 4.0$ ). FS consists of 4 dipole magnets (D1-D4), two time projection chambers (T1,T2) and three drift chamber packages (T3-T6). The particle identification is done by combining time-of-flight measurements in the hodoscopes H1 and H2 with measurements in the threshold Cherenkov counter C1 and the Ring Imaging Cherenkov Counter (RICH). This allows for particle identification in the momentum range 1-20 GeV/c in the forward spectrometer. The mid-rapidity spectrometer has two TPCs (TPC1 and TPC2), a dipole magnet (D5) for momentum measurements, a time-of-flight wall (TOFW), and a segmented gas Cherenkov detector (GASC) for particle identification in the momentum range  $p \leq 5$  GeV/c. The momentum resolution is typically  $\delta p/p \leq 0.01p$ , which is sufficient for tracking considerations and the spectral measurements. A set of beam-beam counters provide the

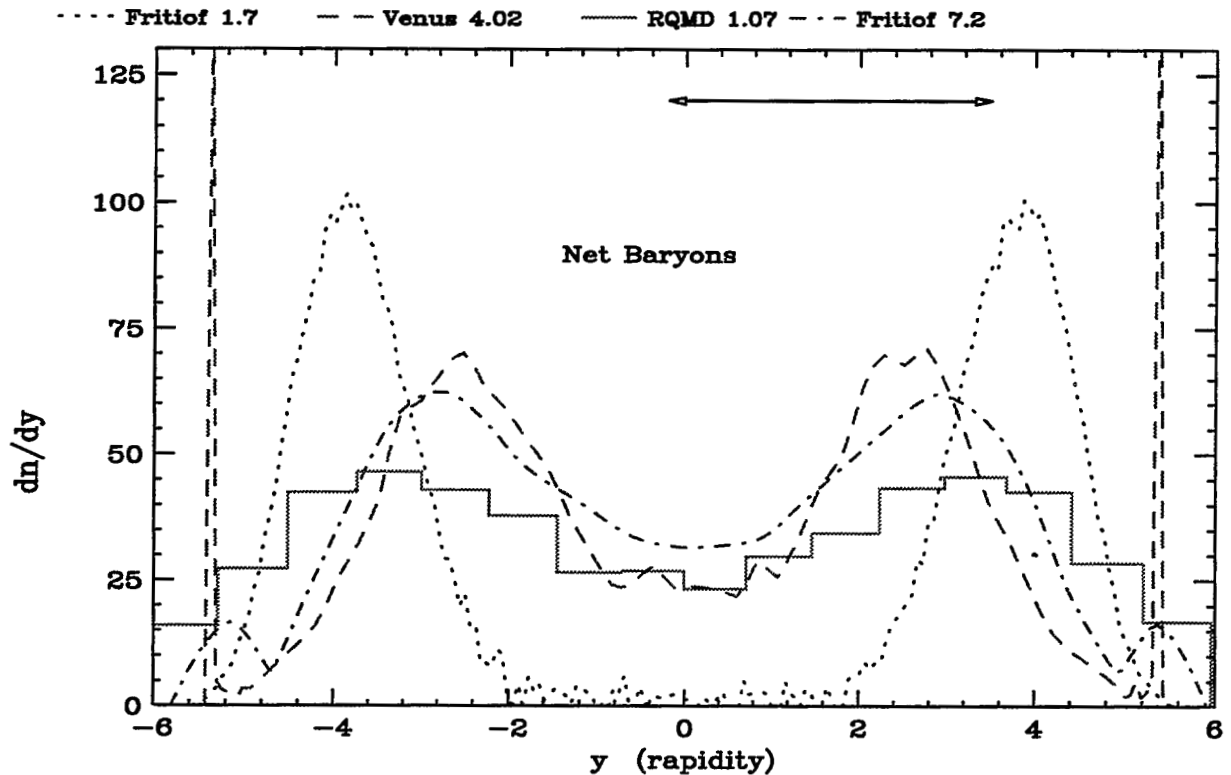


FIG. 2. Predicted rapidity density distributions for central Au+Au reactions using different models as indicated by the linetype. The rapidity range to studied by BRAHMS is indicated by the arrows.

initial trigger and vertex information as well as the start time for the time-of-flight measurements. The silicon multiplicity array will be used to characterize the centrality of the collisions by measurements of the charged particle multiplicities in the region  $-2.5 \leq \eta \leq 2.5$ .

### III. SOFT HADRON MEASUREMENTS

The dominant part of the particle spectra is the soft part with transverse momenta  $p_t \leq 1\text{GeV}/c$ . Particle spectra have been studied in elementary pp ( $p\bar{p}$ ) over a wide range of energies covering the RHIC energy regime. Even with this knowledge in hand it is not trivial to extrapolate to nucleus-nucleus collisions. It has been learned from heavy ion reactions at AGS and SPS, see e.g. [5], that the heavy ion collisions cannot be considered a super-position of elementary nucleon-nucleon collisions, but that multiple collisions and collective effects are important to a proper description of the experimental data. At the much higher energies considered here it is likely that additional many-body effects, even for a pure hadronic description, have to be taken into account. Understanding of the reaction mechanism will clearly come from systematic studies of pp to p-nucleus and nucleus-nucleus reactions.

One of the basic questions is what is the amount of stopping, i.e. the mean rapidity

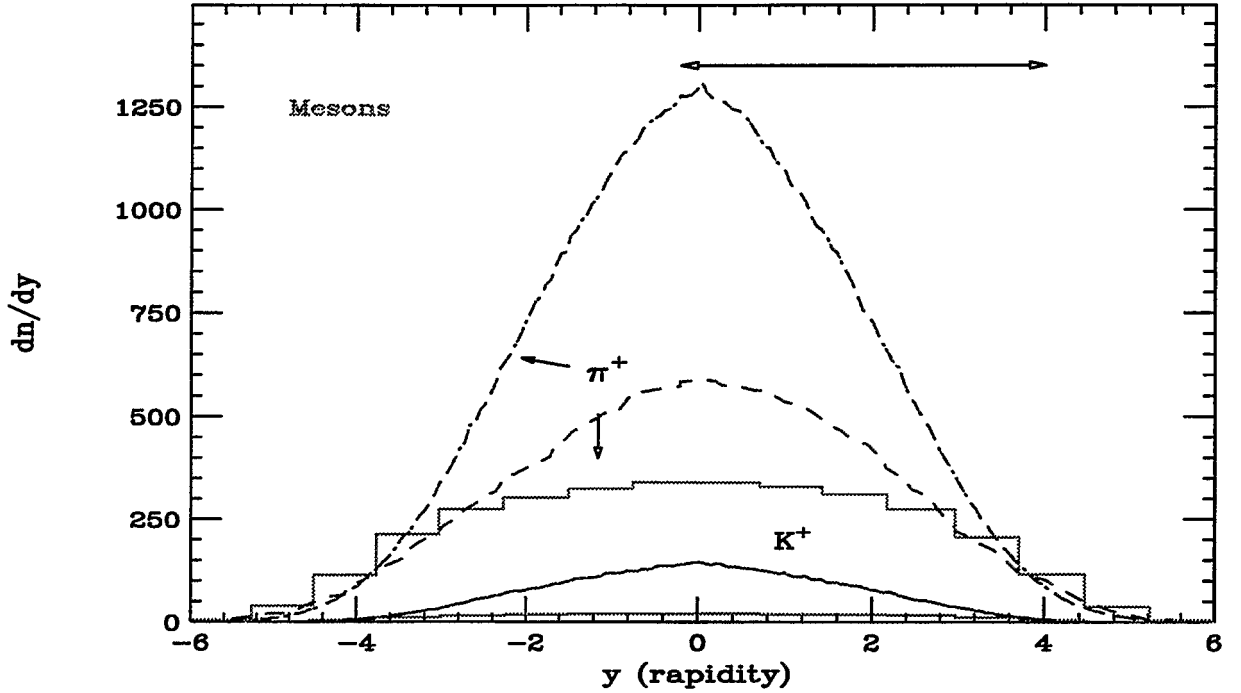


FIG. 3. Predicted rapidity density distributions for  $\pi^+$  and  $K^+$ .

shift of projectile nucleons, see e.g. [6], and how high is the net baryon density in the central region of Au+Au collisions. In fig. 2 is shown the prediction for the net baryon density  $\frac{dn}{dy}$  for 4 different models successfully used to describe pp and nucleus-nucleus reactions at lower energies. These are Fritiof 1.7 [7], Fritiof 7.2 [8], Venus [9], and RQMD [10]. The predicted mean rapidity losses are in the range of 1.7-3.1. The coverage of BRAHMS is shown by the arrow. Even though the fragmentation region in the view of pp (i.e. 4-5) is outside the range, the measurements do cover the region  $y \leq 3.8$  sufficiently to map and study the stopping in nucleus-nucleus collisions at RHIC.

The predictions for meson production are given in figure 3. The experiment will essentially cover the complete distribution for  $\pi$  and K, and can address details of the shape and particle yields. The predictions vary almost a factor of 4 at mid-rapidity, so with this in mind the spectrometers were designed to handle the highest expected values.

The correlation of like-bosons as a function of the relative momenta can provide a measure of the space-time extent of the emission source [11,12]. Pair correlation coupled with single-particle measurements is thought to help in providing a good understanding of the dynamics which control the evolution from the initial hot dense phase to the system at freeze-out. A detailed description of the HBT capabilities can be found in [4], in particular regarding the measurements and sensitivity in the mid-rapidity spectrometer. Here is shown an example of the kind of measurement which can be done at the higher rapidities utilizing the Forward Spectrometer. The pion correlations were simulated using a simple gaussian correlation function  $C(q) = 1 + \lambda e^{-(q^2 R^2 + q_0^2 \tau^2)}$ , where  $q$  is the magnitude of the relative 3-momentum,  $R$  the source radius,  $q_0$  the relative energy, and  $\tau$  the lifetime parameter. Here  $\tau$  was explicitly set to 0. Pairs of pions were accepted through the spectrometer at  $10^\circ$  with an acceptance of  $1 \leq p \leq 3$  GeV/c. The extracted correlation function for 100,000  $\pi^+$  pairs is shown



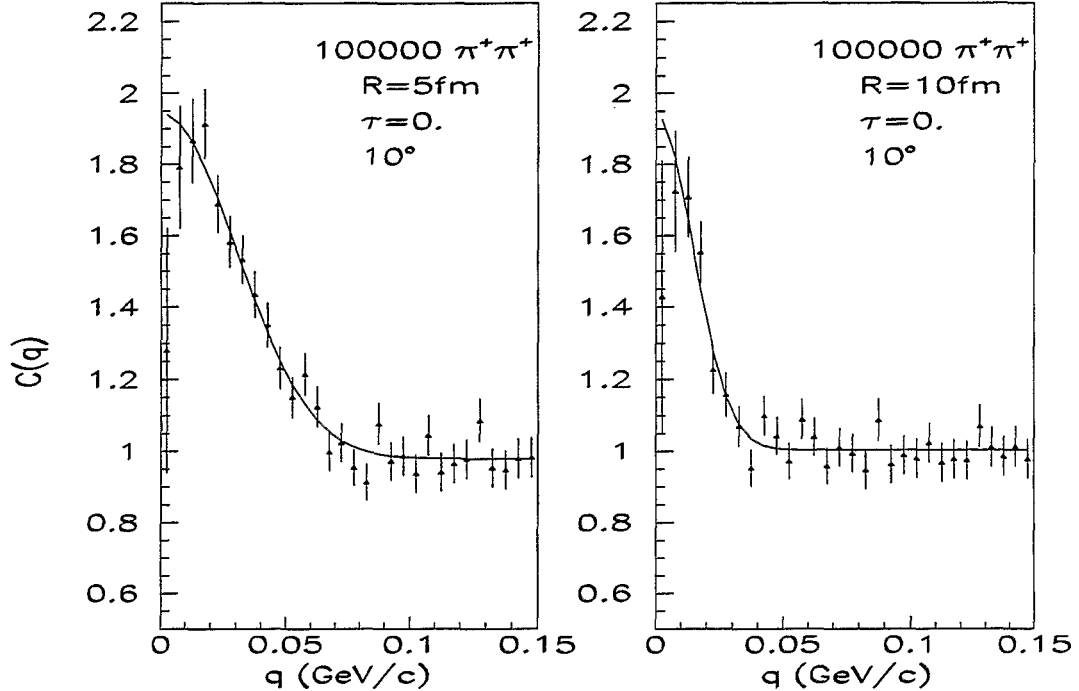


FIG. 4. Estimated results of two-particle correlation measurements at 10 deg.

for two representative samples with  $R=5$  and  $10$  fm. The simulation illustrates that for a limited range of rapidity and momenta the forward spectrometer has sufficient resolution and two-particle separation to make modest measurements of pion-correlation functions.

#### IV. HIGH $P_T$ MEASUREMENTS

In contrast to the heavy ion experiment carried out so far at AGS and SPS, initial hard scattering processes are important for the reaction dynamics at RHIC. The importance is known from the mini-jet production at ISR energies and as evident in the inclusive hadron spectra measured from  $\sqrt{s} = 50 - 1800$  GeV in p+p reactions. A hard component is observed for  $p_t \geq 1.0$  GeV/c. This hard component has two aspects of consequence in heavy ion reactions. The initial fast parton scattering contribute significantly to the formation and equilibration of a hot dense system [13] and to the particle production. Nuclear effects such as jet quenching and gluon shadowing are expected and can be studied in inclusive mini-jet distributions [15]. The prediction from the HIJING model and the Parton Cascade model [14] of the total charged particle rapidity distributions on this is shown in fig.5. The various physical processes are turned on successively. The parton shadowing is determined mainly from the gluon structure function, and the quenching is dominated by the gluon brehmsstrahlung energy loss in the nuclear medium. It is observed that depending on the rapidity region the different processes contribute with different weights. Likewise,  $p_t$  dependencies are present. Measurements at different rapidities, and in a  $p_t$  in a range as large as possible, up to 5-6 GeV/c, will be a mean to experimentally determine constrains on the various mechanisms. Comparison between different collision systems will also be important

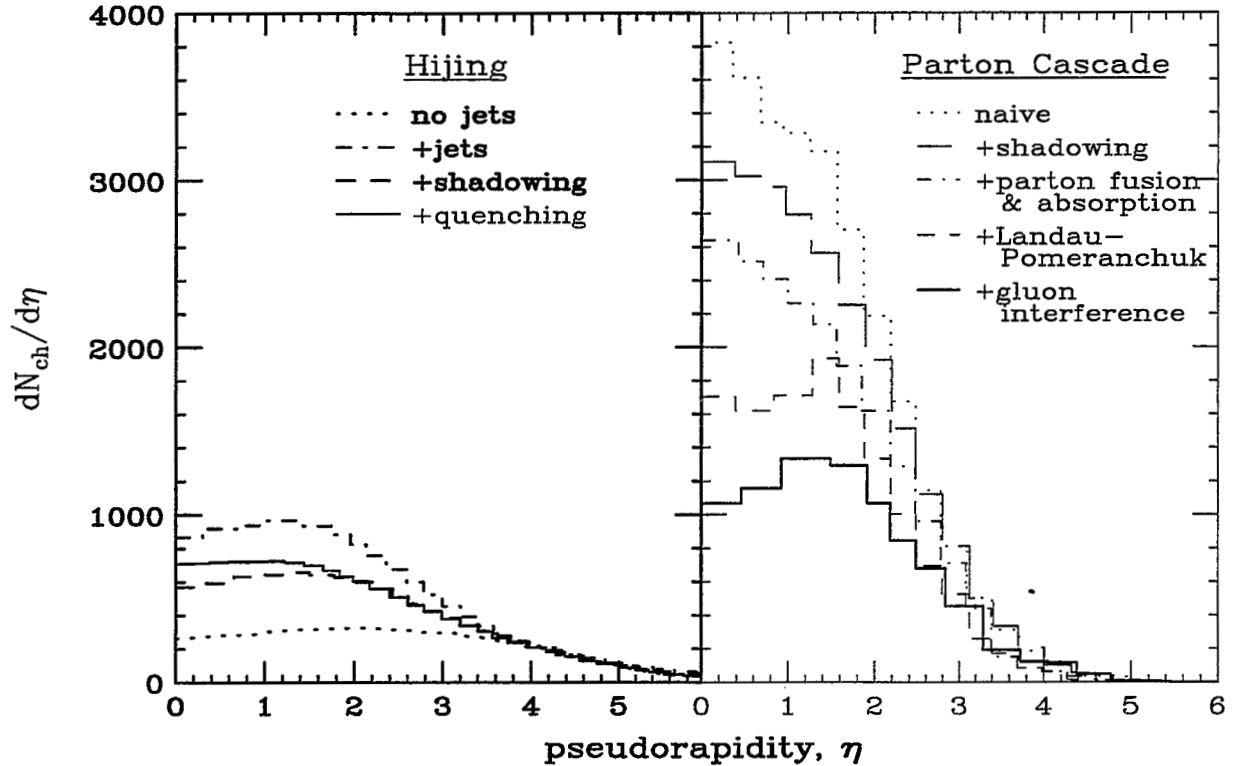


FIG. 5. Prediction for  $dn/d\eta$  for charged particle distributions

for this task.

As an example of the feasibility of this kind of studies, a simulation was performed for a measurement of  $\pi^+$  at rapidity 2 in central Au+Au collisions. A sample of pions from a distribution with inverse slope parameter of 170 MeV (in  $m_t$ ) and a  $\frac{dn}{dy}$  of 200 was fed through the GEANT simulation of the forward spectrometer and the  $p_t$  spectrum reconstructed in two settings of the magnetic field. The resulting  $p_t$  spectrum which can be obtained in about 1 week of running is displayed in fig.6. In about another week the measurements can be extended to about 6 GeV/c with similar statistics using larger bins in  $\Delta p_t$  of .5 GeV/c. This demonstrates that high quality spectra can be collected up to rather high values of  $p_t$ . It should be stressed that these measurements are for identified hadrons, and thus can also be done for kaons, protons, and anti-protons, studying the flavor dependence.

## ACKNOWLEDGMENTS

This paper has presented the design and some expectations of the BRAHMS spectrometer, which is supported by a collaboration consisting of about 35 physicist from BNL, CRN-Strasbourg, The Niels Bohr Institute, Texas A&M, New York University, Harbin Technical University, U.C. Berkeley Space Sciences Laboratory, University of Kansas, and Jagelloian University-Krakow This work was supported by the US Department of Energy under contract DE-AC02-76CH00016.

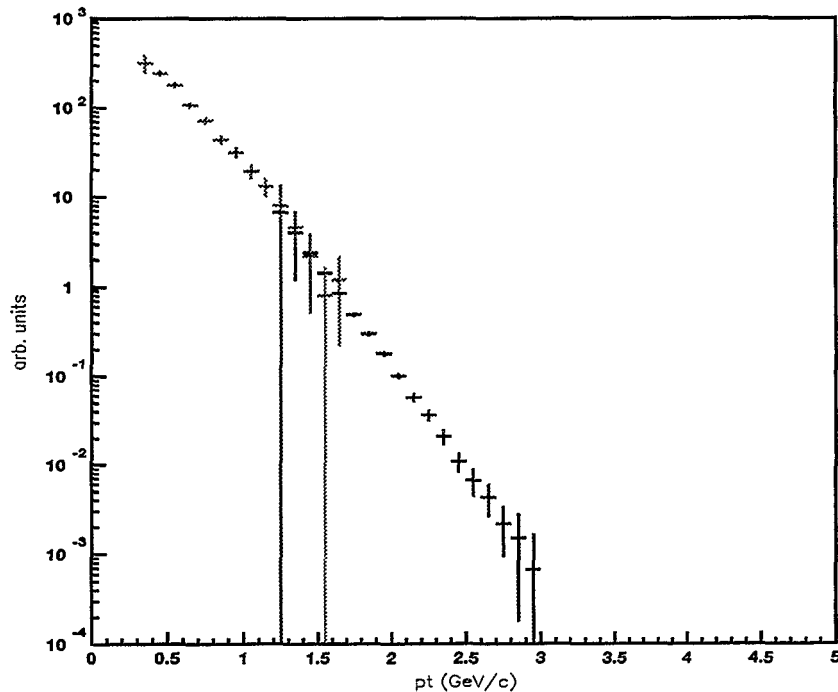


FIG. 6. Predicted  $p_t$  spectrum for  $\pi$  at  $y=2.0$  as measured in about 1 week of running for Au+Au central collisions.

## REFERENCES

- [1] BRAHMS conceptual Design Report, October 1994, BNL-62018; WWW URL <http://rsgi01.rhic.bnl.gov/export1/brahms/WWW/brahms.html>
- [2] F.Videbæk, Nucl. Phys. A566 (1994) 299c
- [3] B. Moskowitz, Proceedings of the Pre-Conference Workshop QM95.
- [4] D. Beavis, Proceedings of the Pre-Conference Workshop QM95.
- [5] Z.Chen (these proceedings), B.Jacak (these proceedings) and references therein.
- [6] F.Videbæk and Ole Hansen, Phys. Rev. C52 (1995) 2684
- [7] B.Andersson, G.Gustafson and B.Nielsson-Almquist, Nucl.Phys.B281(1987)289
- [8] H.Pi, Comp. Phys. Comm 71 (1992) 173
- [9] K.Werner Z. Phys. C42 (1989) 85
- [10] Th.Schönfeld, H.Stöcker, W.Greiner and H.Sorge, Mod.Phys.Lett A8 (1993) 2631
- [11] G.Goldhaber *et al.* Phys.Rev.120(1960) 300.
- [12] F.B.Yano and S.E.Koonin, Phys. Lett. 78B (1978) 556
- [13] E.Shuryak. Phys. Rev. Lett. 68 (1992) 3270.
- [14] K.Geiger Phys. Rev. D47 (1993) 133
- [15] X.N.Wang and M.Gyulassy, Phys. Rev. D44 (1991)3501; X.N.Wang these proceedings.

# Early Results from Minimax: A Disoriented Chiral Condensate Search at the Tevatron

C. C. Taylor

*Department of Physics*

*Case Western Reserve University*

*Cleveland, Ohio 44106-7079, USA*

Representing the MiniMax Collaboration<sup>1</sup>

We present early results from an experimental search (T-864, MiniMax) for Disoriented Chiral Condensate (DCC) at the Fermilab Tevatron Collider at  $\sqrt{s} = 1.8 \text{ TeV}$ . In order to analyze the data on joint charged-particle/photon distributions, we have identified robust observables with many desirable properties. These observables are insensitive to many efficiency corrections and the details of the modeling of the primary pion production mechanisms while maintaining sensitivity to the production of DCC, as opposed to the generic, binomial-distribution, partition of pions into neutral and charged species. The formalism is applied to the MiniMax data.

## I. DISORIENTED CHIRAL CONDENSATES

There has recently been renewed interest in semiclassical mechanisms of pion production in high-energy collisions of hadrons and of heavy ions. [2] One hypothesis in particular is that pieces of strong-interaction vacuum with an unconventional orientation of the chiral order parameter may be produced in high energy collisions. This disoriented chiral condensate (DCC) is then supposed to decay into a coherent semiclassical pion field having the same chiral orientation.

The primary signature of this mechanism is the presence of large, event-by-event fluctuations in the fraction,  $f$ , of produced pions that are neutral. Conventional mechanisms of particle production, including those used in standard Monte Carlo simulations, predict that the partition of pions into charged and neutral species is governed by a binomial distribution which, in the limit of large multiplicity, leads to a sharp value of  $f \approx 1/3$ . We refer to this as *generic* pion production. On the other hand, for the decay of a pure DCC state the distribution of neutral fraction is very different,  $p(f)df = 1/(2\sqrt{f})df$ , in the limit of large multiplicity. Some other production scenarios involving the common feature of coherent final states lead to identical  $f$  distributions.

Theoretical considerations, together with the interpretation of some reported cosmic ray phenomena [3] in terms of DCC, suggest that the one should look in the forward direction in high energy collisions at Tevatron energies. In addition, DCC pions are expected to be of comparatively low  $p_t$ .

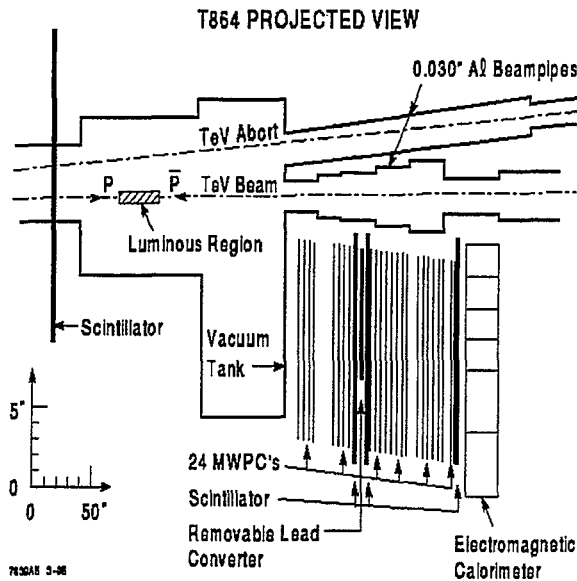


Figure 1: The MiniMax Detector

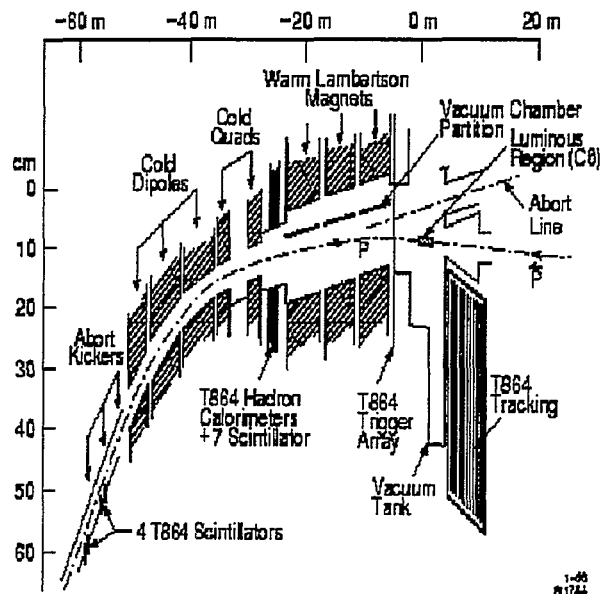


Figure 2: Upstream Instrumentation

## II. THE MINIMAX DETECTOR

With the above considerations in mind, the MiniMax collaboration (Fermilab T-864) has carried out an exploratory search for DCC at the C0 collision area of the Tevatron collider. Proposed in April 1993, the experiment completed running in January 1996.

Figure 1 shows the layout of the detector in the vicinity of the collision region.

Charged particles are identified by reconstructing tracks through a telescope of 24 MWPC's which have an acceptance of radius  $r \approx 0.65$  in  $(\eta, \phi)$  space, centered on  $\eta = 4.1$ . Gamma rays are identified by reconstructing tracks originating from conversions in a  $1 X_0$  lead converter which can be remotely inserted after the eighth chamber of the tracking telescope. In addition, an electromagnetic calorimeter is located behind the last chamber. The wire chambers are mounted behind a thin (0.25 in) window in the large vacuum tank. Scintillator is placed on the far side of the vacuum tank, behind the lead converter, and immediately in front of the electromagnetic calorimeter. Coincidences between the arrays, in time with the beam passage, provide the trigger. Because of substantial interactions of forward secondaries with the beampipe beneath the detector, the floor, etc., occupancies in the chamber are quite high. While this poses substantial challenges in track reconstruction, a corollary is that the trigger is extremely efficient, recording some 35–40 mb of the inelastic cross section.

MiniMax also has instrumentation in the upstream proton direction (see Figure 2). Of particular interest are the scintillators located about 50-60 m from the collision point. These counters are sensitive to final state p-bars with Feynman- $x \sim 0.85-0.95$ , and thus constitute a tag for diffractive events.

### III. ANALYSIS CHALLENGES AND ROBUST OBSERVABLES

Even from this It should be clear, even from this very brief description of the experiment, that we face many challenges in trying to infer either the presence or absence, within limits, of DCC signals from the data. The MiniMax acceptance is small, so that it is improbable that both  $\gamma$ 's from a  $\pi^0$  enter the detector acceptance. The conversion efficiency per  $\gamma$  is about 50%. Not all  $\gamma$ 's come from  $\pi^0$ 's. Not all charged tracks come from  $\pi^\pm$ 's. The multiplicities are rather low, because of the small acceptance, so that statistical fluctuations are very important. Detection efficiencies for charged tracks and  $\gamma$ 's are momentum-dependent and are not the same. Efficiency functions may be dependent upon the observed multiplicity or other parameters. The efficiency for triggering when no charged track or converted  $\gamma$  is produced within our acceptance is relatively low and different from that for events in which at least one charged particle or converted  $\gamma$  is detected.

Nevertheless, we find that there do exist observables which are robust in the sense that, even in the presence of large (uncorrelated) efficiency corrections and convolutions from produced  $\pi^0$ 's to observed  $\gamma$ 's, the observables take very different values for pure DCC and for generic particle production. Each such observable is a ratio, collectively referred to as  $R$ , of certain bivariate normalized factorial moments, that has many desirable properties. The  $R$ 's do not depend upon the form of the parent pion multiplicity distribution. The  $R$ 's possess definite and very different values for pure generic and pure DCC pion production. The  $R$ 's are independent of the detection efficiencies for finding charged tracks, provided these efficiencies are not correlated with each other or with other variables such as total multiplicity or background level. The  $R$ 's are independent of the magnitude of the null trigger efficiency. Some of the  $R$ 's are also independent of the  $\gamma$  efficiencies in the same sense as above. In the remaining cases, the  $R$ 's depend only upon one parameter,  $\xi$ , which reflects the relative probability of both photons from a  $\pi^0$  being detected in the same event.

### IV. GENERATING FUNCTIONS AND ROBUST OBSERVABLES

Generating function techniques have been extremely useful in studies of multiparticle production. Most practical studies, however, have considered the properties of a single species (usually charged particles) at a time. In the case of DCC, however, formal tools for the study of the joint distribution of charged particles and photons are required; the MiniMax collaboration has devoted substantial effort to developing such tools. [4]

The starting point is the generating function for factorial moments of the number of observed charged particles and gamma rays,

$$G(z_{ch}, z_\gamma) = \sum_{n_{ch}, n_\gamma=0}^{\infty} p(n_{ch}, n_\gamma) z_{ch}^{n_{ch}} z_\gamma^{n_\gamma}. \quad (1)$$

where  $p(n_{ch}, n_\gamma)$  denotes the probability distribution for the observation of  $n_{ch}$  charged particles and  $n_\gamma$  gamma rays in a multiparticle event within a given phase-space region. The partial derivatives of  $G(z_{ch}, z_\gamma)$  evaluated at  $z_{ch} = z_\gamma = 1$  generate the factorial moments:

$$f_{i,j} \equiv \left( \frac{\partial^{i,j} G(z_{ch}, z_\gamma)}{\partial z_{ch}^i \partial z_\gamma^j} \right)_{z_{ch}=z_\gamma=1}. \quad (2)$$

TABLE I. Values of  $r_{i,j}$  from the data and Monte Carlo; errors are statistical only

$r_{i,j}$	PYTHIA and GEANT	pure DCC	DCC and GEANT	Data
$r_{1,1}$	$1.01 \pm .02$	0.500	$0.56 \pm .01$	$0.98 \pm .01$
$r_{2,1}$	$1.02 \pm .05$	0.333	$0.40 \pm .03$	$0.99 \pm .02$
$r_{3,1}$	$1.09 \pm .14$	0.250	$0.34 \pm .05$	$1.03 \pm .04$

For example, we have,  $f_{1,0} = \langle n_{ch} \rangle$ ,  $f_{0,1} = \langle n_\gamma \rangle$ , etc.

Under assumptions implicit in properties of the robust observables outlined above, it can be shown that

$$G(z_{ch}, z_\gamma) = \int_0^1 df p(f) \sum_N P(N) [f(\epsilon_0 + \epsilon_1 z_\gamma + \epsilon_2 z_\gamma^2) + (1-f)(1 - \epsilon_{ch}) + \epsilon_{ch} z_{ch}]^N, \quad (3)$$

where  $\epsilon_{ch}$  is the probability of observing a charged pion,  $\epsilon_i$  are the probabilities of observing  $i$  gamma rays from the decay of a  $\pi^0$ , and  $p(f) = \delta(f - \hat{f})$  if the partition of parent pions into charged and neutral species is binomial with neutral fraction  $\hat{f}$ , and  $p(f) = 1/(2\sqrt{f})$  for a DCC.

Defining normalized bivariate factorial moments  $F_{i,j} = f_{i,j}/(f_{1,0}^i f_{0,1}^j)$ , one can show that the quantities  $r_{i,1} = F_{i,1}/F_{i+1,0}$  are robust in the sense introduced above, and take the values  $r_{i,1}(generic) = 1$  for generic (binomial) distribution of neutral and charged pions, and  $r_{i,1}(DCC) = 1/(i+1)$  for a DCC. In addition, the  $r_{i,j} = F_{i,j}/F_{i+j,0}$ ,  $j > 1$  depend on only the single (detector dependent) parameter  $\xi$  related to  $\epsilon_2$ .

## V. EARLY RESULTS

Table I shows the measured values of lower-order ratios of the factorial moments. The results were found to be independent of the run conditions, independent of the converter thickness or composition, and the same in events with or without a diffractive tag. The data are consistent with the generic production mechanisms. Comparison between the different trigger samples, and between the calculated and Monte Carlo [5] corrected values suggest the errors due to systematic effects are in the 5% range. We believe we are sensitive to admixtures of DCC mechanisms to the 10 – 20% level. More work is needed, however, to place a limit on the quantity of DCC we may observe. These values are dependent on the model used to mix DCC into the generic fragmentation.

## VI. ACKNOWLEDGMENTS

This work has been supported in part by the U.S. Department of Energy, the National Science Foundation, the Gugenheim Foundation, the Timken Foundation, the Ohio Super-

computer Center, and the Case Western Reserve University Provost's Fund. The hospitality of the organizers of the RHIC Summer Study '96 was much appreciated.

## VII. REFERENCES

---

- [1] See the MiniMax webpages, <http://fnmine.fnal.gov> for public information about the MiniMax experiment, including a collaboration list and links to papers which have been released.
- [2] For a review, K.Rajagopal, in *Quark-Gluon Plasma 2*, ed. R.Hwa, World Scientific, 1995, HUTP-95-A013.
- [3] C.M.G.Lattes, Y.Fujimoto and S.Hasegawa, *Phys. Rep.* **65** 151 (1980).
- [4] T.Brooks *et al*, Analysis of Charged-Particle/Photon Correlations in Hadronic Multiparticle Production. Submitted to *Phys. Rev. D*.
- [5] GEANT Detector and Simulation Tool, CERN, PM0062 (1993).  
T. Sjostrand *CERN-TH.6488/92 (PYTHIA 5.6 Manual)*



# Spin Physics at RHIC

M. J. Tannenbaum

*Brookhaven National Laboratory, Upton, NY 11973 USA*

## Abstract

Operation of RHIC with two beams of highly polarized protons (70%, either longitudinal or transverse) at high luminosity  $\mathcal{L} = 2 \cdot 10^{32} \text{ cm}^{-2} \text{ sec}^{-1}$  for two months/year will allow the STAR and PHENIX detectors to perform high statistics studies of polarization phenomena in the perturbative region of hard scattering where both QCD and ElectroWeak theory make detailed predictions for polarization effects. The collision c.m. energy,  $\sqrt{s} = 200 - 500 \text{ GeV}$ , represents a new domain for the study of spin. Direct photon production will be used to measure the gluon polarization in the polarized proton. A new twist comes from W-boson production which is expected to be 100% parity violating and will thus allow measurements of flavor separated quark and antiquark ( $u, \bar{u}, d, \bar{d}$ ) polarization distributions. Searches for parity violation in strong interaction processes such as jet and leading particle production will be a sensitive way to look for new physics beyond the standard model, one possibility being quark substructure.

## I. SPIN PHYSICS AND RHI PHYSICS ARE COMPLEMENTARY

The structure of the nucleon, including its spin structure, are fundamental issues of the utmost significance. To quote from a recent article in Physical Review C [1] "The nucleon-nucleon ( $NN$ ) interaction is fundamental to nuclear physics.  $NN$  data serve as tests of the strong interaction and as input to microscopic models of the nucleus." One of the principal objectives of the Heavy Ion program at RHIC is to study nuclear matter under extreme conditions of high temperature and density, the domain of non-perturbative QCD. As QCD is a gauge theory of the strong interactions in which helicity plays a fundamental role [2-4] as "charge", the complementarity of Spin Physics and RHI Physics is evident.

## II. SPIN PHYSICS AT BNL—A LONG TRADITION

BNL has a long and distinguished history in spin physics. In fact, Sam Goudsmit, the co-originator of the concept of spin [5], was one of the early BNL senior staff members and chairman of the Physics Department throughout most of the 1950's [6]. Other highlights include the neutrino helicity measurement [7], major contributions to the physics of the acceleration and storage of polarized beams [8], the AGS spin physics program [9], the 1982

International Spin Symposium [10], and the theory of the systematics of  $W^\pm$  production at hadron colliders including parity violation effects [11].

### A. How we were able to get Polarized Protons at RHIC

In the early 1980's, the first Snowmass meeting [12], the transition from ISABELLE to the 'CBA' [13,14] and the AGS spin program stimulated lots of thinking about spin physics at hadron colliders. Work continued intermittently until January 1990 when the approval of RHIC caused a renaissance. This led to the Polarized Collider Workshop [15] at Penn State in November 1990 where the RHIC Spin Collaboration (RSC), a collaboration of accelerator physicists, theoretical physicists and experimental physicists with a common interest in spin, was formally initiated.

A proposal (R5) was submitted to the BNL HENP Program Advisory Committee in September 1992, for a program of Spin Physics using the RHIC Polarized Collider [16,17], which included a general section—covering an overall view of the physics and a detailed conceptual design for the spin rotators, siberian snakes, and polarimeters which would be necessary to operate RHIC with polarized protons—followed by specific proposals by PHENIX and STAR for experiments to survey spin phenomena using the two major heavy ion detectors [18]. After 3 additional PAC presentations (for spin only), several technical reviews and a major external spin physics review in June 1995, the project “came onto the mass shell” in September 1995 with the signing of the BNL-RIKEN Agreement on Spin Physics—RIKEN, The Institute of Physical and Chemical Research, a non-profit research institute supported by the Science and Technology Agency of Japan, will provide \$20M for the accelerator components and a second muon arm in PHENIX to implement the BNL-RIKEN RHIC/Spin program.

Over this long period, we were fortunate to receive many positive reviews. One my favorites is from the June 1993 Technical Review, *“The proposal has the flavor of the application of an ingenious technological invention (siberian snakes) to make possible exciting physics research (polarization physics) reminiscent of the application of stochastic cooling to obtain  $\bar{p}p$  beams for  $W$  and  $Z$  in the CERN SPS.”*<sup>a</sup>

### III. WHY RHIC?

The use of RHIC to study the interactions of highly polarized protons ( $\geq 70\%$ ), with a luminosity in excess of  $2 \cdot 10^{32} \text{ cm}^{-2} \text{ s}^{-1}$ , and c.m. energy from 50 to 500 GeV, with dedicated operation for two months a year, will open up a totally new field in elementary particle physics and fill a vital gap in the world's accelerators. Both longitudinally and transversely polarized protons will be provided at the interaction regions, and frequent polarization sign reversal will allow the systematic errors to be minimized (see Fig. 1). This facility would be unique in the ability to perform parity-violating measurements with hadrons and polarization tests of QCD including polarized structure function measurements

---

<sup>a</sup>In case you forgot, that project got the Nobel Prize.

of gluons and flavor-separated quarks and anti-quarks. Polarization will be exploited to test fundamental symmetries in strong interactions and to search for new effects beyond the standard model.

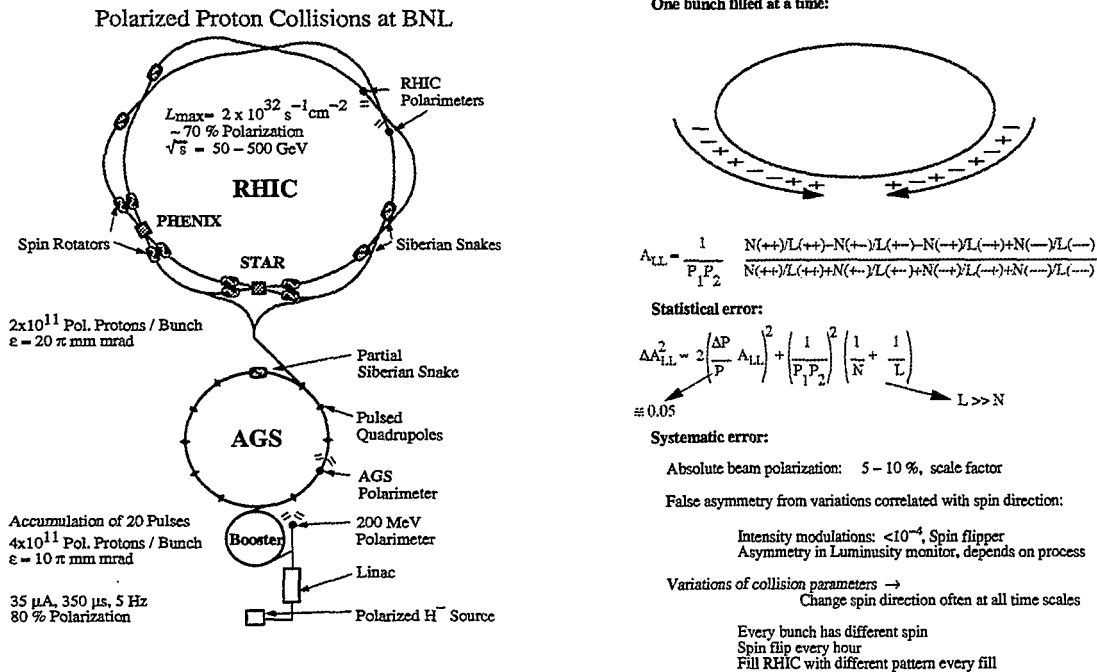


FIG. 1. a) Scheme for Polarized Proton Collisions at RHC. b) Scheme for bunch polarization to minimize systematic errors—figures from Tom Roser.

The simplest description of spin physics at RHC would be proton structure physics, the exploration of the constituents of the proton with a resolution approaching  $10^{-17}$  cm, corresponding to a mass scale of 2 TeV.<sup>b</sup> For many experiments, it would be preferable to run the machine at c.m. energy 200 GeV, rather than the nominal 500 GeV, to obtain the large values of Bjorken  $x$ , ( $x > 0.3$ ), required to effectively transmit the polarization of the protons to the constituent quarks and gluons. Also, the existence of  $p - p$  collisions in the energy range  $\sqrt{s} = 200 - 500$  GeV will permit the study of some classical reactions like the total cross section and elastic scattering [19] as a complement and extension of the CERN and Tevatron  $p - \bar{p}$  measurements.

RHC offers an extraordinary combination of energy, luminosity and polarization. This facility would be unique in the ability to perform single-spin parity violating measurements both in  $p - p$  and  $p + A$  collisions, and two-spin parity violating measurements in  $p - p$  collisions. Also, the utilization of polarized nuclei is possible in principle, and, for the cases of polarized  $d$  or  $^3\text{He}$ , under active study.

<sup>b</sup>The sensitivity to mass scales beyond the c.m. energy will be explained in due course.

## IV. HELICITY ASYMMETRY MEASUREMENTS

Spin effects can be observed with fine precision since they involve the measurements of asymmetries. The effect of systematic errors in the detectors and accelerator can be minimized by frequent polarization sign reversal and careful preparation of the initial polarized beams to give equal luminosities in all polarization states (see Fig. 1b). The goal is to polarize the beams for all proton runs including the possibly extensive  $\sqrt{s} = 200$  GeV comparison runs for the Relativistic Heavy Ion (RHI) program. Experiments not interested in polarization will obtain the spin-averaged result to a high accuracy.

### A. $A_{LL}$ —Parity Conserving Two-Spin Longitudinal Asymmetry

The polarization of a longitudinally polarized proton beam has two possible states, parallel to the momentum (‘+’ helicity) or opposite to the momentum (‘-’ helicity). In asymmetry definitions at RHIC, care must be taken to account for the possibility of large parity violating effects. We use the notation  $\sigma^{++} = N^{++}/L^{++}$  for the measured cross section with both beams having ‘+’ helicity, where  $N^{++}$  is the measured number of events for an integrated luminosity  $L^{++}$ , with analogous notation for the other helicity combinations.

The two-spin parity-conserving longitudinal asymmetry,  $A_{LL}$  is defined:

$$A_{LL} = \frac{1}{P_1 P_2} \frac{\sigma^{++} + \sigma^{--} - \sigma^{+-} - \sigma^{-+}}{\sigma^{++} + \sigma^{--} + \sigma^{+-} + \sigma^{-+}} \quad (1)$$

where  $P_1$  and  $P_2$  are the polarizations of the two beams. If parity is conserved, the theoretical cross sections obey the relations  $\sigma^{++} = \sigma^{--}$  and  $\sigma^{+-} = \sigma^{-+}$ , leading to the more conventional definition:

$$A_{LL} = \frac{1}{P_1 P_2} \frac{\sigma^{++} - \sigma^{+-}}{\sigma^{++} + \sigma^{+-}} \quad (2)$$

### B. Parity Violating Asymmetries ( $PVA$ 's)

Three [20] parity violating asymmetries can be measured with longitudinally polarized beams. In the first case, only one beam is polarized, and the cross section difference is measured for the two helicity states of the polarized beam. This is  $A_L$ , the single spin Parity Violating Asymmetry:

$$A_L = \frac{1}{P_1} \frac{\sigma^- - \sigma^+}{\sigma^- + \sigma^+} \quad (3)$$

A second case involves two polarized beams with the same helicities, which are both flipped e.g. from left-handed (–) to right-handed (+). This is the symmetric two-spin parity-violating asymmetry [13] ( $A_{LL}^{PV}$ )

$$A_{LL}^{PV} = \frac{1}{P_1 P_2} \frac{\sigma^{--} - \sigma^{++}}{\sigma^{--} + \sigma^{++}} \quad (4)$$

which can be twice as big as  $A_L$  for special cases [13,20]. There is also the anti-symmetric two-spin parity-violating asymmetry [20] where the beams have opposite helicities.

### C. Statistical Errors on Asymmetries

Assuming equal integrated luminosity for each spin configuration, with  $N$  total number of events summed over the relevant spin configurations, e.g.  $N = N^{++} + N^{--} + N^{+-} + N^{-+}$  or  $N = N^+ + N^-$ , the error on the measured asymmetry  $A$  is approximately:

$$\delta A_{LL} = \frac{1}{P_1 P_2} \sqrt{\frac{1 - A^2}{N}} \quad \text{and} \quad \delta A_L = \frac{1}{P} \sqrt{\frac{1 - A^2}{N}} \quad . \quad (5)$$

For the purposes of this article, it is assumed that the statistical error in the number of events is the dominant error, with much smaller systematic errors. The challenge will be to achieve both these results in the actual experiments.

## V. GOALS AND CAPABILITIES OF THE RHIC/SPIN PROGRAM

The philosophy of the RHIC/Spin program is to use the existing major detectors [18], which are designed for Relativistic Heavy Ion Physics, to make a survey of a wide variety of spin effects in polarized  $p - p$  collisions for many specific channels over a large range of kinematic variables ( $m, p_T$ ). Conventional longitudinal spin effects, single and double transverse spin asymmetries and a general parity violation search will be made in all channels. Although spin physics is notable for its surprises, there are several channels for which precise and clear-cut predictions exist so that rates and sensitivities can be given. The desired measurements for polarized proton physics focus on the traditional hard processes, direct photons, jets (directly or via leading particles— $\pi$  for light quarks, leptons for  $c$  or  $b$  quarks), high-mass lepton pair production (Drell-Yan), high-mass vector mesons via leptonic or semileptonic decay including  $J/\Psi$ ,  $\Upsilon$ ,  $W^\pm$ ,  $Z^0$ .

In general, the heavy ion detectors are designed with ultra-high granularity to cope with the expected charged particle multiplicity of  $dn/dy \sim 1000$  in Au+Au central collisions. Although the detectors tend to be optimized at low values of transverse momentum where soft multiparticle production plays a major role in the thermalized physics of nuclear collisions, the high granularity and high resolution make them better in many ways for measuring hard scattering in their limited apertures than the ‘conventional  $4\pi$ ’ collider detectors. For instance, STAR, which emphasizes hadron physics, can reconstruct jets and di-jets over the full azimuth and nearly  $\pm 1$  unit of pseudorapidity; while PHENIX, a very highly segmented, high resolution detector with a smaller aperture, concentrates on measurements of leptons (both  $e^\pm$  and  $\mu^\pm$ ) and photons at the highest luminosities, with very selective triggers.

### A. Luminosities for Rate Calculations and Sensitivity Estimates

The expected luminosities for polarized proton at RHIC are  $\mathcal{L} = 2 \times 10^{32} \text{ cm}^{-2} \text{ sec}^{-1}$  at  $\sqrt{s} = 500 \text{ GeV}$ ,  $\sim 1$  event/crossing, and  $\mathcal{L} = 8 \times 10^{31} \text{ cm}^{-2} \text{ sec}^{-1}$  at  $\sqrt{s} = 200 \text{ GeV}$ . It is assumed that the  $\sqrt{s} = 500 \text{ GeV}$  run is dedicated for spin physics and, since the goal is to polarize the beams for all proton runs, the 200 GeV data are collected during comparison runs for the RHI program. The polarization of both beams is taken as  $P_1 = P_2 = 70\%$ . The physics sensitivity calculations at each  $\sqrt{s}$  are based on runs of  $4 \times 10^6$  seconds, or

about 100 days with a duty factor of  $\sim 50\%$ , which leads to the integrated luminosities  $\int \mathcal{L} dt = 8 \times 10^{38} \text{ cm}^{-2}$  at  $\sqrt{s}=500 \text{ GeV}$  and  $\int \mathcal{L} dt = 3.2 \times 10^{38} \text{ cm}^{-2}$  at  $\sqrt{s}=200 \text{ GeV}$ . Optimistically, these initial runs could be accomplished during the first two years of RHIC operation. It is worthwhile to point out that the  $800 \text{ pb}^{-1}$  integrated luminosity is  $\sim 20$  times the total of the entire CERN collider program,  $\sim 6$  times the present total of the Tevatron collider (Run I), and comparable to the integrated luminosity anticipated for the Tevatron 3-4 year 'Run II' which is planned to start in 1999.

## VI. QCD AND HADRON COLLISIONS

The cross section for hard processes in  $p-p$  collisions at c.m. energy  $\sqrt{s}$  is taken to be a sum over the constituent reactions

$$a + b \rightarrow c + d \quad , \quad (6)$$

where the c.m. system for the constituent scattering is not generally the same as the  $p-p$  c.m. system since the constituents have momentum fractions  $x_1$  and  $x_2$  of their respective protons. Thus, in the  $p-p$  c.m. system, the constituent c.m. system has rapidity,  $\hat{y} = \frac{1}{2} \ln \frac{x_1}{x_2}$ , and invariant mass-squared,  $\hat{s} = x_1 x_2 s$ , where

$$x_1 = \sqrt{\frac{\hat{s}}{s}} e^{\hat{y}} \quad x_2 = \sqrt{\frac{\hat{s}}{s}} e^{-\hat{y}} \quad . \quad (7)$$

If  $a(x_1)$ ,  $b(x_2)$ , are the differential probabilities for constituents  $a$  and  $b$  to carry momentum fractions  $x_1$  and  $x_2$  of their respective protons, e.g.  $u(x_1)$ , then the overall  $p-p$  reaction cross section in lowest order (LO) of  $\alpha_s$  is

$$\frac{d^3 \sigma}{dx_1 dx_2 d \cos \theta^*} = \frac{s d^3 \sigma}{d\hat{s} d\hat{y} d \cos \theta^*} = \sum_{ab} a(x_1) b(x_2) \frac{\pi \alpha_s^2(Q^2)}{2\hat{s}} \Sigma^{ab}(\cos \theta^*) \quad , \quad (8)$$

where  $\Sigma^{ab}(\cos \theta^*)$ , the characteristic subprocess scattering angular distributions (see Fig. 2a), and  $\alpha_s(Q^2) = \frac{12\pi}{25} \ln(Q^2/\Lambda^2)$ , the strong coupling constant, are fundamental predictions of QCD [21,22].

By contrast, the quantities  $a(x_1)$  and  $b(x_2)$ , the "number" distributions of the constituents, are empirical—they need to be measured. However, in a triumph of the Standard Model, these distributions are related (for the electrically charged quarks) to the structure functions measured in Deeply Inelastic lepton-hadron Scattering (DIS), e.g.

$$F_2(x, Q^2) = x \sum_a e_a^2 a(x, Q^2) \quad (9)$$

where  $e_a$  is the electric charge on a constituent. The evolution of the structure functions with  $Q^2$  is a higher-order QCD effect in hadron collisions, but is the leading order QCD effect in DIS.

It is important to realize that for fixed  $x_1$ ,  $x_2$ , the hard scattering cross section is proportional to  $1/s$

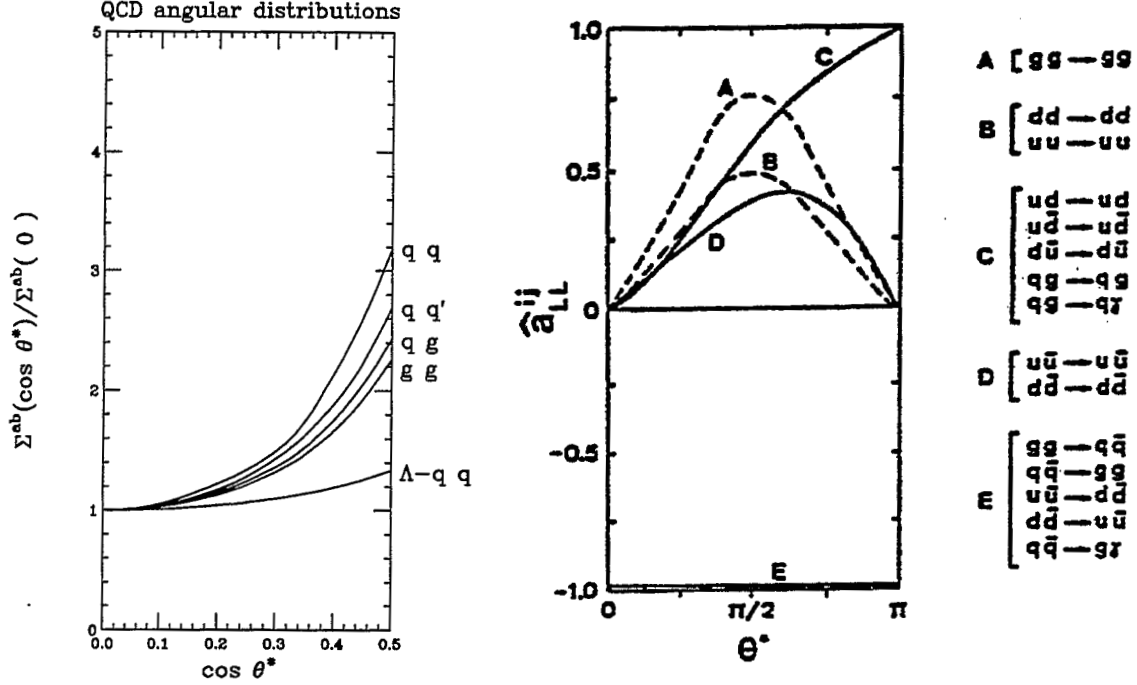


FIG. 2. Characteristic QCD Subprocess angular distributions: (a) scattering; (b) spin asymmetry.  $\theta^*$  is the scattering angle in the constituent c.m. system.

$$\frac{d^3\sigma}{dx_1 dx_2 d\cos\theta^*} = \frac{1}{s} \sum_{ab} a(x_1)b(x_2) \frac{\pi\alpha_s^2(Q^2)}{2x_1x_2} \Sigma^{ab}(\cos\theta^*) \quad (10)$$

so that lower  $s$  leads to larger  $x$  for a given luminosity. Also, the structure functions fall precipitously with increasing  $x$ , which further leads to sharply falling cross-sections with increasing  $\hat{s}$  for a given  $s$ . This explains why RHIC is better than higher energy colliders for attaining values of  $x \sim 0.3$  where polarization effects are important.

### A. Spin QCD

The two-spin longitudinal asymmetry for the constituent reaction (Eqs. 6, 8) is

$$A_{LL}(a + b \rightarrow c + d) = \frac{\sigma^{++} - \sigma^{+-}}{\sigma^{++} + \sigma^{+-}} \quad (11)$$

$$= \frac{\Delta a}{a} \frac{\Delta b}{b} \hat{a}_{LL}(a + b \rightarrow c + d) \quad , \quad (12)$$

where  $\Delta a(x)$  is the helicity asymmetry of the constituent structure function  $a(x)$

$$\Delta a(x) = a^+(x) - a^-(x) \quad (13)$$

and the '+' and '-' refer to constituents with the same or opposite helicity as the parent proton. The spin asymmetry of the subprocess [3,4]

$$\hat{a}_{LL}(a + b \rightarrow c + d) \quad (14)$$

is a fundamental prediction of QCD (see Fig. 2b), which has never been verified—to my knowledge.

## VII. SPIN STRUCTURE FUNCTIONS AND TESTS OF QCD

The predicted QCD constituent polarization asymmetries of Fig. 2b are enormous at the constituent level. However at the observational level, the effect is greatly diluted [15] because the proton polarization is not appreciably transmitted to the constituents, unless  $x \geq 0.3$ . At the outset of the RHIC/Spin program, we assume that QCD is valid and use Eqs. 11, 12 to determine the spin structure functions.

### A. The Spin Structure Function of the Gluon—Direct Photon Production

$A_{LL}$  in direct photon production should be a clean measurement of the spin dependent gluon structure function since the dominant subprocess in  $p-p$  collisions is

$$g + q \rightarrow \gamma + q \quad , \quad (15)$$

with  $q\bar{q} \rightarrow \gamma + g$  contributing on the order of 10%. This small contribution from the annihilation channel can be neglected in the first measurements of  $\Delta G(x)$ . Predictions [23] for  $A_{LL}$  (in NLO) are surprisingly large, in the range 5% to 20%.

This is one of the favorite QCD reactions in hadron physics [24], since there is direct and unbiased access to one of the interacting constituents, the photon. The only problem is the huge background of photons from  $\pi^0$  and  $\eta$  decays which produce a *fake* direct  $\gamma$  signal. This background is effectively eliminated [16,25] by  $\pi^0$  reconstruction and gamma isolation cuts. By applying both of these rejection methods, the purity of direct photon candidates will be excellent. Spin effects from any residual  $\eta$  background can be measured and corrected.

The high segmentation of the PHENIX EM calorimeter, which is driven by the issues of occupancy and energy resolution in the high multiplicity, low  $p_T$  environment of Heavy Ion Collisions, allows the two gammas from  $\pi^0$  decay to be resolved [16] for  $p_T(\pi^0) \leq 30\text{GeV}/c$ . In STAR, the calorimeter is less segmented and a ‘shower-max’ detector is used for  $\gamma/\pi^0$  separation. However, the large solid angle allows the recoil jet to be detected so that the full constituent kinematic quantities  $x_1$  and  $x_2$  can be reconstructed. Similarly, di-jet production can be detected and used to measure the gluon spin structure function in the appropriate kinematic region.

To summarize, here is a subject with precise theoretical predictions and no experimental tests. It cries out for measurements—which can best, if not only, be done using longitudinally polarized proton beams.

## VIII. PARITY VIOLATION IN HADRON COLLISIONS

The field of Parity Violation in hadron collisions has traditionally been the domain of “*ultra high precision*” physicists. The parity violating asymmetry in the total proton-proton cross section has been measured to be  $\sim 3 \times 10^{-7}$  at 1.5 GeV/c,  $2.6 \times 10^{-6}$  at 6 GeV/c laboratory momenta, and predicted to be “large”  $> 10^{-4}$  at RHIC energies [26].



## A. “Large” effects at RHIC?

However, at RHIC there are other conventional parity violating effects which are predicted to be much larger. For instance, in inclusive jet production—the leading strong interaction process at RHIC— $A_{LL}^{PV}$  due to the interference of gluon and  $W$  exchange at the constituent level is estimated [13,27] to be  $\sim 0.8\%$ , at jet  $p_T = m_W/2$ ;  $\sim 0.5\%$ , at  $p_T = 50$  GeV/c;  $1\%$ , at  $p_T=70$  GeV/c; and  $2\%$ ,  $p_T=95$  GeV/c at  $\sqrt{s}=300$  GeV. Of course, a more spectacular effect at RHIC will be the opening up of a totally new regime of hadron physics, a situation in which parity violating effects are **dominant**. This concerns the direct production of the Weak Bosons  $W^\pm$  and  $Z^0$ . The most spectacular channel is the leptonic decay  $W^\pm \rightarrow e^\pm + X$ , where the  $X$  means that the measurement is via the inclusive  $e^\pm$  channel with no “missing energy” detection. This is a textbook example [28] of a process with virtually no background. The predicted  $PVA$  is really **HUGE** at production [11], on the order of **UNITY**. Both PHENIX and STAR have respectable counting rates (see Table I) bringing towards reality something that I only dared to dream just a few years ago [29], “*By measuring the PVA for the reaction  $W \rightarrow e + X$  as a function of  $\sqrt{s}$ , the spin dependent structure functions of the proton can be measured at values of  $x \sim m_W/\sqrt{s}$ .*”

## B. “Yesterday’s sensation is today’s calibration...”

An article by Bourrely and Soffer [20] has now presented the formalism for proton structure function measurements using the parity violating asymmetry of  $W^\pm$  and  $Z^0$  production. This really brings to mind Val Telegdi’s statement, partially quoted above. In the standard model, the differential cross section for the reaction

$$pp \rightarrow W^\pm + \text{anything} \quad (16)$$

is given in leading order [20] by the quark-antiquark fusion reactions  $u\bar{d} \rightarrow W^+$  and  $\bar{u}d \rightarrow W^-$ . The parity violating single-spin asymmetry for  $W^+$  production is given by [20]

$$A_L^{W^+}(y) = \frac{\Delta u(x_1, M_W^2)\bar{d}(x_2, M_W^2) - \Delta\bar{d}(x_1, M_W^2)u(x_2, M_W^2)}{u(x_1, M_W^2)\bar{d}(x_2, M_W^2) + \bar{d}(x_1, M_W^2)u(x_2, M_W^2)} \quad (17)$$

and with the reasonable assumption that  $\Delta u\Delta\bar{d} \ll u\bar{d}$ , the two-spin and single-spin  $PVA$ ’s are simply related by [20]

$$A_{LL}^{PV}(y) = A_L(y) + A_L(-y) \quad . \quad (18)$$

The sensitivity to unknown spin structure functions is generally much larger for the  $W^-$  than the  $W^+$ , which is easy to understand by simple arguments [20]. Near  $y = 0$ , the  $PVA$ ’s are given to a good approximation by

$$A_L^{W^+} = \frac{1}{2} \left( \frac{\Delta u}{u} - \frac{\Delta\bar{d}}{\bar{d}} \right) \quad \text{and} \quad A_L^{W^-} = \frac{1}{2} \left( \frac{\Delta d}{d} - \frac{\Delta\bar{u}}{\bar{u}} \right) \quad , \quad (19)$$

and  $\Delta u/u$  is large and well measured [30]. For large positive rapidity,  $x_1 \gg x_2$ , so that  $A_L^{W^+} \simeq \Delta u/u$ ,  $A_L^{W^-} \simeq \Delta d/d$ ; similarly at large negative rapidity,  $x_1 \ll x_2$ ,  $A_L^{W^+} \simeq -\Delta\bar{d}/\bar{d}$ ,  $A_L^{W^-} \simeq -\Delta\bar{u}/\bar{u}$ .

The expected sensitivities for spin-structure measurements in PHENIX with the latest Bourrely and Soffer polarized structure functions [31] are shown in Fig. 3. Table I gives an overall PHENIX/STAR comparison. The structure functions assumed in Fig. 3 [20] give huge single-spin asymmetries,  $A_L^{W^\pm}$ , as previously advertised. An amusing feature of the single-spin asymmetry is that the variables  $x_1$  and  $x_2$  can be distinguished in the otherwise symmetric  $p - p$  collision. Also, single-spin asymmetries could be used in  $p + A$  collisions to measure the evolution of the spin-dependent sea quark structure functions in nuclei—a combination of the two most famous “EMC effects.” This could be the birth of *Structure Function Physics* using parity violation as a tool.

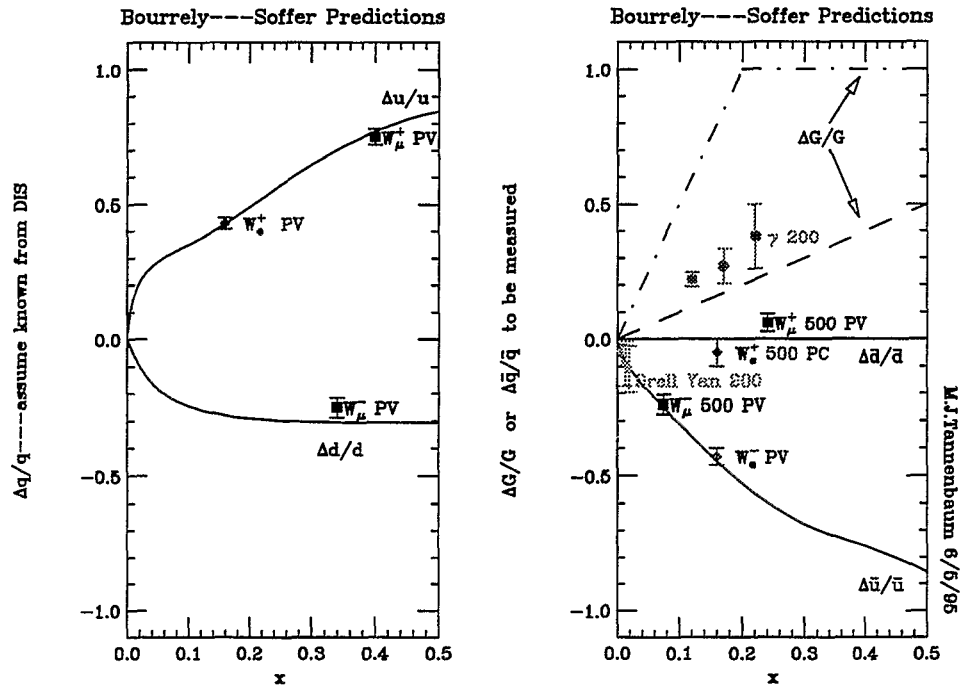


FIG. 3. Expected sensitivities for spin-structure function measurements in PHENIX shown with Bourrely-Soffer distributions [31] for  $800 \text{ pb}^{-1}$  at  $\sqrt{s} = 500 \text{ GeV}$  and  $320 \text{ pb}^{-1}$  at  $\sqrt{s} = 200 \text{ GeV}$

### C. New Physics—Surprises

In my opinion, the most exciting feature of the study of parity violation in hadron interactions is the possibility of surprises. There are essentially no measurements of, or searches for, parity violation in hadron reactions at high energies ( $\sqrt{s} \geq 10 \text{ GeV}$ ). *THIS FIELD IS TOTALLY UNEXPLORED*. In the standard model, no parity violation is expected in strong interactions. Of course, this is probably a consequence of the fact that nobody ever looked. But, to quote Maurice Goldhaber (who was quoting astronomers), “The absence of evidence is not the evidence of absence.” Thus, there are limitless possibilities beyond the standard model for parity violating effects in hadronic interactions since the subject has hardly been studied. Perhaps the B quark production mechanism is 30% parity violating...

TABLE I. RHIC Spin Collaboration: PHENIX/STAR Comparison

	PHENIX	STAR
$W^\pm \rightarrow l^\pm + X$	$e^\pm$ : 15K $W^+$ , 3K $W^-$	$e^\pm$ : 72K $W^+$ , 21K $W^-$
Parity Violation, $\Delta\bar{q}$	$\mu^\pm$ : 9K $W^+$ , 10K $W^-$	
$Z^0 \rightarrow l^+l^-$	$e^+e^-$ : 120 $Z^0$	$e^+e^-$ : 4200 $Z^0$
Transversity $h_1(x), \bar{u}(x)$	$\mu^+\mu^-$ : 700 $Z^0$	
Direct $\gamma$ ( $\Delta G$ )	Highly Segmented EMCAL Resolve $\pi^0$ $p_T \leq 25$ GeV/c	Showers Max Detector $\gamma$ , $p_T < 20$ GeV/c
$\gamma$ +Jet ( $\Delta G$ )	Away-Jet 15% efficiency via leading particle.	$\gamma$ + Jet $\Delta G(x)$ , $x < 0.2$
JETS ( $\Delta G, PV$ )	$\pi^0$ 's as Leading Particles	Full Jets $ \eta  \leq 0.5$
Di-Jets	$\pi^0$ pairs	$\geq 10^6$ Di-jets
Drell-Yan ( $\Delta\bar{q}, \Delta_T\bar{q}$ )	$\mu^+\mu^-$ : 30K pairs mass 9 to 12 GeV	$e^+e^-$ : 37K pairs mass 9 to 12 GeV
$J/\psi \rightarrow l^+ + l^-$ ( $\Delta G?$ )	200K $e^+e^-$ ; $\geq 1M$ $\mu^+\mu^-$	Sizable rates for $e^+e^-$ trigger only at high $p_T$
$\Upsilon \rightarrow \mu^+\mu^-$	25K events	

#### D. My Criteria for the Maximum Discovery Potential

Parity Violation searches at RHIC satisfy all

##### My Criteria for The Maximum Discovery Potential:

- Look where most theorists predict that nothing will be found.
- Look in a channel where the known rates from conventional processes are small, since low background implies high sensitivity for something new.
- Be the first to explore a new domain—something that has never been measured by anybody else.

I feel that parity violation searches offer, at the present time, the same discovery potential as di-lepton searches in the 1970's.

#### E. A timely illustration—Quark Substructure (?)

It is difficult to predict surprises. However, as an example of something that might happen, a recent extension of the standard model has included a new parity violating interaction due to quark substructure [32]. One possible explanation of the several generations of quarks and leptons is that they are composites of more fundamental constituents, with a scale of compositeness  $\Lambda_c \gg 100$  GeV. The intriguing feature of composite models of quarks

and leptons is that the interactions generally violate parity, since  $\Lambda_c \gg M_W$ . The parity-violating asymmetry then provides direct and much more quantitative tests for substructure than other methods. The sensitivity to quark substructure is, of course, model dependent. One model of quark substructure [32] contains an explicitly parity-violating left-left contact interaction between quarks, which results in a *PVA* in jet production [13,14], as well as a slight increase in the jet cross section at large  $p_T$  (See Fig. 4a).<sup>c</sup> Without the *PVA* handle, detectors at the Tevatron are limited to searching for substructure by deviations of jet production from QCD predictions at large values of  $p_T$ . It is difficult to prove that a small deviation is really due to something new. The latest CDF measurement [33] is a case in point (see Fig. 4b). If the “% Difference from NLO QCD” were “% Parity Violation”, the parity-violating signature would be a **clear indication of new physics** [29,34]. The limit is presently [33]  $\Lambda_c \cong 1.4 - 1.6$  TeV.

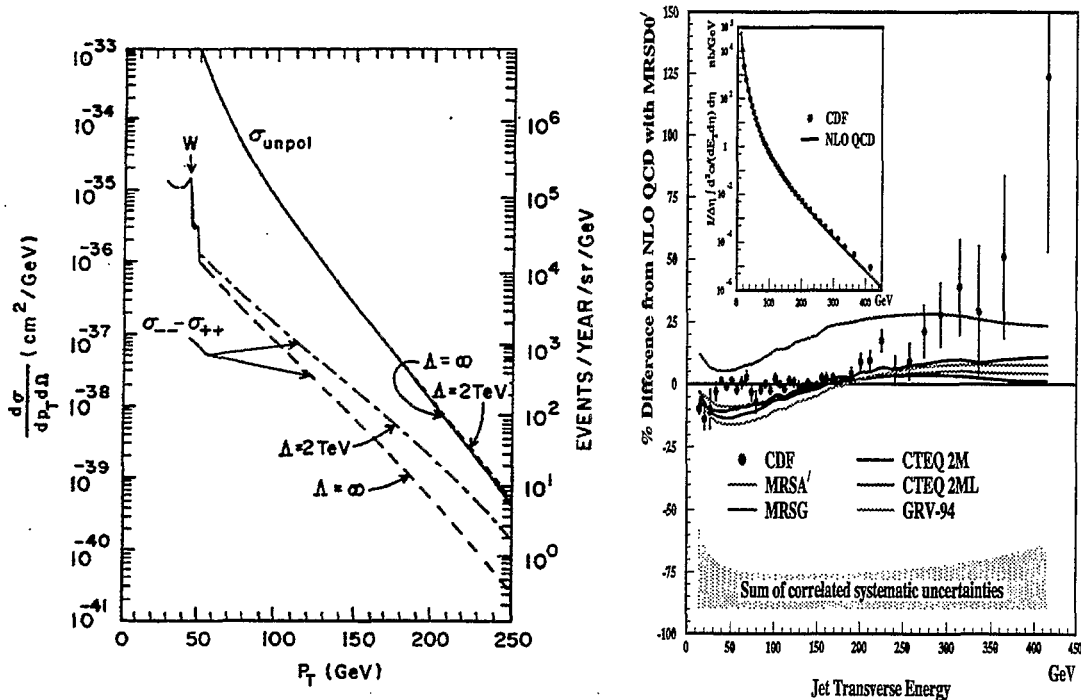


FIG. 4. a) Prediction [13,14] from 1983 for the effect of Quark Substructure on inclusive jet cross section with and without Parity Violation capability. b) Latest CDF [33] Inclusive jet cross section and ratio to NLO QCD.

Although this limit is well above the RHIC c.m. energy, the *PVA* signature provides such a sensitive probe that the substructure could be measured at RHIC up to values of  $\Lambda_c \sim 2 - 3$  TeV. The limit of the sensitivity is set by the standard model *PVA* in inclusive jet production due to the interference of gluon and *W* exchange in the constituent scattering!

<sup>c</sup>There is a factor of 4 dilution of the substructure effect in the spin-averaged cross section [13] in this model.

(See Fig. 5.) The latest calculation [35] of the substructure  $PVA$  for jet production at RHIC by Taxil and Virey (with sensitivity estimates for  $\Delta\eta = 1$  jet acceptance, typical of STAR) nicely illustrates the potential for new physics discoveries at RHIC by the search for Parity Violating Asymmetries in strong interaction processes.<sup>d</sup>

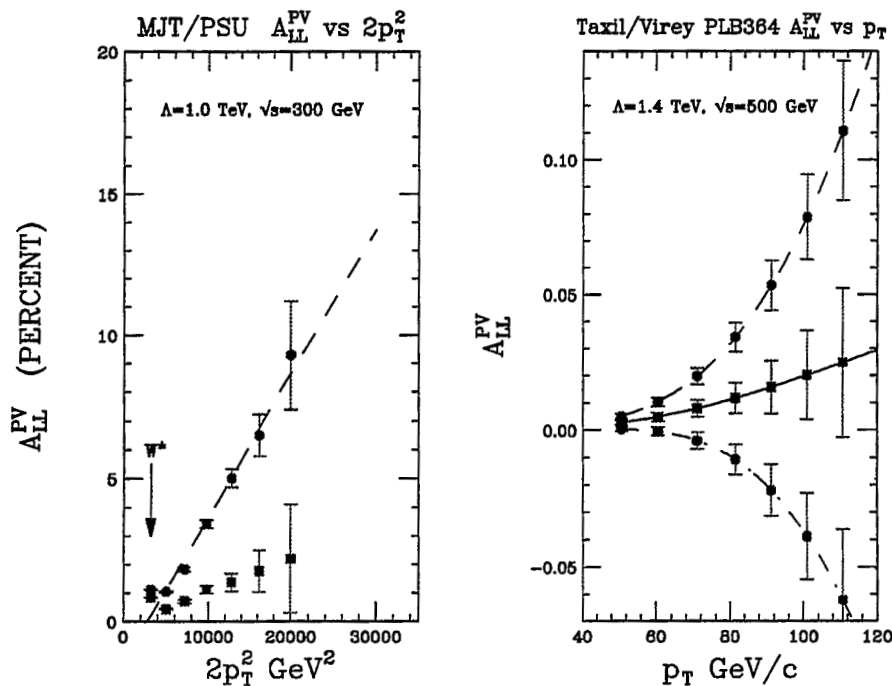


FIG. 5. a) Predicted [13,29] single jet  $A_{LL}^{PV}$  for quark substructure  $A = -1$  (circles) versus  $2p_T^2 \sim -\hat{t}$ . The squares are the standard model  $PVA$  from  $W^\pm$  production (arrow) and  $W$ -gluon interference. b) Latest calculation for RHIC [35] versus  $p_T$  for substructure with  $A = \pm 1$  (circles) and  $W$ -gluon interference (squares). The errors on (b) indicate sensitivity estimates for RHIC.

## IX. ACKNOWLEDGEMENT

This work has been supported by the U. S. Department of Energy under contract number DE-AC02-76CH00016. I would like to thank the members of the RSC, the BNL and RIKEN directorates, and the PHENIX, STAR and PP2PP collaborations for their cooperation and support.

## REFERENCES

- [1] M. W. McNaughton, *et al.*, *Phys. Rev.* **C53**, 1092 (1996).

<sup>d</sup>Of course, if the effect is in the gluon structure function as some claim [36], we measure that too.

- [2] See, for example, J. F. Owens, *Rev. Mod. Phys.* **59**, 465 (1987)
- [3] J. Babcock, E. Monsay and D. Sivers, *Phys. Rev.* **D19**, 935 (1979).
- [4] N. S. Craigie, K. Hidaka, M. Jacob and F. M. Renard, *Phys. Rep.* **C99**, 69 (1983).
- [5] G. E. Uhlenbeck and S. Goudsmit, *Naturwiss.* **13**, 953 (1925); *Nature* **117**, 264 (1926). See also, C. N. Yang in Reference [10].
- [6] Thanks to Bob Crease for confirming this tidbit.
- [7] M. Goldhaber, L. Grodzins and A. W. Sunyar, *Phys. Rev.* **109**, 1015 (1958).
- [8] See, for example, E. D. Courant in *High Energy Physics with Polarized Beams and Polarized Targets, Proceedings of the 1980 International Symposium*, Eds. C. Joseph and J. Soffer (Birkhauser, Basel, 1981), pp 102-109.
- [9] D. G. Crabb, *et al.*, *IEEE Trans. Nucl. Sci.* **NS-26**, 3202 (1979). Also see, for example, L. G. Ratner in Reference [10], pp 412 - 418.
- [10] *AIP Conf. Proc.* **95**, *High Energy Spin Physics-1982*, Ed. Gerry M. Bunce (American Institute of Physics, New York 1983).
- [11] F. E. Paige, T. L. Trueman and T. N. Tudron, *Estimates of W production with polarized protons as a means of detecting its hadron jet decays*, *Phys. Rev.* **D19**, 935 (1979); R. F. Peierls, T. L. Trueman and L.-L. Wang, *Estimates of production cross sections and distributions for W bosons and hadronic jets in high-energy pp and p̄p collisions*, *Phys. Rev.* **D16**, 1397 (1977).
- [12] G. Bunce, *et al.*, *W, Z<sup>0</sup> Production at a PP collider*, Proceedings of the 1982 DPF Summer Study on Elementary Particle Physics and **Future Facilities**, June 28-July 16, 1982, Snowmass, CO, eds. R. Donaldson, R. Gustafson and F. Paige, pp 489-499.
- [13] F. E. Paige and M. J. Tannenbaum, *QCD Tests with Polarized Beams at CBA*, BNL-33119, March 1983 (unpublished).
- [14] R. Longacre and M. J. Tannenbaum, *QCD Tests and Large Momentum Transfer Reactions at CBA*, BNL-32888, March 1983 (unpublished). See also CBA Newsletter 4, March 1983, BNL; and R. Ruckl, *J. Phys.* **46** (1985) C2-55, T. L. Trueman, *ibid.* C2-721.
- [15] *Proceedings of the Polarized Collider Workshop*, University Park, PA (1990), eds J. Collins, S. Heppelmann and R. W. Robinett, AIP conf. proc. No. 223, (AIP, New York, 1991).
- [16] M. Beddo, *et al.*, *Proposal on Spin Physics Using the RHIC Polarized Collider*, submitted August 19, 1992, BNL; Update submitted Sept 2, 1993.
- [17] See, also, G. Bunce, *et al.*, *Polarized protons at RHIC*, *Particle World*, **3**, 1 (1992).
- [18] For further information see <http://www.rhic.bnl.gov/>
- [19] PP2PP Collaboration, W. Guryn, *et al.*, *Experiment to Measure Total and Elastic p-p cross sections at RHIC*, Updated Version, September 1995, BNL.
- [20] Claude Bourrely and Jacques Soffer, *Parton Distributions and Parity-Violating Asymmetries in W<sup>±</sup> and Z Production at RHIC*, *Phys. Lett.* **B314**, 132 (1993).
- [21] R. Cutler and D. Sivers, *Phys. Rev.* **D16**, 679 (1977); **D17**, 196 (1978).
- [22] B. L. Combridge, J. Kripfganz and J. Ranft, *Phys. Lett.* **70B**, 234 (1977).
- [23] A. P. Contogouris, *et al.*, *Phys. Rev.* **D48**, 4902 (1955).
- [24] H. Fritzsch and P. Minkowski, *Phys. Lett.* **69B**, 316 (1977). Also, see, for example, *Proceedings of the International Workshop on QUARK GLUON PLASMA SIGNATURES*, Strasbourg, 1990, eds. V. Bernard, *et al.* (Editions Frontieres, Gif-sur-Yvette, France, 1991).

- [25] M. E. Beddo, H. Spinka and D. G. Underwood, ANLHEP internal report, June 25, 1992.
- [26] T. Goldman and D. Preston, *Prediction of a Large Parity-Violating Total Cross Section Asymmetry at High Energies*, *Phys. Lett.* **168B**, 415 (1986).
- [27] G. Ranft and J. Ranft, *Phys. Lett.* **87B**, 122 (1979); F. E. Paige, in *Workshop on the Production of New Particles*, Madison WI, 1979, (BNL-27066).
- [28] G. Altarelli and L. DiLella, *Proton-Antiproton Collider Physics*, (World Scientific, Singapore, 1989).
- [29] M. J. Tannenbaum, *Polarized Protons at RHIC*, in reference 15.
- [30] E143 Collaboration, K. Abe *et al.*, *Phys. Rev. Lett.* **74**, 346 (1995).
- [31] Claude Bourrely and Jacques Soffer, *Nucl. Phys.* **B445**, 341 (1995).
- [32] E. J. Eichten, K. D. Lane and M. E. Peskin, *Phys. Rev. Lett.* **50**, 811 (1983).
- [33] CDF Collaboration, F. Abe, *et al.*, *Phys. Rev. Lett.* **68**, 1104 (1992); *ibid.* **77**, 438 (1996). See also New York Times, Feb 8, 1996.
- [34] P. Taxil, *Beyond the Standard Model with Polarized Beams at Future Colliders*, in reference 15.
- [35] P. Taxil, J. M. Virey, *Phys. Lett.* **B364**, 181 (1995).
- [36] J. Huston, *et al.*, *Phys. Rev. Lett.* **77**, 446 (1996).

# The PHENIX Physics Program

William A. Zajc

*Department of Physics, Columbia University, NY, NY 10027*

*zajc@nevis1.columbia.edu*

## Abstract

The PHENIX detector is one of two large detectors being built for the Relativistic Heavy Ion Collider (RHIC) at Brookhaven National Laboratory. RHIC will provide colliding beams of relativistic (100 A · GeV) heavy ions as well as polarized protons at  $\sqrt{s} = 500$  GeV. The physics capabilities of the PHENIX detector for the heavy ion portion of the RHIC program are briefly outlined here.

## I. INTRODUCTION

When completed in early 1999, RHIC [1] will provide a unique facility for exploring the hadronic structure of bulk nuclear matter. No other machine will be capable of accelerating such a broad range of species (protons to Au nuclei) to such high energies (maximum energy per beam of  $\sim \frac{Z}{A} \cdot 250$  GeV) with such intense luminosities ( $\sim 2 \times 10^{26}$  cm<sup>-2</sup> s<sup>-1</sup> for Au-Au collisions). It is thought that collisions of the heaviest ions at the highest RHIC energies are the precise tool necessary to form the quark-gluon plasma (QGP) [2], while the range of species and energies available from RHIC provides the necessary ingredients for the systematic exploration of any new phenomena observed.

With these opportunities come immense experimental challenges. Experiments must be designed to accommodate extremely high particle densities ( $\frac{dN}{dy} \sim 1000$  at central rapidities), and from such events extract evidence for a phase transition in a highly transient environment. PHENIX [3] is one of two large experiments at RHIC designed for this purpose.

## II. PHILOSOPHY

### A. General

Designing an experiment to search for QGP formation in relativistic heavy-ion collisions is a daunting task. A plethora of signals have been proposed, but none of them have the distinguishing feature of incontrovertibility (as opposed to, say, the discovery a new particle). In fact, even the sign of the effect may be in dispute [4]. Furthermore, many of the proposed signatures have been derived on a theoretical light-cone rather than on an experimental one, as shown in Figure 1. For instance, the “cleanliness” of electromagnetic probes is true only if one considers the detection channel for the first  $\sim 10^{-22}$  seconds. However, at times far later



than this, but far shorter than any experimental timescale, one must deal with conversions (internal and external) and decays.

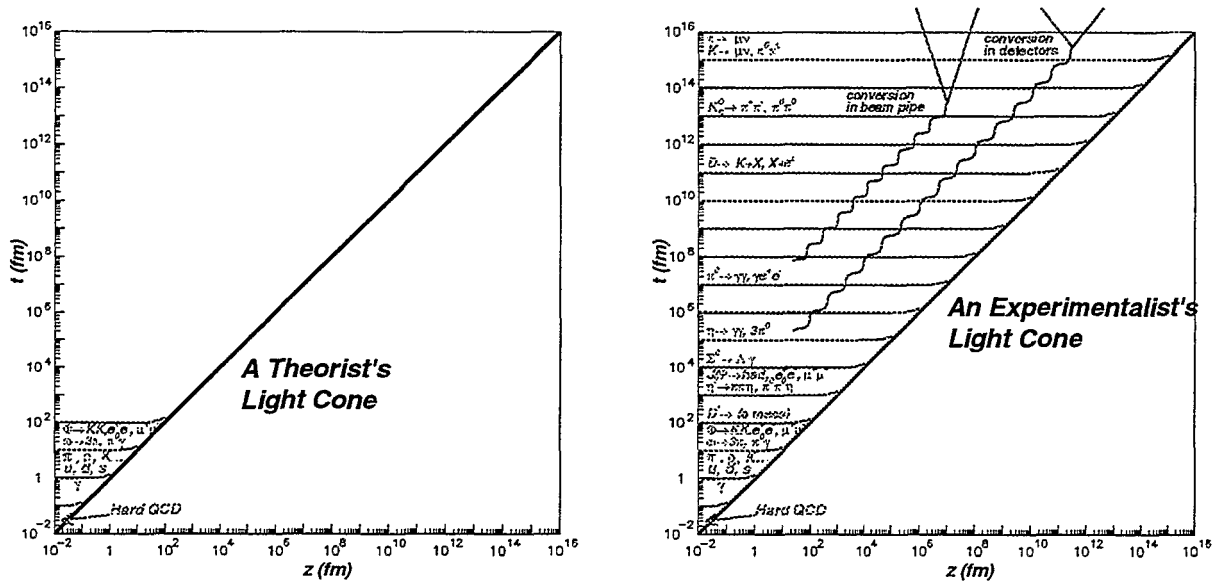


FIG. 1. A pictorial description comparing the fundamental processes contributing to QGP signatures versus some of the additional backgrounds important in their experimental detection.

The situation that confronts an experimentalist is thus one in which the vector sum of theoretical opinion on likely signals is consistent with zero. Even greater uncertainty surrounds predictions of the *rate* for QGP production. Nonetheless, even knowing what one doesn't know can help in framing an approach to the problem:

- **Observation #1:** The QCD phase transition will not be “seen” at RHIC.

While it would be nice if the plasma were to manifest itself in one or several unambiguous events, it would be folly to base an experimental program on such wishful thinking. This is especially true given that we already know that there is no (single) set of events that proves QCD is the correct theory of the strong interactions. Instead it has emerged as a consistent framework for describing the observed phenomena. A conservative strategy to QGP detection should accommodate this possibility.

**Implication #1:** *Avoid single-signal detectors.*

- **Observation #2:** There are no\* cross-sections at RHIC.

\* Except

- $\sigma_{GEOM} \sim$  few barns
- $\sigma_{CENTRAL} \sim (1-10)\% \cdot \sigma_{GEOM}$
- but  $\sigma_{QGP} \sim \sigma_{CENTRAL}??$

This is a fundamental difference between heavy-ion physics and  $Z^0$ -hunting. Estimates of the energy threshold for QGP formation are notoriously unreliable, and there is

essentially no theoretical guidance as to *probability per collision* of plasma formation. This has the obvious experimental consequence:

**Implication #2:** *Preserve high-rate and triggering capabilities.*

- **Assumption #3:** Expect the unexpected.

This item is perhaps more theological than the previous two. Nonetheless, it is important to realize that RHIC opens up an entirely new energy regime for heavy ion collisions, where for the first time hard processes and low- $x$  behavior play an important role. Again, the implication here may be a little less clear, but one might argue:

**Implication #3:** *Don't trigger till you have to.*

It is an instructive exercise to examine the extent to which each of the RHIC experiments follows these guideline. Space does not permit such an analysis here, but it is worth noting that the development of Disoriented Chiral Condensates as a potential phase transition signature post-dates the design of the four RHIC experiments, but each of them has some reasonable sensitivity to this signal.

## B. PHENIX-Specific

The PHENIX approach to RHIC physics is simple to state: *Search for the “simultaneous” appearance of new phenomena in as many channels as possible, as a function of some “external” parameter.* Each of the quoted words warrants some explanation. “Simultaneous” does not necessarily mean in the same event. Instead, it implies that for some class of events, the various new phenomena appear at or near the *same* value of the “external” parameter. This parameter may be anything, but a few obvious candidates suggest themselves:

- The *mass* of the colliding ions.
- The  $\sqrt{s}$  of the colliding ions.
- The *energy density* of the collision.

These are not all independent quantities (for instance, it is likely that the energy density will grow with as  $A^{1/3}$  and logarithmically with  $\sqrt{s}$ ), so an important second-order goal will be establishing the “best” such external parameter.

Which channels [5] are likely to be of interest in such an approach? A simple enumeration of potential signals quickly produces the answer “ALL!”:

### 1. Deconfinement (Debye Screening)

$$- R(\Upsilon) \sim 0.13 \text{ fm} < R(J/\psi) \sim 0.29 \text{ fm} < R(\psi') \sim 0.56 \text{ fm} \\ \Rightarrow \text{Electrons, Muons}$$

### 2. Chiral Symmetry Restoration

$$- \text{Mass, width, branching ratio of } \phi \rightarrow e^+e^-, K^+K^- \text{ with } \delta M \leq 5 \text{ MeV.} \\ \Rightarrow \text{Electrons, Muons, Charged Hadrons}$$

- Baryon susceptibility; color fluctuations: Anti-baryon production  
⇒ Charged Hadrons
  - DCC's: Isospin fluctuations  
⇒ Photons, Charged Hadrons
3. Thermal Radiation of Hot Gas
- Prompt  $\gamma$ , Prompt  $\gamma^* \rightarrow e^+e^-, \mu^+\mu^-$   
⇒ Photons, Electrons, Muons
4. Strangeness and Charm Production
- Production of  $K^+, K^-, K_s^0$  mesons  
⇒ Hadrons
  - Production of  $\phi, J/\psi, D$  mesons  
⇒ Electrons, Muons
5. Jet Quenching
- High- $p_T$  jet via leading particle spectra  
⇒ Hadrons, Photons
6. Space-Time Evolution
- HBT Correlations of  $\pi^\pm, \pi^\pm, K^\pm K^\pm$   
⇒ Hadrons

The executive summary, of course, is that is highly desirable to measure in one experiment electrons, muons, photons, and charged hadrons. Is it possible to measure this ambitious list of phenomena in central A-A collisions at RHIC in one detector (at finite cost)? The PHENIX answer to this question is "Yes" (if one measures over finite intervals).

### III. THE PHENIX APPARATUS

The PHENIX collaboration has chosen to measure electrons, photons and hadrons in the central region  $|y| < 0.35$ , and muons in the rapidity slice  $1.2 < |y| < 2.5$ . This approach results in a four-armed design, as shown in Figure 2, consisting of two central arms, each covering  $90^\circ$  of azimuth, and two full-azimuth muon arms.

The central magnet produces a roughly axial magnetic field in the central region for momentum analysis of charged particles. Each central arm contains three tracking sub-systems: A drift chamber (DC) with one-sided drift cells in "X" for measuring in  $r-\phi$  and with similar cells in small-angle stereo for  $z$  measurement, three layers of pixel pad chambers (PC1, 2 and 3) for determining space points on the trajectories, and a time-expansion chamber (TEC) to provide both tracking and particle ID via  $dE/dx$  and transition radiation. PC1 and PC2 are separated by a  $\sim 140$  cm gas volume for the Ring Imaging Cerenkov (RICH) detector, which is read out by phototubes located on the magnet pole tips. The gas volume, filled with atmospheric pressure ethane ( $\gamma_{th} \sim 25$ ), identifies electrons. The outermost

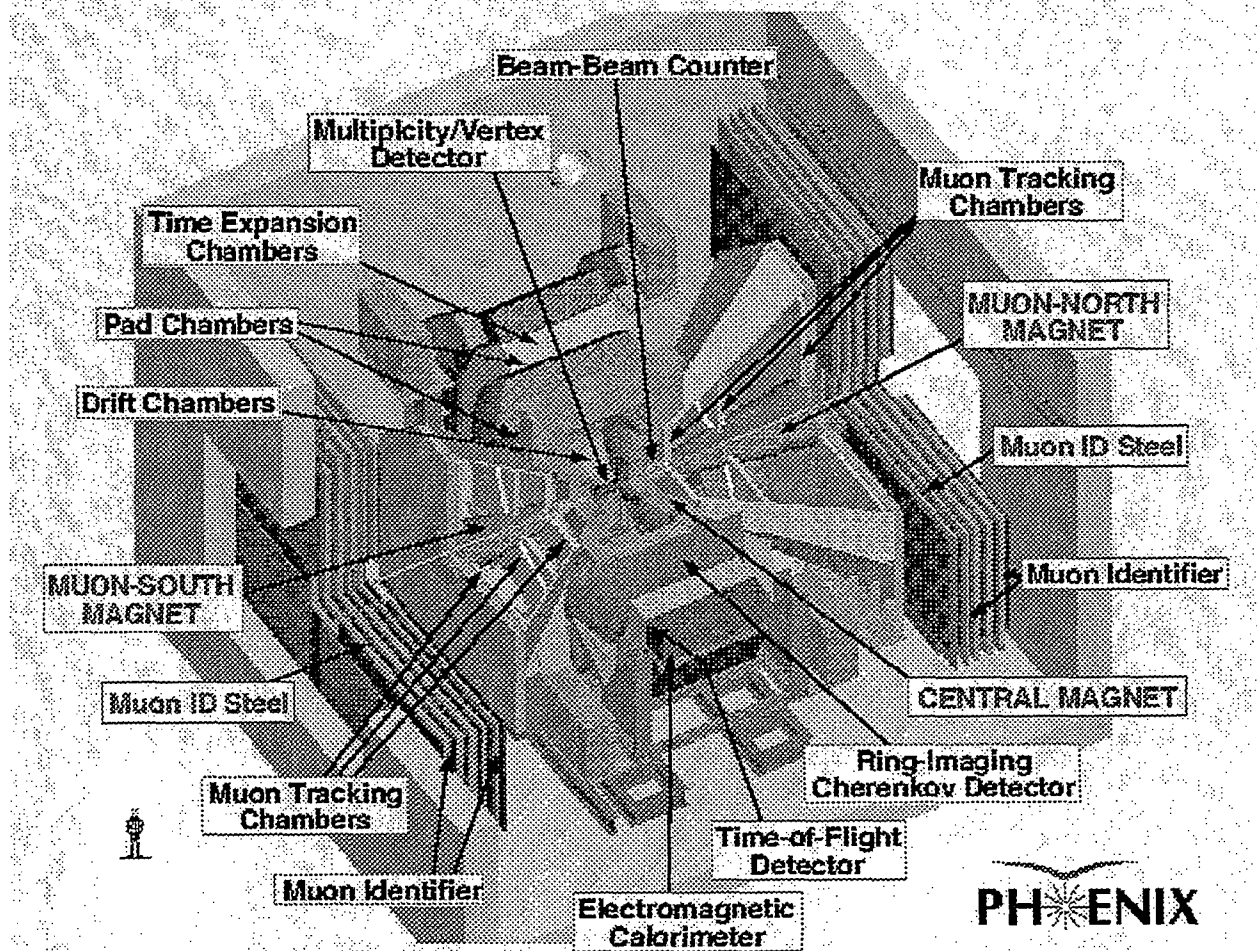


FIG. 2. The PHENIX detector. The central detector arm on the far side of the detector is the West arm; the right-hand muon arm is the North arm.

detectors in the central arm are very finely segmented ( $\Delta\eta \times \Delta\phi \sim 0.01 \times 0.01$ ) PbGl (West arm) and Pb-Scintillator (both arms) electromagnetic calorimeters for measuring photons and electrons. A precision ( $\sigma_t \sim 80$  ps) time-of-flight array covering half the azimuth of the West arm will be used to identify charged hadrons in this aperture.

The two large conical structures apparent in Figure 2 are the North and South muon magnets, which (with the aid of a central cylindrical “pistons” produce a roughly radial magnetic field. Muons in the angular range  $10^\circ < \theta < 35^\circ$  are momentum analyzed in three stations of cathode strip chambers (CSC’s). Identification of the muons is based on their penetration through up to five layers of steel absorber, which is interspersed with limited streamer tubes (LST’s) for readout. It should be noted that an important “component” of the muon detection system is passive, namely, absorbers consisting of the central magnet steel and additional material, designed to absorb produced hadrons before their decays produce muons.

As stated in Section II B, the PHENIX approach to studying heavy ion collisions at RHIC relies on the correlation of many channels with respect to some “external” parameter. One such quantity is the total charged multiplicity measured in the region  $|\eta| < 2.5$  by

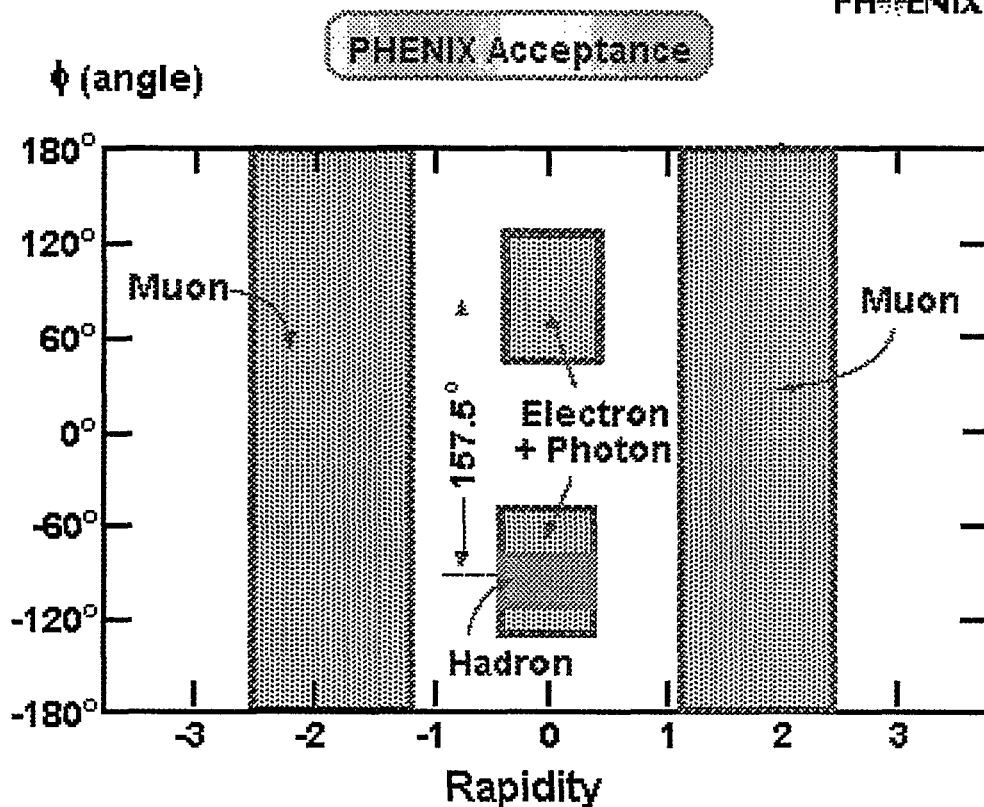


FIG. 3. The acceptance regions of the PHENIX central and muon arms.

the Multiplicity Vertex Detector (MVD), which consists of Si strips and pads covering the full azimuth. The MVD also provides on-line determination of the vertex (used in higher-level triggering). Another important source of vertex information are the Beam-Beam (BB) counters, which consist of two arrays of 64 phototubes each, detecting relativistic charged particles via Cerenkov light in the interval  $3 < |\eta| < 4$ . These counters also provide the essential Start time used in TOF analysis.

As emphasized in Section II, the lack of definitive cross-section predictions for QGP formation argues for building an experiment with the highest possible rate capabilities. The front end electronics (FEE), data acquisition (DAQ) and trigger systems of PHENIX have been designed to perform, for all colliding species, at luminosities an order-of-magnitude greater than the nominal design luminosity of RHIC. As shown in Figure 4, this is an extremely challenging task—while the rate at which data is produced in PHENIX is roughly independent of colliding species, the magnitude of this number is large ( $\sim 2$  GB/s). More importantly, the nature of the data varies from very small events occurring at very high rate (pp at  $\sim 1$  MHz) to very large events at small rate (Au-Au at  $\sim 1$  kHz). Regardless of species, the PHENIX FEE can read out the entire detector at a sustained rate of 25 kHz. Collision rates which exceed the input bandwidth of the system must be reduced by the Level-1 trigger; rates which exceed the output bandwidth of the system (20 MB/s) must be further reduced by higher-level triggers based on the physics content of the events.

# PHENIX DAQ

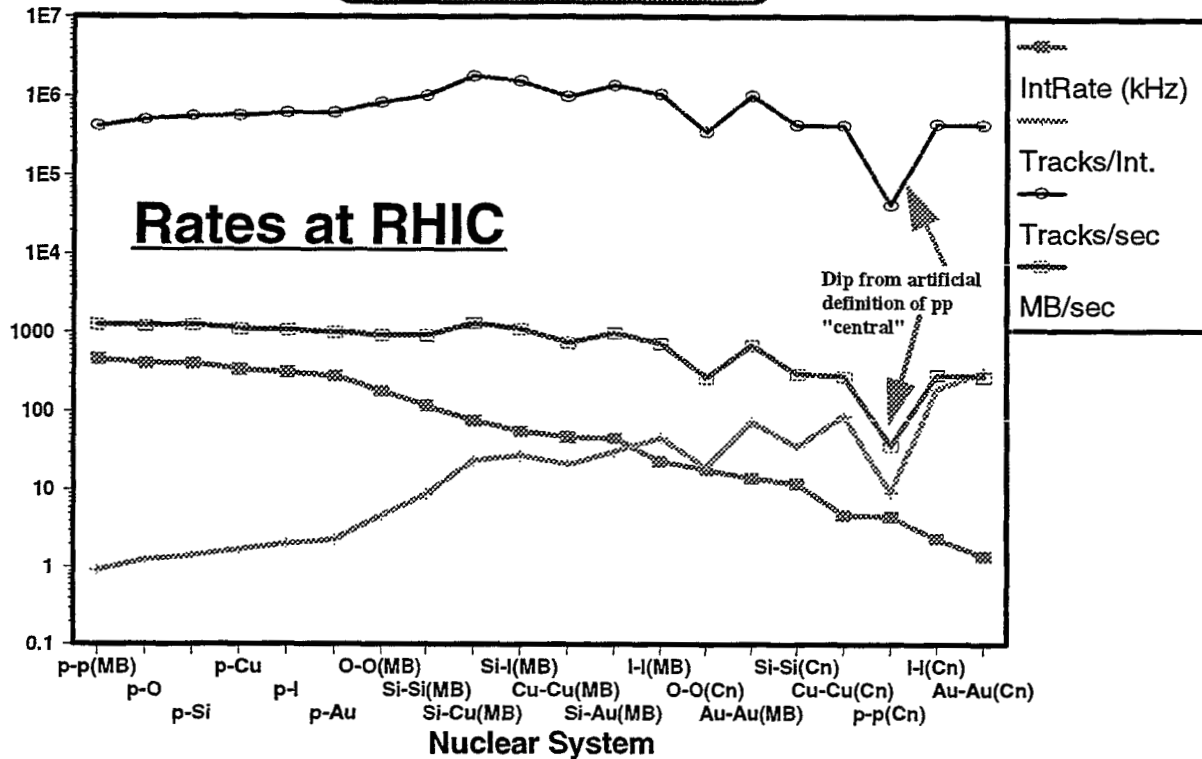


FIG. 4. Collision rates and PHENIX data volumes at RHIC for (roughly) 10 times design luminosity.

## IV. PHENIX PHYSICS

### A. Hadron Physics

The tremendous data volumes implicit in Figure 4 are generated almost entirely by hadrons. This fact, together with the large apertures and sophisticated DAQ systems found in RHIC experiments, implies that measurements which normally require weeks in fixed-target programs can be made in days or even hours at RHIC. A good illustration of this is the rate for correlation physics, shown in Figure 5. There a *three-pion* correlation function for a source with longitudinal, outward and sideward radii  $R_L = R_O = R_S = 6$  fm is shown as measured in the PHENIX aperture, for a greatly restricted subset of the three-particle phase space, namely all  $q_L < \hbar/R_L$  and all  $q_S < \hbar/R_S$ . The resulting correlation function is then plotted versus the “out” component between particles 1 and 2. The data are for a simulation of  $10^5$  central Au-Au events; at design luminosity this corresponds to less than one hour of data-taking(!).

Recently much attention has been focused on an explicit indicator of a second-order phase transition that appears in the hadronic sector, the Disoriented Chiral Condensate (DCC)

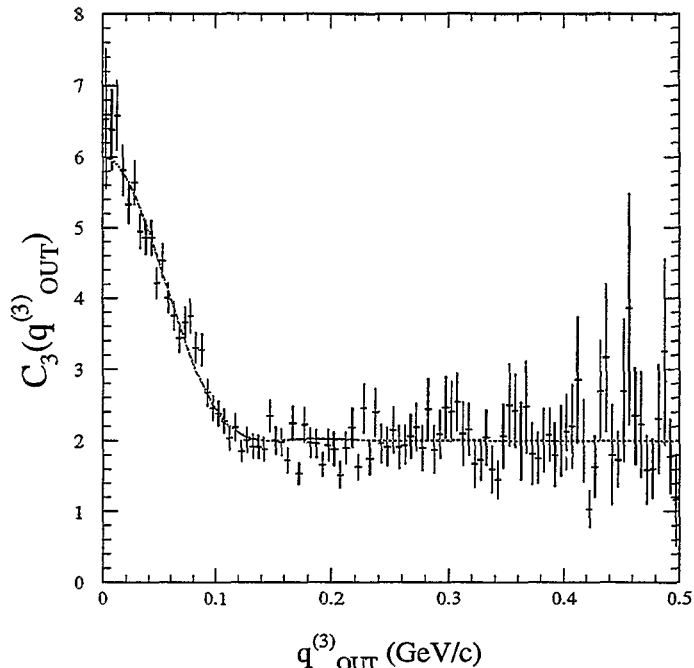


FIG. 5. The three-pion correlation function for triplets from  $10^5$  central Au-Au events as measured in the PHENIX high-resolution hadron sector.

[6], which results in non-Poissonian fluctuations in the yield of charged and neutral pions (particularly at low transverse momenta). Due to its finely segmented EmCal, PHENIX has a unique ability to identify DCC's through their effect on the  $\pi^0$  spectrum. For instance, fluctuations in the MVD's event-by-event reconstruction of the charged-particle pseudorapidity spectrum in the region  $|\eta| < 2.5$  (Figure 6) can be correlated with the number of low- $p_T$  clusters in the EmCal.

## B. Electron Physics

PHENIX has made a concerted effort to optimize the detectors in the central arms for electron and photon detection. Much of the interest centers on the decays of the vector mesons to electron pairs. Figure 7 (from the PHENIX Conceptual Design Report [7]) shows a dielectron mass spectrum for  $\sim 3 \times 10^7$  central Au-Au events in the PHENIX central arms, with clear peaks above the combinatoric background containing several thousand  $\omega$ 's, a thousand  $\phi$ 's and several hundred  $J/\Psi$ 's. (Since these mesons are produced hadronically, their abundances are large; the only reason these rates are "small" is the  $\sim 10^{-4}$  branching ratio to  $e^+e^-$ .) In fact, the time to acquire  $\sim 3 \times 10^7$  pairs is

- $\sim 10$  weeks at  $\frac{1}{100}$  design luminosity
- $\sim 1$  week at  $\frac{1}{10}$  design luminosity
- $\sim 1$  week at design luminosity (without a trigger)
- $\sim 1$  week at  $10\times$  design luminosity (without a trigger)

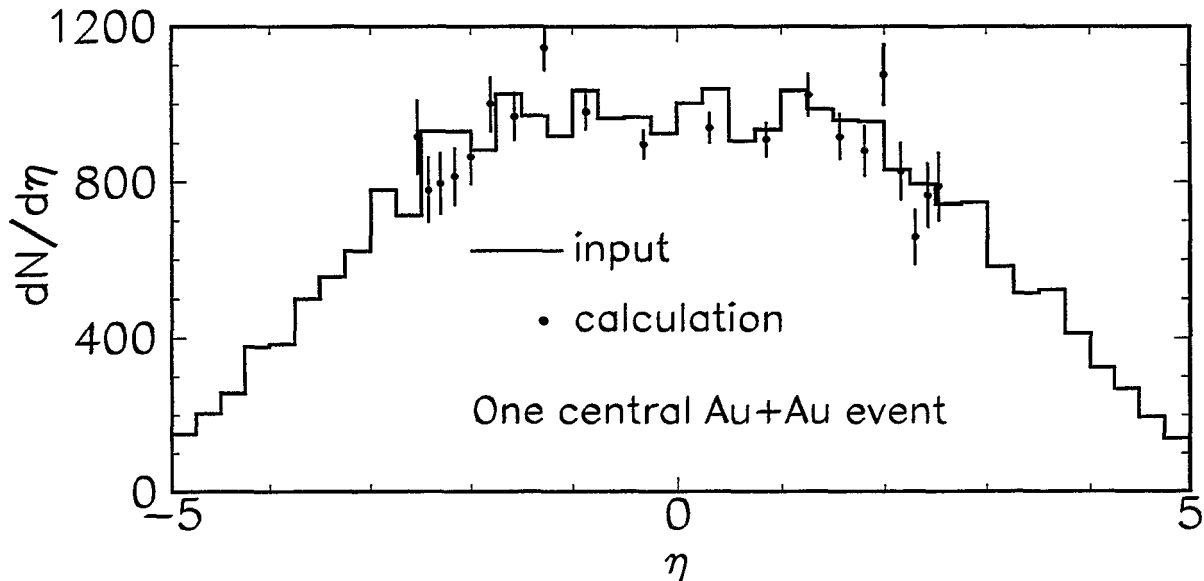


FIG. 6. Reconstruction of the charged-particle distribution for one central Au-Au event using the Multiplicity Vertex Detector, versus the input distribution.

That is, at design luminosity RHIC produces central Au-Au collisions at roughly an order-of-magnitude greater rate than PHENIX can accept. Clearly a trigger to select the “interesting” events is called for. It is absolutely inadequate to declare “interesting” as “having an  $e^+e^-$  pair”, as shown in Figure 8, which plots the rejection factor available by triggering on electrons in the PHENIX aperture [8]. Since there are several such electrons per central Au-Au event, a more sophisticated strategy will be required to preserve DAQ bandwidth for comparatively rare  $J/\Psi$ ’s. Such “physics-based” triggers are under active study at the moment, and will likely be implemented at Level-2.

### C. Direct Photons

Direct photons are thought to be emitted copiously by the plasma, and escape the interacting matter with essentially no interaction. As such, they are in principle superb diagnostics of thermal history of the collision [10]. In practice, their experimental detection is extremely challenging, since the overwhelming background from hadronic decays (dominantly  $\pi^0$ ’s and  $\eta$ ’s) must first be measured and eliminated [11]. This requires a finely segmented electromagnetic calorimeter augmented with charged-particle tracking, as deployed in the PHENIX central arms. The precise details of determining  $\pi^0$  and  $\eta$  yields as a function of multiplicity and transverse momentum will not be dealt with here; the reader is referred to Refs. [3,7,12,13].

The very large combinatoric background at low transverse momentum is substantially reduced at higher  $p_T$  values. In fact, if there is substantial jet quenching the direct photon yield may even exceed the hadronic yield for  $p_T > \sim 12$  GeV [9], as shown in Figure 9. Here



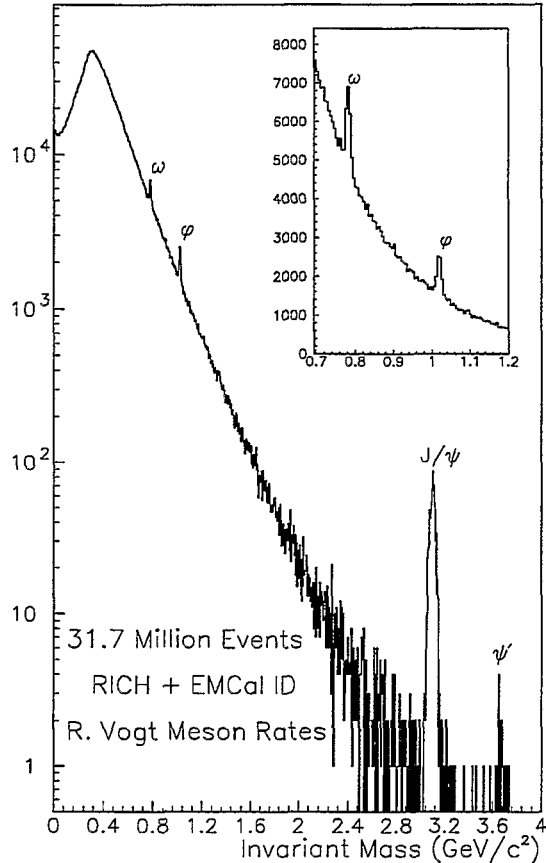


FIG. 7. The dielectron pair mass spectrum expected in the PHENIX central aperture from  $\sim 3 \times 10^7$  events.

we have the happy situation of one plasma signature (jet quenching [14]) helping another (direct photons). The only problem appears to be one of rate, and is not terribly serious: At design luminosities, the predicted yield at  $p_T \sim 12$  GeV/c of  $\frac{dN}{dydp_T} \sim 10^{-5}$  GeV $^{-1}$  gives a rate in the PHENIX aperture of one photon per hour (in a 1 GeV/c bin). This is a case where a trigger is straightforward, since the number of clusters in the EmCal with this energy per central Au-Au event is well below unity, so that live-time can be preserved by rejecting events not satisfying this condition. Correspondingly, the rate can be increased almost linearly by raising the luminosity above the design value. If such gains can be achieved, this opens up the exciting possibility of directly observing the effect of jet quenching on the fragmentation function by using the photon as a tag [15], and examining the particle distribution opposite to it.

#### D. Muons

Much of the physics discussed in Section IV B is also measured in the North and South muon arms. As shown in Figure 10, clear peaks for the various vector mesons emerge after a like-sign subtraction. Note in particular that the spectrum extends beyond  $M_{\mu\mu} = 10$  GeV, which allows for measurement of the  $\Upsilon$ . Due to its very small Bohr radius ( $\sim 0.13$  fm), measurement of the  $\Upsilon$  should be instrumental in understanding the systematics of  $J/\Psi$

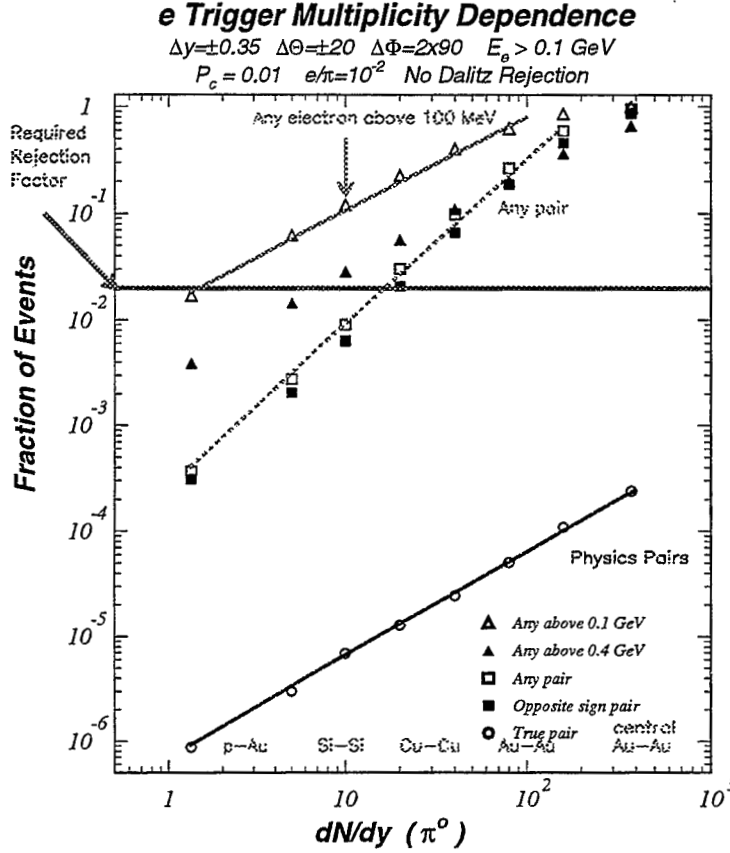


FIG. 8. The fraction of events containing various electron signatures in the PHENIX aperture, as a function of the  $\pi^0$   $dN/dy$ .

	PHENIX Central Au + Au	PHENIX Min. bias Au + Au	FNAL E772
$\rho \rightarrow \mu^+ + \mu^-$	> 300K	> 1M	-
$\phi \rightarrow \mu^+ + \mu^-$	> 139K	> 500K	-
$J/\psi \rightarrow \mu^+ + \mu^-$	700K	3M	100K
$\psi' \rightarrow \mu^+ + \mu^-$	10K	24K	12K
$\Upsilon \rightarrow \mu^+ + \mu^-$	2160	9K	17K
D-Y (4-9 GeV)	~ 24K	~ 100K	450K
$\sqrt{s}$ (GeV)		200	39
$x_F$		-0.3 to 0.3	0 to 0.6
$p_T$ (GeV)		0-10	0-2.5
$x_2$		~ $10^{-4}$ -0.2	~ 0.03-0.27

TABLE I. Comparison of some PHENIX muon performance to the fixed-target experiment E772 at Fermilab. The yields are calculated for 3000 hours of running [16].

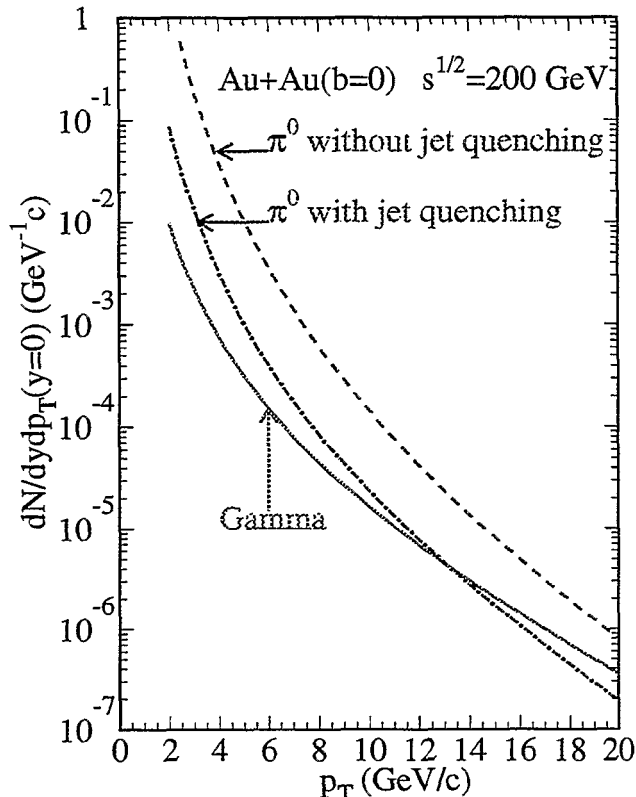


FIG. 9. The direct photon spectrum for central Au-Au collisions versus the  $\pi^0$  background with and without jet quenching [9].

and  $\psi'$  suppression. The mass region between the  $J/\Psi$  and the  $\Upsilon$  is dominated by open charm production (see the next section). Table I demonstrates that the performance of the PHENIX muon systems compares very well [16] to the FNAL experiment E772, which has been a leader in exploring the production of heavy vector mesons in p-A collisions.

### E. Charm

While the discussion of electron physics in Section IV B concentrated on measurement of the vector mesons, observed as peaks in the dilepton pair mass, there is also substantial interest in the dilepton continuum, since virtual photons, just as real ones, diagnose the thermal evolution of the plasma. The penalty in rate from the extra factor of  $\alpha$  must be paid, but the enormous backgrounds from the  $\pi^0$  and  $\eta$  that so affect the direct photon measurement are absent. This optimistic scenario led many researchers circa 1990 to advocate measurement of the thermal dileptons yield as a plasma probe.

Since then, it has become clear that dileptons do provide substantial information on the evolution of the interacting matter, but via the production of open charm rather than by thermal mechanisms [17]. That is, the thermal spectrum lies one to two orders-of-magnitude below the charm signal, as shown in Figure 11. (Ironically, even the lepton pairs in thermally

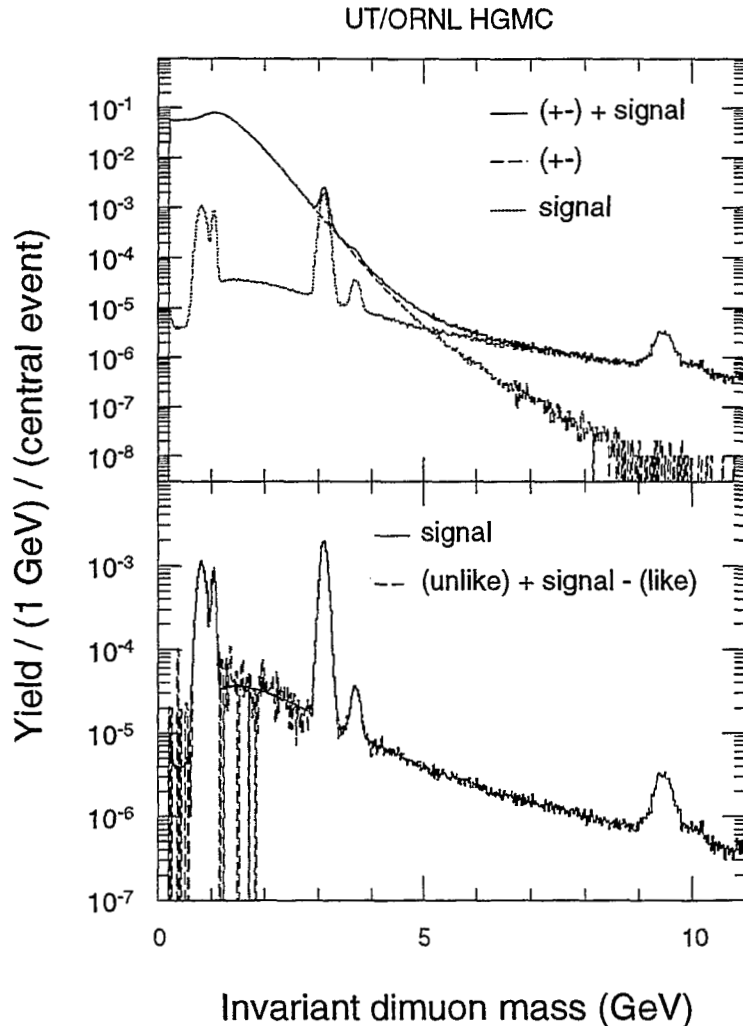


FIG. 10. The PHENIX North Muon arm spectrum before and after subtraction of a like-sign combinatoric background.

produced charm exceeds the directly produced thermal dileptons.) This dominance of the charm signal has prompted several authors to suggest using it rather than thermal dileptons as the canonical probe of the initial densities [19–21].

Accumulating sufficient high-mass muon and electron pairs will be a relatively straightforward procedure for the PHENIX experiment, as indicated by Table I. However, extracting the physics components of the spectrum will be a challenging task, even after a like-sign subtraction to remove the uncorrelated background. Two different techniques will help isolate the charm contribution: First, as emphasized by Tannenbaum [22], the production of single electrons at large transverse momenta is dominated by charm decays. The work of Akiba [18] shown in Figure 12 demonstrates the sensitivity of the  $e/\pi$  ratio for  $p_T > \sim 1.5$  GeV/c to the charm yield, and thus to the nuclear shadowing. A second approach relies on PHENIX's capability for measuring  $e - \mu$  coincidences (some hint of the rates may be obtained by comparing panels a, b and c of Figure 11). Since the first method does not have a combinatoric background, while the second covers a much larger rapidity interval, taken together these techniques will provide us with an excellent handle on the systematics inherent in any such measurement. Finally, it should be noted that the all-important shadowing of the gluon

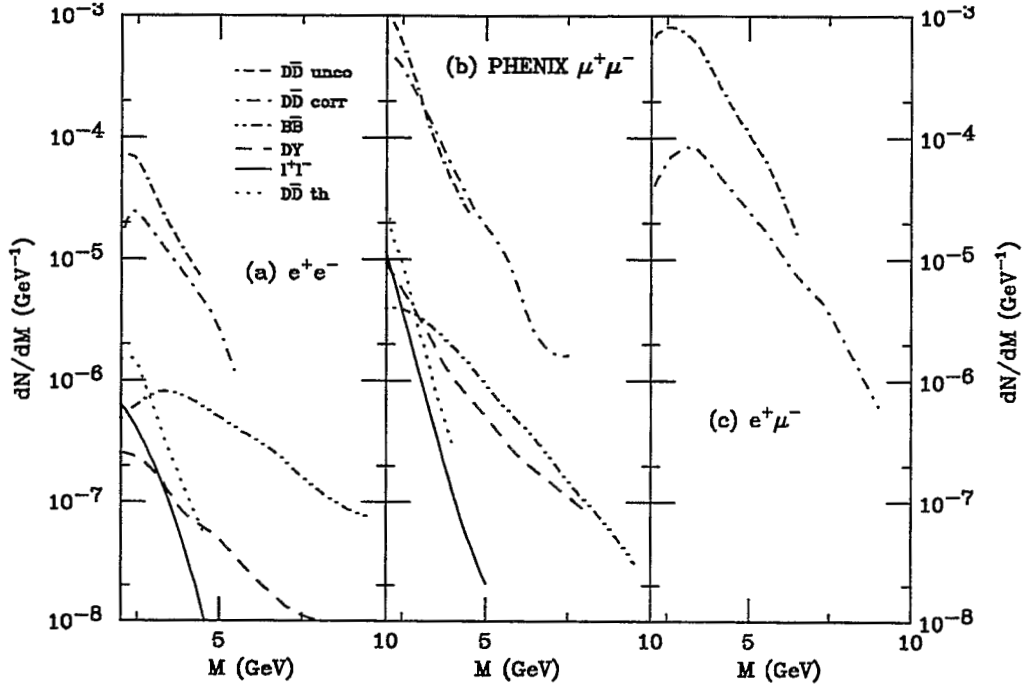
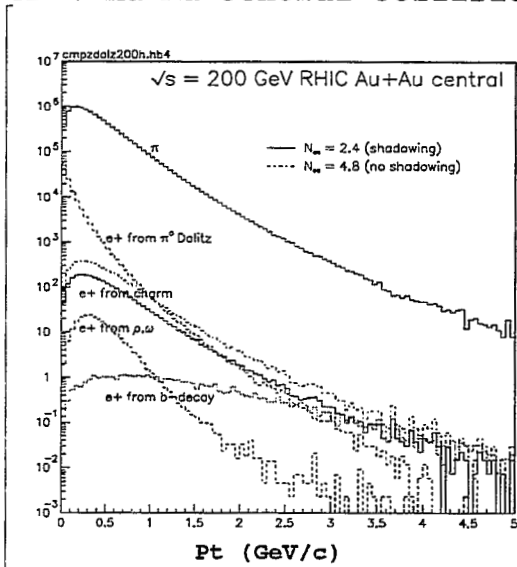


FIG. 11. Contributions to the dilepton spectrum as measured in PHENIX. The “D  $\bar{D}$  uncorr” curve is for dileptons originating from different  $c \bar{c}$  pairs; “D  $\bar{D}$  corr” curve is for dileptons originating from the same  $c \bar{c}$  pair. (From Ref. [17].)

**“single electron” spectrum in  
Rhic Au+Au central collisions**



**e/pi ratio at Rhic Au+Au**

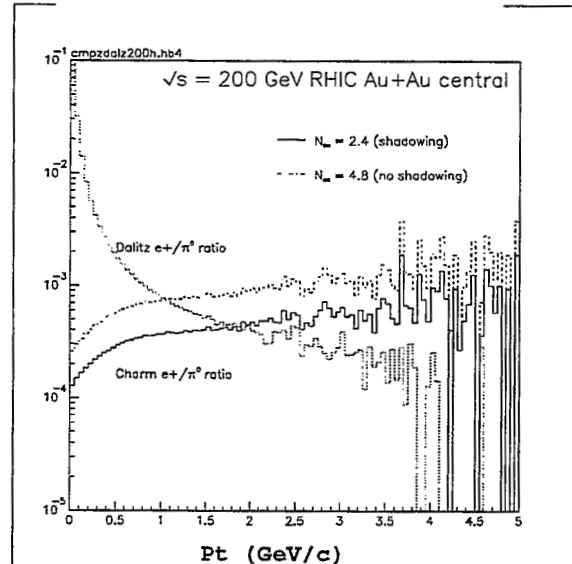


FIG. 12. The contributions to the single electron transverse momentum spectrum, as compared to pions (left hand side), and the resulting  $e/\pi$  ratio (right hand side), as calculated in Ref. [18], for no shadowing ( $N_{cc} = 4.8$ ) and shadowing ( $N_{cc} = 2.4$ ).

structure functions in nuclei may be measured directly in PHENIX using charm yields from p-A collisions, as recently suggested by Lin and Gyulassy [21].

## V. CONCLUSIONS

The broad range of probes made accessible by the PHENIX apparatus make it both an ideal first-generation “discovery” experiment as well as the basis for a second-generation “characterization” facility. We eagerly await the surprises RHIC will provide in 1999 and beyond.

## VI. ACKNOWLEDGMENTS

It is a pleasure to acknowledge the extensive contributions of my many PHENIX colleagues to this work, as well as useful conversations with S. Gavin, M. Gyulassy, Z. Lin, K. Rajagopal, R. Vogt and X. Yang. This work was supported by the United States Department of Energy Grant DOE-FG02-86ER-40281.

## REFERENCES

- [1] The most up-to-date information concerning RHIC may be found at <http://www.rhic.bnl.gov/>.
- [2] For a review of recent work in the field, see these conference proceedings, and *Proceedings of Quark-Matter '96* (Twelfth International Conference on Ultra-Relativistic Nucleus-Nucleus Collisions), Heidelberg, Germany, May 20-24, 1996 (to appear in Nucl. Phys. A).
- [3] The most up-to-date information concerning the PHENIX experiment may be found at [http://rsgi01.rhic.bnl.gov/~phenix/phenix\\_home.html](http://rsgi01.rhic.bnl.gov/~phenix/phenix_home.html).
- [4] For instance,  $J/\Psi$  enhancement was once advertised as the signature for plasma formation (J. Milana, *Phys. Rev. Lett* **62**, 2921,1989). More recently, the *direction* of the mass shift on various vector mesons due to chiral symmetry restoration was vigorously debated at this workshop.
- [5] Here *channel* refers to the observation of a particular final-state particle (e.g., electrons), as distinct from *signals* (e.g., enhancement of the  $e^+e^-$  pair-mass spectrum in the continuum below the  $\rho$ ).
- [6] For a review of recent work, see “The Chiral Phase Transition in QCD”, by K. Rajagopal, in *Quark-Gluon Plasma 2*, edited by R. Hwa, World Scientific, 1995, and also the contribution of K. Rajagopal to this workshop.
- [7] *The PHENIX Conceptual Design Report*, 29-Jan-93.
- [8] T. Awes, private communication.
- [9] X.N. Wang, in the proceedings of this workshop.
- [10] *Photons and Lepton Pairs— The Deep Probes of the Quark-Gluon Plasma*, P.V. Ruuskanen, NATO Advanced Study Institute on Particle Production in Highly Excited Matter, Lucca, Italy, July 1992.

- [11] *Physics from Photon and Di-Lepton Spectra*, G.R. Young, NATO Advanced Study Institute on Particle Production in Highly Excited Matter, Lucca, Italy, July 1992.
- [12] *PHENIX CDR Update*, Nov-93.
- [13] The most current information regarding the EmCal and its performance may be found at <http://www.rhic.bnl.gov/phenix/WWW/emcal/emcal.html>.
- [14] M. Gyulassy and M. Plumer, Phys. Lett. **B243**, 432 (1990).
- [15] Xin-Nian Wang, Zheng Huang, and Ina Sarcevic, Phys. Rev. Lett. **77**, 231 (1996).
- [16] M. Leitch, private communication.
- [17] S.Gavin *et al.*, Phys. Rev. **C54**, 2606 (1996).
- [18] Y. Akiba, in Physics with the Collider Detectors at RHIC and the LHC, Proceedings of the Pre-Conference Workshop, Quark Matter '95, Monterey, CA, J. Thomas and T. Hallman, eds., UCRL-ID-121571, pp. 131-142 (1995).
- [19] B. Muller and X.N. Wang, Phys. Rev. Lett. **68**, 2437 (1992).
- [20] K. Geiger, Phys. Rev. **D48**, 4129-4145 (1993).
- [21] Z. Lin and M. Gyulassy, Phys. Rev. Lett. **77**, 1222-1225 (1996).
- [22] *Charm in PHENIX- a signal or a background?*, M.J. Tannenbaum, to appear in Heavy Ion Physics.

**VI.**

**Summary**



# The Phases of QCD

E. Shuryak

*Physics Department, State University of New York  
Stony Brook, NY 11794*

## Abstract

In the recent years we have learned that light quarks play a crucial role in QCD-like theories, transforming it to many different phases. We review what is known about them, both from lattice and non-lattice approaches. A particularly simple mechanism of the QCD chiral restoration phase transition is discussed first: it suggests that it is a transition from randomly placed tunneling events (instantons) at low  $T$  to strongly localized tunneling-anti-tunneling pairs at high  $T$ . Many features of the transition found on the lattice can be explained in this simple picture. Very relevant for RHIC, this approach predicts a strong non-perturbative interaction between quarks *above* the phase transition. It also predicts that QGP-like phase sets in at *zero* temperature, provided few more light quark flavors are added to QCD. Finally, we also discuss possible experimental signatures of the QCD phase transition. One issue is CERN dilepton data, possibly related with “dropping” masses of  $\rho$ ,  $A_1$  mesons. Another is direct manifestation of a *softness* of EOS (smallness of pressure/energy density) in the phase transition region in flow and even the global lifetime of the system.

## I. INTRODUCTION

My topic is to review our current understanding of critical phenomena in QCD (and its close relatives). But before that, let me comment on a somewhat different type of critical phenomena discussed in one (late) session of the workshop, the so called “self-organized criticality” exemplified by the famous sand piles. Not being an expert in this field, I still dare to suggest that the RHIC summer workshop itself is a perfect example of this phenomenon. Indeed, only several years ago many of the participant of RHIC project (experimentalists, accelerator people and even most of the theorists) would not even listen to a talk with such title as mine. (This is commonly described by exponentially decaying correlations, with rather short correlation length.) Now, with common goals and concerns about directions future experiments at RHIC will follow, we are all well inside “one correlation length”. This is clearly a phase transition in its own right.

Returning to QCD, let me start with the comment that during the last few years we have learned about many new phases, which the gauge theories may have. Of course, the one we are going to look for experimentally is still the *chirally symmetric Quark-Gluon Plasma* (QGP), in which the charge is *screened* [1] rather than confined. Recent unexpected findings

suggest that it may have completely new features, such as preserve some hadronic modes as a bound states [2].

However, theory predicts some other phases which has taught us many new lessons. In particular, it seems that QGP may exist even at *zero* temperature in QCD with about 5-7 light fermions. Even more flavored QCD, with 7-16 light quarks, is expected to be in even stranger *conformal* phase, an extended relative of a condition commonly studied only at the second order phase transition points. Similar phases are proven to exist in supersymmetric extension of QCD, in which there were recently a significant advances due to Seiberg and Witten.

In addition, we have learned about some *unwanted* phases, such as (i) the *Aoki phase* appearing in lattice studies with Wilson fermions (see Ukawa review) and (ii) the *Stephanov phase* appearing in quenched lattice simulations with the non-zero chemical potential.

As emphasized by T.D.Lee in his opening talk, before thinking about “small” (the particles) one should first clearly understand “large” (the phase one actually is in): as we will see it is a very good advice to these lattice calculations indeed.

The bottom line of this talk is the crucial (but still not quite well understood) role of light fermions, generating all these phases of QCD. In particular, compare the phase transition found in “quenched” calculations ( $N_f = 0$ ) and those with  $N_f = 2 - 3$  dynamical quarks. The former case has a “deconfinement” phase transition at high  $T_c \approx 260 MeV$ , while the latter show a “chiral restoration” transition at much lower  $T_c \approx 150 MeV$  <sup>1</sup> Unlike at normal ( $T=0$ ) conditions, at  $T \approx T_c$  physical quantities are very sensitive to such little details as the mass value of the strange quark. Therefore we are still not quite sure about the *order* of the transition: the latest lattice results [3] incline again toward the 1-st order in the real world.

But do we understand why the transitions happen? Is there a simple picture which can explain its microscopic mechanism? Can we build a working model, reliable enough to provide some guidance in delicate questions relevant to experimental observables?

Qualitative explanations of why the QCD phase transition takes place are often done in an over-simplified way, emphasizing the “overlapping” hadrons in a bag-model-type picture. But such pictures give all numbers <sup>2</sup> and physics wrong. Pure gluodynamics is an especially good example: at  $T_c \approx 260 MeV$  the density of glueballs is negligible since even the lightest one has a mass of about 1.7 GeV! Looking at the low-T side of this transition it is impossible to tell why it happens. The same is qualitatively true for the chiral restoration: on the hadronic side the matter is still relatively dilute. But the reason why the phase transition happens is very simple: just two very different phases happen to have *the same free energy*. The lesson: one cannot understand a QCD phase transition without a *quantitative* model for *both* phases.

---

<sup>1</sup>By changing the quark masses from light to heavy continuously, it was shown that these two transitions are indeed different phenomena, separated by a large gap in which there is no transition at all.

<sup>2</sup>For example, the MIT bag model literally predicts QGP formation in heavy ion collisions at unrealistically small (BEVALAC/GSI) energies.

The energetics of the “deconfinement” and “chiral restoration” transitions is entirely different, suggesting different physics. The former has huge latent heat, few  $GeV/fm^3$ , so that probably all of the non-perturbative vacuum energy density (proportional to the “gluon condensate”) is “melted” in it. This is not the case for “chiral restoration” in QCD: large portion of the gluon condensate should actually survive it [4]. What is this remaining “hard glue” or “epoxy”, as Gerry Brown called it? Why, unlike “soft glue” does it not produce a quark condensate? Can it affect quark interactions and hadronic masses?

The major “non-lattice” approaches to the problem include: (i) models based on particular effective Lagrangians, like the sigma model or chiral effective Lagrangians models [5,6]; (ii) QCD sum rules at finite temperature/density [7]; (iii) the interacting instanton liquid model (IILM) [2,8].

*Effective Lagrangians* are very powerful tools at *low* temperatures: with parameters fixed by data one can indeed accurately account for effects due to non-zero occupation factors. However, they are clearly “one-sided”, unable to deal with QGP. In principle, *QCD sum rules* are *not* limited to a description of only hadronic phase: the structural changes can be adequately described by VEV of different operators, or “condensates”. However, since in practice those are unknown, people use simplifications. The most popular one is “vacuum dominance”, reducing average values of any quark operators to powers of  $\langle \bar{q}q \rangle$ , therefore missing non-perturbative effects above  $T_c$ .

Among theory issues discussed intensely during the last couple of years [9–12] is the fate of the U(1) chiral symmetry. It cannot be exactly restored, as suggested in [10], but its violation certainly is dramatically reduced at  $T \approx T_c$ . In practice it means that  $\eta_{non-strange}$  (a combination of  $\eta, \eta'$ ) and isovector scalar (we call  $\delta$ ) may be nearly as light as a pion.

One very important issue (which should have been discussed more) is what happens with the QCD phase transition for larger number of quark flavors  $N_f$ . Several phase transition lines are expected there, the lowest probably being the chiral symmetry restoration at  $T=0$ .

## II. A MECHANISM FOR THE CHIRAL PHASE TRANSITION

The main point of this talk is that due to recent developments it becomes increasingly clear what is the *microscopic mechanism* underlying this phase transition. It is *rearrangement* of instantons, from relatively random liquid at low  $T$  to a gas of instanton anti-instanton “molecules”<sup>3</sup>. These  $\bar{I}I$  molecules are the “epoxy” mentioned above: at  $T > T_c$  they indeed do not create the *quark* condensate but contribute to the *gluon* one. Furthermore, they generate new type of the inter-quark interaction, and may even create hadronic states, even above  $T_c$ !

Several events lead to these developments: (i) Demonstration that “instanton vacuum” explains the QCD correlation functions and hadronic spectroscopy at  $T=0$  [13,2]; (ii) Lattice confirmation of instanton liquid parameters and of the dominant role in general [14,15] ;

---

<sup>3</sup>Note a similarity to Kosterlitz-Thouless transition in O(2) spin model in 2 dimensions: there are paired topological objects (vortices) in one phase and random liquid in another.

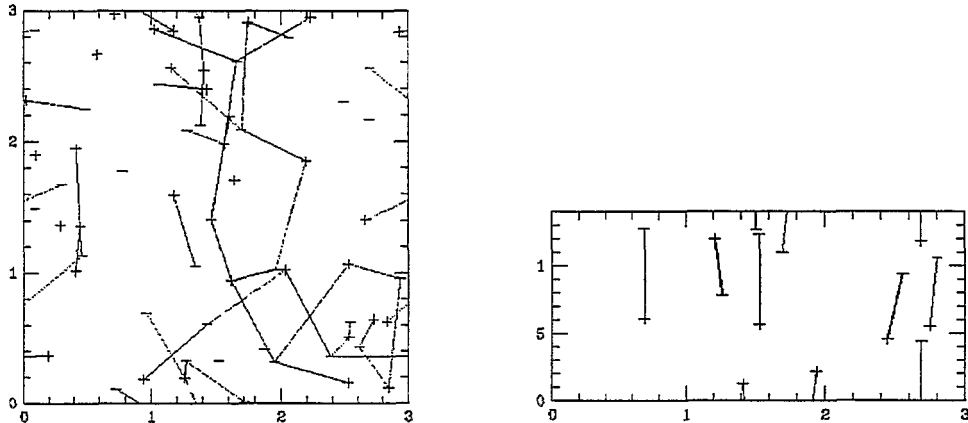


FIG. 1. Typical instanton configurations for temperatures  $T=76$  and  $158$  MeV.

(iii) As shown in [16] instantons cannot be screened<sup>4</sup> at  $T < T_c$ ; (iv) Confirmation of this statement on the lattice [17]; (v) Discovery of polarized  $\bar{I}I$  molecules at  $T \approx T_c$  [19]; (vi) Numerical simulations [2] and analytic studies [8] of the phase transition in the interacting instanton ensemble.

It is very easy to explain what happens at  $T \approx T_c$  in this approach. Recall that finite temperature is described in Euclidean space-time by periodic boundary conditions, with the Matsubara period  $1/T$ . So a rising  $T$  means a decreasing box, and when it fits to the size of one  $\bar{I}I$  molecule, one gets a “geometric” transition. In Fig. 1 from [2] one can see it clearly. (The plots show projections of a four dimensional box into the  $z$  axis-imaginary time plane. Instantons and anti-instanton positions are indicated by  $+$  and  $-$  symbols. The lines correspond to strongest fermionic “bonds”.) Notice that molecules are strongly “polarized” in the time direction and that they are separated by half Matsubara box in time  $\Delta\tau = 1/(2T)$ .<sup>5</sup>

In a series of recent numerical simulations [2] it was found that like QCD, the instanton model has *second* order transition for  $N_f = 2$  massless flavors, but a *weak first order* one for QCD with physical masses. Furthermore, the thermodynamic parameters, the spectra of the Dirac operator, the  $T$ -dependence of the quark condensate and various susceptibilities, the screening masses are all consistent with available lattice data.

### III. PHASES OF QCD WITH MORE QUARK FLAVORS

In this section we discuss further the role of quarks in QCD, adding more flavors to it. If we add too much of them, namely  $N_f > 33/2$  (here and below we imply 3 colors), the

<sup>4</sup>Previously considered scenario based on the “instanton suppression” does not in fact work until rather high  $T$ , well in the QGP domain, and thus it cannot be the reason for the phase transition.

<sup>5</sup>Thus one can even find the approximate phase transition temperature. The molecule fits onto the torus if  $4\rho \simeq 1/T_c$ , and with known instanton size  $\rho \simeq 0.35$  fm one gets  $T \simeq 150$  MeV, close enough to the observed one.

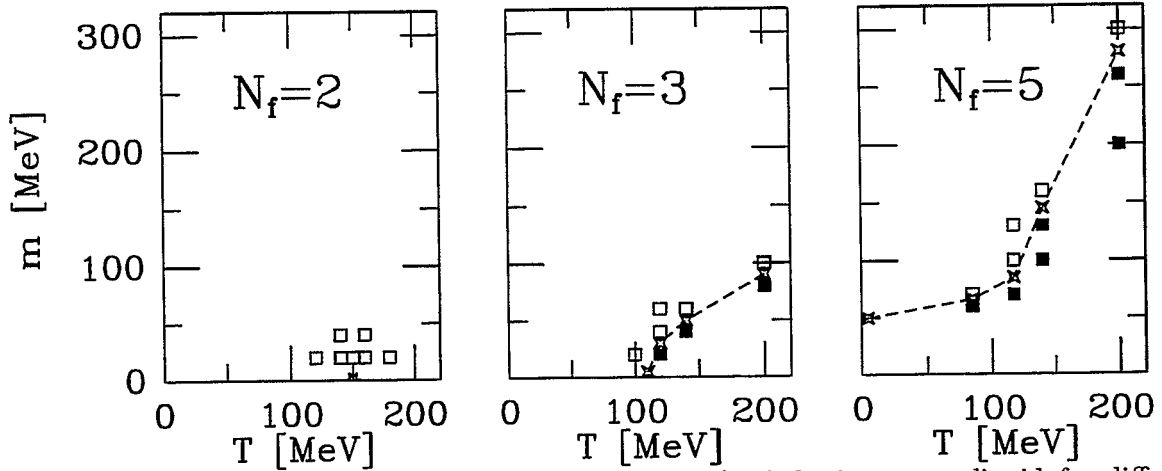


FIG. 2. Phase diagram (temperature-quark mass plane) of the instanton liquid for different numbers of quark flavors,  $N_f=2,3$  and 5. The open squares indicate non-zero chiral condensate, while solid one indicate that it is zero. The dashed lines show the approximate location of the discontinuity line.

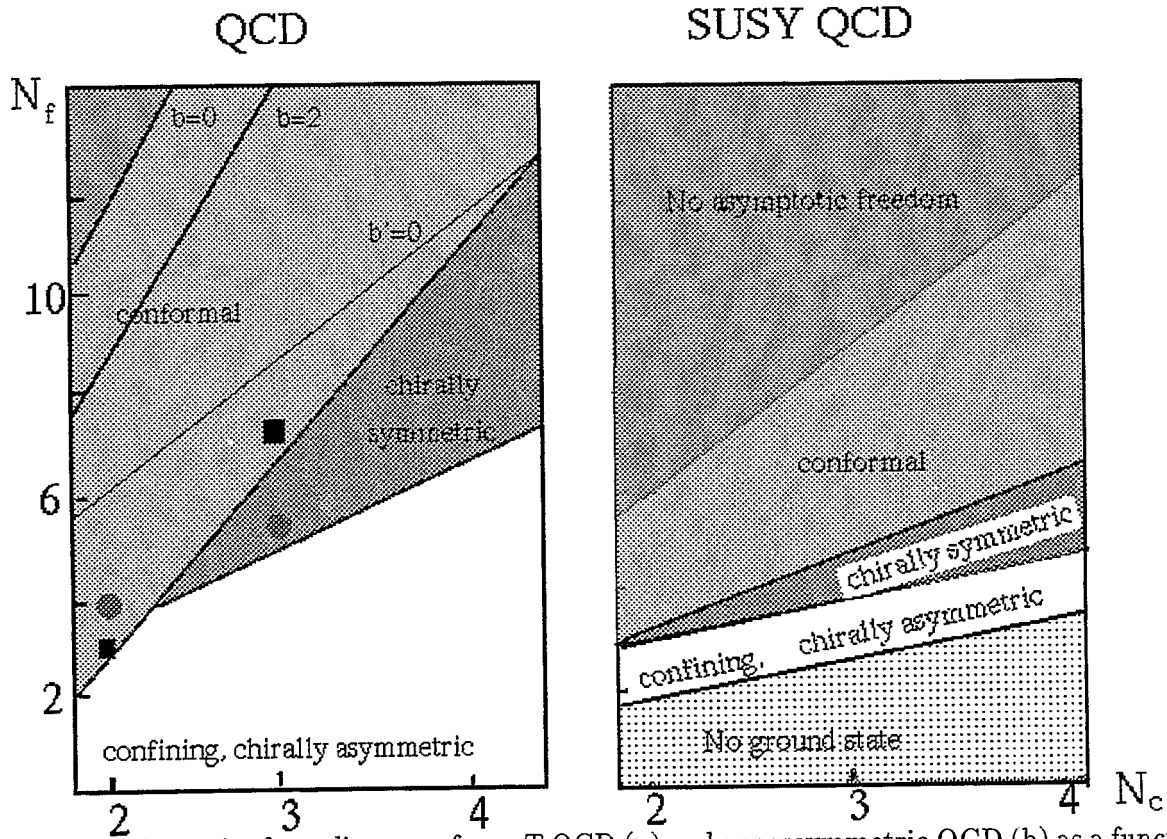


FIG. 3. Schematic phase diagram of zero T QCD (a) and supersymmetric QCD (b) as a function of the number of colors  $N_c$  and the number of flavors  $N_f$ . Squares show where lattice calculations have found the infrared fixed point, dots are where the instanton ensemble is purely “molecular”, with the unbroken chiral symmetry.

asymptotic freedom is lost and we get *uninteresting* field theory with a charge growing at small distances, basically a theory as bad as QED! So our “most flavored” QCD (with 16 flavors, and work out way down from it (see fig 3). The phase we are in there is actually rather simple one, known as the Banks-Zaks conformal domain [25]. It has the infrared fixed point at small coupling  $g_*^2/16\pi^2 = -b/b' \ll 1$  ( $b, b'$  are the one and two-loops coefficients of beta function). It happens in the perturbative domain, so the charge is small both at small and large distances. There are no particles in this phase, and all correlators decay as powers of the distance. In this phase the non-perturbative phenomena like instantons are exponentially suppressed,  $\exp(-const/g_*^2)$ . However, as one decrease the fermion number, the fixed point  $g_*^2$  moves to larger values and eventually disappears. Lattice simulations of multi-flavor QCD were recently reported in [26]. These authors studied QCD with up to 240 flavors. Studying the sign of the beta function in the weak and strong coupling domains, they confirmed the existence of an infrared fixed point as low as at  $N_f = 7$ .

It is not known which phase we find next, at  $N_f = 5 - 6$ , most probably it is the so called Coulomb phase (basically QGP).

The results of the interacting instanton model are summarized by Fig.2(b-d) show how one singular point at  $N_f = 2$  develops into the discontinuity line for  $N_f = 3$ . The value of  $T_c$  goes down with increasing  $N_f$  and at  $N_f = 5^6$  one finds that the chiral symmetry is restored even at  $T=0$ , provided quarks are light enough.

New lattice results have been presented at this meeting by R.Mawhinney for QCD with  $N_f = 4$ . Details can be found in his (and N.Christ’s) talk, and I should only say that when they have extrapolated the measured masses to quark masses  $m \rightarrow 0$ , they have found a dramatic significant drop in chiral symmetry breaking effects, such as  $\pi - \sigma, \rho - a_1, N - N^*(1/2^-)$  splittings, very much unlike the  $N_f = 0 - 3$  studied before. It suggests that chiral restoration is nearby, very similarly to what was found in the instanton calculations.

Finally, we return to Figure 3, and explain its rhs, showing similar phase diagram for the  $N=1$  SUSY QCD based on [27]. Not going into details, let me only mention that the vacuum is now definitely dominated by instanton-antiinstanton molecules, and their contribution can be calculated without problems (in QCD subtraction of perturbation theory is a great one). There are two phases which are impossible in QCD: a case without the ground state (molecule force the system toward infinite Higgs VEV) and also a funny situation with chiral symmetry unbroken but confinement (hadrons exist but are degenerate in parity). It is amusing that chiral symmetry is restored at  $N_f = N_c + 1$ , similar to what was found in QCD in the instanton model. Also note, that in this case the existence of the Coulomb phase is a proven fact.

---

<sup>6</sup>Note that  $N_f = 4$  case is missing. It is because I have found the condensate to be small and comparable to finite-size effects. In order to separate those one should do calculations in different boxes, which is time consuming.

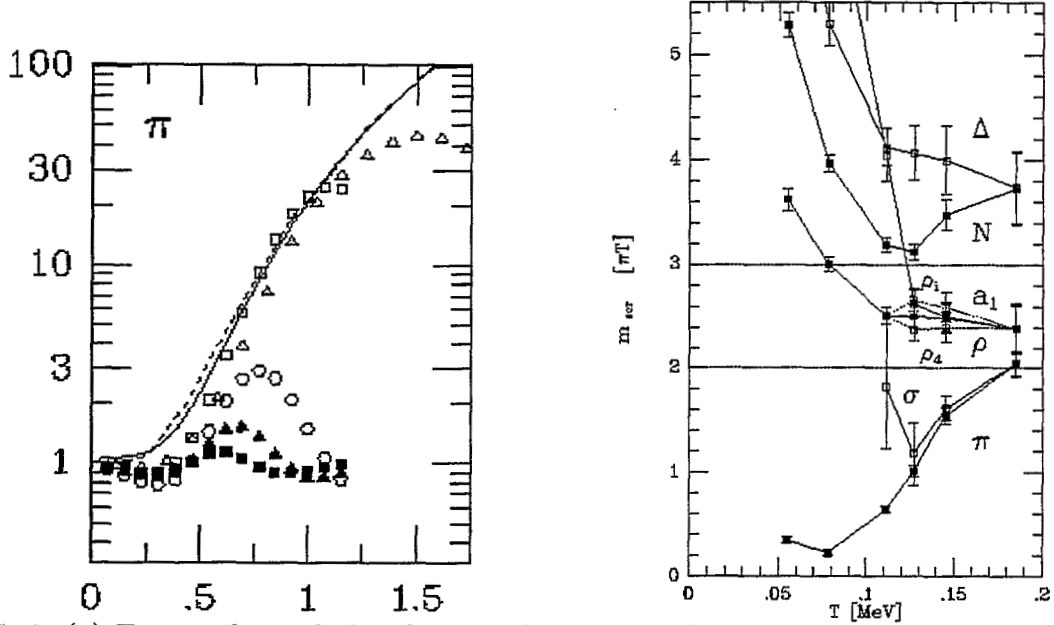


FIG. 4. (a) Temporal correlation function for the pion (divided by the one corresponding to free massless quarks) versus distance (in fm). Solid triangles and squares are for  $T = 1, 1.13T_c$ , open triangles, squares and hexagons for  $T = 0.43, 0.6, 0.86T_c$ , respectively. (b) T-dependence of the screening masses (given in units of  $\pi T$ ) calculated from the ILM. Note that at chiral restoration the partners ( $\sigma, \pi$ ), ( $\rho, a_1$ ) become identical.

#### IV. INTER-QUARK INTERACTION AND HADRONS NEAR AND ABOVE $T_C$

It is well known that the nucleon effective mass in nuclear matter is reduced, and there are also indications that  $m_\rho$  does the same [37]. Among approaches predicted “dropping masses” at high T the simplest (and the most radical) one is Brown-Rho scaling. According to it all hadronic masses get their scale from  $\langle \bar{q}q \rangle$ , and therefore vanish at  $T \rightarrow T_c$ . This idea is supported by the QCD sum rules, provided the “vacuum dominance” approximation is used. However it is not so in a vacuum made of the instanton molecules, because they generate non-zero average values for some fermionic operators, even when  $T > T_c$  and  $\langle \bar{q}q \rangle = 0$ . Those operators can be treated as new non-perturbative inter-quark interaction, which can be described by the following (Fierz symmetric, color-singlet only) Lagrangian [22]

$$\mathcal{L}_{mol\ sym} = G \left\{ \frac{2}{N_c^2} [(\bar{\psi}\tau^a\psi)^2 - (\bar{\psi}\tau^a\gamma_5\psi)^2] - \frac{1}{2N_c^2} [(\bar{\psi}\tau^a\gamma_\mu\psi)^2 + (\bar{\psi}\tau^a\gamma_\mu\gamma_5\psi)^2] + \frac{2}{N_c^2} (\bar{\psi}\gamma_\mu\gamma_5\psi)^2 \right\} + \mathcal{L}_8, \quad (1)$$

which has Nambu-Jona-Lasinio-type form and the coupling constant is proportional to density of molecules  $G = \int n(\rho_1, \rho_2) d\rho_1 d\rho_2 \frac{1}{8T_{IA}^2} (2\pi\rho_1)^2 (2\pi\rho_2)^2$ . Here,  $n(\rho_1, \rho_2)$  is the tunneling probability for the IA pair and  $T_{IA}$  is the corresponding overlap matrix element,  $\tau^a$  is a four-vector with components  $(\vec{\tau}, 1)$ . The effective Lagrangian (1) was determined by averaging over all possible molecule orientations. Near the phase transition, molecules are polarized and all vector interactions are modified according to  $(\bar{\psi}\gamma_\mu\Gamma\psi)^2 \rightarrow 4(\bar{\psi}\gamma_0\Gamma\psi)^2$ .

Numerical simulations [2] and analytic studies [23]<sup>7</sup> have been used to calculate both *spatial* and *temporal* correlation function. The former exponentially decay with the so called “screening masses”: their T-dependence for a number of hadronic channels is shown in Fig.(4)(b) [2] show overall agreement with lattice ones. Especially important is strong attraction in scalar-pseudoscalar channels, shifting these masses down from their high-T asymptotic,  $M/\pi T = 2$ . This attraction is also clearly seen in temporal correlation functions as well. For example, the pion correlators at several T are shown in Fig.(2)(a). They all have upward enhancement, which is absent in other channels (such as  $\rho$ ). Fit of the correlator suggests that pion survives the phase transition and exist at  $T > T_c$  as a (non-Goldstone) massive bound state. Most other hadrons “melt” into constituent quarks. Those have no effective mass but effective energy (or “chiral mass”) above  $T_c$ . Unfortunately, accuracy of the calculations done so far does not allow to get information about the fate of vector and axial mesons, the major players in the next section.

Unfortunately, the temporal correlators are very difficult to get on the lattice: there are only few points in time direction. The best data we can compare with [24] definitely show attraction in the pion channel at  $T > T_c$ , which is absent in vector ones.

## V. THE $U(1)_A$ RESTORATION?

The fate of the  $U(1)_A$  anomaly at finite temperature has received a lot of attention lately. A number of authors have emphasized that a (partial)  $U(1)_A$  restoration may be the case, with rather dramatic observable consequences [9,11,29]. Indeed, recall that at  $T=0$  the  $\eta' - \pi$  mass difference is larger than all other meson mass splittings, and any tendency for it to shrink would therefore strongly affect the whole spectroscopy<sup>8</sup>.

It is well known that this splitting and the  $U(1)_A$  anomaly are related with the topological charge, or well isolated instantons. It was argued in [9] that those should be very rare in the ensemble at  $T > T_c$ , because all instantons are “paired” into molecules. The density of isolated instantons above  $T_c$  is small  $O(m^{N_f})$ , but due to zero modes the quark propagators contribute a factor  $1/m$ , and some results are finite in the chiral limit<sup>9</sup>. So, a significant drop in the strength of the  $U(1)_A$  anomaly around  $T_c$  is expected, although to non-zero value. It was further suggested in [9] that instead of dealing with  $\eta'$  (which involve a complicated

---

<sup>7</sup>Those are directly analogous to the BCS theory of superconductivity, but with the instanton-induced interactions like (1).

<sup>8</sup>An interesting situation arises for  $N_f \geq 3$  massless flavors. In this case, the anomaly does not affect the  $\eta'$  correlation function above  $T_c$  [31,28,33]. If chiral symmetry is unbroken, extra zero modes cannot be absorbed by the condensate, and the 't Hooft vertex only contributes to  $2N_f$ -point correlators. For  $N_f = 3$  this means that the  $\eta'$  and  $\pi$  are degenerate above  $T_c$ , but the singlet and non-singlet  $\Lambda$  are split.

<sup>9</sup>Another way to explain it is to say, that for  $m=0$  the individual instantons are absent in the vacuum, but can be created by the operators themselves.



flavor mixing pattern), it is more convenient to look at a difference between  $\pi$  and its  $U(1)_A$  partner isovector scalar  $\delta$ .

Such measurements have been done, both on the lattice and in the instanton model. *All* of them observe that the difference of  $\pi - \delta$  susceptibilities indeed drops dramatically at  $T_c$ , indicating a move toward the  $U(1)_A$  restoration.

However, the calculations disagree about what exactly is its value at  $T > T_c$ . The problem is the  $m \rightarrow 0$  limit, which is very difficult to do in practice. Then the conclusion is sensitive to extrapolations: MILC collaboration [32] has fitted it quadratically  $\chi_\pi - \chi_\delta = C1 + m^2 C2$  and gets a non-zero  $C1$ , but extensive results from the Columbia group (see their data in N.Christ's talk) have shown that the linear fit is much better, and it leads to  $\chi_\pi - \chi_\delta \rightarrow 0$ .

In the instanton calculations [2] the value is clearly non-zero (although it is not accurately determined yet). So, it seems that here we (for the first time) see a serious qualitative disagreement with lattice simulations at  $T > T_c$ . This can be seen explicitly from the form of the Dirac spectrum. In the one we have calculated there are still quasi-zero modes due to isolated instantons, while in Columbia ensemble those seem to be completely absent. Why this happens remains unclear.

The problem of  $\eta\eta'$  mixing at finite  $T$  was studied in more detail in [30]. The most important conclusion is that there is a tendency towards ideal mixing, a separation of strange and non-strange component. However, contrary to others, it is shown that for  $T > T_c$  the anomaly only can operate in the non-strange sector, with  $\bar{u}u$  transition into  $\bar{d}d$  being proportional to  $m_s$ . It is claimed that non-strange component may be rather heavy.

In summary, a clear tendency toward diminishing of the role of  $U(1)$  anomaly at  $T \approx T_c$  is observed, but quantitative results for  $T > T_c$  are still missing. If (as Columbia data suggests) it is vanishingly small, we would have 8 rather than 4 massless modes (for  $N_f = 2, m = 0$ ), and understand why it moved away from  $O(4)$  indices to the first-order ones. However, the instanton calculations show that it is not so small.

## VI. THE PHASE TRANSITION AT FINITE BARYON DENSITY: THE OLD AND THE NEW PUZZLES

First attempts to introduce the non-zero chemical potential associated with baryon number have been done in *quenched* approximation a decade ago [34]. It was found that a very strange thing (referred as the "old puzzle") happens. At small  $\mu$  as expected, nothing depends on it, till some threshold  $\mu_c$  is reached. But instead of finding a threshold to be around the constituent quark mass  $\mu_c \approx m_N/3$ <sup>10</sup>, they have found it at  $\mu_c \approx m_\pi/2$ . Those are not too different if quark bare mass is large, but if it goes to zero the latter value vanishes. That means that in the chiral limit some states with non-zero baryonic number exist (and can be excited) at arbitrarily small  $\mu$ . There are no such states in the real world, so why lattice data have found them?

---

<sup>10</sup>By tradition, lattice people just put  $\mu$  in the Dirac operator without extra coefficients, which means that in their units quarks have baryonic charge 1, not 1/3.

For ten years it was not clear why, but the phenomenon was not a numeric artifact, and it has been since then seen in many other calculations. The resolution of the puzzle was recently made by Stephanov [35]. He has pointed out, that it is “quenching” the QCD partition function which one should blame. Interestingly enough, it turns out that elimination of the quarks can be done in two very different ways. In both one writes in the bosonic partition function the factor  $[\det(i\hat{D} + i\mu\gamma_0 + im)]^{N_f}$  coming from the integration over fermions, and then takes  $N_f \rightarrow 0$ . This factor is real at  $\mu = 0$  and complex otherwise, so it can be written as a modulus and a phase. Stephanov has shown that the usual quenching corresponds to the limit, in which one keeps modulus and ignores the phase<sup>11</sup>.

Putting the absolute value of the determinant means that anti-quarks have a conjugate operator, with the opposite sign of the chemical potential  $\mu \rightarrow -\mu$ : so instead of having the baryonic charge -1 they also have it equal to 1, like quarks. Then mesons  $\bar{q}\Gamma q$  may have the baryon charge 2, and the massless excitations excited at small  $\mu$  are nothing else but such pions. Those exist in the Stephanov (unwanted) phase, in which the baryon number is spontaneously broken by the quark condensate<sup>12</sup>, which also obtains the baryon charge.

Another talk we had on the lattice data at finite baryon density have been given by M.Lombardo. This time it is based on rather complicated algorithm and strong coupling limit, but it is unquenched and includes the determinant as is, with its phase.

A good news is the excitation to non-zero baryonic density happens around the expected threshold value. But the bad news is the excitation starts about 30% lower it and is more smooth compared to what one expects on the basis of the temperature value involved. So, we still see some unusual baryonic states being excited, like some nuclei or nuclear matter with unexpectedly large binding energy. I do not know any explanation of this puzzle.

## VII. “DROPPING MASSES” IN THE EXPERIMENT?

Already at QM93, CERN dilepton experiments have provided first preliminary indications for a signal, significantly exceeding the theoretical expectations (e.g. [38]). Later CERES has found dramatic excess of dileptons at  $M_{e^+e^-} < m_\rho$ . In spite of multiple attempts by theorists to explain it by “conventional sources”, it was found to be impossible<sup>13</sup>. A list of “unconventional” explanations (more or less in a chronological order) include: (i) dropping  $m_\rho$  [39,40]; (ii) pion occupation numbers at low momenta are very high [41];

---

<sup>11</sup>One can do this also without the limit, at finite  $N_f$ : such approach was suggested and studied separately by Gocksch [36].

<sup>12</sup>In fact Stephanov has found boundaries of this phase and many interesting details about distributions of Dirac eigenvalues at non-zero  $\mu$ , both in the wrong (no phase) and right (with the phase) ensembles, using a particular model of chiral restoration based on random matrix approach. Unfortunately, we have no time to discuss it here.

<sup>13</sup>In fact, I have never before seen that rather involved calculations by several groups agree so well, as far as the shape of spectra of  $M_{e^+e^-}$  is concerned.

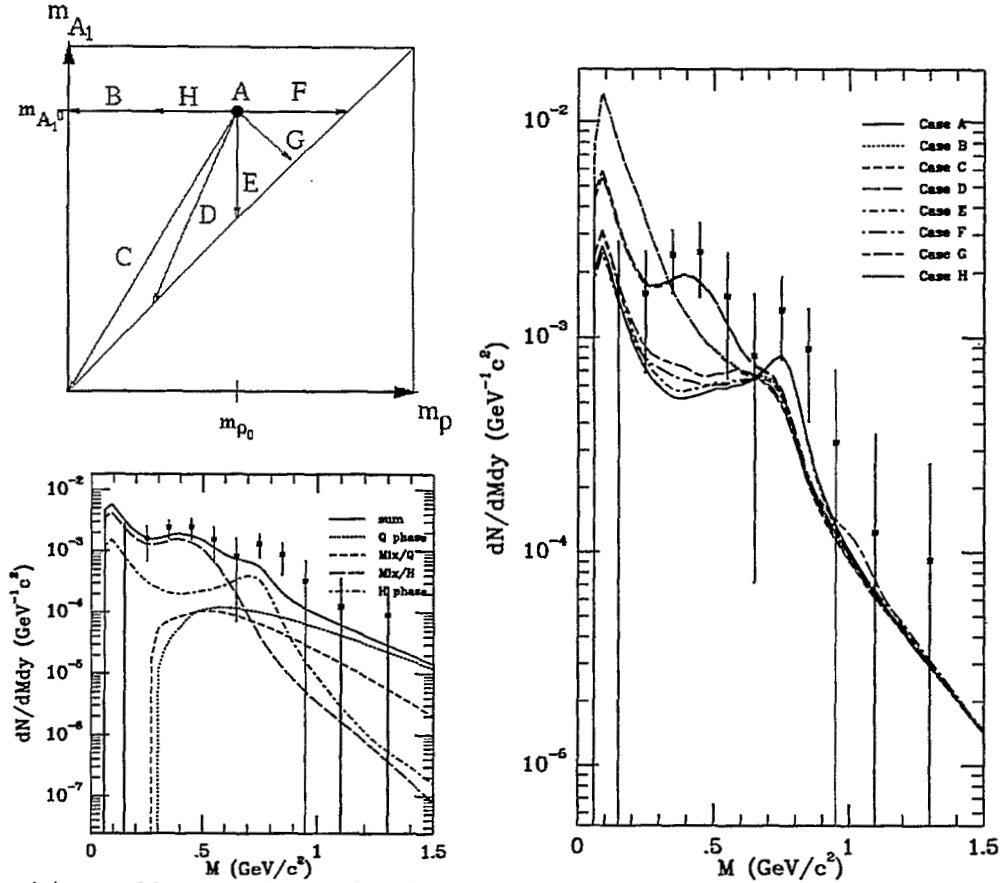


FIG. 5. (a) Possible scenarios of chiral restoration in  $m_\rho - m_{a_1}$  plane, (b) the dilepton spectra corresponding to them (CERES data are shown with background from hadronic decays subtracted); (c) the most favorable case D is shown in details, with contribution from different stages. The dominant one is clearly the long-dashed one, or hadronic part of the mixed phase.

(iii) a very long-lived fireball [38]; (iv) dropping  $m_{\eta'}$  [11,12]; (v) a modified pion dispersion curve [42]; (vi) dropping  $m_{A_1}$  [43].

I will only discuss the  $\rho - A_1$  story, with brief remarks about others. (ii) The observed low- $p_t$  excess of pions (over thermal spectra) can indeed lead to a dramatic increase in low-mass dilepton yield. However, it is most probably due to resonance decays or effects of collective potentials. Both are late-stage phenomena, which hardly affect the early-stage dilepton production. (iii) Even if the long-lived fireball would appear at 200 GeV/A (which is hardly possible) it was found to produce about the same  $M_{e^+e^-}$  spectrum as the usual space-time scenarios, so it does not work. (iv) Above we have indeed suggested that  $m_{\eta'}(T)$  should drop more than any other mass: however in order to account for CERES data one should increase yield of “escaping  $\eta'$ ” by too huge a factor. (In connection to U(1) restoration issue, however, it would be extremely interesting to measure the  $\eta'$  yield, though.)

The “dropping  $m_\rho$ ” idea is very well known, and it seems to be about the only one which can explain the dilepton data. It was studied in details by Li,Ko and Brown [40] in the cascade model based on Walecka-type model with attraction mediated by a scalar field. With much simpler hydro-based approach we have also verified, that one can get a very good description of CERES data by making the rho mass T-dependent, *without* any changes in

standard thermal rate formulae or in space-time evolution.

A point I want to make though is that “dropping  $m_\rho(T)$ ” are not consistent with chiral symmetry restoration, unless *modifications of its chiral partner  $a_1$*  follow. Relation between the two were made e.g. in the contents of Weinberg-type sum rules [44]. Both states should become identical at  $T_c$ , so  $m_\rho(T_c) = m_{A_1}(T_c)$ . Important role of  $a_1$  for production of photons and dileptons was discussed in [52,38,45,46]: we have used rather general expressions recently derived in [47]<sup>14</sup> Possible scenarios of how chiral restoration may proceed are shown in the  $m_\rho - m_{A_1}$  plane in Fig.5(a). For example, path G corresponds to ref. [5], while C corresponds to Brown-Rho scaling. The corresponding dilepton spectra are shown in Fig.5(b): the variant D, with  $m_\rho(T_c) = m_{A_1}(T_c) \sim (1/2)m_\rho(0)$ , does the best job, and Fig.5(c) we show contribution of separate stages in this scenario. The  $A_1$  contribution is mainly at small  $M_{e^+e^-}$ , where CERES acceptance is low and background rather high. Still, with some effort one may be able to dig out the  $A_1$  contribution, using other information (especially the  $p_t$  distribution). Note finally, that none of the scenarios mentioned above happen to violate current upper limit on the direct photons are set by WA80 [48].

#### Equation of State

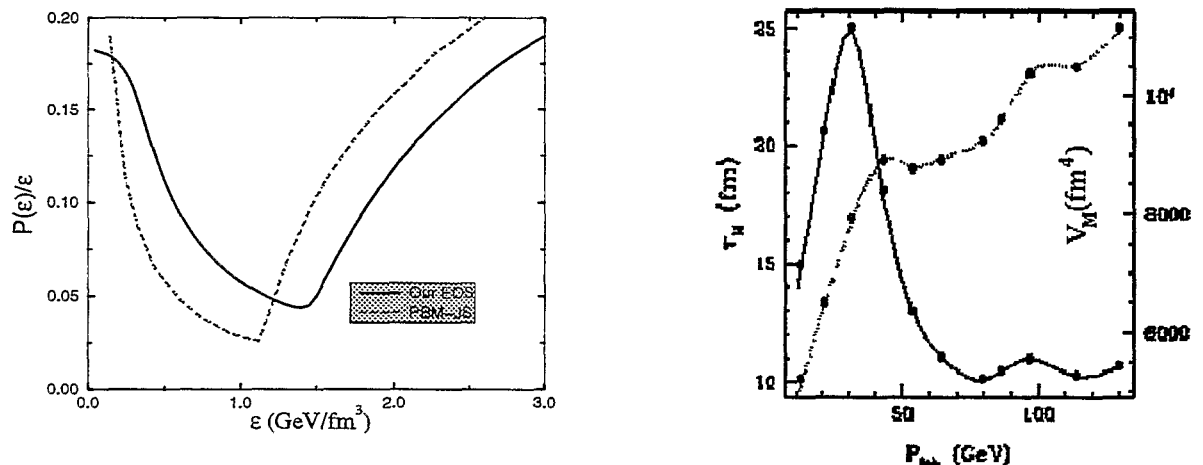


FIG. 6. (a) The EOS in hydro-relevant coordinates for resonance gas and QGP. The solid line is for zero baryon number, the dashed line is for  $\mu_b = 0.54 \text{ GeV}$ . The minimum is the “softest point” discussed in the text. (b) Solid line (and left scale) show the lifetime in the center, the dashed line (and the right scale) shows the space-time volume occupied by the mixed phase ( $T \approx T_c$ ).

### VIII. FLOW, THE “SOFTNESS” OF THE EOS, AND THE FIREBALL LIFETIME

Our last topic deals with a more straightforward approach to observable signal of the QCD phase transition: instead of hunting for “dropping masses” we look instead at the effect of “dropping pressure”. The ratio  $p/\epsilon$ , pressure normalized to the energy density, is shown in Fig.6(a) we show how this ratio depends on  $\epsilon$ . The existence of the “softest point”,

<sup>14</sup>In order to explain why  $a_1$  is important, let us go “backward in time”: it is the first hadronic resonance which may be excited in a collision of a photon, real or virtual, with a pion.

the minimum of this ratio, is clearly seen. Our second point: in those (hydro relevant) plot the curves with and without baryon density look similar in many models: compare the two curves in Fig.6.

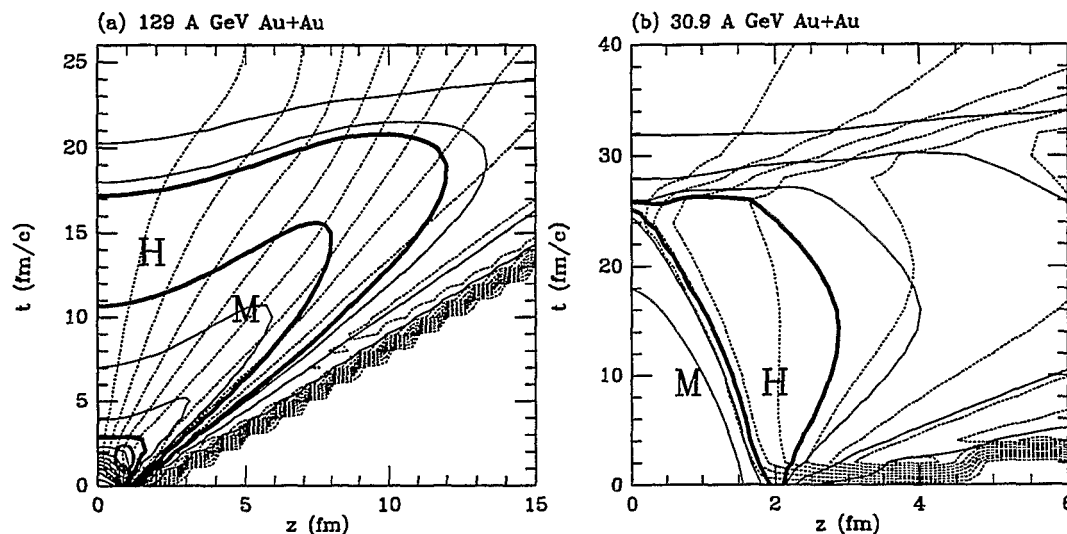


FIG. 7. Space-time picture of AuAu collisions at SPS energies (a) and at the “softest point” (b). Solid lines correspond to fixed energy density while the short-dash lines are contours of fixed longitudinal velocity. Q,M,H stands for Quark, Mixed and Hadronic phases. Note qualitative difference between the two figures, as well as different time scales.

Effect of the “softness” of EOS at  $T \approx T_c$  on transverse *radial* flow was discussed for a long time [53,54]<sup>15</sup>. More radical (and more controversial) idea was proposed in [49], where it was suggested that it can affect the *longitudinal* expansion and thus the global lifetime of the excited system in some energy window. In this workshop we had a detailed talk by D.Rischke, where he has shown that the effect of “softness” of EOS increases the lifetime at RHIC energies by about factor 2.

It was shown in [49] that, due to softness of the EOS, there exists a *window* of collision energies in which the secondary acceleration of matter is completely *impossible*. Thus, *if* stopping does occur, a very long-lived fireball should be formed.

To study this idea semi-quantitatively, a simple 1-fluid relativistic hydrodynamic model was used<sup>16</sup>. Our lattice-based EOS shown (in unusual form) in Fig.6(a) have smooth crossover in a *narrow* temperature interval  $\Delta T \sim 5$  MeV at  $T_c = 160$  MeV the energy density jumps by about an order of magnitude.

As the collision energy is scanned down, from 200 A GeV (SPS) to 10 A GeV (AGS), we

<sup>15</sup>The issue was strongly oversimplified: in fact, transverse velocity is the integral over the whole history, and initial “softness” is only part of the story. Our hydro studies have shown, that the *mean* flow velocity is not sensitive to EOS at early stages, although there are modifications of the shape of its *distribution*.

<sup>16</sup>The major uncertainties are in the initial conditions: we assumed that *half* of the total energy is stopped.

found three radically different scenarios: **(I)** At SPS one starts in the QGP phase, therefore longitudinal explosion quickly restore ultra-relativistic longitudinal motion, even if stopping a la Landau takes place, and expansion resembles the Bjorken picture, (see Fig.7 (a)): **(II)** As the initial energy density passes the softest point, the QGP phase disappears and so does rapid longitudinal expansion. Instead we find a *slow-burning* fireball. For the heavy nuclei and initial conditions we discuss, the burning front moves mostly in the compressed longitudinal direction (see Fig.7 (b)). The total lifetime of the fireball appears to be nearly as long as predicted for RHIC, but of course it is kind of upper bound on the effect. **(III)** At still lower energies burning process becomes more spherical, and ordinary expansion is developed. The main result, shown in Fig.6(b), is a significant *peak* in a lifetime.

Remarkably enough, these completely different scenarios lead to not-so-different spectral. With little fitting of the initial conditions, they can be made consistent with available data. Thus, one-particle spectra alone is not enough, and details about the space-time picture has to come from analysis of flow and HBT.

How one can test these unusual predictions and try to locate the “softest point” experimentally? First of all, it seems that it is above the AGS domain<sup>17</sup>, so one should rather scan downward at SPS. The following ideas are discussed in literature: (i) Look for maximal lifetime (or minimum of the HBT parameter  $\lambda$ ) [49]; (ii) Look for the *minimum* of the “directed” flow in the collision plane [50]; (iii) Look for the nearly isotropic distribution of dileptons, produced in the long-lived fireball [49].

## ACKNOWLEDGMENTS

This talk is based on works done my collaborators, especially with T.Schaefer and C.M.Hung. I benefited from multiple discussion of the topics involved with G.Brown. During the workshop strong interaction with fellow co-organizers N.Christ, M.Creutz, M.Gyulassy and S.Kahana has shaped the interesting discussions we had. This work is partially supported by the US Department of Energy under Grant No. DE-FG02-88ER40388.

## REFERENCES

- [1] E. V. Shuryak. *Zh. Eksp. Teor. Fiz. (Sov. Phys. JETP)*, 70, 408 ,1978.
- [2] T. Schäfer and E. V. Shuryak. *preprints, Stony Brook, SUNY-NTG-95-22,23 hep-ph/9509337,9512384*. Phys.Rev.D, in press.
- [3] K. Kanaya. *Nucl.Phys.B (Proc.Suppl)*, 47:136, 1996.
- [4] V. Koch and G. E. Brown. *Nucl. Phys.*, A560:345, 1993.
- [5] R.D.Pisarski. *Phys. Rev.*, .D52:3773, 1995.
- [6] T. Hatsuda and T. Kunihiro. *Phys. Rep.*, 247:221, 1994.

---

<sup>17</sup>Preliminary results from the E802 AGS experiment reported studies of HBT which indicate significant growth of lifetime for the most central Au Au collisions [51].

- [7] T. Hatsuda, H. Shiomi, and H. Kuwabara. LIGHT VECTOR MESONS IN NUCLEAR MATTER. UTHEP-331, Mar 1996. 33pp. Submitted to Prog. Theor. Phys. e-Print Archive: nucl-th/9603043.
- [8] E. Shuryak and M. Velkovsky. A Mean Field approach ..., SUNY-NTG-95-20, hep-ph/9603234.
- [9] E. V. Shuryak. *Comm. Nucl. Part. Phys.*, 21:235, 1994.
- [10] Thomas. D. Cohen. The High Temperature Phase of QCD and  $U(1)_A$  Symmetry. hep-ph/9601216.
- [11] J. Kapusta, D. Kharzeev, and L. McLerran. *Phys. Rev.*, D53:5028, 1996.
- [12] Xin nian Wang, 1996. Talk at INT/RHIC Seattle workshop, Jan.96.
- [13] E. V. Shuryak and J. J. M. Verbaarschot. *Nucl. Phys.*, B410:37, 1993.B410:55, 1993. T. Schäfer, E. V. Shuryak, and J. J. M. Verbaarschot. *Nucl. Phys.*, B412:143, 1994.
- [14] M. C. Chu, J. M. Grandy, S. Huang, and J. W. Negele. *Phys. Rev.*, D49:6039, 1994.
- [15] C. Michael and P. S. Spencer. *Nucl. Phys. (Proc. Suppl.)*, B42:261, 1995.
- [16] E. Shuryak and M. Velkovsky, *Phys. Rev.* D50: 3323 ,1994
- [17] M. C. Chu and S. Schramm. *Phys. Rev.*, D51:4580, 1995.
- [18] Y. Iwasaki, K. Kanaya, S. Sakai, and T. Yoshie. *Nucl. Phys. (Proc. Suppl.)*, B34:314, 1994.
- [19] E.-M. Ilgenfritz and E. V. Shuryak. *Phys. Lett.*, B325:263, 1994.
- [20] I.I. Balitsky and A. V. Yung. *Nucl. Phys.*, B274:475, 1986.
- [21] N. Seiberg, *Phys. Rev.* D49, 6857 ,1994.
- [22] T. Schäfer, E. V. Shuryak, and J. J. M. Verbaarschot. *Phys. Rev.*, D51:1267, 1995.
- [23] E. Shuryak and M. Velkovsky, 1996. SUNY-NTG-95-20.
- [24] G. Boyd, S. Gupta, F. Karsch, and E. Laerman. *Z. Phys.*, C64:331, 1994.
- [25] T. Banks and A. Zaks. *Nucl. Phys.*, B82:196, 1982.
- [26] Y. Iwasaki, K. Kanaya, and S. Kaya. Phase structure of qcd for general number of flavors, 1996. Talk at Lattice-96, St Louis.
- [27] N. Seiberg. *Phys. Rev.*, D49:6857, 1994.
- [28] S. H. Lee and T. Hatsuda. *Phys. Rev.*, D to be published, 1996.
- [29] Z. Huang and X.-N. Wang. *Phys. Rev.*, D to be published, 1996.
- [30] Thomas Schaefer. The axial anomaly in QCD at finite temperature, INT preprint, Seattle, hep-ph/9608373.
- [31] T. Schäfer and E. V. Shuryak. *Phys. Rev.* D to be published, 1996.
- [32] C. Bernard, T. Blum, C. E. DeTar, et al. Thermodynamics for two flavor QCD, report to Lattice-96, hep-lat/9608026.
- [33] N. Evans, S. D. H. Hsu, and M. Schwetz. *Phys. Rev.*, D to be published, 1996.
- [34] I. Barbour, Nasr-Eddine Behilil, E. Dagotto, F. Karsch, A. Moreo, M. Stone, H.W. Wyld *Nucl. Phys.* B275:296, 1986.
- [35] M.A. Stephanov *Phys. Rev. Lett.* 76:4472-4475, 1996. e-Print Archive: hep-lat/9604003
- [36] A. Gocksch *Phys. Rev.* D37 (1988) 1014.
- [37] G.E. Brown, M. Rho, M. Soyeur *Nucl. Phys.* A553 (1993) 705c-708c.
- [38] L. Xiong and E. Shuryak, *Phys. Lett.* **B333**(1994)316.
- [39] M. Hofman et al. *Nucl. Phys.*, A556:15c, 1994.
- [40] G.Q. Li, C.M. Ko, and G.E. Brown. *Phys. Rev. Lett.*, 75:4007, 1995.
- [41] B. Kaempfer, P. Koch, and O.P. Pavlenko. *Phys. Rev.*, C49:1132, 1994.

- [42] Chungsik Song, V. Koch, Su Houng Lee, and C.M.Ko. *Phys. Lett.*, B366:379, 1996.
- [43] C.M. Hung and E. Shuryak. Dilepton production in heavy ion collisions, SUNY-NTG, 1996.
- [44] J. Kapusta and E. V. Shuryak. *Phys. Rev.*, D49:4694, 1994.
- [45] Chungsik Song. *Phys. Rev.*, C 47:2861, 1993.
- [46] Chungsik Song, Che Ming Ko, and C. Gale. *Phys. Rev.*, D 50:1827, 1994.
- [47] J.V.Steel, H.Yamagishi, and I.Zahed. Dilepton and Photon emission rates from a hadronic gas, hep-ph/9603290.
- [48] P.Stankus, 1996. Measuring direct photons..., Talk at INT/RHIC Seattle workshop, Jan.96.
- [49] C.M. Hung and E. Shuryak. *Phys. Rev. Lett*, 75:4003, 1995.
- [50] Dirk H. Rischke and Miklos Gyulassy. *Nucl. Phys.*, A597:701, 1996.
- [51] M.Baker. Intriguing centrality dependence of the Au Au Source size at the AGS, Talk at Snowbird workshop, Feb.1996.
- [52] Li Xiong, E.Shuryak, G.E.Brown, *Phys.Rev.D*46 (1992) 3798; C.Song, *Phys.Rev.C*, 47 (1993) 2861.
- [53] E. Shuryak and O. V. Zhirov, *Phys. Lett.* **89B**, 253-255 (1979).
- [54] L. van Hove, *Z. Phys. C* **21**, 93 (1983); K. Kajantie, M. Kataja, L. McLerran and P. V. Ruuskanen, *Phys. Rev. D* **34**, 2746 (1986); S. Chakrabarty, J. Alam, D. K. Srivastava, B. Sinha, *Phys. Rev. D* **46**, 3802 (1992).



# Hard Processes at RHIC

A.H. Mueller

*Physics Department, Columbia University  
New York, New York 10027*

## Abstract

A summary of the “Hard Processes” part of the RHIC workshop on Heavy Ions is given. The early stages of a high energy heavy ion collision are reviewed. The questions of induced energy loss and the broadening of the  $p_{\perp}$ -distribution of high energy jets in nuclear matter and in a quark-gluon plasma are discussed. Similarities with a number of theoretical issues in small-x physics are noted.

## I. PREFACE

Of the topics covered at this RHIC Workshop it seems clear that “Phenomenology” is at present the core of heavy ion theory. The success of the RHIC experimental program may depend, to a large extent, on how much progress can be made in the phenomenology of relativistic heavy ion collisions during the next ten years. We have seen a vigorous discussion of many of these issues at this workshop. Hard (perturbative) physics enters when one probes a heavy ion collision and in the very early stages of the collision. It is on these questions that is the focus of the present talk. I shall only cover issues that are directly related to the quark-gluon plasma, and I note in passing that many of the issues related to the early stages of an ultra-relativistic heavy ion collision are quite similar to similar issues presently under active discussion in small-x physics at Fermilab and HERA.

## II. EARLY STAGES OF A RELATIVISTIC HEAVY ION COLLISION

### A. The geometry

At very high energies, and in the center of mass, the small-x partons which contribute to the energy produced in the central unit of rapidity are located in a single layer, in the longitudinal direction, in each of the ions immediately before the collision. This layer of partons is of longitudinal extent  $\Delta z \approx 1/k_{\perp}$ , so for semi-hard partons the relevant longitudinal scale is  $\Delta z = 0.1 - 0.2 fm$  while for soft physics, probably not well represented by partons,  $\Delta z \approx 1/2 - 1 fm$ . In the transverse directions the partons are located in a disc of size  $R = 6-7 fm$ , for a large nucleus, while the size of each parton obeys  $\Delta x_{\perp} \sim 1/k_{\perp}$ . Thus partons which are hard  $k_{\perp} \geq 2 GeV$  are rather dilute in the nucleus and so interact weakly in an ion-ion collision. Perturbative QCD should work well for studying how many of these partons

are freed during the ion-ion collision. For those partons having  $k_{\perp} \leq 1\text{GeV}$  the density of partons is sufficiently great, and the interaction sufficiently strong, that perturbation theory may not be reliable.

## B. The initial condition and shortly thereafter

Calculations were described by Eskola [1] where one considers the production of  $k_{\perp} \geq 2\text{GeV}$  partons, during a time  $t \leq 0.1 - 0.2\text{fm}$ , for a small impact parameter Pb-Pb collision. There are about 300 such partons (gluons) freed per unit rapidity during the collision leading to

$$\frac{dE_T^{\text{Hard}}}{dy} \approx 600\text{GeV}. \quad (1)$$

The density of these partons, immediately after they are freed, is about

$$\rho \approx \frac{300}{\pi R^2} \approx 3/\text{fm}^2 \quad (2)$$

which is only about a 10% occupation of the area available. Thus the initial system of semi-hard partons is rather dilute. There is a good chance that this energy is equilibrated through further parton branching and interaction. This is one of the key questions to be answered by good Monte Carlo calculations of the early times after a heavy ion collision, and there is vigorous effort in this direction [2,3].

In addition to the energy freed in semi-hard parton interactions there is also the estimate

$$\frac{dE_T^{\text{soft}}}{dy} \approx 200 - 300\text{GeV} \quad (3)$$

extrapolated from proton-proton data. However, it is not clear that such an extrapolation is reliable. In an ion-ion collision the soft physics part of the interaction is taking place in an environment of (perhaps) large color fluctuations due to semi-hard production which is an environment quite different from that of a proton-proton collision.

If one lowers the cutoff to  $k_{\perp} = 1\text{GeV}$  in the calculation of semi-hard partons one finds that about 1000 gluons are freed in a head-on Pb-Pb collision leading to  $\frac{dE_T^{\text{hard}}}{dy} \approx 1\text{TeV}$  and  $\rho \approx 10/\text{fm}^2$ . Now the initial state is fairly dense, though the perturbative calculation may still be indicative if not a precise evaluation of the initial conditions in the collision.

One of the key elements in heavy ion phenomenology is a good Monte Carlo for the early stages of the collision. Such a Monte Carlo needs to have the semi-hard interactions of the collision as well as soft hadron production. In addition, the Monte Carlo should be able to follow the evolution of the system up to the time when equilibration sets in. It is a great challenge to develop a realistic Monte Carlo which can be used at RHIC and at LHC.

In the meantime it would be amusing to follow a simpler, and less realistic, approach where one simply ignores soft physics, and follows the evolution of the semi-hard gluons down to some moderately small mass scale where one then converts gluons to hadrons by "Local Parton Hadron Duality," LPHD. This procedure works quite well in  $e^+e^-$  annihilation. Perhaps it gives reasonable results in heavy ion collisions also. It is a "simple" context to

study such perplexing questions as how, and if, an effective screening comes in to cut off infrared divergences in the pre-equilibrium distributions. [2-4]

### III. INTERACTIONS OF PARTONS IN NUCLEI AND IN THE QUARK-GLUON PLASMA <sup>5,6</sup>

There have been some experimental studies of the interaction of high energy quarks and gluons in nuclei mainly through measurements of the broadening of the  $p_{\perp}$  - spectrum of  $\mu$ -pairs and  $J/\psi$ 's in proton nucleus collisions as a function of the atomic number A. There is very little data concerning energy loss of high energy quarks and gluons in nuclei. However, there have been wide discussions about the possibility that the loss of energy of quarks and gluons in matter might furnish a signal for quark-gluon plasma formation.

#### A. $p_{\perp}$ -broadening

Suppose a high energy quark jet has been produced in hot or cold QCD matter through a hard collision. As the jet passes through the matter it encounters essentially random color fields with coherence lengths of a fermi or less. These color fields add to the initial transverse momentum that the jet may have had and thus broadens the  $p_{\perp}$  spectrum of the jet. The same is true for the  $\mu$ - pair spectrum produced by a hard incoming quark which annihilates on an antiquark in the matter. Because of the essentially random character of the  $p_{\perp}$  - kicks given to the quark locally in the matter one expects that the increase in the width of the  $p_{\perp}^2$ -distribution should grow linearly with the length of material that the quark passes through. The theory for this process is now under good theoretical control, except for an overall normalization which sets the scale for the "typical" transverse momentum given to the quark during a scattering. An estimate of the  $p_{\perp}$  - broadening is

$$\langle p_{\perp}^2 \rangle \approx \left( \frac{L}{10fm} \right) \begin{matrix} 5GeV^2(Hot Matter, QGP) \\ 1/2GeV^2(Cold Matter) \end{matrix} \quad (4)$$

with L the length of the matter traversed by the quark.

#### B. 3.2 Radiative energy loss induced by a medium<sup>6</sup>

The problem of the loss of energy of a high energy electrically charged particle as it passes through atomic matter is a classic problem in electrodynamics and was first solved by Landau, Pomeranchuk and Migdal (LPM). The suppression of radiation due to coherence of photon radiation from different regions of the medium has come to be known as the LPM effect. Recently, there has been intense study of the analogous effect in QCD with the hope that radiative energy loss could furnish a signal for quark gluon plasma formation. An estimate for the radiative energy loss of a quark in matter is

$$\Delta E = \left( \frac{L}{10fm} \right)^2 \cdot \begin{matrix} 30GeV(HotMatter, QGP) \\ 2GeV(ColdMatter) \end{matrix} \quad (5)$$

A peculiarity of this result is that the radiative energy loss grows quadratically with the length of matter that the quark passes through. This comes about because the energy loss is dominated by the energy of the highest energy gluon whose formation time is less than or equal to the length of the medium. Setting

$$L = \tau_{form} \equiv \frac{2k}{k_{\perp}^2}, \quad (6)$$

with  $k$  the momentum of the radiated gluon, and taking  $k_{\perp}^2 \propto L$  as given in (4) immediately gives  $k \propto L^2$  as in (5).

The estimates in (4) and (5) are very crude and should be taken as indicative of the possibility that the interaction of high energy quarks and gluons is much more intense in hot matter as compared to cold matter. To a large extent this is likely a straightforward reflection of the higher density of quarks and gluons in hot matter.

### C. How to measure energy loss

The basic partonic reaction  $q + g \rightarrow q' + \gamma$ , occurring as the hard part of a hard proton-nucleus or nucleus-nucleus reaction, can be used to measure the energy loss of the final quark,  $q'$ , as it passes through the medium. [7] By measuring a large transverse momentum for the  $\gamma$ , which is unaffected by the medium, one has a measurement of the  $q'$  at the moment it is produced in the collision. By measuring the energy of these final  $q'$  after it has passed through the medium one gets a measure of the energy loss of quarks in matter. This reaction has another nice feature for ion-ion collisions. By measuring the  $\gamma$  one has a "trigger" on an outgoing jet. Without such a trigger minimum bias fluctuations will likely make jet measurements impossible in an accelerator like RHIC. Estimates suggest that 10 GeV  $\gamma$ 's will be quite abundant at RHIC while 15 GeV transverse momenta may be difficult to achieve because of the smallness of the cross section of production.

## IV. DENSE PARTONIC SYSTEMS AT $T = 0$

The most fascinating part of small- $x$  physics is the study of partonic systems whose density is so high that each parton strongly interacts with neighboring partons even though the QCD coupling,  $\alpha$ , is small. The traditional gluon distribution of the proton

$$xG(x, Q^2) \approx 3(1-x)^5 \quad (7)$$

represents three gluons per unit rapidity, having transverse size  $\Delta x_{\perp} \sim 1/Q$ , in the proton. If  $Q^2 \geq$  a few GeV [2] this corresponds to a rather dilute system. Recently at HERA values of  $xG(x, Q^2)$  between 20 and 30 have been measured at very small values of  $x$ . These measurements have been performed at values of  $Q^2$  such that the gluons are still quite dilute in the proton. However, in the region  $Q^2 \approx 1 \text{ GeV}^2$ , where the idea of partons still makes sense, and at small  $x$  one may reach that region where there is a considerable overlap of partons leading to high field strengths and some sort of saturation effect. This is likely also for the case at RHIC energies for heavy ions as suggested by our discussion in Section 2. In small- $x$  physics there is a strong effort underway to understand what happens when one

reaches high parton densities in a proton's wavefunction. It is likely that this understanding will have application to heavy ion physics also.

The relationship between unitarity constraints and saturation (high field strengths) is an intriguing and not well understood aspect of high energy QCD. To illustrate this relationship compare very high energy scattering in a center of mass frame with that of a laboratory frame. To simplify the problem, and eliminate the usual nonperturbative QCD of bound states, imagine that the colliding hadrons are heavy quarkonium states with wavefunctions consisting of a heavy quark a heavy antiquark and some number of gluons. We shall give a very classical picture of the scattering which is dominated by gluons.

In the center of mass frame

$$\sigma = \sigma_0 \cdot N^2 \quad (8)$$

where  $\sigma$  is the onium-onium cross section,  $\sigma_0$  the gluon-gluon cross section, and the  $N$  the number of gluons in the onium wavefunction. ( $N$  depends on energy as  $N = N(Y/2) = e^{c\alpha Y/2}$  with  $Y = \ln E^2$ .) The gluons in the onium have transverse size about equal to  $R$ , the onium radius, so  $\sigma_0 \approx \alpha^2 R^2$ . Thus, the unitarity limit  $\sigma \approx \pi R^2$  is reached when  $N \sim 1/\alpha$  or  $\frac{dN}{dY} = 0(1)$ . The typical field strength squared goes like  $\frac{dN}{dY}$  so field strength are not very large and the gluons in each of the colliding onia can be considered to be weakly interacting with each other. Thus unitarity is a weak coupling, perturbative, problem.

Now look at the same problem in a frame where one of the onia is at rest. The onium at rest consists only of a heavy quark and a heavy antiquark. Now

$$\sigma \approx \alpha^2 R^2 N(Y) \quad (9)$$

which gives the same result as before, for equal total rapidity  $Y$ , with  $N(Y) \sim 1/\alpha^2$ . But  $N(Y) \sim 1/\alpha^2$  means that the typical field strength  $F_{\mu\nu}$  is of size  $1/g$  so that in a rest frame unitarity looks equivalent to the strong coupling (saturation) problem. It is one of the important tasks over the next few years to clarify the relationship between unitarity and saturation. For heavy ion reactions the  $Q^2$ -value at which saturation sets in likely gives the scale of those gluons which will dominate the free energy in the central unit of rapidity.

## ACKNOWLEDGMENTS

This work is supported in part by the Department of Energy under GRANT DE-FG02-94ER-40819.

## REFERENCES

- [1] K. Eskola, these proceedings.
- [2] D. Kahana, these proceedings.
- [3] K. Kinder-Geiger, these proceedings.
- [4] B. Mueller, these proceedings.
- [5] G. Sterman, these proceedings.

- [6] Y. Dokshitzer, these proceedings.
- [7] X.N. Wang, these proceedings.

# Summary talk on chiral symmetry and Disoriented Chiral Condensates

Robert D. Pisarski

*Department of Physics, Brookhaven National Laboratory, Upton, New York 11973-5000, USA*

## Abstract

I summarize the talks at the RHIC '96 Summer School on chiral symmetry and Disoriented Chiral Condensates.

This summary reviews what I found interesting during the talks on chiral symmetry. There were a few talks on various aspects of chiral symmetry, followed by many talks on one particular aspect, that of Disoriented Chiral Condensates, *DCC*'s.

## I. ZAHED: QUANTUM ACTION PRINCIPLE

Zahed [1] presented an alternate approach to effective theories for chiral symmetry. His starting point is rather abstract, involving a quantum action principle and a master equation. In the end, however, he ends up with something rather concrete.

For example, he starts with the general expression for  $\pi$ - $\pi$  scattering, and writes it as a series of terms. To do so, all he needs is the interpolating formula for the pion field in terms of the axial current. The first three terms which he obtains are most familiar, involving a tree term as would arise from the lowest order in a effective (nonlinear) theory, a second term from the exchange of a  $\rho$ -meson, and a third term from the exchange of a  $\sigma$ -meson. Rather interestingly, he is not putting in these mesons by hand, but finds terms which have a natural interpretation as the exchange of these mesons.

There is a fourth term which remains; this involves the connected four-point function of currents. This last term has no natural interpretation as the exchange of any particle, and does not arise from an effective theory. The major assumption which he makes is that this last term can be neglected. It presumably represents the sum of many higher order processes which eventually arise, such including the exchange of two  $\rho$ -mesons, higher order terms in the derivative expansion of an effective theory, and the like.

He then uses experimental data to fix the first three terms in his expansion. Doing so, he finds an excellent fit to the  $\pi$ - $\pi$  phase shift at energies below  $1\text{GeV}$ . Since he is using experimental input to fix the terms corresponding to  $\rho$ -meson and  $\sigma$ -meson exchange, this agrees with the results found in more explicit approaches.

Zahed then went on to discuss various features of dilepton production at nonzero temperature, as perhaps explains the excess of dielectrons seen above  $2m_\pi$  and below  $m_\rho$  in the CERES experiment. He observed that a shifted  $\rho$  mass, as suggested is relevant for these experiments by G. Brown, C. M. Ko, and others, is only effective if the width of the  $\rho$ -meson decreases strongly with temperature. This is a matter of the area under the peak

being (approximately) constant, so that unless the width gets small, the height won't be sufficiently large to explain the data.

In this vein, the important effect is not the width at one loop order, but that at two loop and beyond. This is not simply because the coupling constant is strong, and so higher order effects are always large; after all, a one loop estimate gets the  $\rho$ -meson width right to about 20% at zero temperature. Rather, it is that at nonzero temperature the effects of collisional broadening first enter at two loop order, and can be significant. Haglin [2] has estimated the effects of collisional broadening, and finds that they can be large; for example, the thermal lifetime of the  $\omega$  meson becomes not  $25fm/c$ , as at zero temperature, but  $\sim 4fm/c$ .

## II. HATSUDA: DROPPING VECTOR MESON MASSES

Hatsuda [3] summarized various approaches to how the light vector meson masses -  $\rho$ ,  $\omega$ , and  $\phi$  - drop in nuclear matter. This included an approach based upon sum rules and effective theories, such as Quantum HadroDynamics. I would only add the qualification that at least in effective theories, such behavior is often built into assumptions about the nature of the relevant couplings. It is not clear to me that more general couplings, still consistent with chiral symmetry, cannot produce different behavior.

What I found interesting, however, is that he estimated the effects of collisional broadening not at finite temperature, but at finite density, and find that they are small. While this is not the same limit as investigated by Haglin, one would expect qualitatively similar results, and the difference is striking. Clearly more complete calculations are required, since the crucial question experimentally is not so much whether or not vector meson masses change with temperature and/or density — they surely do — but how the widths change. In particular, experimentally the cleanest signature would be if the relatively narrow vector mesons, such as the  $\omega$  or the  $\phi$ , became broad in the quark-gluon plasma. If the width of the  $\omega$ , say, is near its value at zero temperature, then most  $\omega$ 's decay outside of the plasma, and it will be difficult to see signs of thermal  $\omega$ 's.

## III. TYTGAT: SOFT PIONS

Tytgat [4] described work with myself on the nature of chiral symmetry breaking in a thermal distribution. Here I wish only to make the following point. Many authors, including especially Shuryak [5], have used specific models to argue that the pion dispersion relation changes in a medium, becoming “flatter”. That is, not only does the effective mass of the pion change, but the pion acts as if it has a nonzero velocity less than one, with a dispersion relation of the form  $\omega_{eff}(p) = \sqrt{v^2 p^2 + m_{eff}^2}$ . We showed that this type of dispersion relation follows not just from the properties of specific models, but is a most general feature of chiral symmetry breaking in a medium. This greatly supports the type of scenarios advocated by Shuryak [5].



#### IV. WELDON: NEW PEAKS IN THE QUARK GLUON PLASMA

Weldon [6] gave a speculative and most interesting talk on how new bound states could arise in the quark-gluon plasma. At first sight, this appears completely contradictory. After all, at very high temperatures our picture is of a (more or less) weakly coupled plasma, in which one would not expect any bound states. However, near the point of phase transition, we know that the  $\sigma$  meson and the  $\pi$ 's are special, since at a point of (second order) chiral phase transition they have zero mass, and so are, of necessity, strongly bound. So perhaps there are other channels in which there is also strong binding (although perhaps not as strong as for the critical modes!).

It is known from perturbative calculations that there are new fermionic quasiparticles in hot gauge theories, sometimes dubbed "plasminos" (although there is nothing supersymmetric about them). Weldon showed that these states are not special to perturbation theory, but arise generally as a type of quasiparticle hole. I use the term plasmino for ease of discussion.

Weldon then observes that besides the usual particle antiparticle bound states, it is also possible to have particle plasmino bound states. Since these states arise from finite temperature effects, they are not generally Lorentz covariant; for example, there is one state in which a particle and a plasmino are sandwiched between the Dirac matrices  $\gamma_0\vec{\gamma}$ ; this state has  $J^{PC} = 1^{--}$ , and so can couple to virtual photons.

What about binding? In a random instanton model, it is found that not only the  $\sigma$  and  $\pi$ , but also precisely these  $1^{--}$  particle plasmino states should experience strong binding, since all involve states with opposite chirality. This in itself is very interesting, and presumably is indicative of something much more general going on beyond the approximations of a random instanton model.

The crucial question is that of width's. Collisional broadening would seem to be a crucial matter for these type of states; for example, the fermions (and plasminos) themselves will acquire thermal widths. However, perhaps all is not as bleak as it sounds: if the real parts of the masses of these states are related to pions, perhaps so are the imaginary parts. Thus perhaps the width of such states is no worse than that of pions. Of course, if pions *do* have large thermal widths even about the point of phase transition, then things are pretty bleak. But there is no general reason for this to be.

Indeed, I would suggest that if such states arise, and are strongly bound, then it is probably indicative of some extension of chiral symmetry at work, tying together the  $\sigma$  meson, pions, and these new bound states together.

#### V. WANG: HOT $\eta$ 'S

Wang [7] discussed the changes of the  $\eta'$  and especially the  $\eta$  mass with temperature. It is known that if the anomaly (or more precisely, gluonic fluctuations in the topological charge density squared) decreases at a given temperature, then the mixing of the pseudogoldstone bosons goes from being nearly an ideal  $SU(3)$  to being nearly eigenstates of pure flavor. For example, if the anomaly evaporates, the  $\eta'$  becomes pure  $\bar{s}s$ , the  $\eta$  pure  $\bar{d}d$ , and the  $\pi^0$  pure  $\bar{u}u$ . Further, the mass of this thermal  $\eta$  naturally decreases as it loses its strangeness. Consequently, one might hope to see an enhancement in the relative abundance of  $\eta$  mesons.

The crucial question is whether chemical equilibrium is lost before thermal equilibrium. The former is determined by  $\eta\eta \rightarrow \pi\pi$ , while the latter by the this process, as well as  $\eta\eta \rightarrow \eta\eta$  and  $\eta\pi \rightarrow \eta\pi$ . Consequently, one expects chemical equilibrium to be lost before thermal, the relevant question is how big is the difference. Using a reasonable parametrization of the linear  $\sigma$  model, Huang and Wang [7] find that  $T_{chemical} \sim 168MeV$ , while  $T_{thermal} \sim 139MeV$ . Thus there is some window in which one might hope to see an enhanced abundance of  $\eta$ 's. Of course all of these temperatures are characteristic of freeze out temperatures in a hadronic gas, so we will have to wait for experiment to see.

## VI. DISORIENTED CHIRAL CONDENSATES, DCC'S

I now turn to a discussion of the work done on DCC's. There were a large number of talks on this subject; since they form a coherent subject, I discuss them collectively.

Rajagopal [8] gave an excellent pedagogical introduction, to which I refer the reader. The essential point to emphasize is that many of the preconceptions which one has from other contexts are inappropriate for DCC's. The basic idea of DCC's cannot, in essence, be wrong: in some manner, one wants to "whack" the chiral alignment of the  $QCD$  vacuum, and see how it realigns to the correct vacuum. This is manifestly a process out of equilibrium, in which being more out of equilibrium will help to magnify the effect. Since one is wrenching the alignment of the vacuum, it is a problem of soft physics, which should manifest itself in phenomenon at small transverse momentum ( $p_t$ ) and high multiplicity. The standard signal is to look for a change in the ratio of neutral pions to the total number of pions,

$$\mathcal{R} = \frac{\langle 2n_\gamma \rangle}{\langle n_{ch} + 2n_\gamma \rangle} \quad (1)$$

Here  $n_{ch}$  is the number of charged pions, and  $n_\gamma$  the number of photons, where on average each  $\pi^0$  gives two photons. On average the ratio  $\mathcal{R}$  is the isospin symmetric value of  $1/3$ ; the question is whether the fluctuations are entirely Poissonian, or have some other component. In this vein, while in hadronic physics it sounds rather radical to look for fluctuations in isospin conservation, in terms of spin models it is not. Consider a magnet aligned along the  $z$  axis, say. If one hits the magnet with some random field, it will precess around in some arbitrary fashion. Thus if one hits it hard, one will see individual events in which the spin is pointing in the  $x$  or  $y$  directions. This is all DCC's really are, are spins temporarily misaligned. What is usually referred to as DCC's is more specific: it is a distribution which is flat in isospin space, so that the probability distribution is not  $\delta(\mathcal{R} - 1/3)$ , as we expect, but  $1/(2\sqrt{\mathcal{R}})$ . While such a definition is useful, in terms of testing models and the like, I stress the generality of the concept beyond this particular distribution.

Given this, it is also worth emphasizing that how DCC's manifest themselves in  $pp$  (or  $\bar{p}p$ , or  $pA$ ) collisions is presumably very different from that in  $AA$  collisions. The latter involves many particles at the outset, and the problem is in obtaining large enough regions in which the chiral vacuum is misaligned. For the former, one is looking for correlations in relatively small regions of space-time. Thus there is no reason to expect the dynamics of the two to be related.

There were three talks on experimental searches for DCC's. Wyslouch [9] discussed the search using  $WA98$  from the  $Pb - Pb$  run at CERN. They have presently analyzed 1% of

the data, and have no candidate events at present. Taylor [10] described the progress of the MiniMax detector at Fermilab's Tevatron in  $\bar{p}p$  collisions. Lastly, Busza [11] described how the PHOBOS detector for AA collisions at RHIC can be used to look for DCC's. In all of these experiments, a basic experimental problem is that the means used to measure the number of charged pions is inevitably very different from that used to measure the number of neutral pions, which are measured as one half the number of photons. Thus the crucial problem is in ensuring that the kinematic limits imposed by the detection of one type of particle overlaps with that of the other.

Taylor [10] presented a clever idea for further observables to measure. Instead of looking at one particle observables, as above, he suggested looking at correlations, such as

$$\mathcal{R}_1 = \frac{\langle n_{ch} n_\gamma \rangle \langle n_{ch} \rangle}{\langle n_{ch} (n_{ch} - 1) \rangle \langle n_\gamma \rangle} \quad (2)$$

The advantage of this quantity is that one need not look at fluctuations: an isospin symmetric distribution will give  $\mathcal{R}_1 = 1$ , while a distribution of  $1/(2\sqrt{\mathcal{R}})$  gives  $\mathcal{R}_1 = 1/2$ .

On the theoretical side, there were a variety of talks, related to the possibility of DCC's emerging in AA collisions. They can be summarized by observing that driving the system as strongly out of equilibrium as possible tends to amplify any possible effect. For example, one can distinguish between a quench and annealing. In a quench, one starts with a system in which the wavefunction is that of a high temperature state, but one assumes that the potential evolves very quickly to that at zero temperature. Thus the system suddenly finds itself in the wrong minimum, and long wavelength modes become unstable, until the system rolls down into the true (chirally asymmetric minimum). In contrast, with annealing, the potential evolves smoothly, and the minimum rolls down as the potential evolves. Rajagopal [8] talked about his work with Wilczek, in which a quench is assumed, and finds large pion fluctuations. Asakawa [12] explicitly compared a quench to annealing, and found that the largest fluctuations occurred under a quench.

Another important effect is from expansion. In a thermal system one wants the system to expand as slowly as possible, so that the temperature changes slowly, and the system remains in equilibrium. For DCC's, in contrast, expansion is beneficial, and tends to drive the system even further out of equilibrium. This was first stressed by Gavin and Muller [13]. Randrup [14] included the effects of transverse expansion classically, and showed that the largest instabilities occurred with fully three-dimensional, as opposed to one-dimensional expansion. Similar results have also been obtained in a large-N expansion by Lampert, Dawson, and Cooper [15]. The large-N results are interesting because, while confined to infinite N, are valid quantum mechanically. Lampert et al find that in fully three dimensional expansion, while the size of the DCC region is not enhanced per se, that the number of produced particles is. This is something which can only be seen by a fully quantum mechanical treatment.

I conclude with some speculations about how DCC's might arise in a realistic model. A well known problem is how to get enough pions out of a chirally misaligned vacuum. This is because the energy density of a phase in which the condensate is misaligned is of order

$$\epsilon \sim m_\pi^2 f_\pi^2. \quad (3)$$

This quantity must vanish like  $m_\pi^2$ , since for a massless pion, the vacuum is truly degenerate, and it should cost nothing to realign it. The remaining mass dimension is then naturally

made up by the pion decay constant  $f_\pi \sim 93MeV$ , which is the natural mass scale for chiral physics. The point is that this is a rather small number of pions per  $fm^3$ , easily less than one. So how can one hope to see a large number of soft pions coming from anywhere?

I would like to suggest that this is because one is counting the energy density wrong. Consider a string model, in which pions are described as strings with quarks at the end. Then most of the energy density comes from the gluons in the string, with relatively little coming from the ends. Of course, since gluons have no flavor, the chiral dynamics is determined entirely by the quarks at the ends. But with this simple construct, there is no problem, at least naively, with getting enough energy density to make a lot of pions. One just stuffs strings.

Indeed, consider the following quandry. It is known that the order of the phase transition at finite temperature is crucially dependent upon the number of flavors, and so is fixed by the chiral symmetry. On the other hand, all simulations, whether for zero (quenched), or two, or three flavors, all find a large increase in the entropy in a narrow region of temperature. This large increase in entropy simply cannot be described by the effective model appropriate for the chiral phase transition, a linear  $\sigma$  model. The reason is obvious, since the transition in the  $\sigma$  model is only related to a few modes becoming massless, there is no way for a large entropy to emerge. Perhaps this would have a natural description in terms of a chiral string model: the entropy would be that of deconfined strings, but the order is controlled by the chiral properties. Of course this is merely wishful thinking.

Consider then a string model, as discussed by Ferreiro [16], to imagine what a DCC would be like. Before doing so, we need to imagine how to get a lot of little strings out of one big string. In string models, the probability of a string snapping is usually taken to be some constant value along the length of the string. While this is surely fine on average, one can imagine some small fraction of events in which the following happens. Suppose the string starts out as an "accordion", with a wave function with lots of nodes in it. As the accordion stretches, it snaps at the nodes, to produce lots of strings with approximately equal length. How then to get a DCC? Assume that the accordion is surrounded by a "sheath" in which the chiral vacuum is misaligned. Since this is only a sheath around the original string, there is no problem with the energy density. The accordion stretches, but presumably the sheath remains misaligned, to produce a large number of strings aligned in the same chiral direction.

Obviously this picture is little more than just that, a picture. However, it does show that it is at least possible to obtain a DCC in a string picture. Further, the distribution of particles is much different from that expected from other pictures, as the particles of the DCC would be spread out, more or less evenly, along rapidity. (MiniMax assumes that they will be bunched up in rapidity, as a blob of "Baked Alaska" which comes at the detector.) Regardless of the generation of DCC's, such a picture should be able to make predictions about the distribution of particles created in  $pp$  or  $\bar{p}p$  collisions for a large number of particles, and so testable.

In the end, what is most exciting about DCC's is that it is leading us to think about new kinds of physics in new regions of physics. And yet which are experimentally measurable. In physics, what could be sweeter?

## REFERENCES

- [1] I. Zahed, these proceedings.
- [2] K. Haglin, nucl-th/9604036.
- [3] T. Hatsuda, "Light vector mesons at finite density", these proceedings.
- [4] M. Tytgat, "On the physics of a cool pion gas", these proceedings.
- [5] E. V. Shuryak, Phys. Rev. D **42**, 1764 (1990).
- [6] H. A. Weldon, "New mesons in the chirally symmetric plasma", these proceedings.
- [7] Z. Huang and Xin-Nian Wang, "Consequences of partial  $U_A(1)$  restoration", these proceedings.
- [8] K. Rajagopal, these proceedings.
- [9] B. Wyslouch, these proceedings.
- [10] C. C. Taylor, these proceedings.
- [11] W. Busza, these proceedings.
- [12] Y. Asakawa, these proceedings.
- [13] S. Gavin and B. Muller, Phys. Lett. B329, 486 (1994).
- [14] J. Randrup, these proceedings.
- [15] M. A. Lampert, J. F. Dawson, and F. Cooper, Phys. Rev. D54, 2213 (1996).
- [16] E. G. Ferreira, these proceedings.

## List of Participants

Aronson, Samuel H.  
Brookhaven National Laboratory  
Upton, NY 11973  
aronson2@bnl.gov

Asakawa, Masayuki  
Columbia University  
New York, NY 10027  
yuki@nuc-th.phys.nagoya-u.ac.jp

Bak, Per  
Brookhaven National Laboratory  
Upton, NY 11973  
bak@bnlux1.bnl.gov

Baltz, Anthony J.  
Brookhaven National Laboratory  
Upton, NY 11973  
baltz1@bnl.gov

Blum, Thomas C  
Brookhaven National Laboratory  
Upton, NY 11973  
tblum@wind.phy.bnl.gov

Bond, Peter D  
Brookhaven National Laboratory  
Upton, NY 11973-5000  
bond1@bnl.gov

Busza, Wit  
Massachusetts Inst. Tech.  
Cambridge, MA 02139  
busza@mit.edu

Chen, Ziping  
Brookhaven National Laboratory  
Upton, NY 11973  
zchen@bnl.gov

Chiku, Suenori  
University of Tsukuba  
Tsukuba, Ibaraki 305, Japan  
sue@nucl.ph.tsukuba.ac.jp

Christ, Norman H  
Columbia University  
New York, NY 10027  
nhc@phys.columbia.edu

Creutz, Michael  
Brookhaven National Laboratory  
Upton, NY 11973  
creutz@bnl.gov

Dokshitzer, Yuri  
CERN  
Geneva 23, Switzerland  
yuri@surya11.cern.ch

Dover, Carl B  
Brookhaven National Laboratory  
Physics Department  
Upton, NY 11973-5000

Emery, Victor J  
Brookhaven National Laboratory  
Upton, NY 11973  
emery@cmth.phy.bnl.gov

Eskola, Kari J.  
CERN  
Geneva 23, Switzerland  
kjeskola@surya20.cern.ch

Gavin, Sean  
Brookhaven National Laboratory  
Upton, NY 11973  
gavin1@bnl.gov

Gonzalez-Ferreiro, Elena  
U. of Santiago de Compostela  
E-15706, Spain  
elena@gaes.usc.es

Guryn, Wlodek  
Brookhaven National Laboratory  
Upton, NY 11973  
guryn@bnl.gov

Gyulassy, Miklos  
Columbia University  
New York, NY 10027  
gyulassy@nt1.phys.columbia.edu

Hallman, Timothy  
Brookhaven National Laboratory  
Upton, NY 11973  
hallman@bnldag.ags.bnl.gov

Harris, John W  
Yale University  
New Haven, CT  
harris@lbl.gov

Hatsuda, Tetsuo  
University of Tsukuba  
Tsukuba, Ibaraki 305, Japan  
hatsuda@nucl.ph.tsukuba.ac.jp

Hemmick, Thomas  
SUNY at Stony Brook  
Stony Brook, NY 11790  
thomas.hemmik@sunysb.edu

Islam, Muhammad M  
University of Connecticut  
Department of Physics  
Storrs, CT 06269-3046

Jacak, Barbara V.  
Los Alamos National Laboratory  
Los Alamos, NM 87545  
jacak@lanl.gov

Kahana, David  
SUNY @ Stony Brook  
Upton, NY 11973  
dkahana@bnlnth.phy.bnl.gov

Kahana, Sidney H  
Brookhaven National Laboratory  
Upton, NY 11973  
kahana@bnlkah.phy.bnl.gov

Kapusta, Joseph I  
University of Minnesota  
Minneapolis, MN 55455  
kapusta@physics.spa.umn.edu

Karsch, Frithjof  
Universitat Bielefeld  
D-33501 Bielefeld, Germany  
karsch@physik.uni-bielefeld.de

Kinder-Geiger, Klaus  
Brookhaven National Laboratory  
Upton, NY 11973  
klaus@bnlnth.phy.bnl.gov

Kirk, Thomas B  
Brookhaven National Laboratory  
Upton, NY 11973  
tkirk@bnl.gov

Kovar, Dennis  
Department of Energy, ER 23-GTN  
Washington, DC 20545  
dennis.kovar@der.doe.gov

Lee, T.D.  
Columbia University  
Physics Department  
New York, NY 10027

Levin, Eugene M  
LAFEX, CBPF  
Rio de Janeiro, RJ, Brazil  
levin@lafex.cbpf.br

Lin, Ziwei  
Columbia University  
New York, NY 10027  
zlin@nt1.phys.columbia.edu

Lombardo, Maria-Paola  
HLRZ (Julich)/DESY (Hamburg)  
D-52425 Julich, Germany  
lombardo@h1rz31.hlrz.kfa-juelich.de

Ludlam, Thomas W  
Brookhaven National Laboratory  
Upton, NY 11973  
ludlam@bnl.gov

Matsui, Tetsuo  
Kyoto University  
Kyoto 606, Japan  
matsui@yukawa.kyoto-u.ac.jp

Mattiello, Raffaele  
SUNY at Stony Brook  
Stony Brook, NY 11790  
raffaele.mattiello@sunysb.edu

Mawhinney, Robert  
Columbia University  
New York, NY 10027  
rdm@phys.columbia.edu

McGrory, Joseph B  
U.S. Department of Energy  
Germantown, MD 20874-1290  
joe.mcgrory@oer.doe.gov

Millener, D. John  
Brookhaven National Laboratory  
Upton, NY 11973  
millene1@bnl.gov

Mueller, Alfred H.  
Columbia University  
Department of Physics  
New York, NY 10027

Mueller, Berndt  
Duke University  
Durham, NC 27708  
muller@phy.duke.edu

Muronga, Azwinndini  
University of Cape Town  
Cape Town, South Africa  
muronga@physci.uct.ac.za

Nagamiya, Shoji  
Columbia University  
New York, NY 10027  
nag@nevis.columbia.edu

Oda, Minoru  
Inst. for Advanced Studies  
Kyoto 619-02  
Japan

Ohta, Shigemi  
RIKEN  
Saitama 351-01, Japan  
ohta@lattice.riken.go.jp

Ozaki, Satoshi  
Brookhaven National Laboratory  
Upton, NY 11973  
ozaki@bnl.gov

Paige, Frank E  
Brookhaven National Laboratory  
Upton, NY 11973  
paigel@bnl.gov

Pang, Yang  
Columbia University / BNL  
New York, NY 10027  
pang@bnl.gov

Papazoglou, Panajotis  
Goethe Universitaet Frankfurt  
Frankfurt am Main D-60054, Germany  
papazo@th.physik.uni-frankfurt.de

Pisarski, Robert D  
Brookhaven National Laboratory  
Upton, NY 11973  
pisarski1@bnl.gov

Prakash, Madappa  
SUNY at Stony Brook  
Stony Brook, NY 11794  
madappa.prakash@sunysb.edu



Rajagopal, Krishna  
Harvard University  
Cambridge, MA 02138  
rajagopal@huhepl.harvard.edu

Randrup, Jorgen  
Lawrence Berkeley Natl. Lab.  
Berkeley, CA 94720  
randrup@nsdssd.lbl.gov

Rischke, Dirk H  
Columbia University  
New York, NY 10027  
drischke@nt1.phys.columbia.edu

Samios, Nicholas P  
Brookhaven National Laboratory  
Upton, NY 11973  
samios@bnl.gov

Shin, Ghi R  
The Andong National University  
Andong, Kyungpook 760-749, South Korea  
gshin@anu.andong.ac.kr

Shuryak, Edward  
SUNY at Stony Brook  
Stony Brook, NY 11790  
edward.shuryak@sunysb.edu

Sorge, Heinz  
SUNY at Stony Brook  
Stony Brook, NY 11790-3800  
sorge@nuclear.physics.sunysb.edu

Stephanov, Michel  
University of Illinois  
Physics Department  
Urbana-Champaign, IL 68101

Sterman, George  
SUNY at Stony Brook  
Stony Brook, NY 11790  
sterman@insti.physics.sunysb.edu

Stoecker, Horst  
Goethe Universitaet Frankfurt  
Frankfurt am Main, Germany  
stoecker@uni-frankfurt.de

Strikman, Mark  
Pennsylvania State University  
University Park, PA 16802  
strikmman@phys.psu.edu

Tannenbaum, Michael J  
Brookhaven National Laboratory  
Upton, NY 11973  
sabin@bnldag.ags.bnl.gov

Taylor, Cyrus  
Case Western Reserve  
Cleveland, OH 44106  
cctopo.cwru.edu

Trueman, Larry  
Brookhaven National Laboratory  
Upton, NY 11973  
trueman1@bnl.gov

Tytgat, Michel  
Brookhaven National Laboratory  
Upton, NY 11973  
mtytgat@wind.phys.bnl.gov

Ukawa, Akira  
University of Tsukuba  
Kyoto 606, Japan  
matsui@jpnyctp.ukawa.kyoto-u.ac.jp

Vance, Stephen E  
Columbia University  
New York, NY 10027  
svance@nt2.phys.columbia.edu

Videbaek, Flemming  
Brookhaven National Laboratory  
Upton, NY 11973  
videbaek@hi2.hirg.bnl.gov

Vogt, Ramona L  
Lawrence Berkeley Natl. Lab.  
Berkeley, CA 94720  
vogt@nsdssd.lbl.gov

Wyslouch, Boleslaw  
Massachusetts Inst. of Tech.  
Cambridge, MA 02139  
wyslouch@mit.edu

Wang, Xin-nian  
Lawrence Berkeley Natl. Lab.  
Berkeley, CA 94720  
xnwang@lbl.gov

Yazaki, Koichi  
University of Tokyo  
Bunkyo-ku, Tokyo 113, Japan  
tky@vax.phys.u-tokyo.ac.jp

Weldon, Arthur H.  
West Virginia University  
Morgantown, WV 26506  
un021604@wvnmms.wvnet.edu

Zahed, Ismail  
SUNY at Stony Brook  
Stony Brook, NY 11794  
zahed@nuclear.physics.sunysb.edu

Weneser, Joseph  
Brookhaven National Laboratory  
Upton, NY 11973  
weneser@bnlnth.phy.bnl.gov

Zajc, William A  
Columbia University  
Irvington, NY 10533  
zajc@nevis1.columbia.edu

Werner, Klaus  
Universite de Nantes  
44070 Nantes Cedex 03, France  
werner@nanhp3.in2p3.fr

Zhang, Bin  
Columbia University  
New York, NY 10027  
bzhang@nt1.phys.columbia.edu

Wiese, Uwe-Jens RC  
Massachusetts Inst. of Tech.  
Cambridge, MA 02139  
wiese@mitlus.mit.edu